UNIVERSIDAD COMPLUTENSE DE MADRID

FACULTAD DE CIENCIAS QUÍMICAS

Departamento de Química Física I

TESIS DOCTORAL

Simulación del equilibrio de fases del agua: cristales plásticos, constantes dieléctricas y disoluciones

MEMORIA PARA OPTAR AL GRADO DE DOCTOR

PRESENTADA POR

Juan Luis Aragonés Gómez

Director

Carlos Vega de las Heras

Madrid, 2013

“El éxito es aprender a ir de fracaso en fracaso sin desesperarse“

Winston Churchill

En esta memoria se presentan varios estudios de simulación por ordenador sobre las propiedades del agua. En particular, se ha investigado el comportamiento de diferentes fases en condiciones extremas: a 0K, a altas presiones y en presencia de un campo eléctrico. Finalmente, y puesto que se trata de una de las disoluciones más comunes en la tierra, se ha estudiado la solubilidad del cloruro sódico en agua, así como el punto de fusión de varios haluros alcalinos.

Simulación del equilibrio de fases del agua: cristales plásticos, constantes dieléctricas y disoluciones.
Juan Luis Aragonés Gómez

Simulación del equilibrio de fases del agua:

cristales plásticos, constantes dieléctricas y disoluciones.

Juan Luis Aragonés Gómez

Madrid, 2012

Universidad Complutense de Madrid
Facultad de Ciencias Químicas
Dpto. Química-Física I

Simulación del equilibrio de fases del agua: cristales plásticos, constantes dieléctricas y disoluciones.

Memoria para optar al grado de
Doctor en Ciencias Químicas
por

Juan Luis Aragonés Gómez

Director: Prof. Carlos Vega de las Heras

Madrid, 2012

A mi padre.

Muchas son las personas que me ha enseñado,
pero es mi padre quién me ha dado la lección
más importate de todas: No rendirse nunca.

Agradecimientos

Esta página, la más difícil de escribir de toda la tesis, marca el final de un viaje alucinante que empezó cuando cursaba cuarto curso de la licenciatura. Recuerdo que los Miércoles a última hora teníamos clase de Química-Física avanzada, impartida por el profesor Carlos Vega. Una de esas tardes, al finalizar la clase, me acerque a Carlos con una de mis infinitas dudas. Una vez resuelta, surgió otra, y luego otra. Carlos fue resolviendo una duda tras otra y, llevándome a la siguiente. En todos los ejemplos que utilizaba aparecía el agua, unas veces como molécula aislada, otras en “un vaso de agua". En algún momento de la conversación me dijo que fuésemos a su despacho, que me enseñaría una película en la que se podía ver como cristalizaba el agua en contacto con un bloque de hielo. Sin saber muy bien de que iba todo esto, ahogado en curiosidad, le seguí hasta su despacho. Una vez allí, se colocó a los mandos de su ordenador y no paró de hablar sobre el agua y la “sociología de sus moléculas". Lo que más me impresiono, más incluso que todas esas moléculas moviéndose frenéticamente sobre un fondo azul, fue la pasión con la que Carlos hablaba de todo esto. Así fue como Carlos me hizo morder el gusanillo de la ciencia. Hoy, mucho tiempo después de aquel Miércoles, sigo caminado detrás de Carlos exactamente igual que entonces: lleno de curiosidad, hipnotizado por su pasión y divirtiéndome a cada paso. Además de haberme enseñado un oficio, me has enseñado a apasionarme por la ciencia. Por esto, tus consejos, tu apoyo y tu dedicación, muchas gracias. Espero poder corresponderte algún día.

El siguiente en la larga lista de personas que me han ayudado durante estos años es José Luis. Contigo también he disfrutado de la ciencia, e igual que Carlos, me has mostrado tu pasión y dedicación. Nunca podré olvidar todos esos días en los que, a últimisima hora, discutíamos sobre alguna fascinante propiedad del agua frente a la pantalla de tu ordenador, que recordaba insistentemente que era hora de irse a casa. Son momentos como estos los que vienen a mi cabeza cuando todo se vuelve demasiado frustrante. Gracias por enseñarme al jl científico y la excepcional persona que hay detrás. Otra persona fundamental para el desarrollo de esta tesis ha sido Luis. Tanto profesional como personalmente he podido disfrutar de su compañía; brillante científico, mejor persona. Igual que Eva, que me aguanto durante los primeros años de tesis y con la que he compartido despacho, trabajo y grandes momentos. Dejaste un gran vacío y se te ha echado mucho de menos. Agradecer también a mi compañera Maria su apoyo incondicional, siempre dispuesta a echar una mano y mejorar la presentación de todos los trabajos. Todo mi agradecimiento para Carl, sin él los días de trabajo habrían sido mucho más duros. He descubierto un compañero inmejorable, del que he aprendido valiosas lecciones.

Más recientemente se han sumado a la lista de agradecimientos Mac, Eduardo y Chantal. Gracias a Mac, que además de resolver mis dudas sobre Gromacs, me ha hecho pasar buenos ratos y olvidar el trabajo en momentos de desesperación. La llegada de Eduardo y Chantal ha hecho que este último año haya sido muy estimulante, tanto personal como científicamente. He podido conocer a dos personas geniales, con las que he tenido el placer de compartir algo más que trabajo. Agradecer en especial a Chantal toda su dedicación desinteresada. He perdido la cuenta de las cervezas que te debo por todas las veces que me has ayudado y aconsejado, muchas gracias.

Gracias a todos los amigos que me habéis apoyado en los buenos y malos momentos. Especialmente a los que lleváis acompañándome tantos años, ya lo sabéis, soy un incondicional

vuestro! Muchas gracias: Desio, Pol, Vence, Fer, Chencho, Putto, Lex, Txele, Ruben, Ñañe, Chule y muchos más, que espero disculpen el límite de espacio. Gracias a Emilio, todo ha sido mucho más fácil gracias a ti. Gracias por alejarme de la realidad con tu: “Un PES.....?"; el día mejoraba cuando oía esta semi-pregunta. Tu apoyo como amigo empequeñece toda la ayuda que me has prestado con el trabajo, aguantando todas mis charlas y corrigiendo todos mis escritos. Creo que no vale con un muchas gracias, tendré que salvarte la vida en un par de ocasiones para compensar.

Entra aquí una nueva incorporación a mis páginas de agradecimiento. Gracias Lauri, por aguantarme a mi, mis ensayos y mis drafts, pero más importante, por darme ilusión y motivación.

Para finalizar, y por eso más importante, todo mi agradecimiento a mi familia. Cuando pienso en la suerte que tengo de haber caído en esta familia me emociono. Son muchas vuestras virtudes, pero por lo que realmente os quiero es por vuestros “defectos", espero que disculpéis los mios. Que estas lineas sirvan de disculpa/agradecimiento, porque sois vosotros los que más habéis sufrido este doctorado. Perdonar mis ausencias, tanto físicas como mentales. Sois todos geniales. Abuelos, abuelas, tíos, tías, primos, primas....no puedo nombrarlos a todos. Mi agradecimiento a mis primos, Juanan y Alberto, por su apoyo a toda la familia cuando yo no pude estar.

Gracias a mi Madre, que con su ejemplo me ha enseñado a enfrentarme a la vida. Siempre he sabido que eres una madre excepcional, pero cuando he tenido conciencia del mundo y su asqueroso funcionamiento, he comprobado que además eres una persona excepcional, la mejor persona que conozco. Admiro tus ganas y forma de afrontar las adversidades, tu eres la que nos mantiene en perpetuo movimiento. Gracias a mi Padre, al que dedico esta tesis y echo de menos cada día. Todas las mañanas de estos últimos años atendistes mis dudas, divagaciones e ilusiones, siempre me diste tu opinión y consejo, y lo hiciste sin decir una sola palabra, gracias. Él, junto con mi madre, son mis referentes. Sólo aspiro a ser la mitad de bueno que ellos. Gracias también a mis dos hermanos, Nacho y Jesús, porque sin ellos nada sería posible. Sois vosotros en los que me miro y busco consejo.

Resumen

El agua es una sustancia fascinante. En nuestro planeta es una de las moléculas más abundantes, y se presenta en varias de sus formas. La gran mayoría de las propiedades del agua suponen un comportamiento anómalo respecto al comportamiento general de otras sustancias formadas por moléculas de tamaño y características similares. La simulación por ordenador es una herramienta tremendamente útil para comprender el comportamiento macroscópico de las sustancias a partir de parámetros moleculares. En esta tesis se han estudiado algunas de las propiedades del agua mediante simulación. Para ello es necesario definir los parámetros moleculares de la molécula de agua, y existen una gran variedad de modelos de potencial de agua. Cada uno de ellos presenta ventajas e inconvenientes. Siguiendo los pasos de Whalley, propusimos un test para evaluar la calidad de los modelos de agua con unos rápidos y sencillos cálculos, el *test de Whalley*.

El agua en forma líquida interviene en una gran cantidad de procesos biológicos, geológicos y atmosféricos. Lo que la convierte en la *matriz de la vida*. En fase sólida presenta uno de los diagramas de fases más complejos, con al menos 16 estructuras cristalinas diferentes. En esta tesis se aborda el estudio de la región de altas presiones del diagrama de fases del agua. Durante este estudio se encontraron dos fases de cristal plástico a altas presiones, no descritas hasta la fecha. Llevar a cabo medidas experimentales en esta región del diagrama de fases es tremendamente complicado, por lo que existe cierto desacuerdo entre las medidas de distintos grupos. Creemos que estas discrepancias pueden ser debidas a la existencia de una fase de cristal plástico.

También se ha llevado a cabo el estudio de las constantes dieléctricas de los hielos, y sobre el efecto que tiene la aplicación de un campo eléctrico sobre el diagrama de fases del agua. Para ello ha sido necesario incluir movimientos de rotación de anillos para muestrear correctamente el desorden de protón. Gracias a la correción de los resultados de simulación con el momento dipolar efectivo de la molécula de agua, para tener en cuenta la diferencia en la polarización de la molécula en función del entorno químico, se han realizado predicciones cuantitativas del efecto de un campo electrico sobre las transiciones de fase del agua.

Finalmente, y ya que la alta constante dieléctrica del agua la convierte en el disolvente universal, hemos estudiado la solubilidad del NaCl en agua. Los cálculos de solubilidad involucran el cálculo del potencial químico del soluto sólido. De manera que para que un modelo de potencial de NaCl sea capaz de reproducir la solubilidad en agua, debe ser capaz de predecir correctamente las propiedades de la sal pura. Por esta razón, también se han estudiado las propiedades de coexistencia sólido–líquido para varios modelos de potencial de NaCl y otros haluros alcalinos monovalentes.

Palabras Claves: *simulación, agua, hielo, constantes dieléctricas, campos eléctricos y disoluciones.*

Índice general

CAPÍTULO 1

Introducción

"*The full area of ignorance is not mapped.*
We are at present only exploring the fringes."
John D. Bernal

El objetivo principal de esta tesis ha sido avanzar en el conocimiento de las propiedades del agua. Para ello hemos estudiado el equilibrio de fases del agua mediante simulación por ordenador.

Los elementos más abundantes en el universo son hidrógeno, helio, oxígeno y carbono, en ese orden. Y el helio es un elemento inerte, así que desde el punto de vista de la composición química, el agua no es nada especial. Pero siguiendo este mismo argumento, tampoco lo sería la vida basada en el carbono (tal y como la concebimos), el elemento químicamente más versátil y cuarto más abundante. Pero lo cierto es que lo son, tanto la vida como el agua son algo especial. Tendemos a pensar que las cosas son especiales o únicas cuando no comprendemos su funcionamiento o comportamiento. ¿Es el agua una sustancia especial debido a nuestra ignorancia o realmente tiene algo que la hace especial? Aunque en una primera impresión el agua no nos parezca algo muy llamativo; aparece en todos los lugares, en todo momento y en varias formas. Lo cierto es que es la sustancia mas increíble con que nos podemos encontrar. Y por suerte para nosotros, la encontramos en todos lados. Precisamente estos tres factores, su abundancia, recurrencia y nuestra falta de conocimiento, hacen que el agua este rodeada de un aura de misticismo. Transciende de lo químico o lo físico, se ha convertido en un símbolo de vida, pureza, fuerza, adaptación, maternal, desastre natural, etc... Muchas son las investigaciones que se han llevado a cabo sobre como el agua interviene en procesos biológicos: plegamiento y estabilidad de proteínas [1, 2], interacciones enzima-substrato [3], solvatación de iones, ciencia espacial [4] y un largo etcétera. Este papel fundamental en procesos biológicos es lo que nos ha llevado a tener una visión mística de esta molécula. Se la llama molécula de la vida, matriz de la vida [5, 6]... Pero entra en juego en muchos más procesos. El agua hace posible la gran mayoría de procesos de transferencia de energía en nuestro planeta. Controla el tiempo en nuestro esférico hogar, moviliza enormes cantidades de energía gracias a las corrientes oceánicas. De esto he podido ser testigo durante mi estancia en la Universidad de Minnesota, en Minneapolis, donde los tornados originados en el "Tornado Alley´´ (callejón de los tornados) eran semanales. También es el soporte de transferencia de energía en sistema hidrodinámicos, y en química es el disolvente universal. Tiene un papel fundamental en infinidad de procesos geológicos y atmosféricos. A lo largo de este estudio vamos intentar restar algo del simbolismo que rodea al agua de la única forma posible, conociendo como es y como se comporta. En general, la descripción científica de mitos y leyendas es decepcionante, pero como veremos, esto no ocurre con el agua, conocerla es todavía mas fascinante que cualquier mitificación posible.

Los intentos por conocer y entender el agua se remontan a los inicios de la ciencia, cuando el agua todavía era uno de los cuatro elementos –tierra, aire, fuego y agua–. Y han sido muchas las teorías falsadas, en términos del filósofo de la ciencia Karl Popper [7]. Y es que

según él mismo, esta es la única forma objetiva que tiene el conocimiento epistémico de avanzar, esquivando la subjetividad humana. Pero fueron Bernal y Fowler, cuya formación era en sólidos, los que hicieron la primera aproximación a la estructura del agua líquida como la entendemos hoy día, con su magistral trabajo del 1933: *A theory of water and Ionic Solutions, with Particular Reference to Hydrogen and Hydroxyl Ions* [8]. Se apartaron de las ideas de la época para las que el agua estaba formada por varias clases diferentes y distintivas de agua. Adoptaron un modelo *uniformista*, centrándose en la estructura media del agua líquida. Basándose en resultados de difracción de rayos X, y tomando como punto de partida el hielo, mostraron una imagen de la estructura del agua completamente diferente a las propuestas hasta el momento. El hielo I_h está formado por moléculas de agua en una disposición tetraédrica formando enlaces de hidrógeno con sus cuatro moléculas vecinas, lo que genera una estructura muy abierta. Bernal y Fowler propusieron que, de forma análoga al hielo I_h, el agua está formada por una red tetraédrica de moléculas de agua, pero en este caso los tetraedros se van distorsionando al aumentar la temperatura (alejarse del hielo I_h), de manera que la estructura deja de ser tan abierta y la densidad aumenta. Esta distorsión debilita los enlaces de hidrógeno, pero la estructura del agua de Bernal y Fowler no se basaba en la ruptura de los enlaces sino en la distorsión progresiva de los tetraedros al alejarnos del hielo. Sin embargo, el modelo de Bernal y Fowler no es capaz de tener en cuenta todas las medidas experimentales. Esto es debido a que se intenta dar una imagen estática de algo que está en continuo cambio. Si observásemos durante un tiempo, o tuviésemos varias instantáneas, podríamos hacernos una idea de como es el proceso. Esto nos permite hacerlo la simulación por ordenador. La imagen que se obtiene mediante simulación de la estructura del agua líquida es: una red continua, irregular y dinámica de enlaces de hidrógeno, en la cual cada molécula enlaza a otras cuatro mediante enlaces de hidrógeno (raras veces a tres o cinco), pero lo hace formando tetraedros distorsionados. Debido a esto, la red de enlaces de hidrógenos es mas débil e irregular, y las moléculas ocupan parcialmente los huecos que quedaban libres en la estructura del hielo I_h aumentando la densidad. Similar a la estructura de Bernal, pero con la novedad de una red de enlaces de hidrógeno dinámica, en continuo cambio. La idea fundamental, y huella dactilar de la estructura del agua líquida, es que cada molécula de agua forma un tetraedro más o menos distorsionado con las cuatro moléculas vecinas mediante enlaces de hidrógeno, en promedio.

La simulación por ordenador nace en Los Alamos durante el proyecto Manhattam. Pero es después del lanzamiento de la bomba atómica, en 1949, cuando se construye el primer ordenador electrónico digital (MANIAC). De esta manera se abría un amplio abanico de posibilidades de investigación científica hasta ese momento inalcanzables. Metropolis desarrolló, junto a Teller, John von Neumann, Stanislaw Ulam, y Robert Richtmyer, los llamados métodos de Monte Carlo, basados en el muestreo de importancia, y conocidos como algoritmos de Metropolis [9]. A partir de este momento, y a través de los años, la simulación se ha convertido en una herramienta fundamental en el estudio del comportamiento de sistemas moleculares. La simulación permite estudiar propiedades macroscópicas de un sistema a partir de los parámetros moleculares del mismo. En función de estos parámetros se definen las interacciones ente las moléculas del sistema. No es posible conocer de manera exacta el potencial de interacción entre las moléculas, y la única “máquina´´ capaz de resolver de forma exacta todas las interacciones entre las mismas es la naturaleza. Así que, es conveniente saber que se está haciendo y hasta donde se puede llegar con las aproximaciones realizadas antes de sacar conclusiones. Dependiendo de los objetivos del estudio y técnicas disponibles, se utilizarán diferentes aproximaciones, y unos modelos de interacción u otros.

No fue hasta 1969 cuando Barker y Watts llevaron a cabo la primera simulación de agua [10]. Poco después les siguieron Rahman y Stilliger [11]. En un principio, el interés se centró en la búsqueda de un modelo de potencial razonable que permitiese comprender la física del agua líquida. Sin embargo, el estudio de las fases sólidas del agua ha recibido una atención menor. Los primeros en realizar simulaciones de las distintas fases de hielo fueron Morse y Rice [12], que analizaron el comportamiento de varios modelos de agua en la descripción de algunos hielos. El estudio de las transiciones de fase llego un poco más tarde. Primero se estudio el equilibrio líquido–vapor [13–15], y más recientemente se han podido estudiar los equilibrios sólido–líquido y sólido–sólido [16–22]. Desde entonces ha sido mucho el trabajo en esta dirección, y han sido muchos los modelos de potencial propuestos para el agua. Además, el aumento de la capacidad de los ordenadores ha permitido el cálculo de más propiedades, y ésto el desarrollo de nuevos modelos de potencial de agua usando estas propiedades como objetivo.

La gran mayoría de los esfuerzos en simulación de agua han estado orientados al estudio de las fases fluidas. Pero en fase sólida, el agua presenta uno de los diagramas de fases más complejos e interesantes, compuesto por al menos 16 fases sólidas. Desde el trabajo pionero de Tamman [23], quien descubrió los hielos II y III y dió nombre al hielo I, y el colosal trabajo de Bridgman en el 1912 [24], calculando metódicamente las líneas de coexistencia de los hielos I, II, III V y VI, ha sido mucho el trabajo realizado en este área. Hoy en día sigue siendo una parcela activa de investigación. En los últimos años se han seguido encontrando y proponiendo nuevas fases sólidas. El reciente descubrimiento de los hielos XIII y XIV [25], y la predicción de nuevas estructuras cristalinas [26, 27], modifican el “dibujo"del diagrama de fases con relativa frecuencia. Existen dos estrategias en la búsqueda de nuevas fases sólidas. La primera se basa en la búsqueda de fases ordenadas de protón de los hielos desordenados conocidos. Los hielos pueden ser ordenados o desordenados de protón atendiendo a las posibles orientaciones que toma la molécula de agua en la estructura cristalina. En el caso de las fases ordenadas de protón (II, XI, IX, VIII, XIII, XIV) a los átomos de hidrógeno se les puede asignar posiciones cristalográficas, es decir, las moléculas de agua tienen una orientación determinada en estas estructuras. Cada estructura ordenada de protón tiene una estructura cristalina gemela de alta temperatura en que los protones están desordenados (I_h, I_c, III, V, VI, VII, IV y XII). En estas estructuras, todas las orientaciones que pueden tomar las moléculas de agua compatibles con la estructura cristalina son aproximadamente isoenergéticas. La búsqueda de fases ordenadas de protón de las fases desordenadas conocidas ha sido una parcela de investigación muy activa en los últimos años con los descubrimientos de los hielos XIII y XIV (fases ordenadas de los hielos V y XII, respectivamente) [25]. La última fase ordenada que faltaba por emparejar ha sido recientemente sintetizada, el hielo XV [28], fase ordenada del hielo VI. La única fase que queda por emparejar es el hielo II, hielo ordenado de protón para el que no se conoce fase desordenada. La segunda es la búsqueda de nuevas fases sólidas en la región de altas presiones del diagrama de fases. Esta es una rama muy activa. Se han hecho predicciones mediante simulación de la posible existencia de fases de cristal plástico [29, 30], sólidos superiónicos [31] y la simetrización de los protones de la molécula de agua (hielo X) a altas presiones [32]. Sin embargo, la comunidad simuladora de agua no centró su interés en las fases de hielo hasta hace relativamente poco tiempo, pese a los acertados apuntes de Whalley en esta dirección [33]. Whalley ya dejó caer la idea de que el modelado de agua tendría que usar las fases sólidas de agua como examen para evaluar la calidad de los modelos de potencial de agua.

En el 2004, Sanz *et al.* calcularon por primera vez el diagrama de fases del agua me-

diante simulación para los modelos SPC/E y TIP4P [22]. En este trabajo se demostró que el modelo TIP4P, descendiente del modelo de Bernal y Fowler, da una descripción cualitativa del diagrama de fases, y superior a la del modelo SPC/E. Esta fue la primera vez que se usó el diagrama de fases del agua como criterio para evaluar la calidad de un modelo de agua. Gracias a lo que enseñan los hielos sobre la física del agua, y escogiendo como propiedad de ajuste la temperatura del máximo en densidad, huella dactilar del agua líquida, se parametrizó el modelo TIP4P/2005 [34]. En 2009 se llevo a cabo un test de calidad para varios modelos de potencial incluyendo varias propiedades del agua líquidas y de los hielos [35]. El modelo TIP4P/2005 resultó ser el mejor modelo de los sometidos al test. En 2011 este examen se amplió y mejoró [36], constatando la superioridad del modelo TIP4P/2005 en la descripción de las propiedades del agua. En esta última evaluación de los modelos de agua también se acotan los limites de aplicabilidad de un modelo como el TIP4P/2005, rígido y no polarizable, y cuales son las mejoras que se pueden introducir, y a que propiedades afectarán.

En 1984 Whalley estimó las energías de varias fases sólidas de agua (hielos) en el cero de presión y temperatura mediante la extrapolación de las lineas de coexistencia hasta 0 K para varios pares de fases. La idea de Whalley era que estos valores serían útiles para evaluar los potenciales de interacción entre moléculas de agua. La idea de Whalley es brillante, pero la comunidad científica no estaba preparada y su trabajo pasó desapercibido. Pero en el año 2007, aplicamos las ideas de Whalley a varios potenciales sencillos de agua. Comprobamos que con unos sencillos y rápidos cálculos es posible comprobar si un modelo será capaz de reproducir cualitativamente el diagrama de fases del agua [37]. Propusimos que cualquier modelo de agua que pretenda ser un modelo realista de agua, debe ser capaz de pasar el *test de Whalley*. Este test es especialmente adecuado para evaluar la calidad de los cálculos cuánticos que se están llevando a cabo de hielos, tanto *ab initio* como de DFT, donde las simulaciones se llevan a cabo a 0 K. Slater y colaboradores han recogido esta idea y están aplicando el *test de Whalley* a sus cálculos cuánticos de hielos [38–41]. El test de Whalley también se está usando en simulaciones clásicas para evaluar la calidad de los modelos de potencial flexibles [42, 43] y en simulaciones de *path integral* [44–47]. Además de evaluar la calidad de un modelo de potencial, el test de Whalley puede aplicarse como test de consistencia en el cálculo de diagramas de fases. La evaluación de un diagrama de fases implica un gran número de cálculos relacionados, y es relativamente sencillo equivocarse. El test de Whalley puede aplicarse para comprobar la consistencia de los cálculos que se llevan a cabo en la evaluación de un diagrama de fases.

Durante los últimos años, el estudio de la zona de altas presiones del diagrama de fases del agua está siendo una parcela muy activa de investigación, tanto experimental como de simulación. Con el avance de las técnicas de alta presión y el desarrollo de la ingeniería en las medidas de difracción de neutrones a altas presiones, se han llevado a cabo nuevas medidas de la línea de fusión del hielo VII, aunque los resultados de diferentes grupos no siempre concuerdan [48–52]. También ha levantado mucho interés el llamativo hielo X [32, 53]. Asimismo, se está aventurando la posible existencia de un sólido superiónico de tipo-II a presiones superiores a los 45 GPa [31]. En esta tesis se incluyen los estudios llevados a cabo en la región de altas presiones para varios modelos de potencial (Capítulos 7 y 8). En estos trabajos se propone la existencia de dos fases de cristal plástico que han sido halladas para todos los modelos de agua estudiados. Además, se analiza y discute la zona de altas presiones del diagrama de fases, y se ponen en contexto los resultados experimentales disponibles en la bibliografía. Uno de estos trabajos fue elegido como portada en el fascículo de su publicación.

La molécula de agua en materia condensada se polariza de forma significativa. En fase líquida, cada molécula de agua siente un campo eléctrico fluctuante generado por las moléculas vecinas. Esto, supone en principio un incremento del momento dipolar de cada molécula. Sin embargo, el momento dipolar de una única molécula en fase condensada no es una propiedad accesible experimentalmente. Se han realizado cálculos *ab initio* que indican que el momento de la molécula de agua aumenta en fase líquida respecto al que posee la molécula aislada. La determinación del momento dipolar de una molécula de agua en una simulación *ab initio* tampoco es inequívoca. Depende de una elección arbitraria para el reparto de la densidad de carga entre las moléculas del sistema. A pesar de la definición ambigua de los momentos locales en fase condensada, es posible asociar dipolos a las moléculas individuales en términos de la localización de máximos de las funciones de Winner (MLWF) [54].

Parrinello *et al.* [55] calcularon que en el agua líquida las moléculas de agua presentan una distribución de momentos dipolares entre 2 y 4 Debyes, que comparado con el momento dipolar de una molécula aislada (1.85 D), supone un incremento muy significativo. Esto podría explicar el valor "anormalmente´´ alto de la constante dieléctrica del agua, propiedad que le confiere al agua su efectividad disociando especies iónicas. En vista de todo esto, hemos estudiado las propiedades dieléctricas del agua líquida y sus fases sólidas (9 y 10). En el primer trabajo se estudia el desorden de protón en los hielos, y se racionaliza el estudio de las constantes dieléctricas. Se calcularon las constantes dieléctricas del agua líquida y sus fases sólidas para varios modelos de potencial. Ninguno de estos modelos, rígidos y no polarizables, es capaz de reproducir simultáneamente la constante dieléctrica del líquido y del hielo I_h. No obstante, los resultados obtenidos para el modelo TIP4P/2005 revelan una simple explicación para este fracaso. Se debe al hecho de que el momento dipolar de la molécula de agua presenta un momento dipolar entorno a 2.3 D para estos modelos mientras que el valor estimado para la molécula en fase condensada es cercano a 3 D [56, 57]. Mediante el escalado de momento dipolar del modelo comprobamos que los resultados están en buena concordancia con los experimentales para todas las fases condensadas del agua. En el segundo trabajo se estudió cual es el efecto sobre el equilibrio de fases del agua de aplicar un un campo eléctrico. En él se describe la aplicación de avanzadas técnicas de simulación para predecir la influencia de aplicar un campo eléctrico sobre los equilibrios de fase: sólido–sólido, sólido–líquido, y líquido–vapor. Este trabajo amplía el conocimiento sobre las propiedades del agua aportando los primeros datos cuantitativos sobre los cambios inducidos por un campo en el diagrama de fases del agua, y las predicciones sobre la anisotropía de la constante dieléctrica de todas las fases cristalinas relevantes.

Cuando un material dieléctrico se somete a un campo eléctrico éste se polariza en la dirección del campo aplicado. Cuando el sistema es isotrópico, la polarización es paralela al campo eléctrico. En cambio cuando el sistema es anisotrópico la polarización no es igual en todas las direcciones del espacio. El tensor dieléctrico es por tanto una magnitud tensorial. Este es el caso de algunos hielos, donde la estructura cristalina impone ciertas restricciones y direcciones preferentes de polarización. El tensor dieléctrico de estos hielos no ha sido medido todavía. Se han hecho intentos por resolver el tensor dieléctrico del hielo I_h, no obstante sigue habiendo discrepancias sobre si se comporta isotrópicamente o anisotrópicamente [58, 59]. La predicciones hechas en este trabajo pueden ser comprobadas experimentalmente, y esperamos que este trabajo estimule investigación experimental en este campo. Parte de este trabajo fue realizado en la Universidad de Minnesota en colaboración con el Prof. I. Siepmann.

La última parte de la tesis se centra en el estudio de las sales (Capítulo 12) y la mezcla agua/NaCl (Capítulo 11). La importancia biológica del agua está fuera de toda duda, pero lo que encontramos en las células no es agua pura. Muy a menudo encontramos también sales en el medio celular. No existiría la vida tal y como la conocemos si el agua no fuese capaz de ionizar sales. En todos los organismos vivos, desde una bacteria hasta una célula nerviosa, el consumo de energía es activado por bombas de iones. El agua es el único líquido capaz de disociar iones en la extensión necesaria. Hay otros líquidos en los que las sales se disocian, pero la solubilidad es muy baja, y por tanto, no tienen las propiedades que tiene el agua. En este trabajo calculamos la solubilidad del NaCl en agua SPC/E para varios modelos de interacción sal–agua. A pesar de la importancia de las disoluciones de sales en agua, no hay muchos trabajos de simulación sobre esta temática en la literatura. Esto es debido a la complejidad del problema. La solubilidad de una sal es la concentración a la que los potenciales químicos del sólido y del soluto en disolución se igualan a unas condiciones termodinámicas dadas. Por un lado, hay que calcular el potencial químico de la sal sólida, y luego ser capaces de calcular el potencial químico de la sal en disolución. Los primeros trabajos es esta línea fueron los de Lynden-Bell *et al.* [60] y Ferrario *et al.* [61, 62]. En los últimos años, debido al aumento de la capacidad computacional de los ordenadores y la aparición de nuevas técnicas de simulación, está habiendo un repunte en los estudios de solubilidad de sales mediante simulación [63–65]. Los valores calculados por distintos grupos no siempre concuerdan. Así que este es un buen momento para establecer un punto de referencia en el cálculo de solubilidades mediante simulación.

La solubilidad del NaCl en agua requiere el cálculo del potencial químico del NaCl sólido. Por tanto, es interesante comparar cuantitativamente la capacidad de los distintos modelos de potencial de NaCl para reproducir las propiedades del NaCl puro. Por esta razón, también evaluamos las propiedades del equilibrio sólido-líquido de este sistema. En este trabajo calculamos la temperatura de fusión (a presión normal) del cloruro sódico para los modelos de potencial: Tosi–Fumi, Smith–Dang y Joung-Cheatham. Comprobando que el modelo de Tosi–Fumi es el que predice una temperatura de fusión (T_f=1084 K) más próxima al valor experimental (1074 K). Además del NaCl, Tosi–Fumi parametrizaron un gran número de haluros alcalinos monovalentes. Con el objetivo de confirmar si el modelo de Tosi–Fumi predice correctamente la temperatura de fusión de otros haluros alcalinos tipo NaCl, calculamos la temperatura de fusión del resto de haluros alcalinos mediante la técnica de integración Gibbs–Duhem hamiltoniana (sección 5.2.2). Para ello usamos como punto inicial la temperatura de fusión del NaCl. También utilizamos la técnica de coexistencia directa sólido–líquido para calcular las temperaturas de fusión, y así confirmar la validez de los cálculos de energía libre realizados.

Pese a todo el trabajo realizado y todo lo aprendido sobre el agua, los estudios de agua, tanto experimentales como de simulación, están lejos de concluir, y han tenido un repunte en los últimos años. En los últimos años se han estudiado problemas como la existencia de un segundo punto crítico a baja temperatura en el agua [66–73], la nucleación de hielo [74–77], la existencia de varios tipos de fases sólidas amorfas a bajas temperaturas [78–80] y las propiedades del hielo en su superficie [81]. A todo esto ha ayudado el desarrollo de nuevos modelos de potencial que mejoran la descripción física del agua o que hacen computacionalmente accesibles problemas fuera de escala hasta la fecha [82]. Además, existe un esfuerzo cada vez mayor en la racionalización del modelado de agua, como se demuestra en los trabajos [35, 36].

Los modelos de agua utilizados en esta tesis, son modelos rígidos y no polarizables. Aunque en la bibliografía existen otro tipo de aproximaciones a la molécula de agua, nosotros hemos optado por enfocar el estudio del equilibrio de fases del agua usando este tipo de potenciales empíricos. Obviamente el agua no es una molécula rígida con 3 ó 4 cargas puntuales estratégicamente colocadas. La intencionalidad de estos modelos simples es tratar de reproducir la característica más importante en la descripción del agua en sus fases condensadas: el enlace de hidrógeno. Lo que convierte al agua en un líquido tan especial es el enlace de hidrógeno y su motivo tetraédrico, casi inalterable. Sin embargo, la realidad de la molécula de agua es mucho más compleja. Los ángulos y distancias de enlace fluctúan, la nube electrónica se modifica para cada configuración nuclear, al ser tan ligero el átomo de hidrógeno los efectos cuánticos nucleares son significativos, etc... Un tratamiento riguroso de la molécula de agua implicaría resolver la ecuación de Schrodinger para cada configuración y llevar a cabo simulaciones de *path integral* para el movimiento nuclear. Ante la imposibilidad técnica de acometer esta empresa, pues está fuera de escala para el estudio de las propiedades de un sistema en materia condensada hemos optado por parcelar el problema. Como primera aproximación, estudiaremos hasta donde podemos llegar con una descripción clásica, rígida y no polarizable de la molécula de agua. Una vez que hayamos aprendido la física del problema y sepamos que propiedades son reproducibles con esta visión simplista de la molécula de agua, podremos estudiar cuales son los ingredientes necesarios para obtener una descripción más realista. Y así ir completando todas las parcelas hasta obtener una visión completa del problema, y de que es lo físicamente relevante para cada cuestión en particular.

Algunos apuntes sobre el agua y sus fases

Comentaremos brevemente cuales son las características principales de la molécula de agua, la asociación con otras moléculas de agua, y como esto puede explicar sus propiedades “anómalas". Siguiendo el esquema de Bernal, para entender la estructura del agua líquida y sus propiedades, las relacionaremos con las de sus fases sólidas. En primer lugar, consideremos las características principales de una única molécula de agua y las que se derivan del tipo de interacción entre las moléculas:

1. La molécula de agua está compuesta por un átomo de oxígeno y dos átomos de hidrógeno. Como el átomo de hidrógeno es muy ligero, los efectos cuánticos nucleares pueden ser significativos.

2. En promedio, la molécula de agua forma un ángulo H-O-H de 104.5^o, próximo a una ángulo tetraédrico ideal (109.5^o), de manera que es posible la formación de estructuras tetraédricas con estos ángulos.

3. La distribución de carga en la molécula no es perfectamente tetraédrica, es más bien asimétrica. La imagen clásica de los pares de electrones no enlazantes es una sobresimplificación. La carga negativa se debería considerar como una única región difusa próxima al oxígeno, y las cargas positivas sobre los hidrógenos. De manera que la geometría que se deriva de la distribución de cargas es más trigonal que tetraédrica, como ya apuntaba en el 1933 el modelo de Bernal y Fowler.

4. El núcleo repulsivo de la molécula se desvía significativamente de la esfericidad.

5. Dos moléculas de agua forman enlaces de hidrógeno. Esta interacción es más fuerte ($\approx$ 10 k_BT) que las fuerzas atractivas de tipo dispersivo, y es mayor que las fluctuaciones térmicas a temperatura ambiente ($\approx$ 3 k_BT).

6. En fase condensada, cada molécula de agua forma enlaces de hidrógeno con cuatro moléculas vecinas, dos como aceptor y dos como dador. Esta característica conforma el motivo tetraédrico típico de las fases condensadas de agua. La formación de enlaces de hidrógeno 2+2, tiene importantes consecuencias en el comportamiento del agua en materia condensada.

7. La polarización de la molécula de agua inducida por los dipolos de las moléculas vecinas produce un aumento del momento dipolar de la molécula en fases condensadas. El alto valor de la constante dieléctrica del agua líquida y los hielos es consecuencia de este incremento del momento dipolar de la molécula.

Aunque la distribución de cargas en la molécula de agua no es tan tetraédrica como siempre nos han contado, al formar los enlaces de hidrógeno tienden a adoptar esta disposición con dos moléculas formando enlaces de hidrógeno aceptores con la molécula central, y otras dos enlaces dadores (apuntando a las posiciones virtuales de los pares de electrones no enlazantes). Si conectamos todas las moléculas del sistema de manera que cada molécula de agua se encuentre en un entorno tetraédrico formando cuatro enlaces de hidrógeno con las moléculas que la rodean, entonces obtendremos la estructura del hielo I_h (Fig. 1.1). Esta estructura es muy abierta, la red de enlaces de hidrógeno forma hexágonos que dan lugar a canales abiertos a lo largo de la estructura. Esto es consecuencia de las restricciones orientacionales que impone el que cada molécula forme cuatro enlaces de hidrógeno con sus cuatro

moléculas vecinas. Las distancias O-O y los ángulos O-O-O en esta estructura son prácticamente homogéneos en toda la estructura, presentando solamente pequeñas desviaciones entre unos y otros.

Figura 1.1: Estructura cristalina del hielo Ih. El eje cristalográfico c es perpendicular al plano del papel. En esta configuración los protones están desordenados, de manera que los hidrógenos están ocupando una de las seis posibles orientaciones de la molécula de agua compatibles con las reglas de los hielos.

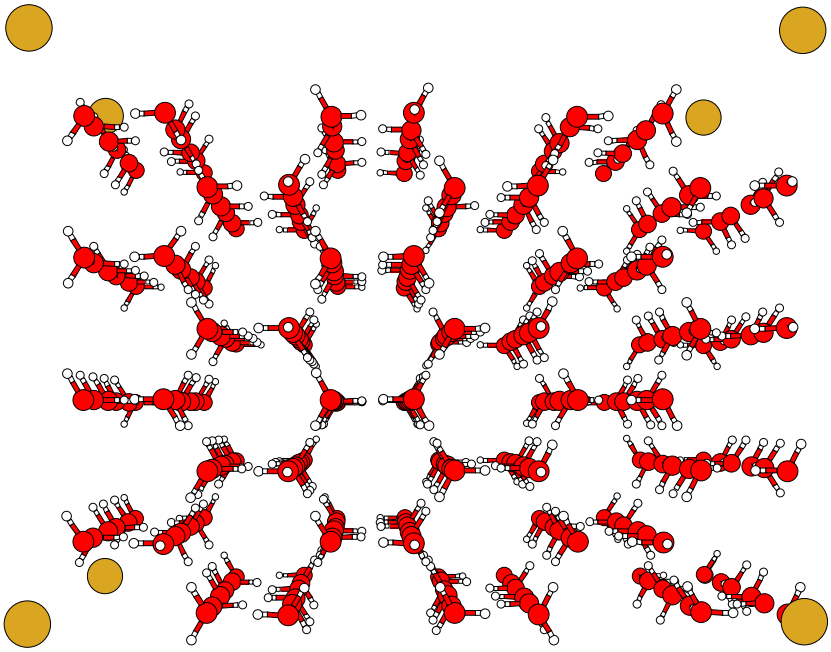

Hay muchas más estructuras cristalinas posibles además del común hielo I_h (Fig. 1.2). Todas las demás estructuras cristalinas son estables a mayores presiones que el hielo I_h, de manera que deben ser más densas, y por tanto menos abiertas. La organización de las moléculas que tiene el hielo ordinario, con cuatro moléculas coordinadas en torno a la central, es común a todas las estructuras sólidas, incluso al agua líquida. Así que la única posibilidad para que las moléculas ocupen un volumen menor es distorsionar la geometría tetraédrica (modificando los ángulos O-O-O). Cuanto más se incrementa la presión, mayor será la distorsión. Pero el límite de distorsión es de 30^o respecto al ángulo tetraédrico ideal, ya que el enlace de hidrógeno es fuertemente direccional. De esta manera es posible construir los hielos II, III, IV y V. Cuando los ángulos y distancias de enlace ya no pueden aumentar más sin romper enlaces de hidrógeno, las moléculas de agua pueden reorganizarse de otra forma a fin de mantener la coordinación de cuatro moléculas y reducir el volumen que ocupan. La coordinación de cuatro moléculas se mantiene y la estructura se acomoda para reducir el volumen mediante la formación de enlaces de hidrógeno que pasen a través de los anillos hexagonales de enlaces de hidrógeno. De esta manera, se pueden relajar los ángulos y distancias de enlace. Mediante este mecanismo de ocupar los huecos vacíos y entrecruzar redes de enlaces de hidrógenos se pueden describir las estructuras de los hielos VI, VII y VIII. En los tres últimos, para los que la región de estabilidad se encuentra a muy altas presiones, la única forma de reducir el volumen es formar dos redes de enlaces de hidrógeno interpenetradas e independientes. Así por ejemplo, el hielo VII esta formado por dos redes de enlaces

de hidrógeno independientes e interpenetradas de hielo I_c (estructura tipo diamante). En este tipo de hielos, cada molécula de agua tiene hasta ocho vecinas pero solo forma enlace de hidrógeno con cuatro.

Figura 1.2: Diagrama de fases del agua. Se representan las estructuras cristalinas de la mayoría de las fases sólidas, estables y metaestables. Nótese que los hielos IV y XII son metaestables en la zona de estabilidad del hielo V. Figura tomada de la Ref. [83].

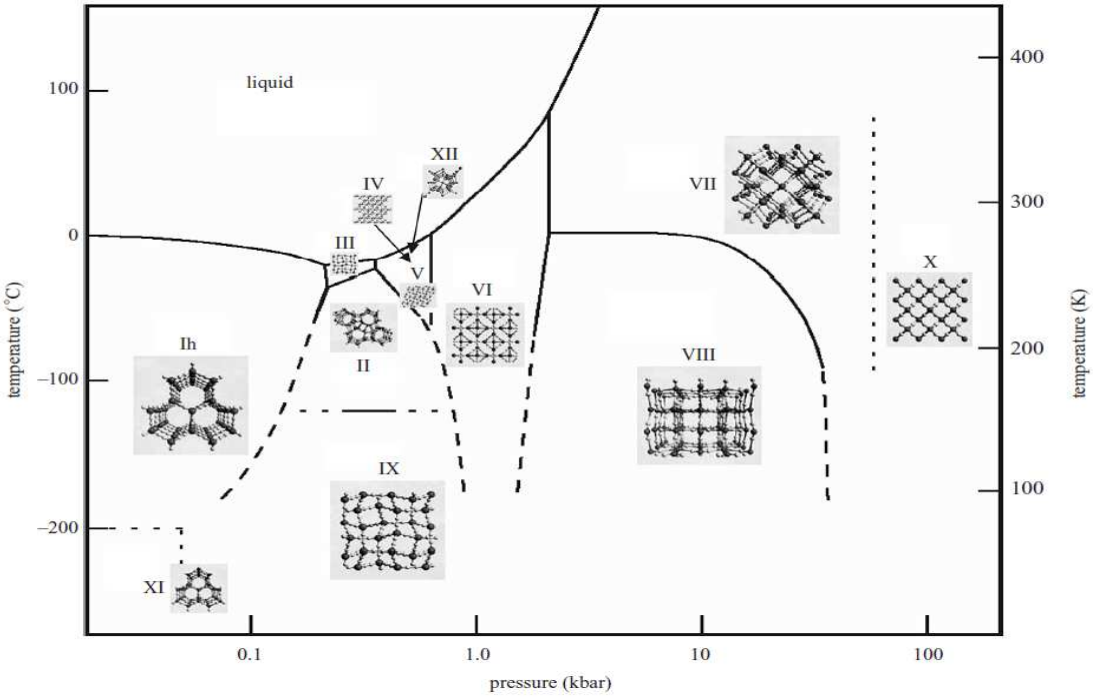

Los hielos se pueden dividir en dos familias. Aquellos en los que los hidrógenos ocupan posiciones cristalográficas definidas, denominados ordenados de protón, y los hielos para los que los hidrógenos no tienen posiciones cristalográficas definidas, desordenados de protón. Todas estas estructuras cristalinas se organizan siguiendo unas pautas generales, que se conocen como las *reglas de Bernal-Fowler* o *reglas de los hielos*:

1. En los hielos, cada átomo de oxígeno está unido a dos átomos de hidrógeno, es decir, las fases sólidas del agua están formadas por moléculas de agua íntegras.

2. En el enlace entre dos oxígenos vecinos debe haber un único átomo de hidrógeno.

3. Como consecuencia del punto anterior, cada molécula de agua está rodeada, en primera esfera de coordinación, por otras cuatro moléculas en una disposición más o menos tetraédrica.

4. Todas las configuraciones de protón que satisfagan las condiciones anteriores son igualmente probables.

Según esto, en los hielos desordenados de protón existirán muchas configuraciones que satisfacen las reglas de los hielos, y todas serán igualmente probables. Esto genera una diferencia de entropía entre las fases ordenadas y desordenadas que se conoce con el nombre de entropía de Pauling. En 1935, Pauling hizo una estimación, mediante argumentos probabilísticos, del número de configuraciones de protón compatibles con las reglas de los hielos [84], y así calculó cual es la entropía debida al desorden de protón: $S = Nk_B ln\left(\frac{3}{2}\right)$.

Ahora que hemos descrito la estructura de las fases sólidas del agua, veamos como es la estructura del agua líquida, y como las “anomalías"del agua se pueden entender a partir de ésta. En el agua líquida, al igual que en las fases sólidas, las moléculas de agua forman enlaces de hidrógeno entre ellas. Como hemos visto es un tipo interacción fuerte, intermedio entre las fuerzas de Van der Waals y el enlace covalente. Esto explica la primera de las “anomalías"del agua, es un líquido a temperatura ambiente, debido a que la interacción entre moléculas de agua es fuerte. El agua líquida es más densa que el hielo I_h. Para la mayoría de la sustancias sucede lo contrario, ya que al disminuir la temperatura y ordenarse las partículas el empaquetamiento que se alcanza es mayor, y la fase sólida es más densa que la líquida. Como ya hemos visto, la estructura del hielo I_h es muy abierta debido a las restricciones orientacionales que impone la coordinación tetraédrica de las moléculas. De manera que para que la estructura del agua líquida sea más densa que la del hielo I_h, los huecos que aparecen en la estructura del hielos I_h (Fig. 1.1) deben ocuparse. Para esto, los tetraedros que forman las moléculas mediante los enlaces de hidrógeno se van distorsionando al aumentar la temperatura, y así fundir el hielo, lo que provoca un aumento de la densidad. Pero también al aumentar la temperatura aumenta el movimiento de las moléculas, con lo que aumentan las distancias entre las mismas, lo que provoca una disminución de la densidad. Así que compiten dos efectos, por una lado la expansividad térmica (normal) y por otro, la distorsión de la red tetraédrica de enlaces de hidrógeno. Esto se traduce en un valor máximo en la densidad a la temperatura de 4^o C, el famoso máximo en densidad del agua (TMD).

Como hemos visto, lo que hace del agua una sustancia tan especial es el enlace de hidrógeno y la organización de las moléculas en disposición tetraédrica mediante enlaces de hidrógeno dador:aceptor (2:2). Además, el hecho que la carga negativa no se encuentre sobre los virtuales pares de electrones no enlazantes, permite que la formación de enlaces de hidrógeno aceptores sea versátil, pudiendo darse estructuras locales trigonales o tetragonales lo que tiene una importancia biológica fundamental en la estabilización de estructuras de macromoléculas. Otra de las características fundamentales del agua, y de enorme relevancia biológica y química, es su alta constante dieléctrica, que permite al agua ionizar sales.

Todas la propiedades anómalas del agua, a nuestros ojos no resultan anómalas. *Water, water everywhere...*(The Rime of the Ancient Mariner), tenemos interiorizado su comportamiento, aparece en todos los lugares de nuestra vida cotidiana. Algunas de sus anomalías las podemos encontrar en otras sustancias, pero lo transcendental es: ¿Podemos encontrar todas esas anomalías juntas en alguna otra sustancia? Eso es lo que hace verdaderamente especial al agua, la acumulación de singularidades. Existen otras sustancias que presentan alguna de las características del agua, pero no hay ninguna que las presente todas [83]. El agua forma una red tetraédrica de enlaces de hidrógeno muy rígida respecto a las fluctuaciones térmicas a temperatura ambiente, por lo que esperaríamos una movilidad molecular mucho menor de la que presenta. Esto es debido a la existencia de defectos en esta coordinación tetraédrica. Esta combinación de rigidez y movilidad molecular es la que hace del agua una sustancia tan importante en procesos biológicos.

Algunos apuntes sobre los hielos.

El diagrama de fases del agua es tremendamente complejo. Exhibe un gran número de fases sólidas, 16, incorporando el recientemente descubierto hielo XV [28]. Presenta varios puntos triples, y un punto crítico, aunque se discute la posible existencia de un segundo punto crítico a bajas temperaturas. En la Figura 1.2 se presenta el diagrama de fases del agua experimental junto con una representación de la estructura cristalina para la mayoría de las fases estables y metaestables. Los hielos estables que se conocen son: I_h, II, III, V, VI, VII, VIII, X y XI. A parte de las fases estables termodinámicamente, también se han caracterizado experimentalmente las siguientes fases metaestables: I_c, IV, IX, XII, XIII, XIV y XV. El hielo X, en el que el agua pierde su identidad como molécula, no puede ser estudiado con modelos rígidos como los utilizados en esta tesis. Los hidrógenos no están enlazados a ningún oxígeno, sino que son compartidos por oxígenos vecinos. Además, sería posible concebir alguna estructura sólida que no se encuentre en la naturaleza, ni como fase estable ni como metaestable, y que, sin embargo, apareciera en el diagrama de fases de estos modelos.

Las estructuras de los hielos son muy diversas. Las hay cúbicas (I_c, VII), romboédricas (II) o tetragonales (III, VI, VII, IX, XI, XII), monoclínicas (V) o hexagonales (I_h). Algunas tienen pocas moléculas por celda unidad –4 el Ih– mientras que otras presentan celdas unidad muy complejas –28 el V–. Hay estructuras poco compactas, como el hielo I_h de densidad $\approx 0.9 g/cm^3$, y otras con empaquetamientos muy eficientes, como el hielo VII de densidad $\approx 1.6 g/cm^3$. Sin embargo, hay una serie de características comunes a todos los hielos:

- Las posiciones de los oxígenos forman una red ordenada en todos ellos. Sin embargo, los hidrógenos no cumplen la misma premisa. Algunos hielos presentan posiciones cristalográficas definidas para los átomos de hidrógeno (hielos ordenados de protón), en cambio en otros la orientación de las moléculas de agua no sigue un patrón ordenado a lo largo de la red cristalina (desordenados de protón).

- Cada oxígeno está rodeado, en primera esfera de coordinación, por otros cuatro oxígenos que forman un tetraedro más o menos distorsionado según la estructura.

- Los hielos están formados por moléculas de agua. Entre cada dos oxígenos vecinos hay siempre situado un hidrógeno. Este hidrógeno está enlazado covalentemente al oxígeno con el que forma la molécula de agua y establece un enlace de hidrógeno con el otro oxígeno. Este último apartado resume las reglas del hielo que establecieron Bernal y Fowler en 1933 [8]. De esta manera, y teniendo en cuenta la coordinación tetraédrica de los oxígenos, un oxígeno se rodea por cuatro hidrógenos; dos de ellos unidos por enlace covalente y los otros dos unidos por enlace de hidrógeno.

Obedeciendo las reglas de los hielos de Bernal y Fowler se pueden construir, en una red de N oxígenos, $\approx \left(\frac{3}{2}\right)^N$ estructuras distintas con las orientaciones de las moléculas de agua desordenadas. Este número fue deducido por Pauling dos años más tarde de que Bernal y Fowler publicaran las reglas del hielo [85]. Así se origina una entropía de degeneración $S = Nk_B \ln(3/2)$ que supone una estabilización extra para aquellos hielos en los que los átomos de hidrógeno están desordenados. Los hielos pueden ser clasificados en tres familias atendiendo a las posiciones de los átomos de hidrógeno en la estructura cristalina:

- **Hielos ordenados de protón.** En este tipo de hielos los átomos de hidrógeno tienen posiciones cristalográficas definidas, o lo que es lo mismo, en la celdilla unidad cada molécula de agua tiene una orientación determinada. En este tipo de estructuras no existe la contribución de Pauling a la entropía, puesto que no hay configuraciones degeneradas.

- **Hielos desordenados de protón.** En este tipo de hielos los átomos de hidrógeno están distribuidos de forma aleatoria siguiendo las reglas de Bernal y Fowler. Para obtener configuraciones de desorden de protón compatibles con las reglas de Bernal y Fowler hemos usado el algoritmo de Buch *et al.* [86]. Es un algoritmo de tipo topológico, en el que no se introduce ningún sesgo termodinámico. Entre cada dos oxígenos vecinos hay dos posibles posiciones en las que un hidrógeno puede situarse. Una de ellas covalentemente enlazado a un oxígeno y formando un enlace de hidrógeno con el otro, y la otra, al revés. En el algoritmo de Buch y colaboradores, inicialmente se coloca al azar, entre cada dos oxígenos vecinos, un hidrógeno en una de las dos posiciones. Así tendremos una estructura que inicialmente no está formada por moléculas de agua. Algunos oxígenos se habrán quedado con más de dos hidrógenos y otros con menos en este proceso de asignación de hidrógenos al azar. Ahora empezamos haciendo movimientos de salto de hidrógenos escogidos al azar de una posición a la otra. El movimiento será aceptado si acarrea un decrecimiento de la diferencia del número de hidrógenos covalentemente enlazados a los oxígenos involucrados, y rechazado en caso contrario. Si la diferencia queda igual, el movimiento es aceptado con una probabilidad del 50 por ciento. La aplicación del algoritmo conduce a una red que tiene un hidrógeno entre cada dos oxígenos vecinos y que está formada por moléculas de agua, es decir, en un hielo. Sin embargo, hay que comprobar que la estructura formada presenta, como sucede con el hielo en la naturaleza, momento dipolar total cero. Si es así, tenemos una configuración inicial válida, si no es así, hay que volver a comenzar con el algoritmo de Buch desde el principio hasta dar con otra estructura candidata. Todas las configuraciones desordenadas de protón tienen energías muy similares. Propiedades que no varíen mucho de unas configuraciones a otras (i.e. funciones de distribución radial, energía, etc...) se pueden evaluar a partir de una única configuración. Sin embargo, para propiedades que varíen notablemente de unas a otras, como la polarización, es necesario tener en cuenta varias configuraciones para calcular estas propiedades promedio.

- **Hielos parcialmente desordenados.** Los hielos III y V presentan desorden parcial de protón [87]. En los hielos desordenados de protón las dos posibles posiciones que puede adquirir un hidrógeno entre dos oxígenos vecinos tienen índices de ocupación del 50 por ciento. Esto no es así en estos dos hielos, en los que las dos posibles posiciones del hidrógeno no son cristalográficamente equivalentes, y hay que modificar ligeramente el algoritmo de generación de la configuración inicial para respetar los índices de ocupación experimentales. Primeramente, la distribución inicial de los hidrógenos no es al azar entre cada par de posiciones adyacentes, sino que se colocan en una o en otra con probabilidades iguales a los índices de ocupación. El criterio de aceptación de un movimiento de salto de un hidrógeno a su posición adyacente se establece en dos etapas [88]: En la primera se decide si se hace un movimiento o no, y en la segunda si se acepta o no éste movimiento. Definimos la diferencia ocupacional, Δs, como la diferencia entre los índices de ocupación de una posición de hidrógeno y su adyacente. En la etapa 1 se decide hacer un movimiento con probabilidad:

$$min\left[1, \exp[-w(\Delta s_{exp} - \Delta s_{act})]\right] \tag{1.1}$$

siendo Δs_{exp} la diferencia ocupacional experimental y Δs_{act} la que hay en la estructura que estamos generando. w es un parámetro que determina la anchura de la distribución de índices de ocupación y que se comprobó que con un valor entre 0.5 y 1 producía configuraciones con índices de ocupación razonablemente similares a los prescritos. Una vez que se decide hacer un movimiento, este se acepta o se rechaza de acuerdo al criterio de la diferencia entre los hidrógenos covalentemente enlazados a cada oxígeno (etapa 2), como en el algoritmo original de Buch y colaboradores. Como en el caso de los hielos totalmente desordenados, una vez que se genera una estructura que cumple las reglas del hielo, hay que comprobar que su momento dipolar total sea cero antes de considerarla como válida.

El hielo I_h, que es el hielo estable a presión atmosférica y por debajo de cero grados centígrados, pertenece al sistema cristalino hexagonal con 4 átomos por celdilla unidad. Tiene desorden total de los hidrógenos y pertenece al grupo espacial $P6_3/mmc$. Destacan los canales hexagonales que presenta la estructura (Fig. 1.3). Es una red muy poco empaquetada, con muchas oquedades. De hecho, su densidad es menor de la del líquido con el que coexiste. Esto no sucede así con los hielos estables a más altas presiones, que son más densos que el líquido con el que están en equilibrio. Debido a la menor densidad del hielo I_h respecto a la fase líquida, la pendiente de la línea de coexistencia líquido–I_h es negativa. Mientras que para el resto de las fases sólidas que coexisten con el líquido, todas de mayor densidad éste, la pendiente de la linea de coexistencia líquido–sólido es positiva.

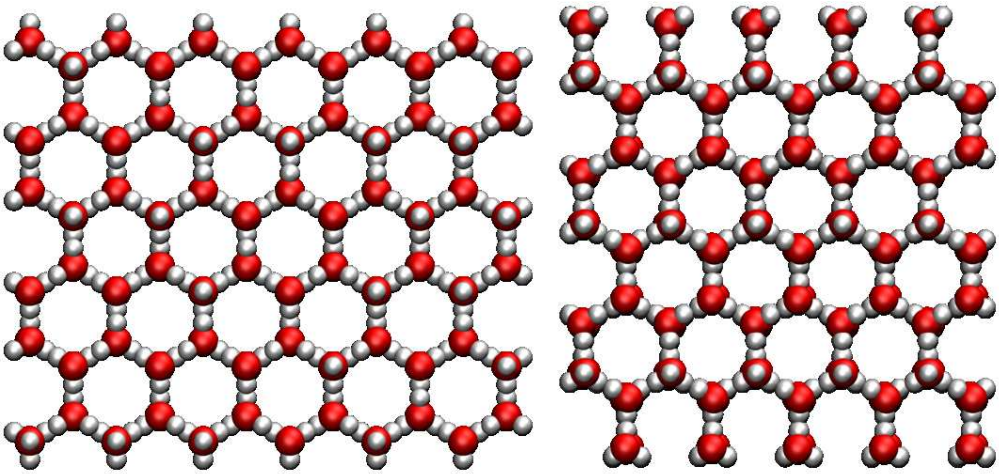

Figura 1.3: Izquierda: estructura cristalina del hielo I_h vista desde el plano basal. Derecha: estructura del hielo XI, fase ordenada de protón del hielo I_h. Las bolas rojas representan los átomos de oxígeno y las blancas los átomos de hidrógeno. Se puede apreciar como en el hielo I_h los hidrógenos presentan un patrón desordenado, mientras que en el hielo XI no. Tomadas de la Ref. [89].

El hielo I_c, es una variante metaestable del I_h. Tiene una densidad prácticamente idéntica al I_h. Las posiciones de los oxígenos forman una estructura cúbica tipo diamante, y las

posiciones de los protones están desordenadas (Fig. 1.4). Al igual que en el hielo I_h, cada oxígeno se coordina con otros cuatro formando tetraedros perfectos. Pertenece al grupo espacial $Fd3m$.

El hielo II puede obtenerse a partir del hielo hexagonal a 198 K y 300 MPa o por expansión de hielo V a 238 K, pero no es fácil obtenerlo por enfriamiento de hielo III. La celdilla unidad es de simetría romboédrica ó trigonal (Grupo espacial R(-3), $C222_1$; Clase de Laue mmm). En el hielo II, a diferencia de los hielos I_h y I_c, los protones están ordenados. Algunos de los enlaces de hidrógeno están torsionados y, por lo tanto, son más débiles que los enlaces de hidrógeno en el hielo hexagonal. La celda unidad está formada por 12 moléculas de H_2O y los parámetros de celda son: a=7.78 y α=113.1^o [90]. La celda unidad consiste en un hexámero en forma de silla unido mediante un enlace de hidrógeno a otro hexámero en casi plano (Fig. 1.4). Nosotros hemos utilizado una superceldilla hexagonal que contiene 36 para generar la estructura. Una celdilla unidad hexagonal puede ser descrita por tres celdas romboédricas. De manera que podemos construir una supercelda hexagonal para el hielo II. A partir de la supercelda hexagonal, y por analogía con la estructura del hielo I_h, para la que es conocida una configuración ortorrómbica, es posible obtener una supercelda ortorrómbica para el hielo II. La ventaja de contar con una configuración de hielo II de simetría ortorrómbica es evitar la aparición de problemas asociados a los cambios de volumen que se llevan a cabo en la simulación, ya que de ésta manera los ángulos de la caja de simulación son ángulos rectos. La configuración hexagonal de hielo II es sencilla de conseguir a partir de los datos cristalográficos. Cada celda hexagonal contiene 36 moléculas de agua (3 celdas unidad romboédricas). La celda unidad ortorrómbica estará formada por 2 celdas hexagonales y, por tanto, contendrá 72 moléculas de H_2O.

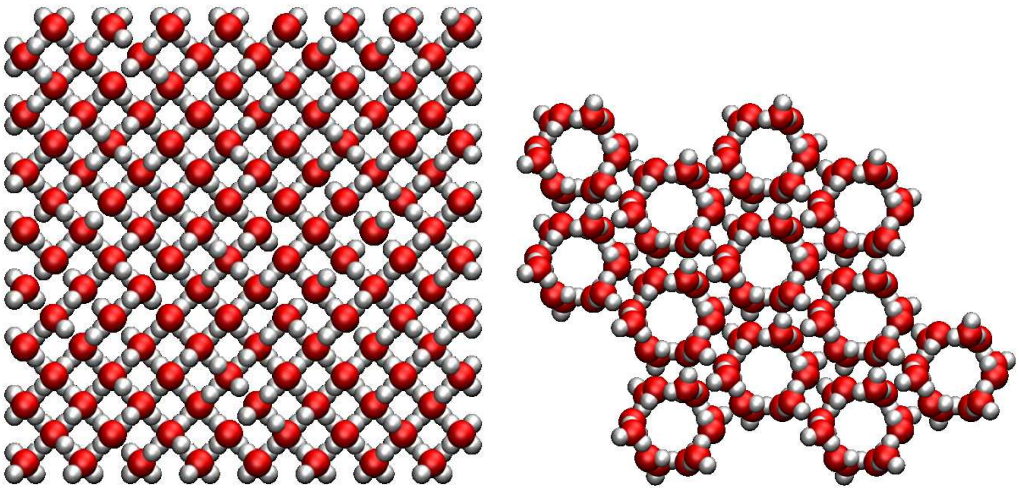

Figura 1.4: Izquierda: estructura cristalina del hielo I_c, fase cúbica desordenada de protón y metaestable respecto al hielo I_h. Derecha: estructura del hielo II, fase ordenada de protón. Se pueden apreciar canales hexagonales similares a los de la estructura del hielo I_h. Las bolas rojas representan los átomos de oxígeno y las blancas los átomos de hidrógeno. Tomadas de la Ref. [89].

El hielo III se forma por calentamiento del hielo II. El desorden de las posiciones de los protones es parcial y variable con la temperatura. Es la fase con el dominio de estabilidad

más pequeño en el plano $p - T$, y separa el líquido del hielo II en un margen de unos 10 grados. Tiene una celdilla tetragonal de 4 moléculas y pertenece al grupo $P4_12_12$ (Fig. 1.5). Puesto que ocupa una posición central en el diagrama de fases del agua coexiste con un gran número de fases, y presenta varios puntos triples. La fase hermana ordenada de protón del hielo III, es el hielo IX (Fig. 1.5).

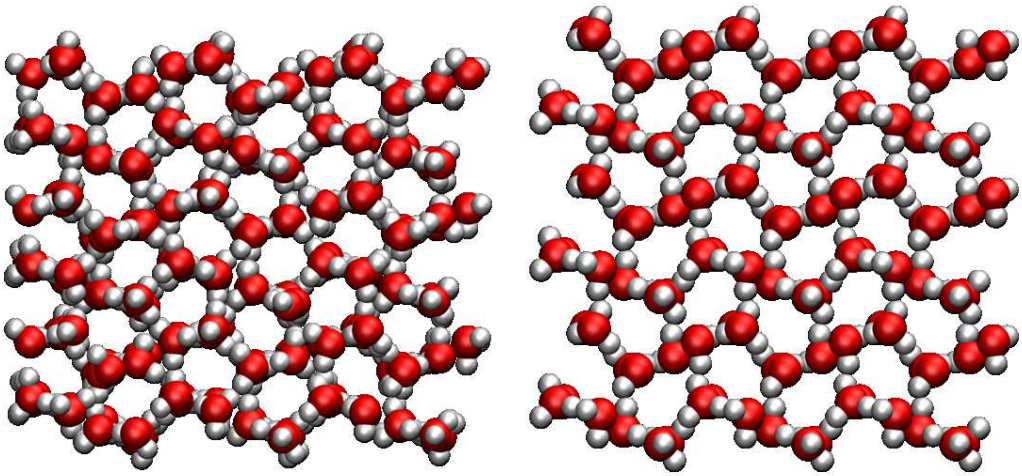

Figura 1.5: Izquierda: estructura cristalina del hielo III, de simetría tetragonal y protones parcialmente desordenados. Derecha: estructura del hielo IX, fase ordenada de protón del hielo III. Las bolas rojas representan los átomos de oxígeno y las blancas los átomos de hidrógeno. Tomadas de la Ref. [89].

El hielo IV es metaestable y se forma, con determinados agentes de nucleación, subenfriando el agua líquida a la zona de estabilidad de los hielos III, V o VI. La orientación de las moléculas está desordenada, tiene una celdilla unidad romboédrica con 4 moléculas y pertenece al grupo espacial $R3c$ (Fig. 1.6). Las primeras evidencias de su existencia fueron encontradas por Bridgman en 1912, pero no fue aislado hasta 1935.

El hielo V es la estructura más complicada de los hielos, tiene una celda unidad monoclínica de 28 moléculas (Fig. 1.8). Es uno de los dos hielos, junto con el III, cuyo desorden en las posiciones de los hidrógenos se ha constatado que es parcial. Pertenece al sistema cristalino $A2/a$. En su estructura contiene anillos formados por 4, 5, 6 y 8 moléculas de agua.

El hielo VI ocupa una extensa región en el diagrama de fases. Tiene una celda tetragonal con 4 moléculas. Como la mayoría de los hielos, tiene los hidrógenos desordenados, pero presenta la característica peculiar de formar dos subredes interpenetradas, pero no interconectadas, de enlaces de hidrógeno. Esto quiere decir que siguiendo el camino que marcan los enlaces de hidrógeno, podemos ir de un oxígeno hasta otro cualquiera de una misma subred, pero no a otro oxígeno de la otra subred, porque no hay enlaces de hidrógenos entre oxígenos de distintas subredes. Pertenece al sistema cristalino $P4_2/nmc$.

El VII es el hielo que convive con el agua a más altas presiones. Está formado por 2 subredes interpenetradas de hielo I_c, originándose un empaquetamiento de los oxígenos cubico centrado en el cuerpo. Por ello su densidad es aproximadamente el doble que la del hielo I_c o

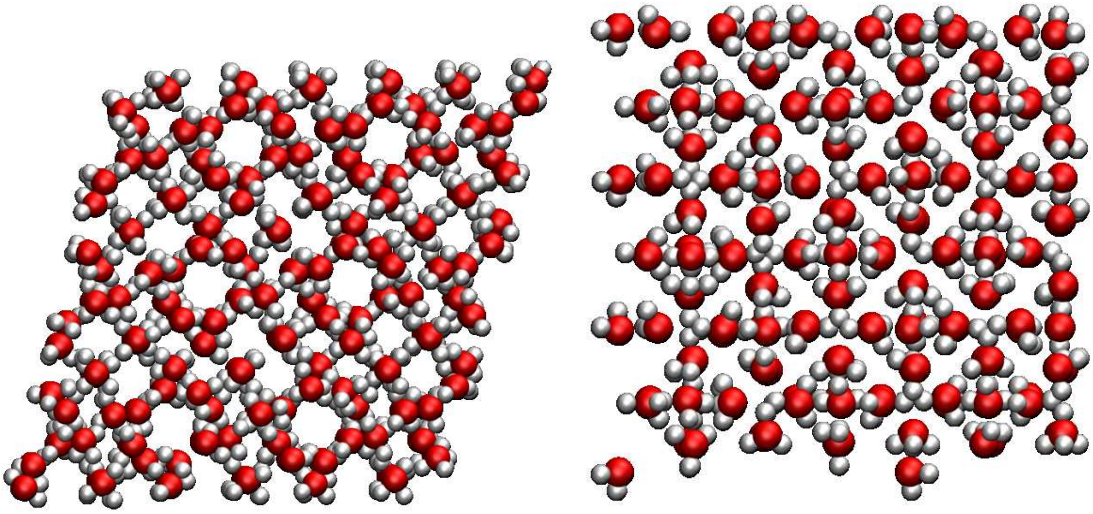

Figura 1.6: Izquierda: estructura cristalina del hielo IV, de simetría romboédrica. Derecha: estructura del hielo VI, formada por dos redes de enlaces de hidrógeno interpenetradas pero no conectadas. Ambas estructuras son desordenadas de protón. Las bolas rojas representan los átomos de oxígeno y las blancas los átomos de hidrógeno. Tomadas de la Ref. [89].

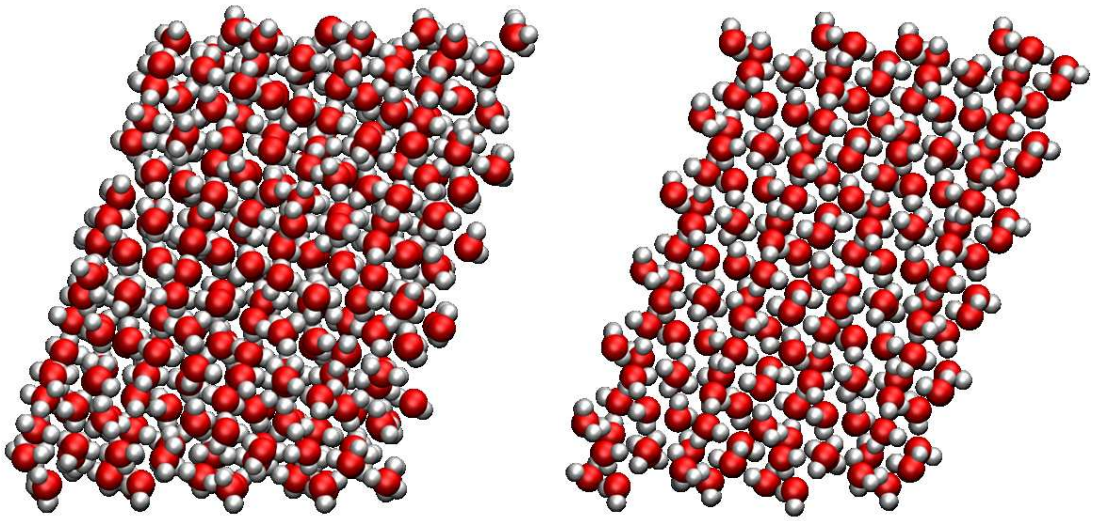

Figura 1.7: Izquierda: estructura cristalina del hielo V, fase parcialmente desordenada de protón. Derecha: estructura del hielo XIII, fase ordenada de protón del hielo V. En ambos casos la simetría del cristal es monoclínica. Las bolas rojas representan los átomos de oxígeno y las blancas los átomos de hidrógeno. Tomadas de la Ref. [89].

el hielo I_h. Al igual que sucedía en el hielo VI las subredes no están interconectadas mediante ningún enlace de hidrógeno. Cada oxígeno tiene otros 8 en primera esfera de coordinación a igual distancia. Cuatro de ellos pertenecen a la misma subred que el átomo central. Dicho átomo forma dos enlaces de hidrógeno como donor con dos de los oxígenos de su misma subred y otros dos como aceptor con los dos oxígenos restantes. La celdilla unidad de la red de oxígenos tiene 2 moléculas. El grupo espacial es $Pn3m$.

El hielo VIII es el resultado del ordenamiento de los hidrógenos en el hielo VII al bajar

la temperatura, junto con una pequeña reestructuración en el empaquetamiento de los oxígenos. En la figura de la configuración inicial generada se puede ver con claridad cómo los hidrógenos siguen un patrón ordenado a lo largo de estructura. El hielo VIII es tetragonal, con 8 moléculas por celda unidad y pertenece al grupo espacial $I4_1amd$.

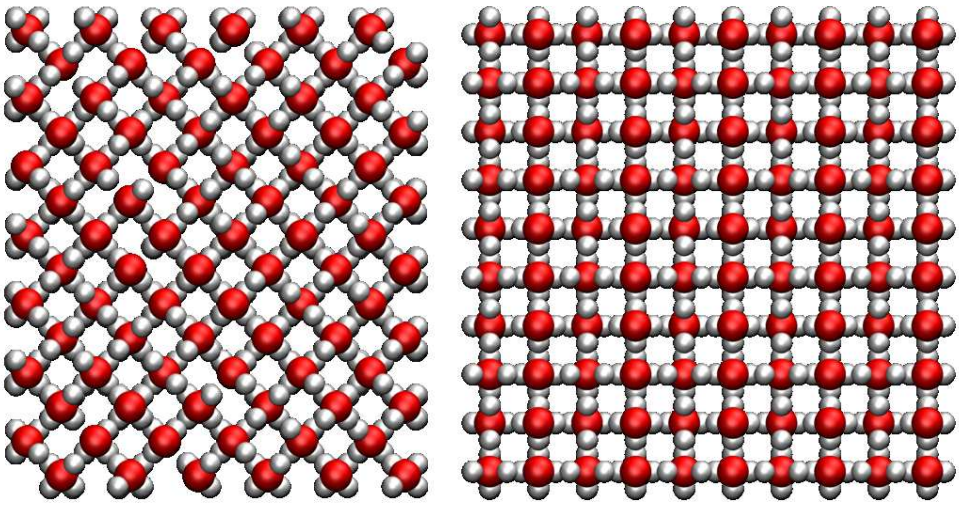

Figura 1.8: Izquierda: estructura cristalina del hielo VII, de simetría cúbica está formado por dos redes de enlaces de hidrógeno tipo hielo I_c interpenetradas pero no interconectadas. Los átomos de hidrógeno, al igual que en el hielo I_c, están desordenados. Derecha: estructura del hielo VIII, fase ordenada de protón del hielo VII. En este caso, la idea de redes interpenetradas no tiene sentido puesto que los protones se han ordenado. Las bolas rojas representan los átomos de oxígeno y las blancas los átomos de hidrógeno. Tomadas de la Ref. [89].

De la misma manera que el hielo VII da origen al VIII cuando se baja la temperatura, el III da lugar al IX por ordenamiento de las orientaciones de las moléculas de agua en la estructura (Fig. 1.5). Como el hielo III, es tetragonal, pero debido al orden de los hidrógenos tiene 8 y no 4 moléculas por celdilla unidad. Pertenece al grupo de simetría $P4_12_12_1$.

Al bajar la temperatura el hielo I_h se ordena y da lugar al XI. Es una fase ferroeléctrica, aunque nosotros hemos utilizado en las simulaciones la variante antiferroeléctrica propuesta por Morokuma *et al.* [91].

El hielo XII, recientemente descubierto [92], es una fase metaestable que aparece en esa conflictiva región central del diagrama de fases donde también están el III, IV, V y IX. Tiene los hidrógenos totalmente desordenados y una deformación bastante grande de los tetraedros de coordinación de los oxígenos. Su celda unidad es tetragonal con 12 moléculas de agua y pertenece al grupo espacial $I42d$.

Los hielos XIII, XIV y XV, también recientemente descubiertos [25, 28], son las fases ordenadas de protón de los hielos V, XII y VI, respectivamente.

Parte I

TEORÍA Y SIMULACIÓN

CAPÍTULO 2

Termodinámica estadística

"*Antes de asombrarte por hechos insólitos,*
preguntale a la estadística qué tienen realmente de insólitos."

La mecánica estadística es la rama de la Física que estudia sistemas macroscópicos desde un punto de vista microscópico. El objetivo es entender y hacer predicciones sobre fenómenos macroscópicos a partir de las propiedades de las moléculas que forman el sistema. Sirve de nexo entre las descripciones termodinámica y mecánica de un sistema. Se explican las propiedades termodinámicas de un sistema a partir de propiedades moleculares del sistema (geometría molecular, interacciones intermoleculares ...). El punto de partida lo constituyen propiedades moleculares descritas por la mecánica clásica o cuántica, que definen el estado del sistema (microestados), y nos permiten asociarlos a un estado termodinámico (macroestados). Los macroestados quedan completamente definidos por unas pocas variables macroscópicas, tales como el número de partículas, el volumen del sistema, la temperatura, presión, energía, etc ... Para definir el estado microscópico del sistema necesitamos conocer las posiciones y velocidades de todas las partículas del sistema en un instante de tiempo, si usamos una descripción clásica del sistema. O bien la función de onda del sistema, si se estudia bajo una descripción cuántica. En cualquiera de los dos casos, el Hamiltoniano del sistema depende del número de partículas y el volumen del sistema. Por tanto, el número de microestados es función de estas dos variables, pero no de la temperatura. No obstante, la energía del sistema sí que dependerá de la temperatura a la que se encuentre. Según esto, existen muchos microestados compatibles con un único macroestado. Así pues, las propiedades macroscópicas del sistema serán un promedio de las mismas en los microestados compatibles.

Para hacernos una idea del número de microestados de un sistema simple, consideremos el problema de la partícula en una caja. Según la mecánica cuántica, para este sistema existe una función de onda (ψ) tal que $\psi * \psi$ es la probabilidad de encontrar una partícula en x,y,z. También sabemos que:

$$\widehat{H}\psi = E\psi \tag{2.1}$$

siendo $\widehat{H} = -\frac{\hbar^2}{2m}\left(\frac{\partial}{\partial^2 x^2} + \frac{\partial}{\partial^2 y^2} + \frac{\partial}{\partial^2 z^2}\right) + \widehat{V}(x,y,z)$. Ésta es una función de valores propios. De manera que hay un número infinito de soluciones, descritas por tres números cuánticos: n_x, n_y, n_z. Así, para una partícula en una caja cúbica, los niveles de energía son:

$$E_{n_x,n_y,n_z} = \frac{h^2}{8mL^2}(n_x^2 + n_y^2 + n_z^2) \tag{2.2}$$

La degeneración (microestados de misma energía) viene dada por el número de formas que el entero $M = \frac{8mL^2}{h^2}E_{n_x,n_y,n_z}$ se puede escribir como la suma de los cuadrados de tres números enteros. Esta ecuación corresponde a una esfera de radio $R = (\frac{8mL^2}{h^2}E_{n_x,n_y,n_z})^{(1/2)}$. De manera que el número de estados será proporcional al volumen de la esfera:

$$\Phi(E) = \frac{1}{8}(\frac{4\pi}{3}R^3) = \frac{\pi}{6}(\frac{8mL^2E}{h^2})^{(3/2)} \tag{2.3}$$

entonces, el número de estados entre $E + \Delta E$ será:

$$\Phi(E + \Delta E) - \Phi(E) = \frac{\pi}{4}(\frac{8mL^2}{\hbar^2})^{(3/2)}E^{1/2}\Delta E \tag{2.4}$$

Para el simple caso de la partícula en una caja, esta degeneración es del orden de 10^{28}. ($E = 3k_BT/2$, $T = 300\ K$, $m = 10^{-22}\ g$, $L = 10\ cm$ y $\Delta E = 0.01E$). Así que para un sistema de N partículas, el número de microestados es enorme.

En la práctica, la termodinámica muestra que es suficiente conocer unas pocas variables macroscópicas del sistema para determinar sus propiedades y comportamiento (basta con 3 en un sistema de un solo componente y una única fase). Un sistema en equilibrio tiene unas propiedades macroscópicas características bien definidas. Microscópicamente, el sistema tiene multitud de microestados compatibles con las mismas condiciones macroscópicas. En el equilibrio, un sistema irá visitando todos los posibles microestados compatibles con el estado macroscópico (N y V dan los niveles de energía E_i). Si medimos una propiedad X del sistema a lo largo del tiempo, podemos calcular el valor promedio de dicha propiedad ($< X >= \frac{1}{t}\int_0^t X(t)\delta t = \bar{X}$). Si podemos contabilizar el número de veces (n_i) que se visita cada microestado (x_i), entonces podremos asociarle una probabilidad a x_i ($p_i = n_i/n$). En consecuencia, podemos escribir el promedio de la propiedad X como:

$$< X >= \sum p_iX_i = \int_{-\infty}^{\infty} g(X)XdX \tag{2.5}$$

con $p_i = g(X_i)dX$. Para calcular el promedio de la propiedad X solo tendríamos que contar el número de veces que toma el valor X_i a lo largo del tiempo. Como las propiedades promedio del sistema quedan fijas al elegir las variables macroscópicas del sistema, se podría tomar un número infinito de sistemas compatibles con esas variables macroscópicas y medir la propiedad X para cada una de esas configuraciones. Al conjunto virtual de microestados compatibles con un mismo estado termodinámico, lo llamamos colectivo. En función de las variables termodinámicas de control (constantes en el sistema) que escojamos para caracterizarlo, los posibles colectivos serán:

- Colectivo microcanónico: N, V, E como variables termodinámicas de control.
- Colectivo canónico: N, V, T como variables termodinámicas de control.
- Colectivo isotermo-isobárico: N, p, T como variables termodinámicas de control.

donde N es el número de moléculas, V el volumen, T la temperatura y p la presión a las que se encuentra el sistema.

A cada posible combinación de números cuánticos le corresponde un microestado. Todos los estados de igual energía son igualmente probables (*principio de igualdad de probabilidades a priori*). Así que, si $\Omega(N, V, E)$ es el número total de microestados (degeneración del sistema), la probabilidad de cada uno de los microestados será:

$$p_i = \frac{1}{\Omega(N, V, E)} \tag{2.6}$$

La función de partición indica el número promedio de estados que son accesibles térmicamente a una partícula a la temperatura del sistema. Consiste en la relación de como las partículas podrían distribuirse en los diferentes estados de la energía. En este caso, $\Omega(N, V, E)$

es la función de partición microcanónica. La condición de equilibrio termodinámico establece que la entropía deber ser máxima (*segundo principio de la termodinámica*), y como el estado de equilibrio corresponde al de máxima probabilidad, es posible demostrar que (Apéndice A):

$$S = k_B ln(\Omega(N, V, E)) \tag{2.7}$$

Esta es la ecuación de Boltzmann, y a partir de ésta se pueden derivar otras funciones termodinámicas alcanzan un máximo o un mínimo en el equilibrio cuando se cambian las variables de control del sistema. En el caso de un sistema a N, V y T constantes, la función termodinámica que marca el equilibrio es la energía libre de Helmholtz, dada por la siguiente expresión (ver Apéndice B):

$$A = -k_B T ln Q(N, V, T) \tag{2.8}$$

$Q(N, V, T)$ es la función de partición en el colectivo canónico, definida como (ver Apéndice B):

$$Q(N, V, T) = \sum_i e^{-\beta E_i(V,T)} \tag{2.9}$$

donde $\beta = \frac{1}{k_B T}$, y el subíndice i representa los niveles de energía del sistema compatibles con N, V. La función de partición es el nexo entre los estados de energía mecanocuántica de un sistema macroscópico y las propiedades termodinámicas del sistema. Si podemos calcular Q como función de N, V y T, entonces podremos calcular las propiedades termodinámicas del sistema en términos de la mecánica cuántica y de los parámetros moleculares. No obstante, las energías $E_i(N, V)$ corresponden a los niveles de energía de un sistema de N moléculas en un volumen V son inaccesibles en la práctica.

Hay muchos problemas en los que el un Hamiltoniano de N cuerpos puede escribirse como la suma de Hamiltonianos de un solo cuerpo (gases diluidos, moléculas poliatómicas...). Cuando esto es posible, la energía del sistema es la suma de las energías individuales. Esto está justificado en el caso de que no haya interacciones entre las partículas del sistema. Para sistemas donde podamos escribir el Hamiltoniano de N partículas como una suma de términos independientes, y si las partículas son distinguibles, entonces el cálculo de la función de partición, $Q(N, V, T)$ se reduce al cálculo de las funciones de partición moleculares ($q(V, T)$).

$$Q(N, V, T) = [q(V, T)]^N \tag{2.10}$$

donde $q(V, T) = \sum e^{-\beta \epsilon_i}$, siendo ϵ_i los estados de energía de cada partícula (o grado de libertad). De esta manera, podemos reducir un problema de N cuerpos (evaluar $Q(N, V, T)$) a un problema de un solo cuerpo (evaluar $q(V, T)$).

Pero las partículas de un sistema no son distinguibles generalmente. Se puede demostrar (página 70, Ref. [93]) que en el caso de partículas indistinguibles, el número de estados cuánticos permitidos para una partícula a temperatura ambiente es mucho mayor que el número de partículas del sistema, de manera que es raro encontrar dos partículas en el mismo estado. Así, la función de partición de un sistema de partículas indistinguibles y no interaccionantes:

$$Q(N, V, T) = \frac{[\sum e^{-\beta \epsilon_i}]^N}{N!} \tag{2.11}$$

¿Pero qué ocurre cuando las partículas de nuestro sistema interaccionan entre si? Para calcular la función de partición de un sistema de N partículas interaccionantes, en un volumen

V y a una temperatura T, tenemos que considerar todos los posibles estados del sistema. Estos corresponden a las posiciones y velocidades de todas la partículas del sistema. La energía del sistema depende, por tanto, de las posiciones y momentos de las partículas. En lugar de realizar el sumatorio, lo reemplazamos por una integral sobre todas las posiciones ($\mathbf{r}^N$) y momentos ($\mathbf{p}^N$) de las partículas del sistema.

$$Q(N,V,T) = \frac{1}{h^{3N}N!}\int d\mathbf{p}^N \int d\mathbf{r}^{\mathbf{N}} exp(-\beta(K(\mathbf{p}^{\mathbf{N}}) + E(\mathbf{r}^N))) \tag{2.12}$$

donde K es la energía cinética total de todas las partículas del sistema. La integración sobre las velocidades de las partículas del sistema se puede resolver de forma analítica, y la función de partición es por tanto,

$$Q(N,V,T) = \frac{1}{N!\Lambda^{3N}}\int d\mathbf{r}^{\mathbf{N}} exp(-\beta(E(\mathbf{r}^N))) \tag{2.13}$$

donde Λ es la función de onda térmica de De Broglie (Λ_i = h / $\sqrt{2\pi m_i kT}$) y $E(\mathbf{r}^N)$ suele aproximarse por la suma de interacciones entre pares de partículas del sistema ($E(\mathbf{r}^N) = \sum_{i<j} U(r_{ij})$). Este potencial de interacción puede ser, por ejemplo, de tipo Lennard-Jones (LJ). En el caso de que el sistema esté compuesto por moléculas, en la función de partición aparecerá la función de partición molecular ($q = q_t q_r q_v q_e$) en la que se incluyen los grados de libertad rotacionales e intramoleculares, ya que es posible separar el Hamiltoniano del sistema en intramolecular e intermolecular.

Como hemos visto hasta ahora, conocida la función de partición $Q(N,V,T)$ del sistema, es posible calcular todas las propiedades termodinámicas (por ejemplo la energía interna). Esto se traduce en una simple receta: Calcula la función de partición Q, y todo lo demás saldrá de aquí. Para sistemas con interacciones ($E(\mathbf{r}^N) \neq 0$) es imposible calcular, ni aproximar, la función de partición (ec. (2.13)). Se podría pensar que $Q(N,V,T)$ podría evaluarse mediante técnicas de integración numérica convencionales como la cuadratura numérica. Sin embargo, resulta imposible evaluar la integral de la ec. (2.13) sobre un grid (malla) en un espacio de fases tan sobredimensionado, puesto que el número de puntos del grid resultaría astronómico. Por ejemplo, para un sistema de $N = 100$, 3 dimensiones y usando un grid muy grosero, de sólo $m = 5$ puntos. Tendríamos que evaluar 5^{300} puntos del grid para cada integrando. Esto es imposible calcularlo incluso en el tiempo de vida del universo. Además, supuesto que seamos capaces de resolver la integral (2.13) de alguna manera, el problema sería que el error numérico es demasiado grande, así que el resultado no sería útil. La razón es que cuando dos partículas solapan, la energía potencial es demasiado grande y el factor de Boltzmann es aproximadamente cero. De hecho, esto es lo que ocurre típicamente en un líquido para la mayoría de configuraciones ($\mathbf{r}^N$), y solo una pequeña parte del espacio de fases tiene una contribución significativa a $Q(N,V,T)$. Por esto tenemos que recurrir a otros métodos que nos permitan estimar la función de partición del sistema, y así estimar propiedades termodinámicas como la energía promedio. En la práctica lo que hacemos es generar configuraciones representativas del sistema, que sigan la función de distribución de probabilidad del colectivo, para promediar las propiedades del sistema (i.e energía interna o la presión). Es aquí donde entra en juego la simulación molecular. La simulación molecular consiste en generar configuración compatibles con las condiciones termodinámicas y que sean significativas en el espacio de fases, y así poder evaluar las propiedades promedio del sistema. Para esto se usan dos técnicas: Dinámica molecular (MD) y Monte Carlo (MC). En la primera se estudia la evolución del sistema con el tiempo resolviendo las ecuaciones de movimiento de Newton para cada una de las partículas del sistema. Mientras que en la segunda,

se generan configuraciones que sigan la distribución de Boltzmann mediante el movimiento aleatorio de las partículas del sistema. Ambas proporcionan resultados equivalentes. Según la hipótesis ergódica, el muestreo temporal y el muestreo sobre las configuraciones debe ser equivalente, puesto que el sistema pasa el mismo tiempo en cada microestado (configuración del sistema).

CAPÍTULO 3

Campos eléctricos: polarización y constante dieléctrica.

"*En este lado de mí*
no existe ciencia ficción"
Cosmonauta (En este lado)

En un material dieléctrico no hay cargas libres, sin embargo, al estar formados por moléculas (formadas por cargas), las moléculas del dieléctrico son afectadas por campos eléctricos. En ausencia de un campo eléctrico las moléculas están orientadas de forma aleatoria debido al ruido térmico. Cuando se aplica un campo eléctrico sobre el material dieléctrico, éste produce una fuerza que se ejerce sobre cada partícula cargada, empujando las partículas positivas en una dirección del campo, y las negativas en sentido opuesto. Sin embargo, estos desplazamientos están limitados por intensas fuerzas restauradoras que se forman por el cambio de la configuración de las cargas de la molécula. El efecto macroscópico es el del desplazamiento de la carga positiva respecto a la negativa, el dieléctrico se ha polarizado. Un dieléctrico polarizado produce un campo eléctrico en los puntos exteriores e interiores del dieléctrico. De manera que la polarización del dieléctrico depende del campo eléctrico total del medio y del campo producido por la propia polarización del dieléctrico. Conviene que definamos que es lo que entendemos por campo eléctrico o campo eléctrico macroscópico. El campo eléctrico (macroscópico) es la fuerza por unidad de carga sobre una carga de prueba sumergida en el dieléctrico, en el límite en que la carga de prueba es tan pequeña que no afecta por si misma a la distribución de carga. En otras palabras, el campo eléctrico macroscópico es el campo promedio en una pequeña región del dieléctrico, pero que contiene un gran número de moléculas.

La polarización del dieléctrico se caracteriza por un momento dipolar eléctrico ($\Delta\mathbf{p}$), que si consideramos un pequeño volumen (Δv) del dieléctrico se define como:

$$\Delta\mathbf{p} = \int_{\Delta v} \mathbf{r} dq \tag{3.1}$$

Esto determina el campo eléctrico producido por este volumen del dieléctrico en puntos distantes (comparados con Δv). Como $\Delta\mathbf{p}$ depende del volumen considerado de dieléctrico, conviene trabajar con el momento dipolar eléctrico por unidad de volumen (**P**):

$$\mathbf{P} = \frac{\Delta\mathbf{p}}{\Delta v} \tag{3.2}$$

P se define en el límite en que Δv se hace muy pequeño desde el punto de vista macroscópico, de manera que **P** se convierte en una función puntual $\mathbf{P}(x, y, z)$, denominada *polarización*.

Ahora calcularemos el campo eléctrico generado por la polarización del dieléctrico en un punto externo al medio dieléctrico. Para ello consideremos un volumen finito de dieléctrico

polarizado (Δv') situado en **r**', de manera que su polarización será **P**(**r**'). Esta polarización genera un campo eléctrico, para el que vamos a calcular su intensidad en un punto **r**, externo al dieléctrico. Calcularemos el potencial eléctrico (ϕ(**r**)) y el campo eléctrico como menos el gradiente de $\phi(\mathbf{r})$.

El potencial eléctrico vendrá dado por el momento dipolar eléctrico ($\Delta\mathbf{p}$) del volumen considerado de dieléctrico (Δv'), ya que el punto considerado (**r**) está suficientemente lejos de Δv'.

$$\Delta\phi(\mathbf{r}) = \frac{\Delta\mathbf{p}(\mathbf{r}-\mathbf{r}')}{4\pi\epsilon_0(\mathbf{r}-\mathbf{r}')^3} = \frac{1}{4\pi\epsilon_0}\frac{\mathbf{P}(\mathbf{r}')(\mathbf{r}-\mathbf{r}')}{(\mathbf{r}-\mathbf{r}')^3}\Delta v' \tag{3.3}$$

$\Delta v'$ debe ser eléctricamente neutro para que se cumpla. En forma diferencial:

$$d\phi(\mathbf{r}) = \frac{1}{4\pi\epsilon_0}\frac{\mathbf{P}(\mathbf{r}')(\mathbf{r}-\mathbf{r}')}{(\mathbf{r}-\mathbf{r}')^3}dv' \tag{3.4}$$

El potencial total se obtiene sumando todas las contribuciones del dieléctrico:

$$\phi(\mathbf{r}) = \frac{1}{4\pi\epsilon_0}\int_{V_0}\frac{\mathbf{P}(\mathbf{r}')(\mathbf{r}-\mathbf{r}')}{(\mathbf{r}-\mathbf{r}')^3}dv' \tag{3.5}$$

$\phi(\mathbf{r})$ se puede calcular fácilmente si se conoce la forma funcional de $\mathbf{P}(\mathbf{r}')$. Como esto no siempre es posible, mediante una transformación matemática sencilla podemos expresar $\phi(\mathbf{r})$ en términos de las *densidades de carga de polarización* (ver apéndice D):

$$\phi(\mathbf{r}) = \frac{1}{4\pi\epsilon_0}\left[\oint_{S_0}\frac{\sigma_P da'}{(\mathbf{r}-\mathbf{r}')} + \int_{V_0}\frac{\rho_p dv'}{(\mathbf{r}-\mathbf{r}')}\right] \tag{3.6}$$

$$= \frac{1}{4\pi\epsilon_0}\int\frac{dq'_P}{(\mathbf{r}-\mathbf{r}')} \tag{3.7}$$

Las nuevas funciones escalares que aparecen en la integrales de la Ec. 3.6, densidad de carga de polarización superficial (σ_P) y la densidad de carga de polarización volumétrica (ρ_p), se obtienen a partir de la polarización (**P**).

$$\sigma_P = \mathbf{P}\cdot\mathbf{n} \tag{3.8}$$

$$\rho_p = -\nabla\mathbf{P} \tag{3.9}$$

donde **n** representa la normal hacia afuera del dieléctrico del elemento de superficie da'. Son densidades de carga de polarización, y es posible darles un significado físico. La densidad superficial de carga de polarización está dada por la componente de la polarización normal a la superficie, y la densidad volumétrica de carga es una medida de la uniformidad de la polarización dentro del material.

Ahora demostraremos como los desplazamientos de las cargas en el dieléctrico generan una densidad de carga neta. La densidad de carga superficial da cuenta de la densidad de carga de cada superficie que no sea paralela al vector de polarización (viene de los extremos de los dipolos que tienen la misma orientación, Fig. 3.1). La densidad volumétrica de carga de polarización representa el exceso de carga del elemento de volumen $\Delta v'$. En el estado no polarizado, cada elemento de volumen del dieléctrico es eléctricamente neutro ($\rho^+ + \rho^- = 0$, donde ρ^+ y ρ^- representan la densidad de carga positiva y negativa, respectivamente). Cuando se polariza el material dieléctrico la carga positiva se desplaza δ^+(x,y,z) y la negativa δ^-(x,y,z). Podemos calcular la densidad de carga positiva que atraviesa un elemento de área

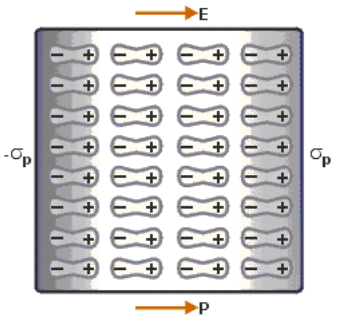

Figura 3.1: Pedazo de material dieléctrico polarizado. Cada elemento de volumen $\Delta v'$ se representa por un dipolo ($\Delta\mathbf{p}$). σ_P representa la densidad de carga superficial.

da' ($\delta^+\delta^+\mathbf{n}da'$), y así el aumento de carga positiva por elemento de volumen $\Delta v'$ durante el proceso de polarización:

$$-\oint_{\Delta S}\rho^+\delta^+\mathbf{n}da' \tag{3.10}$$

donde ΔS es la superficie que limita $\Delta v'$ y $\mathbf{n}$ es la normal hacia afuera del dieléctrico del elemento de superficie da'. Análogamente para el aumento de carga negativa:

$$\oint_{\Delta S}(-\rho^-)\delta^-\mathbf{n}da' \tag{3.11}$$

Así que el aumento total en la carga por elemento de volumen es (teniendo en cuenta $\rho^+ + \rho^- = 0$):

$$-\oint_{\Delta S}\rho^+(\delta^+ - \delta^-)\mathbf{n}da' = -\nabla[\rho^+(\delta^+ - \delta^-)]\Delta v' = \rho_P\Delta v' \tag{3.12}$$

Como $(\delta^+ - \delta^-)$ es el desplazamiento relativo de las densidades de carga positiva y negativa, $\rho^+(\delta^+ - \delta^-)$ es equivalente a la polarización (**P**). Así pues, $\rho_p\Delta v'$ es el exceso de carga o carga neta en un elemento de volumen ($\Delta v'$) del dieléctrico polarizado ($\rho_P = -\nabla P$).

Al principio dijimos que los elemento de volumen del dieléctrico ($\Delta v'$) debían ser eléctricamente neutros, sin embargo acabamos de ver que cuando se polariza el material dieléctrico, los elementos de volumen ($\Delta v'$) tienen una carga neta. El origen de esta paradoja es la transformación matemática que hemos hecho de la Ec. 3.5. Dividimos la contribución de cada elemento de volumen en un término de volumen y otro de superficie. Así que para que se cumpla la premisa de electroneutralidad, la carga total de polarización (suma de la contribución de superficie y de volumen) debe ser cero, y no sólo la contribución de volumen que hemos obtenido mediante la transformación matemática de la Ec. 3.5. Esto es la carga total de polarización:

$$Q_P = \int_{V_0}\left(-\nabla'\mathbf{P}\right)dv' + \oint_{S_0}\mathbf{P}\cdot\mathbf{n}da' \tag{3.13}$$

que se anula como consecuencia del teorema de divergencia (ver apéndice C, $\int_V\left(-\nabla'\mathbf{P}\right)dV = \oint_S -\mathbf{P}\cdot\mathbf{n}da$).

Ahora que tenemos una expresión para el potencial eléctrico $\phi(\mathbf{r})$ generado por un dieléctrico polarizado (Ec. 3.6), el campo eléctrico (**E**) puede obtenerse como menos el gradiente de $\phi(\mathbf{r})$ ($\mathbf{E} = -\nabla\phi(\mathbf{r})$), donde $\nabla(1/(\mathbf{r}-\mathbf{r}')) = -\nabla'(1/(\mathbf{r}-\mathbf{r}'))$.

$$\mathbf{E}(\mathbf{r}) = \frac{1}{4\pi\epsilon_0}\left[\oint_{S_0}\frac{\sigma_P(\mathbf{r}-\mathbf{r}')da'}{(\mathbf{r}-\mathbf{r}')^3} + \int_{V_0}\frac{\rho_p(\mathbf{r}-\mathbf{r}')dv'}{(\mathbf{r}-\mathbf{r}')^3}\right] \tag{3.14}$$

Esta es la expresión analítica para el campo eléctrico en un punto **r** alejado del material, generado por la polarización de un dieléctrico. Puede demostrarse (Págs 86-88 Ref. [94]) que la ecuación 3.6 da la contribución del medio al campo eléctrico en **r**, independientemente de si **r** está dentro o fuera del medio. El campo eléctrico en un dieléctrico es igual al campo eléctrico dentro de una cavidad en forma de aguja contenida en el dieléctrico, siempre y cuando el eje de la cavidad este orientado paralelamente con la dirección del campo. El campo en dicha cavidad es un campo externo y puede calcularse como tal. De manera que la ecuación 3.14 da la contribución del medio dieléctrico polarizado al campo eléctrico en **r**, independientemente de si **r** está dentro o fuera del medio.

El cálculo de **E**(**r**) es directo en los casos en que se conoce la función **P**(**r**). Sin embargo, la polarización se origina como respuesta a un campo eléctrico (**P**(**r**) es una función de **E**(**r**)), lo que complica las cosas. Puesto que no podemos determinar **P**(**r**) porque no conocemos **E**(**r**), y viceversa, debemos recurrir a otro enfoque del problema. Para ello, vamos a obtener una relación entre **P** y **E**.

La ley de Gauss establece que el flujo eléctrico a través de una superficie cerrada arbitraria es proporcional a la carga total encerrada por la superficie, en forma integral:

$$\oint_S \mathbf{E} \cdot \mathbf{n} da = \frac{1}{\epsilon_0} (Q_{tot}) \tag{3.15}$$

donde Q_{tot} es la carga total encerrada en la superficie S, que incluye la carga libre (Q_f) y la carga de polarización (Q_P), que incluye la densidad de carga de la superficie S considerada (σ_P) y densidad de carga volumétrica (ρ_P).

$$Q_P = -\int_S \mathbf{P} \cdot \mathbf{n} da + \int_V (-\nabla \cdot \mathbf{P})\, dV \tag{3.16}$$

Por medio del teorema de divergencia (incluyendo todas las superficies que limitan con el dieléctrico considerado), transformamos la integral de volumen en una integral de superficie. Las densidades de carga superficiales de las cargas libres se cancelan con la densidad de carga superficial de la superficie considerada S (primer término de la ecuación 3.16).

$$Q_P = -\oint_S \mathbf{P} \cdot \mathbf{n} da \tag{3.17}$$

Combinando este resultado con la ley de Gauss (Ec. 3.15)

$$\oint_S (\epsilon_0 \mathbf{E} + \mathbf{P}) \cdot \mathbf{n} da = Q_f \tag{3.18}$$

Esta ecuación establece que el flujo del vector ($\epsilon_0 \mathbf{E} + \mathbf{P}$), que pasa por una superficie cerrada, es igual a la carga libre total introducida en el volumen encerrado por la superficie. Esta cantidad vectorial es el *desplazamiento eléctrico* ($\mathbf{D} = \epsilon_0 \mathbf{E} + \mathbf{P}$). Extendiendo el resultado a una región ΔV, en que toda la carga la esta distribuida como una densidad de carga ρ, entonces:

$$\oint_S \mathbf{D} \cdot \mathbf{n} da = \rho \Delta V \tag{3.19}$$

Dividiendo esta ecuación por ΔV y tomando el límite, obtenemos:

$$\nabla \cdot \mathbf{D} = \rho \tag{3.20}$$

que se conoce por la forma diferencial de la ley de Gauss.

La polarización de un medio dieléctrico tiene lugar debido al campo eléctrico del medio, pero obviamente dependerá de las propiedades de las moléculas que forman el dieléctrico. Desde el punto de vista macroscópico, el comportamiento del material se especifica completamente por la relación: **P** = **P**(**E**) (**E**, campo eléctrico macroscópico), que se determina experimentalmente. Sí **E** varía de un punto a otro dentro del material, entonces **P** variará igualmente y en el mismo sentido (para un dieléctrico isotrópico):

$$\mathbf{P} = \chi(E)\mathbf{E} \tag{3.21}$$

donde $\chi(E)$ es la susceptibilidad eléctrica del material. Sustituyendo la definición que hemos obtenido para el desplazamiento eléctrico ($\mathbf{D} = \epsilon_0\mathbf{E} + \mathbf{P}$) en la ecuación 3.22:

$$\mathbf{D} = \epsilon(E)\mathbf{E} \tag{3.22}$$

$$\epsilon(E) = \epsilon_0 + \chi(E) \tag{3.23}$$

donde $\epsilon(E)$ es la permitividad del material. Para intensidades moderadas de campo eléctrico, $\chi(E)$ y $\epsilon(E)$ son independientes del campo eléctrico, y por eso se suelen expresar como χ y ϵ. Cuando esto ocurre hablamos de dieléctricos lineales, y se cumple:

$$\mathbf{D} = \epsilon\mathbf{E} \tag{3.24}$$

$$\mathbf{P} = \chi\mathbf{E} \tag{3.25}$$

Así, el comportamiento eléctrico de un material queda especificado completamente por su permitividad o su susceptibilidad. Sin embargo, conviene trabajar con una cantidad adimensional, denominada *constante dieléctrica relativa* y definida como:

$$\epsilon_r = \frac{\epsilon}{\epsilon_0} \tag{3.26}$$

Si el campo eléctrico en un dieléctrico se hace muy intenso, empezará a sacar electrones de las moléculas, y el material se convertirá en conductor. El máximo campo eléctrico que puede soportar un dieléctrico se llama *resistencia dieléctrica* (*dielectric breakdown*), que para el agua tiene lugar a campos eléctricos mayores de 0.01 V/nm [95].

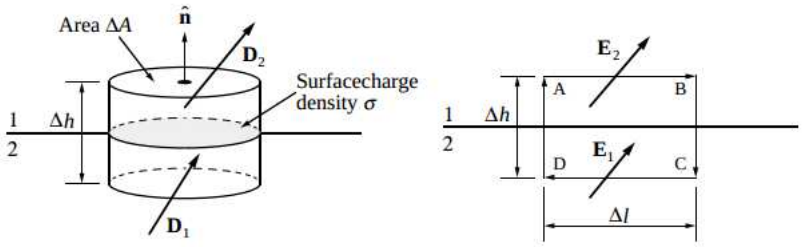

Figura 3.2: Condiciones de frontera sobre los vectores de campo en la zona interfacial entre dos medios. Se pueden obtener aplicando la ley de Gauss a S e integrando $\mathbf{E}d\mathbf{l}$ a lo largo de la trayectoria cerrada $ABCDA$.

Hasta ahora hemos considerado un medio dieléctrico infinito, pero ¿qué ocurre cuando tenemos dos medios con distintas propiedades (dieléctrico$_1$/dieléctrico$_2$ o dieléctrico/conductor)

unidos a través de una interfase? Imaginemos dos medios dieléctricos en contacto. Supondremos una densidad de carga externa (σ) que puede variar de un punto a otro de la zona interfacial. Ahora consideremos una superficie en forma de caja de píldoras S (Fig. 3.2) de espesor infinitesimal ($\Delta h \to 0$) que intersecta la interfase, y encierra un ΔS es ésta. El volumen encerrado es despreciable. Entonces la carga de polarización vendrá dada por:

$$Q_P = \sigma \Delta S + \frac{1}{2}\left(\rho_1 + \rho_2\right) \Delta S \Delta h \tag{3.27}$$

Aplicando la ley de Gauss en forma integral ($\oint_S \mathbf{D} da = Q$) a S:

$$\mathbf{D}_2 \cdot \mathbf{n}_2 \Delta S + \mathbf{D}_1 \cdot \mathbf{n}_1 \Delta S = \sigma \Delta S \left(\mathbf{D}_2 - \mathbf{D}_1\right) \cdot \mathbf{n}_2 = \sigma \tag{3.28}$$

como $\mathbf{n}_2$ es la normal a la interfase:

$$\left(\mathbf{D}_{2n} - \mathbf{D}_{1n}\right) = \sigma \tag{3.29}$$

Es decir, la discontinuidad en la componente normal de $\mathbf{D}$ está dada por la densidad de carga superficial de la carga externa sobre la interfase. O lo que es lo mismo, si la interfase no esta cargada, la componente normal de $\mathbf{D}$ es continua (Fig. 3.2). El campo eléctrico puede calcularse como menos el gradiente de un potencial, de manera que la integral de linea $\mathbf{E} \cdot d\mathbf{l}$ alrededor de cualquier trayectoria cerrada se anula. Entonces:

$$\oint \mathbf{E} \cdot d\mathbf{l} = 0 \tag{3.30}$$

$$\left(\mathbf{E}_2 - \mathbf{E}_1\right) \cdot \Delta \mathbf{l} = 0 \tag{3.31}$$

$$\mathbf{E}_{1,t} = \mathbf{E}_{2,t} \tag{3.32}$$

es decir, la componente tangencial del campo eléctrico es continua al atravesar una zona interfacial. Si la interfase está entre un dieléctrico y conductor, entonces $\mathbf{E} = 0$ en el conductor, y por lo tanto $\mathbf{E}_t$ en ambos medios. $\mathbf{E}$ deberá ser normal a la superficie del conductor (Fig. 3.2).

Si el dieléctrico es lineal, isotrópico y homogéneo, entonces $\mathbf{D} = \epsilon \mathbf{E}$, y aplicando la ley de Gauss (Ec. 3.20) podemos escribir:

$$\nabla \mathbf{E} = \frac{1}{\epsilon} \rho \tag{3.33}$$

como $\mathbf{E} = -\nabla \phi$;

$$\nabla^2 \phi = -\frac{1}{\epsilon} \rho \tag{3.34}$$

que se conoce como la ecuación de Poisson. Por tanto, para este dieléctrico, el potencial eléctrico satisface la ecuación de Poisson. En la mayoría de los casos el dieléctrico no contiene cargas libres distribuidas por su volumen ($\rho = 0$). La carga existe sobre las superficies de conductores o cargas puntuales dentro del dieléctrico. En todos estos casos, se cumple la ecuación de la Laplace en todo el dieléctrico ($\nabla^2 \phi = 0$). Esta ecuación se puede aplicar incluso cuando exista cierta carga superficial (σ) sobre la superficie del dieléctrico. De manera que el problema se reduce a hallar las soluciones de la ecuación de Laplace para determinadas condiciones de contorno.

A nivel microscópico, el promedio del momento dipolar de un dieléctrico ($\mathbf{M}$) bajo el efecto de un campo eléctrico externo $\mathbf{E}_{ex}$ se obtiene a partir de la termodinámica estadística como:

$$\langle \mathbf{M} \rangle_{E_{ex}} = \frac{\int \mathbf{M} e^{-\beta[U - \mathbf{M}\cdot\mathbf{E}_{ex}]} d\Gamma}{\int e^{-\beta[U - \mathbf{M}\cdot\mathbf{E}_{ex}]} d\Gamma} \tag{3.35}$$

donde $\mathbf{M}$ es el momento dipolar instantáneo, U es la energía interna del sistema en ausencia de campo y $d\Gamma$ representa la integración sobre el espacio de configuracional. Esta ecuación hasta primer orden en el campo:

$$\langle \mathbf{M} \rangle_{E_{ex}} = \langle \mathbf{M} \rangle_0 + \beta \langle \mathbf{M}\mathbf{M} \cdot \mathbf{E}_{ex} \rangle_0 - \beta \langle \mathbf{M} \rangle_0 \langle \mathbf{M} \cdot \mathbf{E}_{ext} \rangle_0 \tag{3.36}$$

Para un material dieléctrico, $\langle \mathbf{M} \rangle_0$ se anula. Sin embargo, a lo largo de una simulación, donde el muestreo se limita a una parte del espacio configuracional, podemos encontrar una polarización neta del material. Por esta razón, mantendremos este término. La polarización promedio debida al campo se puede escribir como:

$$\Delta \mathbf{P} = \frac{\beta}{V} \left(\langle \mathbf{M}\mathbf{M} \rangle_0 - \langle \mathbf{M} \rangle_0 \langle \mathbf{M} \rangle_0 \right) \cdot \mathbf{E}_{ext} \tag{3.37}$$

donde $\Delta \mathbf{P} = P_{E_{ext}} - P_0$, y $\mathbf{P}$ es el momento dipolar por unidad de volumen o polarización. La notación $\mathbf{AB}$ representa un par con elementos de matriz $AB_{\alpha,\beta} = A_\alpha B_\beta$. Para un dieléctrico isotrópico, los términos entre paréntesis pueden escribirse como una matriz diagonal, porque la polarización será paralela al campo eléctrico. En cambio, en el caso de dieléctricos anisotrópicos la polarización no es siempre paralela al campo aplicado, y debemos mantener la notación tensorial.

El campo macroscópico dentro de un medio dieléctrico ($\mathbf{E}$) incluye el campo eléctrico externo ($\mathbf{E}_{ex}$) además del campo eléctrico creado por la polarización del material. A nivel macroscópico la polarización es uniforme, y podemos escribir:

$$\mathbf{E} = \mathbf{E}_{ex} + \mathbf{T}_m \cdot \mathbf{P} \tag{3.38}$$

donde $\mathbf{T}_m$ es la integral de volumen sobre el tensor dipolo-dipolo, que dependerá de las condiciones de contorno de la simulación. Debido al tiempo limitado de observación (en una simulación) tenemos que tener en cuenta la presencia de una polarización neta de la muestra. Entonces la ecuación anterior se puede escribir como:

$$\mathbf{E} = \mathbf{E}_{ex} + \mathbf{T}_m \cdot \mathbf{P}_0 + \mathbf{T}_m \cdot \Delta \mathbf{P} \tag{3.39}$$

El segundo término de esta ecuación corresponde al campo microscópico ($\mathbf{E}_0$), creado por el material en ausencia de un campo eléctrico externo. Podemos reescribir la ecuación anterior como:

$$\Delta \mathbf{E} = \mathbf{E}_{ex} + \mathbf{T}_m \cdot \Delta \mathbf{P} \tag{3.40}$$

donde $\Delta \mathbf{E} = \mathbf{E} - \mathbf{E}_0$. Para relacionar esta ecuación con la ecuación 3.36, necesitamos completar la descripción macroscópica con una ecuación constitutiva que relacione el campo y la polarización. De las ecuaciones 3.36 y 3.40 podemos deducir que $\Delta \mathbf{P}$ debe estar linealmente relacionada con $\Delta \mathbf{E}$, así que aceptaremos la siguiente relación constitutiva:

$$\Delta \mathbf{P} = \chi \cdot \Delta \mathbf{E} \tag{3.41}$$

donde χ es el tensor de susceptibilidad del material dieléctrico. La sustitución de la relación constitutiva en la ecuación 3.40 resulta en:

$$\left(\chi^{-1} - \mathbf{T}_m\right) \cdot \Delta\mathbf{P} = \mathbf{E}_{ex} \tag{3.42}$$

Sustituyendo este resultado en la ecuación 3.36, obtenemos:

$$\{\frac{\beta}{V}\left(\chi^{-1} - \mathbf{T}_m\right) \cdot (\langle\mathbf{MM}\rangle_0 - \langle\mathbf{M}\rangle_0\langle\mathbf{M}\rangle_0) - \mathbf{I}\} \cdot \mathbf{E}_{ex} = 0 \tag{3.43}$$

Ya que esta ecuación debe ser cierta para un campo externo arbitrario, está claro que el término entre llaves debe ser igual a la unidad para que la igualdad sea cierta. De manera que el tensor de susceptibilidad es solución de la siguiente ecuación lineal:

$$\chi\left(\mathbf{T}_m + \frac{V}{\beta}\mathbf{F}^{-1}\right) = \mathbf{I} \tag{3.44}$$

donde $\mathbf{I}$ es la matriz unidad, y $\mathbf{F}$ es el tensor de fluctuaciones del momento dipolar ($\mathbf{F} = \langle\mathbf{M}_\alpha\mathbf{M}_\beta\rangle_0 - \langle\mathbf{M}_\alpha\rangle_0\langle\mathbf{M}_\beta\rangle_0$).

El tensor susceptibilidad es la solución general de la ecuación 3.44 para un material dieléctrico anisotrópico. La solución dependerá de las condiciones de contorno, que están explícitamente incluidas en la integral del tensor dipolo-dipolo ($\mathbf{T}_m$). En las simulaciones por ordenador es conveniente suponer que la muestra del material dieléctrico es esférica y está rodeada por un dieléctrico isotrópico. En este caso:

$$\mathbf{T}_m = -\frac{4\pi}{2\epsilon_s + 1}\delta_{\alpha,\beta} \tag{3.45}$$

donde ϵ_s es la constante dieléctrica del medido de alrededor. En el caso de que supongamos que el material dieléctrico está rodeado por un conductor, entonces $\epsilon_s = \infty$ y $\mathbf{T}_m$ puede ser ignorado (el campo aplicado es igual al macroscópico):

$$\chi = \frac{\beta}{V}\mathbf{F} \tag{3.46}$$

Para un medio isotrópico (como un cristal cúbico), el promedio del tensor $\mathbf{F}$ debe ser diagonal para cualquier sistema de referencia, y todos lo elementos de la diagonal principal deben ser iguales entre si. Para sistemas anisotrópicos, $\mathbf{F}$ no es siempre diagonal. Sin embargo, existe algún sistema de coordenadas del cristal para el que $\mathbf{F}$ es diagonal. Los ejes dieléctricos principales vienen dados por la simetría del cristal. Para cristales de simetría tetragonal (hielos III y VI) el sistema de referencia x, y, z, coincide con la dirección de los vectores de la celda unidad a, b, c. Para sistemas de simetría hexagonal (hielos I_h y II), x y z se sitúan sobre los vectores de celda a y c; y se escoge en la dirección perpendicular al plano cristalográfico ac. Con esta elección de ejes, el tensor de susceptibilidad es diagonal. Para cristales de simetría monoclínica o triclínica (hielo V), los ejes x e y se situan sobre los vectores a y b, mientras que el eje z es perpendicular al plano ab [96]. En cualquier caso, cuando tenemos condiciones de contorno conductoras, el problema de encontrar los ejes dieléctricos principales se reduce a la diagonalización de la matriz $\mathbf{F}$.

CAPÍTULO 4

Simulación molecular

"*Sois la mierda cantante y danzante del mundo.*"
Tyler Durden (El club de la lucha).

Como se ha estudiado en el capítulo anterior, la simulación molecular se emplea para generar configuraciones representativas del sistema, y así poder evaluar propiedades promedio del mismo. Las simulaciones de sistemas en materia condensada se llevan a cabo para sistemas con un número pequeño de moléculas (entre 100-10000 partículas). No se pueden simular sistemas de tamaño macroscópico ($\sim 10^{23}$ partículas) porque el tiempo que se requiere para evaluar las interacciones es proporcional a N^2. Pero el usar sistemas tan pequeños tiene una importante desventaja, las moléculas de la superficie tienen energía y propiedades distintas a las que presentan en el seno del sistema (*bulk*). Para evitar los efectos de superficie y aliviar el coste computacional en la evaluación de las interacciones entre las partículas del sistema se usan técnicas especiales que repasaremos a continuación.

4.1. Condiciones de contorno periódicas

El sistema se introduce en una caja de simetría cúbica y se rodea de copias de si mismo (Fig. 4.1). Esto significa que cuando una partícula abandona la caja central, entra en la caja central por el lado contrario. De esta manera, la densidad de partículas de la caja central (y por tanto el sistema entero) se conserva. Al estar el sistema rodeado de copias de si mismo se evitan los efectos de superficie y se obtienen propiedades de *bulk*. En la práctica, la caja de simulación no tiene por qué ser necesariamente cúbica.

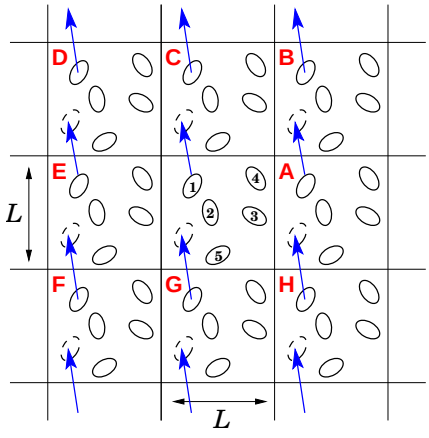

Figura 4.1: Sistema periódico en dos dimensiones. Las moléculas pueden entrar y salir de cada caja a través de las cuatro fronteras. En un ejemplo de tres dimensiones, las moléculas serían libres para cruzar por cualquiera de las seis caras del cubo.

La partícula 1 en la Fig. 4.1 puede interaccionar, en principio, con el resto de las partículas de la caja y con sus réplicas situadas en otras cajas. Sin embargo, es conveniente considerar interacciones únicas entre las réplicas de las partículas, y la elección natural es considerar solo la interacciones con la réplica que esté a la menor distancia interatómica. Esto se conoce como **criterio de imagen mínima**.

En la práctica, la aplicación del criterio de imagen mínima es muy sencilla, basta con tres lineas en el código de simulación. Además, la replicación del sistema no presenta problemas técnicos, no es necesario almacenar las coordenadas de todas las réplicas, solo las de la caja central. La aplicación es igual sea cual sea la simetría de la caja de simulación, no tiene por qué ser necesariamente cúbica.

4.2. Potencial Lennard-Jones

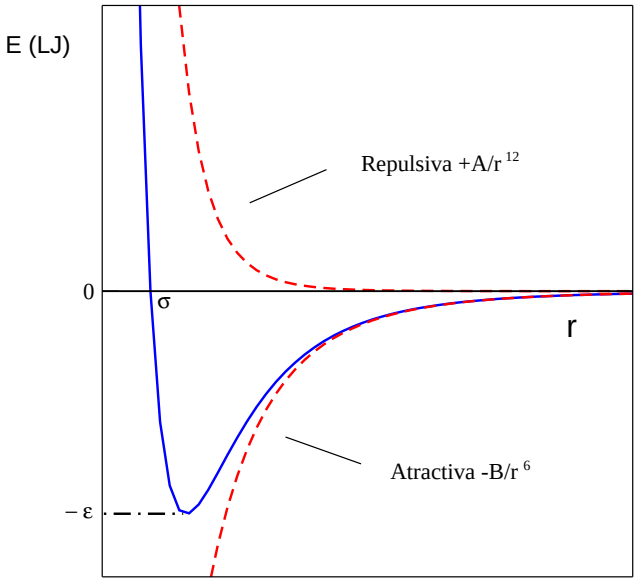

Figura 4.2: Potencial tipo Lennard-Jones (12-6).

El potencial Lennard-Jones (LJ) es el potencial par mas popular para describir las interacciones entre átomos y moléculas. En este modelo, la energía de interacción entre dos átomos a una distancia $r_{ij} = |r_i - r_j|$ es igual a:

$$U_{LJ}(r_{ij}) = 4\epsilon[(\frac{\sigma}{r_{ij}})^{12} - ((\frac{\sigma}{r_{ij}})^{6}] \tag{4.1}$$

donde σ y ϵ son los parámetros del LJ. En este modelo, dos átomos se atraen a largas distancias, pero se repelen a cortas distancias (Fig. 4.2). Como el potencial LJ describe la energía de interacción entre dos partículas, la energía total de un fluido LJ debe ser calculada mediante el sumatorio sobre todos los pares de átomos posibles:

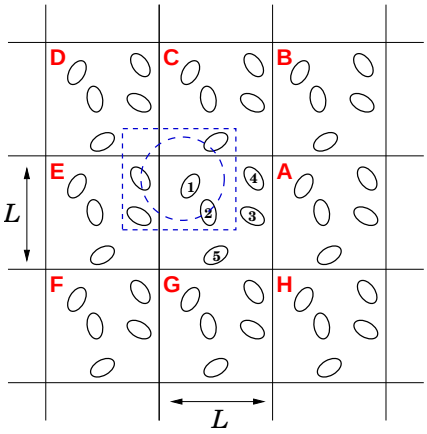

Figura 4.3: Criterio de imagen mínima en un sistema de dos dimensiones. La caja central contiene cinco moléculas. La caja construida en torno al centro de la molécula 1 también contiene cinco moléculas. El círculo quebrado representa la distancia a la que se trunca el potencial.

$$E(\mathbf{r}^N) = \sum_{i=1}^{N-1} \sum_{j=i+1}^{N} U_{LJ}(r_{ij}) \tag{4.2}$$

4.3. Truncamiento del potencial

Las interacciones entre las partículas del sistema dependen de la distancia entre las mismas. Para un sistema formado por N partículas, existen en principio N(N-1)/2 pares, lo que significa que el coste computacional de la energía del sistema es del orden de N^2. Con el objetivo de reducir el número de interacciones, y así el coste computacional, se desprecian todas las interacciones que estén mas alejadas de un radio r_{cut}. Esto reduce el cálculo de interacciones en $\frac{4\pi r_{cut}^3}{3L^3}$. La supresión de interacciones más allá del r_{cut} supone una pequeña perturbación del sistema, de manera que r_{cut} no debe ser muy pequeño (en la práctica, $r_{cut} \approx 2.5 - 4\sigma$). En cualquier caso, r_{cut} debe ser más pequeño que la mitad de un lado la caja de simulación ($r_{cut} \leq \frac{L}{2}$), asegurando así el criterio de imagen mínima.

Es importante darse cuenta de que el resultado de la simulación puede depender de r_{cut} y de cómo se haga. En el caso de interacciones dispersivas (i.e. LJ) el efecto es casi inapreciable. No obstante, en interacciones de tipo coulómbico, que son interacciones de más largo alcance ($U_{coul} \propto r^{-1}$), el truncamiento simple del potencial puede provocar resultados incorrectos.

4.4. Correcciones de largo alcance

Como hemos visto, los resultados de la simulación podrían depender del r_{cut}. Para minimiza esta esta dependencia se suelen incluir correcciones de largo alcance a la energía. La energía entre r_{cut} y $r = \infty$ se puede estimar como [97]:

$$U_{long} = \frac{N}{2} \int_{r_c}^{\infty} \rho u(r)\, g(r)\, d\vec{r} \tag{4.3}$$

Para estimar la corrección de largo alcance a la energía, suele tomarse la aproximación $g(r) \approx 1$ cuando $r > r_c$ (buena aproximación para sistemas homogéneos). ρ es la densidad del sistema $\rho = N/V$ donde N es el número de partículas y V el volumen del sistema. De la ecuación (4.3) se desprende que la corrección de cola es infinita a menos que la función de interacción $u(r)$ decaiga más rápido que r^{-3}. En el caso de interacciones de tipo dispersivo, como las LJ, esta contribución es pequeña, ya que las interacciones decaen rápidamente con la distancia. Sin embargo, en el caso de las interacciones coulómbicas la corrección diverge, pues $U_{coul} \propto r^{-1}$. En este caso, es necesario incluir técnicas especiales, como las sumas de Ewald [97–99], para evaluar las interacciones de largo alcance. El coste computacional de las sumas de Ewald escala con el número de partículas del sistema como $N^{3/2}$, lo que aumenta mucho los tiempos de simulación de sistemas cargados, aunque existen algoritmos basados en las sumas de Ewald que pueden reducir el coste computacional, como el método PME (Particle Mesh Ewald) que escala como $NlogN$ [100].

4.5. Sumas de Ewald

Ahora deduciremos una expresión para calcular la contribución Coulómbica a la energía mediante las sumas de Ewald en un sistema con condiciones de contorno periódicas. Para ello partiremos de un sistema de N_q partículas cargadas y eléctricamente neutro, donde las partículas estarán localizadas en un cubo de $V=L^3$ y tenemos condiciones de contorno periódicas. Para este sistema, la contribución coulómbica viene dada por la siguiente expresión:

$$U_{coul} = \frac{1}{2}\sum_{l=0}^{\infty}\sum_{i}^{N_q}\sum_{j}^{N_q}\frac{q_i q_j}{4\pi\epsilon_0 r_{ij}(l)} \tag{4.4}$$

Donde q_i es la carga de la partícula *i*, r_{ij} es la distancia entre las partículas *i* y *j* y *l* es el número de réplicas. Se está considerando la interacción de una partícula consigo misma (r_{ii}(l=0)), aunque esta contribución la eliminaremos más adelante. La convergencia de esta suma es muy lenta, así que reescribimos la ecuación (4.4) en términos de la densidad de carga (ρ(r)). En la ecuación (4.4), estamos considerando la densidad de carga como una δ-Dirac. La contribución electrostática de cargas puntuales decae como r^{-1}, pero si suponemos que cada carga q_i está rodeada por una distribución de carga difusa de signo opuesto (pero igual carga), entonces el potencial electrostático creado por la partícula *i* se debe solamente a la fracción de q_i que no ha sido apantallada y, a largas distancias tiende rápidamente a 0. Suponemos que el decaimiento de la carga con r sigue una distribución gaussiana (de ancho $\sqrt{2}/\sigma$) (Apéndice E):

$$U_{coul} = \frac{1}{2}\sum_{l=0}^{\infty}\sum_{i}^{N_q}\sum_{j}^{N_q}\frac{q_i q_j}{4\pi\epsilon_0}\frac{2}{\sqrt{\pi}}\int_0^{\infty} e^{-r_{ij}(l)^2\rho^2}d\rho \tag{4.5}$$

Aquí ρ no tiene significado físico. Ahora, la contribución electrostática en un punto r_i debida a las cargas apantalladas se puede obtener rápidamente calculando el sumatorio de la ecuación (4.5) (el potencial debido a las cargas apantalladas decae rápidamente con r). La integral de la ecuación (4.5) se puede dividir en dos contribuciones (ver apéndices E y F) y obtener:

$$E = \frac{1}{2}\sum_{l=0}^{\infty}\sum_{i}\sum_{j}\frac{q_i q_j}{4\pi\epsilon_0}\frac{erfc(gr_{ij})}{r_{ij}} + \frac{1}{2}\sum_{l=0}^{\infty}\sum_{i}\sum_{j}\frac{q_i q_j}{4\pi\epsilon_0}\frac{2}{\sqrt{\pi}}(\int_0^{g} exp(-r_{ij}^2\rho^2)d\rho) \tag{4.6}$$

Donde el primer término es una suma en el espacio real (E_1), que en realidad es la expresión de Coulomb añadiendo la función de error complementaria (ver apéndice G) y el segundo es un sumatorio en el espacio recíproco (E_2). Ahora, la contribución E_1 se puede calcular fácilmente ya que el sumatorio converge rápidamente, puesto que $\frac{erfc(gr_{ij})}{r_{ij}}$ decae rápidamente con r_{ij} (Figura G.1).

Veamos como podemos resolver el sumatorio en el espacio recíproco y obtener E_2. Haciendo uso de la transformada de Fourier podemos transformar el sumatorio sobre las infinitas réplicas del sistema en un sumatorio sobre los vectores de espacio recíproco (ver apéndice H). Como se demuestra en el Apéndice I:

$$\frac{2}{\sqrt{\pi}}\sum_{l} exp(-r_{ij}^2(l)\rho^2) = \frac{2\pi}{V_c}\sum_{\mathbf{G}} \frac{exp(-G^2/(4\rho^2))exp(i\mathbf{G}.(\mathbf{r_j}-\mathbf{r_i}))}{\rho^3} \tag{4.7}$$

De esta manera hemos evitado el sumatorio sobre las infinitas réplicas del sistema. Sustituyendo (4.7) en la contribución de espacio recíproco E_2 (ecuación (4.6)):

$$E_2 = \frac{1}{2}\sum_i\sum_j \frac{q_iq_j}{4\pi\epsilon_0}\frac{2\pi}{V_c}\ [\int_0^g \sum_{\mathbf{G}} \frac{exp(-G^2/(4\rho^2))exp(i\mathbf{G}.(\mathbf{r_j(0)}-\mathbf{r_i(0)}))d\rho}{\rho^3}\ ] \tag{4.8}$$

Sacamos fuera de la integral los términos que no dependen de ρ:

$$E_2 = \frac{1}{2}\sum_i\sum_j \frac{q_iq_j}{4\pi\epsilon_0}\frac{2\pi}{V_c}\sum_{\mathbf{G}} exp(i\mathbf{G}.(\mathbf{r_j(0)}-\mathbf{r_i(0)}))\ [\int_0^g \frac{exp(-G^2/(4\rho^2))d\rho}{\rho^3}\ ] \tag{4.9}$$

La integral que aparece en esta expresión es $\int f'(x)f(x)dx$ y la podemos resolver analíticamente:

$$E_2 = \frac{1}{2}\sum_i\sum_j \frac{q_iq_j}{4\pi\epsilon_0}\frac{4\pi}{V_c}\sum_{\mathbf{G}} \frac{exp(-G^2/(4g^2))}{G^2}exp(i\mathbf{G}.(\mathbf{r_j(0)}-\mathbf{r_i(0)})) \tag{4.10}$$

Esta expresión para la contribución E_2 puede ser reorganizada. Si dividimos el doble sumatorio sobre todas las partículas del sistema es fácil comprobar que:

$$\sum_i\sum_j e^{i(x_j-x_i)} = \sum_j e^{ix_j}\sum_i e^{-ix_i} = zz* = \mid z \mid^2 \tag{4.11}$$

Esto es:

$$\sum_i\sum_j \frac{q_iq_j}{4\pi\epsilon_0}e^{i\vec{G}(\vec{r_j}-\vec{r_i})} = \frac{1}{4\pi\epsilon_0}(\sum_i q_ie^{-i\vec{G}\vec{r_i}})(\sum_j q_je^{j\vec{G}\vec{r_j}})) \tag{4.12}$$

donde cada uno de los sumatorios es un factor de estructura $\rho(\vec{G}) = \frac{1}{V_c}\sum_i q_ie^{i\vec{G}\vec{r_i}}$:

$$\sum_i\sum_j \frac{q_iq_j}{4\pi\epsilon_0}e^{i\vec{G}(\vec{x_j}-\vec{x_i})} = \frac{V_c}{\epsilon_0}\mid \rho(\vec{G}) \mid^2 \tag{4.13}$$

Sustituyendo (4.13) en nuestra expresión para E_2 (ecuación (4.10)):

$$E_2 = \frac{1}{2}\sum_{\vec{G}} \frac{4\pi V_c}{G^2}(\frac{1}{4\pi\epsilon_0})e^{-\frac{G^2}{4g^2}}\mid \rho(\vec{G}) \mid^2 \tag{4.14}$$

En ambos sumatorios (E_1 y E_2) hemos incluido el término r_{ii}(l=0), así que ahora lo eliminaremos. En el sumatorio sobre el espacio real, la interacción de una partícula consigo misma es (self term):

$$E = E_1' + E_2 + \frac{1}{2}\frac{1}{4\pi\epsilon_0}\sum_i \frac{q_i^2 erfc(gr_{ii})}{r_{ii}} - \frac{1}{2}\sum_i \frac{q_i^2}{4\pi\epsilon_0 r_{ii}} \tag{4.15}$$

donde E'$_1$ es igual a E_1 pero sin el término r_{ii} para $l = 0$. Usando $erf(x) = 1 - erfc(x)$ cuando x tiende a cero obtenemos la expresión para la corrección a la energía Coulómbica mediante las sumas de Ewald:

$$U_{coul} = \frac{1}{2}{\sum_{l=0}}' \sum_i^{N_q}\sum_j^{N_q} \frac{q_i q_j}{4\pi\epsilon_0}\frac{erfc(gr_{ij})}{r_{ij}} \tag{4.16}$$

$$+ \frac{1}{2}\sum_{\mathbf{G}}^{N_k} \frac{4\pi V_c}{4\pi\epsilon_0}\frac{exp(-G^2/(4g^2))}{G^2}|\rho(\mathbf{G})|^2 \tag{4.17}$$

$$- \frac{1}{4\pi\epsilon_0}\sum_i^{N_q}\frac{gq_i^2}{\sqrt{\pi}} \tag{4.18}$$

Donde V_c es el volumen de la caja de simulación, $\mathbf{G}$ es el vector del espacio recíproco de la red de cajas de simulación replicadas y N_k es el número de vectores k utilizados en el cálculo de la energía, g es un parámetro de apantallamiento ajustable, $\rho(\mathbf{G})$ equivale a $\sum_{i=1}^{N_q} q_i \exp(i\mathbf{G}\mathbf{r}_i)$ (siendo $\mathbf{r}_i$ las coordenadas en unidades de caja de simulación del punto de carga i, N_q es el número de centros de carga en el sistema, q representa la carga de un centro de interacción electrostática, r_{ij} representa la distancia entre dos centros cargados. La función $\mathrm{erfc}(x)$ es la complementaria de la función error ($1 - \mathrm{erf}(x)$). El radio de corte en espacio real (aplicable al primer término de 4.20) fue $r_c = 8.5$ Å y el parámetro de apantallamiento en espacio de fourier, $g = 1.1/\sigma$ (σ de la interacción LJ). La exploración de parámetros y el número de vectores del espacio recíproco considerado han de ser cuidadosamente escogidos para cada fase cristalina [97, 99]. g es un parámetro que no tiene sentido físico, se ha de optimizar para que la suma converja más rápidamente. Si g es grande, $erfc(gr_{ij})$ decae rápidamente pero exp(-G/4g^2) decae lentamente, y entonces es necesario considerar muchos vectores de espacio recíproco (N_k). Si g es pequeño, pocos vectores de espacio recíproco, pero muchos de espacio real. Es necesario por tanto un compromiso. Queda un último término por tratar, que se refiere a la energía intramolecular. En el caso de moléculas rígidas, el término de energía intramolecular es una constante, y podemos incluirlo al inicio de la simulación. Dado que la molécula de agua, descrita por estos modelos, está formada por varias cargas la contribución coulómbica se puede expresar como una constante dada por:

$$E_{intra} = -\sum_{i=1}^{N_m}\sum_{j=1}^{l-1}\sum_{m=j+1}^{l}\frac{q_{ij}q_{im}}{r_{jm}} \tag{4.19}$$

Con esto, la expresión final para las sumas de Ewald será:

$$\begin{aligned} U_{coul} &= \frac{1}{2}\sum_{l=0}^{'}\sum_{i}^{N_q}\sum_{j}^{N_q}\frac{q_i q_j}{4\pi\epsilon_0}\frac{erfc(gr_{ij})}{r_{ij}} \\ &+ \frac{1}{2}\sum_{\mathbf{G}}^{N_k}\frac{4\pi V_c}{4\pi\epsilon_0}\frac{exp(-G^2/(4g^2))}{G^2}|\rho(\mathbf{G})|^2 \\ &- \frac{1}{4\pi\epsilon_0}\sum_{i}^{N_q}\frac{gq_i^2}{\sqrt{\pi}} \\ &- \sum_{i=1}^{N_m}\sum_{j=1}^{l-1}\sum_{m=j+1}^{l}\frac{q_{ij}q_{im}}{r_{jm}} \end{aligned} \tag{4.20}$$

donde el primer término corresponde a la contribución real, el segundo es la contribución del espacio recíproco, el tercero es el *self-term* y el último la contribución coulómbica intramolecular.

4.6. Método de Monte Carlo

Esencialmente, el método de Monte Carlo se emplea para generar, mediante el movimiento aleatorio de las partículas del sistema, configuraciones que sigan la función de distribución del colectivo. Con estas configuraciones se podrán calcular las propiedades del sistema en dicho colectivo. Vamos a describir el método de Monte Carlo usando un sistema formado por moléculas en el colectivo NpT. Como dijimos anteriormente, en el caso de moléculas aparece un término extra en la función de partición del colectivo, la partición de función molecular (q). Además, se amplia el espacio de fases, ya que ahora las moléculas además de posiciones ($\mathbf{r}^N$) y momentos ($\mathbf{p}^N$) tienen una orientación (ω^N). Así, la función de partición en el colectivo NpT para un sistema formado por moléculas vendrá dada por:

$$Q(N,p,T) = \frac{q^N\beta p}{N!}\int \exp(-\beta PV)V^N dV \int \exp[-\beta U(\vec{s}_1,\omega_1,...,\vec{s}_N,\omega_N;L)]d_1 d_2 ... d_N \tag{4.21}$$

donde $\beta = 1/(k_B T)$, U es la energía intermolecular del sistema, q es la función de partición molecular, $\vec{s}_i$ las coordenadas de la partícula i (x_i, y_i, z_i) en unidades de la caja de simulación (divididas por la longitud del lado de la caja de simulación, L), ω_i las coordenadas angulares normalizadas de la molécula i y el elemento diferencial d_i corresponde a $ds_{xi}ds_{yi}ds_{zi}d\omega_i$. La función de partición molecular, cuando los grados de libertad translacionales y rotacionales pueden tratarse clásicamente, el estado fundamental electrónico es no degenerado, la diferencia de energía con el primer estado electrónico excitado es alta y el análisis del movimiento nuclear puede hacerse en términos de coordenadas normales, viene dada por [93]:

$$q = q_{t'} q_r q_v q_e \tag{4.22}$$

$$q = \left[\left(\frac{2\pi m k_B T}{h^2}\right)^{3/2}\right]\left[\frac{(2\pi k_B T)^{3/2}\Omega(I_1 I_2 I_3)^{1/2}}{s h^3}\right]\left[\prod_j \frac{\exp(-\beta h\nu_j/2)}{1-\exp(\beta h\nu_j)}\right]\left[e^{-\beta D_e}\right],$$

que es el productorio de las funciones de partición translacional dividida por el volumen ($q_{t'}$), rotacional (q_r), vibracional (q_v) y electrónica (q_e) respectivamente. Aquí m es la masa de la molécula, h la constante de Plank, s el número de simetría rotacional, que para el agua vale

2, I_1, I_2, I_3 los momentos principales de inercia, ν_j las frecuencias de los modos normales de vibración, D_e la energía de disociación espectroscópica de la configuración nuclear de equilibrio y Ω el factor de normalización de las coordenadas Ω_i que definen la orientación molecular. Ω se calcula de la siguiente manera:

$$\Omega = \int d\Omega_i = 8\pi^2 \tag{4.23}$$

Ω_i pueden ser, por ejemplo, los ángulos de Euler. Las coordenadas angulares normalizadas se definen fácilmente como $\omega_i = \Omega_i/\Omega$. Los factores correspondientes a las funciones de partición rotacional, vibracional y electrónica de la ecuación 4.22 son adimensionales. El primer factor, que corresponde a la función de partición translacional dividida por el volumen, tiene dimensiones de inversa de longitud al cubo. En este trabajo se ha considerado arbitrariamente que las funciones de partición rotacional, vibracional y electrónica valen 1. De esta manera no obtendremos un valor absoluto para la energía libre, pero el equilibrio de fases no se ve afectado si las funciones de partición rotacional, vibracional y electrónica se hacen 1 en todas las fases consideradas. Del mismo modo, la función de partición translacional dividida por el volumen se igualará siempre a 1 Å^{-3}. Definimos aquí la longitud de onda térmica de de Broglie, Λ, como $q_{t'} = 1/\Lambda^3$, valiendo Λ, en nuestro caso, 1 Å.

Para especificar una configuración perteneciente al colectivo NpT, necesitamos conocer la posición y orientación de todas las moléculas del sistema, y el volumen del mismo. El valor de propiedades como la energía interna (U) o el volumen (V) de cada configuración fluctuará en torno a un valor medio una vez que el sistema se encuentre en equilibrio. El promedio de estas variables es lo que se obtiene como resultado de una simulación NpT. En el equilibrio una configuración 'i´ del colectivo NpT aparece con una probabilidad proporcional al factor de Boltzmann de la configuración en dicho colectivo:

$$P_i \propto \exp[-\beta(U_i + pV_i) + N\ln(V_i)] \tag{4.24}$$

donde V_i y U_i son el volumen y la energía interna de la configuración 'i' respectivamente. Para obtener las propiedades del sistema en equilibrio termodinámico, debemos hacer aparecer las configuraciones con una probabilidad proporcional a su factor de Boltzmann, lo que se consigue mediante el algoritmo de Monte Carlo propuesto por Metropolis *et al.* [9]. Esto permite calcular el promedio de una magnitud X como

$$X = \frac{\sum_{i=1}^{N_c} x_i}{N_c}, \tag{4.25}$$

donde N_c es el número de configuraciones que se generan a lo largo de la simulación y x_i es el valor de la magnitud X en la configuración i. En el algoritmo de Metrópolis las N_c configuraciones se generan haciendo cambios sucesivos a partir de una configuración inicial, que ha de ser representativa del sistema. Es decir, se debe muestrear de forma eficiente el espacio de fases. Para esto, en el algoritmo de Metrópolis, un cambio sobre la configuración i será aceptado de acuerdo a la siguiente probabilidad:

$$P_{acc} = \text{mín}\left(1, \frac{P_{i+1}}{P_i}\right). \tag{4.26}$$

El cociente de las probabilidades de aparición de las configuraciones $i+1$ e i en el colectivo NpT viene dado por el cociente de los factores de Boltzmann de las mismas:

$$\frac{P_{i+1}}{P_i} = \frac{\exp[-\beta(U_{i+1} + pV_{i+1}) + N\ln(V_{i+1})]}{\exp[-\beta(U_i + pV_i) + N\ln(V_i)]} \tag{4.27}$$

De acuerdo a la ecuación 4.26, si $P_{i+1} > P_i$, el cambio se acepta con probabilidad 1. Si $P_{i+1} < P_i$, el cambio se acepta con probabilidad P_{i+1}/P_i. En caso de rechazo, la configuración $i+1$ continuaría siendo igual a la i, y sus propiedades se cuentan de nuevo para el promedio que se hace a lo largo de la simulación según la ecuación 4.25. De esta manera solo muestreamos configuraciones del sistema que, además de seguir la distribución de Boltzmann, son significativas en el espacio de las fases.

El algoritmo de simulación Monte Carlo se lleva a cabo siguiendo el esquema:

1. Se evalúa el factor de Boltzmann de la configuración de partida (i).
2. Se elige una molécula del sistema al azar.
3. Se elige un tipo de movimiento que puede ser de translación, rotación o cualquier otro movimiento que sea representativo del espacio de fases (i.e cambio de volumen, movimientos especiales para el muestreo eficiente del espacio de fases).
4. Se realiza un desplazamiento aleatorio.
5. Se evalúa el factor de Boltzmann de la nueva configuración ($i+1$)
6. Se acepta o rechaza el cambio sobre la configuración i de acuerdo al criterio de Metropolis.
$$\frac{P_{i+1}}{P_i} = \frac{\exp[-\beta(U_{i+1} + pV_{i+1}) + N\ln(V_{i+1})]}{\exp[-\beta(U_i + pV_i) + N\ln(V_i)]} \tag{4.28}$$
7. Se actualizan los promedios del colectivo, se acepte o se rechace el movimiento.
8. Se vuelve al paso 2 con la configuración resultante como configuración i.

La evaluación de factores de Boltzmann es el corazón de una simulación. Fijémonos en todas las variables que aparecen en la exponencial de Boltzmann. La presión p y la temperatura T son constantes que se imponen en el colectivo NpT, y son iguales en todas las configuraciones. La energía interna de una configuración U se halla, en el caso de potenciales par-aditivos, como el sumatorio de la energía entre todos los pares de moléculas del sistema (ec. (4.2)). El volumen V de la configuración se halla muy fácilmente elevando al cubo el lado de la caja de simulación, si la caja es cúbica, o a partir del producto mixto de los vectores que definen la caja de simulación, en el caso de cajas no cúbicas. Los pasos 3 y 4 involucran el cambio de la configuración i para llegar a la $i+1$. Aquí es donde el método de Monte Carlo se muestra como una técnica tremendamente potente. Como ya hemos visto, la generación de configuraciones con un peso significativo en el espacio de fases es de vital importancia. Cuando estamos interesados en propiedades como la energía media del sistema o la densidad, basta con realizar movimientos de translación, rotación de las moléculas y cambios de volumen de la caja de simulación. Si las moléculas tuviesen grados de libertad internos habría que incluir movimientos para muestrear las configuraciones intramoleculares. Pero también es posible llevar a cabo movimientos “no naturales-del sistema con el objetivo de muestrear configuraciones del sistema que son difíciles de observar en una simulación (*rare events*). La tasa de aceptación de este tipo de movimientos es mucho menor que la de movimientos “naturales"del sistema. Movimientos de este tipo se han utilizado en esta tesis para muestrear el desorden de protón de hielos desordenados (ver sección 5.5).

Para rotar una molécula de agua se elegía un centro de interacción al azar sobre el que rotar. A continuación, se generaba un vector al azar con origen en el centro escogido en torno

al cual se giraba la molécula un ángulo comprendido entre $-\phi$ y ϕ. El desplazamiento angular máximo, ϕ, el desplazamiento máximo del centro de masas, δ, y el incremento máximo de los lados de la caja de simulación en los cambios de volumen, ϵ, se ajustaban en la parte de equilibrado de la simulación para que se aceptasen entre un 30 y un 40 % de los movimientos. Superado el equilibrado, los desplazamientos máximos se dejaban fijos durante la obtención de promedios.

Cuando se simulan sólidos, los parámetros de celda son función de estado. En este caso, es importante hacer no sólo cambios de volumen de la caja de simulación, sino también de la forma. Rahman y Parrinello hicieron una extensión del colectivo NpT, con dinámica molecular[101, 102], que nosotros hemos utilizado en su versión para Monte Carlo [103, 104], y que permite muestrear los ángulos formados entre las aristas de la caja de simulación, así como la relación entre sus longitudes. La caja de simulación viene definida por tres vectores (uno para cada lado) y el volumen por el producto mixto de ellos. Un movimiento de cambio de volumen significa modificar independiente las componentes de los tres vectores. Para ello, se le suma a cada componente un número escogido al azar entre $-\epsilon$ y $+\epsilon$, siendo ϵ un parámetro ajustado en el periodo de equilibrado para tener aceptaciones de cambios de volumen en torno al 40 %.

4.7. Dinámica Molecular

Generalmente, una simulación de dinámica molecular se realiza en un sistema de N moléculas en un volumen fijo V y una energía total fija E. Se asignan a las moléculas del sistema unas posiciones y velocidades iniciales, $\vec{r}_i(o)$ y $\vec{v}_i(o)$. Resolviendo las ecuaciones de Newton obtenemos las posiciones $\vec{r}_i(t)$, velocidades $\vec{v}_i(t)$, aceleraciones $\vec{a}_i(t)$, etc. en sucesivos tiempos.

Las moléculas interaccionan a través de un potencial $U(\vec{r}^{\,N})$. Así, para un sistema conservativo:

$$\vec{F}_i(t) = m_i\vec{a}_i(t) = -\frac{\partial\, U(\vec{r}^{\,N})}{\partial\vec{r}_i} \tag{4.29}$$

donde $\vec{F}_i$ es la fuerza actuando sobre la molécula i debido a las interacciones con las otras $(N-1)$ moléculas, $\partial/\partial\vec{r}_i$ es el gradiente con respecto a las coordenadas de la molécula i, y $\vec{r}^N$=$\vec{r}_1$,$\vec{r}_2$,...$\vec{r}_N$. Una vez calculadas las posiciones, velocidades, etc. a partir de la ecuación 4.29 a diferentes tiempos, las propiedades del sistema pueden ser evaluadas promediando las funciones microscópicas apropiadas.

Las ecuaciones del movimiento de Newton no se pueden resolver analíticamente pero sí numéricamente. Lo que se hace es ir evaluando la configuración (posición y velocidad) para cada paso de tiempo. Para integrar las ecuaciones de movimiento se utilizan distintos algoritmos. Uno de estos es el de Verlet. El algoritmo de Verlet está basado en el desarrollo en serie de Taylor de la forma:

$$\vec{r}(t+\delta\ t) = \vec{r}(t) + \vec{v}(t)\delta\ t + \frac{1}{2}\vec{a}(t)(\delta\ t)^2 \tag{4.30}$$

$$\vec{r}(t-\delta\ t) = \vec{r}(t) - \vec{v}(t)\delta\ t + \frac{1}{2}\vec{a}(t)(\delta\ t)^2 \tag{4.31}$$

Si se suman las dos expresiones se obtiene:

$$\vec{r}(t+\delta\ t) = 2\vec{r}(t) - \vec{r}(t-\delta\ t) + \vec{a}(t)(\delta\ t)^2 \tag{4.32}$$

Lo que nos indica que si sabemos donde está una cierta molécula y donde estuvo en el paso anterior, calculando la aceleración se puede estimar donde se encontrará en el paso siguiente.

$$\vec{a}_i = \frac{\vec{F}_i}{m_i} = \frac{-\frac{\partial\, U}{\partial \vec{r}_i}}{m_i} \tag{4.33}$$

δt debe ser muy pequeño para que se puedan resolver con exactitud las ecuaciones del movimiento. A efectos prácticos se suele utilizar $\delta\ t = 10^{-15} s$. Por último, la velocidad asociada a la molécula i se puede determinar a partir de:

$$\vec{v}(t) = \frac{\vec{r}(t+\delta t) - \vec{r}(t-\delta t)}{2\delta t} \tag{4.34}$$

Mediante el método de dinámica molecular se pueden calcular tanto propiedades termodinámicas (al igual que en Monte Carlo) como dinámicas. El colectivo natural de la dinámica molecular es el NVE. No obstante, es posible llevar a cabo simulaciones en otros colectivos mediante la introducción de términos adicionales en la ecuación 4.29, que nos permiten mantener otras variables del sistema constantes. Por ejemplo, en el caso de simulaciones en el colectivo canónico (NVT), la temperatura del sistema se mantiene constante mediante la utilización de un termostato, que nos permite el reescalado de las velocidades de las moléculas del sistema, a fin de que la temperatura del sistema sea constante. En el caso de simulaciones en el colectivo isotérmico–isobárico (NpT), además de un termostato para mantener la temperatura constante, es necesaria la utilización de un barostato que permita fluctuaciones de volumen del sistema, y así mantener la presión constante.

4.8. Modelos de potencial de agua

Ahora estamos en disposición de calcular propiedades promedio de un sistema. El único ingrediente que nos falta es definir las interacciones que existen entre los átomos o moléculas de nuestro sistema. El elemento central de esta tesis ha sido la molécula de agua, así que necesitamos un modelo de potencial para describir las interacciones entre moléculas de agua. Existe una gran variedad de modelos de agua dentro de la aproximación clásica que hemos estudiado. La utilización de cada uno de ellos depende del tipo de estudio. Los hay muy sencillos, como el de Molinero *et al.* [82], cuya principal ventaja es su reducido coste computacional; lo que permite llevar a cabo largas simulaciones de sistemas muy grandes. Otro tipo de modelos son los estudiados en esta tesis, rígidos y no polarizables, que representan una descripción un poco más realista de la molécula de agua, al incluir enlaces de hidrógeno (como una interacción coulómbica). En la Tabla 4.1 se dan los parámetros para varios de estos modelos de potencial de agua. A estos modelos realistas de agua se les puede incluir alguna característica más propia de la molécula de agua, como son la flexibilidad y la polarizabilidad. Esto permite estudiar el efecto de estas características en las propiedades del agua.

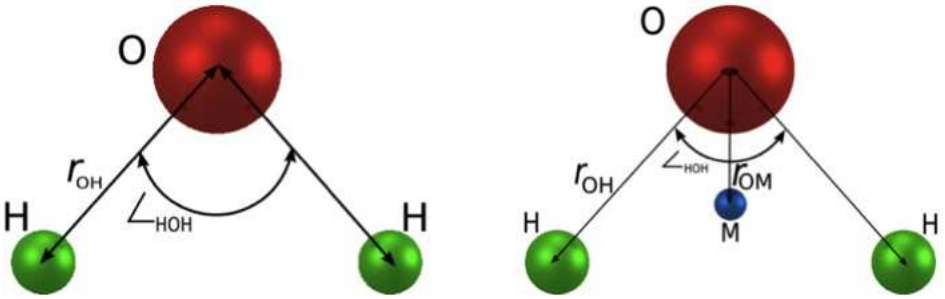

Figura 4.4: Representación esquemática de los modelos SPC/E y TIP4P. Los círculos verdes representan las esferas LJ. Los círculos negros los puntos de carga negativa y los círculos azules los de carga positiva. Las líneas representan los enlaces. Tomada de la Ref. [105].

En este trabajo nos hemos limitado al estudio de algunos modelos de potencial de agua rígidos y no polarizables. En la figura 4.4 se puede ver un esquema de los dos tipos de modelos de potencial más utilizados. Todos estos modelos, presentan un centro Lennard-Jones (LJ) sobre el átomo de oxígeno, y tienen cargas positivas sobre los átomos de hidrógeno. Las diferencias entre ellos están en la geometría de la molécula de agua y principalmente en la ubicación de la carga negativa.

En los modelos SPC, la carga negativa está localizada sobre el átomo de oxígeno y la positiva repartida entre los dos átomos de hidrógeno. No se emplean los valores experimentales de distancias O-H ni ángulos H-O-H; como distancias O-H se emplea 1 Å y para el ángulo formado por los hidrógenos se considera 109.5^{o} . Ambos modelos, SPC y SPC/E fueron propuestos por Berendsen [106]. La diferencia entre uno y otro radica en que la carga para el SPC/E es ligeramente mayor, porque supone que la energía de auto-polarización puede ser sumada a la energía interna del líquido cuando se ajustan los parámetros del potencial a la entalpía de vaporización del agua real[106].

En los modelos TIP, propuestos por Jorgensen [107], se emplean los valores experimentales de distancias O-H y ángulos H-O-H. Tienen un único sitio de interacción Lennard-Jones localizado en la posición del átomo de oxígeno. Las dos cargas puntuales positivas están situadas en las posiciones de los hidrógenos. La diferencia entre los modelos TIP4P, TIP5P y TIP3P radica en la ubicación de la carga negativa. En el modelo TIP4P [107] la carga negativa está localizada en un centro M, localizado a una distancia d_{OM} del átomo de oxígeno en la bisectriz del ángulo H-O-H en dirección a las cargas positivas. En el modelo TIP3P [107], la carga negativa se sitúa sobre el oxígeno. En el modelo TIP5P, propuesto en el 2000 por Mahoney y Jorgensen [108], la carga negativa se divide en dos cargas parciales en las posiciones de los “pares de electrones no enlazantes". Es similar al modelo ST2 [109] utilizado en los 70. Los parámetros de estos modelos han sido ajustados para reproducir determinadas propiedades termodinámicas del agua líquida. En general, estos modelos no son capaces de correctamente el máximo de densidad del agua ni el punto de fusión (el TIP5P sí)[110].

En los modelos TIP4P/Ew[111], TIP4P/2005 [34] y TIP4P/Ice [112], recientemente propuestos, los parámetros han sido ajustados para reproducir las propiedades en las que los otros modelos fallaban. En los modelos TIP4P/Ew y TIP4P/2005 los parámetros han sido ajustados para reproducir el máximo de densidad a presión ambiente del agua líquida en función de la temperatura y, en el TIP4P/Ice para reproducir la temperatura de fusión experimental.

Tabla 4.1: Parámetros de potencial para los distintos modelos de agua: Distancia entre oxígeno e hidrógenos (d_{OH}). Ángulo formado por los hidrógenos (H-O-H). El centro Lennard-Jones está localizado sobre el oxígeno con los parámetros σ y (ϵ/k). Carga del protón (q_H). Momento dipolar y cuadrupolar de la molécula de agua (μ y Q_T) en Debye y Debye por Å, respectivamente.

Modelo	d_{OH} (Å)	H-O-H	σ (Å)	(ϵ/k) (K)	q_H (e)	d_{OM} (Å)	d_{OL} (Å)	μ (D)	Q_T (D Å)
SPC	1.0	109.47	3.1656	78.20	0.41	0	-	2.274	1.969
SPC/E	1.0	109.47	3.1656	78.20	0.423	0	-	2.350	2.035
TIP3P	0.9572	104.52	3.1506	76.54	0.417	0	-	2.347	1.721
TIP4P	0.9572	104.52	3.1540	78.02	0.52	0.15	-	2.177	2.147
TIP4P/Ew	0.9572	104.52	3.1643	81.90	0.524	0.125	-	2.321	2.164
TIP4P/2005	0.9572	104.52	3.1589	93.2	0.5564	0.1546	-	2.305	2.297
TIP4P/ice	0.9572	104.52	3.1668	106.1	0.5897	0.1577	-	2.425	2.434
TIP5P	0.9572	104.52	3.1200	80.51	0.241	-	0.70	2.29	1.560

Respecto al coste computacional, los modelos SPC requieren la determinación de 9 distancias centro-centro, los TIP4P requieren 10 (9 distancias carga-carga y la interacción Lennard-Jones) y el modelo TIP5P necesita 17 (16 distancias carga-carga más la interacción Lennard-Jones). Esto quiere decir que el tiempo necesario para realizar una simulación escala como 9:10:17, respectivamente. Es decir, el TIP5P es aproximadamente el doble de costoso computacionalmente que el SPC. Los modelos TIP4P son un 10 % más caros computacionalmente que el SPC o SPC/E.

CAPÍTULO 5

Metodología

"*Reality leaves a lot to the imagination.*"
John Lennon

Mediante la simulación molecular tenemos acceso a las propiedades termodinámicas promedio del sistema. En ocasiones es necesaria la utilización de técnicas especiales para tener acceso a propiedades que no se pueden calcular de forma inmediata en una simulación. Uno de los objetivos principales de la simulación es el estudio de las transiciones de fase. Las técnicas que se emplean en el estudio de diagramas de fases dependen del carácter de la transición bajo estudio. En este trabajo nos hemos centrado en el estudio de transiciones de fase de primer orden, donde se suelen realizar cálculos de energía libre.

Experimentalmente, la localización de una transición de fase de primer orden es fácil: a la presión y temperatura de la transición, se observará como el sistema inicialmente homogéneo se separa en dos fases, divididas por una interfase. La estrategia a seguir sería, ir variando la presión y/o temperatura del sistema y esperar a que tenga lugar el cambio de fase. Pero en simulación este tipo de estudios no son aplicables para la gran mayoría de sistemas. Por ejemplo, si tenemos un bloque de hielo y queremos saber a que temperatura funde, podríamos ir calentando el sólido a lo largo de una simulación y comprobar a que temperatura funde. Esta forma de abordar el problema no suele tener éxito en simulación por ordenador. En simulación, las transiciones de fase de primer orden presentan histéresis, de manera que el sólido que estamos calentando fundiría a temperaturas por encima de la temperatura de fusión termodinámica. Esto es debido a que la barrera de energía libre que separa ambas fases es demasiado alta cerca de la coexistencia. La altura de la barrera viene dada por la energía libre de la interfase que separa ambas fases. Cuanto mayor es el área interfacial, mayor será la barrera de energía libre que separa ambas fases. Por este motivo el estudio de una transición de fase de primer orden se puede llevar a cabo de dos formas, simulando ambas fases en contacto a través de una interfase ya creada o eliminando la interfase, es decir, simulando ambas fases por separado. El primero se conoce como el método de coexistencia directa. En cambio, existen muchos enfoques posibles en estudios de coexistencia de fases en ausencia de interfase:

1. **Gibbs ensemble**. Se emplea en estudios de coexistencia entre fases fluidas. Se obtiene las propiedades de coexistencia en una única simulación. El sistema está formado por dos cajas separadas en equilibrio "químico´´ y mecánico.

2. **Integración termodinámica**. Permite el cálculo de diferencias de energía libre entre distintos estados del sistema, siempre que no se atraviesen transiciones de fase.

3. **Cristal de Einstein**. Cálculos de energía libre de sólidos.

4. **Simulaciones Gibbs-Duhem**. Se simulan las dos fases por separado y se obtienen las propiedades de coexistencia, conocido un punto inicial de coexistencia. Permite trazar líneas de coexistencia.

5.1. Cálculos de energía libre

Como hemos comentado al principio del capítulo, en simulación, para calcular las condiciones de coexistencia entre dos fases, no es posible modificar una variable termodinámica del sistema y esperar a observar el cambio de fase. Así que el enfoque en el estudio de equilibrio de fases debe ser distinto. Para una sustancia pura, dos fases están en equilibrio cuando sus presiones, temperaturas y potenciales químicos son iguales. El potencial químico del sistema no es una propiedad que pueda ser obtenida de forma directa en una simulación. Es necesario el uso de técnicas especiales. En esta sección estudiaremos las técnicas que se han utilizado en este trabajo para evaluar la energía libre de solidos y líquidos. En todos los casos la estrategia a seguir es similar. Calculamos la diferencia de energía libre entre el sistema de interés y un sistema de referencia, para el que conocemos, o es posible calcular de forma sencilla, su energía libre. Los estados de referencia usados han sido, el cristal de Einstein en el caso de sólidos y un fluido Lennard-Jones en el caso de líquidos. Una vez conocida la energía libre del sistema en unas condiciones de p y T, es posible calcularla para cualquier otro estado termodinámico de la misma fase mediante integración termodinámica.

5.1.1. Integración termodinámica

En la integración termodinámica se integra una cierta función a lo largo de un camino reversible para así obtener la diferencia de energía libre entre los dos estados elegidos. Esto nos permite calcular la diferencia de energía libre entre dos estados termodinámicos de una misma fase. Cuando las variables de integración son magnitudes termodinámicas del sistema como el volumen o la temperatura, es posible comparar con resultados experimentales. A este tipo de integración la denominaremos “no hamiltoniana”, debido a que el hamiltoniano del sistema no varía entre los estados inicial y final. Con la simulación podemos ir más lejos, puesto que es posible también manipular el hamiltoniano con que se describen las interacciones del sistema. De esta manera, los parámetros del potencial intermolecular se convierten en nuevas variables termodinámicas. Por tanto, mediante integración termodinámica se pueden calcular también diferencias de energía libre debidos a un cambio en los parámetros de interacción. A este tipo de integración la denominaremos “hamiltoniana”. A continuación se detalla el uso de ambas variantes de integración termodinámica.

Integración termodinámica no hamiltoniana

Esta variante permite obtener la energía libre en cualquier estado termodinámico de una fase a partir de la energía libre conocida en estado de referencia. Se calcula la diferencia de energía libre entre el estado final y el estado de referencia, de energía libre conocida, integrando la ecuación de estado (EOS) del sistema (obtenida mediante simulaciones NpT o NVT). Hemos utilizado tres tipos de integración termodinámica no hamiltoniana:

a) Cambio de energía libre a lo largo de una isoterma:
Una vez conocida la energía libre de Helmholtz a una densidad $\rho_1 = N/V_1$, podemos calcular la energía libre a otra densidad $\rho_2 = N/V_2$ a la misma temperatura.

De la expresión $dA = -SdT - pdV$ se tiene que

$$\left(\frac{\partial A}{\partial V}\right)_T = -p \tag{5.1}$$

Integrando la ecuación diferencial y dividiendo ambos miembros por Nk_BT se llega a:

$$\frac{A(\rho_2,T)}{Nk_BT} = \frac{A(\rho_1,T)}{Nk_BT} + \int_{\rho_1}^{\rho_2} \frac{p(\rho)}{k_BT\rho^2} d\rho \tag{5.2}$$

Esta es la expresión que utilizaremos para calcular A a la densidad ρ_2 -conocida la EOS- de una isoterma una vez conocida A en un punto de la misma a la densidad de referencia, ρ_1. El integrando se obtiene a partir de simulaciones NpT a distintas presiones a lo largo de una isoterma para tener $p(\rho)$. La función $p(\rho)/k_BT\rho^2$ se evalúa para cada una de las simulaciones y se ajusta a un polinomio en función de ρ, integrable analíticamente.

b) Cambio de energía libre a lo largo de una isóbara:
Nos permite obtener la energía libre de Gibbs a cualquier temperatura (o densidad) de una isóbara a partir de la energía libre conocida a una temperatura de referencia de la isóbara.

La energía libre de Gibbs dividida por la temperatura es

$$\frac{G}{T} = \frac{H}{T} - S \tag{5.3}$$

Diferenciando la expresión anterior

$$d\left(\frac{G}{T}\right) = \frac{1}{T}dH + Hd\left(\frac{1}{T}\right) - dS \tag{5.4}$$

Sustituyendo dH por $TdS + Vdp$ tenemos

$$d\left(\frac{G}{T}\right) = \frac{V}{T}dp + Hd\left(\frac{1}{T}\right) \tag{5.5}$$

Por lo que

$$\left(\frac{\partial(G/T)}{\partial(1/T)}\right)_p = H \tag{5.6}$$

O lo que es lo mismo

$$\left(\frac{\partial(G/T)}{\partial T}\right)_p = -\frac{H}{T^2} \tag{5.7}$$

Integrando la ecuación diferencial y dividiendo por Nk_B se obtiene

$$\frac{G(T_2,p)}{Nk_BT_2} = \frac{G(T_1,p)}{Nk_BT_1} - \int_{T_1}^{T_2} \frac{H(T)}{Nk_BT^2} dT \tag{5.8}$$

Que será la expresión utilizada en este tipo de integración termodinámica. La integral se resuelve haciendo simulaciones NpT a varias temperaturas a lo largo de una isóbara. Se evalúa el integrando a cada una de ellas (($U(T) + pV(T))/Nk_BT^2$) y se ajusta a un polinomio que será integrado analíticamente.

c) Cambio de energía libre a lo largo de una isócora:
Permite obtener la energía libre de Helmholtz a cualquier temperatura (o presión) de una isócora a partir de la energía libre conocida a una temperatura de dicha isócora.
La deducción es totalmente análoga a la integración en isóbaras, pero haciendo uso de A en lugar de G y de dU en lugar de dH. La expresión final queda:

$$\frac{A(T_2,V)}{Nk_BT_2} = \frac{A(T_1,V)}{Nk_BT_1} - \int_{T_1}^{T_2} \frac{U(T)}{Nk_BT^2} dT \tag{5.9}$$

El integrando se obtiene a partir de los resultados de varias simulaciones. En este caso se requiere hacer varios NVT a distintas temperaturas de una isocora. Se evalúa $U(T)/Nk_BT^2$ para cada una de ellas y los puntos se ajustan a un polinomio que se integra analíticamente.

Combinando estos tres tipos de integración termodinámica se puede conocer la energía libre en cualquier estado (p, V, T) a partir de la energía libre conocida en un estado de referencia. La única limitación de la integración termodinámica es que no puede haber cambios de fase en el camino de integración. En una transición de fase, el integrando de cualquiera de los tres tipos de integración termodinámica referidos presenta una discontinuidad. Por tanto, sólo nos podemos mover en los puntos del espacio (p, V, T) que correspondan al dominio de la fase cuya energía libre se conoce. La integración se puede extender a zonas de metaestabilidad, siempre y cuando la fase conserve su estabilidad mecánica. Esto permite, por ejemplo, obtener la energía libre del agua subenfriada, que se conserva largo tiempo en situación de equilibrio metaestable debido a la barrera de energía libre que separa el líquido subenfriado del sólido.

5.1.2. Integración termodinámica hamiltoniana

En este tipo de integración el hamiltoniano del sistema varía entre los estados inicial y final. La variable de integración será un parámetro λ de la función que describe el potencial de interacción del sistema ($U(\lambda)$). Este parámetro puede ser, por ejemplo, el valor de la carga de las moléculas o de σ o ϵ en el caso de una interacción Lennard-Jones. Más adelante aparecerán ejemplos concretos de $U(\lambda)$. Describamos ahora como se realiza la integración termodinámica hamiltoniana.

El parámetro λ es una variable termodinámica de la que depende la energía libre:

$$A(N, V, T, \lambda) = -k_B T \ln Q(N, V, T, \lambda). \tag{5.10}$$

$Q(N, V, T, \lambda)$ es la función de partición que viene dada por (ecuación 2.13):

$$Q(N, V, T, \lambda) = \frac{q^N}{N!} \int \exp[-\beta U(\lambda)] d1...dN \tag{5.11}$$

Derivando ambos miembros de 5.68 con respecto a λ se llega a la ecuación diferencial

$$\frac{\partial A(N, V, T, \lambda)}{\partial \lambda} = -k_B T \frac{\partial \ln Q(N, V, T, \lambda)}{\partial \lambda}. \tag{5.12}$$

La derivada con respecto a λ del logaritmo neperiano de $Q(N, V, T, \lambda)$ es:

$$\begin{aligned} \frac{\partial \ln Q(N, V, T, \lambda)}{\partial \lambda} &= \frac{1}{Q(N, V, T, \lambda)} \frac{\partial Q(N, V, T, \lambda)}{\partial \lambda} \\ &= \frac{-\beta \int [\partial U(\lambda)/\partial \lambda] \exp[-\beta U(\lambda)] d1...dN}{\int \exp[-\beta U(\lambda)] d1...dN} \\ &= -\beta \left\langle \frac{\partial U(\lambda)}{\partial \lambda} \right\rangle_{N,V,T,\lambda} \end{aligned} \tag{5.13}$$

Por lo que

$$\frac{\partial A(N, V, T, \lambda)}{\partial \lambda} = \left\langle \frac{\partial U(\lambda)}{\partial \lambda} \right\rangle_{N,V,T,\lambda}. \tag{5.14}$$

Integrando la ecuación diferencial queda

$$A(N,V,T,\lambda_1) - A(N,V,T,\lambda_0) = \int_{\lambda_0}^{\lambda_1} \left\langle \frac{\partial U(\lambda)}{\partial \lambda} \right\rangle_{N,V,T,\lambda} d\lambda, \tag{5.15}$$

que nos da la diferencia de energía libre de Helmholtz, por integración termodinámica, entre los estados (N,V,T,λ_1) y (N,V,T,λ_0). La integración se hace a N,V y T constantes. Si lo que se busca es la diferencia de energía libre de Gibbs, se obtiene una expresión análoga pero manteniendo N,p y T constantes:

$$G(N,p,T,\lambda_1) - G(N,p,T,\lambda_0) = \int_{\lambda_0}^{\lambda_1} \left\langle \frac{\partial U(\lambda)}{\partial \lambda} \right\rangle_{N,p,T,\lambda} d\lambda. \tag{5.16}$$

La integral 5.15 se resuelve numéricamente evaluando la función $\langle \partial U(\lambda)/\partial\lambda \rangle_{N,V,T,\lambda}$ para distintos valores de λ utilizando simulaciones en el colectivo NVT. El integrando es, por tanto, una función que se obtiene como promedio de las simulaciones. La diferencia de energías libres de Gibbs, ecuación (5.16), requiere la evaluación del integrando en el colectivo NpT.

Del mismo modo que en el caso no hamiltoniano, la integración hamiltoniana tiene la limitación de no poder atravesar transiciones de fase debido a que el integrando ($\langle \partial U(\lambda)/\partial\lambda \rangle$) sufriría una discontinuidad. Por tanto, hay que tener la cautela de asegurarse de que el cambio de hamiltoniano no supondrá un cambio de fases.

Si se conoce la energía libre en uno de los límites de integración (λ_1 ó λ_0), la energía libre en el otro límite puede obtenerse mediante integración termodinámica hamiltoniana. Este método ha sido muy utilizado en esta tesis. En efecto se ha utilizado para calcular la energía libre del agua líquida, de los haluros alcalinos en fase líquida, y de disoluciones de haluros alcalinos. Los métodos utilizados para el cálculo de la energía libre de fases sólidas también son casos particulares de integración termodinámica. En todos los casos, el hamiltoniano del sistema de interés se transformó en otro para el que la energía libre era conocida.

5.1.3. Energía libre de líquidos

Aunque la energía libre de un líquido puede calcularse utilizando varias rutas, en esta tesis la energía libre de todos los líquidos ha sido obtenida mediante integración termodinámica hamiltoniana (sección 5.1.2). Usando integración termodinámica hamiltoniana calculamos la diferencia de energía libre entre el sistema de interés y un sistema de referencia cuya energía libre es conocida. Tanto para evaluar la energía libre del agua líquida, como de haluros alcalinos en fase líquida o de disoluciones acuosas de iones, hemos escogido como referencia un fluido Lennard-Jones, cuya energía libre ha sido determinada por Johnson *et al.* [113] y Nezbeda *et al.* [114].

El camino que conecta el fluido bajo estudio (B) con el de referencia (A) -un Lennard-Jones- se establece a través del siguiente hamiltoniano acoplado:

$$U(\lambda) = \lambda U_A + (1-\lambda) U_B. \tag{5.17}$$

Donde λ es un parámetro que varía entre 0 y 1. Cuando λ vale 0 el hamiltoniano es el del sistema de interés y cuando vale 1 es el del sistema de referencia. Nosotros hemos utilizado una función lineal de λ para definir el camino entre ambos sistemas (aunque no tiene por qué

ser así necesariamente). Según la ecuación 5.15, la diferencia de energía entre A y B vendrá dada por:

$$A_A(N,V,T) - A_B(N,V,T) = \int_0^1 \langle U_A - U_B \rangle_{N,V,T,\lambda} \, d\lambda. \tag{5.18}$$

Siendo $< U_A - U_B >_{N,V,T,\lambda}$ un promedio que puede evaluarse en simulaciones de tipo NVT con un valor determinado de λ. La integral se evalua determinando numéricamente el integrando para distintos valores de λ comprendidos entre 0 y 1.

Como ya se ha comentado en la sección 5.1.1, un aspecto crucial a tener en cuenta cuando se hace integración termodinámica es que no se pueden atravesar transiciones de fase en el camino de integración. Por ello, hay que asegurarse de que en las condiciones N, V, T en las que se hace la integración, tanto el sistema de interés como el Lennard-Jones de referencia están en fase líquida. Esto determina la elección de los parámetros σ y ϵ del sistema Lennard-Jones de referencia. Habitualmente la elección de σ y ϵ se hizo para garantizar que $\rho\sigma^3 \approx 1$ y $T^* = \frac{T}{\frac{\epsilon}{k_B}} \approx 2 - 4$, lo que garantiza que el sistema LJ esta en fase líquida.

5.1.4. Energía libre de sólidos

El cálculo de energía libre de sólidos ha tenido una importancia central en el desarrollo de esta tesis. Buena parte del trabajo realizado se ha centrado en el equilibrio de fases sólido-líquido del agua. Esta metodología también ha sido utilizada en la determinación de temperaturas de fusión y solubilidad del NaCl. En ambos casos se ha empleado el método del cristal de Einstein.

En la región de altas presiones del diagrama de fases del agua encontramos dos fases de cristal plástico para varios modelos de potencial de agua (Capítulos 7 y 8). El método del cristal de Einstein no es aplicable a sólidos con desorden orientacional, así que en esta tesis extendimos el método del cristal de Einstein para el cálculo de energías libres de sólidos con desorden orientacional, como cristales plásticos. Este método se describe en las siguientes secciones.

En hielos con desorden de protón es posible aplicar el método del cristal de Einstein, ya que calculamos la energía libre de una única configuración de enlaces de hidrógeno. Como hemos visto en la sección anterior 5.5, las transiciones entre distintas configuraciones desordenadas no tienen lugar en simulaciones tipo Metropolis. Aquí la clave es calcular la energía libre para una configuración representativa del sistema y luego corregir el resultado con la entropía de Pauling, que corresponde a la entropía debida al desorden de protón. En un futuro sería tremendamente interesante extender el método del cristal de Einstein para el cálculo de energías libre de hielos desordenados de protón, muestreando las posibles configuraciones de enlaces de hidrógeno con el algoritmo de rotación de anillos.

Cristal de Einstein

Este método, propuesto por Frenkel y Ladd en 1984 [115], se ha convertido en un procedimiento muy empleado en el cálculo de energía libre de sólidos [61, 116–125]. La filosofía consiste en utilizar un cristal de Einstein como sistema de referencia y calcular la diferencia de energía libre entre el sistema de interés y el cristal de Einstein. Un cristal de Einstein es un

sólido en el que las unidades constituyentes (átomos o moléculas) están anclados a sus posiciones y orientaciones de equilibrio mediante un potencial armónico y en el que no existen interacciones intermoleculares. Su energía libre se puede calcular de manera analítica para sólidos atómicos y numérica para sólidos moleculares.

Por razones prácticas, que se aclararán más adelante, es conveniente utilizar como sistema de referencia un cristal de Einstein (Ein) que tenga el centro de masas fijo (CM). El camino que hay que recorrer desde el cristal de Einstein con el centro de masas fijo hasta el sólido de interés se puede describir como:

$$A_{sol} = A^{CM}_{Ein-id} + (A^{CM}_{Ein-sol} - A^{CM}_{Ein-id}) + (A^{CM}_{sol} - A^{CM}_{Ein-sol}) + (A_{sol} - A^{CM}_{sol}). \quad (5.19)$$

donde A^{CM}_{Ein-id} es la energía libre del sistema de referencia (cristal ideal de Einstein con el centro de masas fijo). La primera etapa consiste en determinar la diferencia de energía libre entre el cristal ideal de Einstein y el cristal de Einstein con interacciones, ambos con el CM fijo ($\Delta A_1 = A^{CM}_{Ein-sol} - A^{CM}_{Ein-id}$). En la segunda etapa ($\Delta A_2 = A^{CM}_{sol} - A^{CM}_{Ein-sol}$), los muelles del cristal de Einstein con interacciones son gradualmente desenchufados para obtener el sólido de interés (ambos con el centro de masas fijo). Finalmente, el sólido con el CM fijo se transforma en un sólido sin el centro de masas fijo ($\Delta A_3 = A_{sol} - A^{CM}_{sol}$). Podemos reescribir la ecuación 5.19 usando estas definiciones:

$$A_{sol} = A^{CM}_{Ein-id} + [\Delta A_1 + \Delta A_2] + \Delta A_3 \quad (5.20)$$

Veamos como se pueden calcular cada uno de los términos:

1. **Energía del cristal de Einstein con CM fijo.**

   En un cristal de Einstein las moléculas están ancladas a sus posiciones y orientaciones de red mediante unos muelles armónicos. Nos centraremos en el caso de moléculas rígidas no lineales. Aunque el campo traslacional siempre se aplica de la misma manera, la expresión para el campo orientacional depende de la geometría de la molécula a considerar. Aquí se describirá el procedimiento para una molécula con simetría C_{2v}, como es el caso del agua.

   La energía de un cristal ideal de Einstein viene dada por:

   $$U_{Ein-id} = U_{Ein-id,t} + U_{Ein,or} \quad (5.21)$$

   $$U_{Ein-id,t} = \sum_{i=1}^{N} \left[\Lambda_E (\mathbf{r}_i - \mathbf{r}_{io})^2\right] \quad (5.22)$$

   $$U_{Ein,or}(C_{2v}) = \sum_{i=1}^{N} u_{Ein,or,i} = \sum_{i=1}^{N} \left[\Lambda_{E,a} \sin^2(\psi_{a,i}) + \Lambda_{E,b} \left(\frac{\psi_{b,i}}{\pi}\right)^2\right] \quad (5.23)$$

   donde $\mathbf{r}_i$ representa la posición instantánea del punto de referencia de la molécula i, y $\mathbf{r}_{io}$ es la posición de equilibrio de este punto de referencia de la molécula i en el cristal ($\mathbf{r}_i$ fluctuará a lo largo de la simulación pero $\mathbf{r}_{io}$ no). Como hemos comentado, elegimos el CM de la molécula como punto de referencia. De hecho, la función de partición rotacional de la molécula q_r se calcula usando los momentos principales de inercia (I_1, I_2 y I_3) con origen en el centro de masas de la molécula. Las propiedades configuracionales no dependen del punto de referencia. Por este motivo, para calcular propiedades

configuracionales, hay un cierto grado de libertad en la elección del punto de referencia. Aunque la elección del punto de referencia es arbitraria, es conveniente para el cálculo de energías libres que todos los elementos de simetría de la molécula pasen a través del punto de referencia. El término $U_{Ein-id,t}$ de la ecuación 5.22 es un potencial armónico que tiende a mantener las partículas en sus posiciones de red ($\mathbf{r}_{io}$), mientras que $U_{Ein,or}$ representa el campo que fuerza a las moléculas a tomar una orientación determinada. Λ_E, $\Lambda_{E,a}$ y $\Lambda_{E,b}$ son las constantes de acoplamiento de los muelles (no confundir con la longitud de onda térmica de De Broglie Λ). $\Lambda_{E,a}$ y $\Lambda_{E,b}$ tienen unidades de energía y Λ_E de energía dividida por área. Los ángulos $\psi_{a,i}$ y $\psi_{b,i}$ están definidos en términos de dos vectores, $\mathbf{a}$ y $\mathbf{b}$, que especifican la orientación de la molécula. Más adelante, se explicarán en detalle estas dos contribuciones.

La función de partición del cristal ideal de Einstein en el colectivo NVT viene expresada como:

$$Q_{Ein-id} = \frac{1}{N!}\frac{1}{h^{3N}}(q_r q_v q_e)^N \int \exp\left[-\beta \sum_{i=1}^{N} \frac{\mathbf{p}_i^2}{2m_i}\right] d\mathbf{p}_1 ... d\mathbf{p}_N \int \exp\left[-\beta U_{Ein-id}\right] d1...dN \tag{5.24}$$

donde $\mathbf{p}_i = (p_{xi}, p_{yi}, p_{zi})$ representa el momento de la molécula i y $di = d\mathbf{r}_i d\omega_i$, siendo $\mathbf{r}_i$ el vector de posición del punto de referencia de la molécula i y ω_i sus coordenadas angulares normalizadas. La expresión matemática de las funciones de partición moleculares q_r, q_v y q_e se igualarán arbitrariamente a 1 (por lo que se omitirán en adelante). Esta elección no tiene efecto sobre la localización de las transiciones de fase puesto que es la misma para ambas fases.

En el método de Einstein, cada molécula se sitúa en un punto de red. Uno puede calcular energías libres para un sólido donde cada molécula se sitúe en un único punto de red. Sin embargo, no hay que olvidar que existen $N!$ permutaciones posibles. Así, la verdadera energía libre del sistema es aquella que se obtiene para un cierto campo donde cada molécula se sitúa en un punto de red multiplicado por el número de permutaciones posibles (es decir, $N!$). Por esta razón, la función de partición es:

$$Q_{Ein-id} = \frac{1}{h^{3N}} \int \exp\left[-\beta \sum_{i=1}^{N} \frac{\mathbf{p}_i^2}{2m_i}\right] d\mathbf{p}_1 ... d\mathbf{p}_N \int_{*} \exp\left[-\beta U_{Ein-id}\right] d1...dN \tag{5.25}$$

donde ahora la integral se calcula para una permutación dada (*).

La función de partición de un cristal ideal de Einstein con el centro de masas fijo Q_{Ein-id}^{CM}, puede escribirse como:

$$Q_{Ein-id}^{CM} = Q_{Ein,t}^{CM} Q_{Ein,or} \tag{5.26}$$

Finalmente, la energía libre del cristal ideal de Einstein (con el centro de masas fijo) vendrá dado por la suma de una contribución traslacional y otra orientacional:

$$\begin{aligned} A_{Ein-id}^{CM} &= A_{Ein,t}^{CM} + A_{Ein,or} \\ &= -k_B T \ln Q_{Ein,t}^{CM} - k_B T \ln Q_{Ein,or} \end{aligned} \tag{5.27}$$

a) Contribución traslacional: La parte traslacional de la función de partición del cristal de Einstein sin restricción alguna de la posición de su centro de masas viene dada por:

$$\begin{aligned} Q_{Ein,t}^{CM} &= \frac{1}{h^{3(N-1)}} \int \exp\left[-\beta \sum_{i=1}^{N} \frac{\mathbf{p}_i^2}{2m_i}\right] d\mathbf{p}_1 ... d\mathbf{p}_N \\ &\int \exp\left[-\beta \Lambda_E \sum_{i=1}^{N} (\mathbf{r}_i - \mathbf{r}_{io})^2\right] d\mathbf{r}_1 ... d\mathbf{r}_N \end{aligned} \tag{5.28}$$

Ahora imponemos la condición de fijar el CM de los puntos de referencia (oxígenos en el caso de molécula de agua). Esta restricción implica que su posición en cualquier instante no difiera de la inicial:

$$\begin{aligned} \mathbf{R}_{CM} - \mathbf{R}_{CMo} &= 0 \\ \sum_{i=1}^{N} \mu_i \mathbf{r}_i - \sum_{i=1}^{N} \mu_i \mathbf{r}_{io} &= 0 \\ \sum_{i=1}^{N} \mu_i (\mathbf{r}_i - \mathbf{r}_{io}) &= 0 \end{aligned} \tag{5.29}$$

Siendo $\mu_i = m_i / \sum_{i=1}^{N} m_i$, y m_i la masa de la partícula i. Derivando la expresión anterior con respecto al tiempo se obtiene la influencia del centro de masas fijo sobre los momentos de las partículas:

$$\sum_{i=1}^{N} \mathbf{p}_i = 0 \tag{5.30}$$

Incluyendo las restricciones, tanto a las posiciones como a los momentos, en la función de partición del cristal de Einstein se llega a la función de partición del cristal de Einstein con el centro de masas fijo:

$$\begin{aligned} Q_{Ein,t}^{CM} &= \frac{1}{h^{3(N-1)}} \int \exp\left[-\beta \sum_{i=1}^{N} \frac{\mathbf{p}_i^2}{2m_i}\right] \delta(\sum_{i=1}^{N} \mathbf{p}_i) d\mathbf{p}_1 ... d\mathbf{p}_N \\ &\int \exp\left[-\beta \Lambda_E \sum_{i=1}^{N} (\mathbf{r}_i - \mathbf{r}_{io})^2\right] \delta(\sum_{i=1}^{N} \frac{1}{N} (\mathbf{r}_i - \mathbf{r}_{io})) d\mathbf{r}_1 ... d\mathbf{r}_N \end{aligned} \tag{5.31}$$

La contribución traslacional a la energía libre del cristal de Einstein es $-k_B T \ln Q_{Ein}^{CM}$. La resolución de la integral $Q_{Ein,t}^{CM}$ se detalla en el apéndice J. El resultado es:

$$Q_{Ein,t}^{CM} = P^{CM} \left(\frac{\pi}{\beta \Lambda_E}\right)^{3(N-1)/2} (N)^{3/2} \tag{5.32}$$

donde P^{CM} es la parte de momentos de la función de partición del cristal de Einstein con el centro de masas fijo, que no se ha resuelto de manera explícita como la de posiciones porque se cancelará más adelante. La contribución traslacional a la energía libre de un cristal de Einstein con el centro de masas fijo es, por tanto:

$$A_{Ein,t}^{CM} = -k_B T \ln[P^{CM} \left(\frac{\pi}{\beta \Lambda_E}\right)^{3(N-1)/2} (N)^{3/2}] \tag{5.33}$$

b) Contribución orientacional: La restricción de fijar el centro de masas de los puntos de referencia no afecta a la parte de orientaciones de la integral configuracional debido a que la rotación de una molécula con respecto a un eje que pasa por su punto de referencia no supone un desplazamiento del punto de referencia. Así que la contribución orientacional a la función de partición total será independiente del punto de referencia:

$$Q_{Ein,or} = \left[\frac{1}{8\pi^2}\int \exp\left(-\beta u_{Ein,or}\right)\sin\theta d\phi d\theta d\gamma\right]^N \tag{5.34}$$

Para el caso concreto del agua con simetría C_{2v}, vendrá dada por:

$$Q_{Ein,or} = \left[\frac{1}{8\pi^2}\int \exp\left(-\beta\Lambda_{E,a}\sin^2\left(\psi_a\right) - \beta\Lambda_{E,b}\left(\frac{\psi_b}{\pi}\right)^2\right)\sin\theta d\theta d\phi d\chi\right]^N \tag{5.35}$$

El elemento diferencial de las coordenadas angulares normalizadas, ω_i, viene expresado por $d\omega_i = 1/(8\pi^2)\,\mathrm{sen}\,\theta_i d\theta_i d\phi_i d\chi_i$, siendo $8\pi^2$ el factor de normalización de los mismos. θ, ϕ y χ son los ángulos de Euler tal y como se definen en el libro de Gray y Gubbins [126]. (θ) varia entre 0 y π y (ϕ) y (χ) entre 0 y 2π. $\Lambda_{E,a}$ y $\Lambda_{E,b}$ son las constantes de acoplamiento de los muelles. $\psi_{a,i}$ se define como el ángulo formado por el vector $\mathbf{a}$ de la molécula i en una configuración determinada ($\mathbf{a}_i$) y el vector $\mathbf{a}$ de dicha molécula en su orientación de red ($\mathbf{a}_{i,o}$). $\psi_{b,i}$ se define de manera análoga pero con el vector $\mathbf{b}$ en lugar del $\mathbf{a}$. La definición de los vectores $\mathbf{a}$ y $\mathbf{b}$ se esquematiza en la figura 5.1. Los ángulos ψ_a y ψ_b se obtienen a través del producto escalar de los vectores $\mathbf{a}$ y $\mathbf{a}_{i,o}$, y $\mathbf{b}$ y $\mathbf{b}_{i,o}$ respectivamente:

$$\psi_{a,i} = \arccos\left(\frac{\vec{a}_i\cdot\vec{a}_{i,o}}{\mid\vec{a}_i\mid\cdot\mid\vec{a}_{i,o}\mid}\right) \tag{5.36}$$

$$\psi_{b,i} = \arccos\left(\frac{\vec{b}_i\cdot\vec{b}_{i,o}}{\mid\vec{b}_i\mid\cdot\mid\vec{b}_{i,o}\mid}\right) \tag{5.37}$$

por lo que $\psi_{a,i}$ y $\psi_{b,i}$ están definidos entre 0 y π. En este caso se representa una molécula rígida angular con un eje de simetría de orden $n = 2$. El vector $\mathbf{a}$ es la diferencia entre los vectores de enlace ($\mathbf{l}_2$ - $\mathbf{l}_1$) y el vector $\mathbf{b}$ es la suma. El potencial escogido para preservar la orientación del vector $\mathbf{a}$ respeta la simetría de la molécula, repitiéndose el valor del potencial con giros de π radianes (n=2). El valor de $\mathrm{sen}^2(\psi_{a,i})$ oscila entre 0 (cuando $\mathbf{a}_i$ es paralelo a $\mathbf{a}_{i,o}$) y 1 (cuando $\mathbf{a}_i$ es perpendicular a $\mathbf{a}_{i,o}$). El ángulo $\psi_{b,i}$ se divide por π para que también éste término oscile entre 0 (cuando $\mathbf{b}_i$ es paralelo a $\mathbf{b}_{i,o}$) y 1 (cuando $\mathbf{b}_i$ y $\mathbf{b}_{i,o}$ forman un ángulo de 180º) y tener así ambos muelles orientacionales compensados. Aunque se ha representado una molécula triatómica con un eje de simetría de orden 2, el esquema es válido para cualquier molécula rígida, bien sea no lineal o lineal (en cuyo caso se suprimirá el término de $\psi_{b,i}$). Basta con definir $\mathbf{a}$ y $\mathbf{b}$ a partir de dos vectores de enlace, teniendo el cuidado de colocar $\mathbf{a}$ perpendicular al eje de simetría de la molécula.

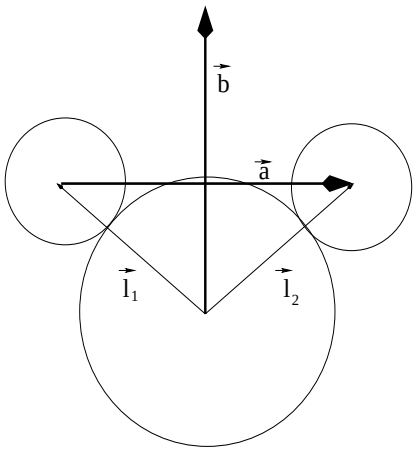

Figura 5.1: Definición de los vectores $\vec{a}$ y $\vec{b}$ en una molécula triatómica rígida con eje de simetría de orden 2. $\vec{a}$ es la resta de los vectores de enlace $\vec{l}_2$ y $\vec{l}_1$ y $\vec{b}$ es la suma.

Arbitrariamente, podemos hacer coincidir el vector $\mathbf{a}_{i,o}$ con el eje z, en cuyo caso el ángulo de Euler θ y el ψ_a son el mismo. Entonces la integral se puede redefinir como:

$$Q_{Eins,or} = \left(\frac{1}{8\pi^2} \int \exp\left(-\beta\Lambda_{E,a} \operatorname{sen}^2(\theta) - \beta\Lambda_{E,b} \left(\frac{\psi_b}{\pi} \right)^2 \right) \operatorname{sen}\theta d\theta d\phi d\chi \right)^N \quad (5.38)$$

El ángulo ψ_b, formado por el vector $\mathbf{b}$ y el $\mathbf{b}_o$ no se identifica, en principio, con ninguno de los ángulos de Euler, sino que es función de todos ellos. La integral resultante puede ser evaluada numéricamente utilizando integración Monte Carlo o a través de una aproximación analítica propuesta por Vega y Monson [127].

Finalmente, la energía libre del cristal de Einstein (con el centro de masas fijo) vendrá dado por la suma de una contribución traslacional y otra orientacional:

$$\begin{aligned} A_{Ein}^{CM} &= A_{Ein,t}^{CM} + A_{Ein,or} \\ &= -k_B T \ln Q_{Ein,t}^{CM} - k_B T \ln Q_{Ein,or} \end{aligned} \quad (5.39)$$

2. **Diferencia de energía libre entre el cristal de Einstein ideal y con interacciones (ΔA_1)**

   Ahora evaluaremos la diferencia de energía libre entre un cristal de Einstein ideal y el cristal de Einstein con las interacciones del sólido de interés, ambos con el centro de masas fijo. La diferencia de energía libre entre dos sistemas arbitrarios, que etiquetaremos como 1 y 2, viene dada por:

$$A_2 - A_1 = -k_B T \ln \frac{Q_2}{Q_1} = -k_B T \ln \frac{\int \exp(-\beta U_2) d1...dN}{\int \exp(-\beta U_1) d1...dN} \quad (5.40)$$

   Multiplicando y dividiendo el numerador del integrando por el factor $\exp(-\beta U_1)$, se obtiene:

$$A_2 - A_1 = -k_B T \ln \left\langle \exp\left[-\beta(U_2 - U_1) \right] \right\rangle_1 \quad (5.41)$$

   donde $\left\langle \exp\left[-\beta(U_2 - U_1) \right] \right\rangle_1$ es un promedio sobre las configuraciones visitadas por el sistema 1. Tomando $U_2 = U_{Ein-id} + U_{sol}$ y $U_1 = U_{Ein-id}$ (siendo U_{sol} el potencial intermolecular del sólido), la expresión anterior se puede reescribir:

$$A_{Ein-sol}^{CM} - A_{Ein-id}^{CM} = -k_B T \ln \left\langle \exp\left[-\beta(U_{sol}) \right] \right\rangle_{Ein-id} \quad (5.42)$$

Luego hay que promediar $exp\left[-\beta(U_{sol})\right]$ a lo largo de las configuraciones de un cristal de Einstein. Esto se lleva a cabo en una simulación NVT con el centro de masas del sistema fijo. Normalmente, no es posible evaluar el cambio de energía libre según está expresado en la ecuación 5.42, debido a que el exponencial $exp(-\beta U_{sol})$ adopta generalmente valores altos que no pueden ser resueltos por el ordenador. Este problema se evita sumando y restando a la energía del sólido U_{sol} la energía de red U_{red}:

$$\Delta A_1 = A^{CM}_{Ein-sol} - A^{CM}_{Ein-id} = U_{red} - k_B T \ln \left\langle \exp\left[-\beta(U_{sol} - U_{red})\right]\right\rangle_{Ein-id} \quad (5.43)$$

que no presenta problemas de divergencia en la exponencial que se promedia.

Si los sistemas 1 y 2 no son muy similares, el sistema 2 visitará, con probabilidad baja, configuraciones energéticamente favorables para el sistema 1, que además tienen un elevado factor de Boltzman $\left\langle \exp\left[-\beta(U_2 - U_1)\right]\right\rangle_1$. Eso ocasionaría un gran error estadístico en la evaluación de la diferencia de energía libre. Por ello, los sistemas 1 y 2 tienen que ser lo más parecidos posible. Por otro lado, cuanto más grande sea la constante de acoplamiento del cristal de Einstein (Λ_E), más se parecerán las configuraciones propias del cristal de Einstein con interacciones a las del cristal de Einstein ideal. Cuando dicha constante tiende hacia el infinito, la energía promedio del sólido en el cristal de Einstein tiende a la energía de red (energía del sólido con todas las moléculas en sus posiciones y orientaciones de equilibrio). Sin embargo, cuanto más alta sea la constante, más largo será el camino termodinámico que va del sólido al cristal de Einstein con interacciones. Por tanto, hay que llegar a un compromiso para optimizar ambas etapas del cálculo de energía libre. Una elección conveniente para $\Lambda_{E,a}$ y $\Lambda_{E,b}$ es aquella que garantice un valor pequeño (alrededor de $0.02Nk_BT$) para el segundo término de la ecuación 5.43. Cuando esto sucede, ΔA_1 es bastante cercano a la energía de red U_{red}.

3. **Diferencia de energía entre el cristal de Einstein con interacciones y el sólido (ΔA_2)**

   En este apartado vamos a calcular la diferencia de energía libre entre el sólido de interés y un cristal de Einstein al que se le añaden las interacciones del sólido, ambos con el CM fijo. Para ellos definimos la energía del sistema en función de un parámetro de acoplamiento λ, de forma análoga a la integración termodinámica hamiltoniana (ver sección 5.1.2):

   $$U(\lambda) = \lambda U_{sol} + (1-\lambda)(U_{Ein-id} + U_{sol}) \quad (5.44)$$

   λ se define entre 0 y 1, así, cuando $\lambda = 0$ se tiene el sólido de Einstein y cuando $\lambda = 1$ obtienes el sólido de interés. La variación de λ es el equivalente matemático a ir desenchufando los muelles armónicos gradualmente. El cambio de energía libre a lo largo de este camino se expresa como:

   $$\begin{aligned} \Delta A_2 &= A(N,V,T,\lambda=1) - A(N,V,T,\lambda=0) = \\ &= \int_{\lambda=0}^{\lambda=1} \left\langle \frac{\partial U(\lambda)}{\partial \lambda} \right\rangle_{N,V,T,\lambda} d\lambda = \\ &= -\int_{\lambda=0}^{\lambda=1} \langle U_{Ein-id} \rangle_{N,V,T,\lambda} \, d\lambda \end{aligned} \quad (5.45)$$

   Esta integral se resuelve numéricamente evaluando el integrando, obtenido en simulaciones NVT, para varios valores de λ. El valor efectivo de las constantes de fuerza de

los muelles en cada simulación viene expresado por $\lambda\Lambda_E$, $\lambda\Lambda_{E,a}$ y $\lambda\Lambda_{E,b}$. Hemos escogido el valor de dichas constantes de tal manera que $\Lambda_E = \Lambda_{E,a} = \Lambda_{E,b}$. Para valores de λ cercanos a 1, las partículas están fuertemente unidas a sus posiciones de red y el cristal tenderá a comportarse como un cristal de Einstein (sin verse afectado por las interacciones intermoleculares) cuya energía, U_{Ein-id}, vale $1/2k_BT$ por grado de libertad. Por el contrario, para valores bajos de λ, los muelles que unen las partículas a sus posiciones de red son muy débiles y, debido a que los átomos o moléculas del sólido podrán separarse mucho de su posición de equilibrio, la energía del cristal del Einstein será muy elevada. Por tanto, el integrando de 5.45 será grande a bajos valores de λ y muy pequeño a altos, lo que hace difícil la evaluación numérica de la integral. En realidad no hemos resuelto la integral 5.45 sino otra que surge como consecuencia de dos cambios de variable. En el primero cambiamos la variable de integración λ por $\lambda\Lambda_E$:

$$\Delta A_2 = A_{sol}^{CM} - A_{Ein-sol}^{CM} = -\int_0^{\Lambda_E} \frac{\langle U_{Ein-id}\rangle_{N,V,T,\lambda}}{\Lambda_E} d(\lambda\Lambda_E) \tag{5.46}$$

Y en el segundo cambiamos $\lambda\Lambda_E$ por $\ln(\lambda\Lambda_E + c)$, siendo c una constante:

$$\Delta A_2 = A_{sol}^{CM} - A_{Ein-sol}^{CM} = \Delta A_2 = -\int_{\ln(c)}^{\ln(\Lambda_E+c)} \frac{\langle U_{Ein-id}\rangle_{N,V,T,\lambda}\,(\lambda\Lambda_E + c)}{\Lambda_E} d(\ln(\lambda\Lambda_E + c)) \tag{5.47}$$

Este segundo cambio de variable es el que resuelve el problema del cambio brusco del integrando a lo largo del intervalo de integración; éste varía suavemente con $\ln(\lambda\Lambda_E + c)$. El integrando se evalúa para distintos valores de $\ln(\lambda\Lambda_E + c)$ distribuidos conforme a un algoritmo de integración gaussiana entre $\ln(c)$ y $\ln(\lambda\Lambda_E + c)$. Mediante simulación molecular se evalúa $< U_{Ein-id} >$ para cada uno de los valores de λ correspondientes a cada punto $\ln(\lambda\Lambda_E + c)$. Se puede apreciar cómo el segundo integrando varía más suavemente con su variable de integración que el primero. El valor utilizado para la constante c ha sido $\exp(3.5)$, tal y como recomiendan Frenkel y Ladd [115].

Si no se fijase el centro de masas, el cristal podría desplazarse como un bloque cuando λ tiende a cero, lo que ocasionaría valores de $< U_{Ein-id} >$ demasiado elevados. En ese caso, se haría necesario la evaluación del integrando en muchos valores de λ cercanos a cero para tener una buena estimación de la integral. Para conseguir un integrando más suave, el centro de masas se fija en la integración.

4. **Diferencia de energía libre entre el sólido y el sólido con el CM fijo (ΔA_3)**

La diferencia de energía libre entre dos sistemas viene dada por el logaritmo neperiano del cociente de las funciones de partición (Eq. 5.40):

$$\Delta A_3 = A_{sol} - A_{sol}^{CM} = -k_BT \ln \frac{Q_{sol}}{Q_{sol}^{CM}} = k_BT \ln \frac{Q_{sol}^{CM}}{Q_{sol}} \tag{5.48}$$

donde Q_{sol}^{CM} viene dado (después de integrar sobre los momentos) por:

$$Q_{sol}^{CM} = \frac{(q_r q_v q_e)^N}{N! h^{3(N-1)}} \int \exp\left[-\beta \sum_{i=1}^{N} \frac{\mathbf{p}_i^2}{2m_i}\right] \delta(\sum_{i=1}^{N} \mathbf{p}_i) d\mathbf{p}_1 ... d\mathbf{p}_N$$
$$\int \exp\left[-\beta U_{sol}(\mathbf{r}_1, \omega_1 ... \mathbf{r_N}, \omega_\mathbf{N})\right] \delta(\sum_{i=1}^{N} \mu_i(\mathbf{r}_i - \mathbf{r}_{io})) d\mathbf{r}_1 d\omega_1 ... d\mathbf{r}_N d\omega_N \tag{5.49}$$

y Q_{sol} viene dado por una expresión similar a Q_{sol}^{CM} pero sin las funciones delta (y con h^{3N} en el denominador en vez de $h^{3(N-1)}$). El factor $N!$ se cancela cuando se calculan energías libres, ya que aparece tanto en Q_{sol} como en Q_{sol}^{CM}. La integración sobre el espacio de momento del sólido sin ligaduras es simplemente la integral del producto de funciones gausianas, cuya solución es:

$$P = \left(\frac{2\pi m k_B T}{h^2}\right)^{(3N)/2} = \left(\frac{1}{\Lambda}\right)^{3N} \tag{5.50}$$

La integral sobre el espacio de momento del sólido con el centro de masas fijo es igual a la integral de los momentos del cristal ideal de Einstein con el centro de masas fijo, el cual se denota como P^{CM}. Sustituyendo las funciones de partición en la ecuación 5.48, se llega a la siguiente expresión:

$$\Delta A_3 = A_{sol} - A_{sol}^{CM} = k_B T \ln\left(\frac{P^{CM}}{P}\right) + \tag{5.51}$$

$$+k_B T \ln \frac{\int \exp\left[-\beta U_{sol}(\mathbf{r}_1, \omega_1 ... \mathbf{r_N}, \omega_\mathbf{N})\right] \delta(\sum_{i=1}^{N}(1/N)(\mathbf{r}_i - \mathbf{r}_{io}))d\mathbf{r}_1\omega_1 ... d\mathbf{r}_N\omega_N}{\int \exp\left[-\beta U_{sol}(\mathbf{r}_1, \omega_1, ..\mathbf{r_N}, \omega_\mathbf{N})\right] d\mathbf{r}_1 d\omega_1 ... d\mathbf{r}_N d\omega_N}$$

La energía de un sistema no se modifica si el sistema se traslada (mientras se mantengan fijas las orientaciones relativas de las moléculas). La consecuencia matemática de este hecho es que $U_{sol}(\mathbf{r}_1, \omega_1, ..\mathbf{r_N}, \omega_\mathbf{N})$ se puede reescribir como $U_{sol}(\omega_1, \mathbf{r}_2^{'}, \omega_2, ...\mathbf{r}_\mathbf{N}^{'}\omega_\mathbf{N})$ donde $\mathbf{r}_i^{'} = \mathbf{r}_i - \mathbf{r}_1$. Además, localizamos el centro de masas del punto de red en el origen del sistema de coordenadas tal que $\sum(1/N)\mathbf{r}_{io} = \mathbf{R}_{CMo} = 0$ y llevamos a cabo el cambio de variables de $\mathbf{r}_1, \mathbf{r}_2, ...\mathbf{r_N}$ a $\mathbf{r}_2^{'}, ...\mathbf{R_{CM}}$, donde $\mathbf{R}_{CM}$ es la posición del centro de masas de los puntos de referencia y, sabiendo que el Jacobiano de esta transformación es N, podemos obtener para el segundo término de la ecuación 5.52:

$$k_B T \ln \frac{\int \exp(-\beta U_{sol}(\omega_1, \mathbf{r}_2^{'}, \omega_2, \mathbf{r}_3^{'}, ...\mathbf{r}_\mathbf{N}^{'}, \omega_\mathbf{N}))\delta(\mathbf{R_{CM}})\mathbf{N}d\omega_\mathbf{1}d\mathbf{r}_\mathbf{2}^{'}d\omega_\mathbf{2}d\mathbf{r}_\mathbf{3}^{'}..d\mathbf{r}_\mathbf{N}^{'}d\omega_\mathbf{N}d\mathbf{R_{CM}}}{\int \exp(-\beta U_{sol})(\omega_1, \mathbf{r}_2^{'}, \omega_2, \mathbf{r}_3^{'}, ...\mathbf{r}_\mathbf{N}^{'}, \omega_\mathbf{N}))\mathbf{N}d\omega_\mathbf{1}d\mathbf{r}_\mathbf{2}^{'}d\omega_\mathbf{2}d\mathbf{r}_\mathbf{3}^{'}..d\mathbf{r}_\mathbf{N}^{'}d\omega_\mathbf{N}d\mathbf{R_{CM}}} \tag{5.52}$$

Después de integrar con respecto a $\omega_1\mathbf{r}_2^{'}\omega_2...\mathbf{r}_\mathbf{N}^{'}\omega_\mathbf{N}$ se obtiene:

$$k_B T \ln \frac{\int \delta(\mathbf{R}_{CM})d\mathbf{R}_{CM}}{\int d\mathbf{R}_{CM}} = k_B T \ln \frac{1}{\int d\mathbf{R}_{CM}} \tag{5.53}$$

La integral en el denominador de la ecuación 5.53 es el volumen disponible para el centro de masas. ¿Cuál es el valor de este volumen? Un interesante comentario ya lo apuntó explícitamente Wilding [128–131] en el que hacía referencia a que la traslación de un cristal como un bloque bajo condiciones de contorno periódicas genera N permutaciones entre las partículas. Cuando contamos el posible número de configuraciones usamos el valor de $N!$ para ir de la ecuación 5.24 a 5.25. De esta manera contamos todas las posibles permutaciones, así, la integral en el denominador de la ecuación 5.53 es el volumen disponible del centro de masas para una permutación dada. Este valor es simplemente V/N. Usando V en vez de (V/N) en el denominador de la ecuación 5.53 ya no sería correcto usar $N!$ para contar el número de permutaciones. En este supuesto, las permutaciones serían contadas dos veces, la primera vez por el factor $N!$, y la segunda debido a la traslación del cristal como un todo (en el volumen V). Por tanto, la expresión correcta que nos queda es:

$$\Delta A_3 = A_{sol} - A_{sol}^{CM} = k_B T\left[\ln(P^{CM}/P) - \ln(V/N)\right] \tag{5.54}$$

Como se puede ver, la expresión para ΔA_3 es general y no depende del potencial intermolecular U_{sol}. Nótese, que también sería correcto usar V en el denominador de la ecuación 5.53 (en el caso en el que el centro de masas se moviera en la totalidad de la caja de simulación) si se usa $(N-1)!$ para contar el número de permutaciones (es decir, contando todas las permutaciones obtenidas por la traslación del cristal bajo condiciones de contorno periódicas). En la ecuación 5.25, uno obtendría un término $(N-1)!/N!$, el cual proporciona un factor de $1/N$ que unido con el término $ln(1/V)$ de la ecuación 5.53 nos da un contribución de $-kTln(V/N)$ (idéntico al obtenido en la ecuación 5.54). Así, ΔA_3 tendrá un término de la forma $-kT\ln(V/N)$ si se consideran $N!$ permutaciones en $A^{CM}_{Eins-id}$ (como en los casos estudiados en el presente trabajo) o tendrá un término de la forma $-kT\ln(V)$ si se incluyen $(N-1)!$ permutaciones en $A^{CM}_{Eins-id}$. Para simplificar, se recomienda unificar en un único término $A^{CM}_{Eins-id}$ y ΔA_3 ya que ambos no dependen de la elección del número de permutaciones incluidas en $A^{CM}_{Eins-id}$.

5. **Expresión final**

$$\frac{A_{sol}}{Nk_BT} = -\frac{1}{N}\ln\left[\left(\frac{1}{\Lambda}\right)^{3N}\left(\frac{\pi}{\beta\Lambda_E}\right)^{3(N-1)/2}(N)^{3/2}\frac{V}{N}\right] + \frac{A_{Ein,or}}{Nk_BT}$$
$$+[\frac{U_o}{Nk_BT} - \frac{1}{N}\ln\langle\exp\left[-\beta(U_{sol}-U_o)\right]\rangle_{Ein}] - \int_{\lambda=0}^{\lambda=1}\left\langle\frac{U_{Ein^{CM}}}{Nk_BT}\right\rangle_{N,V,T,\lambda} d\lambda \quad (5.55)$$

Nótese que P^{CM} no aparece en la expresión final, lo que indica que su valor es irrelevante para el cálculo de energías libres. El término $A_{Ein,or}$ viene dado por la ecuación 5.38 y sólo aparece si estamos tratando con moléculas con grados de libertad orientacionales. El primer término es analítico, mientras que los dos últimos términos se calculan mediante simulación y representan a ΔA_1 y ΔA_2, respectivamente. Obsérvese cómo el argumento del logaritmo del primer término es adimensional: el primer factor (longitud de onda de De Broglie elevada a $3N$) tiene unidades de L^{-3N}, el segundo de $L^{3(N-1)}$ (Λ_E tiene unidades de energía dividida por área) y el tercero de L^3 (siendo L longitud). En nuestras simulaciones, las coordenadas $\mathbf{r}_i$ de las partículas vienen dadas en Å, por lo que Λ_E tiene unidades de Energía/Å^2. Por tanto, el volumen y la longitud de onda de De Broglie de 5.55 deben ser expresados en unidades de Å^3 y Å respectivamente.

Cristales plásticos

En el método del cristal de Einstein calculamos la energía libre de sólidos mediante la aplicación de dos campos externos; uno traslacional que obliga a las moléculas a permanecer en una posición determinada, y otro orientacional que fuerza a las moléculas a adoptar una orientación determinada. Sin embargo, la aplicación de esta metodología a un cristal plástico puede resultar problemática. A valores pequeños del campo orientacional se requieren simulaciones extremadamente largas para garantizar que las moléculas sean capaces de rotar como en un cristal plástico. Para evitar este problema hemos desarrollado en esta tesis un nuevo método para el cálculo de energías libres de cristales plásticos. Con esta nueva metodología evitamos conectar muelles orientacionales a las moléculas. La diferencia con el método del cristal de Einstein tradicional es que para cristales plásticos sólo se emplean muelles traslacionales. Este método fue inspirado en el método de Lindberg and Wang para

el cálculo de constantes dieléctricas de hielos [132].

Igual que para el método original, el sistema de referencia que se ha usado es un cristal de Einstein ideal con el centro de masas fijo. Vamos a describir los pasos para el cálculo de la energía libre de un cristal plástico:

1. **Energía libre de un cristal de Einstein ideal con muelles traslacionales ($A^{CM}_{Ein-id,t}$).** Como hemos visto, en un cristal de Einstein ideal las moléculas están ligadas a sus puntos de red mediante muelles armónicos. En cristales plásticos sólo se usan muelles traslacionales - y no orientacionales -, esto previene la aparición de transiciones a lo largo del camino de integración. La energía del cristal de Einstein vendrá dada por:

$$U_{Ein} = \sum_{i=1}^{N} \Lambda_E (\mathbf{r_i} - \mathbf{r_{i0}})^2 \tag{5.56}$$

donde $\mathbf{r}_i$ representa la localización instantánea de la molécula *i* y $\mathbf{r}_{i0}$ es la posición de equilibrio de la molécula *i*. U_{Ein} es la energía total del término armónico que ancla las moléculas a su posición de red. Λ_E es el parámetro de acoplamiento de los muelles traslacionales y tiene unidades de energía por longitud al cuadrado. La energía de un cristal de Einstein ideal con el centro de masas fijo y muelles traslacionales ($A^{CM}_{Ein-id,t}$) viene dado por[121, 133]:

$$\begin{aligned} A^{CM}_{Ein-id,t} &= -k_B T \ln Q^{CM}_{Ein,t} && (5.57) \\ &= -k_B T \ln[P^{CM} \left(\frac{\pi}{\beta \Lambda_E}\right)^{3(N-1)/2} (N)^{3/2}] && (5.58) \end{aligned}$$

equivalente a la ecuación (5.33).

2. **Diferencia de energía libre entre el cristal de Einstein ideal con muelles traslacionales y un cristal de Einstein con interacciones LJ (ΔA_1).**
Al cristal de Einstein ideal, se le incorporan interacciones intermoleculares en forma de un potencial Lennard-Jones (cuyos parámetros σ y ϵ son iguales a los del modelo de agual que se está considerando). La diferencia de energía libre entre el cristal de Einstein con interacciones LJ (A^{CM}_{Ein-LJ}) y el cristal de Einstein sin interacciones ($A^{CM}_{Ein-id,t}$), ambos con el CM fijo se obtiene de manera equivalente al método del cristal de Einstein clásico (sección 5.1.4):

$$\begin{aligned} \Delta A_1 &= A^{CM}_{Ein-LJ} - A^{CM}_{Ein-id,t} \\ &= U_{lattice} - k_B T \ln < exp[-\beta(U_{sol} - U_{lattice})] >_{Ein-id} && (5.59) \end{aligned}$$

donde $U_{lattice}$ es la energía del sistema cuando las moléculas están fijas a sus posiciones de red (energía de red de un LJ) y U_{sol} es la energía LJ del sistema para la configuración considerada. El promedio se lleva a cabo sobre las configuraciones generadas para un cristal de Einstein ideal.

3. **Diferencia de energía libre entre el cristal de Einstein con interacciones LJ y el cristal de Einstein con las interacciones del cristal plástico (ΔA_Q).**
Evaluaremos ahora la diferencia de energía libre entre un cristal de Einstein con interacciones dadas por el potencial de agua bajo estudio (i.e TIP4P/2005, SPC/E ..) y un cristal de Einstein con interacciones LJ, ambos con el CM fijo. Para evaluar esta diferencia de energía libre, las cargas del modelo de agua se van conectando de forma gradual, mientras se mantienen conectados los muelles traslacionales. El camino que conecta el sistema LJ con el modelo de agua se define como:

$$U(\lambda_Q) = (1-\lambda_Q)U_{LJ} + \lambda_Q U_{water} \tag{5.60}$$

$$\begin{aligned} \Delta A_Q &= A^{CM}_{Ein-sol} - A^{CM}_{Ein-LJ} \\ &= \int_0^1 \langle U_{water} - U_{LJ} \rangle_{N,V,T,\lambda_Q} \, d\lambda_Q \end{aligned} \tag{5.61}$$

donde <U$_{water}$-U$_{LJ}$>$_{N,V,T,\lambda_Q}$ se obtiene a partir de simulaciones NVT a distintos valores de λ_Q. Como sistema LJ de referencia escogemos un potencial con los mismos parámetros LJ que la parte LJ del modelo de agua. De esta manera, <U$_{water}$-U$_{LJ}$>$_{N,V,T,\lambda_Q}$ es simplemente la contribución coulómbica a la energía del potencial de agua U_Q, y la ecuación (8.6) se puede reescribir como:

$$\Delta A_Q = \int_0^1 \langle U_Q \rangle_{N,V,T,\lambda_Q} \, d\lambda_Q \tag{5.62}$$

Como no se usan muelles orientacionales, la moléculas son libres de rotar al principio (cuando $\lambda_Q = 0$) y al final de la integración (cuando $\lambda_Q = 1$) evitando las posibles transiciones de fase a lo largo del camino de integración. La integral se obtiene de numéricamente.

4. **Diferencia de energía libre entre el cristal de Einstein con las interacciones del cristal plástico y el cristal plástico (ΔA_2).**
Ahora, los muelles traslacionales se suprimen gradualmente, igual que para el método tradicional. El cambio de energía libre ΔA_2 entre las moléculas de agua sujetas a sus posiciones de red por muelles armónicos ($A^{CM}_{Ein-sol}$) y el cristal plástico sin muelles (ambos con CM fijo) viene dado por la ecuación (5.45). Igual que en el caso anterior, el integrando cambia varios ordenes de magnitud, por lo que es conveniente, desde el punto de vista numérico, hacer el cambio de variable de $\lambda\Lambda_E$ por ln($\lambda\Lambda_E$+c), donde c es una constante ($c = exp(3.5)$). Esto hace que el integrando sea mucho más suave. La expresión final para ΔA_2 es:

$$\Delta A_2 = -\int_{\ln(c)}^{\ln(\Lambda_E+c)} \frac{\langle U_{Ein-id} \rangle_{N,V,T,\lambda} \, (\lambda\Lambda_E + c)}{\Lambda_E} d(\ln(\lambda\Lambda_E + c)) \tag{5.63}$$

Fijando el CM hemos evitado la cuasi-divergencia del integrando en la ecuación (5.45) cuando λ tiende a cero. Sin esta ligadura, el integrando cambiaría abruptamente en este límite con lo que la evaluación del integrando sería difícil numéricamente.

5. **Diferencia de energía libre entre el cristal plástico con el CM fijo y sin ligaduras (ΔA_3).**
   En el último paso evaluamos la diferencia de energía libre entre el cristal plástico sin ligaduras y el cristal plástico con el centro de masas fijo. El cambio de energía libre de este paso (ΔA_3) se obtiene de la misma forma que para el método del cristal de Einstein, obteniéndose la ecuación (5.54). ΔA_3 no depende de la forma del potencial intermolecular U_{sol}.

La expresión final para la energía libre del cristal plástico es:

$$\begin{aligned} A_{sol} &= (A^{CM}_{Ein-id,t} + \Delta A_3) + \Delta A_1 + \Delta A_Q + \Delta A_2 \\ &= A_0 + \Delta A_1 + \Delta A_Q + \Delta A_2 \end{aligned} \tag{5.64}$$

Juntando los términos $A^{CM}_{Ein-id,t}$ y ΔA_3 (A_0), la contribución P^{CM} se cancela y la expresión final para la energía libre del cristal plástico es:

$$\begin{aligned} \frac{A_{sol}}{Nk_BT} &= -\frac{1}{N}\ln\left[\left(\frac{1}{\Lambda}\right)^{3N}\left(\frac{\pi}{\beta\Lambda_E}\right)^{3(N-1)/2}(N)^{3/2}\frac{V}{N}\right] \\ &+ \left[\frac{U_{lattice}}{Nk_BT} - \frac{1}{N}\ln\left\langle\exp\left[-\beta(U_{sol}-U_{lattice})\right]\right\rangle_{Ein-id}\right] \\ &+ \int_0^1 \left\langle\frac{U_Q}{Nk_BT}\right\rangle_{N,V,T,\lambda_Q} d\lambda_Q \\ &- \int_0^1 \left\langle\frac{U_{Ein-id}}{Nk_BT}\right\rangle_{N,V,T,\lambda} d\lambda \end{aligned} \tag{5.65}$$

5.1.5. Potencial químico de solutos

El equilibrio entre un sólido y una disolución de sus partículas ocurre cuando el potencial químico de las partículas en el sólido y el de las partículas en la disolución se igualan. La concentración a la que esto sucede se denomina solubilidad del sólido en el disolvente y depende de la p y T consideradas.

El método del cristal de Einstein nos permite resolver la primera parte del problema, el cálculo del potencial químico del soluto. El cálculo del potencial químico del sólido en disolución dependerá del tipo de soluto bajo estudio. En el caso de haluros alcalinos en agua el problema se vuelve tremendamente complejo. Además de todos los inconvenientes asociados al cálculo de energías libres, debemos mantener la electroneutralidad del sistema.

Ha habido pocos intentos de evaluar la solubilidad de haluros alcalinos en agua usando diferentes metodologías para el cálculo del potencial químico del soluto. Lynden-Bell *et al.* optaron por hacer un test de Widom [134] de las partículas sin carga por separado y luego, mediante integración termodinámica, calcular el trabajo para cargarlas [60]. Ferrario *et al.* [61] prefirieron convertir los iones, por separado, en partículas de gas ideal. Para mantener la electroneutralidad del sistema en el proceso de cargado se sirvieron de una matriz de carga homogénea opuesta a la de la partícula que se cargaba. Otros autores, prefieren cargar simultáneamente ambos iones para conservar la electroneutralidad [135]. Además, cuando se

carga una partícula en el sistema, hay que tener en cuenta que la interacción con sus imágenes periódicas puede acarrear efectos de tamaño finito que hay que corregir [136]. Más recientemente, Maginn *et al.* [64] y Lisal *et al.* [63], han calculado la solubilidad del NaCl en agua usando el método del colectivo ampliado (*expanded ensemble*) para evaluar la diferencia de potencial químico entre el soluto en disolución y en un estado de referencia. No hemos usado ninguna de las metodologías anteriores para el cálculo del potencial químico del soluto en disolución. Optamos por una aproximación más sencilla, propuesta por Sanz y Vega en el 2007 [137], basada en integración termodinámica hamiltoniana. A continuación se describe la metodología aplicada:

El potencial químico de una sal en disolución se define como:

$$\mu_{AX}^{solution} = \left(\frac{\partial G_{solution}}{\partial N_{AX}} \right)_{T,p,N_{H_2O}} \tag{5.66}$$

donde $G_{solution}$ es la energía libre de la disolución y N_{AX} el número de moléculas de la sal en disolución. Calculamos el potencial químico de la disolución a partir de la energía libre de varias disoluciones a distintas concentraciones de sal manteniendo constante el número de moléculas de agua constante. $G_{solution}$ viene dada por:

$$G_{solution} = A_{solution} + pV_{solution} \tag{5.67}$$

El término $pV_{solution}$ se puede obtener fácilmente en una simulación NpT para una presión, temperatura y composición dadas. La energía libre de Helmholtz de la disolución $A_{solution}$ se puede dividir, a su vez, en dos contribuciones: una residual ($A_{solution}^{res}$) y otra ideal ($A_{solution}^{id}$). Una propiedad termodinámica residual se define como la diferencia entre el valor de dicha propiedad termodinámica en el sistema bajo estudio y la que tendría un gas ideal a la *misma temperatura, densidad y composición*. Según esto, la energía libre de Gibbs puede formularse en términos de las contribuciones residual e ideal:

$$G_{solution} = A_{solution}^{id} + A_{solution}^{res} + pV_{solution} \tag{5.68}$$

$G_{solution}$ se puede calcular a partir de estas tres contribuciones. $A_{solution}^{res}$ la hemos calculado mediante integración termodinámica hamiltoniana desde un fluido Lennard-Jones de referencia (LJ,ref), para el que conocemos su energía libre residual [114], hasta nuestro sistema. En el camino de integración, tanto las moléculas de agua como los iones de la sal son transformados en partículas LJ. El camino de integración se establece a través del siguiente Hamiltoniano combinado:

$$U(\lambda) = \lambda U_{LJ,ref} + (1-\lambda)U \tag{5.69}$$

donde el parámetro de acoplamiento λ conecta el hamiltoniano del fluido LJ de referencia (λ=1) y el de la disolución (λ=0). Según esto, la energía libre residual de la disolución vendrá dada por:

$$A_{solution}^{res} = A_{LJ,ref}^{res} + \int_0^1 \langle U - U_{LJ,ref} \rangle_{N,V,T,\lambda} d\lambda \tag{5.70}$$

$\langle U - U_{LJ,ref} \rangle_{N,V,T,\lambda}$ se obtiene en simulaciones NVT para cada valor de λ, en simulaciones consecutivas, para ayudar al equilibrado del sistema. Puesto que vamos a calcular la solubilidad en condiciones normales de presión y temperatura, estas simulaciones deben realizarse a la densidad de equilibrio del sistema para cada composición, a la presión de 1 bar y T=298 K.

Para obtener $A_{solution}$, sumamos la contribución residual ($A^{res}_{solution}$) y la ideal. La energía libre de Helmholtz de un gas ideal formado por N_{H_2O} y N_{NaCl} viene dada por (taratado como una mezcla ternaria de H_2O, Na^+ y Cl^-):

$$\frac{A^{id}}{k_BT} = N_{H_2O} ln\left(\rho_{H2O}\Lambda^3_{H_2O}\right) + 2N_{NaCl} ln\left(\rho_{NaCl}\Lambda^3_{NaCl}\right) - N_{H_2O} - 2N_{NaCl} \qquad (5.71)$$

donde $\rho_i = \frac{N_i}{V}$. Por conveniencia, hemos tomado el valor de la función de onda térmica de De Broglie para todas las especies (Λ_i) como 1 Å . Esta elección implica que la densidad en la ecuación 11.11 debe ser dada en número de partículas por Å^3. La elección de $\Lambda = 1$ para la disolución es consistente con la hecha para la fase sólida. Una vez conocidas las tres contribuciones a $G_{solution}$ (Ec. 5.68), es posible calcular el potencial químico del NaCl en disolución. Se calculan las contribuciones de cada uno de los términos al potencial químico, es decir, $\mu^{solution,res}_{NaCl}$ y $\mu^{solution,id}_{NaCl}$ (incluimos el término pV en el término residual). $\mu^{solution,res}_{NaCl}$ se obtiene ajustando la suma $A^{res}_{solution}$ y $pV_{solution}$ a un polinomio cuadrático del número de moléculas de NaCl. Por tanto la contribución residual al potencial químico del NaCl es de la forma $\mu^{solution,res}_{NaCl} = (\frac{\partial G^{res}_{solution}}{\partial N_{NaCl}})_{T,p} = A + BN_{NaCl}$. La contribución de la parte ideal al potencial químico de NaCl en disolución se puede obtener de forma analítica (ver Apéndice K):

$$\mu^{id}_{NaCl} = \left(\frac{\partial A^{id}}{\partial N_{NaCl}}\right)_{T,p,N_{H_2O}} = 2ln(\rho_{NaCl}) - \bar{V}\left(\rho_{H_2O} + 2\rho_{NaCl}\right) \qquad (5.72)$$

donde $\bar{V}$ es el volumen molar parcial de NaCl ($\bar{V} = (\frac{\partial V}{\partial N_{NaCl}})_{T,p,N_{H_2O}}$). El potencial químico del NaCl en disolución se obtiene fácilmente sumando ambas contribuciones, ($\mu_{NaCl} = \mu^{solution,id}_{NaCl} + \mu^{solution,res}_{NaCl}$).

Los métodos anteriormente propuestos por otros autores buscaban obtener directamente el potencial químico del soluto. En el método aquí descrito se obtiene indirectamente a partir de cálculos de la energía libre de toda la disolución. Se evitan de esta manera los problemas de electroneutralidad e interacción entre imágenes periódicas que surgen cuando se cargan iones por separado.

5.2. Simulaciones Gibbs-Duhem

Hasta ahora hemos presentado todas las herramientas necesarias para hallar puntos de coexistencia. Sabemos cómo calcular la energía libre de un líquido y de un sólido y cómo, por integración termodinámica no hamiltoniana, obtener la energía libre en cualquier estado termodinámico de una fase. Un punto de coexistencia será aquel en el que nos encontremos con que dos fases a la misma presión y temperatura tenga el mismo potencial químico con un sistema monocomponente. Si nos interesa calcular diagramas de fase, no podemos conformarnos con un punto de coexistencia, sino que tenemos que ser capaces de obtener la línea de coexistencia completa. Se podría utilizar la integración termodinámica para seguir buscando puntos de coexistencia y trazar así la línea, pero ello supondría un esfuerzo ímprobo. En este apartado veremos cómo se resuelve el problema de manera muy sencilla.

5.2.1. Integración Gibbs-Duhem no hamiltoniana

Kofke, en el año 1993 cayó en la cuenta de la idoneidad de la ecuación de Clapeyron para calcular líneas de coexistencia a partir de un punto [138, 139]. Si dos fases coexisten, sus potenciales químicos (o energías libres de Gibbs por partícula para sustancias puras) son iguales. Se refieren con una letra minúscula a las magnitudes termodinámicas por partícula:

$$\begin{aligned} g_I &= g_{II} \\ dg_I &= dg_{II} \\ v_I dp - s_I dT &= v_{II} dp - s_{II} dT \end{aligned} \tag{5.73}$$

Reordenando se llega a la ecuación de Clapeyron:

$$\frac{dp}{dT} = \frac{s_{II} - s_I}{v_{II} - v_I} = \frac{h_{II} - h_I}{T(v_{II} - v_I)} \tag{5.74}$$

La integración de esta ecuación diferencial nos permite obtener, a partir de un punto inicial, toda la línea de coexistencia. La pendiente de la línea de coexistencia ($\Delta h/T\Delta v$) se obtiene mediante simulación de las fases I y II.

Desde un punto de vista práctico resulta muy conveniente la paralelización de las simulaciones: mientras un procesador calcula la entalpía y el volumen de la fase I, otro hace lo propio con la fase II. Finalizados los cálculos de ambos procesadores, se evalúa la pendiente juntando los resultados de las dos fases, se estima el siguiente punto p, T, y se vuelven a lanzar las simulaciones de cada una de las fases con las nuevas condiciones termodinámicas.

Tal y como está escrita la ecuación de Clapeyron (dp/dT) la temperatura es la variable independiente de la integración. Eso quiere decir que el algoritmo numérico va calculando las presiones de coexistencia para las temperaturas a las que nosotros queremos que lo haga. A efectos prácticos, a veces conviene invertir la ecuación y utilizar la presión como variable independiente. Si la pendiente de la línea de coexistencia, en una representación $p - T$, tiende a cero es más adecuado utilizar la temperatura como variable independiente, mientras que si tiende hacia infinito lo mejor es utilizar la presión:

$$\frac{dT}{dp} = \frac{T\Delta v}{\Delta h} \tag{5.75}$$

Para resolver las ecuaciones diferenciales (5.74) y (5.75) se ha utilizado el algoritmo de integración Runge-Kutta de cuarto orden.

5.2.2. Integración Gibbs-Duhem hamiltoniana

Si consideramos un parámetro del potencial, λ, como variable termodinámica, surge una nueva dimensión en el espacio de fases y se pueden deducir ecuaciones de Clapeyron generalizadas. Veamos cómo se obtienen. Para dos fases I y II que coexisten tenemos que

$$g_I(T, p, \lambda) = g_{II}(T, p, \lambda). \tag{5.76}$$

Diferenciando a ambos lados de la igualdad,

$$v_I dp - s_I dT + \left(\frac{\partial g_I}{\partial \lambda}\right) d\lambda = v_{II} dp - s_{II} dT + \left(\frac{\partial g_{II}}{\partial \lambda}\right) d\lambda, \tag{5.77}$$

aparece un nuevo término con respecto a la ecuación 5.73 debido a la nueva variable λ. Si consideramos λ constante, recuperamos la ecuación de Clapeyron original, que da la coexistencia en el plano $p-T$. Si lo que consideramos constante es la presión o la temperatura, se obtienen otras dos ecuaciones de Clapeyron. Con la presión constante, tenemos una ecuación que nos da la coexistencia en el plano $\lambda - T$ y con la temperatura constante en el λ, p. Veamos cómo queda la ecuación con la presión constante:

$$-s_I dT + \left(\frac{\partial g_I}{\partial \lambda}\right) d\lambda = -s_{II} dT + \left(\frac{\partial g_{II}}{\partial \lambda}\right) d\lambda \tag{5.78}$$

Reordenando:

$$\frac{dT}{d\lambda} = \frac{T[(\partial g_{II}/\partial \lambda) - (\partial g_I/\partial \lambda)]}{h_{II} - h_I} \tag{5.79}$$

Esta ecuación se puede integrar numéricamente. La entalpía se obtiene como promedio de una simulación NpT. De $\partial g/\partial \lambda$ ya hemos hablado en el apartado 5.1.2, donde se explicaba la integración termodinámica hamiltoniana. Es igual al promedio de la derivada del potencial con respecto al parámetro λ que hemos tomado como variable termodinámica:

$$\frac{\partial g}{\partial \lambda} = \left\langle \frac{\partial u(\lambda)}{\partial \lambda} \right\rangle_{N,p,T,\lambda}, \tag{5.80}$$

que se evalúa como promedio en una simulación NpT. La ecuación 5.78 queda:

$$\frac{dT}{d\lambda} = \frac{T(< \partial u_{II}(\lambda)/\partial \lambda >_{N,p,T,\lambda} - < \partial u_I(\lambda)/\partial \lambda >_{N,p,T,\lambda})}{h_{II} - h_I} \tag{5.81}$$

Si en lugar de a presión constante, trabajamos a temperatura constante, se llega a la siguiente ecuación de Clapeyron generalizada, que nos da la coexistencia en el plano $\lambda - p$:

$$\frac{dp}{d\lambda} = -\frac{< \partial u_{II}(\lambda)/\partial \lambda >_{N,p,T,\lambda} - < \partial u_I(\lambda)/\partial \lambda >_{N,p,T,\lambda}}{v_{II} - v_I} \tag{5.82}$$

Las expresiones 5.82 y 5.81 son ecuaciones diferenciales que se pueden integrar numéricamente. Nos dicen cómo varía la temperatura y la presión de coexistencia respectivamente con el parámetro del potencial de interacción λ. Esta herramienta es muy poderosa, pues permite evaluar la influencia de los parámetros del potencial sobre la coexistencia. Por ejemplo, uno podría estar interesado en saber cómo se ve afectada la temperatura de fusión por el valor de la carga de un modelo que describe las interacciones del agua; o cómo varía el punto de fusión de los haluros alcalinos si modificamos los parámetros Lennard-Jones que dan cuenta de las interacciones dispersivas. La integración Gibbs-Duhem hamiltoniana es tremendamente útil en el proceso de reparametrizado de modelos con el fin de mejorar las predicciones de equilibrio de fases de una sustancia real: es capaz de aislar, una por una, la influencia de cada uno de los parámetros del potencial sobre las propiedades de coexistencia [112].

Sin embargo, la utilidad de la integración Gibbs-Duhem hamiltoniana no acaba en analizar la influencia que tienen sobre la coexistencia los parámetros de un solo modelo. Si elegimos como λ un parámetro que conecta los potenciales de dos modelos, podremos calcular las propiedades de coexistencia de uno de ellos dadas las del otro:

$$U(\lambda) = \lambda U_B + (1-\lambda) U_A. \tag{5.83}$$

Si λ vale 0 tenemos el potencial del modelo A, mientras que si vale 1 tenemos el del modelo B. Las ecuaciones 5.81 y 5.82 quedan:

$$\frac{dT}{d\lambda} = \frac{T(< u_B - u_A >^{II}_{N,p,T,\lambda} - < u_B - u_A >^{I}_{N,p,T,\lambda})}{h_{II} - h_I} \tag{5.84}$$

$$\frac{dp}{d\lambda} = -\frac{< u_B - u_A >^{II}_{N,p,T,\lambda} - < u_B - u_A >^{I}_{N,p,T,\lambda}}{v_{II} - v_I} \tag{5.85}$$

Si se conoce el diagrama de fases del modelo A, se dispone de puntos $(T, \lambda = 0)$ para comenzar la integración numérica de la ecuación 5.81 que nos dará -para $\lambda = 1$- puntos del diagrama de fases del modelo B. De la misma manera se aplica la ecuación 5.82, pero esta vez haciendo la integración a temperatura constante y con puntos de partida $(p, \lambda = 0)$.

Integrar las ecuaciones 5.82 ó 5.81 significa estimar las pendientes, $dT/d\lambda$ o $dp/d\lambda$, mediante simulación. La diferencia con la integración Gibbs-Duhem no hamiltoniana es que ahora varía el hamiltoniano durante la integración. Como en el caso de la integración Gibbs-Duhem no hamiltoniana, una paralelización en la que un procesador se encarga de la fase I y otro de la fase II resulta óptima. Al final, las simulaciones de ambas fases juntan sus resultados para evaluar la pendiente y estimar, conforme al algoritmo de integración utilizado, el siguiente punto (T, λ) ó (p, λ). Para integrar estas ecuaciones hemos utilizado también un algoritmo Runge-Kutta de cuarto orden.

5.3. Coexistencia directa

Como vimos al principio del capítulo, en estudios de coexistencia de fases existen dos enfoques posibles. Acabamos de estudiar uno de ellos, que consiste en estimar la energía libre de cada una de las fases por separado, para luego calcular las condiciones y propiedades de coexistencia. Otro posible enfoque consiste en poner en contacto ambas fases a través de una interfase. La presencia de la interfase evita la aparición de histéresis, y las condiciones de coexistencia determinadas de esta forma corresponderán a las condiciones de equilibrio.

Esta técnica fue propuesta por Ladd y Woodcock en 1978 para el estudio del equilibrio líquido-sólido [140–142]. En la caja de simulación introdujeron las fases fluida y sólida en contacto a través de la interfase y llevaron a cabo simulaciones de dinámica molecular (MD) en el colectivo NVE hasta lograr el equilibrio de las dos fases en coexistencia. Pero lo resultados iniciales para un sistema Lennard-Jones no tuvieron mucho éxito. El sistema era muy pequeño y el tiempo de simulación demasiado corto, debido a las limitaciones computacionales de la época. En método se hecho más popular en los últimos años [143–145]. Además del estudio del equilibrio líquido-sólido, esta técnica puede ser utilizada para el estudio del equilibrio sólido-vapor y coexistencia de tres fases (sólido-líquido-vapor) [81, 146].

La técnica es de extrema sencillez. La única parte delicada es generar la interfase. Para ello, se ponen en contacto las dos fases a lo largo de alguno de los ejes de la caja de simulación. Esto va depender del plano cristalográfico del sólido que queramos poner en contacto con la fase fluida. La termodinámica no depende del plano cristalográfico expuesto, pero la cinética del proceso sí es sensible al plano expuesto a la fase fluida, y por tanto las propiedades de la interfase [147]. Para poder juntar ambas fases, deben tener el mismo área por el lado por el que se van a unir. Para ello, se hace un equilibrado previo a las condiciones

termodinámicas de interés de la fase sólida para conseguir una configuración a la densidad de equilibro (y por tanto la forma de la caja de simulación). Fundimos el sólido manteniendo la forma de la caja de equilibrio mediante un proceso no Markoviano [148] para obtener la fase líquida. Finalmente, unimos las cajas del sólido y del líquido a lo largo del eje elegido, dejando un espacio vacío entre ambas. De esta manera evitamos posibles solapamientos entre las moléculas de la interfase. Esta configuración se relaja en una simulación NVT, de manera que las moléculas de la fase fluida pasan a ocupar el espacio vacío.

Se pueden llevar a cabo simulaciones de Monte Carlo o de dinámica molecular (MD), los resultados son equivalentes. Mediante simulaciones MD se pueden calcular propiedades dinámicas como la velocidad de crecimiento cristalino. La técnica de coexistencia directa también puede usarse en los colectivos NVE, NVT, NpT y Np_zT. Cada colectivo presenta ventajas e inconvenientes. La elección del colectivo de simulación dependerá de la información que se quiera obtener. Solo hay dos de estos colectivos (NVE y NVT) para los que es posible alcanzar el equilibrio de dos fases en coexistencia. Para el estudio de propiedades interfaciales, sólo los colectivos que permitan alcanzar el equilibrio deben ser utilizados.

- *Colectivo NVE*. La idea es que el sistema evolucione hacia la temperatura y presión de equilibrio mediante el movimiento de la interfase (aumento de la la cantidad de sólido o de fluido). Si el sistema está por encima de la temperatura de fusión, el sólido fundirá, produciendo un descenso de la temperatura (la energía del sistema permanece constante). Si el sistema está por debajo de la temperatura de fusión, el fluido solidificará y la temperatura del sistema aumentará. La configuración inicial no debe estar alejada de la configuración de equilibrio para garantizar que quede algo de sólido o de fluido al final de la simulación. Al final de la simulación se obtendrán la temperatura y presión de equilibrio. Al no conocer la presión de equilibrio, el parámetro de red que se usa en el plano xy (que permanece constante a lo largo de toda la simulación) puede no corresponder al valor de equilibrio para el sólido a la presión de coexistencia. Y el estrés introducido modifica la energía libre del solido, y por tanto su temperatura de fusión.

- *Colectivo NVT*. El sistema evoluciona hacia el equilibrio mediante el cambio de la cantidad fase fluida o sólida. En este caso, se modifica la presión hasta los valores de coexistencia. La cantidad de calor desprendido o absorbido en la cristalización o fusión, es ajustado de forma inmediata por el termostato, y por tanto el equilibrio se alcanza más rápidamente que en simulaciones NVE. Es esta transferencia de calor con el termostato la que controla la velocidad de cristalización y fusión (suelen ser mayores que los valores experimentales). Igual que en el NVE, al sólido no se le permite que relaje en el plano xy, y el sistema podría presentar estrés.

- *Colectivo NpT*. En este tipo de simulaciones solucionamos los dos problemas mencionados anteriormente: la dificultad del sistema para alcanzar el equilibrio térmico (es decir, la lentidud en la transferencia de calor), y la posibilidad de estrés en el sólido. Se llevan a cabo simulaciones NpT anisotrópicas, en las que se permite que todos los lados de la caja de simulación varíen de forma independiente. Como el volumen puede fluctuar, el sólido es capaz de relajar hasta la configuración de equilibrio, y como la temperatura es fija, la transferencia de calor ocurre rápidamente gracias al termostato. El problema es que no es estrictamente correcto realizar simulaciones a presión cons-

tante en presencia de una interfase. Esto se debe a que las componentes tangencial y normal del tensor de presiones no son iguales. Sin embargo, si se elige un sistema suficientemente grande en la dirección perpendicular a la interfase, el error que se introduce debido a la presencia de la interfase será pequeño. Como la presión y temperatura permanecen fijas, no es posible tener una interfase en equilibrio. El procedimiento para determinar las propiedades de coexistencia es el siguiente. A una presión dada, se llevan a cabo varias simulaciones a diferentes temperaturas. Si la temperatura está por encima de la temperatura de fusión (T_f) el sólido fundirá, y la energía del sistema aumentará. Si por el contrario la temperatura está por debajo de la T_f, el líquido solidificará y la temperatura del sistema disminuirá. De esta manera es posible establecer un límite superior e inferior para la T_f.

- *Colectivo Np_zT*. Hemos mencionado antes que, debido a la interfase las componentes normal y tangencial del tensor de presiones son diferentes, y por tanto no es correcto realizar simulaciones a presión constante en presencia de una interfase. La forma correcta sería permitir cambios en la forma de la caja sólo a lo largo del eje normal a la interfase (en el caso de que la interfase sea paralela al plano-xy, sería el eje z). El procedimiento para determinar propiedades de coexistencia sería análogo al descrito anteriormente, sin embargo en este caso, es necesario preparar la configuración inicial para cada valor de p_z y T para eliminar la posible aparición de estrés a lo largo de las direcciones x e y.

5.4. Gibbs Ensemble

Hemos visto dos formas de abordar el estudio del equilibrio de fases usando la simulación por ordenador. Una indirecta, en la que se evalua la energía libre de cada fase independientemente. La razón por la que usamos esta forma indirecta en simulación es debido a que los sistemas que se estudian son demasiado pequeños. Si atacamos el problema de forma directa, simulando las dos fases en contacto a través de una interfase, la mayoría de las partículas del sistema se encontraran en la interfase o cerca de esta. La fracción de partículas en la interfase depende del tamaño del sistema, sistemas con menos de 1000 partículas están dominados por la interfase. Por tanto, debemos utilizar sistemas relativamente grandes (entre 1000-4000 partículas) para obtener propiedades de coexistencia fiables. El problema es que sistemas tan grandes requieren tiempos muy largos de equilibrado y el coste computacional es muy grande.

El método de *Gibbs ensemble*, propuesto por Panagiotopoulos [149], presenta las ventajas de los dos enfoques anteriores y pocas desventajas. Con este método el equilibrio de fases se puede estudiar con una única simulación, lo que implica una reducción significativa del tiempo de cálculo. La única desventaja es que su aplicación se limita a sistemas fluidos no muy densos. El método depende de que se consigan un número razonable de inserciones de partículas de una fase en otra que permita alcanzar el equilibrio. Una consecuencia de esto es que no es un método muy eficiente en el estudio de sistemas muy densos. Sin duda, la gran ventaja del método del *Gibbs ensemble* es que el sistema encuentra por si mismo las condiciones de de coexistencia entre las dos fases.

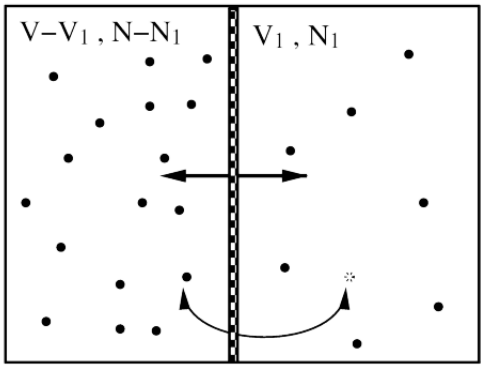

Figura 5.2: Representación esquemática del colectivo de Gibbs, el que un sistema formado por dos volúmenes V_1 y V_2 fluctúan de forma acoplada e intercambian partículas a través de una membrana permeable. El sistema global esta a N, V y T constantes. Tomada de la Ref. [97]

La condición de equilibrio entre dos o más fases (I, II, ...) es que la presión (P_I = P_{II} = ...), temperatura (T_I = T_{II} = ...) y potenciales químicos (μ_I^α = μ_{II}^α = ...) de todas las especies sean iguales. Por tanto, el mejor "colectivo´´ para el estudio de equilibrio de fases sería el μpT. Pero este no es un colectivo propiamente dicho. Un colectivo debe tener al menos una propiedad extensiva (V, N, ...) que permanezca constante. El método del *Gibbs ensemble* funciona porque aunque la *diferencia de potenciales químicos* entre las fases es constante nula, el valor absoluto está indeterminado. Del mismo modo, aunque implícitamente, se impone que la diferencia entre las presiones de las dos fases sea nula, el valor absoluto de p está indeterminado.

Veamos como se lleva a cabo una simulación en el colectivo de Gibbs. Imaginemos dos cajas de simulación separadas por una membrana permeable (Fig. 5.2). Las dos cajas se mantienen a T constante, el volumen total de las dos cajas también es constante, aunque la membrana puede desplazarse, es decir, el volumen de las cajas puede fluctuar de forma acoplada. El número de partículas del sistema también es una constante, aunque pueden atravesar la membrana, de manera que el número de partículas en cada caja varía a lo largo de la simulación. Según esto, los tipos de movimientos necesarios para muestrear el colectivo son 4: movimientos de traslación y rotación (en el caso de moléculas), cambios de volumen e intercambio de partículas entre las dos cajas del sistema (Fig. 5.3).

La función de partición de un sistema de N partículas distribuidas en dos volúmenes V_1 y $V_2 = V - V_1$, donde las partículas interaccionan unas con otras en el volumen 1 pero se comportan como un gas ideal en el volumen 2 ($U(\mathbf{r_2}^{N-n_1}) = 0$):

$$Q(N, V_1, V_2, T) = \sum_{n_1=0}^{N} \frac{V_1^{n_1}(V - V_1)^{N-n_1}}{\Lambda^{3N} n_1!(N - n_1)} \int d\mathbf{r_2}^{N-n_1} \int d\mathbf{r_1}^{n_1} exp(-\beta U(\mathbf{r_1}^{n_1})) \quad (5.86)$$

donde $\mathbf{r_i}$ representa la posición y orientación de la partícula i. Ahora, supongamos que las partículas de los volúmenes 1 y 2 poseen las mismas interacciones intermoleculares, y que los volúmenes V_1 y V_2 pueden variar de manera que el volumen total permanece constante

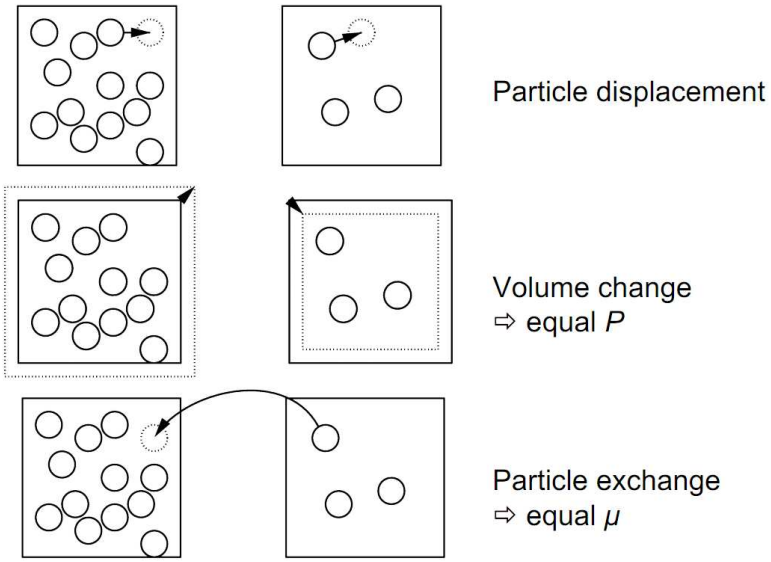

Figura 5.3: Representación esquemática de los movimientos que tienen lugar en el método de Gibbs ensemble. Movimientos de traslación, cambio de volumen e intercambio de partículas. Tomada de la Ref. [97]

($V = V_1 + V_2$). De esta manera, podemos integrar sobre el volumen V_1, y obtenemos la función de partición [97, 149, 150]:

$$\begin{aligned} Q_G(N,V,T) &\equiv \sum_{n_1=0}^{N} \frac{1}{V\Lambda^{3N} n_1!(N-n_1)} \int_0^V dV_1 V_1^{n_1} (V-V_1)^{N-n1} \\ &\times \int d\mathbf{r_1}^{n_1} exp(-\beta U(\mathbf{r_1}^{n_1})) \int d\mathbf{r_2}^{N-n_1} exp(-\beta U(\mathbf{r_2}^{N-n_1})) \end{aligned} \quad (5.87)$$

Con la función de partición del colectivo de Gibbs (ecuación (5.87)) podemos calcular cuál es la probabilidad de encontrar una configuración con n_1 partículas en la caja 1 con un volumen V_1, y posiciones ${r_1}^{n_1}$ y ${r_2}^{N-n_1}$:

$$P(n_1, V_1, \mathbf{r_1}^{n_1}, \mathbf{r_2}^{N-n_1}) \propto \frac{V_1^{n_1}(V-V_1)^{N-n_1}}{n_1!(N-n_1)} exp(-\beta(U(\mathbf{r_1}^{n_1}) + U(\mathbf{r_s}^{N-n_1}))) \quad (5.88)$$

a partir de la cual podemos derivar las reglas de aceptación para los intentos de movimiento en las simulaciones en el colectivo de Gibbs.

El esquema que se sigue en una simulación Gibbs ensemble es el siguiente (Fig. 5.3). Cada ciclo de Monte Carlo se elige aleatoriamente un tipo de movimiento a realizar:

1. **Desplazamiento aleatorio de una partícula en cada una de las cajas**.

   Este tipo de movimientos se realizan exactamente igual que en una simulación NVT, donde la probabilidad de aceptación viene dada por:

   $$acc(o \to n) = min(1, exp(-\beta(U(\mathbf{r_n}^{n_1}) - U(\mathbf{r_o}^{n_1})))) \quad (5.89)$$

   donde o es la configuración antes del movimiento y n después del movimiento.

2. **Cambio de volumen de manera que el volumen total del sistema permanezca constante**.

   Para un cambio de volumen de la caja 1 de ΔV, $V_1^n = V_1^o + \Delta V$, el ratio de pesos estadísticos de las configuraciones antes y después (superíndices o y n, respectivamente) viene dado por:

$$\frac{P(n)}{P(o)} = \frac{(V_1^n)^{n_1}(V - V_1^n)^{N-n_1}}{(V_1^o)^{n_1}(V - V_1^o)^{N-n_1}} \frac{exp[-\beta U(\mathbf{r_n}^N)]}{exp[-\beta U(\mathbf{r_o}^N)]} \tag{5.90}$$

   Imponiendo la condición de balance detallado obtenemos la regla de aceptación para el cambio de volumen:

$$acc(o \to n) = min\left(1, \frac{(V_1^n)^{n_1}(V - V_1^n)^{N-n_1}}{(V_1^o)^{n_1}(V - V_1^o)^{N-n_1}} exp([-\beta U(\mathbf{r_n}^N) - U(\mathbf{r_o}^N)]\right) \tag{5.91}$$

   Este tipo de movimientos se aplica de forma muy similar a una simulación NpT.

3. **Transferencia de una partícula al azar de una caja a otra**.

   Vamos a suponer que eliminamos una partícula de la caja 1 y la insertamos en la caja 2. El ratio de pesos estadísticos de las configuraciones viene dado por:

$$\frac{P(n)}{P(o)} = \frac{n_1!(N - n_1)!V_1^{n_1-1}(V - V_1)^{N-(n_1-1)}}{(n_1 - 1)!(N - (n_1 - 1))!V_1^{n_1}(V - V_1)^{N-n_1}} exp[-\beta U(\mathbf{r_n}^N) - U(\mathbf{r_o}^N)] \tag{5.92}$$

   e imponiendo la condición de balance detallado:

$$acc(o \to n) = min\left(1, \frac{n_1(V - V_1)}{(N - n_1 + 1)V_1} exp([-\beta U(\mathbf{r_n}^N) - U(\mathbf{r_o}^N)]\right) \tag{5.93}$$

   Esta etapa de transferencia de partículas es un proceso complicado. Cuando se inserta una partícula de forma aleatoria, es probable que solape con alguna otra del sistema, por lo que la energía de interacción sería muy grande y el movimiento sería rechazado (ec. (5.93)). De manera que la eficacia en el muestreo es muy pequeña. Esto es más complicado cuanto más denso es el sistema. Hay que ajustar los parámetros del sistema para hacer este muestreo lo más eficiente posible. En el caso del agua la inserción es todavía más compleja, porqué la molécula no sólo debe encontrar un hueco, también debe encontrar una orientación adecuada. Las interacciones en el agua, debido a la formación enlaces de hidrógeno son fuertemente direccionales. En el trabajo publicado en *Physical Review Letters* (Capítulo 10) calculamos el equilibrio líquido–vapor del agua en presencia de un campo eléctrico. Para mejorar la eficiencia en la inserción de moléculas de agua, combinamos las simulaciones de *Gibbs ensemble* con *configurational bias* [151]. El método *configurational bias* consiste en generar k posibles orientaciones para cada intento de inserción, y luego seleccionar una de ellas con una probabilidad dada por:

$$p(b_n) = \frac{exp[-\beta u^{or}(b_n)]}{\sum_{j=1}^{k} exp[-\beta u^{or}(b_n)]} \tag{5.94}$$

   donde b_n corresponde a una de las k posibles orientaciones y $u^{or}(b_n)$ es la energía que le corresponde a cada configuración. De esta manera aseguramos que la configuración energéticamente más favorable se escogerá con mayor probabilidad, y aumentamos la eficiencia en la inserción de moléculas de agua en fase líquida.

5.5. Movimientos de rotación de anillos

La mayoría de procesos moleculares tienen lugar en una escala de tiempos accesible a la simulación. Sin embargo, existen procesos que están fuera del alcance ya que los tiempos en los que tienen lugar son mucho más largos, se conocen como *"rare events´´*. En estos casos, también es necesario incluir movimientos especiales para poder muestrear correctamente el espacio de configuraciones. Un ejemplo de este tipo de movimientos, es la *rotación de anillos*. Este tipo de movimientos se ha empleado en esta tesis para el estudio del desorden de protón de hielos.

Como hemos visto, los hielos pueden clasificarse en dos familias: hielos en los que los protones están ordenados (hielos II, XI, IX, VIII, XIII, XIV), y aquellos en los que los protones están desordenados (I_h,I_c, III, V, VI, VII, IV, XII). En estos últimos, los oxígenos se sitúan en posiciones cristalográficas bien definidas, mientras que los hidrógenos pueden ocupar cualquiera de las generadas por las seis posibles orientaciones de las moléculas de agua en una red tetraédrica. Son, por tanto, cristales rotacionalmente desordenados, aunque el número de configuraciones posibles está limitado a aquellas que obedezcan las reglas de Bernal-Fowler [8]. Las posibles configuraciones desordenadas están separadas por barreras de energía grandes (del orden de dos enlaces de hidrógeno), y por tanto el muestreo de las orientaciones dentro del cristal es muy lento e ineficiente cuando se utilizan únicamente los movimientos convencionales de traslación y rotación. Las transiciones entre diferentes configuraciones desordenadas son *"rare events´´*. Chan *et al.* [152] calcularon que el tiempo de relajación para el hielo I_h a 250 K es de $168\ \mu s$, y Johari y Whalley [153] estimaron que, a 100 K este tiempo de relajación sería de varios años. Por esta razón, es necesario incluir movimientos especiales en la simulación para muestrear de forma eficiente las posibles configuraciones desordenadas de protón.

En el algoritmo de Metropolis estándard sólo se incorporan intentos de desplazamiento y de rotación. Estos movimientos solo muestrean pequeñas vibraciones de red, pero no son capaces de modificar la red de enlaces de hidrógenos impuesta al inicio de la simulación. Para muestrear correctamente el desorden de protón son necesarios movimientos colectivos de reorganización, que implican la rotación cooperativa de las moléculas de agua sobre un anillo. En esta tesis hemos implementado el algoritmo de rotación de anillos propuesto por Rick y Haymet [154], que es una extensión a modelos *off lattice* del algoritmo original propuesto por Stillinger y Rahman para modelos de red tetraédricos (tetrahedral lattice models) [155].

El algoritmo de rotación de anillos consta de dos pasos. El primero consiste en encontrar un anillo cerrado de enlaces de hidrógeno en el cristal mediante un camino aleatorio. El segundo paso consiste en generar nuevas posiciones para los protones mediante el cambio del patrón de enlaces de hidrógeno del anillo formado, imponiendo que se cumplan las reglas de Bernal-Fowler. El algoritmo se describe a continuación (Fig. 5.4):

1. Búsqueda de un anillo de enlaces de hidrógeno

   a) Se elige de forma aleatoria una molécula *i*.

   b) Se elige aleatoriamente una de las cuatro moléculas vecinas de *i*, por ejemplo la molécula *l*.

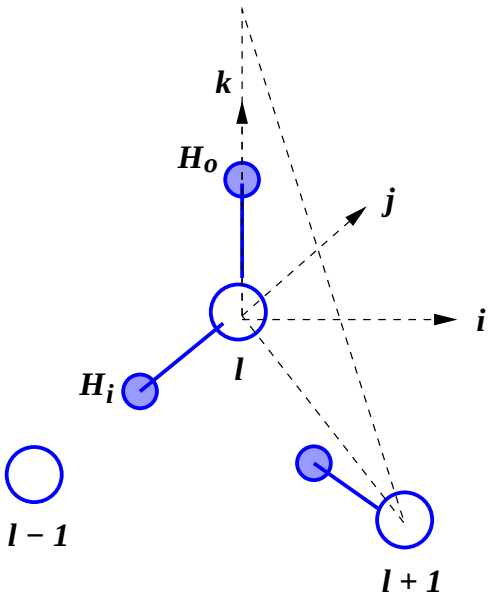

Figura 5.4: Representación esquemática de la rotación de anillos. H_i es el protón dador en el anillo que contiene los oxígenos $l-1$,l y $l+1$. La molécula *l* se rota sobre el vector **k** un ángulo τ, dado por el ángulo diedro entre los planos $H_o - O_l - O_{l-1}$ y $H_o - O_l - O_{l+1}$. De esta manera, el enlace $O_l - H_i$ que estaba contenido en el plano $H_o - O_l - O_{l-1}$, pasa a estar sobre el plano $H_o - O_l - O_{l+1}$. Tomada de la Ref. [156].

c) Si *l* forma un enlace de hidrógeno dador con *i*, entonces se elige aleatoriamente una de las dos moléculas vecinas de *l* que forman enlace de hidrógeno dador con *l*. Al contrario, si *l* forma enlace de hidrógeno aceptor con *i*, se escoge una de las dos vecinas de *l* que forman enlace aceptor con *l*.

d) Se continua este camino aleatorio hasta que encontremos la conexión entre dos moléculas del anillo (Fig. 5.5), no necesariamente con la primera molécula. En sistemas finitos, este camino puede cruzar la caja de simulación en algún punto. Con condiciones de contorno periódicas, el anillo se cierra con la imagen periódica de una de las moléculas del anillo (Fig. 5.6).

e) Se calcula la energía de las N moléculas del anillo antes del movimiento (E_a).

2. Generar nuevas posiciones para los protones

a) Cada molécula *l* del anillo de N moléculas se rota sobre el eje O_l-H_o, donde H_o es el hidrógeno que no forma enlace de hidrógeno con las moléculas de anillo. Las moléculas se rotan un ángulo τ.

b) El ángulo τ corresponde al ángulo diedro formado por los planos $H_o - O_l - O_{l-1}$ y $H_o - O_l - O_{l+1}$. De esta manera, el ángulo de rotación se acomoda instantáneamente a geometrías distorsionadas de la red.

c) Se calcula la energía de las N moléculas del anillo después del movimiento (E_b).

3. El movimiento se acepta o rechaza de acuerdo a Metropolis, la probabilidad de aceptación es igual a $min(1, e^-(E_b - E_a)/kT)$.

Este es el algoritmo original propuesto por Rick y Haymet. Nosotros hemos añadido un paso previo para optimizar la búsqueda de anillos. En simulaciones de hielos, las moléculas

de agua solo vibran en torno a su posición de red. Esto quiere decir que las moléculas vecinas a una dada son las mismas a lo largo de toda la simulación. Así, para reducir el coste computacional, antes de iniciar la simulación construimos una lista de los enlaces de hidrógeno dadores y aceptores de cada molécula de agua. Esta lista evita tener que calcular las moléculas vecinas y los enlaces dadores/aceptores durante la búsqueda de anillos. La lista se actualiza cada vez que se acepta un movimiento de rotación de anillo.

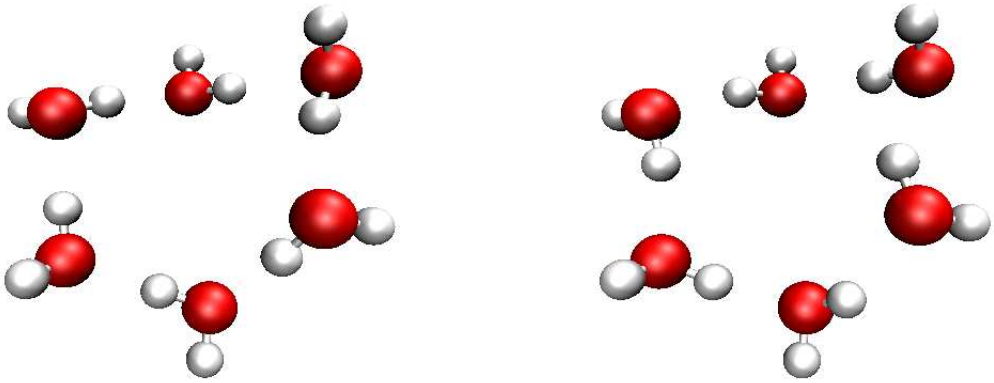

Figura 5.5: Anillo cerrado formado por seis moléculas de agua unidas mediante enlaces de hidrógeno antes del movimiento de rotación (izquierda) y después del movimiento de rotación (derecha).

La topología de los anillos que se pueden encontrar en un cristal fue estudiada por Rahman y Stillinger [155]. Los anillos que aparecen se pueden clasificar en tres tipos: (i) Anillos cerrados de seis moléculas (Fig. 5.5), (ii) Anillos cerrados de más de seis moléculas (Fig. 5.7) y (iii) Anillos percolantes (Fig. 5.6), aquellos que abarcan una dimensión lineal de la caja de simulación y son cerrados gracias a las condiciones de contorno periódicas. En principio todas las configuraciones con desorden de protón podrían ser visitadas. Pero la probabilidad de aceptación de las rotaciones de anillo es fuertemente dependiente del tamaño del anillo. La mayoría de anillos que se encuentran en un hielo I_h están formados por seis moléculas, para los que el ratio de aceptación es pequeño pero significativo. Al aumentar el número de moléculas en un anillo, la tasa de aceptación va disminuyendo. Esto es un problema en el caso de la evaluación de la constante dieléctrica, y en el estudio de transiciones entre fases ordenadas y desordenadas, ya que en ambos casos se requiere el muestreo de anillos percolantes. Este tipo de anillos involucran un elevado número de moléculas, ya que deben tener una extensión del orden de la longitud de la caja de simulación. Así, cuanto mayor sea el tamaño del sistema, menor será la tasa de aceptación de este tipo de movimientos. Por eso conviene utilizar sistemas no demasiado grandes en el estudio de la constante dieléctrica.

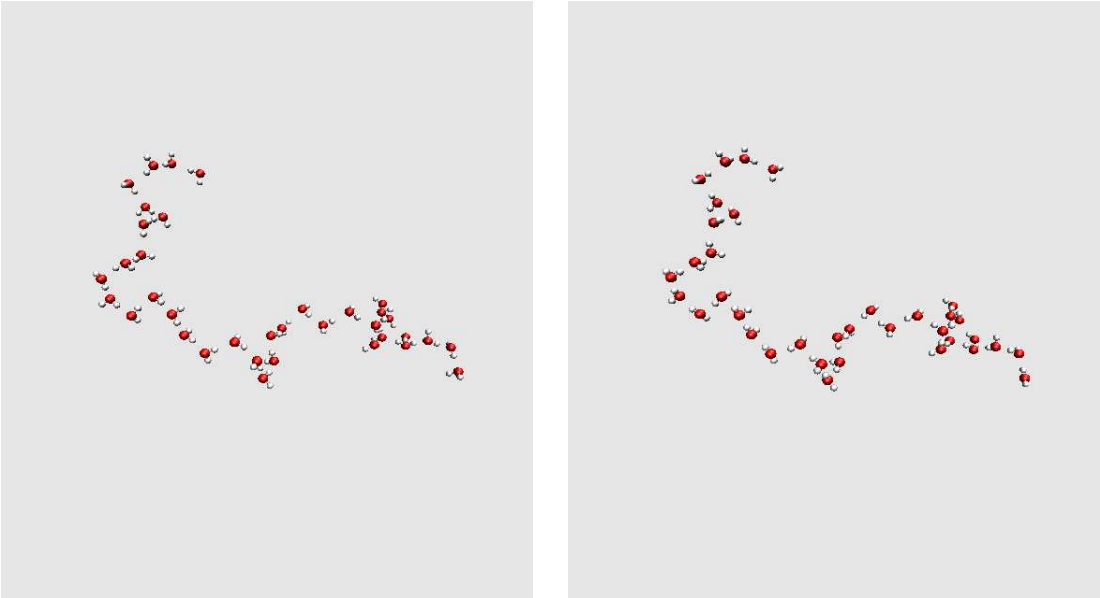

Figura 5.6: Anillo de 37 moléculas de agua unidas por enlaces de hidrógeno que percola una dimensión entera de la caja de simulación, y está virtualmente cerrado por las condiciones de contorno periódicas. A la izquierda antes del movimiento de rotación y a la derecha después de la rotación de todas las moléculas que forman el anillo.

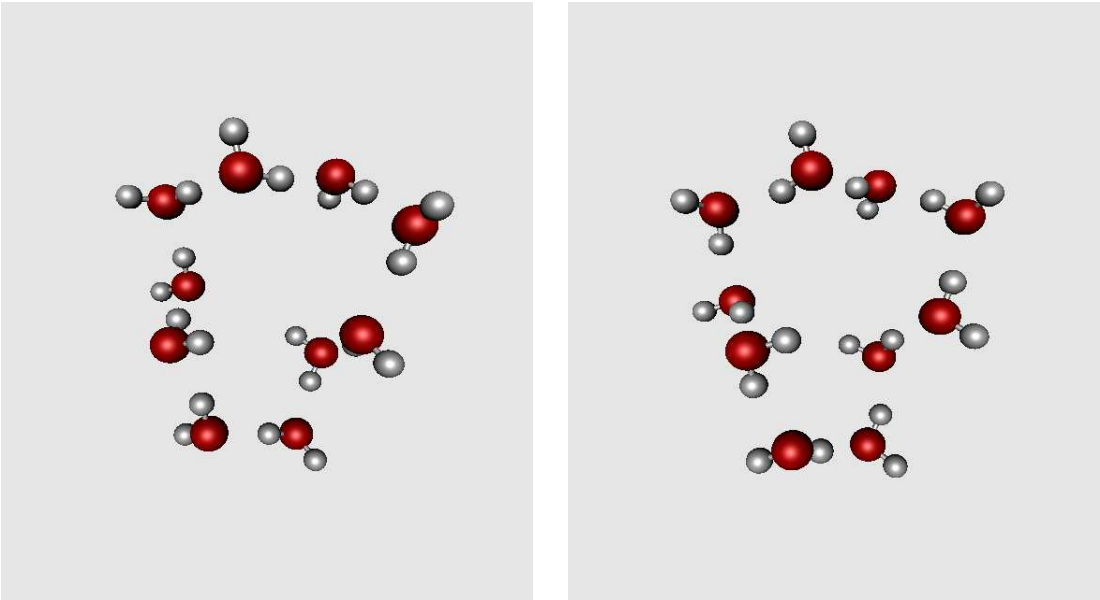

Figura 5.7: Anillo cerrado formado por diez moléculas de agua unidas mediante enlaces de hidrógeno antes del movimiento de rotación (izquierda) y después del movimiento de rotación (derecha).

Parte II

RESULTADOS

CAPÍTULO 6

Properties of ices at 0 K : a test of water models

J.L. Aragones[1], E.G. Noya[1], J.L.F. Abascal[1] and C. Vega[1]

[1] *Dep. Química Física, Fac. Química, Universidad Complutense de Madrid, 28040,Madrid, Spain*

Journal of Chemical Physics, **127***, 14518 (2007)*

Abstract

The properties of ices I_h, II, III, V and VI at zero temperature and pressure are determined by computer simulation for several rigid water models (SPC/E, TIP5P, TIP4P/Ice and TIP4P/2005). The energies of the different ices at zero temperature and pressure (relative to the ice II energy) are compared to the experimental results of Whalley [E. Whalley, J. Chem. Phys. 81, 4087, 1984]. TIP4P/Ice and TIP4P/2005 provide a qualitatively correct description of the relative energies of the ices at these conditions. In fact, only these two models provide the correct ordering in energies. For the SPC/E and TIP5P models, ice II is the most stable phase at zero temperature and pressure whereas for TIP4P/Ice and TIP4P/2005 ice I_h is the most stable polymorph. These results are in agreement with the relative stabilities found at higher temperatures. The solid-solid phase transitions at 0 K are determined. The predicted pressures are in good agreement with those obtained from free energy calculations.

Introduction

Taking into account the importance of water, it is not surprising that thousands of simulation studies of water have been performed since the the pioneering works of Barker and Watts [10] and Rahman and Stillinger [11]. Besides since water is the medium where life takes places, describing water interactions is also important when performing simulation studies of biological molecules in solution. For this reason the search of a water potential that describes in a satisfactory way its properties has been a very active area of research in the last years [157, 158]. Many water potentials have been proposed in the literature. The potential parameters are typically obtained to match the experimental density and enthalpy of vaporization of real water. In this way some successful potentials have been proposed. This is the case of SPC [159], SPC/E [106], TIP4P [107] and TIP5P [108]. In these models [157] water is treated classically as a rigid non-polarizable molecule with the positive charge often located at the hydrogen atoms and a Lennard-Jones (LJ) interaction site located on the oxygen atom. Differences appear in the location of the negative charge. When the negative charge is located on the oxygen atom one has the family of models with three interaction sites such as TIP3P [107], SPC, and SPC/E. When the negative charge is located on the H-O-H bisector

the model has four interaction sites, as it is the case of TIP4P. When the negative charge is located on the “lone pair electrons´´ one has a model with five interaction sites as TIP5P.

The emphasis when developing potentials has been the ability of the potential to reproduce the properties of liquid water. The existence of several types of amorphous phases at low temperatures [79, 160, 161], and the possible existence of a liquid-liquid phase transition in water [69, 162–164] has extended the interest in water to the low temperature region. The study by computer simulation of the solid phases of water has received less attention. The experimental study of the properties of ices and of the phase diagram of water has spanned the entire 20th century, starting with the pioneering work of Tammann and Bridgman [23, 58, 83, 165–167] up to the recent discovery of ices XII, XIII and XIV [25, 92]. Compared to the liquid, the study of ices by computer simulation has been more limited. In 1982 Morse and Rice [168] performed a systematic study of the ability of the water potential models available in the seventies to reproduce the properties of several water polymorphs. Since then the interest in determining ice properties from computer simulation has been growing steadily [17, 26, 40, 56, 117, 169–182]. It seems of interest to study by computer simulation the performance of the different water potentials to describe the properties of the solid phases of water (ices) as this may help to improve our understanding of water interactions.

Motivated by this our group has studied in a systematic way the performance of SPC/E, TIP4P and TIP5P to describe the properties of ices [22, 88, 183–187]. We have found that SPC/E and TIP5P yield a bad prediction of the phase diagram of water [22, 188]. In fact, for these models, ice II was more stable than ice I_h at normal pressure and, besides, ices III and V were found to be metastable phases. Moreover, the melting temperature predicted by SPC/E models was quite low [187]. With respect to their ability to reproduce the densities of the different solid polymorphs, it has been found that SPC/E and TIP5P overestimate the density of ices by about 3 per cent and 8 per cent, respectively [22, 186]. The failure of these models is in contrast with the success of the TIP4P model [107] which is the natural descendent of the very first model of water proposed by Bernal and Fowler [8]. In fact, the TIP4P model is able to predict reasonably well the phase diagram of water [22]. It predicts ice I_h as the stable solid phase at ambient pressure. The prediction of the densities for the different solid phases of water appears as reasonable (it overestimates the experimental densities by about two per cent) [186]. The main failure of the model seems to be a melting point about 40 K below the experimental value.[17, 22, 81, 144, 189, 190] In view of these results, it was more or less obvious that the parameters of the TIP4P model could be modified slightly to yield improved performance. It is with this idea in mind that the TIP4P/Ice [112] and TIP4P/2005 [34] models were proposed. TIP4P/Ice [112] reproduces the melting temperature of water and TIP4P/2005 reproduces the maximum in density of liquid water at room pressure (the impossibility of reproducing simultaneously the temperature of maximum density and the melting point for non-polarizable models has been reported recently [110]). Besides providing good phase diagrams the two new models TIP4P/Ice and TIP4P/2005 predict quite well the densities of the different ice polymorphs; the typical deviation with respect to the experiment is about -1 % for TIP4P/Ice [112] and about 1 % for TIP4P/2005 [34].

In 1984 Whalley determined the experimental values of the energies of different ice polymorphs (relative to that of ice I_h) at zero temperature and pressure [33]. The goal was to provide data that could be useful to validate different water potentials. As stated in his paper “effective potentials that are used to simulate water ought to be tested on the many phases of ice before being treated as serious representations of liquid water". In another subsequent work published in 1987, Handa, Klug and Whalley determined the relative energies of the ices at zero pressure for a temperature close to 150 K. In this paper the zero temperature, zero pressure energies of ices I_h, II, III, V and VI will be determined for several water models. In

particular, we shall consider SPC/E, TIP5P and TIP4P/2005 and TIP4P/Ice. Our interest is to check whether these simple models are able to describe the experimental values of the relative energies of the different ice polymorphs. A second benefit of the study is that it will allow to determine the transition pressures at zero temperature between the different ice polymorphs (the same was already illustrated by Whalley using experimental data). We shall focus our attention mainly on the transition between ice I_h and ice II. This is especially important since as stated above ice II has been found to be more stable than ice I_h at the melting point for the models SPC/E and TIP5P and it would be of interest to establish whether this is also true at zero temperature and pressure. An extra benefit of this zero temperature calculations is that they allow to test in an indirect way the validity of previous free energy calculations. Indeed the coexistence pressures at zero temperature obtained from free energy calculations should be in agreement with those obtained from the direct determination of the properties of the ices at zero temperature and pressure.

Properties at zero temperature

The third law of thermodynamics states that for a pure substance the entropy becomes zero at 0 K provided the substance appears in a perfectly ordered crystalline form. It is then important to clarify several issues related with the properties of the systems when they approach 0 K. The first concerns the limiting behavior of the thermodynamic properties at 0 K and the appearance of the coexistence lines between two phases at 0 K (see Ref. [191] for interesting annotations on the low temperature phase stability in connection to the Third Law of Thermodynamics). It is also important to know how a classical statistical mechanics treatment affects the results at these conditions. Finally we want to discuss here possible methods for the calculation of coexistence properties between two phases at 0 K. In particular, we are interested in the calculation of the coexistence pressure. If we denote as H, V and S the molar values of the enthalpy, volume and entropy, respectively, then the Clapeyron equation can be written as

$$\frac{dp}{dT} = \frac{\Delta H}{T\Delta V} = \frac{\Delta S}{\Delta V}. \tag{6.1}$$

This means that the slope of a certain coexistence curve is the entropy change ΔS divided by the volume change ΔV. In general, the difference in volume between two coexisting solid phases is not zero even at zero temperature. The entropy change depends on the considered transition. According to the Third Law of Thermodynamics, the entropy of a perfectly ordered solid is zero at 0 K. Thus, solid-solid phase transitions between perfectly ordered phases show zero slope at 0 K. When one or both of the solid phases are not completely ordered, they have residual entropy at zero temperature and then the slope of the coexistence curve is not null even at zero temperature. It is well known that a number of solid phases of water present residual entropy at zero temperature [85]. This is the case of ice I_h, III, V and VI. In these structures the oxygens are located on a lattice but the hydrogen atoms are disordered. However ice II is proton ordered and then it has zero entropy at 0 K. Thus, the coexistence curves ice I_h-ice II, III-II, V-II and VI-II present non zero slope when approaching 0 K.

The idea of Whalley was to estimate the differences in energy between ices at 0 K from the known experimental values of the coexistence pressures at that temperature. Let us briefly summarize the procedure used by Whalley. At zero temperature the condition of chemical equilibrium between two phases, labeled as phase A and B, respectively, is given by:

$$U_A(p_{eq}, T=0) + p_{eq}V_A(p_{eq}, T=0) = U_B(p_{eq}, T=0) + p_{eq}V_B(p_{eq}, T=0) \tag{6.2}$$

where U is the (molar) internal energy and p_{eq} is the coexistence pressure. Hence, phase transitions between solid phases at zero temperature occur with zero enthalpy change. In the following we shall drop the $T = 0$ K indication but it should be understood that the thermodynamic analysis in the rest of this Section is only valid at 0 K. The change of internal energy at the equilibrium pressure between phases A and B can be obtained from the previous expression as

$$U_B(p_{eq}) - U_A(p_{eq}) = p_{eq}[V_A(p_{eq}) - V_B(p_{eq})] \tag{6.3}$$

This equation can be further transformed. Let us define $\Delta X = X(B) - X(A)$ where X is a certain thermodynamic property. If one assumes that the isothermal compressibility κ_T does not depend on pressure, it follows[33] that

$$\Delta U(p = 0) = -p_{eq}\Delta V(p = 0) + \frac{1}{2}p_{eq}^2\Delta(V\kappa_T) \tag{6.4}$$

This equation was used by Whalley to estimate $\Delta U(p = 0)$ from the knowledge of $\Delta V(p = 0)$, p_{eq} and $\Delta(V\kappa_T)$. Notice that whereas Eq.(6.3) is exact, Eq.(6.4) contains an approximation. The previous equation can be simplified even further if one assumes (which is a quite good approximation for ices) that $\Delta(V\kappa_T) = 0$. Then it follows

$$\Delta U(p = 0) = -p_{eq}\Delta V(p = 0) \tag{6.5}$$

In summary, Eq.(6.3) is exact, Eq.(6.4) is an approximation which will be denoted here as first order approximation, and Eq.(6.5) is another approximation which will be referred to as zero order approximation. The nice feature of the zero order approximation is that it allows to estimate the coexistence pressure from the values of ΔU and ΔV at zero pressure

$$p_{eq} = -\Delta U(p = 0)/\Delta V(p = 0) \tag{6.6}$$

In this study we shall perform classical Monte Carlo simulations at 0 K for several water models and for several solid structures. The coexistence pressures will be obtained either exactly from Eq.(6.2) (*i.e*, equating the enthalpies of the two phases at coexistence) or more simply from the zero order approximation Eq.(6.6).

Before continuing it seems important to discuss the properties of systems at 0 K when treated with classical statistical mechanics. Of course thermodynamic relations like the Clapeyron equation are still valid within a classical treatment (thermodynamics relations also hold for classical systems except for the laws related to the third principle of thermodynamics). However within classical statistical mechanics ΔS is in general different from zero at 0 K. This is because the entropy is not null at 0 K. In fact, within classical statistical mechanics the entropy diverges to $-\infty$ as the temperature approaches zero [192]. This can be seen by using the following reasoning. As shown in Fig. 6.2, in a classical treatment, the heat capacity at constant pressure (C_p) is not zero even at 0 K (the slope of the internal energy U remains finite up to 0 K). The heat capacity has two contributions: the ideal term ($6R/2$) and the residual contribution, which we have seen that is also finite and positive. Therefore, within a classical statistical mechanics formalism, C_p is finite and positive at 0 K. The entropy at a given temperature can be computed as:

$$S(T) = S(T = 0) + \int_0^T \frac{C_p}{T}dT \tag{6.7}$$

As C_p is finite and positive, the term C_p/T diverges as the temperature approaches zero. On the other hand the entropy increases with the temperature or, what is the same, the entropy decreases as the temperature is lowered. As C_p/T diverges at 0 K and the entropy decreases

as the temperatrure goes down, the entropy must go to minus infinite as the temperature approaches zero. However, in spite of this divergence of the entropy at 0 K, the differences in entropy between different solid phases remain finite. For instance, for hard spheres the entropy goes to minus infinity when the density tends to that of close packing whereas the difference in free energy between the fcc and hcp close packed structures remains finite [193–195]. As a consequence, the coexistence lines between solid phases will present a non zero slope in the p-T plane.

Simulation details

Simulations have been performed for the SPC/E, TIP5P and the two recently proposed models TIP4P/Ice and TIP4P/2005 models. Since SPC/E [106] and TIP5P [108] have been often described in the literature we shall just refer to the original references. TIP4P/Ice [112] and TIP4P/2005 [34] correspond to slight modifications of the TIP4P [107] model. The main differences between TIP4P and TIP4P/Ice is a larger value of the charge located on the H atoms and a larger value of the dispersion energy of the LJ interaction site. The parameters of the TIP4P/2005 are just intermediate between those of TIP4P and TIP4P/Ice. NpT Monte Carlo (MC) simulations have been performed for the following solid structures of water: ice I_h, II, III, V, and VI. In the simulations described in this work the LJ potential was truncated at 8.5 Å for all the phases. Standard long range corrections were added to the LJ energy. Ewald sums were used to deal with the long range electrostatic forces. The real part of the electrostatic contribution was also truncated at 8.5 Å. The screening parameter and the number of vectors of reciprocal space considered had to be carefully selected for each crystal phase [97, 99]. The number of molecules used for ice I_h, II, III, V and VI was 288, 432, 324, 504 and 360, respectively. These system sizes guarantee that the smallest edge of the simulation box is always larger than twice the cutoff in the potential.

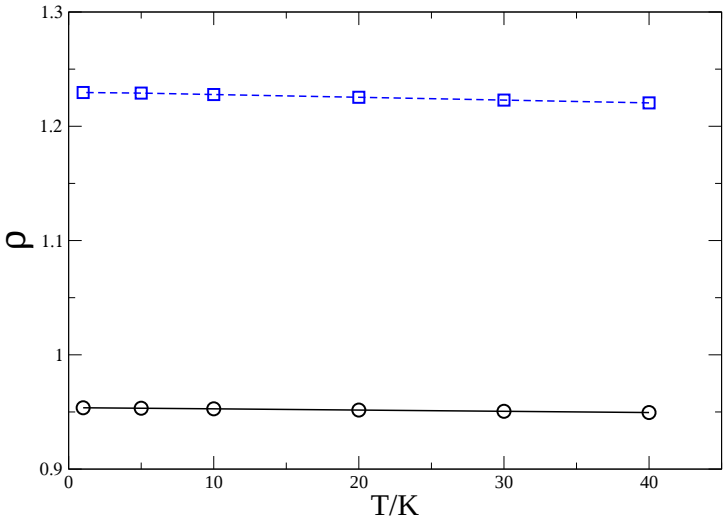

Figura 6.1: Densities (in g/cm^3) of ice I_h (solid line and open circles) and of ice II (dashed line and open squares) for the TIP4P/2005 model of water along the $p = 0$ isobar.

Since the considered solid structures are not cubic [I_h (hexagonal), II (trigonal), III and VI (tetragonal) and V (monoclinic)] anisotropic NpT MC simulations (Parrinello-Rahman like

[102, 196]) were necessary for the solid phases, thus allowing both the shape and the relative dimensions of the unit cell to change. For the proton disordered phases (I_h and VI) the algorithm of Buch *et al.* [86] was used to generate an initial configuration where the hydrogens are disordered (but not the oxygens) and satisfying the ice rules [8, 85] with a negligible dipole moment. The remaining disordered polymorphs, ice III and ice V, required some additional care as they are known to exhibit only partial disorder [87]. In view of this, the algorithm given in Ref. [86] was generalized [88] to construct an initial configuration with biased occupation of the hydrogen positions. Ice II presents proton ordering and thus crystallographic information was used to generate an initial solid configuration [197].

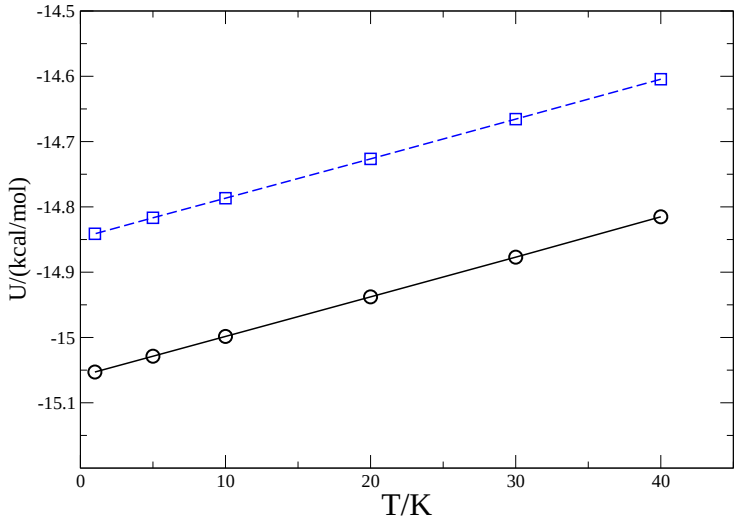

Figura 6.2: Internal energies of ice I_h (solid line and open circles) and of ice II (dashed line and open squares) for the TIP4P/2005 model of water along the $p = 0$ isobar

To obtain the zero temperature-zero pressure properties, several consecutive Parrinello-Rahman NpT simulations (at zero pressure) were performed between 40 K and 1 K. The simulation started at 40 K and after a run of about 20000 cycles for equilibration plus 40000 cycles to obtain thermodynamic averages the temperature was changed to a lower value (a cycle is defined as a trial move per particle plus a trial volume change). The final configuration of a run was used as the initial configuration of the next run at a lower temperature. Fig. 6.1 shows the densities of TIP4P/2005 along the zero pressure isobar. In Fig. 6.2 the residual energies of TIP4P/2005 along the zero pressure isobar are presented. As it can be seen in both figures, these properties vary linearly with temperature. Hence, the properties at 0 K can be obtained by fitting the simulation results to a straight line. Notice that the non-zero slope of the results presented in Figs. 6.1 and 6.2 are due to the classical treatment of the model. According to the Third Law of Thermodynamics, both the coefficient of thermal expansion α and the heat capacity C_p should go to zero as the temperature goes to zero. For the particular case of SPC/E simulations were also performed for other isobars (besides the zero pressure isobar). In particular, for ices I_h and II, simulations were performed for the following pressures $p = -500, -1000, -1500, -2000, -2500$ bar (the reasons for choosing negative pressures in the case of the SPC/E will be clarified in the next section).

In this work we have also performed Gibbs-Duhem simulations[138, 198] to determine the coexistence line between ices I_h-II for the models SPC/E, TIP5P, TIP4P/2005 and TIP4P/Ice. Gibbs-Duhem simulations allow to determine the coexistence line between two phases provided that an initial coexistence point is known. The Gibbs-Duhem technique is just a numerical integration (using simulation results to estimate the volume and enthalpy change between phases) of the Clapeyron equation. For the I_h-II coexistence line initial coexistence points for a number of water models are available from a previous work [187]. For the integration of the Clapeyron equation a fourth-order Runge-Kutta method algorithm is employed. Typically six to seven temperatures were chosen to integrate the coexistence line between ices I_h and II from 150 K up to temperature of about 20 K. The rest of simulation details (size of the system, cutoff, anisotropic scaling) were identical to those used in the NpT simulations along the isobars. In Table I the results of the Gibbs-Duhem simulations along the I_h-II coexistence line are presented. For each model, the coexistence properties at selected temperatures (the initial temperature, one or two intermediate temperatures and the final temperature) are given. We report the equilibrium pressure, volume change, enthalpy change, entropy change and slope of the melting curve. A simple inspection of Table I shows that the enthalpy change of the transition goes to zero when the temperature approaches zero. The entropy change also varies along the transition although it does not tends to zero when the temperature vanishes. The slope of the coexistence line does not change much with temperature so that the coexistence lines between these two solid phases do not deviate much from a straight line. Thus, the coexistence pressure at 0 K may be simply obtained by extrapolation of the results at a slightly higher temperature. The properties along the I_h-II coexistence line as obtained from Gibbs-Duhem simulations are plotted in Fig. 6.4.

Results

Let us start by presenting the results for the properties of the different ices at zero pressure and temperature. In Table 6.2 the internal energies and densities are given for the TIP4P/Ice, TIP4P/2005, SPC/E and TIP5P models. The internal energies differ significantly from one model to another. The higher internal energies (i.e the less negative value) correspond to TIP5P. This can be understood since the parameters of this model were chosen to match the experimental enthalpy of vaporization. The order of magnitude of the energies of SPC/E and TIP4P/2005 are similar because these models reproduce the experimental enthalpy of vaporization only when a self-polarization term is taken into account [106]. Finally the lowest values (*i.e.*, the largest in absolute value) are given by the TIP4P/Ice because this model provides an enthalpy of vaporization much higher than the experimental one (even when the self-polarization term is added) which is required to match the ice I_h experimental melting temperature [112]. In Table 6.2 the results corresponding to the ice polymorph with the lowest energy at zero temperature and pressure are presented in bold characters. For TIP4P/Ice and TIP4P/2005 ice I_h is the structure with the lowest energy. However for SPC/E and TIP5P the lowest internal energy corresponds to ice II. Thus, for TIP4P/2005 and TIP4P/Ice ice I_h is the stable phase at zero pressure and temperature whereas for SPC/E and TIP5P the stable phase is ice II.

Tabla 6.1: Simulation results for the transition between ices I_h and II as obtained from Gibbs-Duhem simulations. The changes in the properties of the coexisting phases are calculated as the values for ice II minus those for ice I_h. The change in volume is given in cm^3/mol, the enthalpy change in kcal/mol, the entropy change in cal/K and the slope dp/dT in bar/K. The initial coexistence point was taken from Ref. [187].

T/K	p/bar	ΔV	ΔH	ΔS	(dp/dT)
TIP4P/Ice					
180	2790	-0.224	-0.0906	-0.503	5.21
120	2490	-0.229	-0.0587	-0.489	4.95
60	2210	-0.233	-0.0300	-0.500	4.98
10	1960	-0.236	-0.0050	-0.498	4.90
TIP4P/2005					
160	2900	-0.218	-0.0849	-0.530	5.64
80	2470	-0.226	-0.0405	-0.506	5.20
20	2160	-0.230	-0.0092	-0.457	4.62
SPC/E					
150	-498	-0.234	-0.1122	-0.748	7.43
90	-940	-0.238	-0.0660	-0.735	7.17
20	-1430	-0.241	-0.0140	-0.683	6.57
TIP5P					
150	-587	-0.209	0.0186	0.124	-1.37
90	-500	-0.207	0.0122	0.136	-1.52
25	-391	-0.205	0.0041	0.163	-1.85

Tabla 6.2: Properties of several ice polymorphs at $T = 0\ K$ and $p = 0$ for popular water models.

Ice	TIP4P/Ice	TIP4P/2005	SPC/E	TIP5P
		U(kcal/mol)		
I_h	**-16.465**	**-15.059**	-14.691	-14.128
II	-16.268	-14.847	**-14.854**	**-14.162**
III	-16.140	-14.741	-14.348	-13.320
V	-16.049	-14.644	-14.169	-13.101
VI	-15.917	-14.513	-13.946	-12.859
		ρ(g/cm^3)		
I_h	0.938	0.954	0.981	1.045
II	1.212	1.230	1.279	1.326
III	1.169	1.184	1.181	1.200
V	1.277	1.297	1.325	1.383
VI	1.363	1.385	1.413	1.471

Let us now compute the coexistence pressures between the different ice phases. It is interesting to analyze first the performance of the zero order approximation given by Eq.(6.6).

According to this approximation, in order to determine the coexistence pressure it is sufficient to know the internal energy and density at zero density and pressure. Within this approximation, the coexistence pressure at 0 K for the ice I_h-ice II line is -1590 bar for the SPC/E model. For the same model we have obtained by computer simulation the properties of ices I_h and II at several pressures along the zero temperature isotherm. From these results it is possible to determine exactly the location of the phase transition at zero temperature (from the condition of equal enthalpy between the two phases).

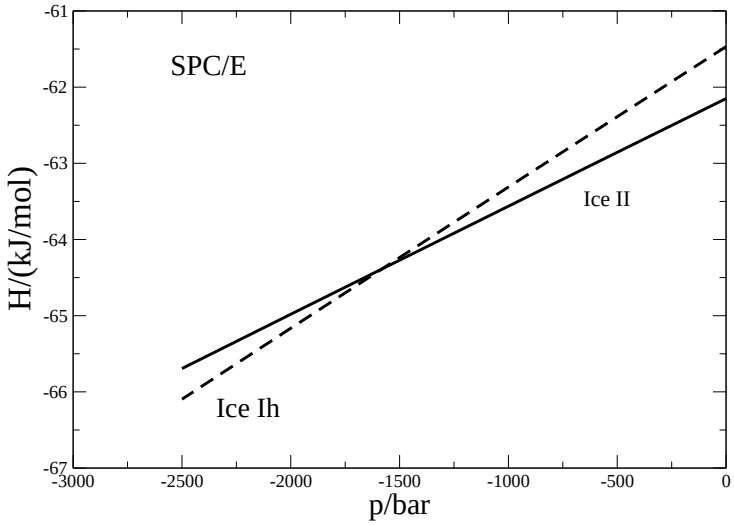

Figura 6.3: Enthalpies of ices I_h and II at zero temperature for the SPC/E model of water.

In Fig. 6.3 the enthalpies of SPC/E for these two ices are shown. The enthalpies of ices I_h and II cross at a pressure of about -1570 bar. This is the coexistence pressure obtained in a rigorous way. As it can be seen both estimations agree quite well which guarantees that the error introduced by the zero approximation is small. For this reason it will be used in the rest of this work to determine the coexistence pressures.

Tabla 6.3: Coexistence pressures (in bar) between solid phases at $T = 0\ K$. The experimental values were taken from Whalley.[33] d is a measure of the departures of the predictions for a given model from the experimental values (see the text).

Phases	Experimental	TIP4P/Ice	TIP4P/2005	SPC/E	TIP5P
I_h-II	140 ± 200	1900	2090	-1590	-390
I_h-III	2400 ± 100	3580	3630	4600	15250
II-V	18500 ± 4000	12120	11230	58270	79600
II-VI	10500 ± 1000	8920	8530	28410	40690
III-V	3000 ± 100	2920	3060	4530	4610
V-VI	6200 ± 200	6210	6210	11010	12950
d		4	4	8	26

The coexistence pressures calculated within the zero order approximation are presented in Table 6.3. We leave aside for the moment the comparison with the experimental coexistence pressures. The first thing to note from the results of Table 6.3 is that the coexistence pressure between ice I_h and ice II occurs at negative pressures for SPC/E and TIP5P. In fact, for the SPC/E model at zero temperature, ice I_h is more stable than ice II only at pressures below -1590 bar. For TIP5P the situation is not as dramatic as that for SPC/E, ice I_h being more stable than ice II at pressures below -390 bar. For TIP4P/2005 and TIP4P/Ice the I_h-II transition occurs at positive pressures so that ice I_h is more stable than ice II for a certain range of positive pressures. A second important question is to analyze whether the coexistence pressures obtained from zero Kelvin calculations agree with the results from Gibbs-Duhem simulations. This is a severe test since any error in the free energy calculation of the solid phases or in the determination of the initial coexistence point or in the Gibbs-Duhem integration along the coexistence line gives rise to discrepancies. Therefore the comparison constitutes a cross check of the calculations. In Table 6.4 the coexistence pressures for the TIP4P/2005 model extrapolated to 0 K from the Gibbs-Duhem simulations are compared to the values predicted from the zero Kelvin calculations. The agreement is satisfactory. This provides further evidence of the correctness of the phase diagram computed for TIP4P/2005. It is also interesting to point out that the melting temperature of ice I_h obtained from free energy calculations was found in agreement with the melting temperature obtained from direct fluid-solid coexistence runs [144] and from surface melting simulations [81]. Therefore the melting temperatures as determined from free energy calculations seem to be correct for this model (and for other models as well). This type of cross-checking is worth especially taking into account that free energy calculations of molecular solids are somewhat involved [19, 22, 115, 199–201]. In summary, the above commented calculations provide further evidence of the validity of the phase diagram computed for the TIP4P/2005. Because of this, and considering that some coexistence lines (II-V, V-VI and II-VI) have been extended to lower temperatures than those previously reported for this model, we present in Fig. 6.5 the resulting phase diagram of TIP4P/2005 including the new coexistence points.

Tabla 6.4: Coexistence pressures at 0 K (in bar) for TIP4P/2005 as obtained from extrapolation of the Gibbs-Duhem coexistence lines and from the analysis of the properties of the ices at zero temperature.

Phases	Gibbs-Duhem	Eq.(6.6)
I_h-II	1990	2090
I-III	3600	3630
II-V	11530	11230
II-VI	9080	8530
V-VI	5990	6210

We now focus on the coexistence pressure between ices I_h and II for different water models. We have also plotted in Fig. 6.4 the predicted pressures using the calculations at 0 K (circles). It may be seen that these predictions agree quite well with the extrapolated values of

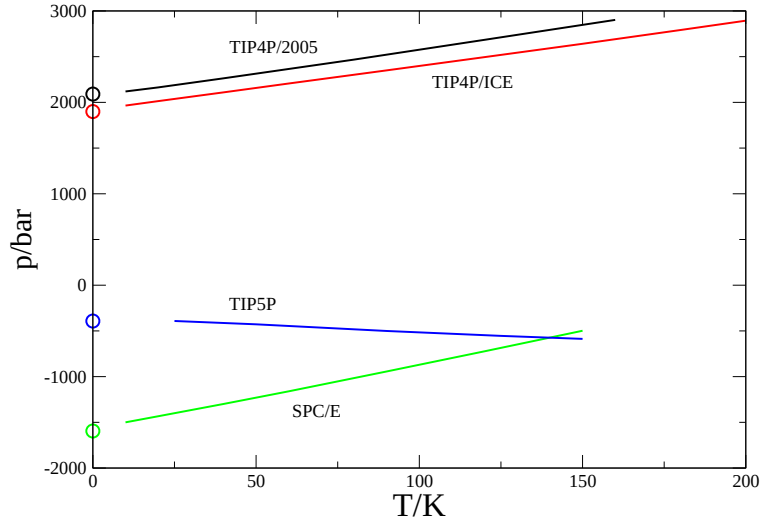

Figura 6.4: Coexistence lines between ices I_h and II as obtained from Gibbs-Duhem simulations for TIP4P/2005, TIP4P/Ice, SPC/E and TIP5P models (solid lines). The symbols represent the coexistence pressures as obtained from the properties of the systems at zero temperature.

the Gibbs-Duhem simulations for the I_h-II coexistence line. Therefore, both set of results are mutually consistent. It is clear that ice II is more stable than ice I_h at zero temperature and pressure for the SPC/E and TIP5P models. For the TIP5P model the slope of the I_h-II line is negative (this is because for this model the enthalpy of ice II is higher than that of ice I_h along the coexistence curve). This is an anomalous behavior since for the rest of the models the enthalpy of ice I_h is higher than that of ice II along the coexistence curve. Because of the negative slope the transition pressure between ices I_h and II at high temperatures (for instance at the temperature of the normal melting point) is lower than at 0 K. In summary, for TIP5P at positive pressures ice II would be more stable than ice I_h at any temperature up to the melting point. For the SPC/E model the stability of ice I_h increases with temperature. Since for this model the ice I_h melting point is around 215K [110, 144], either ice I_h does not appear on the phase diagram at positive pressures or appears just in a very small region of the phase diagram in the vicinity of the melting point. On the contrary, for TIP4P/Ice and TIP4P/2005 the transition between ice I_h and ice II occurs at positive pressures at any temperature in accordance with the experimental observation. Thus, the calculations in the region close to 0 K reinforce previous reports about the dependence of the relative stability of these ice polymorphs on the water models [22, 110].

Let us finally compare the computer simulation results for these models to the experimental data. First of all we compare the transition pressures between ices at 0 K (see Table 6.3). In order to give a numerical value more or less representative of the accuracy of the results and, taking into account the disparity of the values, we have calculated the mean weighted deviations:

$$d = (1/N) \sum w|p_{model} - p_{expt}| \tag{6.8}$$

using the inverse of the experimental uncertainty as a weighting function w. The results for TIP5P do not agree with the experimental values. The d value indicate that the departures of the TIP5P predictions from the experimental equilibrium pressures are (in average) more

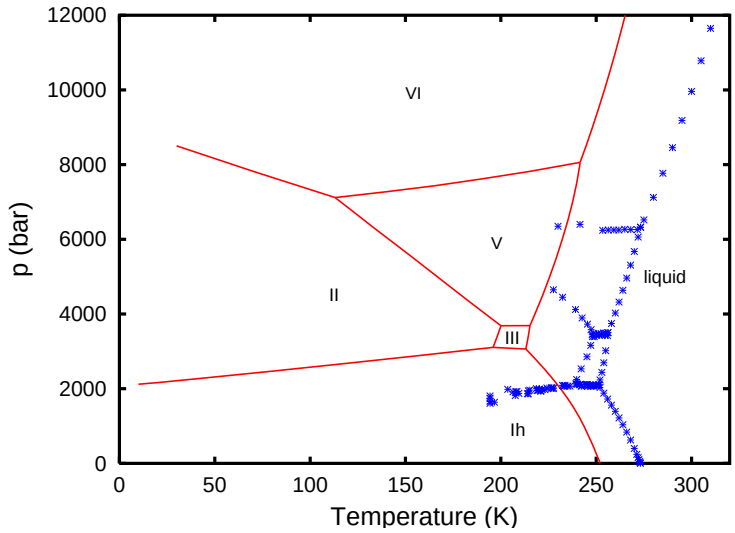

Figura 6.5: Phase diagram of the TIP4P/2005 model of water as obtained from free energy calculations and Gibbs-Duhem simulations

than 25 times larger than the experimental uncertainty. The only exception is the ice I_h-II transition for which the difference with respect to the experimental value is relatively small. The same applies, although to a minor extend, to the coexistence pressures yielded by the SPC/E model. The predictions for TIP4P/2005 are quite similar to those for TIP4P/Ice so we shall use the latter model for our discussion. As it can be seen, the calculations for the TIP4P/Ice model are in reasonable agreement with the experimental values. Although the largest difference with experiment is that for the II-V coexistence, the discrepancy is in this case only slightly larger than the experimental uncertainty. The differences for the other solid-solid lines are lower than 2000 bar. The more significant departures appear when ice I_h is one of the coexistence phases (*i.e.*, I_h-II and I_h-III transitions). In the case of the I_h-II coexistence the model overestimates the equilibrium pressure by about 1800 bar, a value considerably larger than the experimental uncertainty. Taking into account the simplicity of the model (rigid, non-polarizable and classical) the predictions appear as quite reasonable. Probably the predictions of the TIP4P/Ice and TIP4P/2005 models represent the limit of what can be achieved by simple water models.

Finally we present the relative energies of the ice phases at 0 K. The energy of ice II will be taken as the zero of energies so that all the energies will be referred to that of ice II. In Table 6.5 the relative energies (with respect to that of ice II) of the different ice polymorphs (at zero temperature and pressure) are presented. Again, the predictions for TIP5P and SPC/E do not agree with experiment. These models predict rather poorly the relative energies of the different ices polymorphs. Therefore it is not surprising that they yield poor predictions for the phase diagram of water. In particular, the positive value of the relative energy of ice I_h, indicates that ice II is more stable than ice I_h at the considered thermodynamic state as commented before. The relative energies predicted by the TIP4P/Ice and TIP4P/2005 are quite satisfactory. For both models, the difference of the predicted energies respect to the experimental values is (in average) lower than 0.1 kcal/mol. Both models predict that the internal energy of ices at zero temperature and pressure increases in the order I_h, II, III, V, and VI which is in

Tabla 6.5: Relative internal energies (in kcal/mol) of several ice polymorphs with respect to ice II at zero temperature and pressure for the TIP4P/Ice, TIP4P/2005, SPC/E and TIP5P water models. For comparison, the experimental measurements of Whalley[33] are also included. d is the mean deviation with respect to the experimental results (calculated as in Eq.6.8 with $w = 1$ and with the pressures replaced by the relative internal energies).

Phase	TIP4P/Ice	TIP4P/2005	Exp	SPC/E	TIP5P
I_h	-0.197	-0.212	-0.014	0.163	0.034
II	0	0	0	0	0
III	0.128	0.106	0.201	0.506	0.842
V	0.219	0.203	0.213	0.686	1.061
VI	0.351	0.334	0.373	0.908	1.303
d	0.07	0.08		0.37	0.62

agreement with experiment. It is indeed gratifying that such simple models are able to capture the ordering of the energies of the ice phases. The correct ordering guarantees a qualitatively correct phase diagram. The relative energy of ices III, V and VI with respect to ice II is described quite well by these models. The main discrepancy is related to the energy of the ice I_h with respect to ice II. This relative energy is found to be negative both in experiment and in the TIP4P/2005 and TIP4P/Ice models (so that ice I_h is the most stable phase at zero temperature and pressure). However, the difference between the experimental value and the one obtained in the simulation is larger for this polymorph than for the other ices. Thus, the stability of ice I_h with respect to the rest of the polymorphs (ices II, ices III, V and VI) is overestimated in the TIP4P/Ice and TIP4P/2005 models. It is worth to mention that whereas the density of ice I_h in TIP4P/Ice is around 0.93 g/cm^3, the densities of the rest of ices are in the range $1.20 - 1.36$ g/cm^3. This important difference in density may affect the zero point energies (not taken into account in classical simulations) which can also be different in low density (I_h) and high density ices (II, III, V, VI). It may also have some effect on the effective dipole moment of the water molecule in such a different environments. Further work (*e.g.*, path integral simulations or evaluation of the phonon dispersion curve, inclussion of polarizability) is needed to clarify the origin of this feature.

Tabla 6.6: Relative internal energies (in kcal/mol) between ices at zero pressure for temperatures around 150 K. Experimental results were taken from Ref. [202] except for ice XII that were taken from Ref. [203]. Ice VIII melted for the SPC/E model at zero pressure and a temperature of 124 K.

Ice	T(K)	TIP4P/Ice	TIP4P/2005	Exp.	SPC/E	TIP5P
I_h	162	-0.194	-0.209	0.004	0.164	0.038
II	162	0.000	0.000	0.000	0.000	0.000
III	143	0.132	0.112	0.230	0.511	0.874
V	144	0.231	0.218	0.235	0.704	1.083
VI	143	0.354	0.338	0.352	0.918	1.313
XII	150	0.304	0.295	0.307	0.830	1.277
VIII	124	1.903	1.798	0.650	—	2.449

Up to now we have compared the relative internal energies between ices at 0 K. However, in a later work, Whalley et al. [202] also reported the relative internal energies of the different ices at zero pressure and temperatures around $T = 150$ K. These were determined from calorimetric measurements. In Table 6.6 the relative internal energies at zero pressure are compared for the different ices. Notice that the temperature at which the comparison is made is not the same for all solid phases. As before we take as zero energy that of ice II at 162 K. Then the displayed result for the experimental energy of, let us say, ice III (0.23 kcal/mol) means that the internal energy of ice III at zero pressure and 143 K is 0.23 kcal/mol higher than that of ice II at 162 K (the zero of energies). As it can be seen in Table 6.6 the experimental energies reported by Whalley *et al.* from calorimetric measurements are quite similar to those given at 0 K. Both sets of experimental results are mutually consistent and they also show that the difference in internal energies between ices at zero pressure does not depend much on temperature. The relative energies for the different water models presented in Table 6.6 are quite similar to those already discussed for the 0 K case. In addition to the energies of ices I_h, II, III, V and VI, the internal energies of ice VIII and XII are also given (those of ice XII were taken from Ref. [203]). TIP4P/Ice and TIP4P/2005 again describe quite well the energy of ice XII. However none of the models predicts correctly the energy of ice VIII. The energy of ice VIII for all models is much higher that found in experiment. This may explain why ice VIII appears in the phase diagram of SPC/E and TIP4P at a much higher pressure that found in experiment [22].

Conclusions

In this work the properties (density and internal energy) of ices I_h, II, III, V and VI at zero temperature and pressure have been obtained from computer simulations. The following models have been considered, namely, SPC/E, TIP5P, TIP4P/Ice and TIP4P/2005. It is found that ice II is the most stable phase at 0 K for SPC/E and TIP5P models. Ice I_h is the most stable phase for TIP4P/2005 and TIP4P/Ice models. The phase transitions between the different solid phases occurring at 0 K have also been calculated. Only TIP4P-like models predict the equilibrium pressures reasonably well. Besides, the coexistence pressures calculated using the properties at 0 K agree quite well with those obtained from Gibbs-Duhem simulations (with an initial point obtained from free energy calculations). Both sets of results are fully consistent which is a guarantee of the validity of the free energy calculations and phase diagram predictions. It was mentioned above that Gibbs-Duhem simulations require an initial coexistence point which is typically obtained from free energy calculations. Since the transition pressures determined from the zero order approximation are in good agreement with those obtained from Gibbs-Duhem simulations, one could (naively) think that free energy calculations may not be needed to determine solid-solid coexistence lines. In principle, one could determine the transition pressure at 0 K from the zero order approximation (or better from the isoenthalpic condition) and then use it as the initial point to perform Gibbs-Duhem integration starting at 0 K. Unfortunately, this is not possible. The reason is that at 0 K both ΔH and T are null so that its ratio (ΔS) which certainly adopts a finite value can not be determined. Gibbs-Duhem simulations can start from 0 K, but only if ΔS is known. Obviously, ΔS can only be obtained through free energy calculations. In summary, although runs at 0 K enable to check the consistency of phase diagram calculations, they do not allow by themselves to draw the phase diagram of a certain model.

The relative energies of the different polymorphs have been computed and compared to the experimental values reported by Whalley more than 20 years ago [33]. In general the relative energies between ices are quite small (about 0.2 kcal/mol). For this reason their correct prediction is a quite difficult test to pass for water models. Besides water models pass the test with quite different marks! TIP5P fails completely in predicting the relative energy of the different ices polymorphs. The results of SPC/E, although better than those for TIP5P, are not satisfactory either. The relative energies predicted by TIP4P/Ice and TIP4P/2005 agree reasonably well with experiment, the main difference being an overstabilization of ice I_h. Further work is needed to clarify the origin of this discrepancy for TIP4P-like models although it is likely that quantum effects and polarizability may be responsible of the difference. It would be of interest to determine the relative stability between ices [204] from first principles (i.e ab initio calculations) although very precise calculations would be required.

As to why some models are more successful than others we have shown recently that the balance between dipolar and quadrupolar forces varies significantly among the water models, and that this has a deep effect on the appearance of the phase diagram [205, 206]. Notice that in order to predict the phase diagram correctly two conditions are required. First the relative stability of the different ices should be predicted correctly (this guarantees a good description of the solid-solid coexistence lines). The calculations presented in this work illustrate that this is indeed achieved by TIP4P/2005 and TIP4P/Ice models. Second the relative stability of the ices with respect to the liquid should also be described correctly. This second aspect is not discussed in this work. We just should point out that TIP4P/2005 and TIP4P/Ice predict [144, 187] a melting point for ice I_h of about 252 K and 272 K, respectively (to be compared with the experimental value of 273.15 K). Therefore these models describe also quite well the relative energy of the ices with respect to the liquid, the error in the melting point of these models being about 20 K and 1 K, respectively. In the case of the TIP4P/2005 the critical temperature [207] and surface tension [208] of water are reproduced with extraordinary accuracy. Therefore, TIP4P/2005 is able to provide a coherent view of the phase diagram of water from the low temperature limit up to the critical point. Probably, significant further improvement can only be achieved by the addition of polarizability [209] and quantum effects [210, 211].

Acknowledgements

This work was funded by grants FIS2007-66079-C02-01 from the DGI (Spain), S-0505/ESP/0229 from the CAM, MTKD-CT-2004-509249 from the European Union and 910570 from the UCM. E.G.N. wishes to thank the Ministerio de Educación y Ciencia and the Universidad Complutense de Madrid for a Juan de la Cierva fellowship. We would like to thank B.Slater, E.Sanz and L.G.MacDowell for helpful discussions.

CAPÍTULO 7

The phase diagram of water at high pressures as obtained by computer simulations of the TIP4P/2005 model: the appearance of a plastic crystal phase

J.L. Aragones[1], **M.M. Conde**[1], **E.G. Noya**[1] **and C. Vega**[1]

[1] *Dep. Química Física, Fac. Química, Universidad Complutense de Madrid, 28040,Madrid, Spain*

Physcal Chemistry Chemical Physics, **11***, 543-555 (2009)*

Abstract

In this work the high pressure region of the phase diagram of water has been studied by computer simulation by using the TIP4P/2005 model of water. Free energy calculations were performed for ices VII and VIII and for the fluid phase to determine the melting curve of these ices. In addition molecular dynamics simulations were performed at high temperatures (440K) observing the spontaneous freezing of the liquid into a solid phase at pressures of about 80000 bar. The analysis of the structure obtained lead to the conclusion that a plastic crystal phase was formed. In the plastic crystal phase the oxygen atoms were arranged forming a body center cubic structure, as in ice VII, but the water molecules were able to rotate almost freely. Free energy calculations were performed for this new phase, and it was found that for TIP4P/2005 this plastic crystal phase is thermodynamically stable with respect to ices VII and VIII for temperatures higher than about 400K, although the precise value depends on the pressure. By using Gibbs Duhem simulations, all coexistence lines were determined, and the phase diagram of the TIP4P/2005 model was obtained, including ices VIII and VII and the new plastic crystal phase. The TIP4P/2005 model is able to describe qualitatively the phase diagram of water. It would be of interest to study if such a plastic crystal phase does indeed exist for real water. The nearly spherical shape of water makes possible the formation of a plastic crystal phase at high temperatures. The formation of a plastic crystal phase at high temperatures (with a bcc arrangements of oxygen atoms) is fast from a kinetic point of view occurring in about 2ns. This is in contrast to the nucleation of ice Ih which requires simulations of the order of hundreds of ns.

Introduction

The study of the phase diagram of water started its way with the pioneering work of Tammann [23, 212] and Bridgman [24, 165, 213], who obtained a number of different solid phases for water. The story has not ended yet since in the last decade new solid phases have been discovered, as it is the case of ice XII [92], discovered in 1998 by Lobban, Finney and Kuhs and ices XIII and XIV discovered just two years ago by Salzmann et al. [25]. In addition to the existence of new phases, water presents a number of interesting questions, as the possibility of a liquid-liquid transition [69, 163], the relation between the different amorphous phases [79], the possibility of partial proton ordering [87] and the aspect of the phase diagram at high temperatures and pressures. Water is an important molecule since its liquid phase constitutes the "matrix of life"[5, 6]. Getting a molecular understanding of the behaviour of water [83] appears as an interesting and challenging goal. For this reason thousands of computer simulation studies have been reported since the pioneering work of Barker and Watts [10] and Rahman and Stillinger [11]. Most of the studies have focused on the liquid phase. The study of the solid phases have received less attention. Morse and Rice [168] analyzed the performance of early water models to describe the different solid phases of water. In the recent years we have analysed the performance of several popular models (SPC/E [106] and TIP4P [107]) to describe the solid phases of water and its phase diagram [22, 185, 187, 188]. It was realized that TIP4P could be modified slightly to yield an overall better description of the water phase diagram. In this way we proposed two new models TIP4P/2005 [34] and TIP4P/Ice [112], the first describing correctly the maximum in density of water and the second reproducing the melting point temperature of ice Ih. After analysing the behaviour of these two models for other properties (diffusion coefficients, surface tension, vapour-liquid equilibria) it has been concluded that TIP4P/2005 provides a quite reasonable description of the properties of water. In fact it reproduces reasonably well the densities and relative energies of the water polymorphs [37, 214, 215], the vapour-liquid equilibria [207], the diffusion coefficient [34], the surface tension [208] and the structure of the liquid and solid phase (as given by the radial distribution functions). In the original paper where TIP4P/2005 was proposed it was shown that it provides a reasonable description of the phase diagram of water [34] at low and moderate pressures where the polymorphs Ih, II, III, V and VI are thermodynamically stable. However, the high pressure and high temperature region was not considered. One of the goals of this paper is to determine the high temperature and the high pressure part of the phase diagram including the high pressure polymorphs, namely ices VII and VIII.

Another issue which motivated this research was the possibility of obtaining by computer simulation the nucleation of ice from liquid water. In principle, by cooling water at room pressure in a computer simulation, there is the possibility of nucleating ice Ih (or Ic). Svishchev and Kusalik [170] were able to nucleate ice from liquid water by using an external field. Attempts to obtain ice from water without external fields were unsuccessful until the seminal work of Matsumoto, Saito and Ohmine [171], who in 2002 observed by the first time the nucleation of ice from liquid water after very long runs (hundreds of ns). After these first attempts several other authors have been able to nucleate ice from water. Vrbka and Jungwirth [216] nucleated ice from water in a very long run using a slab of liquid in contact with its vapour. Quigley and Rodger [217] nucleated ice by introducing bias in the simulations (via the metadynamics technique [218]). However, it is fair to say that nucleating ice Ih (or Ic) from liquid water in a computer simulation is rather difficult, and this can be achieved only either performing very long runs or introducing bias within the simulations. However, in a very recent experimental study following previous work [219], Dolan et al. [220] showed that the formation of ice VII, from water occurs in a few nanoseconds when the temperature was around 400K. In their work, Dolan et al.

Tabla 7.1: Parameters of the TIP4P/2005 model. The distance between the oxygen and hydrogen sites is d_{OH}. The angle formed by hydrogen, oxygen, and the other hydrogen atom is denoted by H-O-H. The LJ site is located on the oxygen with parameters σ and ϵ/K. The charge on the proton is q_H. The negative charge is placed in a point M at a distance d_{OM} from the oxygen along the H-O-H bisector.

d_{OH} (Å)	H-O-H	σ(Å)	ϵ/k_B(K)	q_H(e)	d_{OM}(Å)
0.9572	104.52	3.1589	93.2	0.5564	0.1546

[220] suggested that such low nucleation time could be studied by computer simulation. We intend to address this issue in this paper.

In the present work we shall determine by using free energy calculations the high pressure region of the phase diagram of the TIP4P/2005 model. On the other hand we shall use this model to analyse if the nucleation of ice VII from the liquid does indeed occur in a few ns. As it will be shown the answer is positive, and besides, as a surprise a new solid phase is found for water. This new solid phase is a plastic crystal phase. It will be shown that for TIP4P/2005 this plastic crystal phase is thermodynamically stable with respect to ices VII and VIII in the region of high pressures and temperatures. The plastic crystal has also been found two months ago by Takii, Koga and Tanaka [221] for the TIP5P and TIP4P models of water. It would be of interest to determine if this plastic crystal phase does indeed exist for real water, especially taken into account that the interest in the high pressure phases of water is growing [222, 223]. If so, that would be, ice XV (the precise value of the roman numeral depends on the order ices are found experimentally).

Simulation details

In this work Monte Carlo simulations have been performed for ices VIII, VII and liquid water. The TIP4P/2005 model will be used. This a rigid non-polarisable model, with a distribution of charges, similar to that of the TIP4P model. A Lennard-Jones (LJ) site is located on the oxygen atom, positive charges are located on the hydrogen atoms, and the negative charge is located in the H-O-H bisector. The parameters of the model are given in Table I. The TIP4P/2005 model improves the description of water properties significantly with respect to the original TIP4P model [35] and is becoming popular in computer simulations of water [224–227]. A critical comparison of the performance of the model with respect to other water models has been presented recently [35].

Ice VIII is formed by two sub-lattices, which are interpenetrated but not interconnected [58, 166]. In one of the sublattices all dipole moments of the water molecules are aligned along the negative direction of the vector **c** of the unit cell, whereas in the other sublattice all dipole moments are aligned along the positive direction of the **c** vector of the unit cell. Thus the net dipole moment of ice VIII is zero. Protons are ordered in ice VIII. Thus an initial configuration of ice VIII can be obtained easily from the neutron diffraction experimental data [228] (adjusting slightly the bond length and angles from the experimental values to those of the TIP4P/2005 model). Ice VII is formed by two ice Ic sublattices which are interpenetrated but not interconnected. Ice VII is a proton disordered phase [166, 229, 230]. The initial configuration of ice VII was obtained by generating first an ice Ic lattice, with no net dipole moment and satisfying the Bernal Fowler rules [8, 85]. The algorithm of Buch et al. [86] was used to obtain such a proton disordered configuration. A second ice Ic lattice was obtained in the same way. After these two independent ice Ic configurations were obtained, we generated the initial

configuration of ice VII but putting together the two ice Ic sublattices, so that they are interpenetrated but not interconnected. Thus, the density of ice VII is of about twice the density of ice Ic.

The number of molecules used in the simulations were 600 (ice VIII), 432 (ice VII), 360 (ice VI) and for water we used either 432 or 360. In all cases the LJ potential was truncated at 8.5 Å. Standard long range corrections to the LJ part of the potential were added (i.e., $g(r)$ =1 beyond the cutoff) [99]. Note that this simple prescription (i.e. assuming $g(r)$ =1 beyond the cutoff) might introduce an error in the estimate of the long range correction, especially in solid phases (where g(r) is not one even at large distances). The impact that this might have on the coexistence points is not easy to assess, as the effect is different for different phases and at different densities. By analyzing the internal energy of solid phases for different systems sizes we conclude that the use of the simple prescription $g(r)$ =1 to estimate the long range correction of the LJ part of the potential may introduce an error of about 1.5 % in the determination of coexistence points ,which is enough for the purposes of this work. The importance of an adequate treatment of the long range coulombic forces when dealing with water simulations has been pointed out in recent studies [231–233]. In this work, the Ewald summation technique [97] has been employed for the calculation of the long range electrostatic forces. Isotropic NpT simulations were used for the liquid phase and for ice VII (which is of cubic symmetry) while anisotropic Monte Carlo simulations (Parrinello-Rahman like) [102, 104] were used for ices VIII and VI (both tetragonal). A typical Monte Carlo run involves about 30000 cycles of equilibration and 70000 cycles to obtain averages (defining a cycle as a trial move per particle plus a trial volume change).

The free energy was computed at a certain thermodynamic state for the ices VIII, VII and for liquid water. Once obtained at a certain thermodynamic state the free energy can be computed for any other thermodynamic conditions by using thermodynamic integration. Initial coexistence points were located by imposing the condition of equal chemical potential, temperature and pressure between coexistence phases. In particular we located coexistence points between several phases along the 70000 bar isobar, and along the 400K isotherm. The free energy of the liquid is calculated by computing the free energy change along a reversible path in which the water molecules are transformed into Lennard-Jones spheres by switching off the charges. The free energy of the reference Lennard-Jones fluid is taken from the work of Johnson *et al.* [113]. The free energy of ices VIII and VII was obtained by using the Einstein crystal method [115], or its slightly variant recently proposed by us denoted as the Einstein molecule method [234]. In the case of ice VII, and due to the proton disorder, one must add at the end of the calculation the entropy contribution due to the degeneracy of the structure. Thus was estimated by Pauling [85] to be of about $S/(Nk_B) = ln(3/2)$. Further details about the free energy calculations, both for the liquid phase, and for the solid phases of water can be found in our recent review paper about free energy calculations [133].

Once an initial coexistence point has been determined the rest of the coexistence curve can be obtained by using Gibbs Duhem simulations [138, 198]. Gibbs Duhem simulations, first proposed by Kofke, allow to determine the coexistence line between two phases, provided that an initial coexistence point is known. Gibbs Duhem is just a numerical integration (using simulation results to estimate the volume and enthalpy change between phases) of the Clapeyron equation. For the integration of the Clapeyron equation a fourth-order Runge-Kutta method algorithm is employed. Anisotropic scaling (Rahman Parrinello like) was used to simulate ices VIII and VI (both are tetragonal) and isotropic NpT simulations are used for the liquid and for the solid phases of cubic symmetry (ice VII and the plastic crystal solid). Rest of the details (size of the system, cutoff) were identical to that used in the NpT simulations.

In this work we have also performed Molecular Dynamic simulations to study the formation

of solid phases from liquid water at high temperatures. The choice of Molecular Dynamics (instead of Monte Carlo) allows to determine the time required by the liquid to freeze so that a comparison with experiment is possible. The molecular dynamic simulations were performed with the program Gromacs [235]. In the simulations the temperature is fixed with a Nose-Hoover thermostat [236, 237] with a relaxation time of 2 ps. To keep the pressure constant, an isotropic Parrinello-Rahman barostat [102, 238] was used. The relaxation time of the barostat was 2 ps. The time step used in the simulations was 1 fs. The typical length of the simulations was about 5 ns (five million time steps). The geometry of the water molecule is enforced using constraints. The LJ part of the potential was truncated at 8.5 Å and standard long range corrections were added. The real part of the coulombic potential was truncated at 8.5 Å. The Fourier part of the Ewald sums was evaluated by using the Particle Mesh Ewald (PME) method of Essmann *et al.* [239] The width of the mesh was 1 Å and we used a fourth other polynomial. As it can be seen the conditions of the Molecular Dynamic simulations were quite similar to those used in the Monte Carlo simulations.

Results

Let us start by presenting the results of Molecular Dynamics for the 440K isotherm. This temperature is close to temperature where fast nucleation of ice was observed experimentally [220]. We used 432 molecules in these molecular dynamic simulations. The choice of this number of molecules was motivated by the fact that we were expecting the formation of ice VII at high pressures. This number of molecules (432) would correspond to 216 unit cells (6x6x6) of ice VII. We started our simulations at low pressures (i.e about 10000 bar) where the system is in the liquid phase, and increased the pressure in consecutive runs. The final configuration of a run was used as the initial configuration of the next run. When the pressure was of 80000 bar we observed the spontaneous formation of a solid phase within a few ns. We repeated the runs several times (using different initial configurations) and the formation of the solid phase in less than 5ns was observed in almost all the cases. Thus the nucleation of a solid phase under these thermodynamic conditions can be reproduced easily. In Fig. 7.1 the evolution of the density with time at 440K and 80000 bar is plotted for several independent runs (we performed five independent runs). The nucleation of ice is a stochastic event so that each run freezes in a somewhat different time. However, it is clear that the formation of a solid phase occurs in about 1.5ns for the TIP4P/2005 model in this thermodynamic state (although for one of the five runs performed no freezing was observed after 5ns). Since the package Gromacs allows to visualise the trajectories, it was simple to identify the structure of the solid. The oxygen atoms of the water molecules formed a body centred cubic structure. The surprise was that the molecules of water were rotating rather wildly in the solid phase. Thus the system jumped from the liquid phase into a plastic crystal phase. Notice that ices VIII and VII are not plastic crystal phases, so that the phase obtained spontaneously is a new type of solid. For small system sizes (N=128 and N=432) and NpT simulations the crystal formed tends to be commensurate with the simulation box. However, for larger system sizes or NVT simulations we found more often that the crystal grows in some direction that was not compatible with the simulation box, so that complete crystallisation could not be achieved. In summary, we have observed that the TIP4P/2005 model freezes spontaneously in about 1.5ns (in average) into a plastic crystal phase at 440K. The formation of a plastic crystal, by heating ice VII at constant pressure has also been reported two months ago by Takii, Koga and Tanaka [221] for the TIP5P and TIP4P models. The plastic crystal phase obtained in this work from the liquid is identical to that described by Takii, Koga and Tanaka [221]. Someti-

mes when cooling/compressing liquids, the obtained solid phase is not the most stable from a thermodynamic point of view, but the more favourable from a kinetic point of view. Thus the thermodynamic stability of the plastic crystal phase with respect to ices VIII and VII should be determined.

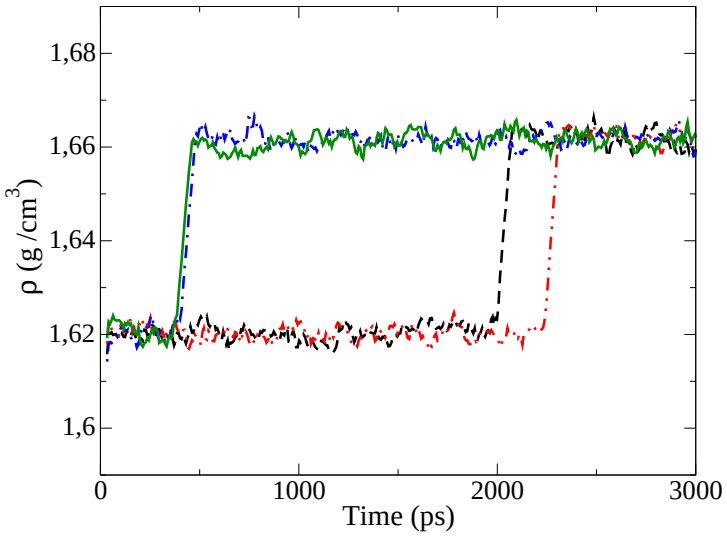

Figura 7.1: MD trajectories for four different initial configurations obtained with Gromacs at 440K and 80000bar. The formation a plastic crystal phase is indicated by the jump in the density (for two of the runs freezing occurs at quite similar times).

After observing the formation of the plastic crystal phase we analysed in detail the mechanical stability of ices VII and VIII when heated along the 70000 bar isobar. Starting at low temperatures, the temperature was increased (in jumps of 10-20K). For each temperature the length of the run was of about 100000 cycles. The final configuration of each simulation was taken as the initial configuration of the next run. For ice VII we observed a jump in the internal energy and density starting at a temperature of about 380K and ending at a temperature of about 390K. Visualisation of several snapshots revealed that the phase obtained at 390K was a plastic crystal phase. The density, radial distribution functions and internal energy were identical to those of the plastic crystal phase obtained from the freezing of the liquid (when compared at the same thermodynamic conditions). This is illustrated for the radial distribution functions in Fig. 7.2.

After a long equilibration at 400K and 70000 bar of the plastic crystal phase obtained by heating ice VII, we proceed to cool the system along the isobar to see if the system was able to return to the original state. The plastic crystal phase was mechanically stable up to 360K, and at a temperature of about 350K, the density and internal energy undergo a jump. The result of this heating-cooling cycle is plotted in Fig. 7.3. The presence of a hysteresis loop indicates clearly the existence of a first order phase transition between ice VII and the plastic crystal phase. In fact the phase obtained by cooling the plastic crystal phase is ice VII.

In Fig. 7.4 the radial distribution functions (O-O, H-H and O-H) of ice VII and of the phase obtained by cooling the plastic crystal phase are shown. As it can be seen they are nearly identical (and the same is true for other thermodynamic properties as density and internal energy) providing further evidence of the fact that the solid phase obtained by cooling the plastic crystal is ice VII. By analyzing the average positions of the water molecules in the

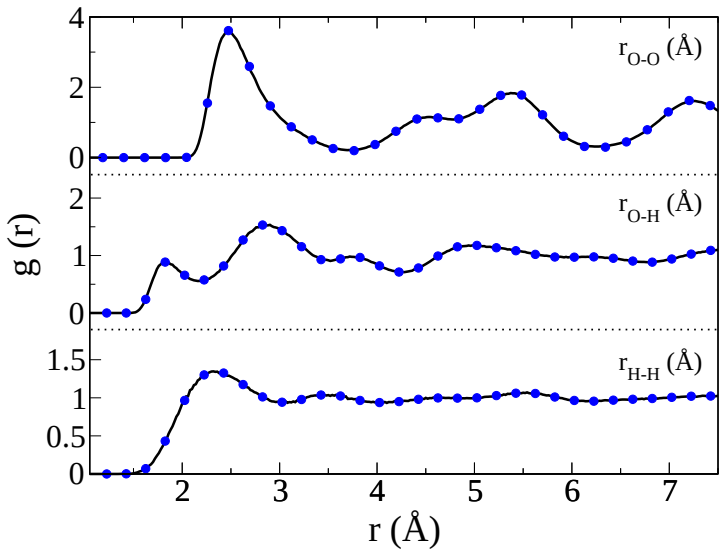

Figura 7.2: Oxygen-oxygen, oxygen-hydrogen and hydrogen-hydrogen radial distribution functions at T=440K and p=80000 bar for the bcc plastic crystal as obtained by isothermal compression of the liquid state (solid line) and by isobaric heating of ice VII (filled circles).

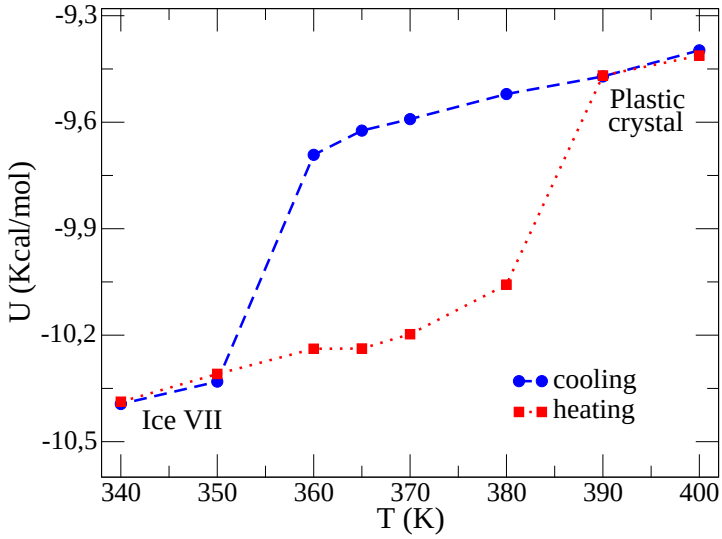

Figura 7.3: Hysteresis loop obtained by heating ice VII to obtain the plastic crystal phase (dotted line) and by cooling the plastic crystal phase to recover ice VII (dashed line). Results were obtained along the 70000bar isobar. The residual part of the internal energy is plotted as a function of the temperature.

phase obtained from the cooling of the plastic crystal phase, we found that the solid was formed by two sublattices which are interpenetrated but not interconnected as in ice VII.

In each of the sublattices each molecule was forming four hydrogen bonds (in two acting as donor and in two acting as acceptor). Therefore, the phase obtained by cooling the plastic crystal phase was indeed ice VII. We have repeated this heating-cooling cycle for the ice VII-plastic crystal transition at several pressures (70000 bar, 65000 bar and 60000 bar). In Table 7.2 the temperatures at which the ice VII to plastic crystal and plastic crystal to ice VII transitions occur are presented.

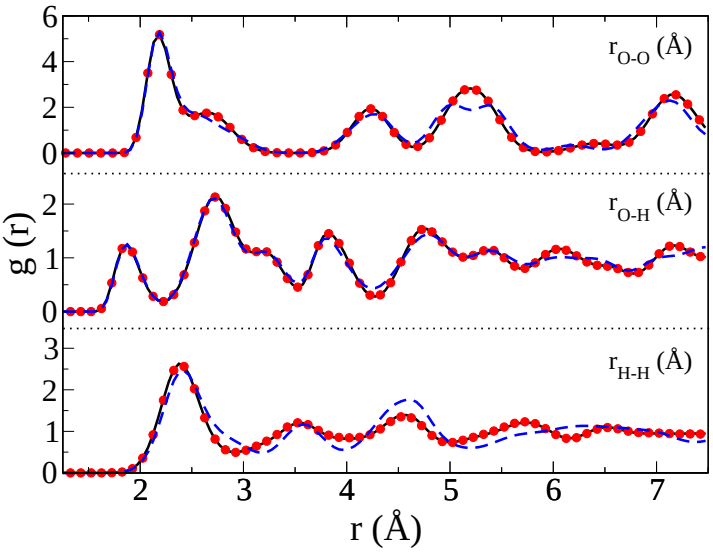

Figura 7.4: Oxygen-oxygen, oxygen-hydrogen and hydrogen-hydrogen radial distribution functions for ice VII (solid line), for ice VII obtained from the cooling of the plastic crystal phase (filled circles) and for ice VIII (dashed-dotted line). The radial distribution functions were obtained at 300K and 70000bar.

Tabla 7.2: Stability limits of ice VII when heated and of the plastic crystal phase when cooled as obtained from NpT simulations at three different pressures.

p/bar	Ice VII-plastic crystal *(heating)*	Plastic crystal-ice VII *(cooling)*
70000	390	350
65000	380	340
60000	360	310

From the results of Table 7.2 it is obvious that the ice VII to plastic crystal thermodynamic phase transition (where the chemical potential of both phases become identical) must be between 350K and 390K when the pressure is of 70000 bar, between 340K and 380K when the pressure is 65000 bar and between 310K and 360K when the pressure is of 60000 bar. Obviously only free energy calculations can determine the precise location of the coexistence point, which must be located between the two temperatures which bracket the hysteresis loop.

We also analysed the mechanical stability of ice VIII when heated along these three isobar. It was found that ice VIII was mechanically stable up to 390K for the p=70000bar isobar, up to 390K for the p=65000bar isobar and up to 380K for the p=60000bar isobar. At higher temperatures ice VIII also becomes a plastic crystal phase. Thus ice VIII becomes mechanically unstable (transforming into a plastic crystal phase) at temperatures similar to those found for ice VII. The mechanical stability limit of ice VIII (where it transforms into a plastic crystal phase) seems to be about 10K higher than that of ice VII. We did not observe any spontaneous transformation of ice VIII into ice VII when heated . This is not to say that this transition does not exist from a thermodynamic point of view (in fact it will be shown later that this transition indeed exists) but rather that the system is not able to overcome the free energy nucleation barrier separating ice VIII from ice VII within the length of our simulations.

In any case for pressures below 70000 bar it is not possible to have neither ice VIII nor ice VII as mechanically stable phases for temperatures above 390K. This provides further evidence that the plastic crystal phase obtained spontaneously from the liquid at 440K must indeed be thermodynamically stable at least at high temperatures. In any case, the definite proof of that will be provided by the free energy calculations.

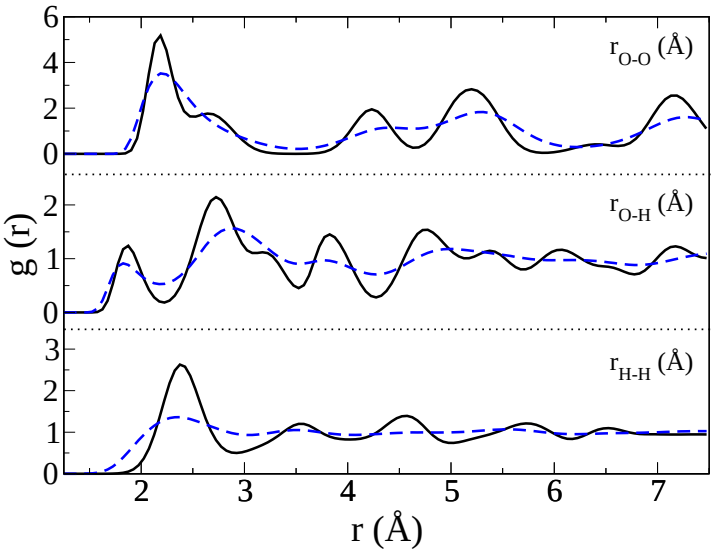

Figura 7.5: Oxygen-oxygen, oxygen-hydrogen and hydrogen-hydrogen radial distribution functions for ice VII at 300K and 70000 bar (solid line) and for the plastic crystal phase at 400K and 70000bar (dashed-dotted line).

In Fig. 7.4 the radial distribution functions of ice VIII are compared to those of ice VII at 300K and 70000 bar. They are clearly different showing that both solids are mechanically stable (and clearly distinguishable) under these thermodynamic conditions.

Let us now present the structural properties for the plastic crystal phase. In Fig. 7.5, the radial distribution functions for the plastic crystal phase at 400K and 70000 bar are compared to those of ice VII at 300K and 70000bar for the O-O, O-H and H-H correlation functions. As it can be seen from the oxygen-oxygen correlation function, the peaks of the O-O distribution in the plastic crystal phase correspond to those of ice VII, although the higher temperature and lower density of the plastic crystal solid provokes peaks with a more diffuse character. Changes in the g_{O-H} distribution function are significant, but the most important change occurs in the g_{H-H} correlation function. It has a liquid like aspect in the plastic crystal solid whereas its long range order is clearly visible in ice VII. Thus the g_{H-H} distribution function is quite useful to identify the existence of a plastic crystal phase.

We have also determined the probability distribution of the polar angles (θ and ϕ of the OH bonds). The x axis is located on the **a** vector of the unit cell, the y axis is located on the **b** vector of the unit cell, and the z axis is located along the **c** vector of the unit cell. The distribution function $f(\theta)$ is defined as :

$$f(\theta) = \frac{N(\theta)}{2N\Delta\theta} \tag{7.1}$$

where $N(\theta)$ denotes the number of OH bonds with polar angle between θ and $\theta + \Delta\theta$ and 2N is the number of OH bonds (i.e twice the number of molecules N). The distribution function

$f(\phi)$ is defined as :

$$f(\phi) = \frac{N(\phi)}{2N\Delta\phi} \tag{7.2}$$

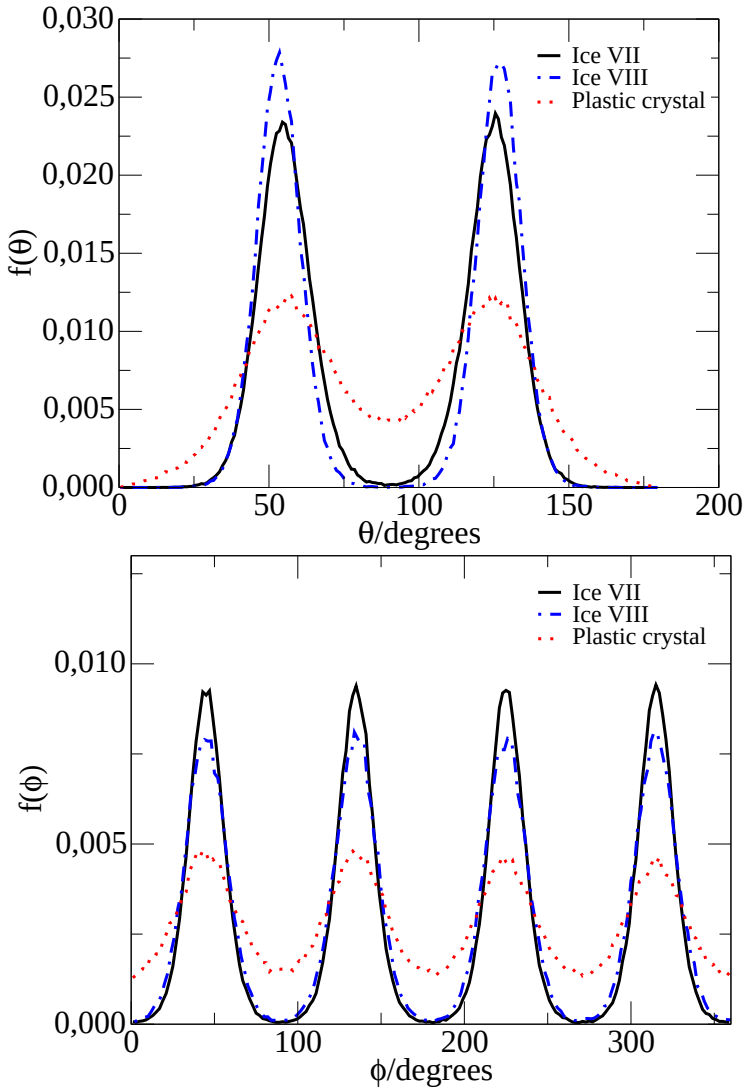

Figura 7.6: a) $f(\theta)$ as a function of θ angle for ices VII (solid line) and VIII (dashed-dotted line) at 300K and 70000bar and for the plastic crystal phase (dotted line) at 400K and 70000bar.
b) $f(\phi)$ as a function of ϕ angle for ices VII (solid line) and VIII (dashed-dotted line) at 300K and 70000bar and for the plastic crystal phase (dotted line) at 400K and 70000bar. For clarity the function $f(\phi)$ of ice VIII has been shifted by 90 degrees to illustrate the similarity with that of ice VII.

In Fig. 7.6 the functions $f(\theta)$ and $f(\phi)$ are presented for ices VIII and VII at 300K and 70000bar. As it can be seen the peaks of $f(\theta)$ are located at 54.74 and $(180 - 54.74)$ where 54.74 is the angle in ice VII between one of the diagonals of the cube and a line connecting the center of two opposite faces. The four peaks in $f(\phi)$ are separated by 90 degrees as it should be. In Fig. 7.6 the functions $f(\theta)$ and $f(\phi)$ are also presented for the plastic crystal phase at 400K and 70000bar. As it can be seen both distributions present less structure than the one of ices VII and VIII. It is also clear that even in the plastic crystal phase the OH vectors

Tabla 7.3: Helmholtz free energy for ices VIII, VII and for the plastic crystal phase. The Gibbs free energy was computed after adding pV to the Helmholtz free energy. The data marked with an asterisk correspond to calculations using the structure ice VII as obtained from the cooling of the plastic crystal. The density is given in g/cm^3.

Phase	T/K	p/bar	ρ	A/Nk$_B$T	G/Nk$_B$T
Ice VIII	300	70000	1.709	-9.36	20.23
Ice VII	300	70000	1.707	-9.75	19.87
Ice VII*	300	70000	1.707	-9.74	19.88
Plastic	400	70000	1.638	-6.46	16.69
Water	300	1292	1.050	-15.45	-14.56

prefer to point out to the contiguous oxygens atoms. Therefore the angular distribution is not uniform even in the plastic crystal phase (i.e the OH vector does not distribute uniformly on the surface of a sphere). The molecules, although able to rotate prefer to point out the OH vectors to any of the 8 O atoms forming the first coordination layer. However, we checked that as the temperature increases the $f(\theta)$ and $f(\phi)$ distributions become somewhat more uniform. In summary the molecules rotate almost freely in the plastic crystal phase, but the OH vectors prefer to point out to the contiguous oxygen atoms. An additional interesting comment is that for ices VIII and VII at 300K and 70000 bar and for the length of the simulations performed in this work , a certain individual molecule presents a fixed value of θ and ϕ (except for a little bit of thermal vibration). However for the plastic crystal phase each individual molecule jumps quite often from one of the peaks of the distribution to another peak. These flipping or jumping moves occur quite often for each molecule within the length of the simulation runs considered here (at 400K in average each flipping requires about 8000 Monte Carlo cycles). The ice VIII to ice VII transition represents the change from proton order to proton disorder within the two sub lattices of the solid, whereas the ice VII to plastic crystal phase transition represents the disappearance of the two sublattices.

Let us now change to the determination of coexistence points. We have determined the free energy for ices VIII, VII and for the plastic crystal phase (Table 8.1). The free energy calculation was performed for ice VIII at 300K and for a density which corresponds to that of the system at 70000 bar. The free energy of ice VII was computed at 300K and for a density which corresponds to that of 70000bar. Finally the free energy of the plastic crystal phase was computed at 400K and for a density which corresponds to that of the system at 70000 bar. Details about the free energy calculations in water solid phases have been provided elsewhere [133]. Let just mention the procedure used to compute the free energy of the plastic crystal phase as it differs from that used for the rest of solid phases of water. Firstly translational springs connecting the oxygen atoms to the lattice positions of the bcc structure were switched on (in the plastic crystal phase the oxygens form a bcc solid). After that, and while keeping the translational springs, the charges of the system were switched off ending with a system of LJ atoms connected by springs to a bcc solid structure. Free energies changes can be computed easily along this path in which the Hamiltonian of the system is changed. Notice that no phase transition occurs along the integration since the system is in a plastic crystal phase along the entire integration path. Finally the free energy difference between a LJ particle connected with translational springs to a bcc lattice, and an ideal Einstein crystal (with springs connecting to the bcc lattice but without intermolecular interactions) is computed by a perturbative approach. This integration path is inspired by a recent article by Lindberg and Wang in which the dielectric

constant of ice Ih was computed by switching off the charges of the molecules while having translational springs [132]. In Table III the free energies for the considered thermodynamic states are reported. Let us just mention, that the Pauling degeneracy entropy was added to the free energy of ice VII. This contribution was not added neither to ice VIII nor to the plastic crystal phase.

As it can be seen the Gibbs free energy of ice VII is smaller than that of ice VIII. Both phases have similar densities and internal energies and the higher stability of ice VII is mainly due to the contribution of the Pauling entropy (which is not present in ice VIII). Therefore for T=300K and p=70000bar ice VII is more stable than ice VIII. By using thermodynamic integration the ice VII to ice VIII transition at 70000 bar has been located at T=69K. In the same way the VII to plastic crystal transition has been located to occur at 377K for a pressure of 70000 bar. This value is consistent with the hysteresis loop found at 70000bar between the temperatures 350 and 390. Finally by using thermodynamic integration the fluid-plastic crystal transition was found to occur at a pressure of $p = 62000bar$ for the 400K isotherm. The fluid-plastic crystal transition was also determined by using direct coexistence simulations. An equilibrated configuration of the plastic crystal phase (432 molecules) was located on the left hand side of a simulation box, and put into contact with an equilibrated configuration of the fluid having 432 molecules. Molecules of the fluid phase overlapping with those of the solid phase at the fluid-solid interface were deleted. Thus the total number of molecules in the direct coexistence simulations was of 858. We then performed MD simulations using Gromacs, while keeping the temperature at 400K. Runs at different pressures were performed. At pressures below the melting point the solid phase will melt, whereas at pressures higher than the coexistence pressure the fluid phase will crystallise. The direct coexistence technique, was pioneered by Ladd and Woodcock [140–142], and used recently by several authors [143, 144, 190, 240–248].

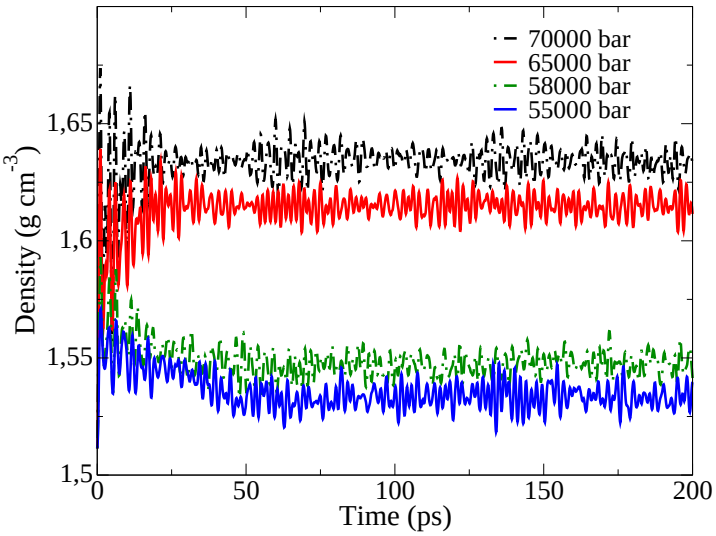

Figura 7.7: Evolution of the density with time as obtained from MD simulations. All results were obtained for T=400K. Lines from the top to the bottom correspond to the pressures 70000,65000,58000 and 55000bar respectively.

In Fig. 7.7, the evolution of the density with time is shown for several pressures. As it can be seen for the low pressures (55000 and 58000 bar) the density decreases quickly indicating the melting of the plastic crystal. For high pressures (i.e 65000, 70000 bar) the density of

the system increases quickly indicating the freezing of the fluid into a plastic crystal phase. Thus the value of 62000 bar obtained from free energy calculations is consistent with the results obtained from direct coexistence simulations [144]. Notice that in the direct coexistence simulations the melting of the plastic crystal, or the freezing of the water occurs in about 0.2ns, which is about two orders of magnitude smaller than the time required to determine accurately the melting point of ice Ih at room pressure by direct coexistence simulations [144]. This is probably due to two different facts. First, the temperature is high (400K instead of the temperature of about 250K used in the ice Ih-water direct interface simulations). Secondly the growth of the crystal is a somewhat more complex process for ice Ih since each water molecule must be located in a certain position and with a certain orientation to allow the ice Ih to grow. However, in the plastic crystal phase, the molecule must find the location, but the orientation is not so important since the molecules are rotating in the plastic crystal phase anyway.

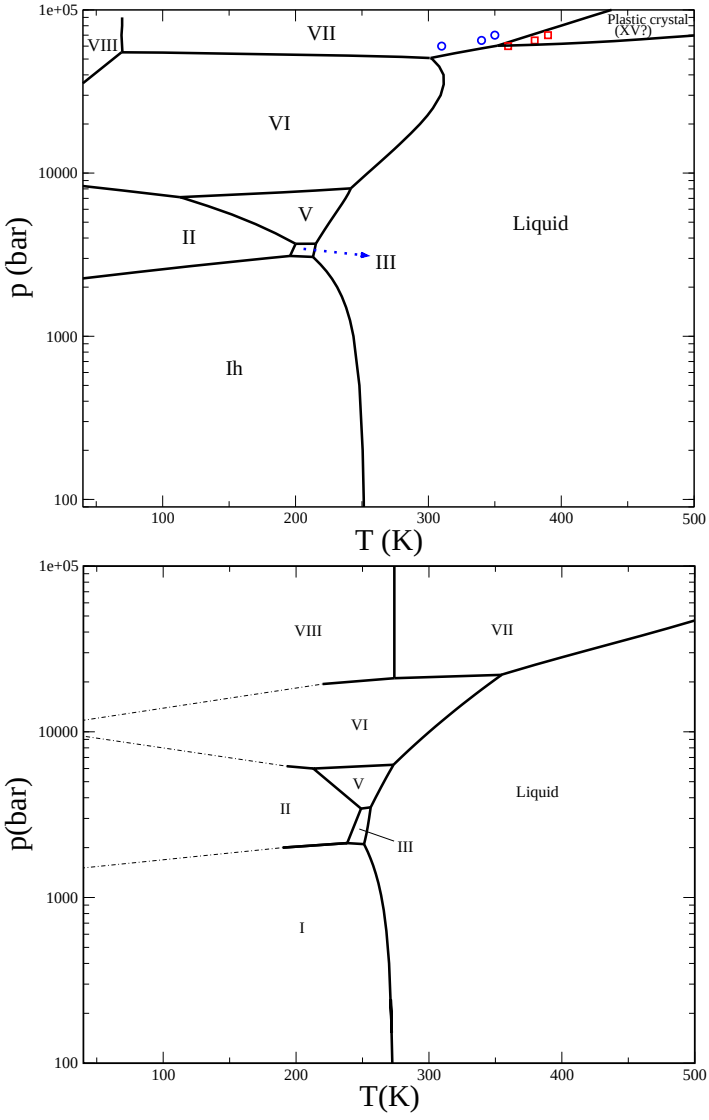

Figura 7.8: a) Global phase diagram for the TIP4P/2005 model. The squares correspond to the stability limit of ice VII when heated, whereas the circles correspond to the stability limit of the plastic crystal phase when cooled. b) Experimental phase diagram of water.

Tabla 7.4: Melting curve of the plastic crystal phase of the TIP4P/2005 as obtained from free energy calculations and Gibbs Duhem integration (with isotropic NpT simulation performed for the fluid and for the cubic plastic crystal phase). The densities are given in g/cm^3. The residual internal energies are given in in kcal/mol.

T/K	p/bar	U_1	U_2	ρ_1	ρ_2
fluid-plastic crystal					
340.00	60193	-10.45	-10.03	1.574	1.622
360.00	60486	-10.24	-9.85	1.572	1.613
380.00	61135	-10.04	-9.73	1.565	1.610
400.00	62000	-9.87	-9.58	1.562	1.609
420.00	63108	-9.75	-9.43	1.565	1.607
440.00	64390	-9.52	-9.30	1.564	1.608
460.00	66042	-9.35	-9.12	1.560	1.607

Once an initial coexistence point has been found for the VIII-VII, VII-plastic and VII-fluid transitions, the rest of the coexistence lines will be obtained by Gibbs Duhem simulations. In Fig. 7.8 these three coexistence lines are plotted. As it can be seen the fluid-plastic crystal and the VII-plastic crystal coexistence lines met at a triple point located around 352K and 60375 bar. This triple point can be used as initial coexistence point of the VII-fluid coexistence line. The fluid-VII coexistence line obtained from Gibbs Duhem simulations has also been plotted in Fig. 7.8. At 300K the Gibbs Duhem integration predicts a fluid-VII coexistence pressure of about 51000 bar, which is consistent with the coexistence pressure predicted from free energy calculations. The melting curve of ice VI intersects the melting curve of ice VII, generating a fluid-VI-VII triple point (the precise location is 301K and 50742 bar). This triple point can be used as initial point for the VI-VII coexistence curve. The VI-VII coexistence curve intersects the VIII-VII coexistence curve at about 55000 bar and 69K. This generates an VI-VII-VIII triple point which can be used to initiate the VI-VIII coexistence line. The global phase diagram of the TIP4P/2005 (including the high pressure phases) is presented in Fig. 7.8. The experimental phase diagram is also presented in Fig. 7.8. The coexistence lines are given in tabular form in Tables 8.2-7.6. The triple points are given in Table 8.4.

As it can be seen the TIP4P/2005 reproduces qualitatively the phase diagram of water. Ice VIII is stable only at low temperatures. The coexistence line between ice VIII and ice VII is almost a vertical line. This is due to the fact that the densities of ices VII and VIII are practically identical for a certain temperature and pressure. There is a certain regime of temperatures where ice VII coexists with the liquid phase. There are three significant qualitative differences between the phase diagram of TIP4P/2005 and the experimental one. The first is that the VIII-VII transition temperature seems to be low as compared to experiment. It seems that models with a TIP4P geometry tend to underestimate the temperature of the order-disorder transitions (between ices having the same arrangement of oxygens but differing in the proton ordering). In fact we found in previous work [188] that also the XI-Ih transition was predicted to occur for the TIP4P model at a temperature lower than found experimentally.

The second is the appearance of a plastic crystal phase for the TIP4P/2005 model. This plastic crystal phase has not been reported so far for real water. The third is the appearance of re-entrant melting in the melting curve of ice VI which is not found in the experimental phase diagram. The reason for the appearance of re-entrant melting in the melting curve of ices (from ice Ih up to ice VI) has been discussed previously [22]. The fluid-VI-VII triple point is located at 301K and 50742 bar, to be compared with the experimental value which is located at a temperature of 355 K and a pressure of about 22000 bar. Thus, it seems that to bring

Tabla 7.5: Melting curves of ices VI and VII for the TIP4P/2005 model as obtained from free energy calculations and Gibbs Duhem integration. The densities are given in g/cm^3. The internal energies in kcal/mol (only the residual part of the internal energy is reported).

T/K	p/bar	U_1	U_2	ρ_1	ρ_2
fluid-VI					
244.97	8540	-12.23	-12.96	1.245	1.359
254.39	10000	-12.02	-12.91	1.265	1.365
265.14	12000	-11.98	-12.84	1.286	1.373
278.27	15000	-11.77	-12.76	1.316	1.385
293.67	20000	-11.55	-12.64	1.365	1.406
303.39	25000	-11.38	-12.55	1.396	1.427
309.21	30000	-11.26	-12.47	1.435	1.447
311.52	35000	-11.21	-12.39	1.464	1.467
311.39	40000	-11.15	-12.32	1.492	1.485
308.14	45000	-11.03	-12.26	1.518	1.503
302.87	50000	-10.98	-12.20	1.542	1.520
293.92	55000	-10.97	-12.15	1.572	1.537
281.74	60000	-10.89	-12.11	1.596	1.553
fluid-VII					
352.00	60375	-10.30	-10.46	1.578	1.663
340.00	58066	-10.42	-10.57	1.570	1.658
320.00	54276	-10.74	-10.74	1.565	1.651
300.00	50988	-10.90	-10.90	1.549	1.646

Tabla 7.6: Solid-solid coexistence lines of the TIP4P/2005 model for the high pressure polymorphs (ice VII,VIII and plastic crystal) as obtained from free energy calculations and Gibbs Duhem integration. The densities are given in g/cm^3. The internal energies in kcal/mol (only the residual part of the internal energy is reported).

T/K	p/bar	U_1	U_2	ρ_1	ρ_2
VII-plastic crystal					
440.00	101354	-8.99	-8.49	1.749	1.728
420.00	90168	-9.44	-8.81	1.729	1.698
400.00	80146	-9.76	-9.19	1.707	1.674
390.00	75596	-9.82	-9.33	1.693	1.659
377.00	70000	-10.04	-9.53	1.681	1.645
360.00	63292	-10.27	-9.79	1.666	1.623
350.00	59665	-10.40	-9.95	1.656	1.617
VII-VIII					
69.70	55000	-11.97	-12.01	1.719	1.718
69.00	70000	-11.67	-11.71	1.758	1.758
69.49	80000	-11.45	-11.48	1.781	1.782
VI-VII					
301.00	50742	-12.19	-10.85	1.523	1.642
280.00	51549	-12.29	-11.03	1.529	1.655
240.00	52454	-12.50	-11.23	1.538	1.669
100.00	54767	-13.15	-11.85	1.567	1.712
50.00	55369	-13.38	-12.06	1.576	1.726
VI-VIII					
69.00	55000	-12.14	-12.02	1.594	1.719
35.00	32974	-12.90	-12.58	1.519	1.660

Tabla 7.7: Triple points of the TIP4P/2005 model of water , between stable phases at high pressures

Phase boundary	T/K	p/bar
fluid-VI-VII	301	50742
fluid-VII-plastic	352	60375
VI-VII-VIII	69	55000

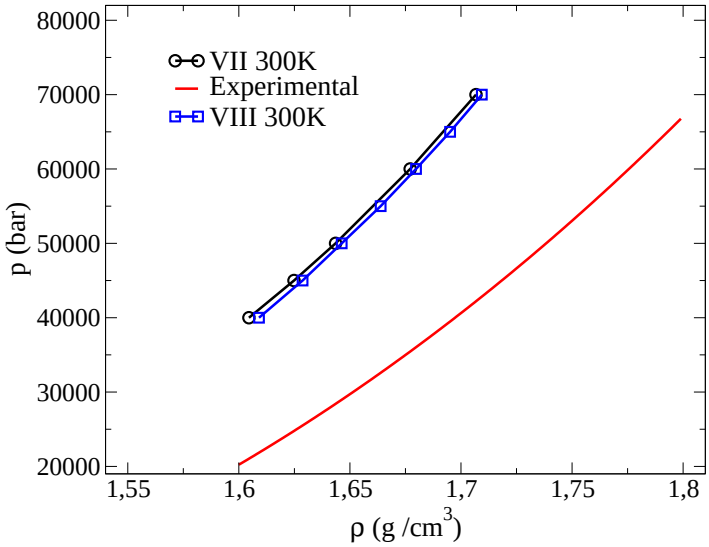

Figura 7.9: Equation of state of ices VII (open circles) and VIII (open squares) for T=300K as obtained from computer simulation for the TIP4P/2005 model. The solid line on the right hand side correspond to the experimental results as given by Fei et al.[249].

the phase diagram of TIP4P/2005 into closer agreement with experiment the stability of ice VII should increase. In this way the fluid-VI-VII triple point would occur at lower pressures and the re-entrant portion of the melting curve of ice VI would occur in the metastable part of the melting curve. In Fig. 7.9 the equation of state of ices VIII and VII at 300K are plotted as a function of pressure. For pressures below 35000 bar ice VIII (as described by TIP4P/2005) is not mechanically stable and melts into a liquid phase. For pressures below 40000 bar ice VII (as described by TIP4P/2005) is not mechanically stable and melts into a liquid phase. As it can be seen for a certain temperature and pressure ice VIII yields a slightly higher density than ice VII (the densities are quite similar anyway as also pointed out by Bartok and Baranyai [227]). As it can be seen the TIP4P/2005 model is not able to describe accurately the experimental values of the densities of ice VII. In fact it tends to underestimate the experimental values of the densities by about 5 per cent. This is striking since the TIP4P/2005 is able to describe the densities of ices Ih, II, III, IV, V, VI, IX and XII (for pressures up to 20000 bar) within an error of about 1 per cent and for liquid water up to pressures of about 40000 bar with an error of about 1 per cent. Thus it seems that there is something wrong in the model which prevents of describing accurately the densities of ices VIII and VII at high pressures. Notice that other water models as SPC, SPC/E and TIP4P do also underestimate significantly the density of ice VII at high pressures. Further work is needed to understand the origin of that. One may suggest that the absence of polarisability, or the use of a non very accurate description of the repulsive part of the potential (by the LJ potential), or even the absence of LJ sites located on the hydrogen atoms (to introduce a further degree of anisotropy) may be responsible. The only model that reproduces the experimental densities of ice VII is TIP5P. This is shown in Table 7.8. However, this is not for free since this model overestimates by about 5-8 per cent [186] the densities of ices Ih, II, III, IV, V, VI, IX and XII. Thus TIP5P reproduces the densities of ice VII, but fails completely in describing the densities of the other polymorphs of water [58, 249, 250].

Let us finish by presenting the value of the dielectric constant of the plastic crystal phase. It should be pointed out that standard computer simulations (MD or standard MC) can not be used to determine the dielectric constant of ices. Typical lengths of the simulations (seve-

Tabla 7.8: Densities of ice VII as obtained from the NpT simulations of this work for the TIP4P/2005 and TIP5P models of water. The experimental data for ice VII are taken from Ref. [249] and for the rest of polymorphs from Ref. [58], except for ice II that was taken from Ref. [250]. Values of the densities of the other polymorphs were taken from Ref. [214] for the TIP4P/2005 model and from Ref. [186] for the TIP5P model.

Phase	T/K	p/bar	ρ/(gcm^{-3})		
			Expt	TIP4P/2005	TIP5P
VII	300	45000	1.718	1.625	1.729
VII	300	70000	1.810	1.707	1.814
I_h	250	0	0.920	0.921	0.976
II	123	0	1.190	1.199	1.284
III	250	2800	1.165	1.160	1.185
IV	110	0	1.272	1.293	1.371
V	223	5300	1.283	1.272	1.331
VI	225	11000	1.373	1.380	1.447
IX	165	2800	1.194	1.190	1.231
XII	260	5	1.292	1.296	1.340

ral ns or hundred of thousands of cycles) are not sufficient to sample the fluctuations of the polarisation of the solid. To compute dielectric constants of ices it is necessary either to introduce special moves within the Monte Carlo program, as those proposed by Rick and Haymet [154, 174] or to use special techniques as that proposed recently by Lindberg and Wang [132]. Thus from our study we could not report the dielectric constant of ices VIII and VII. However we could compute the dielectric constant for the plastic crystal since the molecules are able to rotate rather quickly provoking important fluctuations of the total polarisation. We obtained a value of about 96(10) for the plastic crystal phase at 400K and 70000 bar. The dielectric constant of the plastic crystal phase (assuming it exists in real water) has not been reported. The experimental value [251] of the dielectric constant of ice VII at room temperature and for a pressure of 23300 bar is of 105. Although it is difficult to compare dielectric constants obtained for somewhat different structures (ice VII and the plastic crystal phase are not the same solid), and somewhat different thermodynamic conditions, the comparison between both values appears as reasonable. For liquid water at room temperature and pressure the TIP4P/2005 predicts a dielectric constant of about 60, whereas the experimental value is of 78. Thus the model underestimates the dielectric constant of liquid water by about 20 per cent. Also for ice Ih, TIP4P models seriously underestimate the dielectric constant [132, 154, 174]. Assuming that similar behaviour could be found for liquid water and the plastic ice, the prediction of the model for the plastic crystal phase seems to be lower than the experimental value of ice VII. The absence of polarisability is likely to be responsible for this deviation.

Conclusions

In this work the high pressure region of the phase diagram of water has been determined by computer simulation by using the TIP4P/2005 model. By performing free energy calculations the relative stability of ices VIII and VII, and the melting curve of ice VII was obtained. When compressing water at 440K, the freezing of water into a solid phase occurred in a few

ns. The analysis of the solid allows to conclude that it is formed by a body center cubic lattice of oxygens, with the molecules rotating significantly. In summary a plastic crystal phase. It has also been found that ices VIII and VII transform into a plastic crystal phases at temperatures above 390K and pressures below 70000 bar. By performing free energy calculations the melting curve of the plastic crystal phase and the coexistence lines between the plastic crystal phase and ice VII could be determined. In this way a rather extensive region of the phase diagram for the TIP4P/2005 could be reported by the first time. The possible existence of other solid phases or even of other plastic crystal phases for the model should not be discarded yet. The TIP4P/2005 is able to describe qualitatively the phase diagram of water. The model (in common with the popular SPC/E and TIP4P models) fails to describe the density of ice VII along the room temperature isotherm, and underestimates with respect to experiment the stability of ice VII. This is in contrast with the excellent description provided for other coexistence lines and for the densities of other polymorphs appearing at pressures below 20000 bar. Thus the model does not allow to describe quantitatively the behaviour of water at high pressures. Further work is needed to understand the origin of that. On the other hand the model predicts the existence of a new phase, a plastic crystal phase. Notice that all transitions found between the plastic crystal phase and other phases (liquid or ice VII) were found to be first order, so that if the plastic crystal phase exists in real water there should be a first order phase transition separating it from ice VII. Interestly Takii, Koga and Tanaka suggested that the two set of melting curves reported experimentally at 100000 bar could be due to the fact that these two groups were indeed measuring two different transitions, namely the ice VII to plastic crystal (that would correspond to the temperature of 600K given by Mishima and Endo [252]) and the plastic crystal to liquid phase (that would correspond to the temperature of 687K given by Datchi, Loubeyre and LeToullec [49]). Further experimental work is needed to clarify this point.

It would be of interest to study if such a plastic crystal phase does indeed exist for real water. If so it would corresponds to ice XV (the precise roman numeral may change if other solid phases of water are found experimentally before), and would probably be one of the few cases where computer simulation anticipates an experimental result. In case it exists it may dominate the melting curve of water at high temperatures. The nearly spherical shape of water makes possible the formation of a plastic crystal phase at high temperatures where the strength of the hydrogen bond in k_BT units is rather small and where the molecular shape (i.e repulsive forces) play the leading role in the process of freezing. For hard dumbbells or spherocylinders the maximum anisotropy (as given by the ratio between the bond length and the width of the molecule) which allows the formation of a plastic crystal phase is of about 0.4 [199, 253–257]. Molecules with higher anisotropy freeze into an orientally ordered solid. Thus the formation of plastic crystal phases requires moderate anisotropy in the repulsive part of the potential (the importance of the attractive part decreases substantially at high temperatures). This seems to be the case of water, at least when described as a LJ center plus charges. Besides the experimental importance of finding a plastic crystal phase for water, its presence or absence should also have an impact on the community performing computer simulations of water. Its presence would indicate that current water models are able to predict qualitatively this new feature of the phase diagram of water. Its absence would also be significant since it would indicate that current water models are too spherical and they should be modified so as to predict the disappearance of the plastic crystal phase.

Since a picture is worth a thousand words let us finish by presenting an instantaneous snapshot of ices VII, VIII and of the plastic crystal. This is done in Fig. 7.10. The orientational disorder of the plastic crystal phase is shown clearly in the figure.

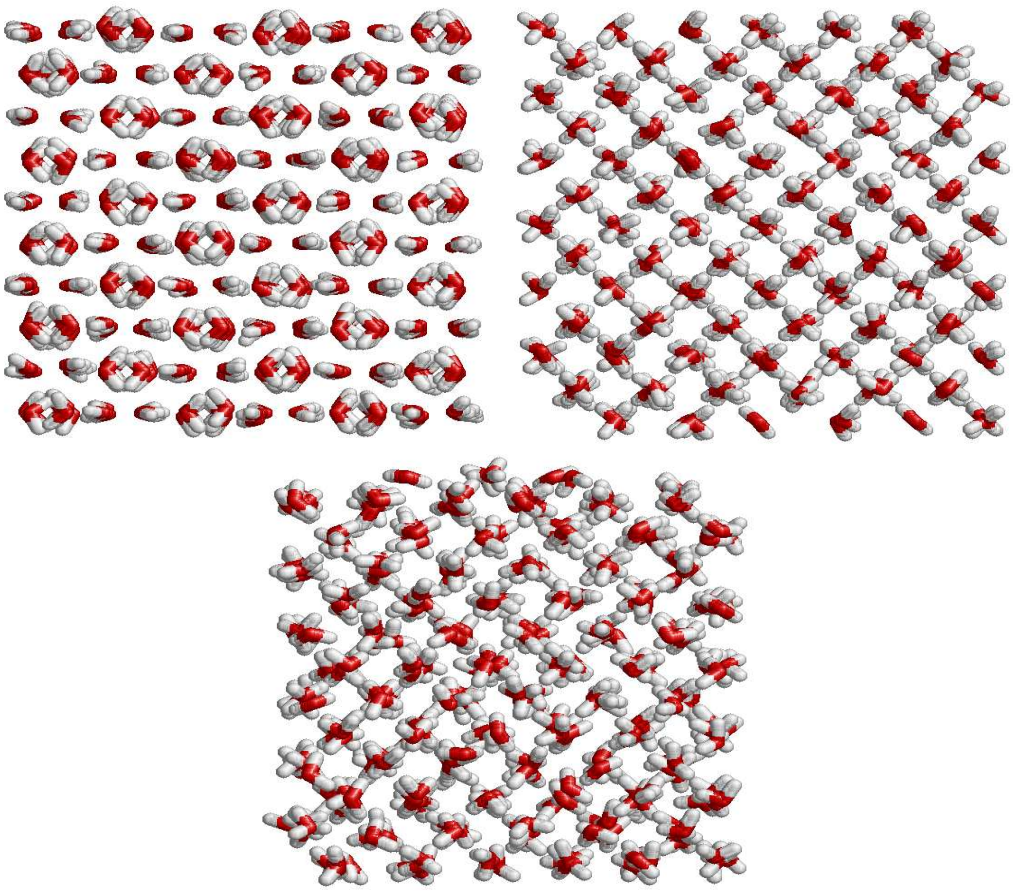

Figura 7.10: Snapshots of ices. a) Snapshot of ice VIII at 300K and 70000bar. b) Snapshot of ice VII at 300K and 70000bar. c) Snapshot of the plastic crystal phase at 400K and 70000 bar.

Acknowledgements

This work was funded by grants FIS2007-66079-C02-01 from the DGI (Spain), S-0505/ESP/0229 from the CAM, and 910570 from the UCM. M.M.Conde would like to thank Universidad Complutense by the award of a PhD grant. J. L. Aragones would like to thank the MEC by the award of a pre-doctoral grant. E.G.N. wishes to thank the Ministerio de Educación y Ciencia and the Universidad Complutense de Madrid for a Juan de la Cierva fellowship. Helpful discussions with L.G.MacDowell and J.L.F.Abascal are gratefully acknowledged.

CAPÍTULO 8

Plastic crystal phases of simple water models

J.L. Aragones[1] **and C. Vega**[1]

[1] *Dep. Química Física, Fac. Química, Universidad Complutense de Madrid, 28040,Madrid, Spain*

Journal of Chemical Physics, **130***, 244504 (2009)*

Abstract

We report the appearance of two plastic crystal phases of water at high pressure and temperature using computer simulations. In one of them the oxygen atoms form a body centered cubic structure (bcc) and in the other they form a face centered cubic structure (fcc). In both cases the water molecules were able to rotate almost freely. We have found that the bcc plastic crystal transformed into a fcc plastic crystal via a Martensitic phase transition when heated at constant pressure. We have performed the characterization and localization in the phase diagram of these plastic crystal phases for the SPC/E, TIP4P and TIP4P/2005 water potential models. For TIP4P/2005 model free energy calculations were carried out for the bcc plastic crystal and fcc plastic crystal using a new method (which is a slight variation of the Einstein crystal method) proposed for these types of solid. The initial coexistence points for the SPC/E and TIP4P models were obtained using Hamiltonian Gibbs-Duhem integration. For all of these models these two plastic crystal phases appear in the high pressure and temperature region of the phase diagram. It would be of interest to study if such plastic crystal phases do indeed exist for real water. This would shed some light on the question of whether these models can describe satisfactorily the high pressure part of the phase diagram of water, and if not, where and why they fail.

Introduction

The phase diagram of water, although relatively well known, is far from being complete. Besides ice Ih, other solid phases were found at the beginning [23, 212, 258] of the last century, towards the end [92] and even in this century [25]. The search of new solid phases has taken two principal routes. The first is the search (at low temperatures) for proton ordered analogous of the high temperature proton disordered ices. This is the research that lead to the discovery of ices VIII [259], XI [260], IX [261], XIII [25], XIV [25] (ice VI being probably the only proton disordered ice for which the proton ordered ice has not yet been found). The second route is the search of new ices at high pressures and/or temperatures. The discovery of ice VII, by Bridgmann [24] and the evidence of ice X [262] illustrate the fact that new solid phases can be found under extreme pressures [223, 228, 263]. Notice that such extreme conditions may be found in other places within the solar system, so this is of interest for the planetary

sciences [264]. However, it must be recognized that performing experiments at high pressures is difficult, and so-far there is not a completely clear understanding of the aspect of the phase diagram of water at high pressures. Even the melting point curve of water at high pressures is a subject of current interest [48–52, 251, 252, 265]. A quick look at Fig. 8.1 (where different experimental measurements of the melting curve of water at high pressures is presented) illustrates the fact that melting lines obtained by various groups are different, and that some consensus about what is happening in this region of the phase diagram of water is required.

Computer simulations of water started with a delay of about 60 years with respect to experiments, the first simulations of water appeared about 40 years ago [10, 11]. At the beginning the interest focused on finding reasonable water models that allowed one to understand the physics of liquid water. The study of phase transitions in water by computer simulation started somewhat later. Firstly the vapor-liquid equilibria was considered [13–15], and more recently the study of fluid-solid and solid-solid equilibria [16–22]. Five years ago we presented for the first time the phase diagram of water as obtained from computer simulations [22], for two water models, the SPC/E [106] and the TIP4P [107] models. It was shown that the TIP4P model was able to provide a reasonable description of the phase diagram of water. The main two defects of the model were that the melting points were too low, and that the freezing pressures were too high above the room temperature. We have since proposed a modified version of the TIP4P model, denoted as TIP4P/2005 [34], that improves the prediction of the melting point temperatures and provides an excellent description of the properties of water [35]. Initially we computed the low pressure region of the phase diagram for the TIP4P/2005 model, showing good agreement with experiment. Later on and motivated by the experimental work of Dolan et al. [220] showing that at 400K and high pressures water freezes in a few nanoseconds, we performed computer simulation studies of the kinetics of freezing at these conditions. It was found [29] that water freezes very quickly in the simulations at these high pressures and temperatures, in clear contrast with the extremely long runs required to freeze water into ice Ih at low temperatures [170, 216, 217, 266]. The surprise was that in the simulations water does not freeze into ice VII but into a new phase, which was a plastic crystal [29]. In this plastic crystal phase the oxygens are located in a bcc arrangement (as in ice VII) but the molecules were able to rotate almost freely (i.e a plastic crystal phase). This plastic crystal (PC) phase was also found by Takii, Koga and Tanaka [221] for TIP5P, and for the TIP4P and SPC/E models. Therefore, it seems at this point necessary to recalculate the high pressure part of the phase diagram of TIP4P and SPC/E to include this new plastic crystal phase that was overlooked in our previous study [22]. This requires free energy calculations for the plastic crystal phase. In this work we shall describe in detail how to perform free energy calculations for these types of solid.

Another issue of interest is the layout of the phase diagram of these rigid water models (TIP4P, TIP4P/2005, SPC/E) at extremely high pressures. In particular it would be of interest to establish if a solid with a fcc arrangement of the oxygens (i.e a close packed structure) may appear for these models at extremely high pressures [221]. As will be shown, this is indeed the case. A plastic crystal phase with an fcc arrangement of the oxygens appears at high pressures and temperatures , allowing a better packing of the molecules than the typical bcc arrangement of ice VII or the bcc plastic crystal. These two plastic crystal phases (bcc and fcc) are also found for the TIP4P and SPC/E models so that they seem to be present in all water models. In these models water is described by a Lennard-Jones center plus additional point charges. At high temperatures, the hydrogen bond energy (in k_BT units) is not sufficient to maintain the hydrogen bonding network and the molecules start to rotate. Once the importance of the charges is reduced, the relatively spherical shape of water makes the existence of a plastic crystal phase possible. Plastic crystal phases are also found experimentally for

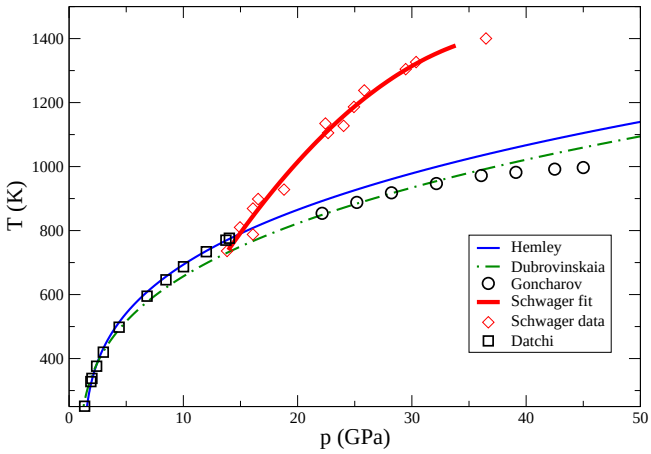

Figura 8.1: Experimental data for the melting curve of the ice VII. Schwager [48], thick solid line and diamonds; Datchi [49], open squares; Hemley [50], thin solid line; Dubrovinskaia [51],dashed-dotted line; Goncharov [52], open circles.

slightly anisotropic molecules as N_2 or O_2 [267].

A word of caution is needed with respect to the conclusions of this work. Our main goal is to accurately determine the complete phase diagram of popular water models. Since these models are used in thousands of simulation studies it is important to know to what extent they can describe satisfactorily the phase diagram of water, and where and why they fail to do so. However, it should be clearly pointed out that SPC/E, TIP4P and TIP4P/2005 are rigid models and they can not describe properly the formation or the breaking of chemical bonds. For this reason these models are completely useless when it comes to understanding the formation of ice X. In ice X, the oxygens form a bcc lattice and the hydrogens are located in the middle of the O-O bonds. Also, at extremely high temperatures a super ionic solid has been proposed [31] (where the oxygens form a lattice and the hydrogens diffuse within the oxygen network). The rigid models of this work cannot describe these situations. Obviously only first principle calculations can do that [31, 32]. Rather the phase diagram presented here corresponds to what approximately would occur in the phase diagram of water in the absence of deformation or breaking of chemical bonds. It will be shown that for these models, water adopts close packed structures at high pressures and plastic crystal phases at high temperatures. Whether real water does indeed form plastic crystal phases or fcc solid structures is an issue that can be solved only by performing experimental work. Experimental studies proving or disproving the existence of a plastic crystal phase for water, should be of great interest not only for the people interested in high pressure studies of water but also for the broad research community performing computer simulations involving water.

Simulation details

We have performed Monte Carlo (MC) and molecular dynamics (MD) simulations for plastic crystal phases of water (bcc and fcc). We have used the TIP4P/2005 [34], TIP4P [107] and SPC/E [106] models. They are rigid and non-polarisable models. A Lennard-Jones (LJ) center is located on the oxygen atom and positive charges are located on the hydrogen atoms. The negative charge is located on the H-O-H bisector for the TIP4P models and on the oxygen for

the SPC/E model. In Ref. [35] one can find a critical comparison of the performance of these three popular water models.

The number of molecules used in the simulations were: 432 for the bcc plastic crystal (which corresponds to 216 units cells (6x6x6)), 500 for the fcc plastic crystal (125 units cells (5x5x5)), 432 for ice VII (216 units cells (6x6x6)), and either 360 or 432 molecules for the fluid phase. In all cases the LJ potential was truncated at 8.5 Å. Standard long range corrections to the LJ part of the potential were added. The Ewald summation technique has been employed for the calculation of the long range Coulombic forces. We have performed isotropic and anisotropic NpT simulations. In the isotropic simulations the volume of the system fluctuates but the shape of the simulation box remains constant. In anisotropic NpT the volume and the shape of the simulation box are allowed to fluctuate [102, 104]. For fluid water and for the cubic solids (ice VII and the two plastic crystals) we used isotropic scaling. In one case anisotropic scaling was used for the bcc plastic crystal to analyze its possible transformation into a fcc plastic crystal through a Martensitic phase transition [238]. A typical Monte Carlo run involves about 30000 cycles of equilibration and 70000 cycles to obtain averages (defining a cycle as a trial move per particle plus a trial volume move).

To determine the phase diagram free energy calculations are required. Free energy calculations can be determined with the Einstein crystal method [115, 121, 257] or a modified version denoted as the Einstein molecule approach [234]. The technique can be used for ices and details have been provided elsewhere [133, 268]. By applying two external fields, one translational forcing the molecules to occupy a certain position, and another orientational forcing the molecules to adopt a certain orientation we have been able to compute the free energy of a number of solid phases of water. However, the application of the technique to plastic crystals may be problematic as at low values of the orientational field very long runs should be performed to guarantee that the molecules are able to rotate as in the plastic crystal. To avoid this issue we have developed a new method for free energy calculations of plastic crystals, which allow us to avoid connecting orientational springs to the molecules. The difference with the traditional Einstein crystal as applied to other ices is that for the plastic crystals only translational springs will be used. The method is inspired in the methodology proposed by Lindberg and Wang to evaluate dielectric constants of ices [132].

An ideal Einstein crystal with the center of mass (CM) fixed is used as the reference system to compute the free energy. Let us describe the different steps to computing the free energy of a plastic crystal:

1. An ideal Einstein crystal is a solid in which the molecules are bound to their lattice positions by harmonic springs. For plastic crystals only translational (and not orientational) springs will be used (this prevents the appearance of phase transitions along the integration). The energy of the ideal Einstein crystal is given by:

$$U_{Ein} = \sum_{i=1}^{N} \Lambda_E (\mathbf{r_i} - \mathbf{r_{i0}})^2 \tag{8.1}$$

   where $\mathbf{r}_i$ represents the instantaneous location of the reference point of molecule *i* and $\mathbf{r}_{i0}$ denotes its equilibrium position. U_{Ein} is a harmonic field that tends to keep the molecules at their lattice positions. Λ_E is the coupling parameter of the translational

springs and has units of energy over a squared length. The free energy of the ideal Einstein crystal (with translational springs) with fixed center of mass (A^{CM}_{Ein-id}) is given by [121, 133]:

$$\begin{aligned} A^{CM}_{Ein-id} &= -k_B T \ln Q^{CM}_{Ein,t} && (8.2) \\ &= -k_B T \ln[P^{CM} \left(\frac{\pi}{\beta \Lambda_E}\right)^{3(N-1)/2} (N)^{3/2}] && (8.3) \end{aligned}$$

where $P^{CM} = \frac{1}{\Lambda^{3(N-1)}} N^{-3/2}$ and Λ is the thermal De Broglie wavelength ($\Lambda = (\frac{h^2}{2\pi m k_B T})^{1/2}$), which has units of length.

2. To the ideal Einstein crystal described above we incorporate intermolecular interactions in the form of a LJ potential (whose parameters σ and ϵ are identical to those of the water model under consideration). The difference in free energy between the the Einstein crystal with LJ interactions (A^{CM}_{Ein-LJ}) and the non-interacting Einstein crystal (A^{CM}_{Ein-id}) both with fixed center of mass can be obtained in a perturbative way as :

$$\begin{aligned} \Delta A_1 &= A^{CM}_{Ein-LJ} - A^{CM}_{Ein-id} \\ &= U_{lattice} - k_B T \ln < exp[-\beta(U_{sol} - U_{lattice})] >_{Ein-id} && (8.4) \end{aligned}$$

where $U_{lattice}$ is the energy of the system when the molecules stand fixed on the lattice position (i.e the LJ lattice energy) and U_{sol} is the LJ energy of the system for the considered configuration. The average is performed over configurations generated for the ideal Einstein crystal.

3. Then we evaluate the free energy difference between an Einstein crystal with water interactions (i.e TIP4P/2005, SPC/E ..) and an Einstein crystal with LJ interactions, both with fixed center of mass. To evaluate this free energy difference, the charges of the water potential are turned on, while keeping the translational springs. The path linking the LJ potential to the water potential is defined as :

$$U(\lambda_Q) = (1 - \lambda_Q) U_{LJ} + \lambda_Q U_{water} \quad (8.5)$$

$$\begin{aligned} \Delta A_Q &= A^{CM}_{Ein-sol} - A^{CM}_{Ein-LJ} \\ &= \int_0^1 \langle U_{water} - U_{LJ} \rangle_{N,V,T,\lambda_Q} \, d\lambda_Q && (8.6) \end{aligned}$$

where $<U_{water}-U_{LJ}>_{N,V,T,\lambda_Q}$ can be obtained in a NVT simulation at a given λ_Q. As the reference LJ potential has the same parameters as the LJ part of the water potential then $<U_{water}-U_{LJ}>_{N,V,T,\lambda_Q}$ is simply the Coulombic contribution to the energy of the water potential U_Q and equation (8.6) can be rewritten as.

$$\Delta A_Q = \int_0^1 \langle U_Q \rangle_{N,V,T,\lambda_Q} \, d\lambda_Q \quad (8.7)$$

Since we are not using orientational springs the molecules are able to rotate at the beginning (when $\lambda_Q = 0$) and at the end (when $\lambda_Q = 1$) of the integration avoiding the possible existence of a phase transition along the integration path. The value of the integral is then obtained numerically.

4. Now the translational springs are turned off gradually. The free energy change ΔA_2 between the water molecules bonded to their lattice positions by harmonic springs ($A^{CM}_{Ein-sol}$) and the plastic crystal with no translational springs (both with fixed CM) is given by :

$$\begin{aligned} \Delta A_2 &= A^{CM}_{sol} - A^{CM}_{Ein-sol} \\ &= -\int_0^{\Lambda_E} \frac{\langle U_{Ein-id} \rangle_{N,V,T,\lambda}}{\Lambda_E} d(\lambda \Lambda_E) \end{aligned} \tag{8.8}$$

Since the integrand changes by several orders of magnitude it is convenient to perform a change of variable [97, 115] from $\lambda\Lambda_E$ to ln($\lambda\Lambda_E$+c), where c is a constant. We shall use $c = exp(3.5)$ which significantly smoothes the integrand. The final expression for ΔA_2 is :

$$\Delta A_2 = -\int_{\ln(c)}^{\ln(\Lambda_E + c)} \frac{\langle U_{Ein-id} \rangle_{N,V,T,\lambda} (\lambda \Lambda_E + c)}{\Lambda_E} d(\ln(\lambda \Lambda_E + c)) \tag{8.9}$$

Fixing the CM avoids the quasi-divergence of the integrand of equation (8.9) when the coupling parameter λ tends to zero. Without this constraint, the integrand would increase sharply in this limit, making the evaluation of the integral numerically involved.

5. The last step is to evaluate the free energy change between a plastic crystal with no constraint and the plastic crystal with a fixed center of mass. The free energy change of this last step ΔA_3 is given by:

$$\begin{aligned} \Delta A_3 &= A_{sol} - A^{CM}_{sol} \\ &= -k_B T \ln \frac{Q_{sol}}{Q^{CM}_{sol}} \\ &= k_B T \left[\ln(P^{CM}/P) - \ln(V/N) \right] \end{aligned} \tag{8.10}$$

where P=$\frac{1}{\Lambda^{3N}}$. ΔA_3 does not depend on the particular form of the intermolecular potential U_{sol}.

The final expression of the free energy of the plastic crystal is

$$\begin{aligned} A_{sol} &= (A^{CM}_{Ein-id} + \Delta A_3) + \Delta A_1 + \Delta A_Q + \Delta A_2 \\ &= A_0 + \Delta A_1 + \Delta A_Q + \Delta A_2 \end{aligned} \tag{8.11}$$

Putting together the A^{CM}_{Ein-id} and ΔA_3 terms (A_0), the P^{CM} contribution cancels out and the final expression of the free energy of the plastic crystal solid is :

$$\begin{aligned}\frac{A_{sol}}{Nk_BT} &= -\frac{1}{N}\ln\left[\left(\frac{1}{\Lambda}\right)^{3N}\left(\frac{\pi}{\beta\Lambda_E}\right)^{3(N-1)/2}(N)^{3/2}\frac{V}{N}\right] \\ &+ \left[\frac{U_{lattice}}{Nk_BT} - \frac{1}{N}\ln\left\langle\exp\left[-\beta(U_{sol}-U_{lattice})\right]\right\rangle_{Ein-id}\right] \\ &+ \int_0^1\left\langle\frac{U_Q}{Nk_BT}\right\rangle_{N,V,T,\lambda_Q}d\lambda_Q \\ &- \int_0^1\left\langle\frac{U_{Ein-id}}{Nk_BT}\right\rangle_{N,V,T,\lambda}d\lambda\end{aligned} \tag{8.12}$$

The first term corresponds to A_0, the second to ΔA_1, the third to ΔA_Q and the last term to ΔA_2.

The free energy was computed at a certain thermodynamic state. By using thermodynamic integration the free energy for other thermodynamic conditions can be obtained easily. The free energy of the fluid phase was obtained as described in our previous work [133]. The chemical potential is easily obtained as $\frac{\mu}{k_BT}=\frac{G}{Nk_BT}=\frac{A}{Nk_BT}+\frac{pV}{Nk_BT}$. Once the free energies (and chemical potentials) for the fluid and for the different solid phases are known initial coexistence points can be located by imposing the condition of equal chemical potential ($\mu_I=\mu_{II}$) at the same temperature and pressure. Having an initial coexistence point the rest of the coexistence curve can be obtained by using Gibbs-Duhem integration [138, 198]. This technique allows one to determine the coexistence line between two phases, provided that an initial coexistence point is known. Gibbs-Duhem is a numerical integration of the Clapeyron equation (and where volume and enthalpy changes are obtained by using computer simulations). The Clapeyron equation is given by :

$$\frac{dp}{dT} = \frac{s_{II}-s_I}{v_{II}-v_I} = \frac{h_{II}-h_I}{T(v_{II}-v_I)} \tag{8.13}$$

The subscripts I and II label the corresponding phases and the thermodynamic properties written with small letters are properties per particle ($x=\frac{X}{N}$). For the integration of the Clapeyron equation a fourth-order Runge-Kutta integration is employed.

In this work free energy calculations were performed only for the TIP4P/2005 model. To obtain initial coexistence points for the TIP4P and SPC/E models of water we shall use Hamiltonian Gibbs-Duhem integration. Hamiltonian Gibbs-Duhem integration is a very powerful technique that allows one to determine the change in the coexistence conditions of a certain coexistence line due to a change of the water potential. In this kind of integration the Hamiltonian of the system is changed through a coupling parameter (so that λ=0 for the initial Hamiltonian and λ=1 for the final Hamiltonian). When the coupling parameter (λ) is introduced within the expression of the potential energy of the system (U(λ)), then a set of generalized Clapeyron equations can be derived. The derivation is as follows. For two phases at coexistence:

$$g_I(T,p,\lambda) = g_{II}(T,p,\lambda) \tag{8.14}$$

If the system is perturbed slightly while preserving the coexistence it must hold that:

$$-s_I dT + v_I dp + (\frac{\partial g_I}{\partial \lambda})d\lambda = -s_{II} dT + v_{II} dp + (\frac{\partial g_{II}}{\partial \lambda})d\lambda \tag{8.15}$$

If the coupling parameter remains constant when performing the perturbation then one recovers the traditional Clapeyron equation (8.13)(coexistence on the p-T plane). If the pressure is kept constant when the perturbation is performed (coexistence on the λ-T plane) then one obtains:

$$\frac{dT}{d\lambda} = \frac{T[\frac{\partial g_{II}}{\partial \lambda} - \frac{\partial g_I}{\partial \lambda}]}{h_{II} - h_I} \tag{8.16}$$

The property $\frac{\partial g}{\partial \lambda}$= <$\frac{\partial u(\lambda)}{\partial \lambda}$>$_{N,p,T,\lambda}$, can be determined easily during the NpT simulations. Then Eq.8.16 can be rewritten as :

$$\frac{dT}{d\lambda} = \frac{T[< (\frac{\partial u_{II}(\lambda)}{\partial \lambda}) > - < (\frac{\partial u_I(\lambda)}{\partial \lambda}) >]}{h_{II} - h_I} \tag{8.17}$$

This generalized Clapeyron equation (8.16) can be integrated numerically (from $\lambda = 0$ to $\lambda = 1$) to obtain the coexistence temperature (at a certain fixed pressure) of the water potential of interest, provided that the coexistence temperature is known for the initial reference potential.

A similar equation can be obtained when a perturbation is performed (whilst keeping the temperature constant). In this case the coexistence pressure of the water potential of interest is obtained (at a certain fixed temperature) provided that the initial coexistence pressure is known for the initial reference potential. The working expression is :

$$\frac{dp}{d\lambda} = -\frac{< (\frac{\partial u_{II}(\lambda)}{\partial \lambda}) > - < (\frac{\partial u_I(\lambda)}{\partial \lambda}) >}{v_{II} - v_I} \tag{8.18}$$

Let us assume that λ is as a coupling parameter leading the system from a certain reference potential U_A to the potential of interest U_B. This can be done with a coupling of the form :

$$U(\lambda) = \lambda U_B + (1 - \lambda)U_A. \tag{8.19}$$

with λ changing from zero (initial reference potential) to one (final potential of interest). The generalized Clapeyron equations can be written as:

$$\frac{dT}{d\lambda} = \frac{T(< u_B - u_A >^{II}_{N,p,T,\lambda} - < u_B - u_A >^{I}_{N,p,T,\lambda})}{h_{II} - h_I} \tag{8.20}$$

$$\frac{dp}{d\lambda} = -\frac{< u_B - u_A >^{II}_{N,p,T,\lambda} - < u_B - u_A >^{I}_{N,p,T,\lambda}}{v_{II} - v_I} \tag{8.21}$$

where u_B is the internal energy per molecule when the interactions between molecules are described by U_B (and analogous definition is used for u_A). If a coexistence point between two phases is known for potential A then integration of the previous equations from $\lambda = 0$ to $\lambda = 1$ allows one to determine the coexistence point between these two phases for potential B. This can be done either by fixing the temperature or the pressure along the integration.

To estimate nucleation times of the plastic crystal phases and to determine the melting point of the fcc plastic crystal phase by direct coexistence technique we have performed Molecular Dynamics (MD) simulations using the program Gromacs [235]. In these simulations

the temperature is kept constant by using a Nose-Hoover thermostat [236, 237] with a relaxation time of 2 ps. To keep the pressure constant, a Parrinello-Rahman barostat [102, 238] (isotropic or anisotropic) was used. The relaxation time of the barostat was 2 ps. The time step was 1 fs and the typical length of the runs was of about 5 ns. The geometry of the water molecules is enforced using constraints. The LJ part of the potential was truncated at 8.5 Å and standard long range correction were added. Ewald sums are used to deal with the long range Coulombic interactions. Coulombic interactions in real space were truncated at 8.5 Å. The Fourier part of the Ewald sums was evaluated using the PME (Particle Mesh Ewald [239]). The width of the mesh was 1 Å and we used a fourth order interpolation.

Results

For the TIP4P/2005 model we found in previous work that ice VII transformed into a bcc plastic crystal at 377K when heated along 70000 bar isobar [29]. We shall now explore the stability of this bcc plastic crystal. It is well known that a bcc solid can transform into a fcc solid, provided that the fcc is more stable, and that one uses anisotropic NpT simulations (Rahman-Parrinello NpT). We shall explore the behavior of the bcc plastic crystal solid when heated along the 70000 bar isobar. The bcc plastic crystal is stable when heating up to temperatures of about 460K (even though we are using anisotropic NpT simulations and it could transform into a fcc solid) but at 480K the properties of the system (energies, densities, and shape of the simulation box) undergo a clear jump. A Martensitic phase transition occurs in which the bcc lattice is transformed into a fcc lattice by increasing the c edge of the bcc structure. The simulation box that was originally cubic for the bcc PC becomes tetragonal (a sketch of the transformation is given in Figure 8.2).

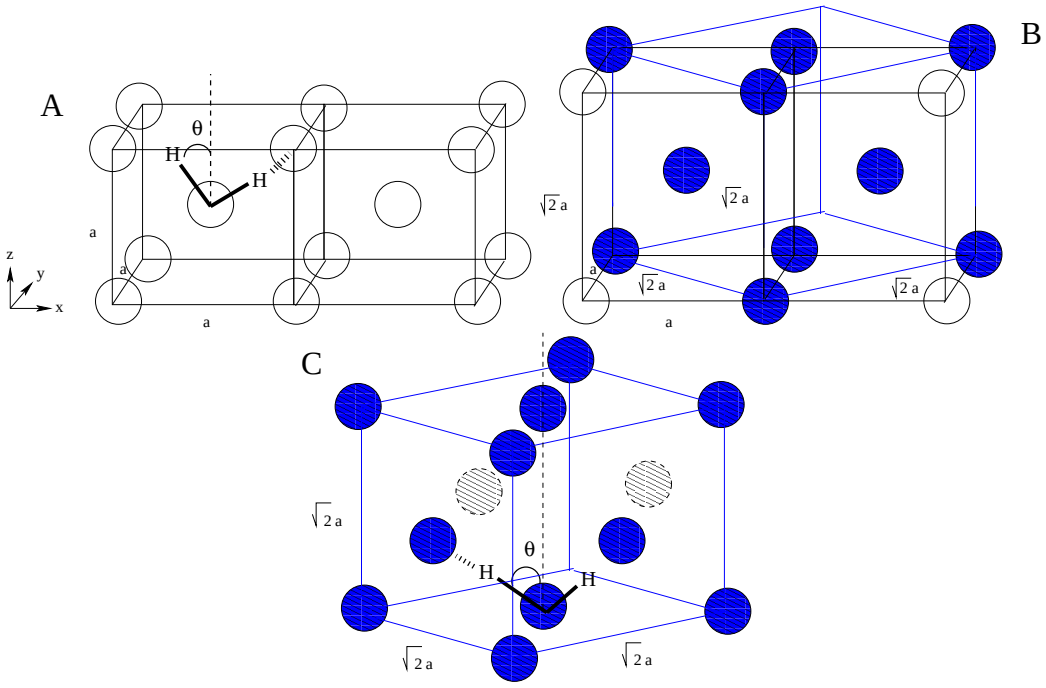

Figura 8.2: (a)Two bcc unit cells. (b) How the fcc lattice can be obtained from two bcc cells. When the z direction is scaled by $\sqrt{2}$a, the crystal is transformed into a fcc lattice. (c) fcc unit cell.

In Fig.8.3 the instantaneous values of the lengths of the sides of the simulation box are

presented for a temperature of 440K and for a temperature of 480K. As can be seen at 440K one sees fluctuations of three sides of identical (in average) lengths. However, for the run performed at 480K one of the sides increases slightly its length at the beginning of the run and after 40000 cycles increases its length dramatically. At the end of the 480K run the length of the sides are a=17.608: b=17.620; c=25.557. As can be seen the ratio c/a is close to c/a=$\sqrt{2}\simeq$1.414 which is the value expected for the ratios of c and a in a Martensitic transformation from a bcc to a fcc solid (see the sketch of Fig.8.2). Therefore, the ratio c/a (actually the ratio between the longest and the shortest sides of the simulation box since since the Martensitic transition may occur also along the x or y axis) is a good order parameter to detect the transformation. In Fig.8.4 the c/a ratio is plotted as a function of temperature for runs performed along the 60000, 70000 and 80000 bar isobars. For the pressure 60000 bar no bcc to fcc transition is observed. For the runs at 70000 bar the transition occurs at about 480K. For the runs at 80000 bar the transition occurs at about 420K. Therefore the transition temperature decreases as the pressure increases. That suggest a negative slope of the bcc-fcc coexistence line. Notice that the jump in Fig.8.4 does not correspond to the true coexistence point (i.e identical chemical potential) between these two phases. Packing considerations favour the fcc structure with respect to the bcc structure. In fact for a r^{-12} potential Wilding [269] has found recently that the fcc structure is more stable than the bcc.

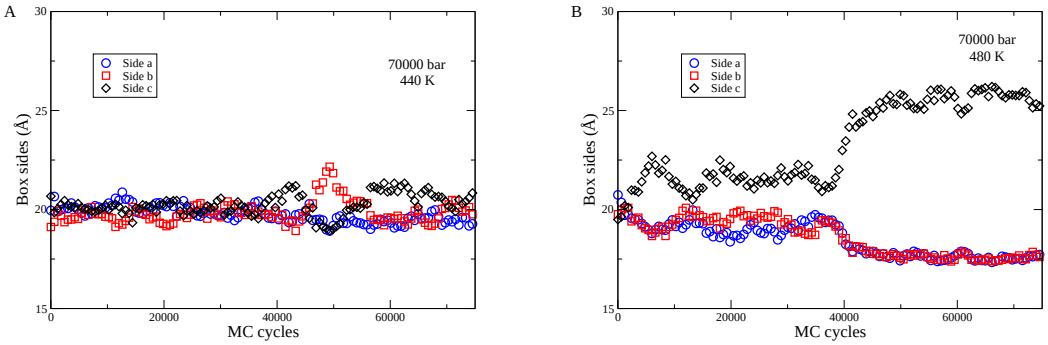

Figura 8.3: Simulation box sides change along the MC run (anisotropic NpT ensemble) for the bcc plastic crystal phase. A) 440 K and 70000 bar. B) 480 K and 70000 bar.

We have found that the fcc PC could also be generated easily by starting from a fcc arrangement of the oxygen atoms (and introducing random orientations). In fact we generated the fcc PC starting from a fcc solid of 500 molecules (i.e 125 unit cells). In Fig.9.3 the oxygen-oxygen radial distribution function (g_{O-O}) is shown. As can be seen the radial distribution function of the the solid obtained from the Martensitic transformation is identical to that obtained from an initial fcc arrangement of oxygens. The radial distribution function of the fcc plastic crystal is clearly different from that of the bcc plastic crystal. In fact the bcc PC shows the first peak of the g_{O-O} at 2.81 Å, the second at 4.59 Å and the third at 5.50 Å, whereas fcc plastic crystal has a first peak at 2.87 Å and the second and third peaks move apart and shift to shorter distances, 4.16 and 5.10 Å, respectively (Figure 9.3).

We have computed the powder x-ray and neutron diffraction patterns. The intensity of the diffraction peaks is obtained as:

$$I = \frac{P(\theta)}{sen(\theta)sen(2\theta)} m_i \mid F_{hkl} \mid^2 \tag{8.22}$$

where m_i is the multiplicity and P(θ) is the polarization factor (in neutron diffraction P(θ)=1

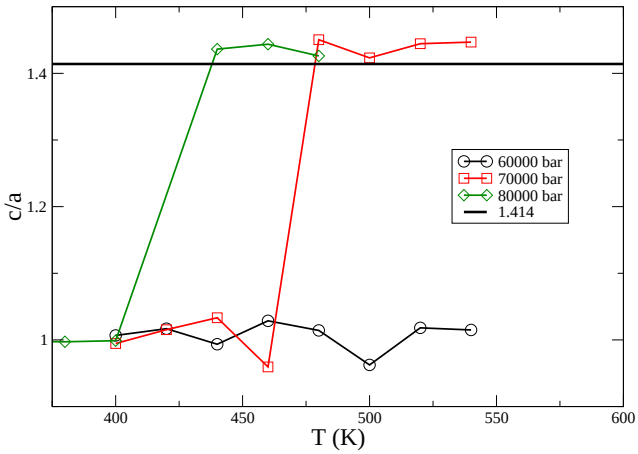

Figura 8.4: Temperature dependence of the c/a ratio at different pressures, 60000 bar (open circles), 70000 bar (open squares) and 80000 bar (open diamonds).

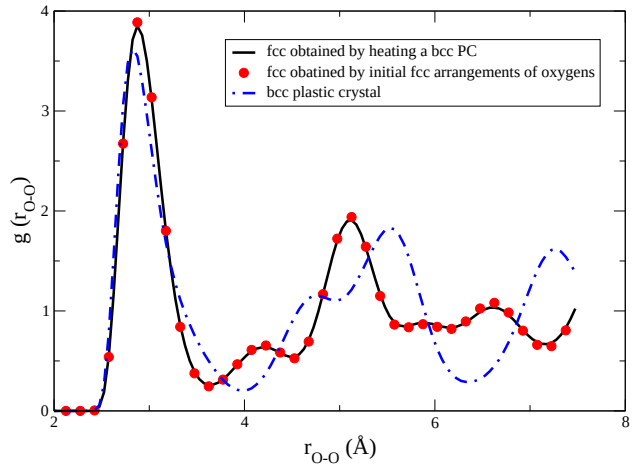

Figura 8.5: Oxygen-oxygen radial distribution functions at T = 440 K and p = 80000 bar for the fcc plastic crystal phase and at T = 440 K and p = 70000 bar for the bcc plastic crystal. Fcc plastic crystal obtained by heating the bcc plastic crystal (solid line), fcc plastic crystal obtained by the fcc lattice of the oxygens (filled circles) and bcc plastic crystal (dashed-dotted line). Notice that, the correct g_{O-O} and g_{O-H} in Figs. 2, 4 and 5 of our previous work [29] are obtained by shifting the curves 0.5 Å to the right.

and in x-ray diffraction P(θ)=($\frac{1+cos^2(2\theta)}{2}$)). In the x-ray diffraction pattern, the F_{hkl} is obtained as:

$$F_{hkl} = \frac{1}{N}\sum_{n=1}^{N} f_n(\theta) e^{2\pi i(hx_n+ky_n+lz_n)} \tag{8.23}$$

where $f_n(\theta)$ is function of θ. Both oxygen and hydrogens were considered and $f_n(\theta)$ was ob-

tained from the fit proposed by Lee *et al.* [270]. The wavelength (λ) used was 0.4 Å [223, 271]. In the neutron diffraction pattern (which was calculated for heavy water) F_{hkl} was obtained as:

$$F_{hkl} = \frac{1}{N}\sum_{n=1}^{N} b_n e^{2\pi i(hx_n+ky_n+lz_n)} \tag{8.24}$$

where the neutron scattering amplitudes (b_n) of the deuteron and the oxygen atom are 0.6671 and 0.5803 fm, respectively and, do not depend on θ [272]. The wavelength used was also 0.4 Å. The number of molecules used in these simulations were 1024 (512 unit cells) and the bcc PC also appears for this system size. Results are presented in Figure 8.6. The main difference between the ice VII and bcc PC x-ray diffraction patterns is the intensity reduction, around 20 %, for the bcc PC peaks and the appearence of more peaks at large 2θ values for the bcc PC. The same results are observed on the neutron diffraction pattern (Figure 8.6B). The intensity reduction of the diffraction peaks is not surprising if one takes into account that in ice VII the hydrogen bonds maintain the location of the oxygen atoms more or less fixed (except for some slight thermal vibration). However in the plastic crystal phases the molecules are free to rotate (frequently forming and breaking hydrogen bonds) so the oxygen atom is able to move significantly from its equilibrium lattice position. The bcc PC diffraction peaks were shifted to lower 2θ values with respect to ice VII due to the lower density of this phase. The conclusion of these results is that one of the signatures of the formation of a plastic crystal phase (say the bcc) will be a significant reduction in the intensity of the diffraction lines with respect to ice VII. Observing the intensity ratio between the *011* and *111* peaks ($\frac{I_{011}}{I_{111}}$) on the neutron diffraction pattern for ice VII and bcc PC, we can see that its value is of about 4 for ice VII and of about 15 for bcc PC. Therefore the ratio $\frac{I_{011}}{I_{111}}$ could be used to detect the apperance of the bcc PC.

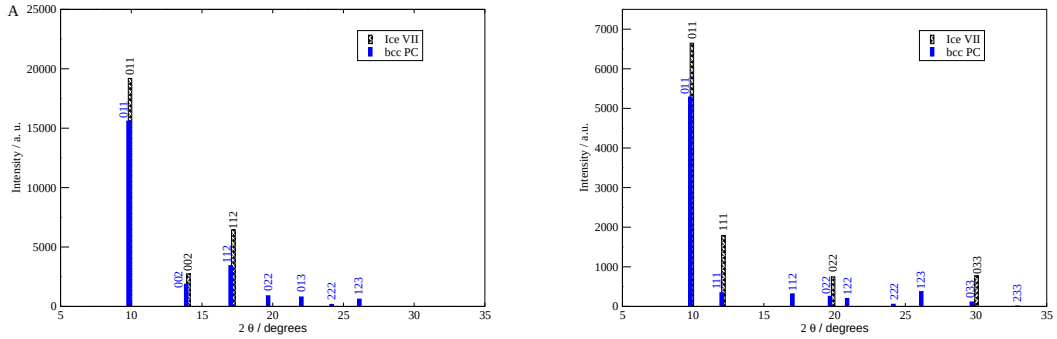

Figura 8.6: (a) Simulated powder x-ray diffraction pattern for ice VII (dashed line) at 70000 bar and 300 K and bcc PC (solid line) at 70000 bar and 400 K. The wavelength used was 0.4 Å. The Miller indices *hkl* are given for each peak. (b) Simulated neutron diffraction pattern for ice VII (dashed line) at 70000 bar and 300 K and bcc PC (solid line) at 70000 bar and 400 K. The wavelength was 0.4 Å. The Miller indices *hkl* are given for each peak.

To gain further understanding of the orientational order in the plastic crystal phases we have also determined the probability distribution of the polar angles (θ and ϕ of the OH bonds). The x axis is located on the **a** vector of the unit cell, the y axis is located on the **b** vector of the unit cell, and the z axis is located along the **c** vector of the unit cell (see Fig. 8.2A and 8.2C). The distribution function $f(\theta)$ is defined as :

$$f(\theta) = \frac{N(\theta)}{2N\Delta\theta} \tag{8.25}$$

where $N(\theta)$ denotes the number of OH bonds with polar angle between θ and $\theta + \Delta\theta$ and 2N is the number of OH bonds (i.e twice the number of molecules N). The distribution function $f(\phi)$ is defined as :

$$f(\phi) = \frac{N(\phi)}{2N\Delta\phi} \tag{8.26}$$

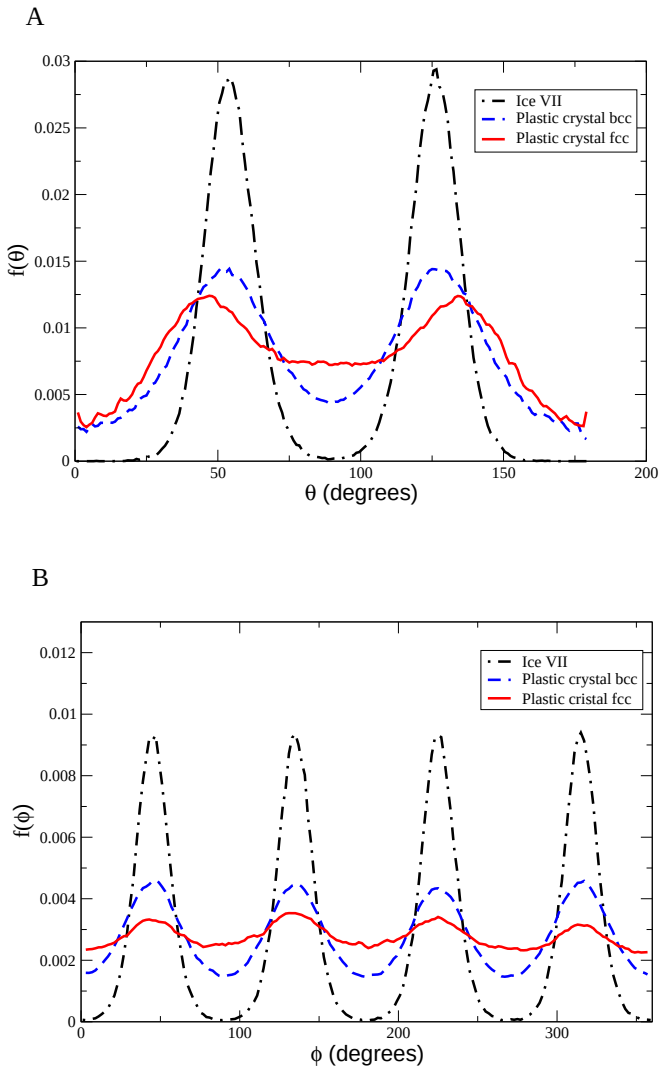

Figura 8.7: (a) f(θ) as a function of θ angle for ice VII (dashed-dotted line) at 300 K and 70000 bar, for the bcc plastic crystal (dashed line) at 400 K and 70000 bar and for the fcc plastic crystal (solid line) at 440 K and 80000 bar. (b) f(ϕ) as a function of ϕ angle for the ice VII (dashed-dotted line) at 300 K and 70000 bar, for the bcc plastic crystal (dashed line) at 400 K and 70000 bar and for the fcc plastic crystal (solid line) at 440 K and 80000 bar.

In Fig. 8.7 the functions $f(\theta)$ and $f(\phi)$ are presented for ice VII at 300 K and 70000 bar, bcc PC at 400 K and 70000 bar and fcc PC at 440 K and 80000 bar. For the plastic crystal phases, bcc and fcc, the distribution functions $f(\theta)$ and $f(\phi)$ are more uniform than those of ice VII. This is due to the fact that in the plastic crystal phases the molecules are able to rotate almost freely. Nevertheless the angular distribution is not uniform even in the plastic crystal phase since the OH vectors still prefer to point out to the contiguous oxygen atoms. For bcc plastic crystal and ice VII the peaks of $f(\theta)$ are located at 54.74 and $(180-54.74)$ where 54.74 is the angle between one of the diagonals of the cube and a line connecting the center of two

Tabla 8.1: Helmholtz free energy for ice VII, bcc plastic crystal phase and fcc plastic crystal phase (as obtained with the Einstein crystal methodology). The Gibbs free energy was computed after adding pV to the Helmholtz free energy. The density is given in g/cm^3. The cubic fcc* phase correspond to the fcc plastic crystal phase obtained by heating the bcc plastic crystal phase.

Phase	Molecules	T/K	p/bar	ρ	A/Nk$_B$T	G/Nk$_B$T
Ice VII	432	300	70000	1.707	-9.75	19.87
Cubic bcc	432	440	80000	1.662	-3.93	19.78
Cubic fcc	500	440	80000	1.679	-4.86	19.23
Cubic fcc*	432	440	80000	1.679	-4.89	19.21
Cubic fcc	500	440	105000	1.749	-3.76	25.80

opposite faces (Figure 8.2A). However, for the fcc plastic crystal the peaks of $f(\theta)$ are located at 45, 90 and 135 degrees. Where 45 and 135 are the angles between one of the diagonals that is connecting the center of two perpendicular faces of the cube and the z edge (Figure 8.2C) and 90 is the angle between the line connecting two oxygens resting on the same plane with the z edge. For the bcc plastic crystal the angles 0, 90 and 180 degrees in the $f(\theta)$ have non-zero probability. This provides some indication that in the bcc plastic crystal the OH vectors point sometimes (while rotating) to second nearest neighbors. For ice VII and the bcc plastic crystal, the angular distribution $f(\phi)$ presents four peaks separated by 90 degrees as should be the case. In the fcc plastic crystal the function $f(\phi)$ is almost uniform, indicating that the molecules can rotate quite freely. For ice VII at 300K and 70000 bar and for the length of the simulations performed in this work, a certain individual molecule presents a fixed value of θ and ϕ (subject to some thermal vibration). However for the plastic crystal phases each individual molecule jumps quite often from one of the peaks of the distribution to another peak. These flipping or jumping moves occur quite often for each molecule within the length of the simulation runs considered here. Another way to see this orientational disorder is by means of the visualization of the MD trayectories. Multimedia mpg files for the MD trayectories of ice VII, bcc PC and fcc PC are provided as electronic supplementary information [**?**].

Let us now determine coexistence points between the different solid phases considered in this work (fluid, ice VII, bcc PC and fcc PC). This requires free energy calculations for the different phases involved. Free energies for the liquid and for ice VII were obtained in our previous work [29]. We have determined the Helmholtz free energy for the bcc PC and fcc PC at 440K and for the densities which correspond to that of the systems at 80000 bar. The free energies are presented in Table 8.1. For the fcc solid we have computed the free energy for a cubic simulation box (500 molecules) and for the tetragonal simulation box obtained from the Martensitic transition of the bcc PC (432 molecules). As can be seen the free energy of these two systems is the same.The small difference may be attributed to the different orientations of the crystallographic planes with respect to the periodic boundary conditions [273]. For the studied thermodynamic state (80000 bar and 440 K), the fcc plastic crystal is more stable than bcc plastic crystal (it has a lower chemical potential). This is consistent with the results presented in Fig. 8.4 where it was shown that when anisotropic NpT simulations were used the bcc PC transformed into an fcc PC. Notice however that it is possible to have a mechanically stable bcc PC at 80000 bar and 440K provided that isotropic NpT simulations are performed (with this type of scaling the bcc PC remains mechanically stable) so it is possible to compute thermodynamic properties even under conditions where the solid is metastable

from a thermodynamic point of view. In Table 8.1 the free energy is presented for two different thermodynamic states of the fcc PC. By using thermodynamic integration it is possible to estimate the free energy at 440K and 105000 bar starting from the value at 440K and 80000 bar. We obtain -3.77 Nk_BT which is good agreement with the value -3.76 Nk_BT obtained from Einstein crystal calculation (Table 8.1).

By using thermodynamic integration the coexistence point between the fluid and the fcc PC has been located at 440 K and 66790 bar. Once an initial coexistence point has been found for the fluid-fcc PC transition, the rest of the coexistence line will be obtained by Gibbs-Duhem integration. The fluid-bcc PC was integrated from the coexistence point given in our previous work at 400 K and 62000 bar, obtained by free energy calculations. The fluid-bcc PC and fluid-fcc PC coexistence lines meet at a triple point located around 570 K and 77124 bar. This triple point can be used as initial coexistence point of the bcc PC-fcc PC coexistence curve. This curve intersects the ice VII-bcc PC coexistence line, generating a new triple point at 393 K and 77179 bar. This triple point was used as initial point for the ice VII-fcc PC coexistence line. The new coexistence lines for the TIP4P/2005 model are given in tabular form in Tables 8.2 and 8.3. The triple points generated by these coexistence lines are shown in Table 8.4. The rest of the triple points of these models can be found in Refs. [29] and [274].

Free energy calculation are somewhat involved and it is convenient to determine coexistence points by an independent procedure. For this reason we also used direct coexistence simulations to determine the fluid-fcc PC transition. The direct coexistence technique, was pioneered by Ladd and Woodcok [140–142]. An equilibrated configuration of a fcc PC phase (500 molecules) was located on the left hand side of the simulation box and put into contact with an equilibrated configuration of the fluid having 500 molecules. We then performed MD simulations using Gromacs, while keeping the temperature at 600 K. We performed several runs at different pressures. In Fig. 8.8, the evolution of the density with time is shown for several pressures. As we can see, for low pressures (70000 and 79000 bar) the density decreases indicating the melting of the fcc plastic crystal. For high pressures (80500 and 90000 bar) the density of the system increases indicating the freezing of the fluid into a fcc PC. This gives a coexistence pressure of about 79750 bar. Thus, the value of about 80000 obtained from free energy calculations is consistent with the results obtained from direct coexistence.

Dolan *et al.* [219, 220], have shown that the formation of a high pressure ice phase (most likely ice VII) from liquid water occurs in a few ns when the temperature is around 400K. By using computer simulations we obtain further evidence of this by nucleating the bcc PC solid from the fluid in a few ns [29]. This nucleation time is small compared to that found previously for ice Ih [266] (hundred of ns). We will attempt here to nucleate the fcc PC solid. We performed MD simulations of the fluid phase with isotropic scaling using 500 molecules in a cubic simulation box (500 molecules is the number of water molecules required to form 125

Tabla 8.2: Melting curves of the plastic crystal phases of the TIP4P/2005 as obtained from free energy calculations and Gibbs Duhem integration (with isotropic NpT simulation performed for the fluid and for the plastic crystal phases). The densities are given in g/cm^3. The residual internal energies are given in in kcal/mol. The * indicate the initial coexistence point.

T/K	p/bar	U_1	U_2	ρ_1	ρ_2
fluid-bcc plastic crystal					
340.00	60193	-10.45	-10.03	1.574	1.622
* 400.00	62000	-9.87	-9.58	1.562	1.609
440.00	64390	-9.52	-9.30	1.564	1.608
460.00	66042	-9.35	-9.12	1.560	1.607
520.00	71653	-8.86	-8.71	1.563	1.615
↓ Metastable					
600.00	80608	-8.20	-8.13	1.575	1.626
700.00	93249	-7.38	-7.37	1.599	1.646
900.00	121380	-5.77	-5.92	1.636	1.690
1000.00	137036	-4.96	-5.15	1.657	1.713
fluid-fcc plastic crystal					
* 440.00	66790	-9.52	-9.06	1.575	1.628
500.00	70691	-9.00	-8.67	1.566	1.629
520.00	72435	-8.86	-8.54	1.569	1.629
540.00	74164	-8.68	-8.44	1.575	1.633
560.00	76115	-8.56	-8.29	1.569	1.635
↑ Metastable					
600.00	80089	-8.21	-8.03	1.571	1.639
650.00	85533	-7.83	-7.71	1.581	1.648
700.00	91508	-7.44	-7.37	1.590	1.657
720.00	93955	-7.30	-7.21	1.593	1.661
740.00	96444	-7.14	-7.09	1.597	1.663
760.00	98973	-6.96	-6.97	1.599	1.667
780.00	101586	-6.81	-6.80	1.602	1.672
800.00	104216	-6.66	-6.67	1.607	1.677
900.00	118027	-5.85	-5.99	1.625	1.698
1000.00	132701	-5.10	-5.28	1.649	1.719

Tabla 8.3: Solid-solid coexistence lines of the TIP4P/2005 model for the high pressure polymorphs (ice VII, plastic crystal bcc and plastic crystal fcc) as obtained from free energy calculations and Gibbs Duhem integration. The densities are given in g/cm^3. The internal energies in kcal/mol (only the residual part of the internal energy is reported). The * indicate the initial coexistence point.

T/K	p/bar	U_1	U_2	ρ_1	ρ_2
VII-bcc plastic crystal					
600.00	250304	-4.13	-3.54	1.979	1.972
550.00	190835	-6.11	-5.50	1.902	1.889
500.00	143221	-7.67	-7.04	1.828	1.810
440.00	101354	-8.99	-8.49	1.749	1.728
400.00	80146	-9.76	-9.19	1.707	1.674
↑					
Metastable					
* 377.00	70000	-10.04	-9.53	1.681	1.645
360.00	63292	-10.27	-9.79	1.666	1.623
350.00	59665	-10.40	-9.95	1.656	1.617
VII-fcc plastic crystal					
* 393.00	77179	-9.94	-9.04	1.703	1.677
414.75	100000	-9.17	-8.34	1.752	1.740
446.94	200000	-6.73	-5.43	1.938	1.935
441.29	400000	-1.19	0.41	2.162	2.168
422.43	500000	1.61	3.29	2.244	2.251
400.00	592309	4.18	5.87	2.309	2.319
300.00	880106	12.12	13.76	2.474	2.489
250.00	980523	14.81	16.41	2.523	2.539
bcc plastic crystal-fcc plastic crystal					
* 570.00	77124	-8.35	-8.22	1.621	1.635
520.00	74646	-8.65	-8.51	1.625	1.639
500.00	74495	-8.75	-8.61	1.630	1.643
460.00	74746	-8.97	-8.78	1.640	1.655
440.00	75551	-9.03	-8.85	1.648	1.661
400.00	78266	-9.20	-8.98	1.666	1.679
380.00	80876	-9.44	-9.02	1.691	1.692

Tabla 8.4: New triple points for the TIP4P/2005, TIP4P and SPC/E models. The rest of the triple points of the models were given in Ref. [29] and [274]

Phases	TIP4P/2005		TIP4P		SPC/E	
	T/K	p/bar	T/K	p/bar	T/K	p/bar
L-VII-bcc	352	60375	322	58929	347	71284
L-bcc-fcc	570	77124	520	73100	683	103426
VII-bcc-fcc	393	77179	363	76091	434	112204

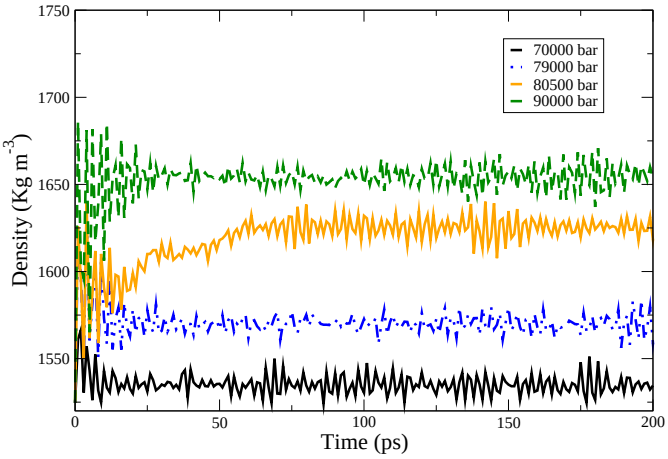

Figura 8.8: Evolution of the density with the time as obtained from direct coexistence MD simulations. All results were obtained for T = 600 K. Lines from the top to the bottom correspond to the pressures 90000, 80500, 79000 and 70000 bar, respectively. For the two first pressures the liquid water freezes, whereas for the last two pressures the solid melts. The estimate coexistence pressure at 600 K is 79750 bar.

unit cells of the fcc plastic crystal 4x(5x5x5)). The simulations were performed at 600K and 100000 bar where the fcc PC is the thermodynamically stable phases. No nucleation of the fcc PC was observed after 12 ns. We then changed strategy and performed, with the same conditions, MD simulations with isotropic scaling of the sides of the simulation box, using a cubic box, containing 432 molecules. This number of molecules (432) correspond to 216 unit cells of a bcc plastic crystal (2x(6x6x6)). In this case we observed in most of the cases the formation of a bcc PC in a few ns (in fact the oxygen-oxygen radial distribution function was clearly that of the bcc PC). With this bcc PC nucleated from the fluid we then performed anisotropic NpT MD simulations. In most of the cases nothing happened, but in one of the runs the bcc PC transformed into an fcc PC through a Martensitic transformation. This typically occurred when the bcc PC obtained was free of defects and with their crystallographic axis aligned with the vectors of the simulation box. The overall picture is that the formation of the fcc PC from the fluid occurs in two steps. Firstly, the bcc PC is formed. Then the bcc PC is transformed into the fcc PC via a Martensitic transition. This two step process is the most likely path to the nucleation of the fcc PC. It seems clear that the free energy nucleation barrier for the formation of the bcc PC from the fluid is lower than the nucleation barrier for the formation of the fcc PC from the fluid [275].

The results of this work make it possible to plot for the first time the complete phase diagram of the TIP4P/2005 model. This is presented in Figure 10.2A. The model provides a qualitatively correct description of the phase diagram of water (see the correct location of ices Ih to VI). It is seen that the two plastic crystals dominate the phase diagram of the TIP4P/2005 model of water for temperatures above 400K. The bcc PC to fcc PC transition presents a small negative slope. The slopes of the melting curves of the bcc PC and of the fcc PC are quite similar and relatively small compared to the slope in the melting curve of the rest of the ices. In fact we found a slope of the melting curve of the PC solids of about 100bar/K at temperatures around 550K. This slope is smaller than the slope found in the melting curve of ices Ih, III, V, VI and VII. In Fig.10.2 (lower panel) the phase diagrams of the TIP4P/2005

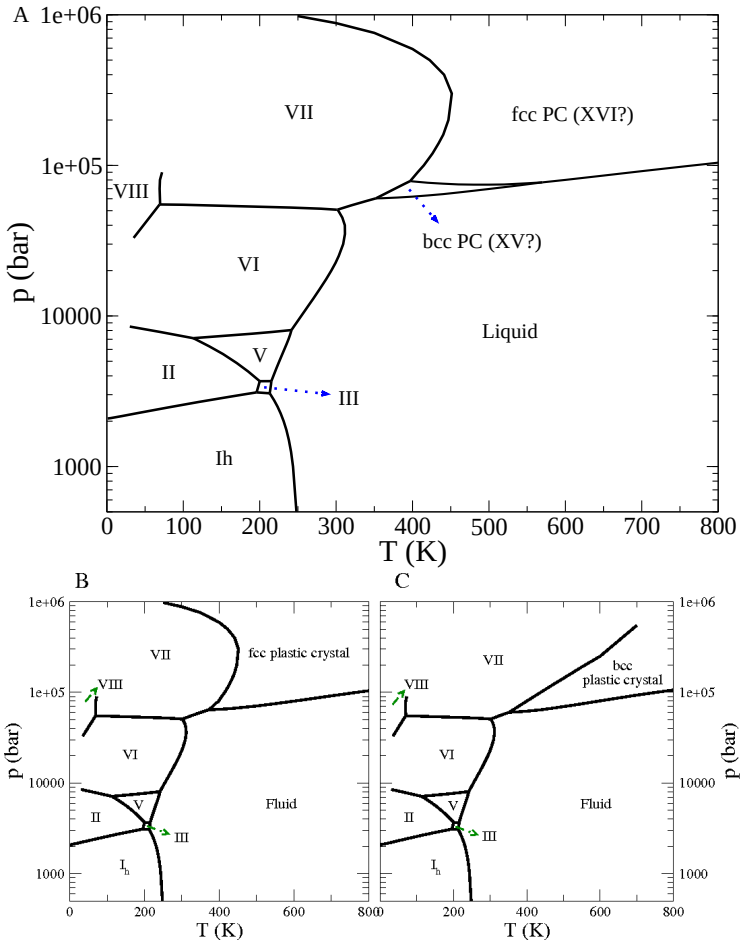

Figura 8.9: a) Global phase diagram for the TIP4P/2005 model. b) What the phase diagram for the TIP4P/2005 model would be like if the bcc plastic crystal phase would be excluded. c) What the phase diagram for the TIP4P/2005 model would be like if the fcc plastic crystal phase would be excluded.

are presented when the bcc PC (Fig. 10.2B) or fcc plastic (Fig. 10.2C) are not considered. These are virtual phase diagrams since for the TIP4P/2005 the fcc PC or bcc PC do indeed exists and the true phase diagram of the model is that of the upper panel. The purpose of the diagram of the Fig. 10.2C is to show that the coexistence curve between ice VII and the bcc PC always presents a positive slope. In other words ice VII is always more dense than the bcc PC at a given temperature and pressure. This is not surprising since both phases present the same arrangement of oxygen atoms, but the localized character of the hydrogen bonds in ice VII provokes a higher density. We do not expect any change in the sign of the slope in the coexistence line between ice VII and the bcc PC. However, in Fig. 10.2B we see a change of slope in the transition between ice VII and the fcc PC. At low pressures ice VII is more dense than the fcc PC (the stronger hydrogen bonds in ice VII compensate the less efficient packing of molecules in the bcc arrangement). However the VII-fcc PC presents re-entrant behavior. In fact a high pressures the fcc PC is more dense than ice VII. This is further illustrated in Fig.8.10A where the equation of state of ice VII and of the fcc PC at 300K are shown, from pressures of about 70000 to extremely high pressures. The crossing in the densities is clear. Notice that the crossing does not indicate any phase transition. The black filled circles in Fig.8.10A indicate the coexistence point as obtained from Gibbs Duhem simulations. At sufficiently high pressures the more efficient packing of the fcc arrangement

of oxygens dominates the physics of the model. The density of the bcc PC is intermediate between that of the fluid and that of ice VII at the same T and p (Fig. 8.10B). The physics of PC has been discussed before for simple models [276] such as hard diatomic molecules [199, 253–255, 277–280].

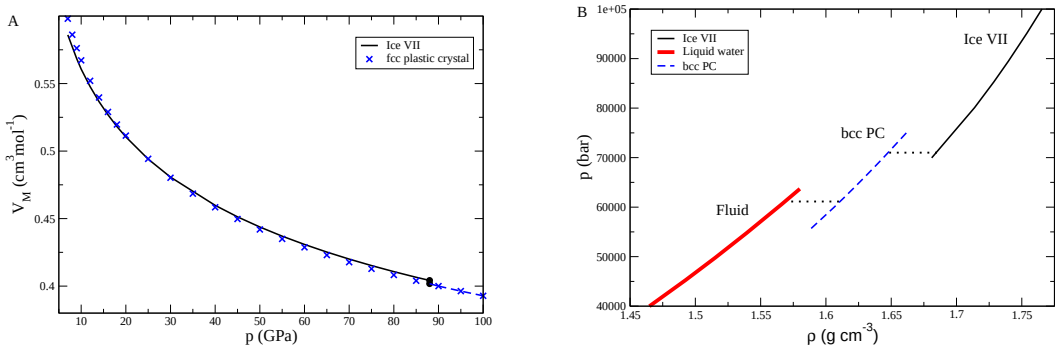

Figura 8.10: a) Equation of state of ices VII (solid line) and fcc PC (crosses) for 300 K as obtained from computer simulation for TIP4P/2005 model. Lines indicate thermodynamic stable phase for each pressure. For low pressures the solid line corresponds to ice VII. At high pressures the dashed line with crosses corresponds to fcc PC. The coexistence point between the two ices is given by the filled circles. b) Equation of state of ice VII (thin solid line), bcc PC (dashed line) and liquid water (thick solid line) for 380 K as obtained by computer simulation for TIP4P/2005 model. The dotted lines gives the coexistence.

Let us now analyze if the plastic crystal phases also appear in other water models such as TIP4P and SPC/E. Although we computed the phase diagram for these two models in our previous work [22] it seems necessary to recalculate the upper part of the phase diagram for at least two reasons. Firstly because we did not consider the possibility of having plastic plastic crystal phases in the phase diagram. Secondly because the free energy calculations for ice VII were performed at a temperature and pressure where the system was already in a plastic crystal phase (443K and a pressure of about 78350 bar). Therefore our free energy calculations for ice VII (reported recently in Ref. [133]) of the TIP4P and SPC/E were incorrect. The rest of free energies and coexistence lines are correct. By performing Hamiltonian Gibbs Duhem integration we estimate an initial coexistence point for the coexistence lines involving ice VII and the PC phases. Once this initial point was located the rest of the coexistence line was obtained by Gibbs Duhem integration. The complete phase diagrams of TIP4P and SPC/E are presented in Fig. 8.11 along with the experimental phase diagram. The phase diagram for the TIP4P model is very similar to that of the TIP4P/2005 model but shifted to lower temperatures by about 20K (this shift is found for instance in the melting point of ice Ih for these two models). The phase diagram of SPC/E is dominated by ice II (ice Ih appears at negative pressures and ices III and V disappear from the phase diagram). The pressure at the fluid-ice VI-ice VII triple point for TIP4P and SPC/E is now about 55000 bar (compared to a value of about 85000 bar reported in our previous work). This new location of the triple point is in better agreement with the experimental pressure at the triple point between ice VI, ice VII and the fluid (which is about 30000 bar). The agreement is not yet quantitative though. It is clear that both PC phases appear in the phase diagram of these two water models. The main difference between SPC/E and TIP4P is the size of the stability region of the bcc PC (larger for the SPC/E). Notice also the change of slope of the ice VIII-ice VII transition observed in the experimental phase diagram. According to our previous discussion of the ice VII- fcc PC transition this change in the slope points to a greater density of the phase on the right (ice

VII) with respect to the phase on the left (ice VIII). It has been suggested [32, 271, 281–284] that the hydrogens become dynamically disordered in ice VII between the two positions along the O-O lines and finally occupies the central location of the O-O lines in ice X. This could provoke a more dense packing in ice VII, explaining the negative slope of the experimental coexistence line between ices VIII and VII (although it would be interesting to know whether ice VIII is affected or not by a similar possible resonance and symmetrization of the hydrogens).

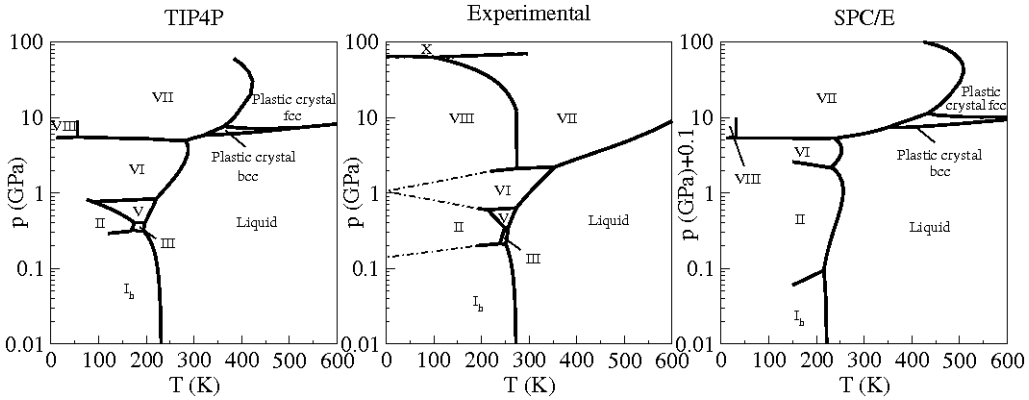

Figura 8.11: Phase diagram of H_2O. Left: simulation results for the TIP4P model; right: simulation results for the SPC/E model; middle: experimental phase diagram. For the SPC/E the coexistence pressures have been shifted by 0.1 GPa to include results for the ice I (which appears for the SPC/E at slightly negative pressures). The Gibbs-Duhem coexistence lines for SPC/E and TIP4P models can be found as electronic supplementary information [**?**].

These plastic crystal phases have not been reported so far for real water. Schwager *et al.* [285] in a very recent experimental study suggests the existence of a new ice phase from 20 to 42 GPa. The structure of this new solid is unknown but the melting curve has been reported. In Figure 8.12 the melting curve reported by Schwager *et al.* is plotted along with the melting curve of ice VII reported by several other groups. In Fig. 8.12A we present the upper part of the phase diagram of TIP4P/2005 as presented in Fig. 10.2C (i.e when the fcc PC solid is not included). The similarity in the slopes between experiment and simulation is striking. In particular the slope of the melting curve reported by most of experimental groups seems to correspond to the ice VII- bcc PC obtained in computer simulations. However, the melting line reported by Schwager *et al.* [285] seems to correspond to the melting curve of the bcc PC obtained in simulations. Notice the small slope of the melting curve reported by Schwager *et al.* [285] As discussed above the small slope of the melting curve is a signature of PC phases. In Fig. 8.12B we compare the fluid-fcc PC and VII-fcc PC coexistence lines with the experimental measurements of the ice VII melting line (i.e when the bcc PC solid is not included). The fluid-fcc PC line is very similar to the melting curve reported by Schwager *et al.* [285] whereas the slope of the VII-fcc PC coexistence line is similar to the rest of the experimental melting lines given for ice VII. The main difference is that there a change of slope in the transition between ice VII and the fcc PC. In view of this, it seems to be reasonable to think that the new phase reported by Schwager could be a plastic crystal phase (it is not clear what it could be, bcc PC or fcc PC). Obviously further work is needed to clarify this. The melting curve of Schwager *et al.* [285] increases its slope for temperatures above 1300K. The sharp increase in the slope of the melting curve could be due to the presence of molecular dissociation and proton diffusion in the solid before melting (typical behavior of type-II super-ionic solids [31]). This can not be reproduced using rigid non-polarisable models and for this reason our simulations do not reproduce the sharp increase in the slope of the melting curve for temperatures greater than

1300 K.

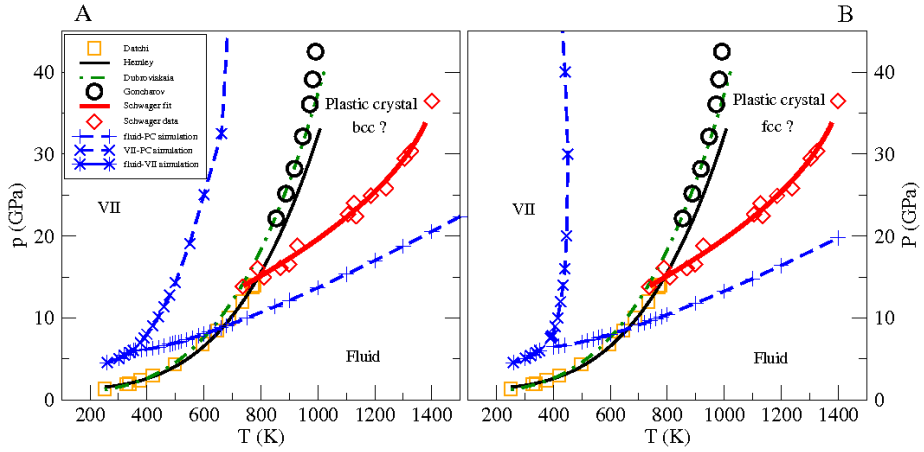

Figura 8.12: Experimental measurements of the ice VII melting curve. The open circles correspond to the Goncharov values Ref. [52], the dashed-dotted line is given by Dubronskaia Ref. [51], the thin solid line correspond to the Lin results Ref. [50], the open squares is taken from Datchi Ref. [49], the diamonds and and the thick solid line is given by Schwanger [48]. Left: The melting curve of the fcc plastic crystal obtained by simulations correspond to the dashed line with pluses, the simulated coexistence curve ice VII-fcc plastic crystal phase is the dashed line with crosses and the dashed line with stars correspond to the simulated melting line of the ice VII. Right: The melting curve of the bcc plastic crystal obtained by simulations correspond to the dashed line with pluses, the simulated coexistence curve ice VII-bcc plastic crystal phase is the dashed line with crosses and the dashed line with stars correspond to the simulated melting line of the ice VII.

Conclusions

In this work the characterization and localization in the phase diagram of water of a new fcc plastic crystal phase has been performed by computer simulation by using the TIP4P/2005 model. This PC was obtained through a Martensitic transformation of the bcc PC. By performing free energy calculations it was further confirmed that it is thermodynamically stable at certain T and p. Details about how to perform free energy calculations for plastic crystal phases of water have been provided. Once the free energies for the fluid, ice VII and the two plastic crystal phases were determined it was possible to determine the upper pressure part of the phase diagram of TIP4P/2005. Melting points predicted by free energy calculations were further confirmed by direct coexistence techniques.

We have recalculated the high pressure region of the phase diagram for the TIP4P and SPC/E models using Hamiltonian Gibbs-Duhem integration. It has been shown that for all these water models these two plastic crystal phases appear in the upper region of the phase diagram. In fact for these water models the melting curves at high temperatures are dominated by the plastic crystal phases.

It would be of interest to study if such plastic crystal phases do indeed exist for real water. As has been seen, the bcc plastic crystal phase (or the fcc PC) could be the new ice phase reported by Schwager et al. [285]. The discrepancies between the melting curve given by Schwager and the rest of the experimental groups could be due to the fact that Schwager is determining the plastic crystal-fluid transition, whereas the other groups may be determining the ice VII- plastic crystal transformation. The presence of plastic crystal phases for real water

would have consequences for the large community performing computer simulations of water. Its presence would indicate that current water models can still provide estimates of the behavior of water even at high pressures (provided that no dissociation of the molecules occurs). Its absence would also be significant since it would indicate that current water models are too spherical and they should be modified so as to predict the disappearance of the plastic crystal phases.

Acknowledgements

This work was funded by grants FIS2007-66079-C02-01 from the DGI (Spain), S-0505-/ESP/0299 from the CAM, and 910570 from the UCM. J. L. Aragones would like to thank the MEC by the award of a pre-doctoral grant. Helpful discussions with L.G.MacDowell, J.L.F.Abascal and E.G. Noya are gratefully acknowledged. We would like to thank Carl McBride for a critical reading.

CAPÍTULO 9

The dielectric constant of ices and water: a lesson about water interactions

J.L. Aragones[1], **L.G. MacDowell**[1] **and C. Vega**[1]

[1]*Dep. Química Física, Fac. Química, Universidad Complutense de Madrid, 28040,Madrid, Spain*

Journal of Physical Chemistry A, **115***, 5745-5758 (2011)*

Abstract

In this paper the dielectric constant has been evaluated for ices Ih, III, V, and VI for several water models using two different methodologies. Using Monte Carlo simulations, with special moves to sample proton disordered configurations, the dielectric constant has been rigorously evaluated. We also used an approximate route in which proton disordered configurations satisfying the Bernal Fowler rules were generated following the algorithm proposed by Buch *et al.* (V. Buch, P. Sandler and J. Sadlej, J.Phys.Chem.B, **102**, 8641 (1998)) and the dielectric constant was estimated assuming that all configurations have the same statistical weight (as Pauling did when estimating the residual entropy of ice). The predictions of the Pauling model for the dielectric constant differ in general from those obtained rigorously by computer simulations because proton disordered configurations satisfying the Bernal Fowler rules can differ in their energies by as much as 0.10-0.30 NkT (at 243K). These differences in energy significantly affect properties that vary from one configuration to another such as polarization, leading to different values of the dielectric constant. The Pauling predictions differ from the simulation results, especially for SPC/E and TIP5P, but yield reasonable results for TIP4P like models. We suggest that for three charge models the polarization factor (G) in condensed phases depends on the ratio of the dipole to the quadrupole moment. The SPC/E, TIP5P, TIP4P, TIP4P/2005, TIP4P/Ice models of water are unable to describe simultaneously both the experimental dielectric constants of water and ice Ih. Non-polarizable models cannot describe the dielectric constants of the different condensed phases of water because their dipole moments (about 2.3 D) are much smaller that those estimated from first principles (of the order of 3 D). However the predictions of TIP4P models provide an overall qualititatively correct description of the dielectric constant of the condensed phases of water, when the dipole moment of the model is scaled to the estimated value obtained from first principle calculations. Such scaling fails completely for SPC/E, TIP3P and TIP5P as these models predict a completely different dielectric constant for ice Ih and water at the melting point, in complete disagreement with experiment. The dielectric constant of ices, as the phase diagram predictions, seems to contain interesting information about the orientational dependence of water interactions.

Introduction

Finding simple water models reproducing as many properties as possible constitutes an important subject of research [83, 286, 287]. Within the Born-Oppenheimer approximation one could obtain condensed matter properties of water exactly by combining path integral simulations (to incorporate quantum effects on the nuclei distribution) with electronic calculations that would provide the energy of a certain configuration of the atoms of the system. Due to computer limitations, it is not possible right now to solve accurately the electronic Schrodinger equation for a system containing about 300 molecules (a typical number required to obtain condensed matter properties), for about 32 slices of imaginary time [288] (a typical number required to describe properly nuclear quantum effects in water) , for about 100 000 time steps (a typical number required to obtain good accuracy in water simulations). Approximations are needed to obtain results within a reasonable time. Approximations can be done either in the description of the nuclear motion (classical versus quantum description) or in the description of the electronic energy (described by an empirical potential or from an approximate treatment of the Schrodinger equation). Thus four approaches to water simulations are possible. The first one is using path integral simulations combined with electronic structure calculations. The second one is combining Newton equations for the motion the nuclei with electronic structure calculations. The third possibility is to use an analytical expression for the water interactions combined with path integral simulations. The fourth possibility is to use an analytical water potential along with classical simulations. The analytical water potentials are typically obtained by proposing an empirical expression and determining its parameters to reproduce either experimental properties (empirical potentials) or ab-initio results (theoretical based potentials).

In the last few years it has become clear that the potential parameters of empirical water potentials should be chosen to reproduce the complete room pressure isobar of water (from 250K to 450K) [35]. In fact we have recently proposed a water model TIP4P/2005 [34] that accurately reproduces the room pressure isobar (and the same is true for the TIP4P-Ew [289] potential). Notice that TIP5P [108] reproduces the location of the maximum in density of water but it fails in reproducing the complete room pressure isobar. The same is true when an empirical potential is used in path integral simulations (TIP4PQ/2005 [44] and the model q-TIP4P/F of Habershon *et al.* [290] both reproduce the room pressure isobar). The TIP4P/2005 is a simple rigid non-polarizable model consisting of a Lennard-Jones (LJ) center and three charges. It is somewhat surprising to see how many properties of water can be described correctly by such a simple model [35, 71, 207]. In particular the model describes quite well the room pressure isobar (by design), the critical temperature and density [207], the diffusion coefficient [34, 71], the isothermal compressibility [71], the coefficient of thermal expansion, the surface tension [208], the viscosity [291], the density of ices [34], the structure of water and ice Ih [34, 214], the relative stability between ices [12, 33, 37], the equation of state up to pressures of about 30 000 bar [34]. The model also provides a qualitative description of the phase diagram of water [22, 29, 34], and predicts the melting point of water with an error of about 23K [34].

The TIP4P/2005 is a simplification of the true interaction between water molecules and consequently must fail to describe some properties. This is certainly the case and the model fails in describing vapor properties (second virial coefficient, vapor pressure and critical pressure). This failure can be understood by considering that the dipole moment of the molecule in the vapor phase is of 1.85 D, whereas the model has a dipole moment of about 2.3 D. The higher dipole moment of the model with respect to that of the isolated molecule is an effective way of accounting for the higher dipole moment of water in the liquid phase with respect to

the vapor phase. The lack of polarizability prevents the model for describing vapor and liquid properties simultaneously. Also we have recently shown that to describe the heat capacity of water and ice nuclear quantum effect should be included [214, 292].

Overall TIP4P/2005 describes quite well the properties of water and when it fails (vapor properties, heat capacities) there is a clear reason (lack of polarizability, classical treatment of nuclei motion) for that. TIP4P/2005 represents an improvement over other more traditional water models such as TIP3P [107], TIP5P [108] or SPC/E [106] in the description of practically all water properties. There is however one important exception: the dielectric constant in the liquid phase at room temperature and pressure. For this property the value predicted by TIP4P/2005 was 60 (thus improving the prediction of the original TIP4P with a value of 54) but clearly inferior to the predictions of the models TIP3P, TIP5P and SPC/E which are 85, 82, and 65 respectively [35] (the experimental value at room temperature and pressure is 78). Motivated by this failure of the model we have decided to investigate in more detail the predictions of the dielectric constant of the model for the solid phases of water (ices). We want to know if the model also fails for other phases besides water, and if the models that are successful in predicting the dielectric constant of water (TIP3P, TIP5P, SPC/E) are also successful or not in the solid phases.

Ices can be divided into two families. Those in which the protons are ordered (ices II, XI, IX, VIII, XIII, XIV) and those in which protons are disordered (Ih, Ic, III, V, VI, VII, IV, XII). From a microscopic point of view the dielectric constant is related to the fluctuations of the total polarization of the system, M. It can be obtained easily (although using long runs [293]) for liquid water and for ices in which the protons are ordered. For ices with ordered protons, the molecules only undergo small vibrations around the equilibrium configuration and for this reason the fluctuations of the total dipole moment are small yielding small dielectric constants (typically less than 5). Thus the behavior of the dielectric constant of proton ordered ices is not particularly exciting. However the situation is completely different for ices with proton disorder. For proton disordered ices many configurations exist that have similar energies, separated by large energy barriers (of the order of two hydrogen bonds). These configurations may present quite different values of the total polarization (M) so the dielectric constants for these ices are usually large (between 90 and 170). Transitions between different disordered configurations are rare events. Chan *et al.* [152] have estimated the relaxation time of ice Ih at 250K to be of about 168 microseconds and Johari and Whalley [153] suggested that it is of the order of several years at 100K. For this reason special moves should be introduced in the simulation of proton disordered ices to obtain dielectric constants. In a series of important papers Rick and coworkers have shown that SPC/E, TIP4P and TIP5P underestimate the dielectric constant of ice Ih by a factor of two or three [154, 233, 294]. These results were confirmed by Wang *et al.* [132]. Recently two of us have found that TIP4P/2005 and TIP4P/Ice also underestimate the dielectric constant of ice Ih [156]. Is there any reason for this failure of all water models studied?

This paper has three goals. The first is to show that the technique proposed by Rick and Haymet [154] can be applied to determine the dielectric constant of other ices (besides ice Ih and V [156]). We shall evaluate the dielectric constant for ices III, V, VI and VII for the TIP4P/2005 and TIP4P/Ice models. Secondly we will compare the dielectric constants obtained for these ices to the experimental results obtained by Whalley [153, 251, 261, 295–297] to test if the failure in describing the dielectric constant of ice Ih, also extends to the other ices. The third goal is to analyze if the Pauling model can be used to estimate the dielectric constant of ices. The Pauling model of ice contains two key ideas [84]. The first one is that the configurations that contribute most to ice properties are those satisfying the Bernal Fowler rules [8]. The second is to assume that all configurations that satisfy the Bernal Fowler rules

have the same statistical weight. In the Bernal Fowler rules, one assumes that ices are formed by water molecules (i.e two H form a covalent bond to each O) and that each water molecule is forming four hydrogen bonds with the nearest water molecules of the solid, in two of them acting as donor and in the other two acting as acceptor. The model was successful in estimating the residual entropy of ice [298, 299] found experimentally and it is natural to ask if the model can be used to describe the dielectric constant of proton disordered ices (Ih, III, V, VI, VII).

In short, the main conclusions of this paper are that the Pauling model can not be used to estimate the dielectric constant of ices (although it yields reasonable predictions for TIP4P models), and that the methodology proposed by Rick and Haymet can be used successfully to determine the dielectric constant of water models in the solid phases (ices). Finally no rigid non-polarizable model of water is able to describe the dielectric constant of ices. However, the results obtained with the TIP4P/2005 provide a simple explanation for this failure. It is simply due to the fact that the model has a dipole moment of about 2.3 D, whereas in condensed phase the dipole moment is closer to 3 D [56, 57, 300–302]. By re-scaling the dipole moment it will be shown that the results are in reasonable agreement for all the condensed phases of water.

Theory and simulation details

For solids the dielectric constant is a tensor. For a rigid non-polarizable model the elements $\epsilon_{\alpha,\beta}$ of this tensor can be calculated in computer simulations (when using Ewald sums and conducting periodical boundary conditions) from the expression [98, 99, 156, 303–306]:

$$\epsilon_{\alpha,\beta} = \delta_{\alpha,\beta} + \frac{4\pi}{kTV}[< M_\alpha M_\beta > - < M_\alpha >< M_\beta >] \tag{9.1}$$

where $\alpha, \beta = x, y, z$ (i.e. a set or orthogonal laboratory frame axes), $\delta_{\alpha,\beta}$ is a Kronecker delta, V is the volume of the simulation box and M_α is the value of the component α of the total dipole moment of the sample (in the absence of an electric field since the previous formula holds within the linear response framework) and the bracket holds for ensemble average. It should be pointed out that for a polarizable model (or in the case of the experimental results) the first term on the right hand side (i.e that with the Kronecker delta) should be multiplied by the infinite frequency value of the tensor component (i.e $\epsilon_{\infty,\alpha,\beta}$). This is typically a small number (i.e for liquid water its value is 1.8, being only slightly larger for ice Ih). For non ferroelectric materials (i.e. water and all the ices considered in this paper) the average value of the component α of the polarization of the sample is zero (i.e $< M_\alpha >= 0$) so that the elements of the dielectric tensor can be written simply as:

$$\epsilon_{\alpha,\beta} = \delta_{\alpha,\beta} + \frac{4\pi}{kTV} < M_\alpha M_\beta > \tag{9.2}$$

Like any other tensor, the values of the components α and β depend on the choice of the laboratory reference frame (i.e. the location of the X, Y, Z axes with respect to the unit cell vectors of the solid). In general, components with α different from β will not be zero. However, there is a choice for the laboratory frame (with respect to the unit cell vectors) that converts the tensor into diagonal form [96]. The three values along the diagonal will be then the three principal dielectric constants and they could be compared to the experimental values. For crystals of cubic (Ic, VII), tetragonal (III, VI) and orthorhombic symmetry the dielectric tensor becomes diagonal when the laboratory frame axes X,Y,Z are located along the **a, b, c** axis of the unit cell. For crystals of hexagonal symmetry (Ih) the dielectric tensor will be diagonal

when X, Z are chosen along the **a** and **c** unit cell vectors respectively, and Y is chosen in the direction perpendicular to **a** [96]. For cubic crystals and fluid phases, the three principal dielectric constants will be identical, and for tetragonal and hexagonal crystals the first two principal dielectric constants will be identical but different from the third one. In the case of ice V (monoclinic) it is more convenient to choose the X, Y axes along the **a** and **b** unit cell vectors respectively, and Z in the direction perpendicular to the **a, b** plane. With this choice the dielectric tensor is not diagonal but could be compared easily to experimental results. In fact with this choice the $xy(yx)yz(zy)$ are zero but the $xz(zx)$ component is non zero. Thus when reporting dielectric constants of solids one should report the three principal dielectric constants. In the case of a monoclinic crystal (ice V) it is more convenient to report four components (xx, yy, zz and xz for the laboratory frame described above). In may cases experimental values of the three principal dielectric constants are not available. Quite often the properties of a powder formed by many small crystals with random orientation with respect to the electric field are measured. In this case the experimental reported dielectric constant, denoted as ϵ, is simply the average of the three principal dielectric constants, which is related to the trace of the the dielectric tensor:

$$\epsilon = \frac{1}{3}(\epsilon_{xx} + \epsilon_{yy} + \epsilon_{zz}) \tag{9.3}$$

The dielectric tensor changes when changing the laboratory frame as $X^{-1}\epsilon_{\alpha,\beta}X$ and this transformation leaves the trace invariant. For this reason, the value of ϵ as given by the trace of the dielectric tensor is invariant to the choice of the laboratory frame. Therefore for the models used in this work one simply obtains :

$$\epsilon = 1 + \frac{4\pi}{3kTV} < M_x^2 + M_y^2 + M_z^2 > \tag{9.4}$$

and this is true regardless of the choice for the laboratory frame. For a polarizable model or in the case of the experiment the first term on the right hand side should be replaced by the infinite frequency dielectric constant ϵ_∞ which does not differ much from one. The previous equation can be rewritten (after dividing and multiplying by N, the number of molecules) as :

$$\epsilon = 1 + \frac{4\pi\rho}{3kT}[\frac{<\mathbf{M}^2>}{N}] \tag{9.5}$$

where ρ is the number density. Experimental measurements of the dielectric constant at a certain T and density allow to determine the experimental value of $[<\mathbf{M}^2>/N]$. Let us now assume that one can identify a characteristic value of the dipole moment of each molecule in the condensed phase. For a non-polarizable model that would just be the dipole moment of the molecule. Then the previous equation can be rewritten as :

$$\epsilon = 1 + \frac{4\pi\rho}{3kT}\mu^2[\frac{<\mathbf{M}^2>}{N\mu^2}] \tag{9.6}$$

Let us define the polarization factor G as the term in brackets in the previous equation so that:

$$G = [\frac{<\mathbf{M}^2>}{N\mu^2}] \tag{9.7}$$

Then the dielectric constant is given by:

$$\epsilon = 1 + \frac{4\pi\rho}{3kT}\mu^2 G \tag{9.8}$$

Thus for a non-polarizable model (in which all molecules have the same dipole moment) the value of G is well defined. Besides the expression for G can be further simplified by noting that :

$$\mathbf{M} = \sum_{i=1}^{i=N} \mu_i \tag{9.9}$$

and then G is simply given by :

$$G =< (\sum_{i=1}^{i=N} \mathbf{u}_i)^2 > /N \tag{9.10}$$

where $\mathbf{u_i}$ is a unit vector along the direction of the dipole moment of the molecule.

If simulations are performed using electronic structure calculations then the value of $[< M^2 > /N]$ is uniquely defined but this is not the case for G. One could still use Eq.9.7 to define G by using the average of the squared dipole moment in the denominator of the expression. However there are several “arbitrary” criteria to distribute the electronic charge density between the molecules that will lead to different values of the average dipole moment μ and consequently to slightly different values of G.

In this work we shall perform computer simulations to determine the dielectric constants (or more generally the dielectric tensor) for several water models and for several ices. In particular we shall consider the proton disordered ices Ih (at 1 bar), Ic (at 1 bar), III (at 2800 bar), V (at 5300 bar), VI (at 11000 bar) and VII (at 70000 bar), and the clathrate structures sI and sII (at 1000 bar). In most of the cases we shall use the TIP4P/2005 model although in a few cases we have determined the dielectric constant for the models SPC/E, TIP4P/Ice and TIP5P. To sample over proton disordered configurations we shall use the efficient algorithm proposed by Rick and Haymet [154] which can be regarded as the extension to non-lattice ice models of the algorithm proposed by Rahman and Stillinger [155]. We refer the reader to the original papers, and to our previous work [156], for a more comprehensive description of the algorithm and here we shall provide only the main details.

Monte Carlo simulations were carried out in the NpT ensemble [99]. Box deformations were considered using the Parrinello–Rahman method [102]. Coulombic interactions were calculated using the Ewald summation technique [97]. Conducting boundary conditions were employed in all simulations. For fluid phases one can use either Ewald sums or the Reaction Field technique [305–308] to obtain the dielectric constant, but for solid phases Ewald sums seems to be the natural choice. Both dispersive and screened–coulombic interactions up to the cutoff distance were calculated by means of an efficient link cell list [309]. The LJ part of the potential and the real space contribution of the Coulombic interactions was truncated at 8.5 Å for all models (except for ices Ic and V with cutoff 6.5 Å) [99]. Usual long range corrections to the Lennard–Jones part of the potential were added.

It is well known that a standard Metropolis algorithm incorporating only displacement and rotation attempts cannot properly sample ice proton disorder. These movements will only sample small lattice vibrations, but are unable to modify the assumed hydrogen bond arrangements. An algorithm for exploring hydrogen bond arrangements was proposed by Rahman and Stillinger for a simple tetrahedral lattice model [155]. This algorithm was also exploited later on to study the order/disorder transition of ice on a lattice [310, 311], and was extended recently for off lattice water models [154]. The method requires first to search for a closed loop of hydrogen bonds. Molecules belonging to the loop have one proton that is bond donor inside the loop (inner bond) and other that is not (outer bond). The attempted move consists in rotating each of the molecules successively about the outer bond by 120 degrees until a full

hydrogen bond arrangement with opposite sense has been established along the loop. The attempted move is accepted or rejected according to the usual Monte Carlo criteria. Whereas this algorithm works well for tetrahedral lattices, the acceptance may become too low in off lattice systems. Rick and Haymet have argued that a greater acceptance is achieved by rotating the molecule such that the new bond lies on the plane formed by the outer hydrogen, the oxygen atom of the rotating molecule and the next oxygen on the loop (see Fig. 2 of our previous paper [156]). The topology of loops in a crystal was studied by Rahman and Stillinger [155]. They found that rings could be classified into three classes. i) True closed loops with six molecules, ii) true closed loops with more than six molecules and iii) percolating loops, which span one full linear dimension of the simulation box and are closed by virtue of the toroidal boundary conditions. By performing a Markov chain [99] over these three type of loops rotations, all the hydrogen bond arrangements may be sampled in principle. Closed loops moves of type i) and ii) change very little the total dipole moment of the simulation box (in fact for a perfect Ih or Ic lattice the change is exactly zero [310]). These moves provoke only small fluctuations in the total dipole moment within the Markov chain. However, percolating loops of type iii) provide dramatic changes in the total dipole moment of the simulation box. For this reason percolating loops are absolutely required to sample properly the fluctuations of the total dipole moment of the sample and to obtain reliable values of the dielectric constant. The probability acceptance of loop rotations (of type ii) or iii)) decreases as the size of the loop increases. The size of the system should be chosen so that there is a small but reasonable probability of accepting moves of type iii) that really contribute to the evaluation of the dipole moment fluctuations. For this reason the algorithm of Rick and Haymet is more efficient for systems of moderate size. In this work, the number of molecules chosen for the simulations was Ih (360),Ic (216), III (324), V (224), VI (360), VII (432), sI (368) and sII (136). For each system 8-12 independent simulations of one million cycles each was done (after an initial equilibration run of about 40, 000 cycles). A cycle is defined as N trial moves (being N the number of molecules of the system). MC translation, rotation and loop moves were performed in the ratio 45:45:10. The error was estimated from the standard deviation between the results of the eight independent runs.

Finally we shall use the Pauling model to estimate the dielectric constant of proton disordered ices. In the Pauling model one assumes that the statistical significantly configurations satisfy the Bernal-Fowler rules and all have the same probability. Therefore to evaluate the dielectric constant of ices using the Pauling model all that is needed is an algorithm that generates configurations satisfying Bernal Fowler without any energetic bias [86, 312]. We used the algorithm proposed by Buch *et al.* [86] to generate these configurations. The algorithm of Buch *et al.* has been used by many authors in the last years to generate proton disordered configurations in the study of ices. The algorithm of Buch *et al.* [86] is of topological type (i.e. no energy or temperature enters in the algorithm). We typically generated 50000 independent configurations satisfying the Bernal Fowler rules. Let us just explain briefly some technical aspect of the calculations. Crystallographic positions (as determined from experimental data) were used to determine the position of the oxygens within the unit cell (the shape of the simulation box was obtained from an NpT run of the ice at the considered T and p). Firstly it should be noted that the $O_1 - O - O_2$ angle between a central oxygen O and two of its nearest neighbors O_1 and O_2 is tetrahedral for ices Ih, Ic and VII but it can adopt values significantly different from the tetrahedral value for ices III, V and VI. An excellent compilation of the O-O-O angles present in ices III, V and VI can be found on the web page of Chaplin [167]. Besides the bond angle of the rigid model (i.e 105.4 for TIP4P and TIP5P models, and 109.5 for SPC/E) will in general be different to the O-O-O angle. Therefore a criterion to determine the precise orientation of the water molecule within the ice should be provided. In this work the orientation of the water molecule was selected in such a way that the H-O-H bisector was coincident with

the $O_1 - O - O_2$ bisector and that the H-O-H is on the same plane as the $O_1 - O - O_2$ (as illustrated in Fig. 9.1). Although there is no a unique criterion to locate the water molecule when forming hydrogen bonds to two nearest neighbors, the criterion chosen here appears to be a reasonable one. An additional advantage of this criterion is that the direction of the dipole moment of each water molecule is the same regardless of the water model considered. Therefore the value of G obtained with this criterion does not depend on the selected water model (of course the dielectric constant will be different since the water models differ in their dipole moment). Notice that the Pauling algorithm can be used to determine anisotropies of the dielectric constant. One can define the tensor:

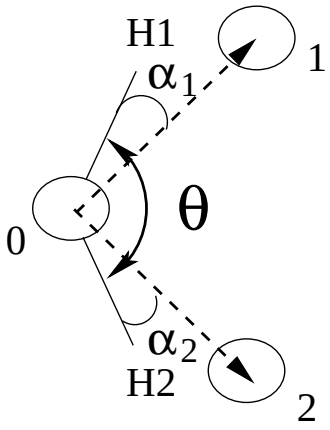

Figura 9.1: Sketch to illustrate the criterion used to determine the orientation of the water molecule within the ice for the Pauling model. The three oxygen atoms and the two hydrogens are on the same plane. The O_1-O_0-O_2 bisector and the $H_1 - O - H_2$ bisector are coincident. According to that α_1=α_2. Notice that the direction of the bisector is the same regardless of the bond angle of the water model θ.

$$G_{\alpha,\beta} =< M_\alpha M_\beta > /(N\mu^2) \tag{9.11}$$

so that the value of G is just the average of the trace of the $G_{\alpha,\beta}$ tensor. The dielectric tensor can be obtained easily from the G tensor using the expression :

$$\epsilon_{\alpha,\beta} = \delta_{\alpha,\beta} + \frac{4\pi\rho}{3kT}\mu^2 G_{\alpha,\beta} \tag{9.12}$$

Results

The Pauling model

The values of the G factor as obtained in this work are presented in Table 9.1. Obviously for the Pauling model the values of G do not depend on temperature (all configurations have the same probability regardless of the temperature) although the dielectric constant still depends on temperature as can be concluded from the inspection of Eq. 14.1. G do not depend on the water model and the reason was described in the previous section (there is a very small dependence on the model through the dependence of the unit cell parameters with the potential model). Ices for which the 4 nearest neighbor oxygens of each oxygen atom form a perfect tetrahedral arrangement (Ih, Ic, VII) present a G factor of 3 (within the statistical uncertainty). This is in agreement with all previous estimates for ices Ih and Ic [313–317]. When the nearest neighbors form a distorted tetrahedron then the G factor is smaller than three, being of 2.5 for

Tabla 9.1: Values of G for several solid phases of water obtained from 50000 proton disordered configurations satisfying the Bernal Fowler ice rules (Pauling model). The values of G at 243K obtained from computer simulations of TIP4P/2005 (this work) are also presented. For SPC/E and TIP5P the values of G for ice Ih were taken from the simulation results of Rick *et al.* [233] For SPC/E the values of G for ices III and VI as obtained in the computer simulations of this work at 243K are also presented.

Phase	Pauling model	TIP4P/2005	SPC/E	TIP5P
I_h	3.02(4)	2.54(5)	1.74(10)	1.40(8)
I_c	3.01(4)	2.54(5)	-	-
III	2.49(3)	2.28(37)	1.24(41)	-
V	2.50(4)	2.70(43)	-	-
VI	2.89(3)	2.85(26)	2.17(88)	-
VII	3.01(5)	2.94(10)	-	-

ice III, 2.5 for ice V and of 2.9 for ice VI. The values of G reported here are in relative good agreement with those estimated by Johari [318–322] which were obtained approximately for the Pauling model counting all possible configurations between a central molecule and the second or third nearest neighbors.

We have also determined the value of the dielectric constant from NpT simulations including loop moves as described in the previous section. The value of G can then be obtained using the expression :

$$G = \frac{(\epsilon - 1)3kT}{(4\pi\rho\mu^2)} \tag{9.13}$$

We found that G depends on T (increasing slightly as T increases) but the changes in the temperature range 200-273K are rather small [156, 323]. Therefore we shall report the value of G at 243K. In Table 9.1, the values of G obtained from NpT simulations for the TIP4P/2005 at the temperature of 243K, are presented. Let us start by discussing the results for ice Ih. For ice Ih the Pauling model yields a value of 3, whereas the simulations results are $G = 2.54$ for TIP4P/2005, 1.74 for SPC/E and 1.40 for TIP5P. The first conclusion to be drawn is that for ice Ih, the Pauling model is unable to predict the value of G obtained in the simulations. Furthermore the value of G found in the simulations changes dramatically from one water potential to another. Thus G is quite sensitive to the charge distribution used to describe Coulombic interactions in the water model. However in a previous work [156] we found that the value of G for ice Ih obtained with the TIP4P, TIP4P/2005 and TIP4P/Ice models was practically the same. This is puzzling since all these water models present a dipole moment close to 2.3 D. A possible explanation is that the value of G depends not on the value of the dipole moment, but rather on the value of the ratio of the dipole to quadrupole moment (μ/Q_T). The suggestion that the quadrupole moment should be used to describe the dielectric constant of water models was first proposed by Rick [294]. For the three TIP4P like models the ratio of the dipole to the quadrupole moment is almost identical and very close to 1.0 $^{-1}$. For the SPC/E the ratio of the dipole to quadrupole moment is of about 1.155 $^{-1}$, and for the TIP5P this ratio is of about 1.46 $^{-1}$ [324]. This suggestion is consistent with the work of Steinhauser *et al.* [293] where it was clearly shown that the value of G for liquid water was practically identical for SPC and SPC/E (two models with different dipole moment but with the

same value for the ratio μ/Q) and quite different for SPC and TIP3P (which present almost the same dipole moment but a different value of the ratio of the dipole to quadrupole moment).

In previous work we have found that the phase diagram of water is quite sensitive to the ratio of the dipole to the quadrupole moment [205, 206, 324]. When this ratio is high (as in SPC/E, TIP3P and TIP5P) one obtains phase diagrams that are not qualitatively correct (with ice II being the stable phase at room pressure and with ices III and V disappearing from the phase diagram). Models with the negative charge located at the H-O-H bisector (as TIP4P or TIP4P/2005) have a dipole/quadrupole ratio of about one and yield qualitatively correct phase diagram predictions. Thus we conclude that both phase diagram predictions, and the values of G, are quite sensitive to the ratio of dipolar to quadrupolar forces. It seems that the different orientational dependence of the potential interactions at long distances between different water models dramatically affects these two properties. In fact the value of G can be rewritten as:

$$G =< \sum_{i=1}^{i=N} \sum_{j=1}^{j=N} (\mathbf{u_i}.\mathbf{u_j}) > /N = 1 + < \sum_{j=2}^{j=N} \mathbf{u_1}.\mathbf{u_j} > \tag{9.14}$$

and thus it is now more clear why G contains information about the orientational dependence of the water interactions.

Let us now focus on the prediction of the Pauling model for the rest of the ices. It is clear that in the particular case of the TIP4P/2005 the Pauling model predictions for ices III, V, VI and VII agree reasonably well with those obtained from the simulations of the model. The largest difference between the Pauling model and the results of TIP4P/2005 are for ice Ih, be the difference is about 15 per cent. In summary, in general the Pauling model can not be used to estimate the value of G for water rigid non-polarizable models. However, it can predict the value of G for TIP4P models with an error below fifteen per cent. Interestingly the Pauling model seems to work better for TIP4P geometries than for SPC/E or TIP5P charge distributions.

What is the experimental value of G? G can not be obtained from experiments since the experimental value of the dipole moment in condensed phases can not be measured. By using DFT and classical molecular dynamics Car *et al.* [56] determined that the average value of the modulus of the dipole moment was 3.09 D for water and 3.32D for ice Ih when using the MLWF criterion to distribute the electronic charge [54]. These values are in line with some other estimates [57, 300–302]. Using the experimental value of the dielectric constant of ice at 273K, i.e 95, one obtains $G = 2.55$, in rather good agreement with the value obtained here for the TIP4P models.

With the Pauling model one assumes that all configurations satisfying the Bernal Fowler rules have the same statical weight. However, the idea that this assumption is not strictly true has been in the air since 1952 [325–327]. To gain further understanding about the typical differences in energy between different proton disordered configurations, we performed MD simulations for about 0.2 ns of 2000 different proton disordered configurations obtained with the algorithm of by Buch *et al.* [86]. The simulations were performed using Gromacs [328], and Ewald sums (using PME to accelerate the calculations [239]), with a cutoff of 8.5 Å for both the LJ part of the potential and for the real part of the Ewald sum. We did not introduce Rick and Haymet Monte Carlo moves during the MD runs, so that in the MD simulations the molecules just vibrate around the equilibrium position without changing the proton configuration. The average potential energies obtained in the MD runs are presented in Figs. 9.2 for ices Ih and III. The energies are shown as a function of the component y of the total dipole moment (M_y). As it can be seen the energies of different proton disordered configurations are quite

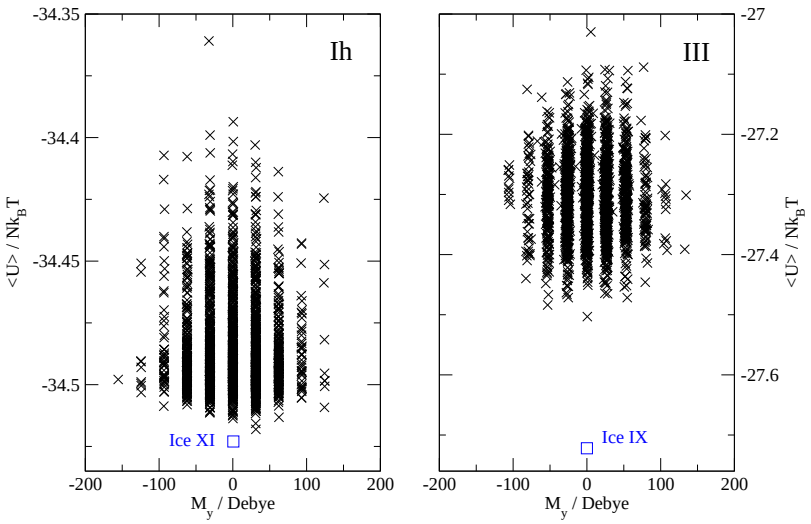

Figura 9.2: Average configuration internal energy (as obtained from MD runs) versus component y of the total dipole moment (M_y) for ice Ih (left) and ice III (right). The results of 2000 different proton disordered configurations satisfying the Bernal Fowler rules are presented. No loop moves were used so that the plotted energies are the average energy of a certain proton disordered configuration. Results for ice Ih were obtained at 200K , 1bar. Results for ice III were obtained at 243K, 2800 bar. The results were obtained using the TIP4P/2005 model. Open squares represents the average configurational energies of the proton ordered phases of the ices I_h and III, ices XI and IX respectively. The proton ordered phase XI corresponds to the antiferroelectric one [91] which is the ground state of this model.

similar but certainly not identical. The distribution of energies seems to be broader for ice III when compared to ices Ih. Differences in internal energies between different proton disordered configurations are of about 0.10NkT for ice Ih and of about 0.30NkT for ice III. Obviously these differences in energy are important for those properties that change significantly from one proton disordered configuration to another as for instance the polarization of the system thus being relevant to understand the value of the dielectric constant of the system. However these differences in energy are not so relevant for those properties that are rather similar in the different proton disordered configurations (as for instance the radial distribution function). In fact in Fig. 9.3 the radial distributions (O-O, H-H and O-H) obtained from a NpT run of a single proton disordered configuration is compared to that obtained from an NpT simulation including loop moves (thus sampling the proton disorder). As it can be seen they are quite similar proving that radial distribution functions of ices can be estimated reasonably well from just a proton disordered configuration.

The dielectric constant of ice: experiment versus water models

In Table 9.2 the dielectric constant for ice Ih obtained in this work and the value of G are compared to that obtained by other authors. There are very few calculations of the dielectric constant of ices for common water models. For ice Ih there are only the results of Rick and Haymet [154, 233, 294] and those of Wang *et al.* [132]. For other ices, the only available results are those of Rick for argon and hydrogen sII clathrate hydrates [329], and those of

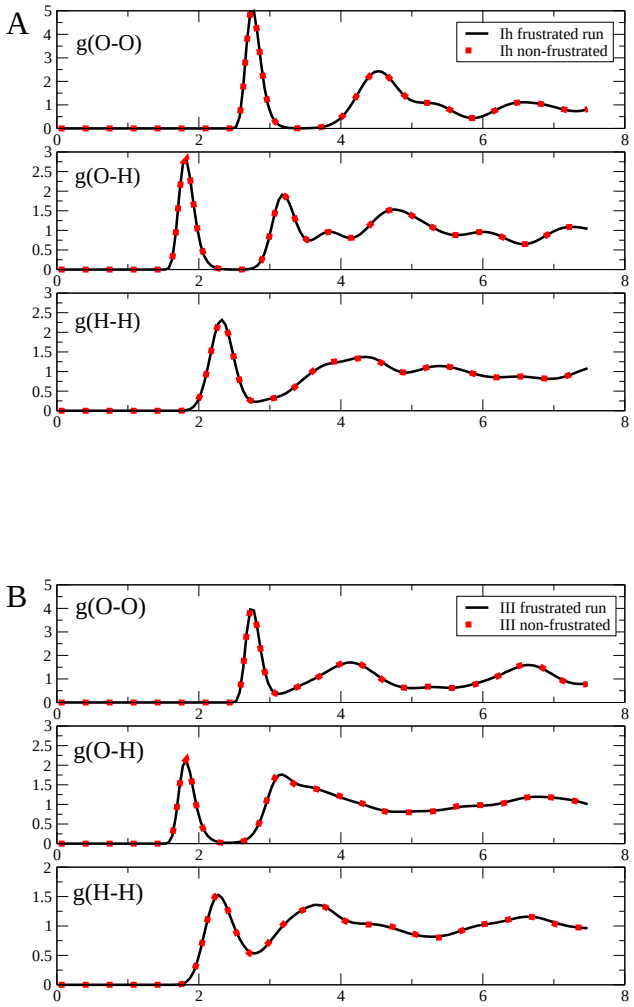

Figura 9.3: A) Radial distribution functions (O-O, H-H, O-H) of ice I_h at 1 bar and 243 K as obtained from MC runs including loop moves (red symbols) and from simulations of a single proton disordered configuration (black solid line). B) Radial distribution functions (O-O, H-H, O-H) of ice III at 2800 bar and 243 K as obtained from MC runs including loop moves (red symbols) and from simulations of a single proton disordered configuration (black solid line)

MacDowell and Vega for ice V [156]. The results of this work are in agreement with those of other authors (i.e they agree within their respective error bars) and that gives us confidence about the methodology used in this work .

In Fig. 9.4 the probability distribution of $p(M_y)$ is shown. The peaks appears for multiples of the total dipole moment of a percolating loop (see the discussion of Rick where it is seen that jumps in M occurs in multiples of the percolating loop [294]). As can be seen, configurations with zero dipole moment have the highest probability.

In Table 9.3 the dielectric constants of ice Ih for TIP4P/2005, SPC/E and TIP5P at 243K and for liquid water at 298K are presented, along with the experimental results. It is obvious that all models fail in describing the dielectric constant of ice Ih, the deviation from experiment

Tabla 9.2: Dielectric constants at room pressure of ice Ih as obtained in this work and in previous work. Notice that for TIP4P and SPC/E Wang and Rick used the experimental value of the density of ice at room T and p (0.92 g cm^{-3}) to obtain G whereas we used the density of the model at room pressure and at the considered T.

Model	Author	T / K	ρ	ϵ	G
TIP4P	Rick, Haymet (2003)	240	0.920	48(1)	2.54(5)
TIP4P	MacDowell, Vega (2010)	240	0.940	47(1)	2.44
TIP4P	Wang (2008)	240	0.920	51(1)	2.7
TIP4P/2005	MacDowell, Vega (2010)	240	0.922	53	2.5
TIP4P/2005	This work	243	0.922	53(2)	2.54(5)
TIP4P/Ice	MacDowell, Vega (2010)	240	0.910	57	2.6
TIP5P	Rick (2005)	240	0.976	30(3)	1.34
TIP5P	This work	243	0.979	31	1.40
Experiment	Whalley (1981)	240		107	
SPC/E	MacDowell, Vega (2010)	200	0.950	49	1.80
SPC/E	Rick, Haymet (2003)	200	0.920	50	1.90
Experiment	Whalley (1981)	200		130	

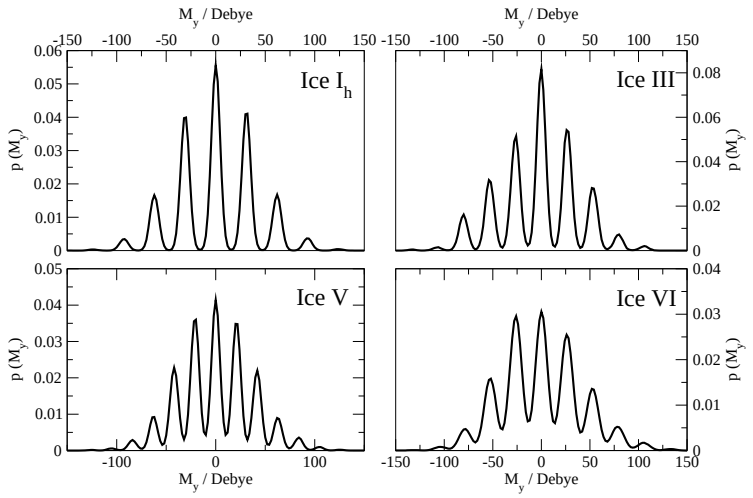

Figura 9.4: Probability distribution of the component y of the total dipole moment (M_y) for ices Ih, III, V and VI obtained from MC runs of the TIP4P/2005 at 243K including loop moves. For each ice the considered pressure is that reported in Table 9.4.

increasing in the order TIP4P/2005, SPC/E, TIP5P. For water the situation is quite different. The model TIP5P overestimates the dielectric constant by about ten per cent. The model SPC/E underestimates the dielectric constant by ten per cent. The model TIP4P/2005 underestimates the dielectric constant by about 25 per cent. In the fluid phase the values of G are larger than those of ice Ih. Large values of G for the fluid phase are not so unusual for water models. For instance Steinhauser *et al.* [293] reported a value of G at room T and p higher than five for the TIP3P model.

Tabla 9.3: Dielectric constants at room pressure for water [34, 35, 71] at 298K and for ice Ih at 243K for several water models. The effective dipole moments $\mu_{efective}$ needed to reproduce the experimental values (assuming that the value of G is constant) of the dielectric constant (78.4 for water at 298K and 107.2 for ice Ih at 243K) are also reported.

Model	Phase	T/K	ρ	ϵ	G	$\mu^{effective}$
TIP4P/2005	Water	298	0.998	59	3.27	2.66
TIP4P/2005	Ih	243	0.922	53	2.54	3.32
TIP5P	Water	298	0.983	91	5.13	2.12
TIP5P	Ih	243	0.979	31	1.40	4.31
SPC/E	Water	298	0.998	70	3.68	2.49
SPC/E	Ih	243	0.946	39	1.74	3.93
Experiment	Water	298	0.998	78.2	-	-
Experiment	Ih	243	0.917	107	-	-

In Fig. 9.5 the experimental dielectric constants of ice Ih and water are presented. Interestingly the experimental curve of the dielectric constants of ice Ih seems to be a continuation of that obtained for liquid water. This suggests the existence of strong tetrahedral ordering in liquid water at the melting point. In fact, these models predict highly tetrahedral ordering of liquid water near the melting point [147]. However, for TIP5P the dielectric constant drops by a factor of three when going from the liquid to the solid phase, in clear disagreement with the experimental results. The results for the SPC/E model are presented in Fig. 9.6. Again, for the SPC/E the dielectric constant drops by a factor of two when going from the liquid phase to ice Ih. In Fig. 9.5 and Fig. 9.6 the results obtained using the TIP4P/2005 model have been included. For this model the dielectric constants of ice Ih and water at the melting point are quite similar (although in this case the value found for the solid phase is somewhat smaller). Obviously all water models (SPC/E, TIP5P, TIP4P/2005) are only approximations to the true interaction between water molecules. What is the origin of the enormous difference between the trends in the experimental values of the dielectric constant and those found for the models? In Table 9.3, we have included in the last column the value of the dipole moment that will bring the predictions of the model in agreement with the experimental values. We are implicitly assuming that the value of G is not affected by the increase of charge required to increase the magnitude of the dipole while keeping the charge distribution. In a previous work Abascal and Vega have shown that for a certain water model the value of the ratio μ/Q [206, 324] is not modified when increasing the magnitude of the charges without changing its location. If the hypotheses that G depends mainly on μ/Q is true, then the value of G of a certain water model would not change significantly when increasing the magnitude of the charges while keeping the charge distribution. In fact the dipole moment increase from TIP4P to TIP4P/2005 to TIP4P/Ice without affecting the value of G (notice that for these three models the charge distribution is practically identical). We have further tested this assumption by evaluating the value of G for ice Ih (at 243K and 1bar) for a TIP4P like toy model, having the following parameters $\mu = 3.32D$, $q_H/e = 0.8014$, $\sigma = 3.2123$ Å , $\epsilon/k = 207.73K$ and $d_{OM} = 0.1546$ Å (this choice of parameters provides a reasonable prediction for the density of ice Ih) [330]. We found that even for this TIP4P toy model (with a very high dipole moment) the value of G was 2.59 , in good agreement with the value found for the TIP4P/Ice (2.53) and TIP4P/2005 (2.54) models at the same thermodynamic conditions. Also for liquid water Steinhauser *et al.* [293], found that the value of G for the SPC and SPC/E models [293] (two models differing in the dipole but having the same value for μ/Q) was practically identical. In fact we have

also found that for ice Ih, the value of G was practically identical for SPC and SPC/E. Thus it seems reasonable to assume that the value of G is affected mostly by the way the charges are distributed but not by their magnitude.

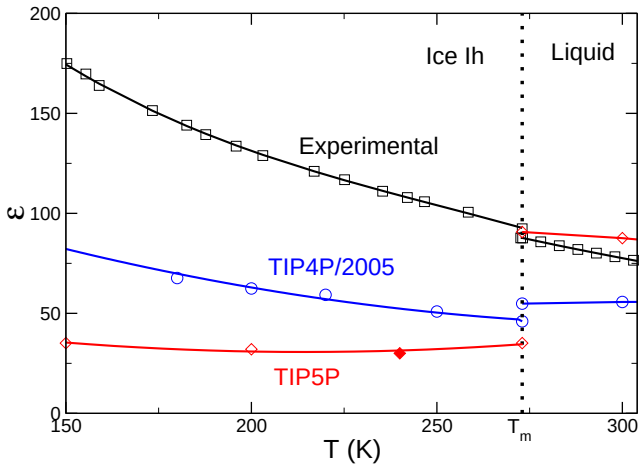

Figura 9.5: Dielectric constant of ice I_h and water for TIP4P/2005 (circles and blue solid lines) and TIP5P (diamonds and black solid lines) compared to the experimental values (squares and black solid lines). The asterisk represents the dielectric constant of the TIP5P model at 240K calculated by Rick [294].

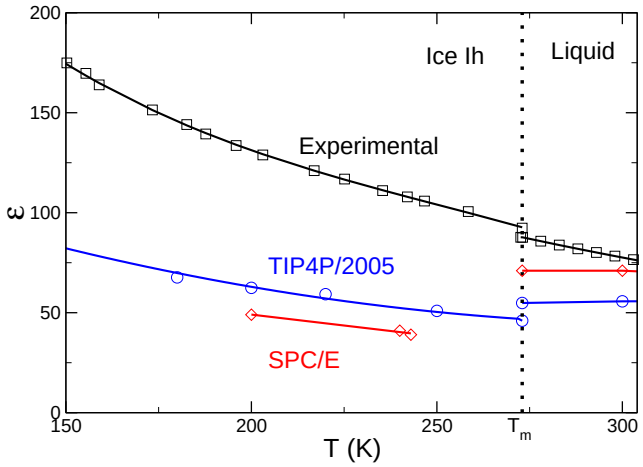

Figura 9.6: Dielectric constant of ice I_h and water for TIP4P/2005 (circles and blue solid lines) and SPC/E (diamonds and red solid lines) compared to the experimental values (squares and black solid lines).

The results of Table 9.3 are surprising. To bring the results of TIP5P in agreement with experiment then the dipole moment in the liquid phase should be of 2.12 D and that of ice Ih of 4.31 D. It is difficult to accept that the dipole moment multiplies by a factor of 2 when going from water to ice Ih. Also it is difficult to accept that the dipole moment of the molecule

in the liquid phase is smaller than that obtained in a cluster of 6 water molecules [331]. Thus it is likely that the TIP5P model provides incorrect estimates of G, the reason being that it incorrectly predicts the orientational dependence of the water interactions. In fact Steinhauser nicely illustrated how the function G(r) (i.e. the value of G obtained including correlations between molecules up to a distance of r) can be related to orientational correlation functions [293]. Atom-atom correlation functions are well described by TIP5P but these functions are just projections of the pair correlation function. The results for SPC/E are more reasonable, but still predicting a dipole moment in ice Ih about forty per cent higher than in the fluid phase. In the case of TIP4P/2005 it predicts that the dipole moment in the solid phase is about twenty per cent higher than in water. Although there is no unique way of determining the molecular dipole moment from first principle calculations (nor experimentally) it seems reasonable to assume that first principle calculations can provide reasonable hints about the ratio of the dipole moment in ice Ih and in liquid water provided that the same criterium is used in both phases to distribute the electronic charge density among the molecules. Values of the dipole moment reported for ice Ih span the range 3.1 - 3.3 D. Values of the dipole moment for liquid water span the range 2.6 - 2.9 D. For instance the AMOEBA model [332] (which yields a good value of the dielectric constant for liquid water) predicts 2.78 D for the liquid and 3.10 D for ice Ih. Using these numbers the ratio of dipole moment of the water molecule in ice Ih and water should be of about 1.1-1.3. The TIP5P model would require a ratio of about 2, the SPC/E requires a ratio of about 1.6 and the TIP4P/2005 would require a ratio of about 1.25. These findings suggest that TIP4P/2005 provides reasonable values of G, and fails in describing the dielectric constant of liquid water because it has a dipole moment of 2.3 D (instead of a value of about 2.9 D that would be more appropriate for liquid water and a value of 3.3 D that would be more appropriate for ice Ih).

To reproduce the energy of water (including nuclear quantum effects effectively through the values of the parameters of the potential), point charge models require a dipole moment of 2.3 D. In fact for about 30 years all rigid non polarizable models designed for water end up with a dipole moment around this value. However, when performing a first principle calculations, the energy of water is reproduced (when including nuclear quantum effects) using a much higher dipole moment. Why is this so? When performing first principle calculations the interaction between water molecules is obtained by solving the Schrodinger equation, whereas it is obtained via an empirical expression when using simple water models. There is no reason to assume that single molecule properties should be identical, when different expressions are used to reproduce the vaporization enthalpy of water which provides an idea of the strength of the intermolecular forces. Although it is gratifying to see how many properties can be reproduce by using a rigid non polarizable model, such simplistic description is not enough to describe either the properties of the gas phase (including small clusters) or the dielectric constants in condensed phases.

In summary, it is unlikely that a non-polarizable model can describe the dielectric constant of the condensed phases of water (one can be successful for one phase, but one will fail dramatically for the other phases). However, at least the results of TIP4P/2005 allow a simple explanation and allow to rationalize the obtained results. The structure predictions are good (i.e good G values) but the dipole moment used is wrong.

It may seem that we are taking our conclusions based only on the results for ice Ih and water too far. Whalley determined the dielectric constant also for ices III, V , VI and VII [153, 251, 261, 295–297]. Therefore, it is possible to test these ideas to other solid phases. In Table 9.4 the dielectric constant for ices Ih, III, V and VI for TIP4P/2005 and TIP4P/Ice, and the sI y sII clathrate structures for TIP4P/Ice are presented. In agreement with our previous

Tabla 9.4: Dielectric constants and G factor for the different ice phases for the TIP4P/2005, TIP4P/Ice, SPC/E y TIP5P models. The experimental values are taken from Ref. [153] (ice I_h), Ref. [261] (ice III), Ref. [295] (ice V), Ref. [297] (ice VI) and Ref. [251] (ice VII). The column labeled as AC gives the probability of acceptance of a trial loop move.

Model	Phase	p / bar	T / K	ρ / g cm^{-3}	U / kcal mol^{-1}	ϵ	G	AC
TIP4P/2005	Liquid	1	298	0.997	-11.43	59	3.27	-
TIP4P/2005	I_h	1	243	0.922	-13.41	53(2)	2.54	0.058
TIP4P/2005	I_c	1	243	0.924	-13.42	53(2)	2.54	0.050
TIP4P/2005	III	2800	243	1.168	-13.33	60(8)	2.28	0.013
TIP4P/2005	III	2800	220	1.175	-13.51	70(6)	2.40	0.011
TIP4P/2005	V	5300	243	1.268	-13.13	77(12)	2.70	0.005
TIP4P/2005	V	5300	180	1.288	-13.60	105(15)	2.69	0.002
TIP4P/2005	VI	11000	243	1.374	-12.99	88(8)	2.85	0.004
TIP4P/2005	VII	70000	243	1.721	-10.90	113(4)	2.94	0.021
SPC/E	I_h	1	243	0.946	-13.02	39(3)	1.74	0.018
SPC/E	III	2800	243	1.193	-13.11	35(11)	1.24	0.002
SPC/E	VI	11000	243	1.396	-12.45	71(35)	2.17	0.004
TIP4P/Ice	Liquid	1.	298	0.993	-11.25	65	3.20	-
TIP4P/Ice	I_h	1	243	0.910	-14.84	57(2)	2.53	0.056
TIP4P/Ice	III	2800	243	1.155	-14.78	75(6)	2.60	0.012
TIP4P/Ice	V	5300	243	1.253	-14.56	76(11)	2.45	0.004
TIP4P/Ice	VI	11000	243	1.355	-14.41	86(17)	2.57	0.003
TIP4P/Ice	sI	1000	243	0.809	-14.58	45(1)	2.46	0.073
TIP4P/Ice	sII	1000	243	0.798	-14.61	43(1)	2.38	0.064
TIP5P	Liquid	1	298	0.983	-9.69	91	5.15	-
TIP5P	I_h	1	243	0.979	-12.41	31(2)	1.40	0.010
TIP5P	I_h	1	200	0.993	-12.79	35(4)	1.29	0.014
TIP5P(Rick data)	I_h	1	240	0.976	-	30(3)	1.34	-
Experimental	Liquid	1	298	0.996	-	78	-	-
Experimental	I_h	0	243	0.917	-	107	-	-
Experimental	III	2300	243	1.155	-	120	-	-
Experimental	V	5000	243	1.258	-	144	-	-
Experimental	VI	11000	243	1.350	-	176	-	-
Experimental	VII	23300	200	1.66	-	127	-	-

discussion the value of G obtained for these two TIP4P like models are quite similar. Experimental results of the dielectric constant have also been included. The average value of the total dipole moment $< \mathbf{M} >$ (in Debye) along the run should be zero if the run is sufficiently long. In most of the cases the average of the dipole moment is smaller than the dipole moment of one or two water molecules. The acceptance probability p of the Rick and Haymet moves is also reported. To obtain the number of successful Rick and Haymet moves one should multiply the length of the runs (8 000 000 cycles) by the number of successfully trial attempts to change the proton disordered configuration (N x (10/100) x AC) where AC is the probability of accepting the trial move which is typically of about 0.003. Thus our runs were able to sample about 600 000 proton disordered configurations. We found that this was sufficient to obtain reliable dielectric constants. More evidence of that is obtained from the plots of the probability distribution of $p(M_y)$ presented in Fig. 9.4. They are symmetric with respect to $M_y = 0$ which is an indirect indication that we are sampling with the same probability configurations with positive and negative values of the polarization along the y axis.

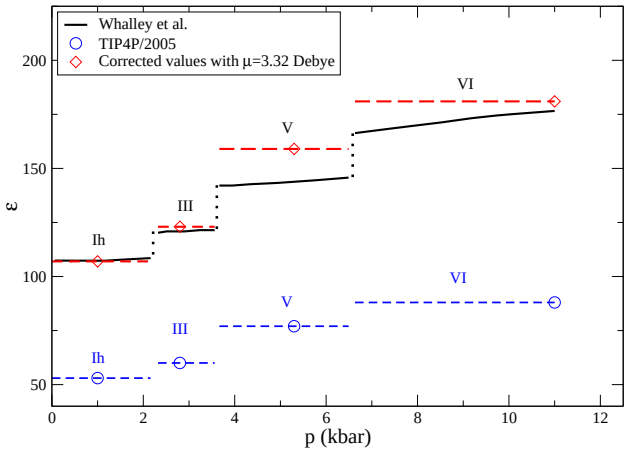

Figura 9.7: Dependence on pressure of the dielectric constant for ices Ih, III, V y VI at 243 K. Dielectric constant obtained for the TIP4P/2005 model (circles and dashed line) compared to the experimental values (black solid lines). Corrected values of the dielectric constant for the TIP4P/2005 with a dipole moment of 3.32 Debye (diamonds and red dashed line).

A comparison of the dielectric constants obtained from experiment and from the simulations of the TIP4P/2005 model is shown in Fig. 9.7. As it can be seen the TIP4P/2005 does not describe the dielectric constant of ices III, V and VI (this is not surprising since it already failed for ice Ih). We know from previous work that the density predictions of TIP4P/2005 for ices and hydrates are quite good [34, 333]. Let us now assume that the model yields reasonable predictions for G and that to compare to experiment one should rescale the molecular dipole moment to a more reasonable value , i.e. 3.32 D. For the time being we shall assume that the dipole moment of water in ices III, V and VI is similar to that of of ice Ih (although not fully correct this appears at least as a reasonable approximation [334]). By scaling the dielectric constant by this dipole moment the corrected values of the dielectric constants for ices Ih, III, V and VI are 107, 123, 159, 181 to be compared with the experimental values of 107, 120, 144, 176. This scaling is also shown in Fig. 9.7. To show that the scaling also provides a way to rationalize the dielectric constant at room pressure in Fig. 9.8 we plot the values of

the dielectric constant of water and ice Ih as a function of temperature at this pressure. The TIP4P/2005 does not match the experimental values of the dielectric constant. However, rescaling the dielectric constants of the TIP4P/2005 using a dipole moment of 3.32 D for ice Ih, and a dipole moment of 2.66 D for water the predictions are in much better agreement with experiment. In summary by using the values of G predicted by TIP4P/2005, and rescaling the value of the dipole moment to a value closer to the value obtained from first principle calculations it is possible for the first time to yield a qualitatively correct description of the dielectric constant of the condensed phases of water.

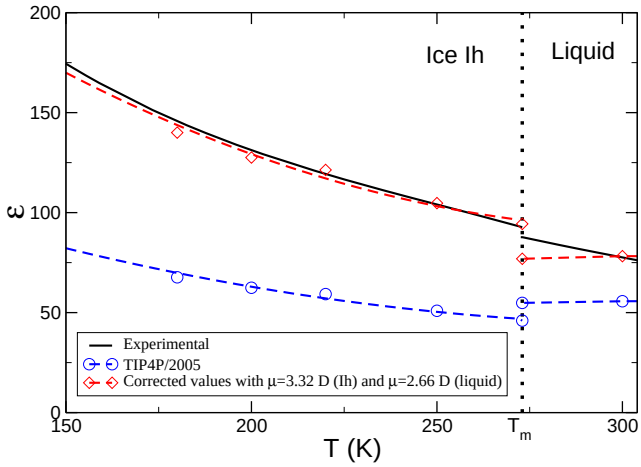

Figura 9.8: Dependence on temperature of the dielectric constant of ice Ih and liquid water. Dielectric constant obtained for the TIP4P/2005 model (circles and dashed line) compared to the experimental values (black solid lines). Corrected values of the dielectric constant for the TIP4P/2005 with a dipole moment of 3.32 D for ice Ih and 2.66 D for the fluid phase (diamonds and red dashed line).

The anisotropy of the dielectric constant

The dielectric constant is a tensor and contains information about the dependence of the response function of the system (polarization which is just the total dipole moment per volume unit) with respect to the electric field. In fact one can write:

$$\mathbf{P} = \epsilon_0(\epsilon - \mathbf{I})\mathbf{E} \tag{9.15}$$

where $\mathbf{P}, \mathbf{E}$ are vectors denoting the polarization of the system and the total electric field acting on the solid (formed by the external electric field and the internal electric field due to the polarization of the sample) and ϵ, $\mathbf{I}$ are the dielectric constant tensor and the identity matrix respectively. In this work we have computed the dielectric tensor for several solid phases. The laboratory frame chosen to compute the dielectric tensor was described in the methodology section. The dielectric tensor was computed along the Monte Carlo runs that included loop moves. We present the results for the TIP4P/2005 model in Table 9.5. For cubic ices (Ic,VII) the three principal values of the dielectric constant are identical (within the error bar) as it should be for a cubic crystal. For ice Ih, the hexagonal symmetry requires two identical components along the X,Y axes and allows a different one along the Z axis. It can be seen that the anisotropy of the dielectric constant of ice Ih (as given by the difference between the Z and the X,Y components) is, at least for the TIP4P/2005 very small. This is in agreement with the

results of Rick for ice Ih using other water models. For the tetragonal crystals (III, VI) the two components X,Y should be identical and different from the component along the Z axis. For ice III this is clearly the case. The components along the X,Y are identical to within the error bar, and clearly different from the component Z. The anisotropy of the dielectric constant in ice III is large and the dielectric constant along the Z axis is less than one third of that along the X,Y axes. For ice VI, the anisotropy is similar to ice III. The components X,Y are equal (within the large error bar obtained in this case) and seems to be larger than the Z component. The results seem to indicate that the dielectric constant along the Z axis is about half of that found along the X,Y axis. For ice V (monoclinic) the XX, YY, ZZ can be different. Notice also that the choice of laboratory frame chosen in this work for ice V has a non-zero XZ component. For ice V it is found that the X,Y components are rather similar. However the value of the dielectric constant along the Z component is roughly half of the value along the Y component. From the results of this work it is suggested that the dielectric constant along the Z axis is significantly smaller (roughly speaking half) than the value of the dielectric constant along the X,Y axis. This has important consequences as it suggest that the energy of ices III, V and VI in the presence of an external electric field would depend significantly on the orientation of the electric field with respect to the crystal (and probable the phase transitions [335]). In fact the energy of a crystal in an electric field **E** is given by the expression [96]:

$$U_{electric} = \frac{\epsilon_0 V}{2}(\epsilon \mathbf{E}).\mathbf{E} = \frac{\epsilon_0 \mathbf{V}}{\mathbf{2}} \sum_{\mathbf{i}} \sum_{\mathbf{j}} \epsilon_{\mathbf{ij}} \mathbf{E_j} \mathbf{E_i} \tag{9.16}$$

It is clear that the energy of a crystal in an electric field will adopt the smallest value when the crystal is aligned to the field along the axis with the smallest value of the principal dielectric constant. It would be quite interesting to determine experimentally the anisotropy of the dielectric constant of ices III, V and VI. To the best of our knowledge nothing has been done in this area. For ice Ih there are some experimental results on the anisotropy of the dielectric constant. However they are contradictory as certain measurements suggest strong anisotropy whereas others suggest small anisotropy [58]. Our results clearly support the presence of small anisotropy for ice Ih.

Finally we have evaluated the anisotropy of the dielectric constant using the Pauling model. The Pauling model allows one to compute the generalized polarization tensor $G_{\alpha\beta}$ which does not depend on temperature. With the choice used in this work to locate the orientation of the molecules within the crystal it does not depend either on the considered water model. The dependence of the dielectric tensor with the water model comes simply from the value of the dipole moment of the model. We have computed the $G_{\alpha\beta}$ tensor using the Pauling model. The obtained dielectric tensor predicted by the Pauling model for the TIP4P/2005 model is shown in Table 9.5. As it can be seen the Pauling model describes reasonably well the average dielectric constants (i.e. the average of the trace) for ices III, V, VI and VII. As previously discussed, the largest difference is found for ices Ih, Ic (although the predictions are still reasonable). Concerning the predictions for the anisotropy it is clear that the Pauling model already predicts a lower value of the dielectric constant along the Z axis for ices III and VI ant to a less extent for ice V. However the predicted anisotropy is smaller than that found in the simulations. We conclude that the Pauling model provides hints about the trends that can be found in the anisotropy of the dielectric constant, but underestimate the anisotropy of the dielectric tensor.

Occupation analysis of the partial proton ordered phases

It is well known from experimental work that ices III and V present partial proton disorder [87, 336–338] and that affects the value of the estimated configurational entropy of those ices

Tabla 9.5: Dielectric tensor of proton disorder phases of ice at 243 K as obtained by computer simulations (including loop moves to sample proton disorder) and using the TIP4P/2005 model. For each ice the pressure was the same as that presented in Table 9.4. For ices Ih, Ic, III, VI and VII the laboratory frame was chosen so that the dielectric tensor is diagonal and for this reason the xz component is zero. For ice V the laboratory frame was chosen so that X,Y, go along the direction of the vectors **a** and **b** of the unit cell and Z was chosen along the direction perpendicular to the **a,b** plane. For this reason the dielectric tensor is not diagonal and there is a non-zero XZ component. We have also included the predictions of the Pauling model for TIP4P/2005. In the Pauling model, the dielectric tensor does not depend on temperature.

Phase	G	ϵ	ϵ_{xx}	ϵ_{yy}	ϵ_{zz}	ϵ_{xz}
TIP4P/2005						
I_h	2.54(5)	53(2)	53(2)	53(2)	53(2)	0
I_c	2.54(5)	53(2)	53(2)	53(2)	53(2)	0
III	2.28(37)	60(8)	80(15)	84(11)	15(5)	0
V	2.70(43)	77(12)	81(22)	97(12)	53(11)	-5(7)
VI	2.85(26)	88(8)	102(40)	115(36)	41(10)	0
VII	2.94(10)	113(4)	111(7)	111(9)	117(5)	0
Pauling Model						
I_h	3.02(4)	63	64	63	63	0
I_c	3.01(4)	63	63	62	63	0
III	2.49(3)	65	71	71	54	0
V	2.50(4)	71	71	76	61	-7
VI	2.89(3)	93	100	99	80	0
VII	3.01(5)	126	124	128	125	0

Tabla 9.6: Fractional occupancy for the hydrogen atoms of ice III and V for the TIP4P/2005 model as obtained from the MC runs of this work when including loop moves. For ice III there are only two types of hydrogen positions labeled as α and β (see Ref.[88] for details about these two kinds of hydrogen positions). An occupancy of 50 % represents full disorder whereas an occupancy of 0 % or 100 % represents full order. For ice V there are four types of hydrogen positions labeled as α, β, γ and δ (see Ref.[88] for details about these four kinds of hydrogen positions). The experimental values are taken from Ref. [87].

Phase	p / bar	T / K	α / %	β / %	γ / %	δ / %
III	2800	243	50.8(3)	25.6(2)	-	-
III	2800	220	50.9(3)	23.2(3)	-	-
III Exp.	2500	240	35(2)	52(4)	-	-
V	5300	243	53(1)	46(1)	55(1)	55(1)
V	5300	180	58(2)	44(2)	55(1)	55(2)
V Exp.	5000	237	43.5(1.5)	29.9(1.6)	50.2(1.2)	76.4 (1.9)

[88]. Proton ordering has also been found of the surface of ice Ih [339, 340]. The simulations of this work which include loop moves allow to analyze the possible existence of partial proton ordering for these ices. In fact one can obtain the populations of the different type of hydrogen positions along the runs. Results for the hydrogen site occupancies for ices III and V obtained from simulations of the TIP4P/2005 model are presented in Table 9.6. The calculated populations are compared to the experimental ones. For ice V the occupancies predicted by the model are close to 50 % (fully disordered). Experimentally for ice V, the populations for hydrogens of type α and γ are close to 50 %, but the populations of type β and δ are clearly different. Notice that the experimental occupancies tend to a value of 50 % as the temperature increases. It is likely that the transition between a proton ordered phase (ice XIII [25]) and a proton disordered phase (ice V) predicted by the TIP4P/2005 occurs at temperatures lower than found experimentally. That was already found for the XI-Ih transition, which occurs at temperatures of about 25K for the model [41, 91, 156], whereas experimentally it occurs at temperature of about 75K. That would explain why for a temperature of about 240K, the model predicts full proton disorder of ice V whereas experimentally there is only partial proton disorder. For ice III, we have found noticeable proton ordering when using the TIP4P/2005 (i.e the occupancies of the different type of hydrogen positions are not of 50 %). In fact in Table 9.6 it can be seen that for TIP4P/2005 the value of α is close to 50 % whereas the value of β is of about 25 % thus indicating partial proton ordering. When comparing the results of the models with those obtained experimentally it is seen that experimentally the value of β is close to 50 % whereas the value of α is of about 35 %. There are two possible explanations for this disagreement between the results of the model and those found experimentally. Either the model fail in describing the experimental trends, or the labeling of α and β used in this work is the opposite to that adopted by Lobban *et al.* [87].

Conclusions

In this work we have computed the dielectric constant of several solid phases of water (ices Ih, III,V and VI) using computer simulations that include moves able to sample the proton disorder. Most of the results were obtained for the TIP4P/2005, although in certain cases results for TIP5P and SPC/E were also obtained. Also the Pauling model was used to estimate

the dielectric constant by generating proton disordered configurations that satisfy the Bernal-Fowler rules and assuming that they have the same probability. Finally we compared the simulation predictions for the dielectric constant to experimental results. The main conclusions of this work are :

- For ices with a perfect tetrahedral coordination the value of G obtained from the Pauling model is 3, whereas for ices that form distorted tetrahedron the value of G decreases slightly to values around 2.6.
- The Pauling model can not be used to estimate the value of the dielectric constant of a certain water model. In fact, for ice Ih, it predicts a value of G of 3, whereas the simulation results for TIP5P and SPC/E yield that the value of G is of 1.4 and 1.9 respectively. However for TIP4P like models the predictions of the Pauling model seem to be closer to those obtained in the simulations.
- Proton disordered configurations satisfying the Bernal-Fowler rules present in general different energies. Thus differences in the value of G between different water models arise from the differences between the successfuly selected configurations.
- Certain thermodynamic properties, for instance radial distribution functions, do not differ much between different configurations satisfying the Bernal Fowler rules. Thus using just an snapshot appears as a reasonable approximation. However, this is not the case of the dielectric constant, since different configurations differ significantly in their respective polarizations.
- For three charge models, it is suggested that the value of the polarization factor G, depends only on the ratio of the dipolar to quadrupolar moment. Therefore we suggest that for three charge models G=G(μ/Q). Increasing the charges for a certain charge geometry modifies the dielectric constant but not the value of G. Thus G, contains information about the orientational dependence of water interactions, and this is in common with phase diagram predictions that were found to be quite sensitive to this ratio.
- Non-polarizable models fail in describing simultaneously the dielectric constant of ice Ih and water. The only models that predicts (in agreement with experiment) a similar dielectric constant for the fluid phase and ice Ih are TIP4P like models. We argue that this model predicts a reasonable value for the ratio of the dipole to quadrupole moment (of about one), whereas other common water models (TIP3P, TIP5P or SPC/E) predict a large value for this ratio.
- When the predictions of the dielectric constants of the TIP4P/2005 are scaled using a dipole moment estimated from first principles, then the model is able to predict qualitatively the dielectric constant of the fluid phase and of the proton disordered ices Ih, III, V and VI.

One concludes that if one wants to describe water by a LJ center and three charges, then the TIP4P geometry provides an overall better description of water. This is somewhat surprising, since the first water model ever, the Bernal Fowler model of water, was indeed a TIP4P like model [8]. The model is able to predict the existence of many ice polymorphs [341]. Interestingly most of the water models developed recently from first principle calculations for small clusters, use a fitting function, in which the negative charge is located at at the H-O-H bisector (as in TIP4P), starting with the pioneering work of Clementi [342], and following with the work of Jordan [343] or Xantheas [344]. Obviously these models also include polarization,

a feature missing in the TIP4P like models. It is likely that the inclusion of polarizability within a TIP4P like geometry [329, 345] will improve the description of the dielectric constant of water in condensed phases.

In summary, common non-polarizable models can not describe the dielectric constant of the condensed phases of water (you can be successful for one phase, but will fail dramatically for the other phases). However, at least the results of TIP4P/2005 allow a simple explanation and a route to rationalize the results. The model yields good estimates of G but the model uses an incorrect value of the dipole moment. It is gratifying to see that by using reasonable values of the dipole moment of water in the fluid and solid phases, the TIP4P/2005 predictions for the dielectric constants are in reasonable agreement with experiment. The inclusion of nuclear quantum effects was crucial to understand the failure of popular water models in reproducing the heat capacity of water [292]. However for the dielectric constant the inclusion of nuclear quantum effects will improve (but not correct) the disagreement between experiment and theory found for TIP4P/2005. In fact, models optimized for path integral simulations have an slightly larger dipole moment than those optimized for classical simulations [44, 290]. For instance q-TIP4P/f has a dipole moment of about 2.35 D , whereas TIP4PQ/2005 has a dipole moment of 2.38D (both values being slightly larger than the value of the TIP4P/2005, namely 2.3D). This increase in the dipole moment would increase slightly the dielectric constant (the value of G is not expected to be modified much by the inclusion of nuclear quantum effects) but will not bring the predictions into agreement to experiment. Thus nuclear quantum effects seems not to be the key to improve the predictions of the dielectric constants obtained by simple non polarizable models. It seems that only including polarization one could describe quantitatively the dielectric constants of water in condensed phases.

Acknowledgments

This work was funded by grants FIS2010-16159 from the DGI (Spain), MODELICO-P2009/-ESP/1691 from the CAM, and 910570 from the UCM. J. L. Aragones would like to thank the MEC by the award of a pre-doctoral grant. We would like to thank J.L.F. Abascal and Carl Mc-Bride for helpful discussions and for a critical reading of the manuscript. One of us (CV) would like to thank to the late Prof. Victoria Buch for very helpful discussions during the Faraday Discussion 141 Conference that took place in Edinburg in August 2008.

CAPÍTULO 10

The phase diagram of water under an applied electric field

J.L. Aragones[1,2], L.G. MacDowell[1], J.I. Siepmann[2] and C. Vega[1]

[1]*Dep. Química Física, Fac. Química, Universidad Complutense de Madrid, 28040,Madrid, Spain*
[2]*Dep. of Chemistry and Chemical Theory Center, University of Minnesota, Minneapolis, Minnesota 55455, USA*

Physical Review Letters, **107***, 155702 (2011)*

Abstract

Simulations are used to investigate by the first time the anisotropy of the dielectric response and the effects of an applied electric field $\mathbf{E}_{\rm ex}$ on the phase diagram of water. In the presence of electric fields ice II disappears from the phase diagram. When $\mathbf{E}_{\rm ex}$ is applied in the direction perpendicular to the ac crystallographic plane the melting temperatures of ices III and V increase whereas that of ice Ih is hardly affected. Ice III also disappears as a stable phase when $\mathbf{E}_{\rm ex}$ is applied in the direction perpendicular to the ab plane. $\mathbf{E}_{\rm ex}$ increases by a small amount the critical temperature and reduces slightly the temperature of the maximum density of liquid water. The presence $\mathbf{E}_{\rm ex}$ modifies all phase transitions of water but its effect on solid-solid and solid-fluid transitions seems to be more important and different depending on the direction of $\mathbf{E}_{\rm ex}$.

Applied electric fields, $\mathbf{E}_{\rm ex}$, modify the properties of all phases of matter but to different extents and, hence, can change the location of phase transitions. The phase diagram of water exhibits a large number of polymorphs. Thus, there is significant interest in exploring the effects of $\mathbf{E}_{\rm ex}$ on the properties of water's condensed phases and on its phase diagram. Attempts have been made to determine whether $\mathbf{E}_{\rm ex}$ affects the melting point of ice Ih [95]. Also, the effects of $\mathbf{E}_{\rm ex}$ on the structural properties of liquid water and on gas-to-particle nucleation rates have been investigated [346, 347], while recently it has been shown that $|\mathbf{E}_{\rm ex}| \leq 0.3$ V/nm leads to relatively small changes for water's vapor–liquid phase envelope [335]. Theoretically it is known that an external field stabilizes phases with high dielectric constant. Since solid phases are generally anisotropic, the relative stabilization will depend on the magnitude and on the orientation of $\mathbf{E}_{\rm ex}$ with respect to the crystal. However, the dielectric constant has been measured only for a limited set of state points for some solid phases of water, either experimentally [295] or from simulation [154, 348] and very little is known as to the anisotropy of its dielectric response [349].

Here, we present a simulation study of the dielectric constant tensor for several solid phases and the effects of $\mathbf{E}_{\rm ex}$ on the phase diagram of water, described by the non-polarizable TIP4P/2005 model [34]. We show that electric fields exhibit a dramatic effect for boundaries

between ordered/disordered phases. Particularly, we find that for $\mathbf{E}_{\rm ex} > 0$, ice II, an ordered phase, is destabilized to the point of completely vanishing from the phase diagram. $\mathbf{E}_{\rm ex}$ applied along the axis of smallest dielectric response further washes out ice III from the phase diagram. It should be recognized that a non-polarizable model with its effective dipole moment $\mu_{\rm eff}$, cannot quantitatively represent the dielectric properties over a wide range of state points. However, we have shown that the dielectric constants of ices can be reproduced reasonably well when the calculated polarization factor, $G_{\rm pol}$, for the TIP4P/2005 model is scaled to account for the difference between the accurate average molecular dipole moment, $\mu_{\rm acc}$, in a given phase and $\mu_{\rm eff}$ of the model [156, 350]. This scaling approach is also used here for the determination of the phase boundaries.

For $|\mathbf{E}_{\rm ex}| > 0$, the dipolar water molecules tend to align with the field direction. For liquid and vapor phases, molecules can re-orient without encountering large barriers, but the situation is different for solid phases. Ices can be divided in to proton-ordered (II, VIII ...) and proton-disordered phases (Ih, III, V, VI ...). Molecular re-orientation is not permitted for proton-ordered phases, whereas the extent of the re-orientation depends on the crystalline structure and thermodynamic state for proton-disordered phases. The relaxation times in proton-disordered structures can be very long (μs) and for this reason it is necessary to bias the simulations (by introducing Monte Carlo moves that sample efficiently the proton re-arrangement) to determine the response of the system under a perturbation such as $\mathbf{E}_{\rm ex}$. We have implemented a rotational loop algorithm [154, 155]. Under the presence of a homogeneous static electric field, **E**, changes in the internal energy U ($K + V_{\rm inter}$) can be written as [351]:

$$\mathrm{d}U = T\,\mathrm{d}S - p\,\mathrm{d}V + \mathbf{E}\,\mathrm{d}\mathbf{M} + \mu\,\mathrm{d}N \tag{10.1}$$

where **M** is the total dipole moment of the system. The value of the electric field **E** is in general different from the applied external field $\mathbf{E}_{\rm ex}$ due to the additional field generated by the polarized surface of the cavity [97] which depends on its geometry and the anisotropy of the dielectric constant [156]. Following Alberty [351] let us define $G_E = G - \mathbf{E}\cdot\mathbf{M}$ and $H_E = H - \mathbf{E}\cdot\mathbf{M}$ that are related through $\partial(G_E/T)/\partial(1/T) = H_E$. Phase transitions at constant $\mathbf{E}_{\rm ex}$, *T* and *p* require that both phases have the same $\mu = G_E/N$. From a microscopic point of view $G_E = -kT\ln(Q')$ with Q':

$$Q' \propto \int \exp(-\beta(V_{\rm inter} + pV - \mathbf{M}\mathbf{E}_{\rm ex} + U_{\rm pol}))d\mathbf{r}^{\mathbf{N}}dV \tag{10.2}$$

When Ewald sums are used (as done in this work) $V_{\rm inter}$ includes the real and reciprocal space contributions to the Coulombic energy of the system. The term $U_{\rm pol}$ is the interaction energy of the system with the polarized surface [97]. Here we shall assume a spherical sample (formed by many simulation boxes) under conducting periodic boundary conditions so that $U_{\rm pol}$ vanishes and **E** and $\mathbf{E}_{\rm ex}$ become identical [97]. Differentiating G_E with respect to $\mathbf{E}_{\rm ex}$ yields $- < \mathbf{M} >$, and its integral allows one to evaluate how G_E changes under the influence of a field as follows

$$G_E(E_{\rm ex}) - G_E(0) = -\int_{E=0}^{E_{\rm ex}} < M_{\parallel} >_{N,p,T,E_{\rm ex}} dE_{\rm ex} \tag{10.3}$$

The integrand of equation (13.4) (i.e., the polarization in the direction of the applied electric field) is easily obtained by performing NpT simulations at different values of $\mathbf{E}_{\rm ex}$, and $G_E(0)$ has been determined by Abascal and Vega for the phase diagram of the TIP4P/2005 water model [34]. Once $G_E(E_{\rm ex})$ has been computed for a specific reference state of each phase, thermodynamic integration in p, T space can be used to locate a point where two phases

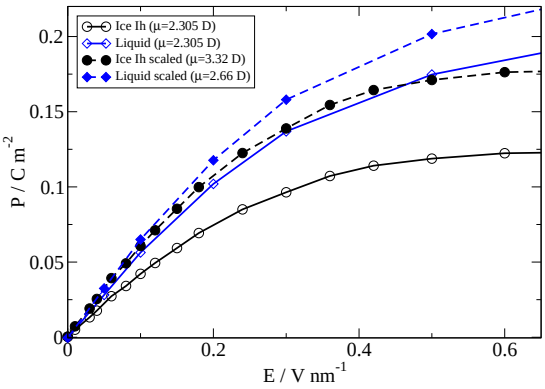

Figura 10.1: (Color online) Polarization (P) as function of $\mathbf{E}$ for the liquid phase (open diamonds and solid line) and the ice Ih phase (open circles and solid line) computed for the TIP4P/2005 model at 250 K and 1 bar. The corresponding values obtained by scaling the magnitude of the molecular dipole moment are indicated by filled symbols and dashed lines. For ice Ih the applied field was on the direction perpendicular to the ac plane and P stands for $P_{\perp ac}$.

coexist. After that Gibbs–Duhem integration [138] is used to trace the coexistence line. Simulation details for the solid-phase simulations (constant-stress ensemble, system size, types of moves) follow those described in our previous work [156, 350].

The polarization response of liquid water and ice Ih to $\mathbf{E}$ is illustrated in Fig. 10.1. For $\mathbf{E} < 0.1$ V/nm, the polarization response is linear for both phases, but the slope is somewhat larger for the liquid phase. For $\mathbf{E} > 0.1$ V/nm, the polarization response is not linear. Let us define the degree of saturation as $S_M = \langle M \rangle / (N\mu_{\rm eff})$. For liquid water values close to unity are obtained for S_M at high $\mathbf{E}$ as the molecules are free to orient their dipoles with the field direction. For ice Ih, however, S_M reaches a limit of ≈ 0.58 at high $\mathbf{E}$ because the geometric constraints of the solid structure of ice Ih prevent complete saturation.

For small $\mathbf{E}$, the polarization of the system $\mathbf{P} = \mathbf{M}/V$ is related to the field strength through the expression $\mathbf{P} = \chi\mathbf{E}$, where χ is the susceptibility tensor given by $\epsilon - \mathbf{I}$ with ϵ and $\mathbf{I}$ being the dielectric constant tensor and the identity matrix [96]. In computer simulations the dielectric constant tensor can be determined either by analyzing the fluctuations of the system dipole [154, 156, 294, 350] or through the polarization response of the system [352]. In this work, we have used the the latter method and applied $\mathbf{E}$ in different crystallographic directions to resolve the anisotropy of the dielectric constant tensor. A comparison with literature data (see Table 10.1) shows good agreement between the two computational approaches.

The dielectric constant tensor exhibits significant anisotropy for ices III, V, and VI. The TIP4P/2005 model under predicts the dielectric constants of liquid and solid phases by about 25 %. However, it predicts correctly the polarization factor, $G_{\rm pol} = \langle M^2 \rangle / N\mu^2$, which contains information about the orientational structure of water, and the underestimation of the dielectric constant is due to $\mu_{\rm eff} = 2.305$ D for this model being too small. First principles studies indicate that the average dipole moment of water molecules in the condensed phases is ≈ 2.7 D for liquid water and ≈ 3.3 D for ice Ih [56, 57]. Thus, the TIP4P/2005 model is capable of predicting qualitatively the effects of $\mathbf{E}_{\rm ex}$ on the phase boundaries, but for quantitative predictions a scaling of the dipole moment to an accurate value $\mu_{\rm acc}$ is needed.

For $\mathbf{E}_{\rm ex} > 0$, G_E is lower than for $\mathbf{E}_{\rm ex} = 0$ (see Eq.(13.4)), and the extent of the reduction is proportional to $< M_{\parallel} >$. Therefore, when $\mathbf{E}_{\rm ex} > 0$, the phase with higher ϵ will become more stable (larger reduction in G_E). Since the dielectric constant is a tensor the effect of an electric field will depend on its direction with respect to the crystal. For ice Ih, the three components are about equal, whereas ϵ for the other ice polymorphs is anisotropic (see Table 10.1). To study

Tabla 10.1: Dielectric constants obtained for the TIP4P/2005 model from equilibrium fluctuations [350] (Fluc) at $\mathbf{E}_{\rm ex} = 0$ and from linear response (LR). For ices III and VI the laboratory frame defining x, y and z is chosen in the direction of the unit cell vectors a, b, and c [96]. For ices Ih and II, x and z are located along a and c; y is chosen in the direction perpendicular to the ac plane (ice II was described with an hexagonal unit cell instead of the trigonal one). With this choice of the laboratory frame the susceptibility tensor is diagonal. For ice V, the x and y axes are located along the a and b vectors and z is perpendicular to the ab plane. The subscripts indicate the statistical uncertainty. Using dipole scaling, the ϵ values increase by $(2.66/2.305)^2$ and $(3.32/2.305)^2$ for the liquid and solid phases, respectively.

phase	p	T	ϵ_{xx}		ϵ_{yy}		ϵ_{zz}	
	(bar)	(K)	LR	Fluc	LR	Fluc	LR	Fluc
L	1	250	58_8	56_3	–	–	–	–
Ih	1	243	49_7	53_2	–	53_2	–	53_2
II	3016	180	2_{13}	–	–	–	–	–
III	2800	243	75_{10}	80_{15}	77_9	84_{11}	4_8	15_5
V	5300	180	79_{10}	75_{25}	118_9	161_{37}	56_8	71_{13}
VI	11000	260	83_{10}	–	–	–	42_8	–
VI	11000	243	–	102_{40}	–	115_{36}	–	41_{10}

the effect of $\mathbf{E}_{\rm ex}$ on the phase diagram of water, we have chosen to apply $\mathbf{E}_{\rm ex}$ in the direction perpendicular to the ac plane (i.e $\mathbf{E}_{\rm ex\perp ac}$) for crystalline phases (c.f. caption to Table 10.1 for details) because ϵ_{yy} is larger than the other components, and this field direction allows for the maximum reduction in G_E for a given field strength. We assume that one studies a single crystal with a well defined orientation with respect to the field. For a polycrystalline sample, the orientations of the micro crystals with respect to $\mathbf{E}_{\rm ex}$ would be random, i.e., leading to broadening of the melting temperature.

A comparison of the phase diagrams computed for the TIP4P/2005 water model at $\mathbf{E}_{\rm ex\perp ac} = 0.3$ V/nm with and without dipole scaling and that in the absence of a field is shown in Fig. 10.2. Our choice of field strength is motivated by previous findings indicating that high fields are needed for statistically significant shifts in the phase boundaries [335]. A field strength of 0.3 V/nm significantly exceeds the dielectric breakdown strength of bulk water samples, but is only three times larger than the 0.1 V/nm reached recently in microfluidic channels [353]. For the TIP4P/2005 model the electric field removes ice II from the phase diagram and shifts the melting temperature of ice Ih down by about 10 K to lower temperatures. It is more interesting to analyze the behavior of TIP4P/2005 when using dipole scaling, since then dielectric constants of condensed phases are reproduced reasonably well [350] so that the predictions of the model should be closer to what is expected to occur in the experiment. With the dipole scaling ice II again disappears from the phase diagram, ice V increases significantly its stability range, the melting point of ices III and V increase by about 15 K and the melting point of ice Ih is hardly affected by the field. This last prediction is consistent with experimental results at lower fields [95]. The key to understand these changes is to realize that phases with high dielectric constant increase their stability at the expense of phases with lower dielectric constant. The melting line of ice Ih at $\mathbf{E}_{\rm ex\perp ac} = 0.3$ V/nm closely traces that found without a field. The reason is that the scaled polarization curves are quite similar for liquid water and ice Ih up to this field strength (see Fig.10.1).

The principal effect of $\mathbf{E}_{\rm ex\perp ac}$ is the displacement of the phase boundaries. The slopes of the phase transitions are not much affected by the field. The only exception is the change of

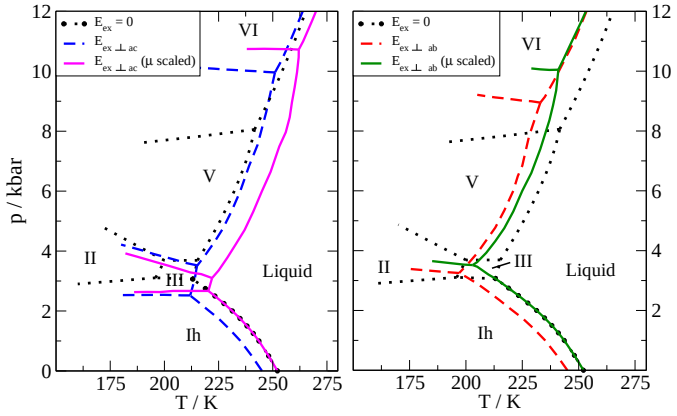

Figura 10.2: (Color online) Phase diagram for the TIP4P/2005 water model. Dotted black, dashed blue, solid magenta, dashed red and solid green lines indicate the phase boundaries for $\mathbf{E}_{\rm ex} = 0$, $\mathbf{E}_{\rm ex\perp ac} = 0.3$ V/nm with $\mu_{\rm eff}$, $\mathbf{E}_{\rm ex\perp ac} = 0.3$ V/nm and dipole scaling using 2.66 and 3.32 D for the liquid and crystalline phases, $\mathbf{E}_{\rm ex\perp ab} = 0.3$ V/nm with $\mu_{\rm eff}$ and $\mathbf{E}_{\rm ex\perp ab} = 0.3$ V/nm and dipole scaling, respectively.

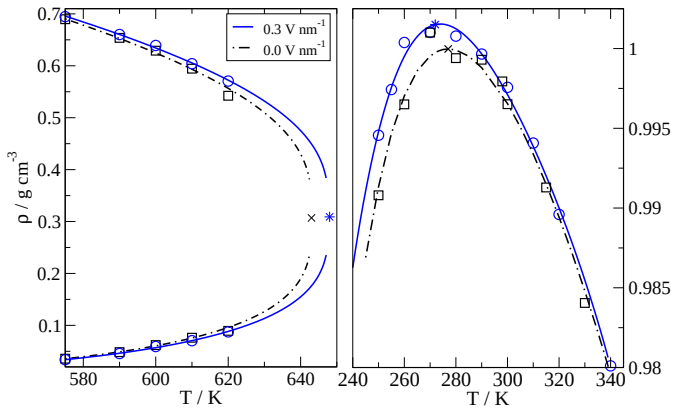

Figura 10.3: (Color online) Vapor–liquid coexistence curve (left) and temperature dependence of the liquid density (right) for the TIP4P/2005 model at $\mathbf{E}_{\rm ex} = 0.3$ V/nm (blue circles and solid lines) and in the absence of a field (black squares and dashed lines). The blue stars and black crosses denote the corresponding critical points and temperatures of maximum density.

slope of the V—VI transition from positive to negative values. This is a consequence of the lower enthalpy of ice V with respect to ice VI in the presence of the field. Another interesting result is obtained when the $\mathbf{E}_{\rm ex}$ is applied perpendicular to the ab plane (Fig. 10.2). Now besides ice II, ice III also disappears from the phase diagram because of its very small value of ϵ_{zz} value.

Let us now focus on the effect of the field on fluid phases. Here, we have also studied the influence of $\mathbf{E}_{\rm ex} = 0.3$ V/nm on the vapor–liquid coexistence curve (VLCC) for the TIP4P/2005 model (without dipole scaling). Gibbs ensemble Monte Carlo [149] simulations were carried out to compute the VLCC, and the simulation and analysis details follow those used previously for the TIP4P model [335]. The VLCC exhibits a small increase in liquid density and small decrease in vapor density in the presence of the field (see Fig. 10.3). The critical temperature is increased from 643 ± 1 to 648 ± 1 K, the critical density is reduced from 0.309 ± 0.004 to 0.307 ± 0.003 g/cm^3, and the normal boiling temperature is increased from 398.5 ± 0.6 to 399.2 ± 0.7 K. The relatively small extent of these shifts agrees well with results for the TIP4P model [335]. One of the fingerprint properties of water is the existence of a density maximum

occurring at $T_{\rm md} = 277$ K (at 1 bar). Here, we find that $T_{\rm md}$ shifts downward to 272 K for $\mathbf{E}_{\rm ex} = 0.3$ V/nm (see Fig.10.3). The preferential alignment of the water molecules with the field direction leads to a slight decrease in the tetrahedral order [335] and an increase in the density especially for $T < 300$ K.

In conclusion, efficient simulation algorithms have been used to investigated the effect of $\mathbf{E}_{\rm ex}$ on the phase behavior of the TIP4P/2005 water model. Dielectric constants obtained from the linear response region are found to be in good agreement with those obtained from fluctuations. The dielectric constants of ices III, V, and VI are highly anisotropic, but this is not the case for ice Ih. With dipole scaling (correcting for the underestimation of μ by the non-polarizable TIP4P/2005 model), the dielectric constants for the condensed phases are in satisfactory agreement with experiment [350]. For anisotropic crystalline phases, the changes in properties depend on the field direction, and we have focused on $\mathbf{E}_{\rm ex\perp ac} = 0.3$ V/nm applied in the direction of the largest diagonal element of the dielectric constant tensor. The main result of this work is the prediction that ice II disappears from the phase diagram, ice V increases significantly its region of stability, the melting temperatures of ices III and V increases by about 15 K and the melting point of ice Ih is hardly affected by $\mathbf{E}_{\rm ex}$. Ice III also disappears when the electric field is applied perpendicular to the ab plane. For fluid phases at $\mathbf{E}_{\rm ex} = 0.3$ V/nm, the vapor–liquid coexistence curve is shifted slightly to higher temperatures ($T_{\rm c}$ increases by 5 K) and $T_{\rm md}$ is shifted downward by the same extent. The structure of cubic ice (Ic) allows for full saturation ($S_M = 1$) [346] and we observe that ice Ic becomes more stable than ice Ih for $\mathbf{E}_{\rm ex} > 0.15$ V/nm at low pressure (withouth dipole scaling) for the TIP4P/2005 model. Thus, a transformation of ice Ih to Ic is not expected at field strength that are experimentally accessible for bulk samples (the dielectric breakdown of bulk water occurs at about 0.01 V/nm [95]). The results of this work support the hypotheses that only very small changes in phase transitions should be expected in the experiments, with the exception of the disappearance of ice II which could indeed be experimentally accesible.

Support from grants FIS2010-16159 and FIS2010-22047-C05-05 (DGI) , P2009/ESP/1691 (CAM) , 910570 (UCM) and CBET-0756641 (NSF) is gratefully acknowledged. J.L.A. would like to thank the MEC for the award of a pre-doctoral grant and for support of an extended visit to Minnesota, EEBB-2011-43743. Part of the computer resources were provided by the Minnesota Supercomputing Institute.

CAPÍTULO 11

Solubility of NaCl in water by molecular simulation revisited

J.L. Aragones[1], **E. Sanz**[1] **and C. Vega**[1]

[1]*Dep. Química Física, Fac. Química, Universidad Complutense de Madrid, 28040,Madrid, Spain*

Journal of Chemical Physics, **Aceptado***, (2012)*

Abstract

In this paper the solubility of NaCl in water is evaluated by using computer simulations for three different force fields. The condition of chemical equilibrium (i.e equal chemical potential of the salt in the solid and in the solution) is obtained at room temperature and pressure to determine the solubility of the salt. We used the same methodology that was described in our previous work (E.Sanz and C.Vega, *J.Chem. Phys.*, **126**, 014507 (2007)) although several modifications were introduced to improve the accuracy of the calculations. It is found that the predictions of the solubility are quite sensitive to the details of the force field used. Certain force fields underestimate the experimental solubility of NaCl in water by a factor of four, whereas the predictions of other force fields are within twenty per cent of the experimental value. Direct coexistence molecular dynamic simulations were also performed to determine the solubility of the salt. Reasonable agreement was found between the solubility obtained from free energy calculations and that obtained from direct coexistence simulations. This work shows that the evaluation of the solubility of salts in water can now be performed in computer simulations. The solubility depends on the ion-ion, ion-water and water-water interactions. For this reason, the prediction of the solubility can be quite useful in future work to develop force fields for ions in water.

Introduction

When a soluble salt is added to water there is a point where further addition of salt does not increase the concentration of salt dissolved in water. Any extra amount of salt added simply precipitates and goes to the bottom of the vessel. The equilibrium concentration of salt dissolved in water in equilibrium with the solid phase of the salt is denoted as the solubility limit of the salt, or simply the solubility. The value of the solubility depends on the salt, the solvent, and the thermodynamic conditions (i.e the temperature and pressure). The presence of salts significantly modify the properties of pure water, and also affect the properties of biological molecules in water [354–356]. Many experimental studies have been performed to analyze these issues [357, 358]. Experimental studies of both thermodynamic and kinetic aspects of the equilibrium between salts and their saturated solutions is also crucial in geological studies [359–363]. Sodium Chloride (NaCl) is one of the most abundant salts available on earth, and for this reason many experimental studies have been devoted to determining the properties of

NaCl solutions, and the effect of NaCl on biological molecules [364, 365]. It is clear that computer simulations can complement these studies by supplying a molecular perspective of the behavior of the system. For this reason many of simulation studies have been devoted to NaCl solutions [177, 366–376] and primitive models of ionic systems[377, 378]. The chemical potential of ions in solution has been calculated in many simulation studies [60, 136, 379–381]. However it is somewhat surprising to realize that the number of studies devoted to determine from molecular simulations the solubility of salts into water is quite small. Ferrario *et al.* determined for the first time the solubility of KF into water using computer simulations [61]. Later on, Sanz and Vega determined the solubility of NaCl into water [137]. The interest in the problem seems to be growing in the last few years. In fact, in 2010 Maginn and co-workers determined the solubility of NaCl in water [64], and quite recently another paper by Lisal and coworkers on the same problem appeared [63]. This recent activity provides some indication that the interest in this problem may increase significantly in the near future. Why is the number of computer simulation studies on solubility is so small? In our opinion the main reason for this is that determining the solubility of a salt in water by computer simulation is not an easy problem. The common route to evaluate the solubility by computer simulation is to determine the chemical potential of the salt in the solid phase and the chemical potential of the salt into water as a function of the composition of the solution. The composition of the solution at which the chemical potential of the salt is identical to that of the pure solid (at a certain T and p) determines the solubility of the salt. Why is that so involved? Firstly because determining the chemical potential of the salt in the solid phase requires in general using special techniques such as the Einstein crystal [115] or Einstein Molecule method [234, 382] that are generally not implemented in standard molecular dynamics (MD) programs. Secondly, the evaluation of the chemical potential of the salt in water is far from trivial, and an accurate evaluation is needed to have a reasonable estimate of the solubility.

Direct coexistence simulations could be an alternative route. The methodology, proposed by Ladd and coworkers has been implemented successfully to the LJ system [140, 141]. It can be also used for molecular fluids as water as shown by Haymet *et al.* [20] and Fernandez *et al.* [144]. For the ice Ih-water equilibrium we have obtained that the melting point temperature obtained from free energy calculations (i.e the thermodynamic route) is identical within the error bar to that obtained from direct coexistence simulations [81]. That constitutes a cross-check of the robustness of the calculations. To the best of our knowledge, the only study of the solubility problem by direct coexistence simulations was undertaken by Joung and Cheatham [65].

The first goal of this paper is methodological. We shall evaluate the solubility of NaCl in water by a thermodynamic route, following the methodology described in our previous work [137] after incorporating some improvements. We shall also determine the solubility from direct coexistence simulations, to illustrate that there is reasonable agreement between the two routes. There is a second motivation for this study. When modeling the solubility of NaCl in water it is necessary to define the potential used for ion–ion, ion–water and water–water interactions. The set of these three potentials will be denoted as the "force field". Since force fields provide only an approximate description of molecular interactions, there is no guarantee that the solubility evaluated by a force field will match the experimental value. In this work we shall explore how much the solubility of NaCl in water differs for different force fields. It will be shown that the solubility obtained for the considered force fields may be quite different. These are bad news since it means that the disagreement with the experimental values can be quite large. However, the sensitivity of the solubility to the force field can be used to discriminate between "good.ªnd "bad"force fields, at least with respect to the solubility problem. It will be shown here that the model proposed by Joung and Cheatham [383] provides a reasonable

estimate of the solubility of NaCl into water. This model represents an improvement with respect to previous models. It is our impression that there is still room for improvement in the area of force field developments for salts in water, and that the solubility could be used as a target property in the development of force fields for this kind of systems.

In summary, in this work we shall try to illustrate that the evaluation of the solubility of NaCl into water by computer simulation is feasible using current computational resources, and that results obtained from thermodynamic integration are reasonably consistent with those obtained from direct coexistence simulations. Also it will be shown that one of the studied models provides a quite reasonable estimate of the solubility of NaCl in water. We do hope that this work attracts more researchers into the interesting problem of the determination of the solubility of salts into water by computer simulation.

Molecular models

In this work the solubility of NaCl in water has been determined for three different force fields. In all cases, the SPC/E model [106] was used to describe the water–water interactions. All previous studies dealing with the solubility of NaCl in water used this water model, so that our choice allows a comparison with the results of other authors. In the SPC/E model positive charges are located on the position of the hydrogen atoms and a negative charge is located on the position of the oxygen atom. Besides the charges, a LJ potential is located on the oxygen atom (Table 12.2). For this model the water molecule geometry is $d(OH) = 1$ Å and $\theta(HOH) = 109.47^{o}$. Let us now present the three force fields considered in this work. In all cases a positive charge of magnitude e and a negative charge $-e$ are located on the position of the Na^{+} cation and Cl^{-} anion, respectively. However the force fields differ in the way that the non-Coulombic part of the ion–ion or ion–water interactions are described.

Force field I (TF)

In the first force field considered in this work the ion–ion interactions are described by the potential proposed by Tosi and Fumi for alkaline halides [384–387]. The potential parameters were fitted to reproduce properties of the pure solid, and for this reason the Tosi–Fumi potential is commonly used in studies of pure salts and melts of ionic systems [123, 388, 389]. The ion–ion potential is given by the expression :

$$u_{ij} = A_{ij} e^{-r_{ij}/\rho_{ij}} - \frac{C_{ij}}{r_{ij}^{6}} - \frac{D_{ij}}{r_{ij}^{8}} + \frac{q_i q_j}{4\pi\epsilon_o r_{ij}} \tag{11.1}$$

The parameters of the ion–ion interactions for NaCl were described in detail in Ref. [137]. Since the Tosi-Fumi potential was aimed to describe pure NaCl, these authors did not provide parameters to describe the water–ion interaction. In their pioneering study of solubility Ferrario *et al.* [61], used the Tosi–Fumi potential to describe the ion–ion interactions (in KF) and a LJ potential to describe the ion–water interactions using the parameters proposed by Smith and Dang [390]. This route was also followed by several authors for NaCl [63, 64, 137]. Thus, the first force field considered in this work, which will be denoted as "TF", is "hybridïn the sense that uses the Tosi–Fumi potential for ion–ion interactions and a LJ type for water–ion interactions. The parameters for the ion–water interactions of the TF potential are presented in Table 12.2.

Force field II (SD)

For the second force field considered in this work both the ion–ion and the ion–water interactions are described by the Lenard–Jones potential. For NaCl in SPC/E water the parameters are presented in Table 12.2, and they have taken directly from the original paper of Smith and Dang [390, 391]. This force field will be simply be denoted as "SD". It is interesting to point out that in the SD force field the ion–water interactions are simply a consequence of applying the Lorentz-Berthelot combinig rules to the ion–ion and water–water interactions. This force field is quite popular in studies of NaCl in water although somewhat surprisingly the solubility of this model has never been computed before.

Force field III (JC)

This force field is similar in spirit to the the SD force field. Again the ion–ion and ion–water interactions are described by a LJ potential. Joung and Cheatham proposed a set of NaCl force field each one tailored for the model considered to describe water [383]. Here we shall focus on the parameters of NaCl in SPC/E water to be consistent with the rest of the results of the paper. Interestingly, even though Joung and Cheatham used a LJ potential to describe ion–ion and ion–water interactions and the SPC/E to describe water, they proposed a set of parameters completely different from those proposed by Smith and Dang [390]. The parameters of this force field are presented in Table 12.2. We shall denote this force field as "JC".

Solubility of salts from free energy calculations

The solubility limit of a salt AX at a certain temperature and pressure is just the concentration of the salt at which the chemical potential of the salt in the solution $\mu_{AX}^{solution}$ becomes identical to that of the the pure solid μ_{AX}^{solid}:

$$\mu_{AX}^{solid} = \mu_{AX}^{solution} \tag{11.2}$$

In this work we shall determine the solubility of NaCl in water at room temperature (298 K) and normal pressure (1 bar). For a certain phase let us denote as N_A the number of cations of a system, N_X the number of anions and N_{AX} the number of molecules of salt. Obviously it always holds that (if the salt is A_iX_j with $i = j = 1$):

$$N_A = N_X = N_{AX} \tag{11.3}$$

Let us denote as N the total number of particles of a certain phase. For the salt in the solid phases it holds:

$$N = N_A + N_X = 2N_{AX} \tag{11.4}$$

whereas for a solution of AX in water N is given by :

$$N = N_A + N_X + N_{H2O} \tag{11.5}$$

Let us first describe the procedure to obtain the chemical potential of salt in the solid phase.

Tabla 11.1: Parameters for the Smith–Dang, Joung–Cheatham and Tosi–Fumi force fields. The crossed interactions are obtained by the Lorentz-Bertheloth combining rules.

LJ interaction	ϵ/k_B (K)	σ ()	Charge	q (e)
		Water SPC/E		
O - O	78.20	3.166	O	-0.8476
			H	0.4238
		Smith–Dang		
Na^+ - Na^+	65.42	2.35	Na^+	+1.0
Cl^- - Cl^-	50.32	4.40	Cl^-	-1.0
Na^+ - Cl^-	57.375	3.375		
Na^+ - O	71.525	2.758		
Cl^- - O	62.730	3.783		
		Joung–Cheatham		
Na^+ - Na^+	177.457	2.159	Na^+	+1.0
Cl^- - Cl^-	6.434	4.830	Cl^-	-1.0
Na^+ - Cl^-	33.789	3.495		
Na^+ - O	117.841	2.663		
Cl^- - O	22.430	3.998		
		Tosi–Fumi		
Na^+ - O	71.52	2.758		
Cl^- - O	62.73	3.783		

Chemical potential of AX in the solid phase

The chemical potential of AX in the solid phase is simply:

$$\mu_{AX}^{solid} = \left(\frac{G_{solid}}{N_{AX}}\right) = \left(\frac{A_{solid} + pV_{solid}}{N_{AX}}\right) \tag{11.6}$$

By performing NpT simulations of the AX solid at room temperature and pressure it is possible to determine easily V_{solid}. The term A_{solid} can be computed by using the Einstein crystal [115] or Einstein molecule [234, 382] methodologies. In these methodologies NVT simulations are performed in which the Hamiltonian of the system is modified from the original solid to one for which the free energy can be computed analytically. Both in the Einstein crystal and Einstein molecule methodologies the reference system consists of non-interacting particles connected to the equilibrium lattice positions by harmonic springs (hence the name Einstein crystal). In the Einstein crystal the center of mass of the system is fixed, whereas in the Einstein molecule the center of mass of just one particle in the system remains fixed. The calculations are performed at the equilibrium density of the system at the considered temperature and pressure. The final expression of the Helmholtz free energy of the solid of Einstein crystal/molecule calculations is [133]:

$$A = A_0 + \Delta A_1 + \Delta A_2 \tag{11.7}$$

The term A_0 is the free energy of the reference system. The analytical expression for A_0 is slightly different in the Einstein crystal and Einstein molecule methodologies (see Ref. [133]).

The term A_1 is just the difference in free energy between an Einstein crystal/molecule with no intermolecular interactions and an Einstein crystal/molecule with intermolecular interactions. The expression used to compute A_1 is the same in the Einstein crystal and Einstein molecule methodologies, being the only difference the choice of the reference point that remains fixed (center of mass of the system or center of mass of a reference particle). The term A_2 gives the free energy difference between the considered solid and a system with intermolecular interactions and additional harmonic springs (of strength Λ_E) connecting the atoms to the equilibrium lattice positions. Again, the expression for A_2 is the same in Einstein crystal/molecule calculations the only being difference the choice of the particle that remains fixed. We refer the reader to the original references for further details, and specially to our review about free energy calculation of solid where the expression and all technical details are provided [133]. It is convenient to assume that the thermal De Broglie wave length of all species is $\Lambda_b = 1$ Å, and that the rotational, vibrational and electronic partition function of all species is one. As discussed in our previous work [133], these arbitrary choices affects the value of the free energy but does not affect phase equilibria (provided the same choice is adopted in all phases). Let us point out that free energies obtained from Einstein crystal calculations are identical to that obtained from free Einstein molecule calculations. The free energy of a solid is unique and does not depend on the computational details. We found that this was indeed the case for hard spheres [234]. The same was found here for NaCl. We computed in all cases the free energy of the solid AX from Einstein crystal and Einstein molecule calculations and found that the free energies obtained by both routes was the same to within the statistical uncertainty. That was also a crosscheck of the calculations since it means that we have computed the free energy of the solid by two somewhat different routes.

The chemical potential of AX in the water phase

The procedure to obtain the chemical potential of the AX salt in solution used in this work is basically that first proposed by Sanz and Vega [137]. However, as will be discussed later some technical details about the practical implementation of the method will differ from the original work. We shall first describe the methodology, and discuss later on the details about how it was implemented in this work.

The chemical potential of an AX salt in water is defined as :

$$\mu_{AX}^{solution} = \left(\frac{\partial G_{solution}}{\partial N_{AX}} \right)_{T,p,N_{H_2O}} \tag{11.8}$$

where $G_{solution}$ is the total Gibbs free energy of the solution and N_{AX} is the number of molecules of salt in the solution. Notice that the number of water molecules should be constant when computing the derivative of the previous expression, in this work $N_{H_2O} = 270$. As usual, the Gibbs free energy of the solution is obtained from the sum of the Helhmoltz free energy $A_{solution}$ and of the $pV_{solution}$ term:

$$G_{solution} = A_{solution} + pV_{solution} \tag{11.9}$$

In short, our strategy is to compute $A_{solution}$ and $pV_{solution}$ for several solutions differing in the number of NaCl molecules N_{AX}, but with the same number of water molecules N_{H_2O}. From the computed value of $G_{solution}$ the chemical potential of the salt in the solution is obtained by the derivative of Eq.(11.8). The $pV_{solution}$ term is obtained easily from the NpT runs. Then, the cumbersome job is to compute $A_{solution}$. The total Helmholtz free energy of the solution can be divided into an ideal and a residual term. A residual property is defined as that of the

real system at the considered thermodynamic state and that of an ideal system at the same temperature, density and composition:

$$A_{solution} = A^{id}_{solution} + A^{res}_{solution} \tag{11.10}$$

The ideal term is obtained from the expression [392]:

$$\frac{A^{id}_{solution}}{k_B T} = N_{H_2O} \ln\left(\rho_{H2O}\Lambda_b^3\right) + 2N_{NaCl}\ln\left(\rho_{NaCl}\Lambda_b^3\right) - N_{H_2O} - 2N_{NaCl} \tag{11.11}$$

where $\rho_i = \frac{N_i}{V}$ and where we have chosen the De Broglie thermal wave length of all species to be Λ_b=1 Å and set the internal partition function of all species to one to be consistent with our previous choice for the solid phase. Notice that we are treating the NaCl water solution as a ternary mixture (although in practice we always take into account that $N_A = N_X$). To compute $A^{res}_{solution}$ the NaCl water solution is transformed into a pure Lennard–Jones fluid for which the residual free energy is known from the empirical expressions of Kolafa and Nezbeda [114], which is basically a reliable fit to simulation results of the LJ fluid. The transformation of the salt solution in a pure LJ fluid is done via a coupling parameter (λ) in the Hamiltonian of the system. The Hamiltonian of the system is written as a function of λ as:

$$U(\lambda) = \lambda U_{LJ,ref} + (1-\lambda)U \tag{11.12}$$

so that when (λ=1) the particles of the system interact through a LJ potential and when (λ=0) one recovers the original salt solution. Then, the residual free energy of the solution can be obtained from Hamiltonian integration as:

$$A^{res}_{solution} = A^{res}_{LJ,ref} + \int_0^1 \langle U - U_{LJ,ref}\rangle_{N,V,T,\lambda} d\lambda = A^{res}_{LJ,ref} + A^{integral} \tag{11.13}$$

For each composition, the integrand of the equation above is computed for several values of λ using NVT runs. The value of the volume corresponds to that of the the system in the original salt solution at the considered temperature, pressure and composition. The parameters of the LJ reference system were $\epsilon_{ref}/k_B = 78.2$ K and $\sigma_{ref} = 3.14$ Å. We check that no transition was detected along the integration path. Basically, all this methodology is the same that used by Sanz and Vega [137]. Let us now describe the improvements over our previous methodology that have been used in this work:

- Improvement 1. Very long runs were used to determine the the density of NaCl solutions. Either runs of one million MC cycles or MD runs of up to 10ns were used to determine with high accuracy the density of each of the considered solutions.

- Improvement 2. The densities obtained from the NpT runs of the solutions were fitted to a polynomial expression as a function of N_{NaCl}. That reduces the noise of each density and probably reduces also the error in the estimate of the density for each composition.

- Improvement 3. The error in the estimate of $A_{solution}$ was reduced significantly. That was consequence of several changes. Firstly, since $A_{solution}$ is computed in NVT runs, the more accurate value of V obtained from the two previous improvements certainly helped to increase the accuracy of the estimate of $A_{solution}$. Secondly, longer NVT runs were used to evaluate the integrand of Eq.(11.13). While in our previous work we used runs of 20000+30000 cycles, here we used runs of 80000+100000cycles. A cycle was defined as a trial move per particle of the system (translation or rotation in the case of water)

plus a trial volume change. Another important feature is that we increased the number of values of λ considered to evaluate the integrand. Whereas in our earlier paper we used Gaussian integration with 11 values of λ, here we have used Simpson integration and the number of values of λ has been increased to 21. The use of Simpson's integration allows more values of λ in regions where the integrand of Eq.(11.13) changes abruptly (region of λ values between 0.95 and 1). Besides since the final configuration of each value of λ was used as initial configuration of the following value of λ this also helps significantly the equilibration of the system. In summary, we have increased the accuracy computing $A_{solution}$.

- Improvement 4. This improvement concerns the evaluation of the derivative of Eq. (11.8), which yields the chemical potential of the salt. In our previous work we fitted $G_{solution}$ to a quadratic function of N_{AX}. As a consequence, is the chemical potential became a linear function of N_{AX}. This is fine when considering a narrow range of concentrations (and that was indeed the aim of our original approach). But it is true that the chemical potential of NaCl in water presents a strong curvature at small concentrations, and this feature (consequence of logarithmic terms in the ideal contribution to the free energy) is not reproduced by the way we performed the analysis. For this reason Lisal *et al.* [63] and Maginn *et al.* [64] have criticized the approach used in our previous study. We admit the criticism and we have modified the way the chemical potential is obtained.

  Let us re-write $G_{solution}$ as:

$$G_{solution} = A^{id}_{solution} + [A^{res}_{solution} + pV_{solution}] = G_1 + [G_2] \tag{11.14}$$

  We have found that G_2 can be fitted quite well by a cuadratic function of N_{AX} (it should be noticed that the $pV_{solution}$ term is quite small as compared to the term $A^{res}_{solution}$) so that :

$$G_2 = A^{res}_{solution} + pV_{solution} = a + bN_{NaCl} + cN^2_{NaCl} \tag{11.15}$$

  According to this, the contribution of these two terms (i.e. G_2) to the chemical potential of NaCl in the solution, which we shall denote as $\mu^{solution}_{NaCl,2}$ is simply:

$$\mu^{solution}_{NaCl,2} = b + 2cN_{NaCl} \tag{11.16}$$

  The second contribution to the chemical potential $\mu^{solution}_{NaCl,1}$ is given by:

$$\mu^{solution}_{NaCl,1} = \left(\frac{\partial A^{id}_{solution}}{\partial N_{AX}}\right)_{T,p,N_{H_2O}} \tag{11.17}$$

  It is possible to show that $\mu^{sol}_{NaCl,1}$ is given by (see Appendix K):

$$\mu^{solution}_{NaCl,1} = \left(\frac{\partial A^{id}_{solution}}{\partial N_{NaCl}}\right)_{T,p,N_{H_2O}} = 2k_BT\ln(\rho_{NaCl}) - k_BT\bar{V}(\rho_{H_2O} + 2\rho_{NaCl}) \tag{11.18}$$

  where $\bar{V}$ is the partial molar volume of NaCl ($\bar{V} = \left(\frac{\partial V}{\partial N_{NaCl}}\right)_{T,p,N_{H_2O}}$). Notice that the derivative of the ideal Helhmoltz free energy is performed while keeping T, p and N_{H_2O} constant (and not while keeping T, V and N_{H_2O} constant). That explains the appearance of a partial volume contribution (see the Appendix K). To calculate Eq. (11.18) we get ρ_{NaCl}, $\bar{V}$ and ρ_{H_2O} from the ρ(NaCl) described in ïmprovemet 2". We have checked that

this is fully equivalent to evaluate numerically the derivative given by Eq. (11.17). The total chemical potential of NaCl in the solution is obtained easily by adding these two contributions:

$$\mu_{NaCl}^{solution} = \mu_{NaCl,1}^{solution} + \mu_{NaCl,2}^{solution} \tag{11.19}$$

For all simulations aimed to compute the chemical potential of NaCl in the solution Ewald sums were used to deal with Coulombic interactions. The LJ and the real part of the Coulombic interactions were truncated at 9 Å . A home made program was used. We checked that the results are totally consistent with those obtained from the MD package Gromacs [235] (see Appendix 11). Standard corrections for the truncation of the potential were used for the LJ contribution. In the Ewald sums the term controlling the convergence of the reciprocal space sum was chosen so that ($\alpha \cdot r_c = 2.98$, 0.29 $^{-1}$ for a cutoff of 9 Å). All NpT runs used isotropic scaling since we are dealing either with fluid phases or with cubic crystals (with the NaCl cubic structure).

Direct coexistence simulations

Experimentally, when a large amount of solid NaCl is introduced into water, one finds that after a certain amount of time, part of the NaCl dissolves into water, and the two phases (the solid NaCl and the NaCl solution) reach the equilibrium. Then the concentration of NaCl in the solution reach the solubility limit. That opens a possible route to determine the solubility of NaCl in water in computer simulations. A block of NaCl is introduced in one side of the simulation box, and water is introduced in the other side, and molecular dynamics simulations are performed (MD) until the system reaches the equilibrium. We performed MD simulations by putting pure NaCl in contact with pure water. Unfortunately this approach was not very useful as no single ion from the solid went to the fluid phase even after 500 ns. What is the reason for this .apparent"disagreement between experiment and simulation? The reason is that the solution of solid NaCl into water is a rare event", since it has a high activation energy and it is necessary to wait times much longer than those used typically in computer simulations to see it. For this reason this does not seem to be a very useful route to determine solubilities (it remains to be studied in future studies if the introduction of defects, kinks, steps or even roughness on the surface of solid the NaCl could help to reduce the time required to see the migration of ions from the solid to the solution.) The second possibility is to introduce solid NaCl in one side of the simulation box and a supersaturated water solution in the other side. Since the solution is supersaturated part of the ions in the solution will precipitate, or in other words will incorporate to the solid phase until the system reaches the equilibrium concentration. Can this second route work? This second route was recently employed by Joung and Cheatham [65]. It will be shown in this work that this second route can indeed be used to determine the solubility, although long runs, of the order of several microseconds, are needed (at least for the force fields of NaCl considered in this work). The reason why still long runs are needed is that the incorporation of ions from the supersaturated solution to the solid phase is still an activated process with a free energy of activation. In fact the ions must get rid of part of the first solvation layer of water molecules before incorporating into the crystal. However it is likely that the activation energy of this process is lower than the activation energy of the opposite one.

Let us now provide some details about direct coexistence (NaCl solid- supersaturated solution) runs. Molecular dynamic simulations were performed using Gromacs [235] (version 4.5). Unfortunately the Tosi–Fumi potential is not implemented within the program Gromacs,

so that direct coexistence simulations were performed only for the SD and JC force fields. A velocity scaling thermostat [393] was used to keep T fixed and a Parrinello-Rahman barostat [102] was used to keep pressure constant. The shape of the simulation box was orthorhombic and the three sides of the simulation box were allowed to vary independently, to avoid the presence of any stress in the solid phase (stress could change the free energy of the solid and affect the solubility). The relaxation time for the thermostat and barostat was of 2 ps. The time step was 2 fs. The LJ interaction was truncated at 8.5 and standard long range correction was employed. Ewald sums were used to deal with the Coulombic interactions. The real part of the Coulombic interaction was truncated at 8.5 , and the reciprocal contribution was evaluated by using PME [100]. The results were obtained by running Gromacs in parallel using 4CPU's. With this number of processors we typically obtained 30 ns/day so that about 3 months were required to determine the solubility of a given force field. Constraints were used to fix the geometry of the molecule of water by using the algorithm LINCS [394] which is quite efficient in runs performed in parallel. The set up of the initial configuration for the MD runs was as follows. The solid NaCl contained in all cases 500 molecules (i.e 1000 ions). In the case of the SD force field the supersaturated solution contained 1523 molecules of water and 156 molecules of NaCl (i.e 312 ions) so that the initial concentration of NaCl in water phase was of about $5.6\ m$. In the case of JC force field the supersaturated solution contained 1215 molecules of water and 156 molecules of NaCl (i.e 312 ions) so that the initial concentration of NaCl in the water phase was of about $7.2\ m$. Therefore the number of particles in our simulations was of about 3000. The x direction was perpendicular to the solid NaCl-water interface. The concentration of NaCl in the supersaturated was obtained as a function of time as follows. Typically after 200 ns, the average density profile of the individual ions Na^+ and Cl^- in water phase was obtained. In general the density of Na^+ and Cl^- was found to be a function of x, except for the central region of the water phase (sufficiently far away from the NaCl-water interface) where we found that the concentrations of Na^+ and Cl^- were practically identical as it should be for a bulk NaCl solution. That also guarantees electroneutrality in the central slab of the water solution. The width of this central electroneutral region was typically larger than 20 Å . The molality of NaCl in the solution was obtained by computing the average number density of NaCl and water in this central slab.

Results

As we have discussed previously, the evaluation of the solubility of NaCl in water involves the calculation of the chemical potential of the salt in the solid phase and it the solution. We shall start by presenting the results for the chemical potential of the pure NaCl solid. The free energy of the NaCl solid was calculated at 298 K and 1 bar by the Einstein crystal/molecule method. The number of ions used in the calculations was $N = 1000$. The potential was truncated at $r_c = 14$ Å , and long range corrections were taken into account by assuming that the radial distribution function was one beyond the cutoff distance. For the TF force field we implemented the Einstein molecule method, whereas for the SD and JC force fields we used the Einstein crystal method. The different contributions to the Helhmoltz free energy (A_0, A_1 and A_2) are presented in Table 11.2. The total value of the free energy, which is the sum of these three terms, is presented in the last column of Table 11.2. In our previous work [137] we calculated the free energy for the TF force field using the Einstein crystal technique. The result of this work, obtained by using the Einstein molecule, is practically identical to that obtained in our previous work. The uncertainty of the free energy calculations presented in this work is of about $0.05\ Nk_BT$, (a quite typical value of the Einstein crystal methodology) .

To obtain the chemical potential of NaCl in the solid phase one simply must add the pV term to the Helmholtz free energy obtained by the Einstein crystal/molecule method. At 298K the contribution of the pV term is quite small (is of the order of $6 \cdot 10^{-4}$ in Nk_BT units), so that G is practically identical to A. The value of the chemical potential of NaCl in the solid phase (given per mol of NaCl) is presented in Table 11.3.

Tabla 11.2: Free energy calculations for NaCl solid for Tosi–Fumi (TF), Smith–Dang (SD) and Joung–Cheatham (JC) potential models at 298 K and 1 bar. The free energy reported in the last column corresponds to the sum of all the terms ($A_0 + \Delta A_1 + \Delta A_2$). The spring constant ($\Lambda_E$) and the number density $\rho = N/V$ given in particles per ^{3} are reported. The number of ions used in the calculations was 1000 and the cut–off was 14 Å. The thermal de Broglie wavelength (Λ_b) was set to 1 , and all components of the internal partition function set to one $q_r = q_v = q_e = 1$. These definitions correspond to our reference state 1 (ref1). EM and EC stands for Einsteim molecule and Einstein crystal calculations respectively.

Model	ρ (N_{ions}/V)	Λ_E/k_BT ($^{-2}$)	A_0/Nk_BT	$\Delta A_1/Nk_BT$	$\Delta A_2/Nk_BT$	A^{sol}/Nk_BT
TF(EM)	0.04360	2500	10.006	-156.85	-6.27	-153.11
SD(EC)	0.03981	4000	10.70	-159.90	-6.37	-155.57
JC(EC)	0.04143	4000	10.70	-159.94	-6.34	-155.58

The numerical values of the chemical potential reported in Table 11.3 depend on the value of the thermal De Broglie wave length (Λ_b) and on the value of the partition function of the internal degrees of freedom. In this work we have set to one the intramolecular partition function and to 1 the thermal de Broglie wave length, labeled as reference state 1 ($\mu_{NaCl}^{sol,ref1}$). Although this arbitrary choice does not affect phase equilibria (provided the same value is used for all phases) it does not allow a a comparison with the experimental values of the chemical potential. It is necessary to correct our simulation results for the different choice of the reference system used in experiments and in this work. This is simply done by adding 386.8 kJ/mol to the simulations results, and correspond to the reference state 2 ($\mu_{NaCl}^{sol,ref2}$) The justification of the value of the shift is described in detail in the Appendix 11. As can be seen, the SD and JC force fields reproduce almost exactly the experimental value of the chemical potential. However the TF force field provides a value that is about 12 kJ/mol higher (about two per cent). It is interesting to note that the chemical potential of NaCl in the solid phase was not used as a target property for determining the potential parameters of the SD and JC force field (and the same is true for the TF force field). The fact that these two force fields, SD and JC, reproduces the experimental value of the chemical potential of the solid should be regarded as a successful prediction of these two models.

We shall now discuss the results for the NaCl solutions. In Fig. 11.1 experimental density of the NaCl in water is compared to the simulation results for the three force fields considered in this work. The predictions of the TF and SD force fields are quite similar and agree quite well with the experimental values for concentrations up to $4\ m$. For higher concentrations these two models seem to underestimate the experimental values. The TF and SD force fields have different ion–ion interactions but the same water–ion interactions. At low concentrations of salt, the ion–ion interactions play a minor role. Ion–ion interactions become increasingly important as the concentration of the salt increases. The density prediction of the JC force field tends to overestimate the experimental values by a small amount. The densities obtained in this work for the TF force field are quite similar to those reported in our previous work (compare the results of Fig. 11.1 of this work with those of Fig. 2a of our previous work [137]). And in both cases it can be seen that the agreement with experiment is excellent. Paluch *et al.*

Tabla 11.3: Chemical potential for the NaCl solid at 298 K and 1 bar for TF, SD and JD models. The first column corresponds to the chemical potential of the solid using our choice of reference system ($\mu_{NaCl}^{sol,ref1}$), and the second column are the shifted values of the chemical potential in order to compare with the experimental value ($\mu_{NaCl}^{sol,ref2}$). The experimental value was taken from Ref. [395].

Model	$\mu_{NaCl}^{sol,ref1}$ / kJ mol^{-1}	$\mu_{NaCl}^{sol,ref2}$ / kJ mol^{-1}
TS	-758.68	-371.88
SD	-770.87	-384.07
JC	-770.92	-384.12
Exp.	-770.82	-384.02

claimed that our 2007 densities for the TF model did not agree with the experimental values [64]. This statement is incorrect as can be seen by simply looking at Fig. 2a of our previous work (where the good agreement with experiment is clearly visible), or more simply converting the tabulated results for the number densities reported in Tables V and X from our previous work to density in g cm^{-3}. This can be done simply by using the formula:

$$\rho(g/cm^3) = \rho(N/^3)(x_{H_2O}M_{H_2O} + x_{Cl^-}M_{Cl^-} + x_{Na^+}M_{Na^+})\frac{10^{24}}{N_{Avo}} \tag{11.20}$$

where x_i is the molar fractions of i (treating the system as a ternary mixture) and M_i is the molecular/atomic weight. For example, since we are using 270 molecules of water, for a system with 25 NaCl molecules, the mol fraction of water is $270/(270+25+25))$ and the molar fraction of Na^+ is $25/(270+25+25)$. For this reason the values presented in Fig. 8 of Ref. [64], labeled as Sanz and Vega, are incorrect.

The density varies smoothly as a function of the concentration of salt. For this reason it seems reasonable to fit the number densities to a quadratic polynomial of the number of NaCl molecules:

$$\rho(N/^3) = d_0 + d_1 N_{NaCl} + d_2 N_{NaCl}^2. \tag{11.21}$$

The coefficients of the fit are presented in Table 11.4. The NaCl concentration in molality units (mol of NaCl per kilogram of water) can be obtained as:

$$m_{NaCl} = \frac{1000 N_{NaCl}}{N_{H_2O} M_{H_2O}} \tag{11.22}$$

Tabla 11.4: Coefficients of the cuadratic fits to the number density $\rho(N/^3)$ as a function of the number of NaCl molecules for the three force fields considered in this work.

Model	$d_0 \cdot 10$	$d_1 \cdot 10^3$	$d_2 \cdot 10^5$
TF	0.3344	0.1149	-0.1507
SD	0.3344	0.1186	-0.1729
JC	0.3355	0.1339	-0.1390

Let us now turn to the calculation of the chemical potential of the solution. Using the fits just described, the density of the NaCl solution was estimated for several numbers of NaCl molecules (remember that the number of water molecules is fixed to 270). The integrand of Eq. (11.13) was computed by using NVT simulations for different values of λ. In Fig. 11.2 the

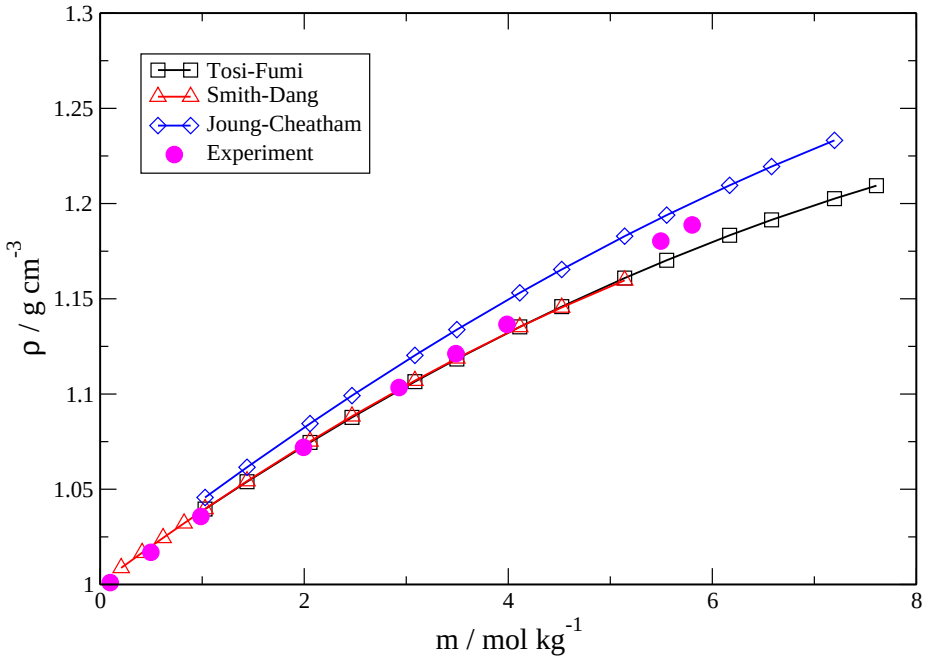

Figura 11.1: Density versus NaCl molality for the considered force fields compared to the experimental values (as indicated in the legend).

integrand is shown for several solutions of the JC force field. In all cases the integrand is quite smooth in the interval of λ from 0.1 to 0.9. The integrand decreases slightly from 0 to 0.1. On the other hand, the integrand decreases quickly λ from $\lambda = 0.9$ to $\lambda = 1$. For this reason we have evaluated the integrand for many values of λ in this region. Notice that the integrand does not diverge either in λ=0 nor in λ=1. The accuracy obtained in this work for determining the integral of Eq. (11.13) is higher than in our previous work [137]. The main reasons are that much longer runs were used and that 21 values of λ, distributed reasonably over the integration range, were used instead of the 11 values of lambda employed in our previous work which used Gaussian integration. Once the integral is evaluated, the following step to compute $G_{solution}$ is to add the residual free energy of the LJ reference fluid ($A^{res}_{LJ,ref}$) [114], the $pV_{solution}$ term and the ideal gas contribution to the Helmholtz free energy (Eq. (11.14)).

We shall start the discussion by presenting the results for the SD force field. In Table 11.5 the different contributions to the Gibbs free energy of the solution (ideal, residual and pV terms) are presented for the SD model. The values reported are free energies expressed in kJ per mol of simulation boxes (neither per mol of water nor per mol of molecules of salt). The value of the $pV_{solution}$ term is quite small compared to the other contributions to the free energy. As described in the previous section, the total value of $G_{solution}$ is divided in two contributions. The first one (G_1) is the $A^{id}_{solution}$ term, and the second one (G_2) is the sum of the $A^{res}_{solution}$ and the $pV_{solution}$ term of Table 11.5. G_2 is plotted as a function of the number of molecules of salt (N_{NaCl}) in Fig. 11.3. The results are quite smooth and can be fitted nicely to a second order polynomial curve. Although not obvious from the figure, we have checked that the sum of squared deviations of the fit is reduced by approximately a factor of two from the the linear to the cuadratic fit whereas further increasing the order of the polynomial did not improve signficantly the fit. The coefficients of the fit are reported in Table 11.6. In our previous work [137] the sum of G_1 and G_2 was fitted to a second order polynomial. That was not a good

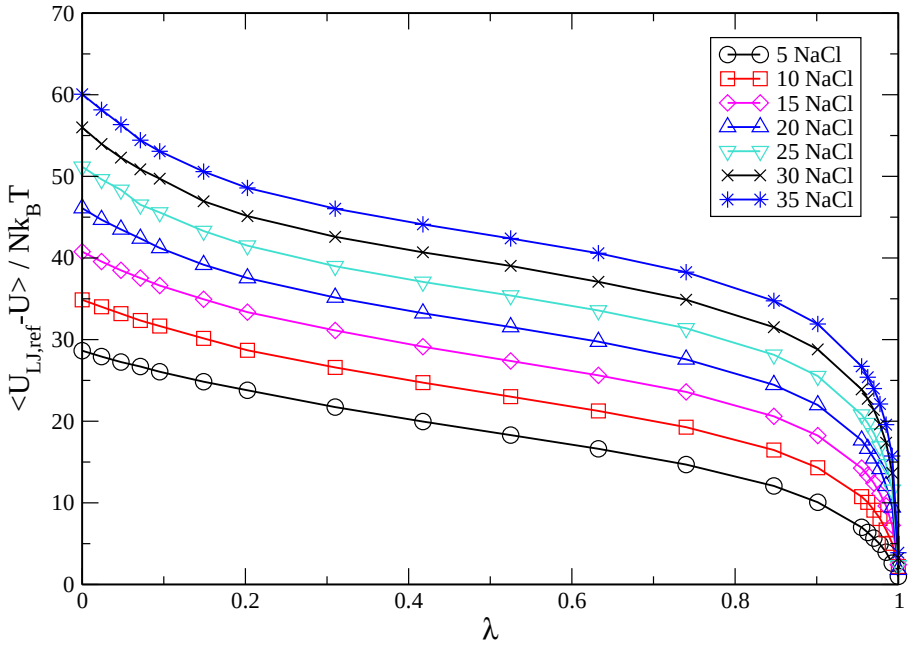

Figura 11.2: Integrand of the transformation of Joung–Cheatham NaCl solution into a Lennard–Jones fluid for several NaCl solutions.

Tabla 11.5: Solution density and terms contributing to the solution Gibbs free energy for the SD model. All the solutions have 270 water molecules. Energies are given in kJ per mol of simulation boxes. The number density $\rho = N/V$ is given in particles per ^{3}. The chemical potential of NaCl is given in kJ per mol of NaCl.

N_{NaCl}	ρ	$G_{solution}$	$A^{integral}$	$A^{res}_{LJ,ref}$	$pV_{solution}$	$A^{id}_{solution}$	m / mol kg^{-1}	$\mu^{solution}_{NaCl,ref2}$ / kJ mol^{-1}
1	0.03356	-11082.05	-9573.96	1485.61	0.488	-2994.18	0.21	-391.5
2	0.03367	-11853.53	-10326.39	1511.91	0.490	-3039.55	0.41	-388.0
3	0.03378	-12629.48	-11085.67	1538.10	0.492	-3082.40	0.62	-385.9
4	0.03389	-13404.25	-11845.24	1564.15	0.494	-3123.65	0.82	-384.5
5	0.03400	-14174.89	-12603.93	1592.00	0.496	-3163.45	1.03	-383.3
7	0.03419	-15700.64	-14102.38	1642.40	0.500	-3241.16	1.44	-381.5
10	0.03445	-18017.48	-16381.43	1716.58	0.507	-3353.14	2.06	-379.5
12	0.03461	-19545.54	-17885.33	1764.88	0.511	-3425.60	2.47	-378.5
15	0.03483	-21833.55	-20137.47	1835.28	0.519	-3531.88	3.08	-377.2
17	0.03495	-23383.65	-21663.36	1880.64	0.524	-3601.45	3.50	-376.4
20	0.03511	-25634.34	-23876.56	1946.01	0.531	-3704.32	4.11	-375.4
22	0.03521	-27173.28	-25389.36	1987.61	0.537	-3772.07	4.52	-374.9
25	0.03533	-29468.87	-27643.45	2046.75	0.545	-3872.71	5.14	-374.1

idea as the G_1 term exhibits a strong curvature. However, it seems quite reasonable to fit the G_2 term to a second order polynomial as it can be seen in Fig. 11.3. The contribution of G_2 to the chemical potential is obtained from the derivative of G_2 with respect to N_{NaCl}. Therefore, this contribution increases linearly with the number of ions in the solution. The contribution of the ideal term to the chemical potential can be obtained easily by obtaining numerically the derivative of G_1 with respect to N_{NaCl} using the previously described polynomial fit of the

number density of the system (Table 11.4). Alternatively, and certainly more elegantly, one can just to compute the partial molar volume of the salt from the fitted values of the densities and using Eα. 11.18.

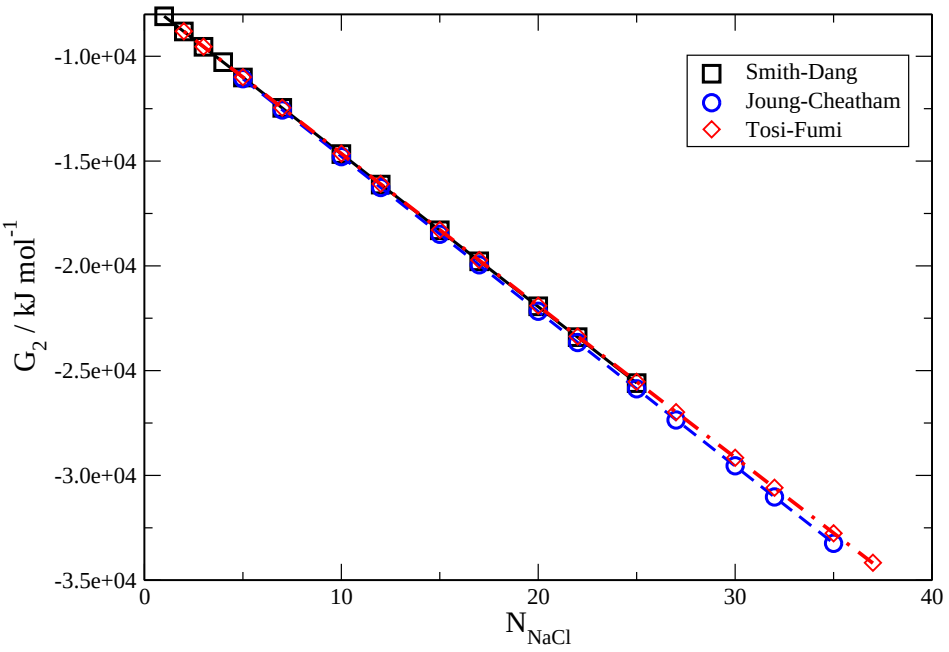

Figura 11.3: G_2 contribution to the Gibbs free energy of the solution as a function of the number of NaCl molecules for the three studied force fields. The units of G_2 are kJ per mol of simulation boxes.

Tabla 11.6: Cuadratic fit coefficients of the G_2 ($A^{res}_{solution} + pV_{solution}$) fits for the three force fields. The units of G_2 are kJ per mol of simulation boxes.

Model	a $\cdot 10^{-4}$	b $\cdot 10^{-3}$	c
TF	-0.7343	-0.7315	0.1588
SD	-0.7354	-0.7311	0.0692
JC	-0.7365	-0.7426	0.0982

Once we have calculated the chemical potential for the solid and for the solution phases we shall estimate the solubility. For the SD force field the results are presented in Fig. 11.4. The experimental values of the chemical potential of NaCl, both in the solid phase and in solution, are also shown. The intersection between the experimental values of the chemical potential occurs at a concentration of $6.15\ m$. This is indeed the experimental value of the the solubility of NaCl in water. The intersection of the chemical potential curves of the SD force field occurs at a concentration of $0.9\ m$. This differs from the experimental value by about 5.2 units of molality. The solubility of NaCl in water predicted by the SD force field is totally incorrect. Since the SD model predicts correctly the chemical potential of the NaCl solid phase, the problem of this model is an incorrect prediction of the chemical potential of the salt in the solution, about 12 kJ/mol higher than the experimental value. It is clear from the results of Fig. 11.4 that the water–ions interactions in the SD force field are somewhat weak, and

should be slightly increased to bring the predictions of the model into closer agreement with the experiment. Of course that should be done without modifying the ion–ion interaction, since otherwise the good agreement with the experiment found for the chemical potential of the solid will be lost. The values of the chemical potential of NaCl in the solution reported recently by Lisal *et al.* [63] for the SD force field are also presented in Fig 11.4. As can be seen our results agree rather well with those of Lisal *et al.*, who use a completely different approach to the calculation of the chemical potential of NaCl in solution. Taking into account the difficulties in the determination of the chemical potential of NaCl in water this is gratifying.

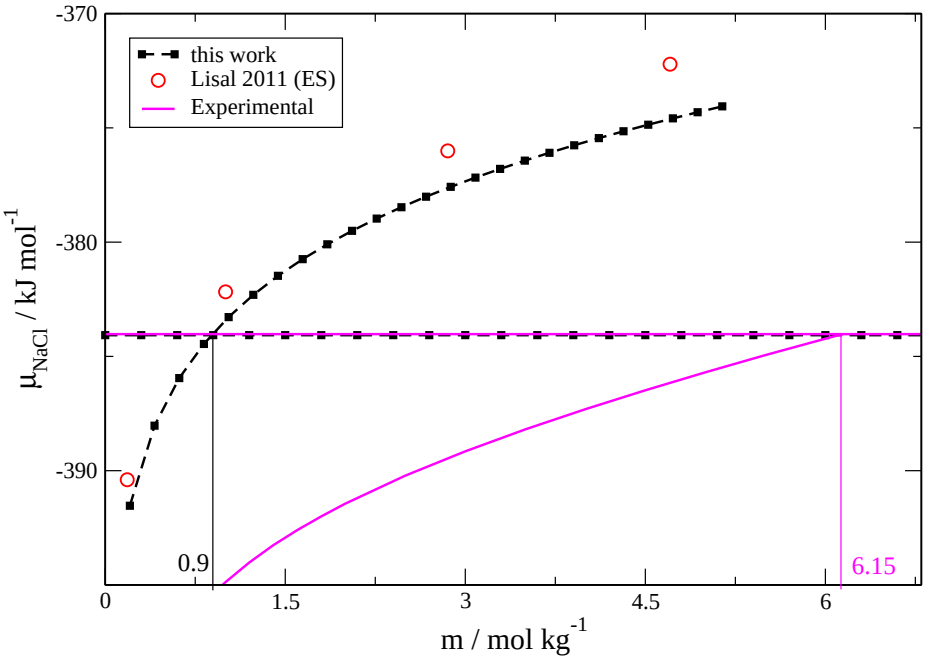

Figura 11.4: Chemical potential of NaCl versus molality for the Smith–Dang force field (black dashed line with filled squares). The red open circles represent the results by Lisal *et al.* using Ewald sumsi [63]. The solid magenta curve corresponds with the experimental values. Horizontal lines represent the chemical potential of the solid; experimental (solid line) and Smith–Dang (dashed line with filled squares).

Let us now turn to the results for the JC model. In Table 11.7 the different contributions to the Gibbs free energy of the system are provided. Once again, we split G into two contributions, G_1 (which just contains $A^{id}_{solution}$) and G_2 with the sum of the other contributions ($A^{res}_{solution}$ and $pV_{solution}$ terms). Again G_2 could be fitted nicely to a second order polynomial (Fig. 11.3) and the coefficients are given in Table 11.6. Taking the derivative of G_1 and G_2 with respect to N_{NaCl}, and adding these two contributions one obtains the chemical potential of NaCl in water. The chemical potentials of NaCl in the solid phase and in the solution are presented in Fig. 11.5, and compared to the experimental values. As mentioned before, the JC force field predicts quite well the experimental value of the chemical potential of the solid. As to the solution , the predictions for the chemical potential are quite reasonable, but slightly higher than the experimental values. The intersect of the two chemical potentials of NaCl occurs at $4.8\ m$, which is the solubility of NaCl that follows from this force field. This is a quite reasonable result since the experimental value is $6.15\ m$. The chemical potential of NaCl in solution obtained by Lisal *et al.* [63] for the JC force field are also presented in Fig. 11.5. The

agreement with this work is quite good. To estimate the solubility of the JC force field Lisal *et al.* used the experimental value of the chemical potential of the NaCl solid [63]. They estimated the solubility to be $4.8\ m$, in perfect agreement with our result. The reason for that is that the chemical potential of NaCl in the solid phase for the JC force field is practically identical to the experimental value. Notice also that the approach of Lisal *et al.* could also be used to estimate the solubility of the SD force field since also for this force field the chemical potential of the model in the solid phase agrees quite well with the experimental value [63]. The good news is that there are at last two models (SD and JC) for which the solubility estimated by two different groups agree within the estimated uncertainty of the calculations.

Tabla 11.7: Free energy components of Joung–Cheatham NaCl solutions at 298 K and 1 bar. All the solutions have 270 water molecules. Energies are given in kJ per mol of simulation boxes. The number density $\rho = N/V$ is given in particles per Å^3. The chemical potential of NaCl is given in kJ per mol of NaCl.

N_{NaCl}	ρ	$G_{solution}$	$A^{integral}$	$A^{res}_{LJ,ref}$	$pV_{solution}$	$A^{id}_{solution}$	m (mol kg^{-1})	$\mu^{solution,ref2}_{NaCl}$ / kJ mol^{-1}
5	0.03419	-14228.47	-12687.63	1618.38	0.49	-3159.71	1.03	-394.0
10	0.03475	-18136.34	-16552.57	1762.66	0.50	-3346.94	2.06	-389.9
12	0.03496	-19681.54	-18083.66	1819.95	0.51	-3418.33	2.47	-388.8
15	0.03525	-22017.13	-20399.75	1905.02	0.51	-3522.91	3.08	-387.3
17	0.03543	-23540.83	-21911.05	1960.99	0.52	-3591.28	3.50	-386.4
20	0.03567	-25858.95	-24210.74	2043.49	0.52	-3692.23	4.11	-385.3
22	0.03583	-27419.62	-25758.86	2097.34	0.53	-3758.63	4.52	-384.5
25	0.03603	-29725.48	-28044.94	2176.05	0.53	-3857.13	5.14	-383.5
27	0.03615	-31278.67	-29584.00	2226.97	0.54	-3922.18	5.55	-382.9
30	0.03632	-33561.22	-31843.50	2300.70	0.55	-4018.97	6.17	-382.1
32	0.03641	-35111.01	-33376.39	2347.90	0.55	-4083.07	6.58	-381.5
35	0.03654	-37419.88	-35657.24	2415.48	0.56	-4178.68	7.20	-380.7

At this point we would like to test the predictions presented so far using a completely different route. The motivation is twofold. Firstly to guarantee that SD and JC force fields present a dramatically different solubility in water (i.e $0.9\ m$ and $4.8\ m$) even though they predict the same chemical potential for the solid phase, close to the experimental value. The second reason is that Joung and Cheatham estimated the solubility for the JC force field using direct coexistence simulations [65]. They performed simulations of solid NaCl in contact with a supersaturated water solution of NaCl of about 0.4 ns. They estimate the solubility for the JC force field was $7.2\ m$. Obviously, this value disagree with the values reported by us and by Lisal *et al.* [63]. To investigate this in further detail we performed direct coexistence molecular dynamic runs. At variance with the work of Joung and Cheatham, the length of our runs was of about 2800 ns (this is about 6-8 times longer than the runs of Joung and Cheatham). The time evolution of the bulk density of NaCl in the solution is presented in Fig. 11.6. The bulk density of NaCl was evaluated in a slab of the solution phase where the effects of the interfaces are negligible. For this reason it is necessary to carry out simulations with a large number of molecules in the solution phase. The initial solution was supersaturated, and the concentration of the salt decreases with time in the first 1000 ns. That means that one cannot simply run for 200–400 ns to estimate the solubility. Notice that the initial concentration of our runs was just the solubility of the two models predicted by Joung and Cheatham from direct coexistence runs [65]. After $1.5\ \mu s$ the concentration of the salt becomes stable, and remains stable for up to one additional microsecond. The results presented in Fig. 11.6 are quite expensive from a computational point of view. It was required to run Gromacs using 4

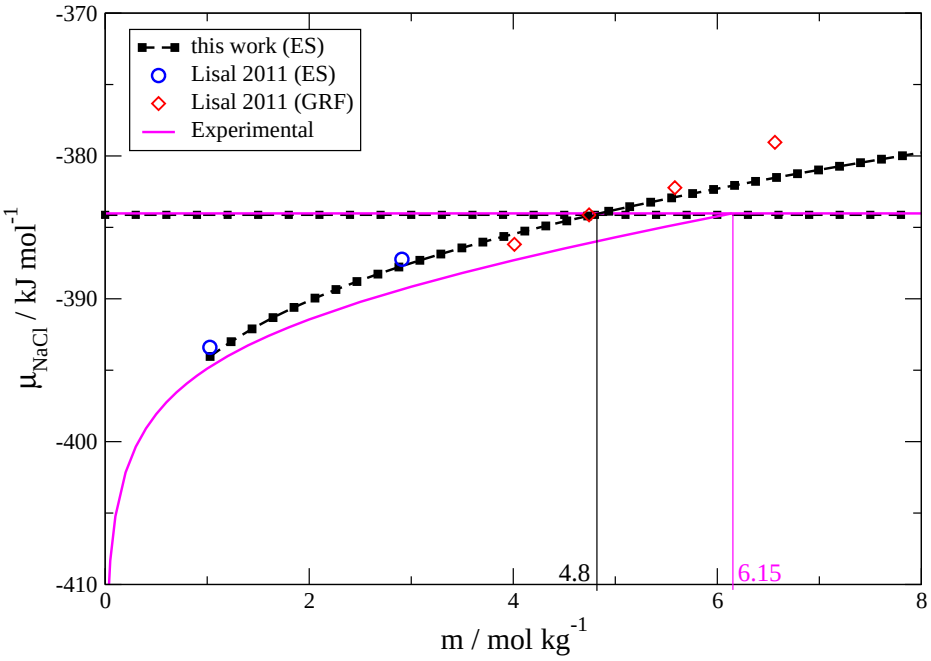

Figura 11.5: Chemical potential of NaCl versus molality for the Joung–Cheatham model (black dashed lines with filled squares). The results of Lisal *et al.* [63] are represented by blue open circles (Ewald Sums) and red open squares (GRF). The magenta solid curve corresponds with the experimental values. Horizontal lines represent the chemical potential of the solid; experimental (solid line) and JC (dashed line with filled squares).

CPU's for about 3 months to obtain these curves. Certainly it would be nice to perform even longer runs to be sure that the concentration of NaCl in water has reached the equilibrium. However this is beyond of our current computer facilities. For this reason we shall assume that the plateau of the salt concentration at times above 1.5 microseconds is just the solubility limit obtained from direct coexistence. The plateau in salt concentration cannot be ascribed to dynamical arrest. We have computed the diffusion coefficient of ions and water for the range of concentration considered in this work. The results are shown in Table 11.8. The water diffusion coefficient decreases as the concentration of salt increases. In fact, the diffusion coefficient of water can decrease up to half its value in the absence of salt. Concerning the ions, the Na^+ presents the smallest diffusion coefficient, its value is roughly one third of water's at the same thermodynamic conditions. The diffusion coefficient of Cl^- is slightly higher than that of Na^+ but smaller than that of water. The typical root mean square displacement of Na^+ ions in our MD simulations was about 775 Å. It is clear that the system is not glassy and that the plateau in the concentration versus time profile can not be due to a dynamic arrest.

Tabla 11.8: Diffusion coefficients at 298 K and 1 bar for the JD model.

N_{NaCl}	$D_{Na^+}\cdot 10^5$ / cm^2 s^{-1}	$D_{Cl^-}\cdot 10^5$ / cm^2 s^{-1}	$D_{H_2O}\cdot 10^5$ / cm^2 s^{-1}
10	0.44(9)	0.93(9)	1.61(9)
20	0.40(2)	0.58(9)	1.04(1)
35	0.22(1)	0.26(5)	0.54(4)

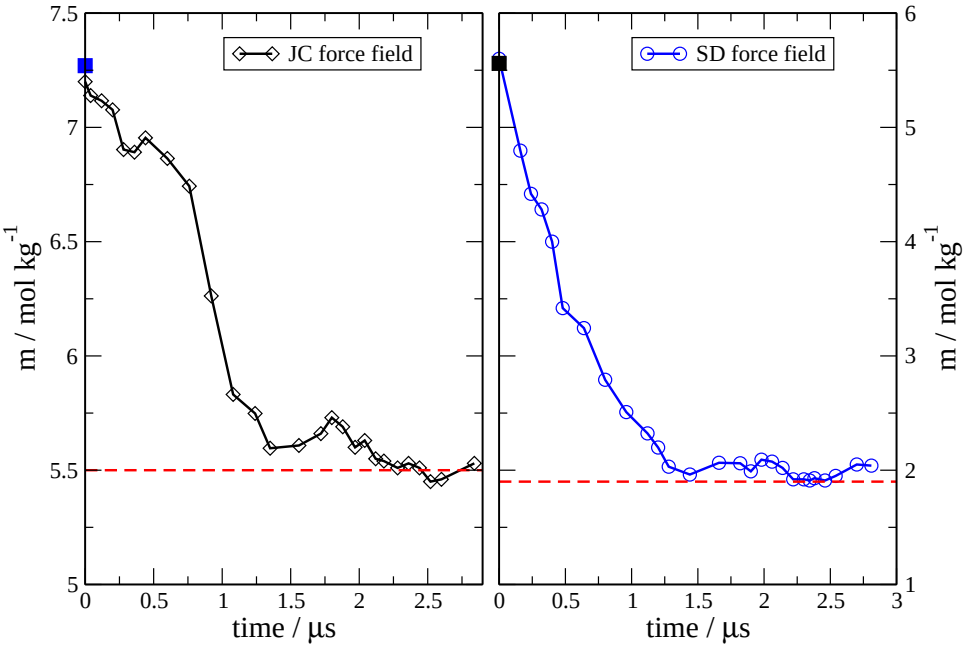

Figura 11.6: Molal concentration of NaCl versus simulation time for Smith–Dang (right) and Joung–Cheatham (left) force fields. The filled squares represent the solubility values reported by Joung and Cheatham in Ref. [65]. Dashed lines indicate the value at which the molality reaches a plateau.

The solubility of the SD and JC force fields obtained from free energy calculations and direct coexistence simulations are presented in Table 11.9. The first thing to notice is that direct coexistence simulations indeed confirm that the solubility of the SD force field is about $4\ m$ units smaller than that of the JC model. And secondly, the difference between the solubility of the SD model from free energy calculations and from direct coexistence simulations is of about $1\ m$ unit. In the case of JC force field this difference is of about $0.7\ m$ units. Which of the two techniques offer the most reliable values? We can not provide a definitive answer to this question. Firstly the hypothesis that still longer runs are needed in the direct coexistence simulations can not be definitely ruled out. It could be that the concentration of the salt in the supersaturated solutions occurs quickly initially, when the system is far from equilibrium, and then the process is much slower since the driving force (i.e the degree of supersaturation) decreases considerably. The only way to clarify this is to perform much longer runs (probably of the order of 10 microseconds). At this point this exceeds our computer capacities, but it could be addressed in future work (the computer speed will always increases year after year). The previous reasoning may lead to the conclusion that the direct coexistence simulations may be less reliable than the free energy results. However this is not completely true. In the direct coexistence simulations the size of the solution was rather large (i.e more than one thousand water molecules and more than one hundred molecules of salt). When implementing free energy calculations we used a smaller system, containing 270 molecules of water and up to about 40 molecules of NaCl. The reason of this choice of the size is three fold. Firstly, because we wanted to perform the calculations using the same size as was used in our previous study. In this way we could compare both results and analyze how to perform accurate calculations for a certain system size. In this work the same technique as in our previous has been used, but the results are more reliable. The second reason is that it is much cheaper to perform very long runs for a small system than for a large one, so that there is also a limit in the computer

power even for free energy calculations. Thirdly, Lisal *et al.* [63] used exactly the same system size (i.e 270 water molecules plus a number of NaCl molecules of up to 40) so that this allows a direct comparison with their results. However, neither this work nor the work of Lisal *et al.* have analyzed in detail the possible existence of finite size effects for the chemical potential of NaCl in the solution [63]. The size of our system is rather small, so that the hypothesis that there may be finite size effects affecting the value of the chemical potential of NaCl in solution when evaluated from free energy calculations cannot be completely ruled out. It is obvious that further work is needed to clarify these issues. Taking all previous points into account, we have decided to report the final value of the solubility of a certain force field in water as the arithmetic average of the value obtained from free energy calculations and that obtained from direct coexistence simulations, and to assign an error bar to the results which is equal to the distance of the two simulations results to the arithmetic average. This estimated value of the solubility is the central result of this work. From the previous discussion we found that the JC force field yields a solubility of $5.1(3)\ m$ whereas the solubility of the SD model is of $1.4(5)\ m$. It is clear that the JC model does a good job in predicting the chemical potential of the solid, the chemical potential of the solution and that of the solubility.

Tabla 11.9: Solubility results for the considered force fields.

Model	solubility / mol kg^{-1}		
	Free energy	Direct coexistence	Recommended
Tosi-Fumi	4.3(3)	-	-
Smith-Dang	0.9(4)	1.9(4)	1.4(5)
Joung-Cheatham	4.8(3)	5.5(4)	5.1(3)

Let us finish the paper by presenting the results for the TF force field. The chemical potential of NaCl for the TF force field obtained in this work are presented in Fig. 11.7 for the solid and for the NaCl solution. Lisal *et al.* have also computed the chemical potential in the solution for this force field [63], and their values are also presented in Fig. 11.7. As can be seen, the agreement between the results of this work and those of Lisal *et al.* is quite good. For the solid phase the chemical potential obtained in this work is practically identical to that reported by us in 2007. The two chemical potentials curves intersect at $4.3\ m$. This value is smaller than our estimate of the solubility reported in 2007, $5.4(8)\ m$ (although it is just slightly larger than the error bar of our calculations estimated in 2007). As already discussed, the change between the value of the solubility of this work and that of our 2007 work is due to some methodological improvements that were introduced: longer runs, more values of the coupling parameter λ in the integration of Eq. (11.13), higher accuracy in the estimate of the densities of the solutions using a fit to describe the densities of the system, and the separation of two contributions when computing the chemical potential. The combined effect of all these changes reduces the solubility by about $1.1\ m$. The chemical potential of NaCl in the solution obtained in this work agrees quite well with that of Lisal *et al.* [63]. To estimate solubilities of salts Lisal *et al.* combine the simulation results for the solution, with the experimental value of the chemical potential of the salt. It is clear from the results of Fig. 11.7 that would yield an incorrect estimate of the solubility for the TF model, because for this force field the chemical potential of the solid phase is rather different from the experimental value. Notice also that the ions will start to agregate/precipitate when the chemical potential of the salt in the solution becomes higher than its value in the solid phase (this kind of agregation has been studied recently by Alejandre *et al.*[396, 397]) and not when its value becomes higher than the experimental value

of the chemical potential of the solid phase. It is interest to notice that although the TF force field does not reproduce well neither the chemical potential of the solid nor that of the solution, it yields a solubility only slightly worse than the one predicted by the JC force field.

Tabla 11.10: Solution density and terms contributing to the solution Gibbs free energy for the Tosi–Fumi model. All the solutions have 270 water molecules. Energies are given in kJ per mol of simulation boxes. The number density $\rho = N/V$ is given in particles per ^{3}. The chemical potential of NaCl is given in kJ per mol of NaCl.

N_{NaCl}	ρ	$G_{solution}$	$A^{integral}$	$A^{res}_{LJ,ref}$	pV	$A^{id}_{solution}$	m / mol kg^{-1}	$\mu^{solution}_{NaCl}$ / kJ mol^{-1}
5	0.03399	-14159.23	-12586.08	1590.08	0.49	-3163.72	1.03	-382.7
7	0.03417	-15696.73	-14095.41	1639.72	0.49	-3241.53	1.44	-380.6
10	0.03444	-17993.39	-16354.88	1714.42	0.50	-3353.43	2.06	-378.1
12	0.03460	-19513.88	-17851.50	1762.97	0.51	-3425.86	2.47	-376.7
15	0.03481	-21818.82	-20119.88	1832.75	0.52	-3532.21	3.08	-374.9
17	0.03495	-23320.83	-21600.19	1880.33	0.53	-3601.50	3.50	-373.8
20	0.03512	-25602.13	-23844.81	1946.41	0.54	-3704.27	4.11	-372.3
22	0.03523	-27137.44	-25357.01	1990.71	0.54	-3771.68	4.52	-371.3
25	0.03536	-29404.79	-27585.35	2052.06	0.55	-3872.05	5.14	-370.0
27	0.03544	-30919.06	-29073.75	2092.35	0.55	-3938.21	5.55	-369.2
30	0.03553	-33197.07	-31308.67	2147.97	0.56	-4036.93	6.17	-368.0
32	0.03558	-34690.91	-32772.77	2183.55	0.56	-4102.25	6.58	-367.2
35	0.03563	-36960.99	-34994.23	2232.51	0.58	-4199.85	7.20	-366.1
37	0.03565	-38433.87	-36432.55	2262.73	0.59	-4264.64	7.61	-365.4

There is still an issue we would like to point out. Paluch *et al.* estimated the solubility of the TF force field to be $0.8\ m$ from free energy calculations [64]. The deviation from the value of the solubility reported in this work ($4.3\ m$) is quite large. Let us investigate the origin of the discrepancy. In Fig. 11.7 the chemical potential of the NaCl solution obtained by Paluch *et al.* [64] is compared with the results of this work and those of Lisal *et al.* [63]. The results of Paluch *et al.* [64] are systematically higher than those obtained by Lisal and us. The difference is not large, but significant (of about 5 kJ/mol). However, only this difference is not sufficient to explain the difference between the solubility of Paluch ($0.8\ m$) and that of this work ($4.3\ m$). There must be something else. The main difference is that the chemical potential obtained by Paluch *et al.* for the pure NaCl solid is 2 k_BT lower than our value. This difference is not due to the accuracy of the free energy calculations of the solid since, as we discussed above, the typical uncertainty in the free energy of the solid phase is of about 0.05 Nk_BT units. The fact that the difference between the two set of values is 2 k_BT is striking. We ascribe the origin of the discrepancy to the inclussion by Paluch *et al.*[64] of an additional -2 k_BT term when computing the chemical potential of the solid phase (see Eq. (7) of their paper [64]). In our opinion this additional -2 k_BT should not be included. In fact by adding a -2 k_BT to our solid free energies the predicted solubility of the SD and JC would have been extremely small and completely different from the value obtained from direct coexistence simulations.

Let us finish this section with a comparison of the chemical potential of NaCl in water as predicted by the different force fields to the experimental results. This comparison is shown in Fig. 11.8. As it can be seen, the chemical potential of the JC force field agrees reasonably well with the experimental results. The results from TF and SD are not so good as they tend to overestimate the chemical potential. The results of the TF and SD are practically identical

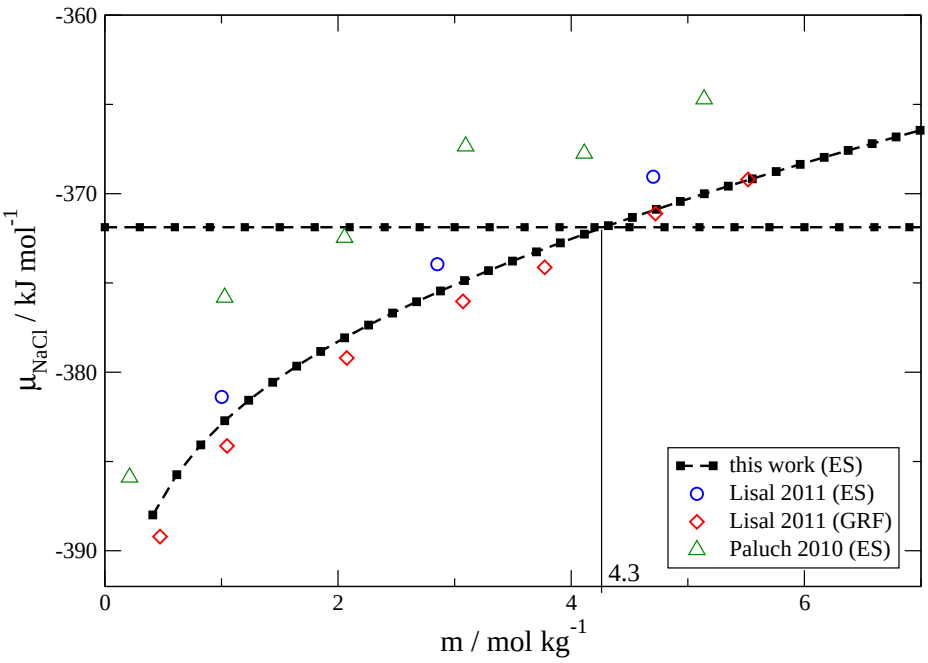

Figura 11.7: Chemical potential of NaCl versus molal concentration for the Tosi–Fumi (black dashed line with filled squares) at 298 K and 1 bar. The values computed by Lisal *et al.* [63] and Paluch *et al.* [64] are also plotted (as indicated in the legend). ES stands for Ewald sums and GRF for generalized reaction field method. Horizontal line represents the solid chemical potential.

up to a concentration of $2\ m$, and are somewhat different for higher concentrations. As it was stated above, the ion–water interaction of the TF and SD force fields are identical. That explains that both models yields practically identical results at low salt concentrations, where the ion–ion interaction are virtually neglected. It seems that the ion–ion interactions start to affect the magnitude of the chemical potential for concentrations above $2\ m$. An interesting conclusion of that is that for salts with very low solubility in water (i.e below $2\ m$) the ion–ion interactions will play a minor role in determining the chemical potential of the salt in water (although, of course they will play a major role in determining the chemical potential of the pure solid phase). That means that for salts with low solubility in water the path to develop a force field is to adjust the ion–ion interactions, first by forcing the model to reproduce the experimental properties of the solid (density and chemical potential), and afterwards to adjust the ion–water interactions to reproduce the experimental values of the chemical potential of the salt in water at low concentrations (or eventually at infinite dilution) . A force field developed in this way will reproduce the chemical potential of both phases and the experimental value of the solubility. When the solubility of the salt in water is high, things are more difficult since the ion–ion interactions will be important not only in determining the chemical potential of the solid phase but also in determining the chemical potential of the salt in water. In any case, it seems a sensible approach to adjust the ion–ion interactions using mostly properties of the pure solid and to adjust the ion–water interactions using the properties of the salt in water [398–400]. It seems that combining rules will not be very useful in the optimization process, and probably the best route is to adjust simultaneously the A-A, X-X and A-X interactions, rather than to obtain the A-X interactions from combination rules. In this respect it is interesting to note that in the TF force field the parameters for the A-X interactions were optimized and not obtained

from any combination rule. Even assuming that the model to describe water is fixed, and assuming two parameters for each interaction, one needs in total 10 parameters to describe all interactions of the system (A-A,X-X,A-X, A–water, X–water).

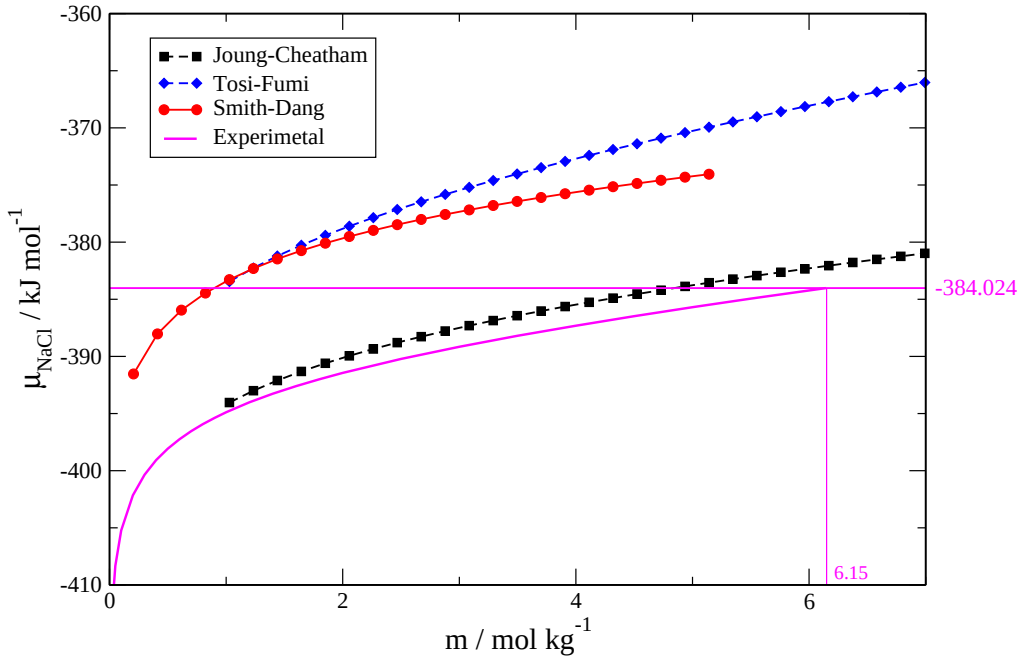

Figura 11.8: Chemical potential of NaCl versus molar concentration for all studied models compared to the experimental values. The dashed horizontal line represents the experimental solid chemical potential. Experimental values were obtained with the mean activity coefficients tabulated in Ref. [401] and the chemical potential at infinite dilution (Ref. [395]).

Conclusions

In this work we have determined the solubility of NaCl in water using computer simulations. Three different force fields were used, and two different methodologies: free energy calculations and direct coexistence simulations. The main conclusions of this work can be summarized as follows:

- The chemical potential of NaCl in the solid phase can be computed with an accuracy of about 0.05 Nk_BT units by using the Einstein crystal/molecule methodology. The SD and JC force fields predict nicely the experimental value of the chemical potential of NaCl in the solid phase. The TF force field overestimates the experimental value.

- The JC force field predicts reasonably well the chemical potential of NaCl in water. The predictions from the TF and SD models are quite similar at low cocentrations and differ somewhat above 2m (where ion–ion interactions become more important). The TF and SD force fields over estimates the experimental value of the chemical potential. The chemical potentials for NaCl in water obtained in this work agree quite well with the values recently obtained by Lisal *et al.* [63] for the three force fields considered.

- The solubilities of the SD, TS and JC models evaluated from free energy calculations are $0.9\ m$, $4.3\ m$ and $4.8\ m$, respectively. The experimental value is $6.15\ m$. The solubility changes quite significantly with the force field. The SD predicts well the chemical potential of the solid and poorly that of the solution, the final result is a poor estimate of the solubility. The JC predicts quite well the chemical potential of the solid and reasonably well the chemical potential of the solution, so that it yields a reasonable estimate of the solubility. The TF does not predict correctly neither the chemical potential of the solid nor that of the fluid phase but still is able to yield a reasonable prediction for the solubility.

- The solubilities of the SD and JC have also been determined from direct coexistence simulations. Runs of 2.8 microseconds were needed to reach a plateau in the concentration of salt. The solubilities found from this route were respectivelty, $1\ m$ and $0.6\ m$ above the values from free energy calculations. Taking into account the difficulties encountered in all the calculations we find the agreement with the free energy route reasonable. However, further work is needed to clarify the origin of the difference (longer runs may be needed in the direct coexistence simulations, or finite size effects in the free energy calculations can affect the value of the chemical potential of the solid). For the time being we recommended value of the solubility is $5.1(3)\ m$ for the JC force field and $1.4(5)\ m$ for the SD force field.

- The solubility of the JC and SD models can be estimated quite well by computing the chemical potential of the solution and assuming that the chemical potential of the model in the solid phase is identical to the experimental value. That was the approach followed by Lisal *et al.* [63] which seems to yield correct results for these two force fields. However, this approach would yield an incorrect value of the solubility for the TF force field, as the chemical potential for the TF force field in the solid phase does not correspond to the experimental value. The assumption that the chemical potential of the solid phase matches the experimental value (implicitly adopted by Lisal *et al.* [63]) will only work for certain force fields but it will fail for others.

- The solubility for the TF force field obtained in this work ($4.3\ m$), somewhat lower than that obtained in our previous work ($5.4(8)\ m$). Longer runs and a more sensible data analysis have increased the accuracy of the calculations. The solubility found in this work still deviates signficantly from the estimate reported by Paluch *et al.* [64]. This is due to a higher value of the chemical potential of NaCl in water reported by Paluch *et al.* as compared to the values reported by Lisal *et al.* [63] and reported in this work. Secondly and more significantly, the chemical potential of the solid phase reported by Paluch is 2 k_BT units lower than the value reported here.

The reader may have the impression that finally there is a reliable force field for NaCl the Joung-Cheatham model. From the results presented so far this is a reasonable conclusion. However, things are not that simple. By using direct coexistence simulations we have determined the melting point of NaCl (i.e the equilibrium between pure NaCl in the solid phase and pure NaCl in the liquid phase). We have found[389] that the melting point was 1286(10) K which is above the experimental value of 1074 K. Thus, even though the JC force field describes well the experimental value of the chemical potential of the NaCl solid at room temperature it yields an incorrect melting point (either because the performance of the model deteriorates at high temperatures or because the model fails to describe the NaCl melt). Remember that the TF force reproduces almost exactly the melting point of NaCl [123, 402]. Definitely, things

are complicated and it is difficult to find a force field that match all these properties. Hopefully one should expect progress on this area of research in the future.

The studies of the solubility of salts in water are scarce, and basically there are only 7 papers dealing with this issue, the seminal work of Ferrario *et al.* [61], the two papers of Lisal *et al.* [63, 403], the paper of Paluch *et al.* [64], the work of Joung and Cheatham [65], and the two studies of our group, this paper and our previous work [137]. It is clear that the interest in the problem has increased significantly in the last five years. Likely more studies will soon come on this interesting problem. It would be of interest to develop a force field for NaCl in water able to describe the experimental value of the solubility, and also develop models for ions obtained either from first principles [404] or from polarizable models [405].

Acknowledgments

This work was funded by grants FIS2010-16159, from the DGI (Spain), MODELICO-P2009/ESP/1691 from the CAM, and 910570 from the UCM. J. L. Aragones would like to thank the MEC by the award of FPI pre-doctoral grant. We would like to thanks C. McBride for a critical reading of the manuscript and J.L.F. Abascal for helpfull discussions.

APPENDIX

Evaluating the contribution of the G_1 term to the chemical potential

The chemical potential of NaCl in the solution is given by the expression:

$$\mu_{NaCl}^{solution} = \left(\frac{\partial G_{solution}}{\partial N_{NaCl}}\right)_{T,p,N_{H_2O}} \tag{11.23}$$

where $G_{solution}$ is the Gibbs free energy (see eq. 11.14). We have splitted $G_{solution}$ in two terms, the first one $G_1 = A_{solution}^{id}$ contains the ideal gas contribution to the Helmholtz free energy of the system. The second one G_2 contained the other contributions to the Gibbs free energy, the residual contribution to the Helmholtz free energy and the p$V_{solution}$ term. The contribution of the G_1 term to the chemical potential will be denoted as $\mu_{NaCl,1}^{solution}$ and is given by :

$$\mu_{NaCl,1}^{solution} = \left(\frac{\partial A_{solution}^{id}}{\partial N_{NaCl}}\right)_{T,p,N_{H_2O}} \tag{11.24}$$

The term $A_{solution}^{id}$ is given by Eq. 11.11. By taking the derivative of $A_{solution}^{id}$ with respect to the number of molecules of NaCl N_{NaCl} while keeping T and p constant one obtains:

$$\left(\frac{\partial (A_{solution}^{id}/k_BT)}{\partial N_{NaCl}}\right)_{T,p,N_{H_2O}} = 2\ln\left(\rho_{NaCl}\right) - 2 + V\left(2\rho'_{NaCl} + \rho'_{H_2O}\right) \tag{11.25}$$

where ρ'_{H_2O} stands for $\left(\frac{\partial \rho_{H_2O}}{\partial N_{NaCl}}\right)_{T,p,N_{H_2O}}$, being $\rho_i = \frac{N_i}{V}$ the number density of component i. The term ρ'_{H_2O} can be written as:

$$\left(\frac{\partial \rho_{H_2O}}{\partial N_{NaCl}}\right)_{T,p,N_{H_2O}} = \frac{\partial\left(\frac{N_{H_2O}}{V}\right)}{\partial N_{NaCl}} = -\frac{N_{H_2O}\left(\frac{\partial V}{\partial N_{NaCl}}\right)}{V^2} = -\frac{N_{H_2O}\bar{V}}{V^2} \tag{11.26}$$

where V stands for the volume of the system and $\bar{V}$ stands for the partial molar volume of NaCl. Similarly, the term ρ'_{NaCl}, that corresponds to $\left(\frac{\partial \rho_{NaCl}}{\partial N_{NaCl}}\right)$, can be written as:

$$\left(\frac{\partial \rho_{NaCl}}{\partial N_{NaCl}}\right)_{T,p,N_{H_2O}} = \frac{1}{V} - \frac{N_{NaCl}\bar{V}}{V^2} \tag{11.27}$$

Taking into account the expressions for ρ'_{NaCl} and ρ'_{H_2O} the last term of Eq.K.3 can be written as:

$$\left(2\rho'_{NaCl} + \rho'_{H_2O}\right) = \frac{1}{V}\left(\frac{-2N_{NaCl}\bar{V}}{V} - \frac{N_{H_2O}\bar{V}}{V} + 2\right) \tag{11.28}$$

so that the final expression for $\mu_{NaCl,1}^{solution}$ is:

$$\left(\frac{\partial (A^{id}/k_BT)}{\partial N_{NaCl}}\right)_{T,p,N_{H_2O}} = 2\ln\left(\rho_{NaCl}\right) - \bar{V}\left(2\rho_{NaCl} + \rho_{H_2O}\right) \tag{11.29}$$

Converting the chemical potential to experimental units.

Let us describe briefly how to convert chemical potentials from the units of this work (which implicitly used 1 Å for the thermal De Broglie wave length and one for the internal partition function to one for all species) to the units used in experimental work which are also the units used by Lisal *et al.* [63] when describing NaCl models in water. Firstly one should use the experimental values of the standard chemical potentials of Na^+ y Cl^-, as taken from NIST-JANAF [395] tables which amount to ($\mu_{Na^+}{}^o = 574.317\ kJmol^{-1}$ and $\mu_{Cl^-}{}^o = -240.167 kJmol^{-1}$) . Implicitly our choice of setting the intramolecular partition function for all species equal to one means that these values were zero in our criterion. We can simply add the sum of these two terms to our chemical potentials. The second point is that our reference state is a system with a particle per Å^3, whereas experimentally the reference state is the volume occupy by a molecule per (kT/p^0) where $p^0 = 1bar$ is the reference pressure. Therefore, the chemical potential of this work can be converted into experimental units by simply adding the constant C :

$$C(kJ/mol) = \mu_{Na^+}(kJ/mol) + \mu_{Cl^-}(kJ/mol) + \frac{2RT}{1000}\ln(k_B T 10^{25}) \qquad (11.30)$$

(where the 10^{25} term arises from a 10^{30} term to convert from m^3 to Å^3 divided by a 10^5 term which 1 bar of pressure in Pascals). By replacing the value of R (8.314 $J/mol/K$) and k_B ($1.3805\ \ 10^{-23} J/K$) one obtains $C = 386.8 kJ/mol$. Thus the chemical potentials of this work can be converted into the units used in experimental work by simply adding this constant C.

Comparing our Monte Carlo to Molecular Dynamics

We have also compared the results obtained using our own Monte Carlo program to those obtained from Molecular Dynamic simulations obtained running Gromacs. In both cases we used NpT simulations at 298 K and 1 bar for a solution composed by 270 water molecules and 10 NaCl molecules (20 ions), $N = 290$. Results are shown in Table 11.11 for JC force field (for a solution of NaCl in water). As it can be the agreement for the densities and internal energies is quite good.

Tabla 11.11: Comparison between number densities and residual internal energies (per mol of particles) obtained with Gromacs and with our MC program for the JC force field at $298K$ and 1 bar.

Method	U (kcal/mol)	ρ(N / Å^{-3})
	Joung-Cheatham	
GROMACS	-17.01	0.0347
MC	-17.02	0.0348
	Smith-Dang	
GROMACS	-16.86	0.0344
MC	-16.88	0.0345

Chemical potential of a binary mixture using a simple model

To show the correctness of the thermodynamic route used in this work to determine the chemical potential of NaCl in water, it is useful to consider a very simple model, for which the calculations can be implemented easily. We shall consider a binary mixture of hard bodies described with a virial expansion , truncated at the second virial coefficient. The expression for the compressibility factor ($Z = p/(\rho kT)$) of the mixture is given by :

$$Z = 1 + B_2\rho \tag{11.31}$$

where $\rho = (N/V) = (N_1 + N_2)/V$ is the total number density of components 1 and 2 and the second virial coefficient of the mixture is defined as :

$$B_2 = \sum\sum B_{ij}x_ix_j \tag{11.32}$$

being x_i the molar fraction of component i and B_{ij} the second virial coefficient between a molecule of type i and a molecule of type j. Since we are assuming hard bodies the virial coefficients will always be positive. The residual contribution to the Helmholtz free energy can be obtained from the expression:

$$A^{res}/(NkT) = \int_0^\rho \frac{(Z-1)}{\rho'}d\rho' = B_2\rho \tag{11.33}$$

The ideal term to the Helmholtz free energy of the mixture is given by :

$$A^{id}/(NkT) = x_1\ln(\rho_1\sigma^3) + x_2ln(\rho_2\sigma^3) - 1 \tag{11.34}$$

where we have assumed that the De Broglie thermal length of the two species is identical and we have set its value to a certain characteristic molecular length σ that will be used as unit of length $\sigma = 1$.

By adding together the ideal and residual terms one obtains for A:

$$A = N_1kT\ln(\rho_1\sigma^3) + N_2kT\ln(\rho_2\sigma^3) - N_1kT - N_2kT + NkTB_2\rho \tag{11.35}$$

Let us compute the chemical potential of component 2, from the expression :

$$\mu_2 = (\frac{\partial A}{\partial N_2})_{T,V,N_1} \tag{11.36}$$

Evaluating the derivatives analytically one obtains:

$$\mu_2 = kT\ln(\rho_2\sigma^3) + 2kT(B_{11}\rho_2 + B_{12}\rho_1) \tag{11.37}$$

The chemical potential can also be obtained from the derivative of the Gibbs free energy $G = A^{id} + A^{res} + pV$ with respect to N_2 at constant T and p :

$$\mu_2 = \left(\frac{\partial G}{\partial N_2}\right)_{T,p,N_1} \tag{11.38}$$

where the derivative is performed at constant pressure. For this simple mixture, the volume of the system at a certain T, p, N_1 and N_2 can be obtained by simply solving a second order polynomial equation. Once this is done, the A^{id}, A^{res} and pV terms are computed trivially from the expression described above. That allows one to compute the Gibbs free energy of the system G as a function of N_2 (for a certain fixed values of T,p,N_1). The derivative of G

with respect to N_2 provides the chemical potential μ_2 from this route. Obviously the two routes (differenciating A with respect to N_2 while keeping T,V and N_1 constant and differenciating G with respect to N_2 while keeping T,p and N_1 constant should be equivalent and should yield the same value of the chemical potential). Let us consider a system with $B_{11}/\sigma^3 = 1$,$B_{22}/\sigma^3 = 3$,$B_{12}/\sigma^3 = 1.6$. Let us assume that $N_1 = 270$ and $N_2 = 50$ and $p/(kT/\sigma^3) = 1$. From the derivative of A , at constant T,V and N_1 we obtained $\mu_2/(kT) = -0.26024$ (-2.39108 being the contribution of the ideal gas term and 2.13084 of the residual free energy term). From the derivative of G , at constant T,p and N_1 we obtained $\mu_2/(kT) = -0.26024$ (-3.68794 from the ideal gas term, 1.21385 from the residual free energy term and 2.21385 from the pV term). Obviously the chemical potential is the same regardless of the thermodynamic route. Notice that the derivative of A is done at constant T,V and N_1, and the derivative of G is done at constant T,p and N_1. In this work we have always evaluated the chemical potential by performing derivatives at constant T,p and N_1 (i.e the number of molecules of water).

CAPÍTULO 12

Calculation of the melting point of alkali halides by means of computer simulations

J.L. Aragones[1], **E. Sanz**[1], **C. Valeriani**[1] **and C. Vega**[1]

[1] *Dep. Química Física, Fac. Química, Universidad Complutense de Madrid, 28040,Madrid, Spain*

Journal of Chemical Physics, **Enviado***, (2012)*

Abstract

In this manuscript we study the liquid-solid coexistence of NaCl-type alkali halides, described by interaction potentials such as Tosi-Fumi (TF), Smith-Dang (SD) and Joung-Cheatham (JC), and compute their melting temperature (T_m) at 1 bar via three independent routes: 1) liquid/solid direct coexistence, 2) free-energy calculations and 3) Hamiltonian Gibbs-Duhem integration. The melting points obtained by the three routes are consistent with each oter. The calculated T_m of the Tosi-Fumi model of NaCl is in good agreement with the experimental value as well as other numerical calculations. However, the other two models considered for NaCl; SD and JC, overestimate the melting temperature of NaCl by more than 200 K. We have also computed the melting temperature of other alkali halides using the Tosi-Fumi interaction potential and observed that the predictions are not always as close to the experimental values as they are for NaCl. It seems that there is still room for improvement in the area of force-fields for alkaline halides, given that most of models are still unable to describe a simple yet important property such as the melting point.

Introduction

Alkali halides are inorganic compounds composed of an alkali metal and a halogen. The most abundant by far is sodium chloride (NaCl). NaCl in its solid form has a cubic structure (usually denoted as NaCl structure) and melts at a relatively high temperature (around 1070 K at ambient pressure) as a consequence of its high lattice energy. NaCl dissolves in polar solvents, such as water, to give ionic solutions that contain highly solvated anions and cations, relevant for the functioning of biological organisms.

In the last century, there have been many thorough studies aimed to quantitatively describe physical properties of alkali halides. Back in 1919, Born developed a numerical model to estimate the energy of an ionic crystal [406]. Later on, on the one side Pauling, based on Born's primitive model, studied the effect of the ions'sizes on ionic salts [407, 408], and on the other side Mayer evaluated the role of polarizability and dispersive forces on alkali halides [384] and proposed, together with Huggins, a generalization of Born's repulsive

energy [385]. More recently, several ion-ion interaction potentials have been developed in order to numerically simulate alkali halides. In 1962 Tosi and Fumi, fitting the Huggins-Mayer dispersive energy to crystallographic data, proposed an empirical potential parametrizing the repulsive part of the NaCl alkali halide interactions [386]. The Tosi-Fumi (TF) potential whose adventages and disadventages have been underlined by Lewis and coworkers [409] was used for the first time in a numerical simulation by Adams and McDonald [410], who simulated alkali halides obtaining a remarkably good agreement between numerical simulations and experimental results. In recent years, the Tosi-Fumi potential has also been used to study liquid/solid phase transitions in alkali halides: on the one side, Valeriani *et al.* studied homogeneous crystal nucleation in molten NaCl [388] and Chen and Zhu carried out homogeneous nucleation studies of other alkali halides, such as KBr [411] and NaBr [412]. On the other side, Zykova-Timan *et al.* studied packing issues related to the interfacial free-energy between the liquid and solid phases [413, 414]. In all these works it was implicitly relevant a knowledge of the melting temperature of the alkali halide at the given pressure. In fact the melting point of NaCl has been determined for the TF model by several groups. In 2003, Anwar *et al.* determined by free energy calculations the melting temperature of NaCl for the Tosi-Fumi model [123]. Similar results were obtained later on by Eike *et al.* [415] and Mastny *et al.* [416]. There are also experimental studies where the melting curves of several alkali halides were determined. Also molecular simulations were carried out to verify and analyze the experimental results [417, 418]. In these works the melting temperature was calculated by direct heating of the solid, hence the thermal instability limit rather that the melting temperature was calculated [419]. Later on, Belonoshko *et al.* performed two-phase simulations of NaCl and LiF to determine T_m [419, 420].

Besides TF, another popular model used to describe NaCl is that was proposed more recently by Smith and Dang (SD) [390, 391] who presented an interaction potential where the ion-ion interactions were Lennard-Jones like. This model potential has become quite popular when studying NaCl in water solutions, even though the properties of its solid phase remain unknown. Similarly to the SD potential, Joung-Cheatham (JC) presented another interaction potential where the ion-ion interactions were Lennard-Jones like and proposed several NaCl force-fields tailored to be used in a water solution [383]. Somewhat surprisingly the melting point of the SD and JC NaCl potentials are still unknown.

The study of alkali halides in water solutions has also been extensive. Simulations of alkali halides dissolved in water have proved useful to study thermodynamic mixing properties, such as the cryoscopic descent of the melting temperature [375]. The properties of alkali halides solutions have been studied at low temperatures in order to localize the hypothesized second critical point of water [163, 366, 369]. The solubility of NaCl in water has also received certain interest [63, 65, 137, 403, 421]. Notice that in order to determine the solubility of a salt, the chemical potential of the solid should be known.

Thus, it is of interest to quantitatively compare several interaction potentials in order to estimate their efficiency in mimicking the properties of NaCl-type alkali halides. To this aim, in this manuscript we evaluate the liquid-solid equilibrium properties of such systems. Perform the study of the melting temperature (at normal pressure) for three alkali halides, emphasizing NaCl, for three interaction models: the Born-Mayer-Huggins-Tosi-Fumi potential (TF) [384–387], the Smith-Dang potential (SD) [390] and the Joung-Cheatham (JC) potential [383]. All three are two-body and non-polarizable model potentials, characterized by repulsive term, a short-range attraction and a long-range Coulombic interaction term. We have calculated the melting temperature (T_m) of NaCl for these potentials using three independent routes: 1) liquid/solid direct coexistence 2) free-energy calculations and 3) Hamiltonian Gibbs-Duhem integration. We have found that the value obtained for the T_m of the TF/NaCl is in good agree-

ment with the experiment, different from the values calculated for the SD/NaCl and JC/NaCl. Therefore we can conclude that the TF/NaCl model is the most suitable for studies of pure NaCl. Using Hamiltonian Gibbs-Duhem integration we have also evaluated T_m for other TF/alkali halides. We have observed that the quality of the results obtained with the TF potential depends on the alkali halide chosen. The TF model provides good predictions for alkali halides that involve K^+, Cl^-, Na^+, Br^- and Li^+ ions, whereas the predictions are poor for alkali halides involving Rb^+ or F^- ions.

The manuscript is organized as follows: we first introduce the interaction potentials of the alkali halides under study, i.e. Born-Mayer-Huggins-Tosi-Fumi potential (TF), the Smith-Dang potential (SD) and the Joung-Cheatham (JC) potential. Then we describe the three simulation routes followed to compute their melting temperature: 1) the liquid/solid direct coexistence 2) the Einstein crystal/molecule for the solid and the thermodynamic integration for the liquid; 3) the Hamiltonian Gibbs-Duhem integration. To conclude we will present our results obtained for different alkali halides.

Simulation methods

The interaction potentials we used are two-body and non-polarizable model potentials, each of them characterized by a repulsive term, a short-range attractive and a long-range Coulomb interaction term. The TF model potential has the following form:

$$U(r_{ij}) = A_{ij}e^{-r_{ij}/\rho_{ij}} - \frac{C_{ij}}{r_{ij}^6} - \frac{D_{ij}}{r_{ij}^8} + \frac{q_i q_j}{4\pi\epsilon_o r_{ij}} \tag{12.1}$$

where r_{ij} is the distance between two ions with charge $q_{i,j}$, the first term is the Born-Mayer repulsive term; $-\frac{C_{ij}}{r_{ij}^6}$ and $-\frac{D_{ij}}{r_{ij}^8}$ are the Van der Waals attractive interaction terms; the last term corresponds to the Coulomb interaction. The parameters A_{ij}, ρ_{ij}, C_{ij} and D_{ij} are given in Table 12.1 for the TF/alkali halides we will discuss in the paper.

Both the SD and the JC model potentials can be written using the following expression:

$$U(r_{ij}) = 4\epsilon\left[\left(\frac{\sigma_{ij}}{r_{ij}}\right)^{12} - \left(\frac{\sigma_{ij}}{r_{ij}}\right)^{6}\right] + \frac{q_i q_j}{4\pi\epsilon_o r_{ij}} \tag{12.2}$$

where r_{ij} is the distance between two ions with charge $q_{i,j}$. The first term is Lennard-Jones-like, and its parameters are given in Table 12.2. The last term in Eq. 12.2 corresponds to the Coulomb interaction. For the JC potential, we are going to use the parameters introduced to simulate NaCl in SPC/E water [383].

For the SD and JC the crossed interaction parameters are obtained using the Lorentz-Berthelot combining rules [422, 423]. It is interesting to point that the TF model was developed to study ionic crystals and pure alkaly halides in the solid phase whereas the SD was obtained to model Na^+ and Cl^- in water. The JC was fitted to model NaCl both in the solid phase and in aqueous solutions. In what follows, we shall refer to ions as particles.

In this manuscript, we compute the melting temperature at 1 bar for different alkali halides. When computing T_m for the TF/NaCl interaction potential, we follow three independent routes: 1) liquid/solid direct coexistence, 2) free-energy calculations and 3)Hamiltonian Gibbs-Duhem integration. For the SD/NaCl and JC/NaCl and for other TF/alkali halides we use the first and the third route.

Tabla 12.1: Parameters of the TF ion-ion interaction potential for all alkali halides from Ref. [410] with units A_{ij}([kj/mol]), ρ_{ij} ([]), C_{ij} ([$^6kj/mol$]) and D_{ij} ([$^8kj/mol$]).

	A_{ij}	ρ_{ij}	C_{ij}	D_{ij}		A_{ij}	ρ_{ij}	C_{ij}	D_{ij}
Na^+/Na^+	40870.5	0.317	101.2	48.2	K^+-K^+	146278.3	0.338	1463.4	1445.3
Na^+/Cl^-	121075.5	0.317	674.5	837.0	K^+-F^-	50507.9	0.338	1174.3	1264.6
Cl^-/Cl^-	336258.6	0.317	6985.7	14031.6	F^--F^-	16349.7	0.338	1120.1	1324.9
K^+-K^+	150084.5	0.337	1463.4	1445.3	K^+-K^+	158069.4	0.335	1463.4	1445.3
K^+-Cl^-	172444.1	0.337	2890.6	4396.2	K^+-Br^-	269108.5	0.335	3613.3	5961.9
Cl^--Cl^-	185751.3	0.337	7497.6	15055.3	Br^--Br^-	429515.0	0.335	12405.6	28304.0
Na^+-Na^+	24805.3	0.340	101.2	48.2	Rb^+-Rb^+	331402.3	0.335	3577.1	4938.2
Na^+-Br^-	98869.2	0.340	843.1	1144.2	Rb^+-Br^-	389655.9	0.335	5961.9	10839.8
Br^--Br^-	369443.6	0.340	11803.4	27099.6	Br^--Br^-	429515.0	0.335	12947.6	29508.5
Rb^+-Rb^+	549956.0	0.318	3577.1	4938.2	Rb^+-Rb^+	405668.1	0.328	3577.1	4938.2
Rb^+-Cl^-	437206.4	0.318	4757.5	8069.7	Rb^+-F^-	93549.4	0.328	1866.9	2408.9
Cl^--Cl^-	325849.0	0.318	7828.8	15657.6	F^--F^-	20224.7	0.328	1138.2	1385.1
Li^+-Li^+	4809.7	0.342	4.4	1.8	Na^+-Na^+	30557.7	0.330	101.2	48.2
Li^+-Cl^-	31327.1	0.342	120.4	144.5	Na^+-F^-	25122.0	0.330	271.0	228.8
Cl^--Cl^-	161885.0	0.342	6684.6	13429.4	F^--F^-	19362.4	0.330	993.7	1204.4

Tabla 12.2: Parameters of the SD (left-hand side) and JC (right-hand side) ion-ion interaction potentials.

	(**SD**) ϵ/k$_B$[K]	σ_{ij}[]	(**JC**) ϵ/k$_B$[K]	σ_{ij}[]
Na^+/Na^+	65.42	2.35	177.457	2.159
Cl^-/Cl^-	50.32	4.40	6.434	4.830
Na^+/Cl^-	57.375	3.375	33.789	3.495

Route 1. Liquid/solid direct coexistence

The first route we follow to compute the melting temperature is by means of the liquid/solid direct coexistence, originally proposed in Ref. [143, 242, 424–426].

To start with, we generate an equilibrated configuration of the NaCl solid phase in contact with its liquid. The procedure we follow to prepare the solid is: first, we obtain an equilibrated configuration of the solid phase at the equilibrium density at 1 bar and the temperature of interest (T$_{ini}$) in an NpT simulation. The liquid is obtained by melting the solid and keeping the box shape at the solid equilibrium density (in the NVT ensemble). Then the liquid phase is equilibrated in an NpT simulation where only box-length changes are allowed along the x-axis (the one perpendicular to the solid-liquid interface), so that the area of the yz-plane remains unchanged. Given that the two phases have been equilibrated with the same y-side and z-side of the simulation box, we "glue"them together along the x-axis allowing an empty layer of 3.5 Å between them to avoid overlapping between solid and liquid particles. Finally, the prepared liquid-solid configuration was equilibrated for a short time in an NpT ensemble

at the temperature of T_{ini}, so that the empty gap between the two phases is naturally filled by the liquid particles.

After having prepared the liquid-solid configuration, we run several anisotropic NpT simulations at different temperatures and always at a pressure of 1 bar. Each box side changes independly, in order not to cause stress in the solid phase. Depending on the temperature, the system evolves towards complete freezing or melting of the sample. Since we do not know the location of the melting temperature, we simulate the system in a wide range of temperatures and identify the melting temperature T_m as the average of the highest temperature at which the liquid freezes and the lowest temperature at which the solid melts.

Route 2. Free-energy calculations

In this route, we first compute the Helmholtz free-energy of both the solid and the liquid phase; next, we estimate the Gibbs free-energy (G) by simply adding pV. To compute the melting temperature we perform thermodynamic integration as a function of temperature at constant pressure to evaluate where the chemical potentials ($\mu = G/N$) of both phases coincide.

To estimate the free-energy of the bulk solid phase we use the Einstein crystal [115] and the Einstein molecule methods [234, 268]. Both methods are based on the calculation of the free-energy difference between the target solid and a reference system at the solid equilibrium-density for the given thermodynamic conditions (obtained with an NpT simulation). The reference system of the Einstein crystal method consists of an ideal solid whose free-energy can be analytically computed (an "Einstein crystal" with the center of mass fixed, the inter-molecular interactions are neglected and particles are bound to their lattice positions by a harmonic potential). The Einstein molecule method differs from the previous one due to the fact that we fix only the position of one molecule: thus, the reference system is now the Einstein crystal with one fixed molecule.

Thermodynamic integration is performed in two steps [133]: 1) we evaluate the free-energy difference (Δ A_1) between the ideal Einstein crystal, where particles, without any inter-molecular interaction are connected to their equilibrium lattice positions by harmonic springs (with strength Λ_E), and the Einstein crystal in which particles interact through the Hamiltonian of the original solid ("interacting" Einstein crystal); 2) next we calculate the free-energy difference (Δ A_2) between the interacting Einstein crystal and the original solid, by means of thermodynamic integration: $U(\lambda) = \lambda U_{sol} + (1-\lambda)(U_{Ein-id} + U_{sol})$), where U_{Ein-id} represents the energy of the interacting Einstein crystal, U_{sol} the one of the original solid, and λ the coupling parameter that allows us to integrate from the interacting Einstein crystal ($\lambda = 0$) to the desired solid ($\lambda = 1$). The final expression of the Helmholtz free-energy $A_{sol}^{NaCl}(T,V)$ coming from the Einstein crystal/molecule calculations is [133]:

$$A_{sol}^{NaCl}(T,V) = A_0(T,V) + \Delta A_1(T,V) + \Delta A_2(T,V) \tag{12.3}$$

where A_0 is the free energy of the reference system, whose analytical expression is slightly different in the Einstein crystal and Einstein molecule (see Ref. [133]). The expression used to compute ΔA_1 and ΔA_2, are the same in the Einstein crystal and Einstein molecule methods (the only difference being the choice of the point that remains fixed in the simulations, whether the system's center of mass or a reference particle's center of mass). It has been shown that, since the free energy of a solid is uniquely defined, its value does not depend on the method used to compute it and the two methodologies give exactly the same results [133]. It is convenient to set the thermal De Broglie wave length of all species to 1 Å, and the internal partition

functions of all species to one. These arbitrary choices affects the value of the free energy but does not affect phase equilibria (provided the same choice is adopted in all phases).

To estimate the free-energy of the bulk liquid we used Hamiltonian thermodynamic integration as in Ref. [123], calculating the free-energy difference between the liquid alkali halide and a reference liquid of known free-energy, for which we choose a Lennard-Jones (LJ). Starting from an equilibrated NaCl liquid, we perturb the Hamiltonian of the system so that each ion is gradually transformed into a LJ atom. The path connecting both states is given by:

$$U(\lambda) = \lambda U^{LJ} + (1-\lambda)U^{NaCl} \tag{12.4}$$

where U^{LJ}/U^{NaCl} are the total energies of the Lennard Jones and NaCl fluids, respectively, and λ is the coupling parameter ($\lambda = 0$ corresponds to NaCl whereas λ=1 to a LJ fluid). The Helmholtz free-energy of a NaCl (A_{liq}^{NaCl}) is computed as:

$$A_{liq}^{LJ}(T,V) = A_{liq}^{NaCl}(T,V) + \int_{\lambda=0}^{\lambda=1} \langle U^{LJ} - U^{NaCl} \rangle_{N,V,T,\lambda} d\lambda = A_{liq}^{NaCl}(T,V) + \Delta A_{liq}^{LJ}(T,V) \tag{12.5}$$

Since the Lennard-Jones free-energy (A_{liq}^{LJ}) is already known [114] and the integral in the Eq. 12.5 (ΔA_{liq}^{LJ}) can be numerically evaluated, we can determine the free-energy A_{liq}^{NaCl} of the liquid alkali halide.

In order to estimate the integral in Eq. 12.5, we choose 20 values of λ between 0 and 1, 10 of them equally spaced from 0.000 to 0.95 and the remaining 10 from 0.95 to 1.000, and integrate each region using the Simpson integration method. This choice originated from then fact that when λ has a value close to 1.0, the integrand changes abruptly dropping to the dispersive energy of a LJ.

The Lennard-Jones free-energy consists of two terms: $A_{liq}^{LJ}(T,V) = A_{liq}^{LJ,id}(T,V) + A_{liq}^{LJ,res}(T,V)$, where $A_{liq}^{LJ,res}(T,V)$ is the excess and $A_{liq}^{LJ,id}(T,V)$ the ideal part. $A_{liq}^{LJ,res}$ for a Lennard-Jones fluid has been already computed for a broad range of temperatures and densities in Ref. [113, 114]. The free energy of the ideal gas of a mixture of N_{Na} and N_{Cl} is given by

$$\frac{1}{k_B T} A_{liq}^{LJ,id}(T,V) = N_{Na} ln(\rho_{Na}\Lambda_{Na}^3) - N_{Na} + N_{Cl} ln(\rho_{Cl}\Lambda_{Cl}^3) - N_{Cl} = N[ln(\rho/2) - 1] \tag{12.6}$$

where N = N_{Na}+ N_{Cl} is the total number of particles in the system with density $\rho = \frac{N}{V}$ (and $\rho_{Na} = \frac{N_{Na}}{V}$ = $\rho_{Cl} = \frac{N_{Cl}}{V}$ = ρ/2) and Λ_i is the De Broglie thermal length (Λ_i = h / $\sqrt{2\pi m_i kT}$), that we arbitrarily set to 1 Å, consistent with our choice for the solid phase.

Route 3. Hamiltonian Gibbs-Duhem integration

The third route we follow to compute the melting temperature is by means of Hamiltonian Gibbs-Duhem thermodynamic integration as in Ref. [187, 427, 428]. Starting from the liquid-solid coexistence point of a reference system (A), the Hamiltonian Gibbs-Duhem thermodynamic integration allows one to compute the coexistence point of the system of interest (whose Hamiltonian is B) by resolving a Clapeyron-like differential equation. In more detail, the Hamiltonian of the initial system (with energy U_A), whose two-phases coexistence point is known, is connected to the one of the final system of interest (with energy U_B), via the following expression:

$$U(\lambda) = \lambda U_B + (1-\lambda)U_A \tag{12.7}$$

where λ is the coupling parameter. When two phases coexist (labeled as I and II): $\mu_I(T,p,\lambda) = \mu_{II}(T,p,\lambda)$, being $\mu = G/N$ the Gibbs free-energy per particle (the chemical potential of

each phase). Therefore, differentiating μ in both phases, we can write generalized Clapeyron equations for two coexisting phases as

$$v_I(T,p)dp - s_I(T,p)dT + \left(\frac{\partial \mu_I(T,p,\lambda)}{\partial \lambda}\right) d\lambda = v_{II}(T,p)dp - s_{II}(T,p)dT + \left(\frac{\partial \mu_{II}(T,p,\lambda)}{\partial \lambda}\right) d\lambda \tag{12.8}$$

where v and s are properties per particle. If λ is constant we recover the well known Clapeyron equation. If the pressure is constant we obtain the slope of the coexistence line in the λ-T plane:

$$\frac{dT}{d\lambda} = \frac{T[(\partial \mu_{II}/\partial \lambda) - (\partial \mu_I/\partial \lambda)]}{h_{II} - h_I} = \frac{T[(\partial \mu_{II}/\partial \lambda) - (\partial \mu_I/\partial \lambda)]}{\Delta h} \tag{12.9}$$

knowing that, at coexistence

$$s_{II} - s_I = \frac{h_{II} - h_I}{T}. \tag{12.10}$$

When a liquid coexists with a solid, ($s_{II} - s_I$) is the melting entropy difference Δs_m, that can be easily computed as $\frac{\Delta h_m}{T_m}$. Δh is obtained from the NpT simulations at (p,λ,T) constants, whereas $\frac{\partial \mu}{\partial \lambda} = \langle \frac{\partial u(\lambda)}{\partial \lambda} \rangle_{N,p,T\lambda}$, computed with an NpT simulation at different values of λ in each phase.

Therefore, using Eq. 12.7, the generalized Clapeyron equation can be written as:

$$\frac{dT}{d\lambda} = \frac{T[\langle u_B - u_A \rangle^{II}_{N,p,T,\lambda} - \langle u_B - u_A \rangle^{I}_{N,p,T,\lambda}]}{\Delta h} \tag{12.11}$$

where u_B/u_A is the internal energy per particle when the interaction between particles is described by U_B/U_A. The numerical integration of the generalized Clapeyron equation in Eq. 12.11 yields the change of the coexistence temperature (at constant pressure) due to the change in the Hamiltonian of the system, starting from the initial coexistence point (where interactions are described by U_A) to the final coexistence point (where interactions are described by U_B).

Simulation Details

When using the liquid/solid direct coexistence route to compute the melting temperature we choose a system containing 1024 [512 solid/512 liquid] and 2000 ions [1000 solid/1000 liquid] in an NpT ensemble. When using the free-energies calculations route to compute the melting temperature, we simulate systems of 512 and 1000 ions (the chosen system sizes being compatible with crystalline structures of 4x4x4 and 5x5x5 unit cells, respectively). And for the Hamiltonian Gibbs-Duhem integration route we simulate systems of 2000 ions.

We simulated NaCl using three interaction potentials: the TF, the SD and the JC interaction potentials. For the other alkali halides considered in this work we used only the TF model potential. In the free-energy calculations and Hamiltonian Gibbs-Duhem integration routes, we truncated the non-Coulomb part of the potential at 10 Å for the 512 ions system and at 14 Å for the 1000 ions system and added tail corrections. We used Ewald sums to deal with Coulomb interactions, truncating the real part of the Ewald sums at the same cut-off as the non-Coulomb interactions and choosing the parameters of the Fourier part of the Ewald sums so that $\alpha \cdot r_c = 2.98$ [97, 99] (α = 0.25 Å^{-1} for the 512 ions system and α = 0.214 Å^{-1} for the 1000 ions system). To calculate T$_m$ for the SD and JC models via direct coexistence we performed NpT Molecular Dynamics simulations (MD) with the Gromacs package [235], where we kept the temperature constant with a Nose-Hoover thermostat [429, 430] with a relaxation

time of 2 ps, and the pressure constant to 1 bar with a Parrinello-Rahman barostat [102] with a relaxation time of 2 ps. In our MD simulations, we allowed the different box lengths to fluctuate independently. We truncated the non-Coulombic part of the potential at 8.5 Å and added tail corrections to both the energy and the pressure. We used Ewald sums to deal with Coulomb interactions, truncating the real part of the Ewald sums at the same cut-off as the non-Coulombic interactions and choosing the Particle Mesh Ewald (PME) method [100] to deal with the Fourier part of the Coulomb interactions, with mesh width of 0.65 Å and a fourth other polynomial. For the TF alkali halides direct coexistence simulations we used NpT Monte Carlo simulations.

In the free-energy calculations, we used the Einstein Crystal and the Einstein Molecule methods to compute the free-energy of the solid phase. We performed an initial equilibration run of the solid in the NpT ensemble of about 10^5 Monte Carlo (MC) cycles to obtain the equilibrium density at the given thermodynamic conditions. We define a MC cycle as a translational trial-move per particle and a trial-volume change. For the thermodynamic integration in the NVT ensemble we carried out 2x10^4 equilibration and 8x10^4 production cycles for every value of λ and simulated 20 values of λ per thermodynamic state. We also used thermodynamic integration to compute the free-energy of the liquid phase. We carried out 8x10^4 equilibration and 18x10^4 production cycles for every value of λ and simulated 21 values of λ per thermodynamic state. Free-energy calculations were performed at 1083 K and 1 bar. To obtain the equilibrium densities at these thermodynamic conditions, we run NpT MC simulations of the liquid and solid phases. Once equilibrated, we used those densities in the free energy calculations.

When performing the thermodynamic integration to compute the free-energy of the liquid phase (route 2), we tested the dependence of our results on the choice of the reference system by performing the thermodynamic integration to two Lennard-Jones models with different parameters: the parameters set $LJ1$ used by Anwar *et al.* [123] and $LJ2$, whose parameters have been chosen in Ref. [114]. Both sets of parameters are represented in Table 12.3.

Tabla 12.3: $LJ1$ and $LJ2$ sets of parameter with units ϵ/k$_B$($[K]$) and σ([]). ρ*=$\rho\sigma^3$ and T*=k_BT/ϵ.

ϵ/k$_B$ [**LJ1]**	σ	ρ*	T*	ϵ/k$_B$ [**LJ2]**	σ	ρ*	T*
537.01	2.32	0.3766	2.02	358.00	3.00	0.8143	3.03

The values of ρ* and T* shown in Table 12.3 are obtained by scaling the density and temperature of the liquid phase of the TF/NaCl at 1083 K and 1 bar to LJ reduced units. The free-energy should be independent of the choice of the LJ reference system. Notice that the free-energy of the LJ system given by the Nezbeda EOS [114] has a lower error when using LJ2 (at ρ*=0.8143 and T*=3.03) rather than at ρ*=0.3766 and T*=2.02 (when using LJ1) due to the proximity of the LJ fluid critical point.

When using the third route to compute the melting temperature, we integrated the Hamiltonian in Eq. 12.7 from the TF/NaCl to the SD and JC potentials and from the TF/NaCl potential to other alkali halides potentials parametrized using TF. In all cases, we simulated 5 values of λ per Hamiltonian Gibbs-Duhem integration.

Results

Let us start by presenting the results for the melting point of NaCl for the models and routes considered in this work.

Route 1. Liquid/solid direct coexistence

Using the liquid/solid direct coexistence technique [424, 425] we determined the melting temperature at 1 bar not only of the TF/NaCl but also of the other NaCl potentials (the Smith-Dang and Joung-Cheatham). After having prepared the equilibrated liquid-solid configuration we performed several anisotropic NpT Monte Carlo simulations (in the case of TF/NaCl) and molecular dynamics simulations with an anisotropic barostat (in the case of SD/NaCl and JC/NaCl) for two different system sizes, N=1024 and N=2000, to analyze the finite-size effects. In Fig. 12.1 we plot the time evolution of the total energy of the TF/NaCl system equilibrated at 1 bar and at different temperatures for the two system sizes.

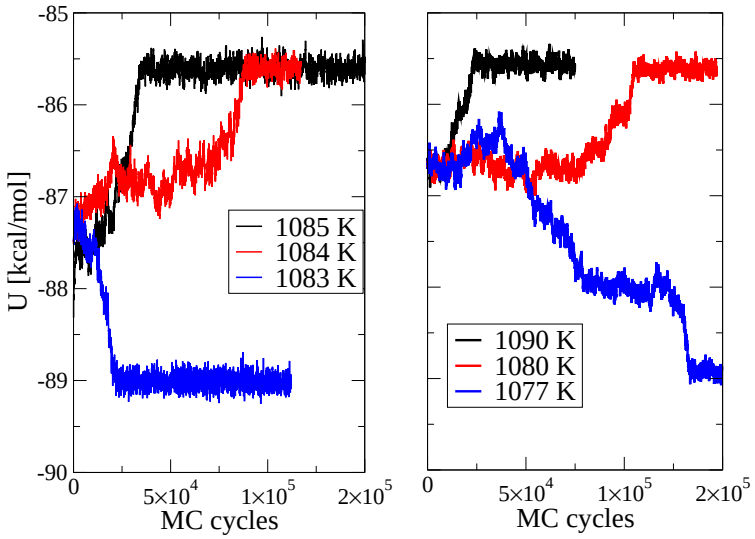

Figura 12.1: Total energy versus MC cycles for the Tosi-Fumi NaCl at T= 1085 K, 1084 K and 1083 K (from top to bottom) for the 1024 particles system (left-hand side) and T= 1090 K, 1080 K and 1077 K (from top to bottom) for the 2000 particles system. Note the same x and y-axis in both plots. The internal energy of the system is expressed in kcal per ion mol.

After an equilibration interval of about 10^4 MC cycles (where the energy stays constant), we observed that when the temperature is below melting the energy decreases until it reaches a plateau with a sudden change of slope, corresponding to the situation where the liquid has fully crystallized. When the temperature is above melting, the energy presents a sudden increase until it reaches a plateau and stays constant: at this stage, the solid has completely melted. The results obtained for the 1024 particles system (left-hand side of Fig. 12.1) shows that when T=1083 K the liquid crystallizes, whereas when T $>$ 1084 K the solid melts: therefore, the estimated melting temperature for the 1024 particles system is T_m=1083(2) K. The results obtained for the 2000 particles system (right-hand side of Fig. 12.1) show that when $<$ 1077 K the liquid crystallizes, whereas when T $>$ 1080 K and 1090 K the solid melts. Therefore, the estimated melting temperature for the 2000 particles system is T_m=1078(2) K. Since the melting temperature decreases when the system size increases, we concluded that there were finite-size effects (although they seemed to be less than 1 %).

Hence, when computing T_m for the remaining interaction potentials, we chose a large enough system with 2000 particles. In Fig. 12.2, we present the time evolution of the total energy of the NaCl/SD and NaCl/JC 2000 particles systems, equilibrated at 1 bar and at different temperatures. The results obtained for the 2000 particles system show that the estimated

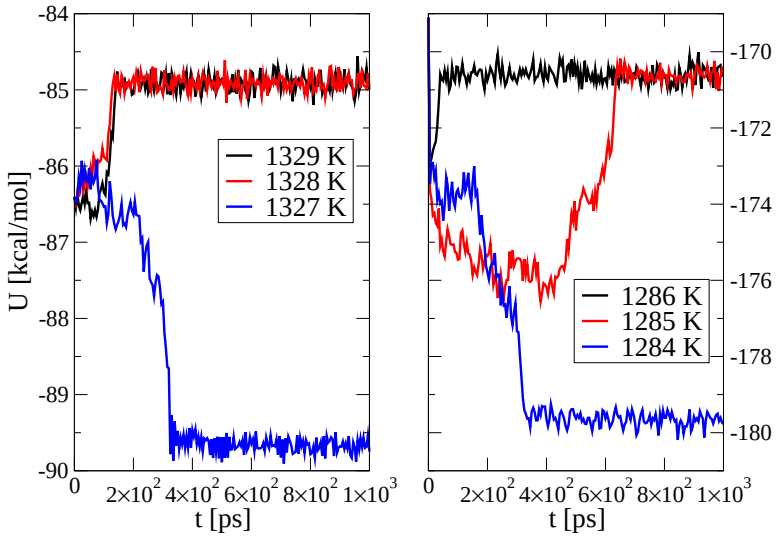

Figura 12.2: Total energy versus time (in picoseconds) for the NaCl/SD system (left-hand side) at T=1329 K, 1328 K and 1327 K (from top to bottom), and for the SD/NaCl system (right-hand side) at T= 1284 K, 1285 K and 1286 K (from top to bottom). Note the different y-axis of both plots.

melting temperature is T_m= 1327(2) K for the NaCl/SD and T_m=1285(2) K for the NaCl/JC, respectively.

From these results, we can already conclude that the potential that gives the melting temperature closest to the experimental one (1074 K) is the Tosi-Fumi. For this reason the TF/NaCl model is the most suitable for simulations of pure NaCl. This conclusion is further confirmed when calculating the melting curve for both TF/NaCl and JC/NaCl potentials. Using Gibbs Duhem integration [138] we calculated the $p-T$ melting curve of the TF/NaCl and the JC/NaCl, presented in Fig. 12.3.

Concerning the results of the TF/NaCl, we observe that at low pressure our calculations recover the experimental slope of the melting curve ($\frac{dp}{dT} = 30.6(5)$ bar/K), in good agreement with previous calculations [123, 416], whereas at higher pressures the slope of the melting line is lower than the experimental one.

On the other hand, concerning the results for the JC/NaCl, we observe that not only the melting temperature, but also the slope of the melting curve does not reproduce the experimental one. The same conclusions can be drawn for the melting enthalpy difference (Δh_m). The calculated melting enthalpy differences for the TF/NaCl, SD/NaCl and JC/NaCl are 3.36 kcal/mol, 4.8 kcal/mol and 4.6 kcal/mol, respectively, that compared to the experimental value (3.35 kcal/mol), confirms the better performance of the TF/NaCl model with respect to the other models.

Route 2. Free-energy calculations

According to the second route, we first computed the Helmholtz free-energy of the solid and liquid phase of the TF/NaCl, and then estimate the Gibbs free-energy of each phase (G) by adding the pV term. After that, we performed thermodynamic integration of G in the (p,T)

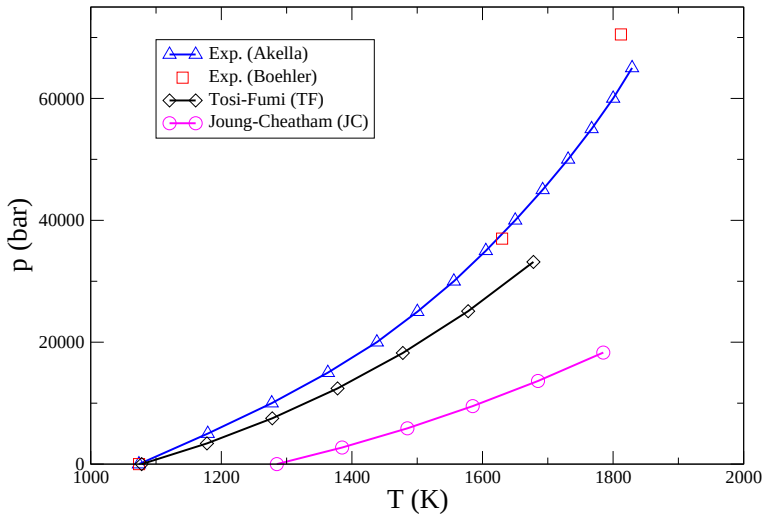

Figura 12.3: Melting curve for the TF/NaCl (open diamonds) and JC/NaCl (open circles). Experimental results are from Ref. [417] (open squares) and Ref. [431] (open triangles).

plane at constant pressure as in Eq. 12.12.

$$\frac{G(T_2,p)}{Nk_BT_2} = \frac{G(T_1,p)}{Nk_BT_1} - \int_{T_1}^{T_2} \frac{H(T)}{Nk_BT^2} dT \tag{12.12}$$

where the enthalpy $H(T) = U(T) + pV(T)$ can be easily obtained in NpT simulations at each temperature. The melting point is defined as the state point where the two phases have the same chemical potentials ($\mu = G/N$).

We computed the free-energy of the NaCl solid phase at 1083 K and 1 bar with Einstein crystal (EC) [115] and Einstein molecule (EM) [234] algorithms. Our results are summarized in Table 12.4, where we present free-energies in Nk_BT units. To determine the normal melting point any temperature could have been selected, the choice of 1083 K (coming from our direct coexistence results) is convenient from a practical point of view since it is expected to be close to the T$_m$ of the model so that the contribution of the second term on the right side of the Eq. 12.12 would be small.

Tabla 12.4: Free energy from the Einstein Crystal/Einstein Molecule for the TF/NaCl solid phase at 1 bar and different temperatures (T) and system size (N being the total number of particles). ρ the number density (N_{ions}/V), Λ_E the spring constant, A_0, ΔA_1, ΔA_2 are the terms in Eq. 12.3 and the free energy of the solid A_{sol}^{NaCl} is represented in the last column and corresponds to $A_0 + \Delta A_1 + \Delta A_2$.

	T[K]	N	ρ (N/Å^3)	$\Lambda_E[k_BT^{-2}]$	A$_0$[Nk$_B$T]	Δ A$_1$[Nk$_B$T]	Δ A$_2$[Nk$_B$T]	A$_{sol}^{NaCl}$[Nk$_B$T]
TF/EM	1083	512	0.03877	500	7.584	-42.77	-6.31	-41.500(9)
TF/EC	1083	1000	0.03856	500	7.583	-42.73	-6.33	-41.481(9)
TF/EM	1083	1000	0.03856	500	7.594	-42.73	-6.34	-41.477(9)

In Table 12.4, we observe a perfect agreement between the free-energy computed with the Einstein Crystal and the one compute with the Einstein Molecule at the same pressure (1 bar), temperature (1083 K) and system size (1000 particles) (see the last column of the second and third row in Table 12.4). Next, in order to evaluate if our calculations at 1 bar and 1083 K are subject to finite-size effects we repeat the evaluation of the free-energy with

Einstein Molecule for two different system sizes, $N = 512$ and $N = 1000$. The free energy difference between both system sizes (last column of the first and third row in Table 12.4) is around 0.02 Nk$_B$T and this will be reflected in the calculation of the melting point.

Having computed the chemical potential of the solid phase, we calculated the Helmholtz free-energy of the liquid phase using two Lennard-Jones reference systems $LJ1$ and $LJ2$ in order to study the uncertainties associated to the choice of the reference system. Our results at 1 bar and T=1083K for the 1000 particles TF/NaCl system are summarized in Table 12.5.

Tabla 12.5: TF/NaCl free energy of the liquid phase (A_{liq}^{NaCl}) as in Eq. 12.5 at 1 bar and T=1083 K. The results presented in the table refer to a system with $N = 1000$ particles and number density of $\rho = 0.03016$ Å^{-3}. ΔA^{LJ} is the integral in Eq. 12.5. $\frac{A_{liq}^{LJ,id}}{Nk_BT} = ln(\rho/2) - 1.00$. $A_{liq}^{LJ,res}$ is obtained from the EOS of Ref. [114].

	ΔA_{liq}^{LJ}[Nk$_B$T]	$A_{liq}^{LJ,id}$[Nk$_B$T]	$A_{liq}^{LJ,res}$[Nk$_B$T]	A_{liq}^{NaCl}[Nk$_B$T]
TF/LJ1	35.95	-5.19	-0.327	-41.47(2)
TF/LJ2	37.12	-5.19	0.837	-41.48(2)

As it is shown in the Table 12.5, the value of the integral (ΔA_{liq}^{LJ}) depends on the choice of the LJ parameters of the reference LJ system. In Fig. 13.4 the integrand of Eq. 12.5 is shown when carrying out the thermodynamic integration from the liquid TF/NaCl to both LJ reference systems $LJ1$ and $LJ2$. It is relevant to stress that, due to the abrupt change of $\langle U^{LJ} - U^{NaCl} \rangle_{N,V,T,\lambda}$ for values of λ close to 1, many points were used in the integration between $\lambda = 0.95$ and $\lambda = 1.00$.

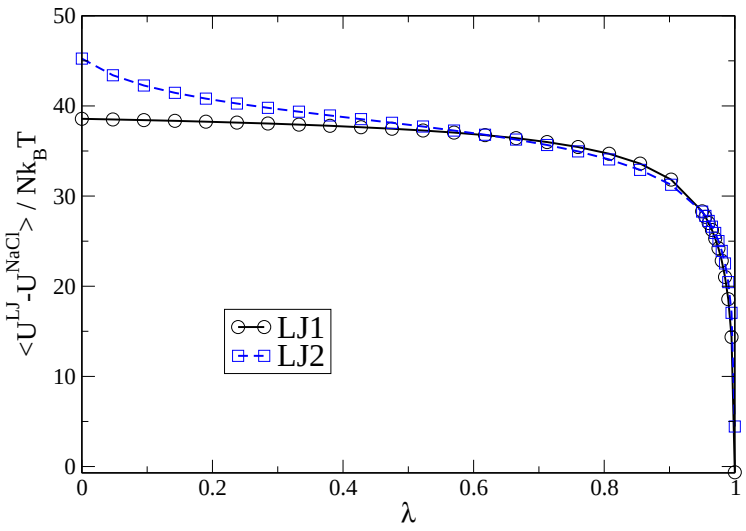

Figura 12.4: $\langle U^{LJ} - U^{NaCl} \rangle_{N,V,T,\lambda}$ from Eq. 12.5 at 1083 K and 1 bar. The two curves correspond to a different set of Lennard-Jones parameters for the reference system: $LJ1$ (open circles) and $LJ2$ (open squares).

To calculate the residual free energy of the reference LJ fluid at our thermodynamic conditions, we used the equation of state (EOS) for the LJ system proposed by Nezbeda *et al.* [114, 432]. Independently on the chosen reference system (whether $LJ1$ or $LJ2$), the two free-energies A_{liq}^{NaCl}[Nk$_B$T] coincide (last column in Table 12.5).

After having computed the Helmholtz free-energy, we estimated the Gibbs free-energy (G) by adding the pV term and performed thermodynamic integration of G at constant pressure

(see Eq. 12.12) where we used NpT MC simulations to compute enthalpy $H(T)$ and to estimate the equation of state of the liquid and solid phases (where a typical MC run consists of 3x10^4 equilibration and 7x10^4 production cycles). The chemical potential of one phase is $\mu = G/N$ and the melting temperature is given by the point at which the two phases have the same chemical potentials. Our results for the TF/NaCl are presented in Table 12.6.

Tabla 12.6: Melting temperature at 1 bar of the TF/NaCl model. The results presented in the table refer to a system with $N = 1000$ particles. The parameters for the interaction potentials of the reference systems ($LJ1$ and $LJ2$) are given in Table 12.3.

	T_m[K]		T_m[K]
TF/LJ1	1083(3)	TF/LJ2	1084(3)

Both results are in perfect agreement with the T_m calculated by direct coexistence. Other EOS could be used to calculate the residual free energy of the reference LJ fluid, such as the one proposed by Johnson *et al.* [433]. When the LJ residual contribution is taken from Johnson *et al.*, the melting temperature turns out to be about 6 K higher than when it is taken from Nezbeda *et al.*. However, it is likely that the EOS proposed by Nezbeda is slightly more accurate than that by Johnson *et al.* [114]. In any case, the differences are small.

Route 3. Hamiltonian Gibbs-Duhem integration

The third route we followed to compute the melting temperature of several alkali halides at 1 bar is by means of the Hamiltonian Gibbs-Duhem thermodynamic integration. We used the TF/NaCl as the reference Hamiltonian (U_A in Eq. 12.7) and integrated the generalized Clapeyron equation (Eq. 12.11) using a 2000-particle system (that is less affected by finite-size effects). From the $\lambda = 1$ point of the Hamiltonian Gibbs-Duhem integration, we could compute the melting entropy difference ΔS_m (being $\Delta S_m = N\Delta s_m$, see Eq. 12.10) and the melting enthalpy difference ($\Delta H_m = N\Delta h_m$) at coexistence. In the following table we present our results for the melting temperature, ΔS_m, reporting also the experimental values of both for each alkali halide, and for ΔH_m.

We checked our Hamiltonian Gibbs Duhem calculations by computing the melting temperature of TF/KF at 1 bar by means of liquid/solid direct coexistence. Figure 12.5 represents the time evolution of the total energy of the TF/KF 2000-particle systems, equilibrated at 1 bar and at different temperatures. From these results we estimate T_m to be 860(5) K, that corroborates the result obtained with the Hamiltonian Gibbs Duhem integration in Table 12.7.

While the Tosi-Fumi potential predicts the NaCl melting temperature in good agreement with its experimental value, the results for the rest of alkali halides are not as accurate. The predictions for KCl and NaBr are reasonable (differing only about 15 K and 10 K from the experiments). Whereas for alkali halides involving Rb or F ions (such as KF, RbBr, RbCl, RbF, LiF and NaF) the calculated values differ strongly from the experimental ones (with deviations of up to 100 K). From this we conclude that the TF model potential, being non-polarizable, fails when describing alkali halides that involve big cations (such as Rb^+) and small anions (such as F^-) ions. In general, when T_m of a given TF/alkali halide is lower than the experimental value, also ΔH_m is smaller than the experiment, so that the predicted ΔS_m is in reasonable agreement with the experimental value for most of the studied alkali halides.

Tabla 12.7: Melting temperatures, ΔS_m and ΔH_m at 1 bar for several alkali halides simulated using the TF interaction potential with units $T_m([K])$, $\Delta S_m([cal/(Kmol)])$ and $\Delta H_m([kcal/mol])$. The experimental values of ΔS_m are from Ref. [434–436]. The bold fonts represent alkali halides for which there are good agreement with the experimental melting temperatures.

Alkali halide	T_m	T_m^{exp}	ΔS_m	ΔS_m^{exp}	ΔH_m	ΔH_m^{exp}
NaCl	**1078(5)**	**1074**	**3.12**	**3.12**	**3.36**	**3.35**
KF	855(15)	1131	2.80	2.98	2.39	3.37
KBr	**1039(15)**	**1003**	**3.17**	**3.03**	**3.29**	**3.04**
KCl	**1035(15)**	**1049**	**3.14**	**3.04**	**3.25**	**3.19**
RbBr	1043(15)	955	3.37	2.88	3.51	2.75
RbCl	1088(15)	988	3.20	2.88	3.48	2.85
RbF	992(15)	1048	3.06	2.88	3.03	3.02
NaF	607(15)	1266	2.13	3.09	1.29	3.91
NaBr	**1018(15)**	**1028**	**3.12**	**3.06**	**3.18**	**3.70**
LiCl	776(15)	887	2.48	2.70	1.93	2.39
LiF	**1006(15)**	**1118**	**2.96**	**2.88**	**2.97**	**3.22**

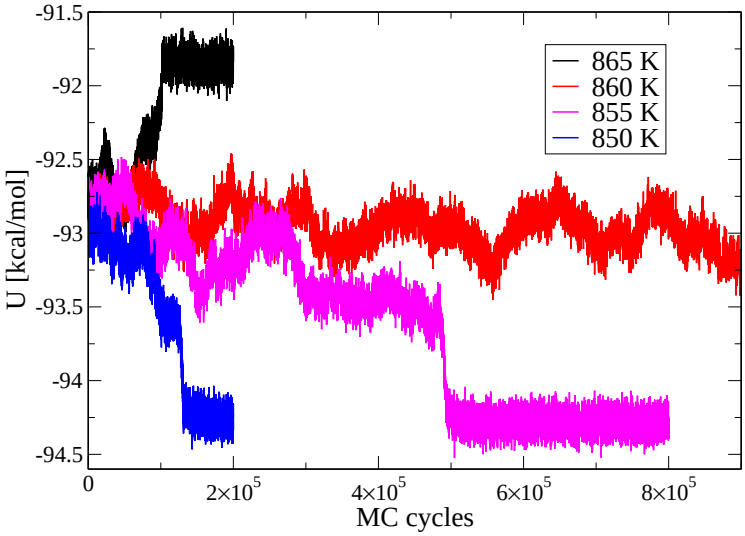

Figura 12.5: Total energy versus MC cycles for TF/KF at T = 865 K, 860 K, 855 K and 850 K (from top to bottom).

Discussions

We now compare our data for the melting temperature of NaCl at 1 bar with other values taken from the literature (see Table 12.8).

Concerning the calculations of the melting temperature with the Tosi-Fumi, we observe that T_m calculated in this work is in good agreement (within the error bar) with the one reported by Anwar *et al.* [123]. They calculated the coexistence pressure at 1074 K and -300 bar. Then, they evaluated the slope of the coexistence curve, $\frac{dp}{dT} = 30 \text{ bar } K^{-1}$, and recalculated the melting temperature at 1 bar obtaining 1064(14) K (nonetheless, using their values, we have obtained the NaCl melting temperature at 1084(14) K, in perfect agreement with our results). Tosatti *et al.* [413] computed the melting temperature via liquid/solid direct coexistence and

Tabla 12.8: Melting temperature of the NaCl computed using TF, SD and JC interaction potentials at 1 bar. All results listed from the references are for a 512 particles system. ρ_{liq} and ρ_{sol} are the liquid and solid densities in gcm^{-3}, respectively. The * represents the recalculated T_m at 1 bar using the values given by Anwar (p_{coex}=-300 bar at 1074 K and $\frac{dp}{dT} = 30 \text{ bar } K^{-1}$).

	T_m[K]	ρ_{liq}	ρ_{sol}
TF/Anwar [123]	1064(14)	–	–
TF/Anwar* [123]	1084(14)	–	–
TF/Tosatti [413]	1066(20)	–	–
TF/de Pablo [416]	1050(3)	–	–
TF/Maginn [415]	1089(8)	–	–
TF/Luo [437]	1063(13)	–	–
TF/this work (N=2000)	1078(5)	1.465	1.876
TF/this work ($N \to \infty$)	1074(5)	–	–
SD/this work	1327(10)	1.216	1.668
JC/this work	1286(10)	1.283	1.746
Experimets/Janz [438]	1074	–	–

obtained a value for T_m in very good agreement with the one obtained in this work. In general, the agreement with the literature data is satisfactory.

When computing the melting temperature of the TF/NaCl model potential via liquid/solid direct coexistence and free-energy calculations we have studied finite-size effects and observed that the value of the melting temperature decreases when increasing the system size. For N=512 we found that T_m= 1100(15) K, for N=1000 T_m=1084(10) K, for N=1024 T_m=1083(2) K and for N=2000 T_m=1078(5) K (where the melting temperature for the 512 and 1000 particles systems has been calculated via free-energy calculations, whereas the melting temperature for the 1024 and 2000 ions system via liquid/solid direct coexistence). Extrapolating to an infinite-size system, we obtain a melting temperature for the TF/NaCl of $T_m(N \to \infty)$ = 1074(5) K. When calculating T_m via Hamiltonian Gibbs-Duhem integration, we have used the value of T_m=1078(5) K as the initial point for the Hamiltonian Gibbs Duhem integration at coexistence. The tabulated values of T_m in Table 12.7 are for systems with N=2000: thus extrapolating for $N \to \infty$, the values of T_m would be 4 K lower than in Table 12.7.

Concerning the calculation of the melting temperature with the Smith-Dang and Joung-Cheatham potentials, we computed these values via two independent routes (liquid/solid direct coexistence and Hamiltonian Gibbs-Duhem integration) and obtained the same results. The T_m of both models is reported here for first time. From our calculations we conclude that these models overestimate the melting temperature of NaCl, being about 200-250 K higher than the experimental value of 1074 K. Therefore, it is clear that the melting temperature that most resembles the experimental one at 1 bar is the one calculated using the TF/NaCl. Although JC/NaCl or SD/NaCl would work for NaCl solutions in water, they seem to be unsuitable for simulations of pure NaCl.

Conclusions

In this manuscript, we have computed the melting temperature at 1 bar for different NaCl-type alkali halides. When computing T_m for the TF/NaCl interaction potential, we have followed

three independent routes: 1) liquid/solid direct coexistence, 2) free-energy calculations and 3) Hamiltonian Gibbs-Duhem integration. For the SD/NaCl and JC/NaCl, we have used the first and third route; whereas for other TF/alkali halides we have applied only the third route.

The results obtained for the T_m of TF/NaCl are in good agreement with other numerical [123, 413] and with experimental results [438], giving T_m= 1078(5) K at 1 bar. For this system, we have also performed a thorough study of finite-size effects, suggesting the minimum system size one should simulate in order to avoid them (around 2000 particles). When computing T_m for the SD/NaCl and JC/NaCl, we find a perfect agreement between the calculations obtained via liquid/solid direct coexistence and Hamiltonian Gibbs-Duhem integration. However, both models overestimate the melting temperature of NaCl by more than 200 K. We have also determined the melting curve for the Tosi-Fumi and Joung-Cheatham models and found that the Tosi-Fumi correctly predicts the behavior of the curve ($\frac{dp}{dT}$) at low pressures, but does not capture the experimental behavior when the pressure increases. Therefore, we conclude that the SD/JC models are unable to reproduce the properties of pure alkali halides.

We have also computed the melting temperature of other alkali halides using the Tosi-Fumi interaction potential and observed that this model gives good predictions for NaCl, NaBr and KCl; whereas for the other alkali halides the predictions are not as good, especially when it concerns Rb^+ and F^- ions. The reason for this probably being that the Tosi-Fumi interaction potential is not polarizable and cannot capture the highly polarizable/polarizability character of these ions. The TF/alkali halide potentials have a serious transferability problem: the same ions present different potential parameters depending on the alkali halide in which they are involved (i.e. the Na-Na interaction is different in NaCl and NaF). In the case of LJ-like models, it seems that is not possible to describe NaCl accurately with a model consisting of point charges and a Lennard-Jones interaction site for each ion when Lorentz-Berthelot rules are used to describe the interaction between cations and anions. An interesting possiblility would be incorporating deviations to the Lorentz-Berthelot combining rules to obtain the crossed interactions between the ions or adjusting these interactions as in the TF model. Thus, it seems there is still room for improvement in the area of alkali-halides salts potential models.

Acknowledgments

This work was funded by grants FIS2010-16159. from the DGI (Spain), MODELICO-P2009/ESP/1691 from the CAM, and 910570 from the UCM. J. L. Aragones would like to thank the MEC by the award of a pre-doctoral grant. C.Valeriani acknowledgments financial support from a Juan de la Cierva Fellowship and from a Marie Curie Integration Grant. E. Sanz acknowledgments financial support from a Ramon y Cajal Fellowship.

Parte III

DISCUSIÓN DE RESULTADOS

CAPÍTULO 13

Discusión integradora

"*Decidamos la verdad democráticamente.*"
Paul Karl Feyerabend

Todos los estudios aquí presentados versan sobre el equilibrio de fases del agua y el estudio de sus propiedades mediante simulación por ordenador. Los siete trabajos aquí expuestos se pueden clasificar en tres bloques según los objetivos del estudio:

1. **Estudio del diagrama de fases del agua**. En este epígrafe se pueden encuadrar los trabajos realizados sobre la región de altas presiones del diagrama de fases (Capítulos 7 y 8) y el *test de Whalley* para evaluar la calidad de los cálculos del diagrama de fases (Capítulo 6).

2. **Campos eléctricos y agua: Constante dieléctrica y efecto de aplicar campos eléctricos sobre el diagrama de fases del agua**. Cálculo de la constante dieléctrica del agua líquida y los hielos (Capítulo 9), y cuál es el efecto de aplicar un campo eléctrico sobre las diferentes transiciones de fase del agua (Capítulo 10).

3. **Cálculo de la temperatura de fusión de sales y su solubilidad en agua mediante simulación**. (Capítulos 11 y 12)

En el 2004 se calculó por primera vez el diagrama de fases del agua para los modelos SPC/E y TIP4P, y se comprobó que daban descripciones muy distintas [22]. Hasta ese momento tampoco había consenso sobre las temperaturas de fusión de los modelos de potencial. Todos los modelos de agua reproducen algunas de las propiedades del agua líquida a presión y temperatura ambiente, pero no todos se comportan igual cuando nos alejamos de las condiciones para las que fueron ajustados. La complejidad del diagrama de fases del agua, con un gran número de fases sólidas, es un excelente territorio para explorar las bondades y defectos de los distintos modelos de potencial. Esta idea de usar los hielos como prueba de calidad de un modelo de potencial fue propuesta por Whalley ya en el año 1984 [33]. Whalley sostenía que cualquier modelo de potencial de agua que pretenda dar una descripción realista de las propiedades del agua, debería ser capaz de reproducir también las propiedades de los hielos. Siguiendo las ideas de Whalley, calculamos la energía en el cero de temperatura y presión para los hielos Ih, II, III, V y VI. A partir de estos resultados obtuvimos las presiones de coexistencia entre pares de fases a 0 K. Si se comparan estos resultados con los que se obtienen mediante el cálculo de las lineas de coexistencia hasta 0 K, la concordancia es muy buena. De manera que es posible estimar el orden de estabilidad de los hielos en el cero de temperaturas con unos cálculos rápidos y sencillos, y a partir de estos estimar las presiones de coexistencia entre los hielos a 0 K (p_{eq}^{0K}). Con estos dos elementos, podemos tener ya una estimación cualitativa del diagrama de fases del agua. Esto

convierte al *test de Whalley* en una potente herramienta para estimar la calidad de un modelo en su capacidad para predecir el diagrama de fases. Ahora, casi 30 años después de que Whalley sugiriese este tipo de test, se está empezando a aplicar para evaluar la calidad de los resultados de simulaciones DFT de hielos [38–41], modelos flexibles de agua [42, 43] y simulaciones de path integral [44–47]. Además, el test resulta ser una herramienta tremendamente útil como test de consistencia en los cálculos de diagramas de fases [439].

El estudio de los hielos y el cálculo de nuevas propiedades del agua motivó el desarrollo de nuevos modelos de potencial con el objetivo de reproducir estas características del agua. Esto dio origen a una nueva serie de modelos de potencial, como los TIP4P/2005 [34], TIP4P/Ew [111], TIP5P [108] y TIP4P/Ice [112]. Los tres primeros fueron ajustados usando la temperatura del máximo en densidad del agua (TMD) como propiedad objetivo. Como hemos visto, la temperatura del máximo en densidad del agua es una de sus señas de identidad. Con la aparición de todos estos nuevos modelos el *test de Whalley* se revela como una herramienta tremendamente útil. Con unos rápidos cálculos podemos predecir que modelos darán una mala descripción del diagrama de fases, como es el caso del modelo TIP5P. Para el TIP5P la fase sólida más estable a la T_f es el hielo II. Y las únicas fases que aparecerían en el diagrama de fases serían los hielos II y VI (Tabla 6.3). Después de estudiar y comparar muchos modelos de potencial de agua, el modelo TIP4P/2005 ha demostrado ser el mejor modelo de agua para simulaciones clásicas [35]. En vista de que teníamos un buen modelo de agua, y que era capaz de reproducir propiedades para las que no había sido ajustado y fuera de los límites del ajuste (un modelo muy robusto), nos propusimos explorar regiones del diagrama de fases inexploradas y de difícil acceso experimental, y el cálculo de propiedades para las que el modelo no había sido parametrizado.

En 2007, Dolan *et al.* [220] observaron la cristalización espontánea de una fase sólida de agua (en palabras del propio Dolan: “most likely ice VII") a altas presiones (70 GPa) en pocos nanosegundos. En simulación la cristalización de agua es un problema de máxima envergadura, porque tiene lugar en una escala de tiempos muy lejos del alcance de la simulación. Por ejemplo, el límite superior experimental de las de tasas de nucleación medidas para el hielo I_h es de $10^{15} m^{-3} s^{-1}$, lo que requeriría 10^9 segundos (≈ 32 años) de una trayectoria de simulación con un sistema de tamaño $\approx 1000 nm^3$. De hecho, la nucleación, y la nucleación de hielo en particular, es un tema de investigación muy activo [74–77]. En vista de los resultados de Dolan, intentamos la cristalización de agua líquida a altas presiones. El resultado fue la cristalización del agua en pocos nanosegundos (Fig. 7.1), pero la fase sólida que se obtuvo no correspondía a la que se esperaría en esa zona del diagrama de fases (hielo VII). En su lugar cristalizó una fase de cristal plástico con la misma simetría que el hielo VII (cúbica centrada en el cuerpo, bcc). Enfriando la fase de cristal plástico se obtuvo hielo VII, y por calentamiento del hielo VII el cristal plástico (Fig. 7.3). Estábamos ante una transición de fase de primer orden. Llevamos a cabo cálculos de energía libre para las fases implicadas y situamos el cristal plástico bcc en el diagrama de fases (Fig. 7.8). Mientras explorábamos los límites de estabilidad del cristal plástico, observamos que éste experimentaba una transición de fase de tipo martensítica (Fig. 8.2) a otro cristal plástico de simetría cúbica centrada en la caras (fcc) al aumentar la presión. Así que también localizamos la región de estabilidad de esta fase plástica fcc, que es la que domina el diagrama de fases a altas presiones para estos modelos (Fig. 8.11). Estudiamos varios modelos de potencial para comprobar que la existencia de cristales plásticos es común a todos los modelos rígidos y no polarizables. Casi de forma simultanea, Tanaka *et al.* [221] observaron también la formación de un cristal plástico en la región de altas presiones del diagrama de fases del agua.

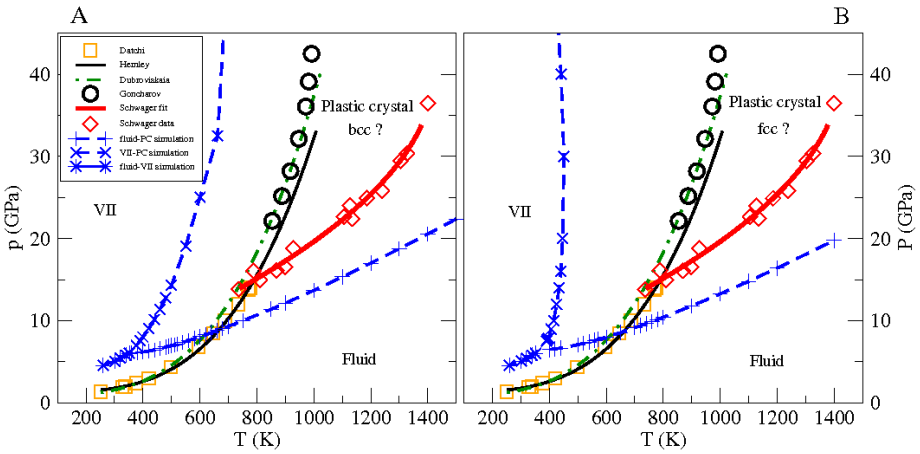

Figura 13.1: Medidas experimentales de la linea de fusión del hielo VII. Los círculos abiertos corresponden a los valores de Goncharov Ref. [52], la línea discontinua con puntos es la medida por Dubronskaia Ref. [51], la línea verde continua corresponde a los resultados de Lin Ref. [50], los cuadrados abiertos son los resultados dados por Datchi Ref. [49], los rombos y la línea gruesa es la linea de coexistencia dada por Schwanger [48]. Izquierda: la línea de fusión del cristal plástico fcc obtenida por simulación corresponde a la línea discontinua con signos más, la curva de coexistencia hielo VII–cristal plástico fcc es la línea discontinua con cruces, y la línea discontinua con asteriscos corresponde a la curva de fusión del hielo VII obtenida por simulación. Derecha: la línea de fusión del cristal plástico bcc obtenida por simulación corresponde a la línea discontinua con signos más, la curva de coexistencia hielo VII–cristal plástico bcc es la línea discontinua con cruces, y la línea discontinua con asteriscos corresponde a la curva de fusión del hielo VII obtenida por simulación.

Cuando la presión es muy alta es difícil llevar a cabo medidas experimentales, lo que explica que varios grupos experimentales presenten resultados dispares en esta zona del diagrama de fases. Estas diferencias podrían explicarse por la existencia de una fase de cristal plástico. En el segundo trabajo de esta serie exploramos esta posibilidad representando los resultados experimentales junto a nuestros resultados de simulación (Fig. 13.1). En vista de estos resultados, todo parece indicar que las discrepancias experimentales podrían explicarse por la existencia de una fase de cristal plástico en la zona de altas presiones del diagrama de fases. Sería altamente relevante la demostración experimental de la existencia o no de un cristal plástico a altas presiones. Ayudaría al modelado de agua, ya que en el caso de que fuesen artefactos de los modelos, habría que ver por qué fallan estos modelos. Una idea es que la parte repulsiva de estos modelos, optimizada para generar un enlace de hidrógeno a una distancia O-O de 2.82 Å, sea demasiado repulsiva para situaciones de alta presión, donde las moléculas están muy juntas. Prueba de esto es que el modelo TIP4P/2005 no es capaz de reproducir la densidad del hielo VII. La estructura del hielo VII puede entenderse como dos redes cristalinas de hielo I_c (tipo diamante) interpenetradas pero no conectadas, de manera que cada molécula de agua tiene 8 moléculas vecinas a la misma distancia, pero sólo forma enlace de hidrógeno con cuatro de ellas. El enlace de hidrógeno es muy direccional, de manera que las moléculas que no forman enlaces de hidrógeno están demasiado penalizadas por la parte repulsiva del LJ. Esto lleva a una desestabilización de la estructura y el hielo VII aparece a presiones muy altas con respecto al experimento.

La calidad de los resultados en la descripción de las propiedades de los hielos y del diagrama de fases cambian de unos modelos de potencial a otros. Los modelos de geometría

TIP4P son superiores a otros modelos como SPC/E, TIP5P y TIP3P en la descripción de las fases sólidas del agua. A pesar de todo, la existencia de fases de cristal plástico es general para este tipo de modelos. Pero existen otras propiedades, como la constante dieléctrica del agua, para las que estos modelos TIP5P, SPC/E y TIP3P predicen valores próximos a los experimentales, mientras que los resultados de los modelos TIP4P se alejan bastante del experimento. A fin de comprender el origen de estas diferencias en los valores de la constante dieléctrica para estos modelos, comenzamos el estudio de las propiedades dieléctricas del agua.

La elevada constante dieléctrica del agua líquida es otra propiedad singular del agua, convirtiéndola en el disolvente universal. Pero no sólo el agua líquida tiene una constante dieléctrica alta, también la tienen algunas de sus fases sólidas. Como hemos comentado, algunos modelos de potencial reproducen la constante dieléctrica del agua líquida. ¿Qué hace que algunos modelos reproduzcan correctamente la constante dieléctrica y otros no? ¿Qué característica de los modelos SPC/E, TIP5P y TIP3P, que no se encuentra en los modelos TIP4P, hace que reproduzcan la constante dieléctrica del agua líquida? Estos modelos que capturan esta característica del agua líquida, ¿reproducen también la constante dieléctrica de las fases sólidas?

Desde el punto de vista microscópico, la constante dieléctrica está relacionada con las fluctuaciones de la polarización total del sistema (M). Las fluctuaciones de la polarización del sistema se puede calcular fácilmente para el agua líquida y los hielos ordenados de protón. Para el agua líquida basta con calcular la polarización del sistema para un gran número de configuraciones a lo largo de una simulación. En los hielos ordenados de protón las moléculas sólo vibran entorno a su posición de equilibrio en la red cristalina. De manera que las fluctuaciones de M son pequeñas, y por tanto el valor de la constante dieléctrica es pequeño. En cambio, en hielos desordenados de protón existen muchas configuraciones de energía similar pero que presentan valores muy distintos de M. De manera que estos hielos suelen presentar valores altos de la constante dieléctrica. Las distintas configuraciones de protón están separadas por altas barreras de energía, por lo que los tiempos de relajación pueden ser muy largos (μs) [153], y es necesario incluir movimientos especiales para muestrear correctamente las distintas configuraciones de protón (sección 5.5).

Incluimos en nuestras simulaciones el algoritmo de rotación de anillos propuesto por Rick y Haymet [154] y calculamos la constante dieléctrica de los hielos I_h, I_c, II, III, V, VI y VII para los modelos TIP4P/2005, TIP4P/Ice, TIP5P y SPC/E (Tabla 9.4). Ninguno de estos modelos es capaz de reproducir la constante dieléctrica de las fases sólidas del agua, incluso aquellos que predecían correctamente la constante dieléctrica del agua líquida. Por tanto, ningún modelo es capaz de reproducir simultáneamente la constante dieléctrica del agua líquida y del hielo I_h. No obstante, los modelos de tipo TIP4P predicen, en concordancia con el experimento, constantes dieléctricas similares para la fases líquida y de hielo I_h a la temperatura de fusión (Fig. 13.2). En cambio, modelos que daban valores de la constante dieléctrica para la fase líquida próximos a los experimentales como el TIP5P, dan valores entre 2 y 3 veces inferiores para el hielo I_h (Fig. 13.2). Esto quiere decir que los modelos tipo TIP4P, aunque no reproducen los valores de la constante dieléctrica para ninguna de las fases, capturan la física del comportamiento de la constante dieléctrica en ambas fases. Esto es, valores similares a la temperatura de fusión. Con el objetivo de entender el origen de este comportamiento calculamos el factor de polarización (G), que para este tipo de modelos rígidos y no polarizables

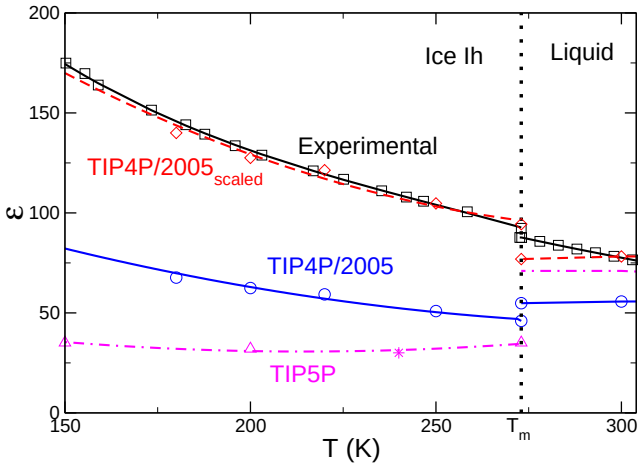

Figura 13.2: Constantes dieléctricas del hielo I_h y agua líquida para el modelo TIP4P/2005 (círculos y líneas continuas azules), TIP5P (triángulos y líneas con puntos magenta) y el modelo TIP4P/2005 reescalado con el valor del momento dipolar efectivo de la molécula de agua en cada fase comparadas con los valores experimentales (cuadrados y lineas continuas negras). El asterisco representa el valor de la constante dieléctrica calculado por Rick [294] para el modelo TIP5P.

se puede escribir como:

$$G =< \sum_{i=1}^{i=N} \sum_{j=1}^{j=N} (\mathbf{u_i}.\mathbf{u_j}) > /N = 1 + < \sum_{j=2}^{j=N} \mathbf{u_1}.\mathbf{u_j} > \tag{13.1}$$

El factor de polarización contiene información sobre la dependencia orientacional de las interacciones entre las moléculas de agua, como se puede ver en la Ec. 13.1. G es el promedio de la orientación de una molécula respecto al resto de moléculas del sistema. Los modelos estudiados presentan valores muy distintos de G (Tabla 9.1), algo desconcertante ya que todos estos modelos presentan valores muy similares del momento dipolar de la molécula de agua. La clave esta en que G no depende del momento dipolar de la molécula de agua, sino que depende mayoritariamente del ratio entre el dipolo y el cuadrupolo de la molécula, algo similar a lo que ocurre con el diagrama de fases [205, 206, 324]. Según esto, si suponemos que el modelo TIP4P/2005 describe correctamente la dependencia orientacional de las interacciones entre las moléculas de agua, es decir, el factor de polarización, entonces el desacuerdo entre el valor de las constantes dieléctricas del modelo y las experimentales para ambas fases es debido al pequeño valor del momento dipolar de la molécula de agua en este modelo (2.305 D) comparado con el que tendría la molécula de agua en fases condensadas y diferente para cada fase.

La molécula de agua presenta distintos valores del momento dipolar dependiendo de la fase en que se encuentre. Lamentablemente, el momento dipolar de una molécula de agua en fase condensada no es una magnitud accesible experimentalmente. Se han estimado los valores del momento dipolar de la molécula agua en fase líquida (2.66 D [57]) y en el hielo I_h (3.3 D [56]) mediante simulaciones *ab initio*. En los modelos empíricos el momento dipolar de la molécula está en torno a 2.3 D, no sólo es inferior al que presenta la molécula de agua en fases condensadas, sino que además es el mismo para ambas fases. Puesto que G parece no depender del valor de las cargas (el ratio μ/Q sólo depende de la distribución de cargas y

no de su valor), podemos aumentar el momento dipolar de la molécula de agua en el modelo sin estropear la descripción de las interacciones entre las moléculas (G). Reescalando los valores de las constantes dieléctricas dadas por el modelo TIP4P/2005 con los valores del momento dipolar que tendría la molécula de agua en cada fase (μ_{eff}), los resultados están cuantitativamente en concordancia con los resultados experimentales (Fig. 13.2). Lo mismo ocurre reescalando la constante dieléctrica de las distintas fases de hielo con el momento dipolar de la molécula de agua en fase sólida (Fig. 9.7). En vista de estos resultados, podemos decir que el modelo TIP4P/2005 no es capaz de reproducir el valor de la constante dieléctrica de las distintas fases de agua. No obstante captura la dependencia orientacional de las interacciones en el agua. Esto quiere decir que el modelo contiene la física de las propiedades eléctricas del agua, pero no reproduce cuantitativamente el valor de la constante dieléctrica porque el momento dipolar del modelo es el mismo para todas las fases (no es polarizable) e inferior al valor de μ_{H_2O} real del agua en fases condensadas.

La constante dieléctrica se puede calcular también mediante la respuesta de polarización de un sistema a un campo eléctrico. Dependiendo de la dirección de aplicación del campo, es posible resolver la anisotropía de la constante dieléctrica. Comprobamos que las constantes dieléctricas que se obtienen por el método de fluctuaciones y el de respuesta lineal son equivalentes (Tabla 10.1), y además resolvimos el tensor dieléctrico para los distintos hielos. El hielo I_h no presenta anisotropía de la constante dieléctrica, mientras que los hielos III, V y VI son marcadamente anisotrópicos. La anisotropía en el tensor dieléctrico es relevante en el caso de aplicación de un campo eléctrico, ya que la energía de interacción con el campo dependerá de la orientación del campo respecto al cristal. La anisotropía de la constante dieléctrica es una propiedad que todavía no ha sido medida experimentalmente, y esperamos que este trabajo anime a verificar los resultados aquí pronosticados.

Sabemos que el modelo TIP4P/2005 reproduce de forma cualitativa las propiedades eléctricas del agua. Estas predicciones pueden hacerse cuantitativas usando los valores del momento dipolar de la molécula de agua en fase condensada. Esto es posible gracias a que el factor de polarización (G), ecuación (14.1), parece depender principalmente del cociente dipolo/cuadrupolo (μ/Q). Así que si aumentamos las cargas del modelo, G no cambia pero sí aumenta el momento dipolar del modelo y podemos reproducir cualitativamente la constante dieléctrica de las distintas fases de agua. Con toda esta información y las técnicas que habíamos puesto a punto, decidimos estudiar el efecto que tiene aplicar un campo eléctrico sobre el equilibrio de fases del agua.

Los campos eléctricos modifican las propiedades de todas las fases de la materia pero en diferente extensión, y por lo tanto, modifican los límites de coexistencia de fases. En presencia de un campo eléctrico las moléculas del sistema tienden a alinear sus dipolos con la dirección del campo, y ésta interacción con el campo modifica la energía libre del sistema, en diferente extensión según la fase. En presencia de un campo eléctrico (**E**) los cambios de la energía interna del sistema ($K + V_{\text{inter}}$) se pueden escribir como:

$$\mathrm{d}U = T\,\mathrm{d}S - p\,\mathrm{d}V + \mathbf{E}\,\mathrm{d}\mathbf{M} + \mu\,\mathrm{d}N \tag{13.2}$$

donde **M** es momento dipolar total del sistema y **E** es el campo eléctrico microscópico, generalmente distinto del campo aplicado o macroscópico ($\mathbf{E}_{ext}$) debido a la polarización de superficie de la cavidad, que depende de su geometría y la anisotropía de la constante dieléctrica. En presencia de un campo eléctrico podemos definir un nuevo potencial termodinámico $G_E = G - \mathbf{E}\cdot\mathbf{M}$ (transformada de Legendre de G) que sólo depende de variables

intensivas del sistema, y se hace mínimo en el equilibrio para un sistema cerrado y a presión, temperatura y campo eléctrico constante. En presencia de un campo eléctrico dos fases de una sustancia pura estarán en equilibrio cuando sus potenciales químicos sean iguales a T, p y $\mathbf{E}_{ext}$ constantes. Así, para un sistema de moléculas rígidas en el colectivo donde N, p, T, $\mathbf{E}_{ext}$ son constantes, G_E viene dado por (después de integrar sobre los momentos):

$$G_E[E_{ext}] = -k_B T ln(Q(N, p, T, E_{ext})) =$$

$$= -k_B T ln[\frac{q^N}{N!} \int exp[-\beta(V_{\text{inter}} + pV - \mathbf{M}\mathbf{E}_{\text{ex}} + U_{\text{pol}}))] d\mathbf{r}^{\mathbf{N}} dV] \tag{13.3}$$

U_{pol} es la energía de interacción del sistema con la superficie polarizada, que bajo condiciones de contorno periódicas conductoras se anula, y **E** y $\mathbf{E}_{\text{ex}}$ se igualan. Para evaluar los cambios de G_E bajo la influencia de un campo eléctrico, diferenciamos G_E respecto a $\mathbf{E}_{\text{ex}}$:

$$G_E(E_{\text{ex}}) - G_E(0) = -\int_{E=0}^{E_{\text{ex}}} < M_{\parallel} >_{N,p,T,E_{\text{ex}}} dE_{\text{ex}} \tag{13.4}$$

Esto quiere decir que, conocidas las condiciones de coexistencia entre dos fases en ausencia del campo, y determinando la polarización en la dirección del campo eléctrico, podemos calcular la integral de la ecuación 13.4 y determinar el cambio de energía libre para cada fase. Entonces, mediante integración termodinámica en el espacio p, T localizamos el nuevo punto de coexistencia de fases. Con este nuevo punto de coexistencia entre fases en presencia de un campo, podemos calcular las líneas de coexistencia mediante integración Gibbs-Duhem.

De esta manera hemos calculado el diagrama de fases para el modelo TIP4P/2005 en presencia de un campo eléctrico (Fig. 13.3). El efecto más notable de aplicar un campo eléctrico es que el hielo II (fase ordenada de protón, $\epsilon \approx 5$), con una destacada región de estabilidad, desaparece del diagrama de fases. Sabiendo que para obtener resultados cuantitativos con el modelo TIP4P/2005 es necesario usar el momento dipolar efectivo de la molécula de agua para cada fase, recalculamos el diagrama de fases en presencia de un campo eléctrico usando $\mu_{H_2O} = 2.66\ D$ para la fase líquida y $\mu_{H_2O} = 3.32\ D$ para las fases sólidas. De esta manera, las predicciones sobre el efecto de un campo eléctrico en el equilibrio de fases del agua serán mucho más realistas (Fig. 10.2). La curva de coexistencia líquido–I_h no se ve apenas afectada cuando aplicamos un campo eléctrico (la constante dieléctrica de ambas fases es prácticamente la misma). En el hielo I_h, desde el punto de vista de la constante dieléctrica aproximadamente isotrópico, la línea de coexistencia con el líquido no se ve afectada por la dirección de aplicación del campo. En cambio, para el resto de hielos, con una marcada anisotropía en ϵ, los efectos del campo dependen de la dirección de aplicación. Cuando aplicamos el campo en la dirección perpendicular al plano ab de los distintos sólidos, los hielos III, V y VI aumentan su región de estabilidad respecto al líquido alrededor de 15 K. Sin embargo, cuando el campo eléctrico es aplicado en la dirección perpendicular al plano cristalográfico ac de los hielos (a lo largo de esta dirección la componente dieléctrica es mínima para todos lo hielos), el hielo III desaparece del diagrama de fases en beneficio del hielo I_h, cuya constante dieléctrica es casi isotrópica. En estas condiciones, los V y VI ceden terreno al líquido. También se evaluó el efecto de aplicar un campo eléctrico sobre el equilibrio líquido–vapor y la temperatura del máximo en densidad (TMD) (Fig. 10.3). El campo eléctrico no tiene un gran efecto sobre las fases fluidas. En presencia de un campo eléctrico la densidad del líquido aumenta levemente y desciende la del vapor, con lo que la temperatura crítica aumenta 5 K. En la misma extensión se reduce la TMD, debido al alineamiento preferencial de las moléculas con el campo, lo que conlleva una reducción del orden tetraédrico y aumento de la densidad.

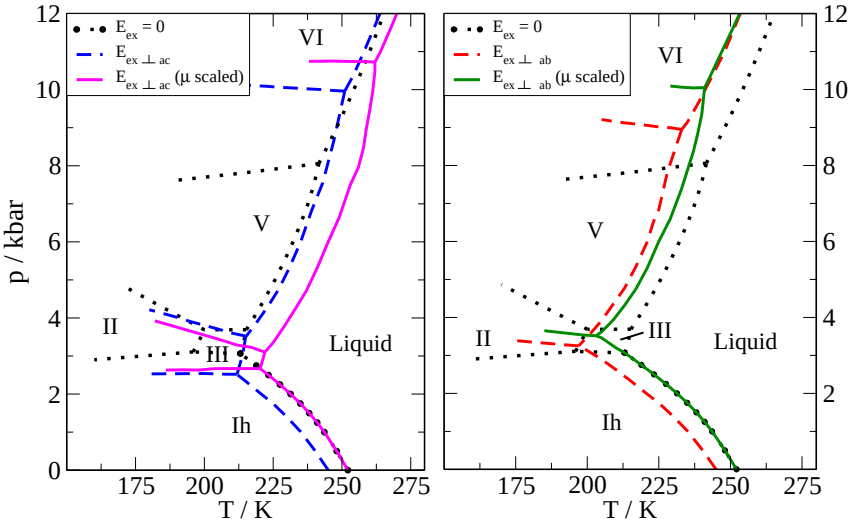

Figura 13.3: Diagrama de fases del modelo TIP4P/2005. La líneas negra de puntos, azul discontinua, magenta continua, roja discontinua y verde continua indican los límites de fase para $\mathbf{E}_{\rm ex} = 0$, $\mathbf{E}_{\rm ex\perp ac} = 0.3$ V/nm con $\mu_{\rm eff}$, $\mathbf{E}_{\rm ex\perp ac} = 0.3$ V/nm y con reescalado del momento dipolar usando 2.66 y 3.32 D para el líquido y las fases sólidas, $\mathbf{E}_{\rm ex\perp ab} = 0.3$ V/nm con $\mu_{\rm eff}$ y $\mathbf{E}_{\rm ex\perp ab} = 0.3$ V/nm y reescalado dipolar, respectivamente.

La consecuencia fundamental de la alta constante dieléctrica del agua es su capacidad para disociar sales. Así que el siguiente paso fue el estudio de las disoluciones de sales en agua, empezando por la sal más común, el cloruro sódico. La disolución más común del planeta y fundamental desde el punto de vista biológico. Para ello, es fundamental determinar la solubilidad de esta sal en agua para distintos modelos de potencial.

Usando la metodología propuesta por Sanz y Vega [137] hemos calculado la solubilidad de disoluciones de NaCl en agua SPC/E usando tres modelos de potencial para el NaCl: los modelos de Tosi–Fumi, Smith–Dang y Joung–Cheatham. En primer lugar se calculó el potencial químico del NaCl sólido con el método del cristal de Einstein (Sección 5.1.4). Para el cálculo del potencial químico del NaCl en disolución se llevó a cabo integración termodinámica hamiltoniana (Sección 5.1.2) desde la disolución hasta un sistema con interacciones tipo Lennard–Jones, sistema de referencia para el que conocemos la energía libre de Gibbs. Se calculó la energía libre de Gibbs para varias disoluciones con diferente número de moléculas de sal y el mismo número de moléculas de agua, y así obtuvimos el el potencial químico, $\mu = \left(\frac{G}{N}\right)_{T,p,N_{H_2O}}$, de la sal en disolución. Con esto pudimos calcular la solubilidad de NaCl en agua para los tres modelos de potencial de NaCl en agua SPC/E. La solubilidad es la concentración para la que se igualan los potenciales químicos del NaCl sólido y del NaCl en disolución. Para comprobar que los resultados obtenidos con esta metodología eran correctos calculamos la solubilidad del NaCl usando la técnica de coexistencia directa. Para ello pusimos en contacto un bloque NaCl sólido con una disolución supersaturada de NaCl en agua. Se llevaron a cabo simulaciones NpT de dinámica molecular hasta alcanzar el equilibrio. Los iones difunden desde la disolución supersaturada hacia el NaCl sólido hasta que se alcanza el equilibrio. En el equilibrio, la concentración de NaCl en disolución marcará la solubilidad del modelo de potencial. El equilibrado de este sistema fue extremadamente largo ya que la disolución estaba altamente supersaturada. La simulaciones tuvieron una duración de aproximadamente 3 μs.

Los valores de solubilidad de NaCl en agua obtenidos por ambas técnicas se dan en la Tabla (11.9). Los resultados que hemos obtenido mediante el cálculo de energías libres de la disolución y con la técnica de coexistencia directa están en buena concordancia, teniendo en cuenta las barras de error. Las diferencias podrían ser debidas a dos factores. El primero es que en las simulaciones de coexistencia directa no se haya alcanzado el equilibrio al final de la simulación. Al principio, cuando la disolución está supersaturada, los iones difunden fácilmente de la disolución al sólido, pero cuando la concentración va disminuyendo, el *driving force* ($\Delta\mu_i$) es menor y se requiere más tiempo para alcanzar el equilibrio. El segundo es que los cálculos de energía libre se han llevado a cabo utilizando sistemas relativamente pequeños (270 moléculas de agua) con el objetivo de poder comparar con los resultados disponibles en la literatura. De manera que podrían existir efectos de tamaño finito. No puede descartarse que al aumentar el tamaño del sistema aumentase la solubilidad. Teniendo en cuenta estos dos factores, el valor recomendado de la solubilidad de cada modelo es la media aritmética de los resultados de los dos métodos. Con en este trabajo creemos haber establecido un valor de referencia que podrá ser utilizado en un futuro en el desarrollo de nuevos métodos de simulación para determinar la solubilidad. Con lo aprendido en este trabajo sobre las sales en disolución, sería tremendamente interesante parametrizar un modelo de sal entorno al modelo de agua TIP4P/2005, el mejor modelo de agua rígido y no polarizable.

El cálculo de la solubilidad de una sal en agua requiere el cálculo del potencial químico de la sal sólida. Por tanto, el que un *force field* reproduzca la solubilidad de una sal en agua, no sólo depende de hacer predicciones razonables del potencial químico del soluto en disolución, también debe reproducir el potencial químico de la sal sólida. Puede ocurrir, como en el caso del modelo Tosi–Fumi, que predice valores del potencial químico de la sal en disolución superiores al experimental pero también para el potencial químico de la sal sólida, con lo que se obtiene un valor razonable de la solubilidad. Mientras que el modelo Smith–Dang, que predice un potencial químico del NaCl sólido muy próximo al experimental, predice valores de solubilidad extremadamente bajos. A concentraciones bajas, dominan las interacciones ion–agua, pero al aumentar la concentración las interacciones ion–ion empiezan a ser importantes. Por todas estas razones es interesante comprobar que modelos de potencial reproducen las propiedades de la sal pura (interacciones ion–ion).

Para ello evaluamos las propiedades sólido–líquido de la sal pura. Calculamos la temperatura de fusión del NaCl para los tres modelos de potencial estudiados: Tosi–Fumi, Smith–Dang y Joung–Cheatham. La temperatura de fusión del NaCl para el modelo Tosi–Fumi calculada está en buena concordancia con los valores que se encuentran en la literatura y con el valor experimental. Algo que no ocurre con los otros dos modelos tipo LJ estudiados para el NaCl.

Además del NaCl, existen más parámetros propuestos por Tosi y Fumi para otros haluros alcalinos monovalentes. Calculamos la T_f del resto de haluros alcalinos encontrando un comportamiento irregular. Las predicciones para las sales KCl y NaBr son razonables (desviaciones de 15 K y 10 K, respectivamente). En cambio, para los haluros alcalinos que contienen los iones Rb o F (KF, RbBr, RbCl, RbF, LiF y NaF), las predicciones son malas, con desviaciones del orden de 100 K. La razón para esto puede ser que el potencial de interacción Tosi–Fumi es no polarizable, y no es capaz de capturar el alto carácter polarizante/polarizable de estos iones. En el caso de los modelos tipo Lennard–Jones (SD y JC), parece que no es posible describir con exactitud el NaCl con un modelo formado por cargas y un centro de interacción LJ. Una posibilidad interesante que podría ser explorada es incluir desviaciones de las reglas de Lorentz–Berthelot para obtener las interacciones cruzadas entre los iones para ajustar la temperatura de fusión del NaCl, y luego ajustar las interacciones ion–agua para reproducir el

valor de la solubilidad.

Para terminar me gustaría contextualizar (en palabras menos amables, criticar) este trabajo. Como se comentó al principio de esta tesis, en simulación se deben hacer aproximaciones. De manera que es importante saber que se está haciendo y hasta dónde se puede llegar antes de sacar conclusiones. Esto, que se aplica a los estudios de simulación, es general a cualquier estudio científico. En este trabajo el agua se ha tratado como una molécula rígida y no polarizable. Ciertamente el agua es mucho más que unas cargas en una determinada posición geométrica. El agua es flexible, posee una nube electrónica que se polariza en presencia de otras moléculas, presenta marcados efectos cuánticos, etc. El objetivo de hacer esta severa simplificación de la molécula de agua es aprender que características de la molécula son importantes para según que propiedades. De esta manera podremos saber, y más importante conocer, cuales son las características moleculares que determinan las fascinantes propiedades del agua. Es un primer paso hacia una descripción cada vez más realista del agua, pero como todo avance científico relevante, *aprendiendo por el camino*.

Resumiendo, soy muy consciente de que estos trabajos no son “la última palabra´´ en el estudio del agua. No obstante, creo que representan un avance en el campo. Casi la totalidad de los trabajos de investigación se sostienen sobre alguna aproximación o axioma, y por tanto son susceptibles de sufrir críticas. Las criticas más útiles son las que hacen mejorar un trabajo, y ojalá este trabajo sea muy criticable, y espero que las que las críticas permitan avanzar en la descripción de esta peculiar sustancia, el agua.

CAPÍTULO 14

Conclusiones

"*Los momentos finales de una experiencia determinan el recuerdo que tenemos de ella.*"
Daniel Kahneman

Como se ha mencionado al inicio de este trabajo, el agua es una sustancia tremendamente interesante e importante, y han sido muchas las lecciones que hemos aprendido a lo largo de nuestros estudios. Aquí se recogen los estudios realizados en la región de altas presiones del diagrama de fases del agua; el cálculo de propiedades dieléctricas de agua e hielos, y su impacto en el equilibrio de fases en presencia de un campo eléctrico; el cálculo de la temperatura de fusión de haluros alcalinos monovalentes, y el estudio de la solubilidad de NaCl en agua. Además de las conclusiones propias de estos estudios, se han extraído otras conclusiones de carácter más general sobre el comportamiento de la molécula de agua en fase condensada y el modelado de agua.

El agua exhibe un gran número de propiedades que la convierten en un líquido muy especial. Pero igualmente fascinante es el increíble número de fases sólidas que se pueden formar. Por esta razón, y como ya anticipó Whalley en 1984 [33], en el modelado del agua no nos debemos olvidar de los hielos. Un buen modelo de agua, además de dar una buena descripción del agua líquida, debe ser capaz de reproducir propiedades de sus fases sólidas.

Modelos sencillos como los aquí estudiados, 1 centro LJ y 3 cargas, son capaces de capturar buena parte de la física del agua. Gracias al estudio llevado a cabo en nuestro grupo durante todos estos años, hemos llegado a un esquema general de hasta donde podemos llegar con estos modelos y como se podrían mejorar cuando se incluyan características de la molécula de agua que no han sido contempladas hasta la fecha. Esta manera de acercarse a la "respuesta final´´ es tremendamente útil, pues permite ir comprendiendo no sólo la física de la molécula de agua, sino que además, al compartimentar el problema, podemos conectar propiedades moleculares con características físicas. Este enfoque nos ha permitido determinar qué se puede esperar, dadas las características generales de un modelo. También hemos aprendido qué implicaciones tienen las aproximaciones realizadas, y cuales son los objetivos a alcanzar en futuros estudios.

Las principales conclusiones que se derivan de los trabajos presentados en esta tesis se enumeran a continuación:

1. El *test de Whalley*, propuesto para evaluar los modelos de agua utilizando las propiedades de los hielos, es una herramienta fácil y rápida que permite tener una primera estimación sencilla del diagrama de fases del agua y conocer la calidad de los resultados de simulación sobre las fases sólidas del agua. Cualquier modelo o descripción de la molécula de agua que pretenda ser realista deberia proporcionar resultados aceptables en esta prueba.

2. Para los modelos de potencial rígidos y no polarizables estudiados, aparecen dos fases de cristal plástico en la región de altas presiones del diagrama de fases a $\approx$ 440 K.

Cuando se comprime agua líquida, esta cristaliza en una fase solida en pocos nanosegundos. La estructura sólida obtenida corresponde a una red cúbica centrada en el cuerpo (bcc) de moléculas de agua que rotan significativamente entorno a sus posiciones de equilibrio, en definitiva un cristal plástico. También es posible transformar los hielos VIII y VII en este tipo de cristal plástico mediante calentamiento. Estas transiciones se pueden entender como un aumento del desorden con la temperatura: el hielo VIII, ordenado de protón, se transforma en hielo VII (desordenado de protón) al calentarse, y el hielo VII se transforma en un cristal plástico al calentarse, en el que las moléculas rotan casi libremente entorno a las posiciones de equilibrio. En las tres estructuras las posiciones cristalográficas de los oxígenos son las mismas. La aparición de una fase de cristal plástico en esta región del diagrama de fases (alta presión y alta temperatura) se entiende, porque a estas presiones la interacción LJ mantiene las moléculas en sus posiciones de red, pero la alta temperatura rompe los enlaces de hidrógeno y las moléculas son capaces de rotar entorno a su posición de equilibrio. Si se comprime el cristal plástico de simetría bcc, se transforma mediante una transición martensítica en un cristal plástico de simetría cúbica centrada en las caras (fcc). Y es esta fase de cristal plástico fcc la que domina el diagrama de fases a altas presiones.

3. Los modelos utilizados infraestiman la estabilidad del hielo VII, que es estable a presiones muy superiores a las experimentales para estos modelos. La estructura del hielo VII puede entenderse como dos redes cristalinas de hielo I_c (tipo diamante) interpenetradas, de manera que cada molécula de agua tiene 8 moléculas vecinas a la misma distancia, pero sólo forma enlace de hidrógeno con cuatro de ellas. La parte repulsiva del centro LJ ha sido ajustada para que la distancia del enlace de hidrógeno sea de 2.82 Å. El enlace de hidrógeno, descrito por una interacción coulómbica, es fuertemente direccional. De manera que las moléculas que no forman enlace de hidrógeno con la central, están energéticamente perjudicadas debido a la parte repulsiva del LJ, lo que se traduce en una inestabilización de toda la estructura. De hecho, la densidad del hielo VII que predice el modelo TIP4P/2005 se desvía notablemente del valor experimental hacia menores densidades. Las moléculas que no forman enlace de hidrógeno están “repelidas"por la parte repulsiva del potencial LJ a distancias superiores a las que se encuentran el el hielo VII. Según esto, de encontrarse experimentalmente alguna de estas fases de cristal plástico sería a presiones inferiores a las que predice el modelo TIP4P/2005, alrededor de 30000 bar.

4. Los hielos desordenados de protón presentan muchas posibles configuraciones de desorden de protón compatibles con las reglas de Bernal-Fowler. Estas configuraciones presentan pequeñas diferencias en la energía; las diferencias de energía entre las distintas configuraciones varían entre 0.1-0.2 Nk_BT para el hielo I_h, y $\approx$0.5 Nk_BT para el hielo III. Ciertas propiedades termodinámicas no varían mucho de una configuración a otra. Sin embargo cada una de estas configuraciones presenta una polarización muy distinta. Por esta razón, la constante dieléctrica de los hielos desordenados de protón es alta (fluctuaciones de la polarización del sistema). Para muestrear correctamente el desorden de protón de hielos desordenados, es necesario incluir movimientos de rotación de anillos.

5. Los modelos de potencial no polarizables no son capaces de reproducir simultánea-

mente la constante dieléctrica del agua líquida y del hielo I_h. Sin embargo, los modelos tipo TIP4P (TIP4P/2005 y TIP4P/Ice) predicen correctamente que $\epsilon_{I_h} \approx \epsilon_{lq}$ a la temperatura de fusión, aunque fallan en la predicción cuantitativa. La constante dieléctrica puede expresarse en términos del factor de polarización (G):

$$\epsilon = 1 + \frac{4\pi\rho}{3kT}\mu^2 G \tag{14.1}$$

Se ha comprobado que el valor de G sólo depende del ratio entre el momento dipolar y cuadrupolar ($G = G(\mu/Q)$). De manera que, incrementando el valor de las cargas sin modificar su distribución, se modifica la constante dieléctrica pero no el valor de G. G contiene información sobre la dependencia orientacional de las interacciones del agua. Así, cuando las predicciones de G del modelo TIP4P/2005 son reescaladas con el momento dipolar estimado para la molécula de agua en las distintas fases condensadas ($\mu^{liq}_{H_2O} = 2.66\ D$ y $\mu^{sol}_{H_2O} = 3.32\ D$) es capaz de reproducir el valor de la constante dieléctrica de la fase fluida y de los hielos I_h, III, V y VI.

6. Aplicando un campo eléctrico a un sistema es posible calcular la constante dieléctrica del sistema a partir de la respuesta de polarización de sistema. Las ϵ calculados mediante respuesta de polarización concuerdan con las obtenidas mediante fluctuaciones. La respuesta dependerá de la dirección de aplicación del campo en fases cristalinas anisotrópicas. Este es el caso del tensor dieléctrico de los hielos III, V y VI, que presenta una fuerte anisotropía. Sin embargo el hielo I_h no presenta anisotropía en el tensor dieléctrico.

7. Los campos eléctricos modifican las propiedades de todas las fases, pero en distinta medida, de manera que cambia la localización de las transiciones de fase. El diagrama de fases del agua presenta un gran número de polimorfos, y hemos estudiado como se modifican las transiciones de fase en presencia de un campo eléctrico. La lineas de coexistencia sólido-líquido no se ven muy afectadas en presencia de un campo eléctrico, ya que la constante dieléctrica del líquido y de los hielos son muy similares, de manera que la respuesta a un campo eléctrico también. Los tránsitos más afectados son los que involucran a dos fases sólidas. El hielo II (ordenado de protón) en presencia de un campo eléctrico desaparece del diagrama de fases del agua. Cuando el campo eléctrico se aplica en la dirección donde el hielo III presenta la componente dieléctrica más pequeña, esta fase también desaparece del diagrama de fases en favor de los hielos I_h y V, que presentan mayor valor de la constante dieléctrica. El efecto de un campo eléctrico sobre las fases fluidas es también pequeño. La temperatura crítica (T_c) aumenta en unos 5 K y la temperatura del máximo en densidad disminuye una magnitud muy similar.

8. Se ha determinado la temperatura de fusión del NaCl para tres potenciales de interacción ión-ión: Tosi-Fumi, Smith-Dang y Joung-Cheatham. El modelo Tosi-Fumi reproduce una temperatura de fusión próxima a la experimental, al contrario que los otros dos modelos. También se calculó la T_f de otros haluros alcalinos monovalentes parametrizados para el modelo Tosi-Fumi y se encontró un comportamiento irregular. Las predicciones para las sales KCl and NaBr son razonables (desviaciones de 15 K y 10 K, respectivamente). En cambio, para los haluros alcalinos que contienen los iones Rb o F (KF, RbBr, RbCl, RbF, LiF y NaF), las predicciones son malas, con desviaciones del

orden de 100 K.

9. Por último, hemos calculado la solubilidad de NaCl en agua SPC/E para tres modelos de interacción ión-ión: Tosi-Fumi, Smith-Dang y Joung-Cheatham, mediante integración termodinámica hamiltoniana y coexistencia directa $NaCl_{solid}$ - $NaCl_{solution}$. Se ha comprobado que el modelo Joung-Cheatham es claramente superior a los demás modelos estudiados en la predición de la solubilidad del NaCl en agua. El modelo JC es superior para simulaciones de disoluciones de NaCl en agua, mientras que el modelo TF es superior para simulaciónes de NaCl puro. Con ambos modelos, y lo aprendido en estos trabajos, tenemos un buen punto de partida para la obtención de un modelo de NaCl que reproduzca tanto la solubilidad del NaCl en agua como la temperatura de fusión.

Parte IV

APÉNDICES

APÉNDICE A

Colectivo microcanónico (N,V,E)

Un sistema aislado con energia E (colectivo N,V,E) viene determinado mecano-cuánticamente por el número de microestados del sistema, $\Omega(N,V,E)$. En un colectivo microcanónico todos los microestados son igualmente probables, de modo que si $\Omega(N,V,E)$ es el número de microestados, la probabilidad de encontrar uno de ellos en el colectivo es $p_i = \frac{1}{\Omega(N,V,E)}$. Supongamos un sistema formado por N moléculas, un volumen V y una energía E, y que esta dividido en dos subsistemas de energía E_1 y $E - E_1$. Entonces, la degeneración del primer subsitema será $\Omega(E_1)$ y la del segundo $\Omega(E - E_1)$. Por tanto, el número de formas de tener energía E_1 en cada uno de los subsistemas será:

$$\Omega(E_1, E - E_1) = \Omega(E_1)\Omega(E - E_1) \tag{A.1}$$

Como todos los microestados son igualmente probables, el valor mas probable de E_1 será aquel al que le correspondan mayor número de microestados. Para hallar este punto, derivamos en la ecuación (D.3), que al ser un producto es más cómodo trabajar con logarítmos:

$$\frac{\partial ln\Omega(E_1, E - E_1)}{\partial E_1} = \frac{\partial ln\Omega(E_1)}{\partial E_1} + \frac{ln\Omega(E - E_1)}{\partial(E - E_1)}\frac{\partial(E - E_1)}{\partial E_1} \tag{A.2}$$

$$\frac{\partial ln\Omega(E_1)}{\partial E_1} = \frac{\partial ln\Omega(E_2)}{\partial(E_2)} \tag{A.3}$$

$$\beta(N_1, V_1, E_1) = \beta(N_2, V_2, E_2) \tag{A.4}$$

La condición de equilibrio establece que si la energía E_1es inicialmente grande, la energía fluirá hasta alcanzar el equilibrio, y viceversa. Análogamente, la termodinámica nos indica que el equilibrio se alcanza al maximizar la entropía, en tal caso se obtiene que ($\frac{\partial S}{\partial E} = \frac{1}{T}$):

$$\left(\frac{\partial S}{\partial E}\right)_1 = \left(\frac{\partial S}{\partial E}\right)_2 \tag{A.5}$$

$$\frac{1}{T_1} = \frac{1}{T_2} \tag{A.6}$$

Entonces, se puede observar que la funcion $ln\Omega$ cumple las mismas propiedades que la función entropía:

1. Al extremarse da lugar al equilibrio del sistema.
2. Se corresponde a una propiedad β, igual en cada subsistema
3. β es una derivada respecto a la energía
4. Es máxima en el equilibrio para N,V,E.

Por tanto, a partir de la función de partición, $\Omega(N, V, E) = \sum p_i$, podemos establecer una relación con la termodinámica:

$$S = k_B ln\Omega \tag{A.7}$$

de donde además se deduce que, $\beta = 1/k_B T$

APÉNDICE B

Colectivo canónico (NVT)

El colectivo microcanónico, aunque es el más fundamental, es poco útil desde el punto de vista operativo. Asi que es necesario adaptar el colectivo a variables termodinámicas mas accesibles. El caso más inmediato es el de las variables de control N,V,T. Esto corresponde a un sistema que está acoplado con un termostato que permite intercambio de energía. Hay intercambio de energía con el entorno y el sistema podría adoptar cualquier valor de la energía E_i con probabilidad p_i. La distribución de energias que maximiza el desorden vendrá dada por las ligaduras:

$$L_1 = \sum p_i - 1 = 0 \tag{B.1}$$

$$L_2 = \sum E_i p_i = \bar{E} \tag{B.2}$$

Entonces tenemos que:

$$dS + \lambda dL_1 + \beta dL_2 = 0 \tag{B.3}$$

$$dS = -k_B \sum (lnp_i + 1) dp_i \tag{B.4}$$

$$dL_1 = \sum dp_i \tag{B.5}$$

$$dL_2 = \sum E_i dp_i \tag{B.6}$$

Resolvemos,

$$\sum (k_B lnp_i + k_B + \lambda + \beta E_i) dp_i = 0 \tag{B.7}$$

de aqui tras despejar p_i:

$$p_i = e^{-1} e^{-\lambda} e^{-\frac{\beta E_i}{k_B}} \tag{B.8}$$

Aplicando la ligadura 1,

$$\sum p_i - 1 = e^{-1} e^{-\lambda} \sum e^{-\frac{\beta E_i}{k_B}} = 0 \tag{B.9}$$

luego

$$e^{-1} e^{-\lambda} = \frac{1}{\sum e^{-\frac{\beta E_i}{k_B}}} \tag{B.10}$$

$$\begin{aligned} p_i &= \frac{e^{-\frac{\beta E_i}{k_B}}}{\sum e^{-\frac{\beta E_i}{k_B}}} \\ &= \frac{e^{-\frac{\beta E_i}{k_B}}}{Z} \end{aligned} \tag{B.11}$$

Para resolver la ligadura 2, escribimos la entropía en función de la p_i obtenida con la ligadura 1:

$$\begin{aligned} -\frac{S}{k_B} &= \sum p_i ln p_i = \frac{1}{Z}\sum e^{\frac{-\beta E_i}{k_B}}(-\frac{\beta E_i}{k_B} - lnZ) \\ &= -\frac{\beta \bar{E}}{k_B} - k_B lnZ \\ -S &= -\beta \bar{E} - k_B lnZ \end{aligned} \tag{B.12}$$

Comparando la ecuación (B.12) con la ecuación de la termodinámica, $A = U - TS$, podemos deducir por analogía que:

$$-S = -\beta \bar{E} - k_B lnZ \tag{B.13}$$

$$-S = \frac{U}{T} - \frac{A}{T} \tag{B.14}$$

De lo que se deduce que, $\beta = 1/k_B T$ y $A = -k_B T lnZ$. Es decir, la distribución canónica es aquella que maximiza el valor de la entropía bajo la condición de una energía promedio del sistema.

APÉNDICE C

Teorema de divergencia

La integral de la divergencia de un vector sobre un volumen V es igual a la integral de superficie de la componente normal del vector sobre la superficie que limita V:

$$\int_V div\mathbf{F}dv = \oint_S \mathbf{F}\cdot\mathbf{n}da \tag{C.1}$$

Consideremos un volumen que se subdivide en un gran número de celdas. Sea ΔV_i el volumen de la i-é sima celda que esta limitada por la superficie S_i. Entonces:

$$\sum_i \oint_{S_i} \mathbf{F}\cdot\mathbf{n}da = \oint_S \mathbf{F}\cdot\mathbf{n}da \tag{C.2}$$

donde en cada integral de la izquierda la normal se dirige hacia fuera del volumen considerado. Puesto que el sentido hacia fuera de una celda es el sentido hacia dentro de adyacente, todas las contribuciones del primer miembro de la Ec. C.3 se anulan excepto aquellas que provienen de la superficie, demostrandose la ecuación. El teorema de divergencia se obtiene haciendo que el número de celdas se aproxime infinito, de modo que el volumen de cada celda tienda a cero.

$$\sum_i \oint_{S_i} \mathbf{F}\cdot\mathbf{n}da = \lim_{\Delta V_i\to 0}\sum_i \left(\frac{1}{\Delta V_i}\oint_S \mathbf{F}\cdot\mathbf{n}\right)\Delta V_i da \tag{C.3}$$

APÉNDICE D

Transformación de la ecuación 3.5

Vamos a transformar la ecuación 3.5 en una forma diferente

$$\phi(\mathbf{r}) = \frac{1}{4\pi\epsilon_0}\int_{V_0}\frac{\mathbf{P}(\mathbf{r}')(\mathbf{r}-\mathbf{r}')}{\mid \mathbf{r}-\mathbf{r}' \mid^3}dv' \tag{D.1}$$

Como $\mid \mathbf{r}-\mathbf{r}' \mid$ viene dado por:

$$\mid \mathbf{r}-\mathbf{r}' \mid = \sqrt{(x-x')^2+(y-y')^2+(z-z')^2} \tag{D.2}$$

entonces

$$\nabla'\left(\frac{1}{\mid \mathbf{r}-\mathbf{r}' \mid}\right) = \frac{\mid \mathbf{r}-\mathbf{r}' \mid}{\mid \mathbf{r}-\mathbf{r}' \mid^3} \tag{D.3}$$

por aplicación directa del operador gradiente en coordenadas cartesianas (derivadas respecto a $\mathbf{r}'$). El integrando de la ecuación 3.5 puede transformase mediante D.3:

$$\frac{\mathbf{P}(\mathbf{r}')(\mathbf{r}-\mathbf{r}')}{\mid \mathbf{r}-\mathbf{r}' \mid^3} = \mathbf{P}\cdot\nabla'\left(\frac{1}{\mid \mathbf{r}-\mathbf{r}' \mid}\right) \tag{D.4}$$

Consideremos la siguiente identidad vectorial sobre la ecuacion D.4,

$$\nabla'\cdot(f\mathbf{F}) = f\nabla'\cdot\mathbf{F}+\mathbf{F}\cdot\nabla' f \tag{D.5}$$

donde f es cualquier función puntual escalar y $\mathbf{F}$ es una función puntual vectorial arbitraria. Si aplicamos esta identidad (Ec. D.5) sobre la ecuación D.4, suponiendo $f = \left(\frac{1}{|\mathbf{r}-\mathbf{r}'|}\right)$ y $\mathbf{F} = \mathbf{P}$ se obtiene:

$$\frac{\mathbf{P}(\mathbf{r}')(\mathbf{r}-\mathbf{r}')}{\mid \mathbf{r}-\mathbf{r}' \mid^3} = \nabla'\cdot\left(\frac{\mathbf{P}}{\mid \mathbf{r}-\mathbf{r}' \mid}\right) - \frac{1}{\mid \mathbf{r}-\mathbf{r}' \mid}\nabla'\cdot\mathbf{P} \tag{D.6}$$

Finalmente, el potencial 3.5 puede expresarse como:

$$\phi(\mathbf{r}) = \frac{1}{4\pi\epsilon_0}\int_{V_0}\frac{(-\nabla'\mathbf{P})\,dv'}{\mid \mathbf{r}-\mathbf{r}' \mid} + \frac{1}{4\pi\epsilon_0}\oint_{S_0}\frac{\mathbf{P}\cdot\mathbf{n}da'}{\mid \mathbf{r}-\mathbf{r}' \mid} \tag{D.7}$$

donde la integral de volumen $\nabla'\cdot\left(\frac{\mathbf{P}}{|\mathbf{r}-\mathbf{r}'|}\right)$ ha sido sustituida por una integral de superficie aplicando el teorema de divergencia (ver apéndice C), y $\mathbf{n}$ es la normal hacia afuera del elemento de superficie da'.

APÉNDICE E

Propiedades de la función Gaussiana

$$f(x) = \frac{1}{\sqrt{2\pi}\sigma} e^{-\frac{(x-x_0)^2}{2\sigma^2}} \tag{E.1}$$

Si $f(x)$ está centrada en 0, normalizada y a=$\frac{1}{2\sigma^2}$.

$$f(x) = \left(\frac{a}{\pi}\right)^{1/2} e^{-ax^2} \tag{E.2}$$

$$\int_0^\infty f(x)dx = \frac{1}{2} \tag{E.3}$$

Entonces y, haciendo $a = r^2$:

$$\frac{2}{\sqrt{\pi}} \int_0^\infty e^{-r^2x^2} dx = \frac{1}{r} \tag{E.4}$$

APÉNDICE F

Cambio de variable en la integral de la ec. (4.5)

$$\int_0^\infty e^{-r_{ij}^2\rho^2}d\rho \tag{F.1}$$

Dividimos esta integral en dos partes:

$$\int_0^\infty e^{-r_{ij}^2\rho^2}d\rho = \int_0^g e^{-r_{ij}^2\rho^2}d\rho + \int_g^\infty e^{-r_{ij}^2\rho^2}d\rho \tag{F.2}$$

Haciendo el cambio de variable $y = r\rho$, cuando $\rho = g$, $y = rg$:

$$\int_g^\infty e^{-r^2\rho^2}d\rho = \frac{1}{r}\int_{rg}^\infty e^{-y^2}dy \tag{F.3}$$

Multiplicando y dividiendo por $\frac{2}{\sqrt{\pi}}$:

$$\int_g^\infty e^{-r^2\rho^2}d\rho = \frac{1}{r}\int_{rg}^\infty e^{-y^2}dy(2/(\pi^{1/2}))((\pi^{1/2})/2) \tag{F.4}$$

donde podemos ver la función error complementaria (ver G):

$$\int_g^\infty e^{-r^2\rho^2}d\rho = \frac{\sqrt{\pi}}{2r}erfc(rg) \tag{F.5}$$

APÉNDICE G

Función error

$$f(x) = \frac{1}{\sqrt{2\pi}\sigma} e^{-\frac{(x-x_0)^2}{2\sigma^2}} \tag{G.1}$$

Cuando x_0 es cero y σ es 1, la función error es:

$$erf(x) = 2\int_0^x \frac{1}{\sqrt{2\pi}} e^{-\frac{x^2}{2}} dx \tag{G.2}$$

Haciendo un cambio de variable $x' = \frac{x}{\sqrt{2}}$

$$erf(x) = 2\int_0^{x'} \frac{1}{\sqrt{2\pi}} e^{-\frac{x'^2}{2}} \sqrt{2} dx' \tag{G.3}$$

Obtenemos la función error:

$$erf(x) = \frac{2}{\sqrt{\pi}} \int_0^{x'} e^{-\frac{x'^2}{2}} dx' \tag{G.4}$$

De donde se deduce la complementaria de la función error:

$$erfc(x) = \frac{2}{\sqrt{\pi}} \int_{x'}^{\infty} e^{-\frac{x'^2}{2}} dx' \tag{G.5}$$

Para la función error y su complementaria se cumple que:

$$erf(x) + erfc(x) = 1 \tag{G.6}$$

Como se puede ver en la Figura G.1 la función $erfc(x)$ decae más rápidamente con x que la función $\frac{1}{x}$. Por esta razón, la convergencia del sumatorio de E_2 (ecuación (4.6)) es más rápida que en el caso de (4.4).

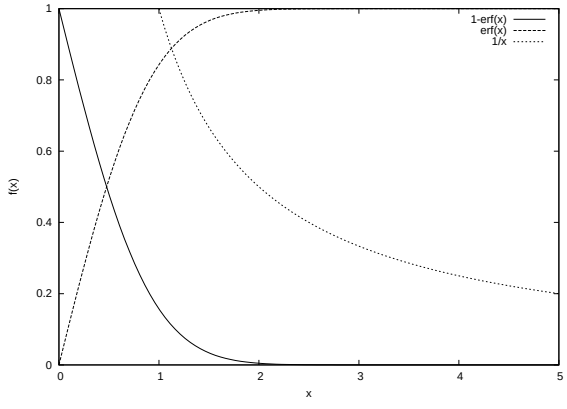

Figura G.1: Funciones erf(x), erfc(x) y 1/x.

APÉNDICE H

Vectores de espacio recíproco

Los vectores del espacio recíproco vienen dados por:

$$\overrightarrow{G} = h\overrightarrow{A} + k\overrightarrow{B} + l\overrightarrow{C} \tag{H.1}$$

donde h,k y l son enteros y $\overrightarrow{A}$, $\overrightarrow{B}$ y $\overrightarrow{C}$ son los vectores de la red recíproca y vienen dados por:

$$\overrightarrow{A} = 2\pi \frac{\overrightarrow{b} \times \overrightarrow{c}}{\overrightarrow{a} \cdot \overrightarrow{b} \times \overrightarrow{c}} \tag{H.2}$$

$$\overrightarrow{B} = 2\pi \frac{\overrightarrow{c} \times \overrightarrow{a}}{\overrightarrow{a} \cdot \overrightarrow{b} \times \overrightarrow{c}} \tag{H.3}$$

$$\overrightarrow{C} = 2\pi \frac{\overrightarrow{a} \times \overrightarrow{b}}{\overrightarrow{a} \cdot \overrightarrow{b} \times \overrightarrow{c}} \tag{H.4}$$

$\overrightarrow{a}$, $\overrightarrow{b}$ y $\overrightarrow{c}$ son los vectores de caja. No es casualidad que se denoten como hkl, ya que la reflexión de los planos hkl ocurre en la dirección del punto $\overrightarrow{G}$ de la red reciproca obtenido con los valores hkl.

APÉNDICE I

Demostración del teorema 4.7

Se define la transformada de Fourier en una dimensión como:

$$\widetilde{f}(k) = \frac{1}{\sqrt{2\pi}} \int_{-\infty}^{\infty} f(x) e^{-ikx} dx \tag{I.1}$$

Una transformada de Fourier asocia una función $f(x)$ con otra función $\widetilde{f}(k)$, que se obtiene mediante la ecuación (I.1). La utilidad de las transformadas de Fourier es que, conocida la función $\widetilde{f}(k)$, podemos averiguar cual es la función $f(x)$ de la que viene mediante:

$$f(x) = \frac{1}{\sqrt{2\pi}} \int_{-\infty}^{\infty} \widetilde{f}(k) e^{ikx} dk \tag{I.2}$$

Se puede comprobar (ver Kregszig, pag. 613) que la transformada de Fourier de una gaussiana es otra gaussiana:

$$\widetilde{f}(k) = \frac{1}{\sqrt{2\pi}} \int_{-\infty}^{\infty} e^{-ax^2} e^{ikx} dx \tag{I.3}$$

$$\widetilde{f}(k) = \frac{1}{\sqrt{2a}} e^{-\frac{k^2}{4a}} \tag{I.4}$$

Esta transformada de Fourier que hemos definido en una dimensión se puede extender a 3 dimensiones:

$$\widetilde{f}(\mathbf{k}) = \frac{1}{\sqrt{2\pi}} \int_{-\infty}^{\infty} f(\overrightarrow{\mathbf{r}}) e^{-i\mathbf{k}\cdot\overrightarrow{\mathbf{r}}} \tag{I.5}$$

donde $\overrightarrow{\mathbf{r}} = (x, y, z)$ y $\mathbf{k} = (k_x, k_y, k_z)$. Así, la transformada de Fourier de una gaussiana en tres dimensiones es:

$$\frac{2exp(-r_{ij}^2\rho^2)}{\sqrt{\pi}} = \frac{\int exp(-k^2/(4\rho^2)) exp(-i\mathbf{k}\cdot\mathbf{r_{ij}}) d\mathbf{k}}{4\pi^2\rho^3} \tag{I.6}$$

Que para el sumatorio sobre las infinitas réplicas del sistema de las condiciones de contorno periódicas es:

$$\frac{2}{\sqrt{\pi}} \sum_l exp(-\mathbf{r_{ij}}^2(l)\rho^2) = \frac{\int exp(-k^2/(4\rho^2)) \sum_l exp(-i\mathbf{k}\cdot\mathbf{r_{ij}}(\mathbf{l})) d\mathbf{k}}{4\pi^2\rho^3} \tag{I.7}$$

Por otro lado, podemos descomponer r_{ij}(l) en (Figura I.1):

$$\mathbf{r_{ij}}(\mathbf{l}) = (\mathbf{r_j}(\mathbf{0}) - \mathbf{r_i}(\mathbf{0})) + \mathbf{r}(\mathbf{l}) \tag{I.8}$$

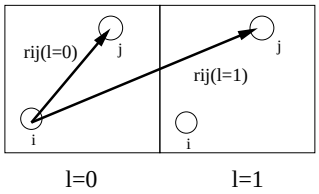

Figura I.1: Esquema del vector r_{ij} en función de las réplicas del sistema

donde r(l) es el vector de translación de la red (contiene el orden del sólido). Si sustituimos (I.8) en la ecuación (I.7):

$$\frac{2}{\sqrt{\pi}}\sum_{l} exp(-r_{ij}^2(l)\rho^2) = \frac{\int exp(-k^2/(4\rho^2))exp(i\mathbf{k}.(\mathbf{r_j}(\mathbf{0})-\mathbf{r_i}(\mathbf{0}))\sum_l exp(i\mathbf{k}.\mathbf{r}(\mathbf{l}))\mathbf{dk}}{4\pi^2\rho^3} \tag{I.9}$$

En esta ecuación (I.9), el sumatorio de la exponencial (exp($i\mathbf{k}\cdot\mathbf{r}(\mathbf{l})$)), es la ecuación de Laue sobre todas las réplicas del sistema. Este sumatorio es 0 a no ser que $\mathbf{k}\cdot\overrightarrow{\mathbf{r}}$ valga nπ, es decir, es distinto de cero cuando miramos un punto de la red recíproca. De manera que:

$$\sum_{l} exp(i\mathbf{k}.\mathbf{r}(\mathbf{l})) = \frac{(\mathbf{2}\pi)^{\mathbf{3}}}{\mathbf{V_c}}\sum_{\mathbf{G}}\delta(\mathbf{k}-\mathbf{G}) \tag{I.10}$$

Y sustituyendo (I.10) en la ecuación (I.9):

$$\frac{2}{\sqrt{\pi}}\sum_{l} exp(-r_{ij}^2(l)\rho^2) = \frac{2\pi\sum_{\mathbf{G}}\int exp(-k^2/(4\rho^2))exp(i\mathbf{k}.(\mathbf{r_j}(\mathbf{l}=\mathbf{0})-\mathbf{r_i}(\mathbf{l}=\mathbf{0}))\delta(\mathbf{k}-\mathbf{G})d\mathbf{k}}{V_c\rho^3} \tag{I.11}$$

Haciendo uso de las propiedades de la función δ de Dirac, la ecuación (I.11) se simplifica a:

$$\frac{2}{\sqrt{\pi}}\sum_{l} exp(-r_{ij}^2(l)\rho^2) = \frac{2\pi\sum_{\mathbf{G}} exp(-G^2/(4\rho^2))exp(i\mathbf{G}.(\mathbf{r_j}(\mathbf{l}=\mathbf{0})-\mathbf{r_i}(\mathbf{l}=\mathbf{0}))}{V_c\rho^3} \tag{I.12}$$

APÉNDICE J

Función de partición del cristal de Einstein con el centro de masas fijo

La contribución traslacional a la función de partición de un cristal de Einstein con el centro de masas fijo es:

$$Q_{Ein,t}^{CM} = \frac{1}{h^{3(N-1)}} \int \exp\left[-\beta \sum_{i=1}^{N} \frac{\mathbf{p}_i^2}{2m_i}\right] \delta(\sum_{i=1}^{N} \mathbf{p}_i) d\mathbf{p}_1 ... d\mathbf{p}_N$$
$$\int \exp\left[-\beta \Lambda_E \sum_{i=1}^{N} (\mathbf{r}_i - \mathbf{r}_{io})^2\right] \delta(\sum_{i=1}^{N} \mu_i (\mathbf{r}_i - \mathbf{r}_{io})) d\mathbf{r}_1 ... d\mathbf{r}_N \tag{J.1}$$

La integral sobre la parte de los momentos no es relevante para calcular energías libres y la incluiremos simplemente como un factor P^{CM}:

$$P^{CM} = \frac{1}{h^{3(N-1)}} \int \exp\left[-\beta \sum_{i=1}^{N} \frac{\mathbf{p}_i^2}{2m_i}\right] \delta(\sum_{i=1}^{N} \mathbf{p}_i) d\mathbf{p}_1 ... d\mathbf{p}_N \tag{J.2}$$

Nos centraremos en la parte configuracional:

$$Z_{Ein,t}^{CM} = \int \exp\left[-\beta \Lambda_E \sum_{i=1}^{N} (\mathbf{r}_i - \mathbf{r}_{io})^2\right] \delta(\sum_{i=1}^{N} \mu_i (\mathbf{r}_i - \mathbf{r}_{io})) d\mathbf{r}_1 ... d\mathbf{r}_N \tag{J.3}$$

Esta integral se puede expresar definiendo un cambio de variable de la forma, $\mathbf{r}_i - \mathbf{r}_{io} = \mathbf{r}_i^{'}$. El Jacobiano de esta transformación es 1, y la integral configuracional se puede reescribir como:

$$Z_{Ein,t}^{CM} = \int \exp\left[-\beta \Lambda_E \sum_{i=1}^{N} (\mathbf{r}_i^{'})^2\right] \delta(\sum_{i=1}^{N} \mu_i \mathbf{r}_i^{'}) d\mathbf{r}_1^{'} ... d\mathbf{r}_N^{'} \tag{J.4}$$

donde la función de la delta de Dirac se define:

$$\delta(\sum_{i=1}^{N} \mu_i \mathbf{r}_i^{'}) = \frac{1}{(2\pi)^3} \int_{-\infty}^{\infty} \exp\left[i\mathbf{k} \cdot \left(\sum_{i=1}^{N} \mu_i \mathbf{r}_i^{'}\right)\right] d\mathbf{k} \tag{J.5}$$

Así, la integral configuracional quedará de la forma:

$$Z_{Ein,t}^{CM} = \frac{1}{(2\pi)^3} \int \exp\left[-\beta \Lambda_E \sum_{i=1}^{N} \left((\mathbf{r}_i^{'})^2 - \frac{i\mathbf{k}}{\beta \Lambda_E} \cdot \mu_i \mathbf{r}_i^{'}\right)\right] d\mathbf{k} d\mathbf{r}_1^{'} ... d\mathbf{r}_N^{'} \tag{J.6}$$

Jugando un poco con el contenido del sumatorio de la integral se obtiene:

$$(\mathbf{r}_i^{'})^2 - \frac{i\mathbf{k}}{\beta \Lambda_E} \cdot \mu_i \mathbf{r}_i^{'} = (\mathbf{r}_i^{'})^2 - \frac{2i\mathbf{k}}{2\beta \Lambda_E} \cdot \mu_i \mathbf{r}_i^{'} + \frac{i^2 k^2 \mu_i^2}{4\beta^2 \Lambda_E^2} - \frac{i^2 k^2 \mu_i^2}{4\beta^2 \Lambda_E^2} \tag{J.7}$$
$$= \left(\mathbf{r}_i^{'} - \frac{i\mathbf{k}\mu_i}{2\beta \Lambda_E}\right)^2 + \frac{k^2 \mu_i^2}{4\beta^2 \Lambda_E^2} \tag{J.8}$$

Por lo que:

$$Z_{ein,t}^{CM} = \frac{1}{(2\pi)^3}\int \exp\left[-\beta\Lambda_E \sum_{i=1}^{N}\left(\left(\mathbf{r}_i^{'} - \frac{i\mathbf{k}\mu_i}{2\beta\Lambda_E}\right)^2 + \frac{k^2\mu_i^2}{4\beta^2\Lambda_E^2}\right)\right] d\mathbf{k}d\mathbf{r}_1^{'}...d\mathbf{r}_N^{'} \tag{J.9}$$

Ahora es conveniente realizar otro cambio de variable:

$$\mathbf{r}_i^{''} = \mathbf{r}_i^{'} - \frac{i\mathbf{k}\mu_i}{2\beta\Lambda_E} \tag{J.10}$$

Para hallar el jacobiano asociado a esta transformación supondremos el sistema más sencillo posible; un sistema con dimensionalidad uno y con dos partículas. El jacobiano, J, viene dado por el siguiente determinante:

$$J = \begin{vmatrix} \frac{\partial \mathbf{r}_1^{'}}{\partial \mathbf{r}_1^{''}} & \frac{\partial \mathbf{r}_1^{'}}{\partial \mathbf{r}_2^{''}} & \frac{\partial \mathbf{r}_1^{'}}{\partial \mathbf{k}} \\ \frac{\partial \mathbf{r}_2}{\partial \mathbf{r}_1^{''}} & \frac{\partial \mathbf{r}_2}{\partial \mathbf{r}_2^{''}} & \frac{\partial \mathbf{r}_2^{'}}{\partial \mathbf{k}} \\ \frac{\partial \mathbf{k}}{\partial \mathbf{r}_1^{''}} & \frac{\partial \mathbf{k}}{\partial \mathbf{r}_2^{''}} & \frac{\partial \mathbf{k}}{\partial \mathbf{k}} \end{vmatrix} \tag{J.11}$$

$$J = \begin{vmatrix} 1 & 0 & \frac{i\mu_i}{2\beta\Lambda_E} \\ 0 & 1 & \frac{i\mu_i}{2\beta\Lambda_E} \\ 0 & 0 & 1 \end{vmatrix} = 1 \tag{J.12}$$

El determinante de una matriz triangular es el productorio de los elementos de la diagonal. Al valer uno el jacobiano del cambio de variable, la integral queda simplificada a:

$$Z_{Ein,t}^{CM} = \frac{1}{(2\pi)^3}\int \exp\left[-\beta\Lambda_E \sum_{i=1}^{N}\left((\mathbf{r}_i^{''})^2 + \frac{k^2\mu_i^2}{4\beta^2\Lambda_E^2}\right)\right] d\mathbf{k}d\mathbf{r}_1^{''}...d\mathbf{r}_N^{''} \tag{J.13}$$

Separando en dos integrales:

$$Z_{Ein,t}^{CM} = \frac{1}{(2\pi)^3}\int \exp\left[-\beta\Lambda_E \sum_{i=1}^{N}(\mathbf{r}_i^{''})^2\right] d\mathbf{r}_1^{''}...d\mathbf{r}_N^{''}\int \exp\left[-\frac{k^2\sum_{i=1}^{N}\mu_i^2}{4\beta\Lambda_E}\right] d\mathbf{k} \tag{J.14}$$

Ambas integrales son de tipo gausiano ($\int_{-\infty}^{\infty} exp(-ax^2)dx = \sqrt{\pi/a}$), cuya solución es:

$$Z_{Ein,t}^{CM} = \frac{1}{(2\pi)^3}\left(\frac{\pi}{\beta\Lambda_E}\right)^{N3/2}\left(\frac{4\beta\pi\Lambda_E}{\sum_{i=1}^{N}\mu_i^2}\right)^{3/2} \tag{J.15}$$

Haciendo un poco más de algebra se llega a:

$$Z_{Ein,t}^{CM} = \left(\frac{\beta\Lambda_E}{\pi}\right)^{3/2}\left(\frac{\pi}{\beta\Lambda_E}\right)^{N3/2}\left(\sum_{i=1}^{N}\mu_i^2\right)^{-3/2} \tag{J.16}$$

o, sencillamente:

$$Z_{Ein,t}^{CM} = \left(\frac{\pi}{\beta\Lambda_E}\right)^{3(N-1)/2}\left(\sum_{i=1}^{N}\mu_i^2\right)^{-3/2} \tag{J.17}$$

Así, se obtiene que la función de partición de un cristal de Einstein con el centro de masas fijo viene dado por:

$$Q_{Ein,t}^{CM} = P^{CM} \left(\frac{\pi}{\beta \Lambda_E} \right)^{3(N-1)/2} \left(\sum_{i=1}^{N} \mu_i^2 \right)^{-3/2} \tag{J.18}$$

Cuando todas las moléculas presentan la misma masa reducida, μ_i se reduce a $1/N$. Por tanto, la ecuación anterior se puede simplificar como:

$$Q_{Ein,t}^{CM} = P^{CM} \left(\frac{\pi}{\beta \Lambda_E} \right)^{3(N-1)/2} (N)^{3/2} \tag{J.19}$$

que corresponde con la expresión final para la energía libre de un cristal de Einstein con el centro de masas fijo. Una expresión explícita para P^{CM} no es necesaria para el cálulo de energías libres de un sólido ya que recordando la ecuación 5.54 se cancela con otro término similar. Sin embargo, no es difícil obtener P^{CM} realizando el mismo formalismo para la ecuación J.2 que el realizado para la ecuación J.3 (con $\mu_i = 1$ y $\Lambda_E = 1/(2m_i)$ y omitiendo el prefactor $h^{3(N-1)}$). Lo que lleva a:

$$P^{CM} = \frac{1}{\Lambda^{3(N-1)}} N^{-3/2} \tag{J.20}$$

Se obtiene que el cociente entre P^{CM}/P adopta el valor de $\Lambda^3 N^{-3/2}$. Si la ecuación J.20 se reemplaza por la ecuación J.19 se obtiene:

$$Q_{Ein,t}^{CM} = \frac{1}{\Lambda^{3(N-1)}} \left(\frac{\pi}{\beta \Lambda_E} \right)^{3(N-1)/2} \tag{J.21}$$

APÉNDICE K

Contribucion ideal al potencial quimico

El potencial quimico del NaCl en disolucion viene dado por la expresion:

$$\mu_{NaCl}^{solution} = \left(\frac{\partial G_{solution}}{\partial N_{NaCl}}\right)_{T,p,N_{H_2O}} \tag{K.1}$$

donde $G_{solution}$ es la energía libre de Gibbs (ver eq. 5.68). Hemos separado la $G_{solution}$ en dos términos, el primero $G_1 = A_{solution}^{id}$ corresponde a la contribución de gas ideal a la energía Helmholtz del sistema. El segundo, G_2 contiene el resto de contribuciones a la energía libre de Gibbs, la contribución residual a la energía Helmholtz del sistema y el término p$V_{solution}$. La contribución del término G_1 al potencial químico se representara por $\mu_{NaCl,1}^{solution}$ y viene dada por:

$$\mu_{NaCl,1}^{solution} = \left(\frac{\partial A_{solution}^{id}}{\partial N_{NaCl}}\right)_{T,p,N_{H_2O}} \tag{K.2}$$

El término $A_{solution}^{id}$ viene dado por la Ec. 11.11. Haciendo la derivada de $A_{solution}^{id}$ respecto al número de moléculas de NaCl (N$_{NaCl}$) a T y p constantes, se obtiene:

$$\left(\frac{\partial (A_{solution}^{id}/k_BT)}{\partial N_{NaCl}}\right)_{T,p,N_{H_2O}} = 2\ln\left(\rho_{NaCl}\right) - 2 + V\left(2\rho'_{NaCl} + \rho'_{H_2O}\right) \tag{K.3}$$

donde ρ'_{H_2O} representa $\left(\frac{\partial \rho_{H_2O}}{\partial N_{NaCl}}\right)_{T,p,N_{H_2O}}$, siendo $\rho_i = \frac{N_i}{V}$ el número en densidad del componente i. El término ρ'_{H_2O} puede escribirse como:

$$\left(\frac{\partial \rho_{H_2O}}{\partial N_{NaCl}}\right)_{T,p,N_{H_2O}} = \frac{\partial\left(\frac{N_{H_2O}}{V}\right)_{T,p,N_{H_2O}}}{\partial N_{NaCl}} = -\frac{N_{H_2O}\left(\frac{\partial V}{\partial N_{NaCl}}\right)_{T,p,N_{H_2O}}}{V^2} = -\frac{N_{H_2O}\bar{V}}{V^2} \tag{K.4}$$

donde V representa el volumen del sistema y $\bar{V}$ el volumen molar parcial de NaCl. Igualmente, el término ρ'_{NaCl}, que corresponde a $\left(\frac{\partial \rho_{NaCl}}{\partial N_{NaCl}}\right)_{T,p,N_{H_2O}}$, se puede escribir como:

$$\left(\frac{\partial \rho_{NaCl}}{\partial N_{NaCl}}\right)_{T,p,N_{H_2O}} = \frac{1}{V} - \frac{N_{NaCl}\bar{V}}{V^2} \tag{K.5}$$

Teniendo en cuenta las expresiones para ρ'_{NaCl} y ρ'_{H_2O} el último término de la Ec. K.3 se puede escribir como:

$$\left(2\rho'_{NaCl} + \rho'_{H_2O}\right) = \frac{1}{V}\left(\frac{-2N_{NaCl}\bar{V}}{V} - \frac{N_{H_2O}\bar{V}}{V} + 2\right) \tag{K.6}$$

así que la expresión final para $\mu^{solution}_{NaCl,1}$ es:

$$\left(\frac{\partial(A^{id}/k_BT)}{\partial N_{NaCl}}\right)_{T,p,N_{H_2O}} = 2\ln\left(\rho_{NaCl}\right) - \bar{V}\left(2\rho_{NaCl} + \rho_{H_2O}\right) \tag{K.7}$$

Bibliografía

[1] C.N. Pace, B.A. Shirley, M. McNutt, and K. Gajiwala. Forces contributing to the conformational stability of proteins. *FASEB J.*, 10:75–83, 1996.

[2] C.N. Pace, S. Trevino, E. Prabhakaran, and J.M. Scholt. Protein structure, stability and solubility in water and other solvent. *Phil. Trans. R. Soc. Lond. B*, 359:1225–1235, 2004.

[3] Y. Pocker. Water in enzyme reactions: biophysical aspects of hydration-dehydration processes. *Cell Mol Life Sci.*, 57:1008, 2000.

[4] J. P. Poirier. Rheology of ices: a key to the tectonics of the ice moons of Jupiter and Saturn. *Nature*, 299:683, 1982.

[5] F. Franks. *Water a matrix of life*. Royal Society of Chemistry, Cambridge, 2000.

[6] P. Ball. *Life's Matrix. A biography of Water*. University of California Press, Berkeley, 2001.

[7] Karl Popper. *The Logic of Scientific Discovery*. 1959.

[8] J. D. Bernal and R. H. Fowler. A theory of water and ionic solutions, with particular reference to hydrogen and hydroxyl ions. *J. Chem. Phys.*, 1:515–548, 1933.

[9] N. Metropolis, A. W. Rosenbluth, M. N. Rosenbluth, A. H. Teller, and E. Teller. Equation of state calculations by fast computing machines. *J. Chem. Phys.*, 21:1087, 1953.

[10] J. A. Barker and R. O. Watts. Structure of water; a monte carlo calculation. *Chem. Phys. Lett.*, 3:144, 1969.

[11] Aneesur Rahman and Frank H. Stillinger. Molecular dynamics study of liquid water. *J. Chem. Phys.*, 55:3336, 1971.

[12] Michael D. Morse and Stuart A. Rice. Tests of effective pair potentials for water: Predicted ice structures. *J. Chem. Phys.*, 76:650, 1982.

[13] Georgios C. Boulougouris, Jeffrey R. Errington, Ioannis G. Economou, Athanassios Z. Panagiotopoulos, and Doros N. Theodorou. Molecular simulation of phase equilibria for water-n-butane and water-n-hexane mixtures. *J. Phys. Chem. B*, 104:4958, 2000.

[14] M. Lisal, W. R. Smith, and I. Nezbeda. Accurate vapour–liquid equilibrium calculations for complex systems using the reaction gibbs ensemble Monte Carlo simulation method. *Fluid Phase Equilib.*, 181:127–146, 2001.

[15] I. F. Will Kuo, C. J. Mundy, B. L. Eggimann, M. J. McGrath, J. I. Siepmann, B. Chen, J. Vieceli, and D. J. Tobias. Structure and dynamics of the aquous liquid-vapor interface: a comprehensive particle based simulation study. *J. Phys. Chem. B*, 110:3738, 2006.

[16] G. T. Gao, X. C. Zeng, and Hideki Tanaka. The melting temperature of proton-disordered hexagonal ice: A computer simulation of 4-site transferable intermolecular potential model of water. *J. Chem. Phys.*, 112:8534, 2000.

[17] Yuji Koyama, Hideki Tanaka, Guangtu Gao, and X.C.Zeng. Melting points and thermal expansivities of proton-disordered hexagonal ice with several model potentials. *J. Chem. Phys.*, 121:7926–7931, 2004.

[18] Hiroki Nada and Jan P. J. M. van der Eerden. An intermolecular potential model for the simulation of ice and water near the melting point: A six-site model of h2o. *J. Chem. Phys.*, 118:7401, 2003.

[19] Margot J. Vlot, Jan Huinink, and Jan P. van der Eerden. Free energy calculations on systems of rigid molecules: An application to the tip4p model of h2o. *J. Chem. Phys.*, 110:55, 1999.

[20] O. A. Karim and A. D. J. Haymet. The ice/water interface: A molecular dynamics simulation study. *J. Chem. Phys.*, 89:6889–6896, 1988.

[21] B. F. Nicholson, P. Clancy, and S. W. Rick. The interface response function and melting point of the prism interface of ice i-h using a fluctuating charge model (tip4p-fq). *Journal of Crystal Growth*, 293:78, 2006.

[22] E. Sanz, C. Vega, J. L. F. Abascal, and L. G. MacDowell. Phase diagram of water from computer simulation. *Phys. Rev. Lett.*, 92:255701, 2004.

[23] G. Tammann. *Kristallisieren und Schmelzen*. Johann Ambrosius Barth, Leipzig, 1903.

[24] P. W. Bridgman. The phase diagram of water to 45000 kg/cm^2. *J. Chem. Phys.*, 5:964, 1937.

[25] C. G. Salzmann, P. G. Radaelli, A. Hallbrucker, E. Mayer, and J. L. Finney. The preparation and structures of hydrogen ordered phases of ice. *Science*, 311:1758–1761, 2006.

[26] G. A. Tribello, B. Slater, and C. G. Salzmann. A blind structure prediction of ice xiv. *J. Am. Chem. Soc.*, 128:12594, 2006.

[27] C. J. Fennell and J. D. Gezelter. Computational free energy studies of a new ice polymorph which exhibits greater stability than ice i-h. *Journal of Chemical Theory and Computation*, 1:662, 2005.

[28] C.G. Salzmann, P.G. Radaelli, E. Mayer, and J.L. Finney. Ice xv: A new thermodynamically stable phase of ice. *Phys. Rev. Lett.*, 103:105701, 2009.

[29] J. L. Aragones, M. M. Conde, E. G. Noya, and C. Vega. The phase diagram of water at high pressures as obtained by computer simulation of the tip4p/2005 model: the apparence of a plastic crystal phase. *Phys. Chem. Chem. Phys.*, 11:543–555, 2009.

[30] J.L. Aragones and C. Vega. Plastic crystal phases of simple water models. *J. Chem. Phys.*, 130:244504, 2009.

[31] E. Schwegler, M. Sharma, F. Gygi, and G. Galli. Melting of ice under pressure. *Proc. Natl. Acad. Sci.*, 105:14779, 2008.

[32] M. Benoit, D. Marx, and M. Parrinello. Tunnelling and zero-point motion in high-pressure ice. *Nature*, 392:258, 1998.

[33] E. Whalley. Energies of the phases of ice at zero temperature and pressure. *J. Chem. Phys.*, 81:4087–4092, 1984.

[34] J. L. F. Abascal and C. Vega. A general purpose model for the condensed phases of water: Tip4p/2005. *J. Chem. Phys.*, 123:234505, 2005.

[35] C. Vega, J. L. F. Abascal, M. M. Conde, and J. L. Aragones. A critical comparison of the performance of different water models. *Faraday Discussions*, 141:251–276, 2009.

[36] C. vega and J.L.F. Abascal. Simulating water with rigid non-polarizable models: a general perspective. *Phys. Chem. Chem. Phys.*, 13:19663–19688, 2011.

[37] J. L. Aragones, E. G. Noya, J. L. F. Abascal, and C. Vega. Properties of ices at 0k : a test of water models. *J. Chem. Phys.*, 127:154518, 2007.

[38] G.A. Tribello, B. Slater, M.A. Zwijnenburg, and R.G.Bell. Isomorphism between ice and silica. *Phys. Chem. Chem. Phys.*, 12:8597–8606, 2010.

[39] G.A. Tribello and B. Slater. A theoretical examination of known and hypothetical clathrate hydrate materials. *Phys. Chem. Chem. Phys.*, 131:024703, 2009.

[40] G. A. Tribello and B. Slater. Proton ordering energetics in ice phases. *Chem. Phys. Lett.*, 425:246–250, 2006.

[41] M.M.Conde, C.Vega, G.A.Tribello, and B.Slater. The phase diagram of water at negative pressures: Virtual ices. *J. Chem. Phys.*, 131:034510, 2009.

[42] M.A. Gonzalez and J.L.F. Abascal. A flexible model for water based on tip4p/2005. *J. Chem. Phys.*, 135:224516, 2011.

[43] S. Habershon and D.E. Manolopoulos. Free energy calculations for a flexible water model. *Phys. Chem. Chem. Phys.*, 13:19714–19727, 2011.

[44] C. McBride, C. Vega, E. G. Noya, R. Ramirez, and L.M.Sese. Quantum contribution in the ice phases: the path to a newempirical model for water: Tip4pq/2005. *J. Chem. Phys.*, 131:024506, 2009.

[45] M.M. Conde and C. Vega. Can gas hydrate structures be described using classical simulations? *J. Chem. Phys.*, 132:114503, 2010.

[46] E.G. Noya, L.M. Sese, R. Ramirez, C. McBride, M.M. Conde, and C. Vega. Path integral monte carlo simulations for rigid rotors and their application to water. *Molec. Phys.*, 109: 149–168, 2011.

[47] E.G. Noya, C. Vega, and C. McBride. A quantum propagator for path-integral simulations of rigid molecules. *J. Chem. Phys.*, 134:054117, 2011.

[48] B. Schwager, L. Chudinovskikh, A. Gavriliuk, and R. Boehler. Melting curve of h_2o to 90 gpa measured in a laser-heated diamond cell. *Journal of Physics: Condensed Matter*, 18:S1177–S1179, 2004.

[49] F. Datchi, F. P. Loubeyre, and R. LeToullec. Extended and accurate determination of the melting curves of argon, helium, ice (h2o), and hydrogen (h2). *Phys. Rev. B*, 61:6535, 2000.

[50] J. Lin, B. Militzer, V. V. Struzhkin, E. Gregoryanz, R. Hemley, and H. Mao. High pressure-temperature raman measurements of h_2o melting to 22 gpa and 900k. *J. Chem. Phys.*, 121:8423, 2004.

[51] N. Dubrovinskaia and L. Dubrovinky. Melting curve of water studied in externally heated diamond-anvil cell. *High Pressure Research*, 23:307–311, 2003.

[52] A. Goncharov, N. Goldman, L. E. Fried, J. C. Crowhurst, I. W. Kuo, C. J. Mundy, and J. M. Zaug. Dynamic ionization of water under extreme conditions. *Phys. Rev. Lett.*, 94: 125508, 2005.

[53] R.J. Hemley, A.P. Jephcoat, H.K. Mao, C.S. Zha, L.W. Finger, and D.E. Cox. Static compression of h2o-ice to 128 gpa (1.28 mbar). *Nature*, 330:737–740, 1987.

[54] N. Marzari and D. Vanderbilt. Mlwf criterion. *Phys. Rev. B*, 56:12847, 2007.

[55] P.L. Silvestrelli and M. Parrinello. Water molecule dipole in the gas and in the liquid phase. *Phys. Rev. Lett.*, 82:3308–3311, 1999.

[56] M. Sharma, R. Resta, and R. Car. Dipolar correlations and the dielectric permitivity of water. *Phys. Rev. Lett.*, 98:247401, 2007.

[57] E.R. Batista, S.S. Xantheas, and H. Jonsson. Molecular multipole moments of water molecules in ice ih. *J. Chem. Phys.*, 112:4546, 1998.

[58] V. F. Petrenko and R. W. Whitworth. *Physics of Ice*. Oxford University Press, 1999.

[59] Isao Minagawa. Ferroelectric phase transition and anisotropy of dielectric constant in ice ih. *J. Phys. Soc. Jpn.*, 50:3669, 1981.

[60] R. M. Lynden-Bell, J. C. Rasaiah, and J. P. Noworyta. Using simulation to study solvation in water. *Pure Appl. Chem.*, 73:1721–1731, 2001.

[61] Mauro Ferrario, Giovanni Ciccotti, Eckhard Spohr, Thierry Cartailler, and Pierre Turq. Solubility of kf in water by molecular dynamics using the kirkwood integration method. *J. Chem. Phys.*, 117:4947, 2002.

[62] R. M. Lynden-Bell and W. A. Steele. A model for strongly hindered molecular reorientation in liquids. *J. Phys. Chem.*, 88:6514, 1984.

[63] F. Moucka, M. Lisal, J. Skvor, J. Jirsak, I. Nezbeda, and W.R. Smith. Molecular simulation of aqueous electrolyte solubility. 2. osmotic ensemble monte carlo methodology for free energy and solubility calculations and application to nacl. *J. Phys. Chem. B*, 115: 7849–7861, 2011.

[64] A.S. Paluch, S. Jayaraman, J.K. Shah, and E.J. Maginn. A method for computing the solubility limit of solids: Application to sodium chloride in water and alcohols. *J. Chem. Phys.*, 133:124504, 2010.

[65] I.S. Joung and T.E. Cheatham. Molecular dynamics simulations of the dynamic and energetic properties fo alkali and halide ions using water-model-specific ion parameters. *J. Phys. Chem. B*, 113:13279–13290, 2009.

[66] M.-C. Bellissent-Funel. Is there a liquid-liquid phase transition in supercooled water? *Europhys. Lett.*, 42:161, 1998.

[67] P. G. Debenedetti and H. E. Stanley. Supercooled and glassy water. *Phys.Today*, 56: 40–46, 2003.

[68] A. Scala, F. W. Starr, E. La Nave, F. Sciortino, and H. E. Stanley. Configurational entropy and diffusivity of supercooled water. *Nature*, 406:166, 2000.

[69] O. Mishima and H. E. Stanley. The relationship between liquid, supercooled and glassy water. *Nature*, 396:329, 1998.

[70] E. La Nave, A. Scala, F. W. Starr, H. E. Stanley, and F. Sciortino. Dynamics of supercooled water in configuration space. *Phys. Rev. E*, 64:36102, 2001.

[71] H. L. Pi, J. L. Aragones, C. Vega, E. G. Noya, J. L. F. Abascal, M. A. Gonzalez, and C. McBride. Anomalies in water as obtained from computer simulations of the tip4p/2005 model: density maxima, and density, isothermal compressibility and heat capacity minima. *Mol. Phys.*, 107:365, 2009.

[72] J.L.F Abascal and C. Vega. Equation of state and compressibility of supercooled water: simulations and experiment. *J. Chem. Phys.*, 134:186101, 2011.

[73] J.L.F. Abascal and C. Vega. Widom line and the liquid-liquid critical point for the tip4p/2005 water model. *J. Chem. Phys.*, 133:234502, 2010.

[74] Y. Viisanen, R. Strey, and H. Reiss. Homogeneous nucleation rates for water. *J. Chem. Phys.*, 119:4680, 1993.

[75] Joonas Merikanto, Hanna Vehkamaki, and Evgeni Zapadinsky. Monte carlo simulations of critical cluster sizes and nucleation rates of water. *J. Chem. Phys.*, 121:914, 2004.

[76] E. B. Moore and V. Molinero. Structural transformation in supercooled water controls the crystallization rate of ice. *Nature*, 479:506–508, 2011.

[77] A. Reinhardt and J.P.K. Doye. Free energy landscapes for homogeneous nucleation of ice for a monatomic water model. *J. Chem. Phys.*, 136:054501, 2012.

[78] Hideki Tanaka. Phase behaviors of supercooled water: Reconciling a critical point of amorphous ices with spinodal instability. *J. Chem. Phys.*, 105:5099, 1996.

[79] Pablo G. Debenedetti. Supercooled and glassy water. *J. Phys. Cond. Mat.*, 15:R1669, 2003.

[80] Stillinger and Frank H. A topographic view of supercooled liquids and glass formation. *Science*, 267:1935, 1995.

[81] C. Vega, M. Martin-Conde, and A. Patrykiejew. Absence of superheating for ice ih with a free surface: a new method for determining the melting point of different water models. *Molec. Phys.*, 104:3583, 2006.

[82] E. B. Moore and V. Molinero. Water modeled as an intermediate element between carbon and silicon. *J. Phys. Chem. B*, 113:4008–4016, 2009.

[83] J. L. Finney. Water ? what is so special about it ? *Phil.Trans.R.Soc.Lond.B*, 359:1145–1165, 2004.

[84] Linus Pauling. The structure and entropy of ice and of other crystals with some randomness of atomic arrangement. *J. Am. Chem. Soc.*, 57:2680, 1935.

[85] L. Pauling. The structure and entropy of ice and other crystals with some randomness of atomic arrangements. *J. Am. Chem. Soc.*, 57:2680–2684, 1935.

[86] V. Buch, P. Sandler, and J. Sadlej. Simulations of H_2O solid, liquid and clusters, with an emphasis on ferroelectric ordering transition in hexagonal ice. *J. Phys. Chem. B*, 102: 8641–8653, 1998.

[87] Colin Lobban, John L. Finney, and Werner F. Kuhs. The structure and ordering of ices iii and v. *J. Chem. Phys.*, 112:7169, 2000.

[88] L. G. MacDowell, E. Sanz, C. Vega, and L. F. Abascal. Combinatorial entropy and phase diagram of partially ordered ice phases. *J. Chem. Phys.*, 121:10145–10158, 2004.

[89] M. M. Conde. *Simulación del equilibrio de fases del agua: hielos e hidratos.* PhD thesis, Universidad Complutense de Madrid, 2011.

[90] B. Kamb. Ice ii: A proton-ordered form of ice. *Acta Cryst.*, 17:1437, 1964.

[91] Ernest R. Davidson and Keiji Morokuma. A proposed antiferroelectric structure for proton ordered ice ih. *J. Chem. Phys.*, 81:3741, 1984.

[92] C. Lobban, J. L. Finney, and W. F. Kuhs. The structure of a new phase of ice. *Nature*, 391:268, 1998.

[93] D. A. McQuarrie. *Statistical Mechanics*. Harper and Row, New York, 1976.

[94] Reitz, Milford, and Christy. *Fundamentos de la teoría electromagnética*. Addison-Wesley Iberoamericana, 1986.

[95] C. A. Stan, S. K. Y. Tang, K. J. M. Bishop, and G. M. Whitesides. Externally applied electric fields up to $1.6x10^5$ v/m do no affect the homogeneous nucleation of ice in supercooled water. *J. Phys. Chem. B*, 115:1089, 2011.

[96] J. F. Nye. *Physical properties of crystals*. Oxford University Press, Oxford, 1985.

[97] D. Frenkel and B. Smit. *Understanding Molecular Simulation*. Academic Press, London, 2002.

[98] Paul Ewald. Die berechnung optischer und electrostatischer gitterpotentiale. *Annalen der Physik*, 64:253, 1921.

[99] M. P. Allen and D. J. Tildesley. *Computer Simulation of Liquids*. Oxford University Press, 1987.

[100] U. Essmann, L. Perera, M. L. Berkowitz, T. Darden, H. Lee, and L. G. Pedersen. A smooth particle mesh ewald method. *J. Chem. Phys.*, 103, 1995.

[101] M. Parrinello and A. Rahman. Crystal structure and pair potentials: A molecular-dynamics study. *Phys. Rev. Lett.*, 45:1196, 1980.

[102] M. Parrinello and A. Rahman. Polymorphic transitions in single crystals: A new molecular dynamics method. *J. Appl. Phys.*, 52:7182–7190, 1981.

[103] P. Najafabadi and S. Yip. *Scr. Metall.*, 17:1199, 1983.

[104] S. Yashonath and C. N. R. Rao. A Monte Carlo study of crystal structure transformations. *Molec. Phys.*, 54:245–, 1985.

[105] C. McBride. *Sklogwiki*, www.sklogwiki.org, 2010.

[106] H. J. C. Berendsen, J. R. Grigera, and T. P. Straatsma. The missing term in effective pair potentials. *J. Phys. Chem.*, 91:6269, 1987.

[107] William L. Jorgensen, Jayaraman Chandrasekhar, Jeffry D. Madura, Roger W. Impey, and Michael L. Klein. Comparison of simple potential functions for simulating liquid water. *J. Chem. Phys.*, 79:926, 1983.

[108] Michael W. Mahoney and William L. Jorgensen. A five-site model for liquid water and the reproduction of the density anomaly by rigid, nonpolarizable potential functions. *J. Chem. Phys.*, 112:8910, 2000.

[109] F. H. Stillinger and A. Rahman. Improved simulation of liquid water by molecular dynamics. *J. Chem. Phys.*, 60:1545–1557, 1974.

[110] C. Vega and J. L. F. Abascal. Relation between melting temperature and temperature of maximum density for the most common models of water. *J. Chem. Phys.*, 123:144504, 2005.

[111] Hans W. Horn, William C. Swope, Jed W. Pitera, Jeffry D. Madura, Thomas J. Dick, Greg L. Hura, and Teresa Head-Gordon. Development of an improved four-site water model for biomolecular simulations: Tip4p-ew. *J. Chem. Phys.*, 120:9665, 2004.

[112] J. L. F. Abascal, E. Sanz, R. Garcia Fernandez, and C.Vega. A potential model for the study of ices and amorphous water: Tip4p/ice. *J. Chem. Phys.*, 122:234511, 2005.

[113] J. K. Johnson, J. A. Zollweg, and K. E. Gubbins. The lennard-jones equation of state revisited. *Molec. Phys.*, 78:591, 1993.

[114] J. Kolafa I. Nezbeda. The lennard-jones fluid: An accurate analytic and theoretically-based equation of state. *Fluid Phase Equilibria*, 100:1–34, 1994.

[115] Daan Frenkel and Anthony J. C. Ladd. New monte carlo method to compute the free energy of arbitrary solids. application to the fcc and hcp phases of hard spheres. *J. Chem. Phys.*, 81:3188, 1984.

[116] C. Vega, E. P. A. Paras, and P. A. Monson. Solid-fluid equilibria for hard dumbbells via monte carlo simulation. *J. Chem. Phys.*, 96:9060, 1992.

[117] Luis A. Baez and Paulette Clancy. Phase equilibria in extended simple point charge ice-water systems. *J. Chem. Phys.*, 103:9744, 1995.

[118] C. Vega and P. A. Monson. Solid-fluid equilibria for quadrupolar hard dumbbells via Monte Carlo simulation. *J. Chem. Phys.*, 102:1361, 1995.

[119] Carlos Vega, Fernando Bresme, and Jose L. F. Abascal. Fluid-solid equilibrium of a charged hard-sphere model. *Phys. Rev. E*, 54:2746, 1996.

[120] A. P. Malanoski and P. A. Monson. The high density equation of state and solid-fluid equilibrium in systems of freely jointed chains of tangent hard spheres. *J. Chem. Phys.*, 107:6899, 1997.

[121] J. M. Polson, E. Trizac, S. Pronk, and D. Frenkel. Finite-size corrections to the free energies of crystalline solids. *J. Chem. Phys.*, 112:5339, 2000.

[122] Enrique de Miguel and Carlos Vega. The global phase diagram of the gay-berne model. *J. Chem. Phys.*, 117:6313, 2002.

[123] Jamshed Anwar, Daan Frenkel, and Massimo G. Noro. Calculation of the melting point of nacl by molecular simulation. *J. Chem. Phys.*, 118:728, 2003.

[124] Felipe J. Blas, Eduardo Sanz, Carlos Vega, and Amparo Galindo. Fluid-solid equilibria of flexible and linear rigid tangent chains from wertheim's thermodynamic perturbation theory. *J. Chem. Phys.*, 119:10958, 2003.

[125] Sander Pronk. *Disorder in entropic solids*. PhD thesis, University of Amsterdam, 2003.

[126] C. G. Gray and K. E. Gubbins. *Theory of molecular fluids*. Clarendon Press, Oxford, 1984.

[127] C. Vega and P. A. Monson. Solid-fluid equilibrium for a molecular model with short ranged directional forces. *J. Chem. Phys.*, 109:9938, 1998.

[128] A. D. Bruce, A. N. Jackson, G. J. Ackland, and N. B. Wilding. Lattice-switch monte carlo method. *Phys. Rev. E*, 61:906, 2000.

[129] N. B. Wilding and A. D. Bruce. Freezing by monte carlo phase switch. *Phys. Rev. Lett.*, 85(24):5138–5141, 2000.

[130] A. D. Bruce and N. B. Wilding. Computational strategies for mapping equilibrium phase diagrams. *Adv. Chem. Phys.*, 127:1, 2003.

[131] G. C McNeil-Watson and N. B. Wilding. Freezing line of the lennard-jones fluid: A phase switch monte carlo study. *J. Chem. Phys.*, 124:064504, 2006.

[132] G. E. Lindberg and F. Wang. Efficient sampling of ice structures by electrostatic switching. *J. Phys. Chem. B*, 112:6436, 2008.

[133] C. Vega, E. Sanz, E. G. Noya, and J. L. F. Abascal. Determination of phase diagrams via computer simulation: methodology and applications to water, electrolytes and proteins. *J. Phys. Condens. Matter*, 20:153101, 2008.

[134] B. Widom. Some topics in the theory of fluids. *J. Chem. Phys.*, 39:2808, 1963.

[135] K. M. Åberg, A. P. Lyubartsev, S. P. Jacobsson, and A. Laaksonen. Determination of solvation free energies by adaptive expanded ensemble molecular dynamics. *J. Chem. Phys.*, 120:3770–3776, 2004.

[136] E.J. Smith, T. Bryk, and A.D.J. Haymet. Free energy of solvation of simple ions: Molecular-dynamics study of solvation of Cl^- and Na^+ in the ice/water interface. *J. Chem. Phys.*, 123:034706, 2005.

[137] E. Sanz and C. Vega. Solubility of kf and nacl in water by molecular simulation. *J. Chem. Phys.*, 126:014507, 2007.

[138] D. A. Kofke. Gibbs-duhem integration: A new method for direct evaluation of phase coexistence by molecular simulation. *Molec. Phys.*, 78:1331, 1993.

[139] David A. Kofke. Direct evaluation of phase coexistence by molecular simulation via integration along the saturation line. *J. Chem. Phys.*, 98:4149, 1993.

[140] A. J. C. Ladd and L. Woodcock. Triple-point coexistence properties of the lennard-jones system. *Chem. Phys. Lett.*, 51:155, 1977.

[141] A. J. C. Ladd and L. Woodcock. Interfacial and co-existence properties of the lennard-jones system at the triple point. *Molec. Phys.*, 36:611, 1978.

[142] J. Cape and L. Woodcock. Molecular dynamics calculation of phase coexistence properties: the soft-sphere melting transition. *Chem. Phys. Lett.*, 59:271, 1977.

[143] O. A. Karim and A. D. J. Haymet. The ice/water interface: A molecular dynamics simulation study. *J. Chem. Phys.*, 89:6889, 1988.

[144] R. G. Fernandez, J. L. F. Abascal, and C. Vega. The melting point of ice ih for common warer models calculated from direct coexistence of the solid-liquid interface. *J. Chem. Phys.*, 124:144506, 2006.

[145] T. Zykova-Timan, D.Ceresoli, U. Tartaglino, and E. Tosatti. Physics of solid and liquid alkali halide surfaces near the melting point. *J. Chem. Phys.*, 123:164701, 2005.

[146] M. M. Conde and C.Vega. Determining the three phase coexistence line in methane hydrates using computer simulations. *J. Chem. Phys.*, 133:064507, 2010.

[147] M. M. Conde, C. Vega, and A. Patrykiejew. The thickness of a liquid layer on the free surface of ice as obtained from computer simulation. *J. Chem. Phys.*, 129:014702, 2008.

[148] Carl McBride, Carlos Vega, and Eduardo Sanz. Non-markovian melting: a novel procedure to generate initial liquid like phases for small molecules for use in computer simulation studies. *Computer Physics Communications*, 170:137–143, 2005.

[149] A. Z. Panagiotopoulos. Direct determination of phase coexistence properties of fluids by monte carlo simulation in a new ensemble. *Molec. Phys.*, 61:813, 1987.

[150] Athanassios Z. Panagiotopoulos. Monte carlo methods for phase equilibria of fluids. *J. Phys. Cond. Mat.*, 12:R25, 2000.

[151] J. I. Siepmann and D. Frenkel. Configurational bias monte carlo: a new sampling scheme for flexible chains. *Molec. Phys.*, 75:59–70, 1992.

[152] R. K. Chan, D. W. Davidson, and E. Whalley. Effect of pressure on the dielectric properties of ice i. *J. Chem. Phys.*, 43:2376, 1965.

[153] G.P. Johari and E. Whalley. The dielectric properties of ice ih in the range 272-133 k. *J. Chem. Phys.*, 75:1333, 1981.

[154] Steven W. Rick and A. D. J. Haymet. Dielectric constant and proton order and disorder in ice ih: Monte carlo computer simulations. *J. Chem. Phys.*, 118:9291, 2003.

[155] Aneesur Rahman and Frank H. Stillinger. Proton distribution in ice and the kirkwood correlation factor. *J. Chem. Phys.*, 57:4009, 1972.

[156] L. G. MacDowell and C. Vega. Dielectric constant of ice ih and ice v: A computer simulation study. *J. Phys. Chem. B*, 114:6089–6098, 2010.

[157] B. Guillot. A reappraisal of what we have learnt during three decades of computer simulations on water. *J. Molec. Liq.*, 101:219–260, 2002.

[158] W. L. Jorgensen and J. Tirado-Rives. Potential energy functions for atomic level simulations of water and organic and biomolecular systems. *Proc. Natl. Acad. Sci.*, 102: 6665–6670, 2005.

[159] H. J. C. Berendsen, J. P. M. Postma, W. F. van Gunsteren, and J. Hermans. *Intermolecular Forces, ed. B. Pullman, page 331*. Reidel, Dordrecht, 1982.

[160] C. G. Venkatesh, S. A. Rice, and A. H. Narten. Amorphous solid water: an x-ray diffraction study. *Science*, 186:927–928, 1974.

[161] O. Mishima, L. D. Calvert, and E. Whalley. Melting ice ih at 77 k and 10 kbar: a new method of making amorphous solids. *Nature*, 310:393, 1984.

[162] O. Mishima, L.D. Calvert, and E. Whalley. An apparently first-order transition between two amorphous phases of ice induced by pressure. *Nature*, 314:76, 1985.

[163] P. H. Poole, F. Sciortino, U. Essmann, and H. E. Stanley. Phase behavior of metastable water. *Nature*, 360:324, 1992.

[164] R. Martoňák, D. Donadio, and M. Parrinello. Evolution of the structure of amorphous ice: From low-density amorphous through high-density amorphous to very high-density amorphous ice. *J. Chem. Phys.*, 122:134501, 2005.

[165] P. W. Bridgman. Water, in the liquid and five solid forms under pressure. *Proc. Natl. Acad. Sci.*, 47:441–558, 1912.

[166] D. Eisenberg and W. Kauzmann. *The Structure and Properties of Water*. Oxford University Press, 1969.

[167] M. Chaplin. Water structure and behavior. *http://www.lsbu.ac.uk/water/*, 2005.

[168] M. D. Morse and S. A. Rice. Test of effective pair potentials for water: Predicted ice structures. *J. Chem. Phys.*, 76:650–660, 1982.

[169] Roger W. Impey, Michael L. Klein, and John S. Tse. Effective pair potentials and the structure of ices viii and ix. *J. Chem. Phys.*, 81:6406, 1984.

[170] Igor Svishchev and Peter G. Kusalik. Crystallization of liquid water in a molecular dynamics simulation. *Phys. Rev. Lett.*, 73:975–978, 1994.

[171] M. Matsumoto, S. Saito, and I. Ohmine. Molecular dynamics simulation of the ice nucleation and growth process leading to water freezing. *Nature*, 416:409–413, 2002.

[172] S. C. Gay, E. J. Smith, and A. D. J. Haymet. Dynamics of melting and stability of ice 1h: Molecular-dynamics simulations of the spc/e model of water. *J. Chem. Phys.*, 116: 8876, 2002.

[173] R. B. Ayala and V. Tchijov. A molecular dynamics study of ices III and V using TIP4P and TIP5P water models. *Canadian Journal of Physics*, 81:11–16, 2003.

[174] S. W. Rick. Simulation of proton order in ice ih. *J. Chem. Phys.*, 122:094504, 2005.

[175] Andras Baranyai, Albert Bartok, and Ariel A. Chialvo. Computer simulation of the 13 crystalline phases of ice. *J. Chem. Phys.*, 123:54502, 2005.

[176] András Baranyai and Albert Bartók. Classical interaction model for the water molecule. *J. Chem. Phys.*, 126:184508, 2007.

[177] L. Vrbka and P. Jungwirth. Brine rejection from freezing salt solutions: A molecular dynamics study. *Phys. Rev. Lett.*, 95:148501, 2005.

[178] M. A. Carignano, P. B. Shepson, and I. Szleifer. Molecular dynamics simulations of ice growth from supercooled water. *Molec. Phys.*, 103:2957–2967, 2005.

[179] J. Slovak and H. Tanaka. Computer simulation study of metastable ice vii and amporphous phases obtained by its melting. *J. Chem. Phys.*, 122:204512, 2005.

[180] V. Buch, R. Martoňák, and M. Parrinello. Exploration of nve classical trajectories as a tool for molecular crystal structure prediction, with tests on ice polymorphs. *J. Chem. Phys.*, 124:204705, 2006.

[181] S. Picaud. Dynamics of tip5p and tip4p/ice potentials. *J. Chem. Phys.*, 125:174712, 2006.

[182] P. Jedlovszky, L. Partay, P. N. M. Hoang, S. Picaud, P. von Hessberg, and J. N. Crowley. Determination of the adsorption isotherm of methanol on the surface of ice. An experimental and Grand Canonical Monte Carlo simulation study. *J. Am. Chem. Soc.*, 128: 15300–15309, 2006.

[183] E. Sanz, C. Vega, J. L. F. Abascal, and L. G. MacDowell. Tracing the phase diagram of the four-site water potential (tip4p). *J. Chem. Phys.*, 121:1165, 2004.

[184] Carl McBride, Carlos Vega, Eduardo Sanz, and Jose L. F. Abascal. Formation of high density amorphous ice by decompression of ice vii and ice viii at 135 k. *J. Chem. Phys.*, 121:11907–11911, 2004.

[185] Carl McBride, Carlos Vega, Eduardo Sanz, Luis G. MacDowell, and Jose L. F. Abascal. The range of meta stability of ice-water melting for the tip4p and spc/e models. *Molec. Phys.*, 103:1, 2005.

[186] C. Vega, C. McBride, E. Sanz, and J. L. Abascal. Radial distribution functions and densities for the spc/e, tip4p and tip5p models for liquid water and ices ih,ic,ii,iii,iv,v,vi,vii,viii,ix,xi and xii. *Phys. Chem. Chem. Phys.*, 7:1450–1456, 2005.

[187] C. Vega, E. Sanz, and J. L. F. Abascal. The melting temperature of the most common models of water. *J. Chem. Phys.*, 122:114507, 2005.

[188] C. Vega, J. L. F. Abascal, E. Sanz, L. G. MacDowell, and C. McBride. Can simple models describe the phase diagram of water? *J. Phys. Cond. Mat.*, 17:S3283, 2005.

[189] G. T. Gao, X. C. Zeng, and H. Tanaka. The melting temperature of proton–disordered hexagonal ice: A computer simulation of 4–site transferable intermolecular potential model of water. *J. Chem. Phys.*, 112:8534–8538, 2000.

[190] J. Wang, S. Yoo, J. Bai, J. R. Morris, and X. C. Zeng. Melting temperature of ice ih calculated from coexisting solid-liquid phases. *J. Chem. Phys.*, 123:036101, 2005.

[191] J. P. Abriata and D. E. Laughlin. The Third Law of Thermodynamics and low temperature phase stability. *Progress In Materials Science*, 49:367–387, 2004.

[192] D. P. Landau and K. Binder. *A guide to Monte Carlo simulations in Statistical Physics*. Cambridge University Press, 2000.

[193] J. Alder, W. G. Hoover, and D. A. Young. Studies in molecular dynamics. v. high-density equation of state and entropy for hard disks and spheres. *J. Chem. Phys.*, 49:3688, 1968.

[194] W. G. Hoover and F. H. Ree. Melting transition and communal entropy for hard spheres. *J. Chem. Phys.*, 49:3609, 1968.

[195] A. D. Bruce, A. N. Jackson, G. J. Ackland, and N. B. Wilding. Lattice-switch monte carlo method. *Phys. Rev. E*, 61:906–919, 2000.

[196] S. Yashonath and C. N. R. Rao. A monte carlo study of crystal structure transformations. *Molec. Phys.*, 54:245, 1985.

[197] C. Lobban, J. L. Finney, and W. F. Kuhs. The p-t dependency of the ice ii crystal structure and the effect of helium inclusion. *J. Chem. Phys.*, 117:3928, 2002.

[198] D. A. Kofke. Semigrand canonical monte carlo simulation: Integration along coexistence lines. In David M. Ferguson, J. Ilja Siepmann, and Donald G. Truhlar, editors, *Monte Carlo Methods in Chemical Physics*, volume 105, page 405. John Wiley and Sons, 1998.

[199] C. Vega, E. P. A. Paras, and P. A. Monson. Solid–fluid equilibria for hard dumbbells via Monte Carlo simulation. *J. Chem. Phys.*, 96:9060–9072, 1992.

[200] C. Vega and P. A. Monson. Solid–fluid equilibrium for a molecular model with short ranged directional forces. *J. Chem. Phys.*, 109:9938–9949, 1998.

[201] I. Saika-Voivod, F. Sciortino, T. Grande, and P. H. Poole. Phase diagram of silica from computer simulation. *Phys. Rev. E*, 70:061507, 2004.

[202] Y. Paul Handa, D. D. Klug, and E. Whalley. Energies of the phases of ice at low temperature and pressure relative to ice ih. *Can. J. Chem.*, 66:919–924, 1988.

[203] C. G. Salzmann, I. Kohl, T. Loerting, E. Mayer, and A. Hallbrucker. The low-temperature dynamics of recovered ice xii as studied by differential scanning calorimetry: a comparison with ice v. *Phys. Chem. Chem. Phys.*, 5:3507, 2003.

[204] A. D. Fortes, I. G. Wood, J. P. Brodholt, and L. Vocadlo. Ab initio simulation of the ice ii structure. *J. Chem. Phys.*, 119:4567–4572, 2003.

[205] J. L. F. Abascal and C. Vega. The melting point of hexagonal ice ih is strongly dependent on the quadrupole of the water models. *Phys. Chem. Chem. Phys.*, 9:2775, 2007.

[206] J. L. F. Abascal and C. Vega. Dipole-quadrupole force ratios determine the ability of potential models to describe the phase diagram of water. *Phys. Rev. Lett.*, 98:237801, 2007.

[207] C. Vega, J. L. F. Abascal, and I. Nezbeda. The vapor liquid from the triple point up to the critical point for the new generation of tip4p-like models: tip4p/ew, tip4p/2005 and tip4p/ice. *J. Chem. Phys.*, 125:034503, 2006.

[208] C. Vega and E. de Miguel. Surface tension of the most populat models of water by using the test-area simulation method. *J. Chem. Phys.*, 126:154707, 2007.

[209] P. Paricaud, M. Predota, A. A. Chialvo, and P. T. Cummings. From dimer to condensed phases at extreme conditions: Accurate predictions of the properties of water by a gaussian charge polarizable model. *J. Chem. Phys.*, 122:244511, 2005.

[210] H. Tanaka. Thermodynamic stability and negative thermal expansion of hexagonal and cubic ices. *J. Chem. Phys.*, 108:4887–4893, 1998.

[211] L. Hernandez de la Peña, M. S. Gulam Razul, and P. G. Kusalik. Quantum effects in ice ih. *J. Chem. Phys.*, 123:144506, 2005.

[212] G. Tammann. nose. *Z.Phys.Chem.*, 68:205, 1910.

[213] P. W. Bridgman. The pressure-volume-temperature relations of the liquid, and the phase diagram of heavy water. *J. Chem. Phys.*, 3:597–605, 1937.

[214] E. G. Noya, C. Menduina, J. L. Aragones, and C. Vega. Eos, thermal expansion coefficient and isothermal compressibility for ices ih,ii,iii,v and vi as obtained from computer simulation. *J. Phys. Chem. C*, 111:15877, 2007.

[215] M. Martin-Conde, L. G. MacDowell, and C. Vega. Computer simulation of two new solid phases of water: Ice xiii and ice xiv. *J. Chem. Phys.*, 125:116101, 2006.

[216] L. Vrbka and P. Jungwirth. Homogeneous freezing of water starts in the subsurface. *J. Phys. Chem. B*, 110:18126, 2006.

[217] D. Quigley and P. M. Rodger. Metadynamics simulations of ice nucleation and growth. *J. Chem. Phys.*, 128:154518, 2008.

[218] A. Laio and M. Parrinello. Escaping free-energy minima. *Proc. Natl. Acad. Sci.*, 99: 12562, 2002.

[219] D. H. Dolan, J. N. Johnson, and Y. M. Gupta. Nanosecond freezing of water under multiple shock wave compression: Continuum modeling and wavw profile measurements. *J. Chem. Phys.*, 123:64702, 2005.

[220] D. H. Dolan, M. D. Knudson, C. A. Hall, and C. Deeney. A metastable limit for compressed liquid water. *Nature Physics*, 3:339, 2007.

[221] Y. Takii, K. Koga, and H. Tanaka. A plastic phase of water from computer simulation. *J. Chem. Phys.*, 128:204501, 2008.

[222] R. Hemley, A. P. Jephcoat, H. K. Mao, C. S. Zha, L. W. Finger, and D. E. Cox. Static compression of h_2o-ice to 128 gpa (1.28 mbar). *Nature*, 330:737, 1987.

[223] M. Somayazulu, J. Shu, C. Zha, A. F. Goncharov, O. Tschauner, H. Mao, and R. Hemley. In situ high-pressure x-ray diffraction study of h_2o ice vii. *J. Chem. Phys.*, 128:64510, 2008.

[224] J. Kolafa, F. Moucka, and I. Nezbeda. Handling electrostatic interactions in molecular simulations: A systematic study. *Collect. Czech. Chem. Commun.*, 73:481, 2008.

[225] P.J. Dyer, H. Docherty, and P.T. Cummings. The importance of polarizability in the modeling of solubility: Quantifying the effect of solute polarizability on the solubility of small nonpolar solutes in popular models of water. *J. Chem. Phys.*, 129:024508, 2008.

[226] A. Ghoufi, F. Goujon, V. Lachet, and P. Malfreyt. Surface tension of water and acid gases from monte carlo simulations. *J. Chem. Phys.*, 128:154716, 2008.

[227] A. Bartok and A. Baranyai. Disorder in ice polymorphs: A monte carlo simulation study. *J.of on Crystalline Solids*, 353:2698, 2007.

[228] W. F. Kuhs, J. L. Finney, C. Vettier, and D. V. Bliss. Structure and hydrogen ordering in ices vi, vii, and viii by neutron powder diffraction. *J. Chem. Phys.*, 81:3612, 1984.

[229] B. Kamb and B. L. Davis. Ice vii, the densest form of ice. *Proc. Natl. Acad. Sci.*, 52: 1433, 1964.

[230] G. P. Johari, A. Lavergne, and E. Whalley. Dielectric properties of ice vii and viii and the phase boundary between ice vi and vii. *J. Chem. Phys.*, 61:4292, 1974.

[231] David van der Spoel, Paul J. van Maaren, and Herman J. C. Berendsen. A systematic study of water models for molecular simulation: Derivation of water models optimized for use with a reaction field. *J. Chem. Phys.*, 108:10220, 1998.

[232] Martin Lísal, Jiří Kolafa, and Ivo Nezbeda. An examination of the five–site potential (tip5p) for water. *J. Chem. Phys.*, 117:8892–8897, 2002.

[233] Steven W. Rick. A reoptimization of the five-site water potential (tip5p) for use with ewald sums. *J. Chem. Phys.*, 120:6085, 2004.

[234] C. Vega and E. G. Noya. Revisiting the frenkel-ladd method to compute the free energy of solids: The einstein molecule approach . *J. Chem. Phys.*, 127:154113, 2007.

[235] D. Van der Spoel, E. Lindahl, B. Hess, G. Groenhof, A. E. Mark, and H. J. C. Berendsen. Gromacs: Fast , flexible and free. *J. Comput. Chem.*, 26:1701, 2005.

[236] S. Nosé. A molecular dynamics method for simulations in the canonical ensemble. *Molec. Phys.*, 52:255–268, 1984.

[237] W. G. Hoover. Canonical dynamics: equilibrium phase-space distributions. *Phys. Rev. A*, 31, 1985.

[238] S. Nosé and M. L. Klein. Constant pressure molecular dynamics for molecular-systems. *Molec. Phys.*, 50:1055–1076, 1983.

[239] U. Essmann, L. Perera, M. L. Berkowitz, T. Darden, H. Lee, and L. G. Pedersen. A smooth particle mesh ewald method. *J. Chem. Phys.*, 103:8577–8593, 1995.

[240] J. Q. Broughton and G. H. Gilmer. Molecular dynamics of the crystal-fluid interface. v. structure and dynamics of crystal-melt systems. *J. Chem. Phys.*, 84:5749, 1986.

[241] R. L. Davidchack and B. B. Laird. Simulation of the hard-sphere crystal-melt interface. *J. Chem. Phys.*, 108:9452, 1998.

[242] J. R. Morris and X. Song. The melting lines of model systems calculated from coexistence simulations. *J. Chem. Phys.*, 116:9352, 2002.

[243] Paras M. Agrawal, Betsy M. Rice, and Donald L. Thompson. Molecular dynamics study of the melting of nitromethane. *J. Chem. Phys.*, 119:9617, 2003.

[244] T. Bryk and A. D. J. Haymet. Ice 1h/water interface of the spc/e model: Molecular dynamics simulations of the equilibrium basal and prism interfaces. *J. Chem. Phys.*, 117:10258, 2002.

[245] J. L. F. Abascal, R. Garcia Fernandez, C. Vega, and M. A. Carignano. The melting temperature of the six site potential model of water. *J. Chem. Phys.*, 125:166101, 2006.

[246] T. J. Frankcombe and G. J. Kroes. Molecular dynamics simulations of type-sii hydrogen clathrate hydrate close to equilibrium conditions. *J.Phys.Chem.C*, 111:13044, 2007.

[247] J. Vatamanu and P. G. Kusalik. Molecular insights into the heterogeneous crystal growth of si methane hydrate. *J. Phys. Chem. B*, 110:15896, 2006.

[248] E. G. Noya, C. Vega, and E. de Miguel. Determination of the melting point of hard spheres from direct coexistence simulation methods. *J. Chem. Phys.*, 128:154507, 2008.

[249] Y. Fei, H.-K. Mao, and R. J. Hemley. Thermal expansivity, bulk modulus, and the melting curve of h2o-ice vii rto 20gpa. *J. Chem. Phys.*, 99:5369, 1993.

[250] A. D. Fortes, I. G. Wood, M. Alfredsson, L. Vočadlo, and K. S. Knight. The incompressibility and thermal expansivity of d2o ice ii determined by powder neutron diffraction. *J. Appl. Cryst.*, 38:612, 2005.

[251] G. P. Johari, A. Lavergne, and E. Whalley. Dielectric properties of ice vii and viii and the phase boundary between ice vi and vii. *J. Chem. Phys.*, 61:4292, 1974.

[252] O. Mishima and S. Endo. xxxxxxx. *J. Chem. Phys.*, 68:4417, 1978.

[253] C. Vega, E. P. A. Paras, and P. A. Monson. On the stability limit of the plastic crystal phase of hard dumbbell solids. *J. Chem. Phys.*, 97:8543–8548, 1992.

[254] E. P. A. Paras, C. Vega, and P. A. Monson. Application of the cell theory to the thermodynamic properties of hard dumbbell solids. *Molec. Phys.*, 77:803, 1992.

[255] C. Vega and P. A. Monson. Plastic crystal phases of hard dumbbells and hard spherocylinders. *J. Chem. Phys.*, 107:2696, 1997.

[256] P. Bolhuis and D. Frenkel. Tracing the phase boundaries of hard spherocylinders. *J. Chem. Phys.*, 106:666, 1997.

[257] P. A. Monson and D. A. Kofke. Solid fluid equilibrium: Insights from simple molecular models. In Ilya Prigogine and Stuart Alan Rice, editors, *Advances in Chemical Physics*, volume 115, page 113. John Wiley and Sons, 2000.

[258] P. W. Bridgman. Water in the liquid and five solid forms, under pressure. *Proc. Amer. Acad. Arts Sci.*, XLVII:441, 1912.

[259] E. Whalley, D. W. Davidson, and J. B. R. Heath. Dielectric properties of ice vii. ice viii: a new phase of ice. *J. Chem. Phys.*, 45:3976, 1966.

[260] Shuji Kawada. Dielectric dispersion and phase transition of koh doped ice. *J. Phys. Soc. Jpn.*, 50:1442, 1972.

[261] E. Whalley, J. B. R. Heath, and D. W. Davidson. Ice ix: An antiferroelectric phase related to ice iii. *J. Chem. Phys.*, 48:2362, 1968.

[262] A. F. Goncharov, V. V. Struzhkin, M. S. Somayazulu, R. J. Hemley, and H. K. Mao. Compression of ice to 210 gpa: Infrared evidence for a symmetric hydrogen-bonded phase. *Science*, 273:218, 1996.

[263] E. Wolanin, Ph. Pruzan, J. C. Chervin, B. Canny, M. Gauthier, D. Häusermann, and M. Hanfland. Equation of state of ice VII up to 106 GPa. *Phys. Rev. B*, 56:5781–5785, 1997.

[264] C. R. Bina and A. Navrotsky. Possible presence of high-pressure ice in cold subducting slabs. *Nature*, 408:844–847, 2000.

[265] Carl W. F. T. Pistorius, Eliezer Rapoport, and J. B. Clark. Phase diagrams of H_2O and D_2O at high pressures. *J. Chem. Phys.*, 48:5509–5514, 1968.

[266] M. Matsumoto, S. Saito, and I. Ohmine. Molecular dynamics simulation of the ice nucleation and growth process leading to water freezing. *Nature*, 416:409, 2002.

[267] David A. Young. *Phase diagram of the elements*. University of California press, 1991.

[268] Eva G. Noya, M. M. Conde, and Carlos Vega. Computing the free energy of molecular solids by the einstein molecule approach: Ices xiii and xiv, hard-dumbbells and a patchy model of proteins. *J. Chem. Phys.*, 129:104704, 2008.

[269] N. B. Wilding. Freezing parameters of soft spheres. *Molecular Physics*, page In press, 2009.

[270] J. D. Lee and H. W. Pakes. Revised analytic constants for atomic scattering factors. *Acta Cryst.*, A25:712, 1969.

[271] E. Wolanin, Ph. Pruzan, J. C. Chervin, B. Canny, M. Gauthier, D. Hausermann, and M. Hanfland. Equation of state of ice vii up to 106 gpa. *Phys. Rev. B*, 56:5781, 1997.

[272] L. Pusztai, O. Pizio, and S. Sokolowski. Comparison of interaction potentials of liquid water with respect to their consistency with neutron diffraction data of pure heavy water. *J. Chem. Phys.*, 129:184103, 2008.

[273] E. de Miguel, R. G. Marguta, and E. M. del Rio. System-size dependence of the free energy of crystalline solids. *Journal of Chemical Physics*, 127:154512, 2007.

[274] Jose L. F. Abascal, Eduardo Sanz, and Carlos Vega. Triple points and coexistence properties of the dense phases of water calculated using computer simulation. *Phys. Chem. Chem. Phys.*, 11:556, 2009.

[275] W. Ostwald. *Zeitschrift fur Physikalische Chemie*, 22:289, 1897.

[276] D. Frenkel and B. M. Mulder. The hard ellipsoid-of-revolution fluid i. monte carlo simulations. *Molec. Phys.*, 55:1171, 1985.

[277] E. P. A. Paras, C. Vega, and P. A. Monson. A generalized van der waals theory of solid-fluid equilibria for nonspherical molecules. *Molec. Phys.*, 79:1063, 1993.

[278] C. Vega and P. A. Monson. Solid-fluid equilibria for quadrupolar hard dumbbells via monte carlo simulation. *J. Chem. Phys.*, 102:1361, 1995.

[279] Sherwin J. Singer and Ruth Mumaugh. Monte carlo study of fluid¿plastic crystal coexistence in hard dumbbells. *J. Chem. Phys.*, 93:1278, 1990.

[280] M. Marechal and M. Dijkstra. Stability of orientationally disordered crystal structures of colloidal hard dumbbells. *Phys. Rev. E*, 77:061405, 2008.

[281] R. J. Hemley, A. P. Jephcoat, H. K. Mao, C. S. Zha, L. W. Finger, and D. E. Cox. Static compression of H_2O ice to 128 GPa (1.28 Mbar). *Nature*, 330:737, 1987.

[282] P. Loubeyre, R. LeToullec, E. Wolanin, M. Hanfland, and D. Hausermann. Modulated phases and proton centring in ice observed by x-ray diffrraction up to 170 gpa. *Nature*, 397:503, 1999.

[283] E. Sugimura, Y. Iitaka, K. Hirose, K. Kawamura, N. Sata, and Y. Ohishi. Compression of h_2o ice to 126 gpa and implications for hydrogen-bond symmetrization: Synchrotron x-ray diffraction measurements and density-functional calculations. *Phys. Rev. B*, 77: 214103, 2008.

[284] M. Benoit, M. Bernasconi, P. Focher, and M. Parrinello. New high-pressure phase of ice. *Phys. Rev. Lett.*, 76:2934, 1996.

[285] B. Schwager and R. Boehler. H_2o: another ice phase and its melting curve. *High Pressure Research*, 28:431–433, 2008.

[286] John L. Finney. The water molecule and its interactions: the interaction between theory, modelling, and experiment. *J. Molec. Liq.*, 90:303, 2001.

[287] Bertrand Guillot. A reappraisal of what we have learnt during three decades of computer simulations on water. *J. Molec. Liq.*, 101:219, 2002.

[288] M. J. Gillan. *The Path-Integral simulation of Quantum Systems*, volume 293 of *NATO ASI Series C*, chapter 6, pages 155–188. Kluwer Academic Publishers, 1990.

[289] Hans W. Horn, William C. Swope, Jed W. Pitera, Jeffry D. Madura, Thomas J. Dick, Greg L. Hura, and Teresa Head-Gordon. Development of an improved four-site water model for biomolecular simulations: TIP4P-Ew. *J. Chem. Phys.*, 120:9665, 2004.

[290] Scott Habershon, Thomas E. Markland, and David E. Manolopoulos. Competing quantum effects in the dynamics of a flexible water model. *J. Chem. Phys.*, 131:024501, 2009.

[291] M. A. Gonzalez and J. L. F. Abascal. The shear viscosity of rigid water models. *J. Chem. Phys.*, 132:096101, 2010.

[292] C. Vega, M. M. Conde, C. McBride, J. L. F. Abascal, E. G. Noya, R. Ramírez, and L. M. Sesé. Heat capacity of water: A signature of nuclear quantum effects. *J. Chem. Phys.*, 132:046101, 2010.

[293] P.H. Hochtl, S. Boresch, W. Bitomsky, and O Steinhauser. Rationalizacion of the dielectric properties of common three-site water models in terms of their force field parameters. *J. Chem. Phys.*, 109:4927, 1998.

[294] S. W. Rick. Simulations of proton order and disorder in ice ih. *J. Chem. Phys.*, 122: 094504, 2005.

[295] G.J. Wilson, R.K. Chan, D.W. Davidson, and E. Whalley. Dielectric properties of ices ii, iii, v and vi. *J. Chem. Phys.*, 43:2384, 1976.

[296] G.P. Johari and E. Whalley. The dielectric relaxation time of ice v, its partial antiferroelectric ordering and the role of bjerrum defects. *J. Chem. Phys.*, 115:3274, 2001.

[297] G.P. Johari and E. Whalley. Dielectric properties of ice vi at low temperatures. *J. Chem. Phys.*, 64:4484, 1976.

[298] W. F. Giauque and J. W. Stout. The entropy of water and the third law of thermodynamics. the heat capacity of ice from 15 to 273 k. *J. Am. Chem. Soc.*, 58:1144, 1936.

[299] J. F. Nagle. Lattice statistics of hydrogen bonded crystals. I the residual entropy of ice. *J. Math. Phys.*, 7:1484, 1966.

[300] Y.S. Badyal, M.L. Saboungi, D.L. Price, S.D. Shastri, D.R. Haeffner, and A. K. Soper. Electron distribution in water. *J. Chem. Phys.*, 112:9206, 2000.

[301] A.V. Gubskaya and P.G. Kusalik. The total molecular dipole moment for liquid water. *J. Chem. Phys.*, 117:5290, 1998.

[302] J.A. Morrone and R. Carr. Nuclear quantum effects in water. *Phys. Rev. Lett.*, 101: 017801, 2008.

[303] Frohlich. no se. *Trans. Faraday Soc.*, 44:238, 1948.

[304] M. Neumann. Dipole moment fluctuation formulas in computer simulations of polar systems. *Molec. Phys.*, 50:841, 1983.

[305] M. Neumann. The dielectric constant of water. computer simulations with mcy potential. *J. Chem. Phys.*, 82:5663, 1985.

[306] M. Neumann. Dielectric relaxation in water. computer simulations with the tip4p potential. *J. Chem. Phys.*, 85:1567, 1986.

[307] O. Steinhauser. Reaction field simulation of water. *Molec. Phys.*, 45:335, 1982.

[308] B. Garzon, S. Lago, and C. Vega. Reaction field simulations of the vapor-liquid equilibria of dipolar fluids : Does the reaction field dielectric constant affect the coexistence properties? *Chem. Phys. Lett.*, 231:366, 1994.

[309] L. G. MacDowell. *Termodinámica Estadística de Moléculas Flexibles: Teoría y Simulación*. PhD thesis, Universidad Complutense de Madrid, 2000.

[310] G.T. Barkema and J. Boer. Properties of a statical model of ice at low temperatures. *J. Chem. Phys.*, 99:2059, 1993.

[311] G.T. Barkema and M.E.J. Newman. Monte carlo simulation of ice models. *Phys. Rev. E*, 57:1155–1166, 1998.

[312] J. A. Hayward and J. R. Reimers. Unit cells for the simulation of hexagonal ice. *J. Chem. Phys.*, 106:1518–1529, 1997.

[313] W. Gobush and C. A. J. Hoeve. Calculation of the dielectric correlation factor of cubic ice. *J. Chem. Phys.*, 57:3416, 1972.

[314] J. F. Nagle. Dielectric constant of ice. *J. Chem. Phys.*, 61:883, 1974.

[315] D.J. Adams. Theory of the dielectric constant of ice. *Nature*, 293:447, 1981.

[316] D.J. Adams. Monte carlo calculations for the ice-rules model, with and without bjerrum defects. *J. Phys. C: Solid State Phys.*, 17:4063, 1984.

[317] A. Yanagawa and J. F. Nagle. Calculations of correlation functions fot two-dimensional square ice. *Chem. Phys.*, 61:883, 1973.

[318] G.P. Johari and S.J. Jones. The orientational correlation tensor in ice i, iii, iv, v and vi. *Phil. Mag. B*, 50:L1–L4, 1984.

[319] G.P. Johari. The dipolar correlation factor and permittivity of ice iv and v. *Phil. Mag. B*, 42:241–255, 1979.

[320] G.P. Johari. The dipolar correlation factor and dipole moment of a water molecule in ice iii. *Phil. Mag. B*, 39:219–228, 1978.

[321] G.P. Johari and E. Whalley. The orientational correlation parameter and the dipole moment of a water molecule in ice vi. *J. Chem. Phys.*, 72:3201, 1978.

[322] G. P. Johari, S. J. Jones, and J. Perez. The orientational correlation tensor in ice-i, ice-iii, ice-iv, ice-v and ice-vi. *Philosophical Magazine B*, 50:L1, 1984.

[323] B. A. Berg, C. Muguruma, and Y. Okamoto. Residual entropy of ordinary ice from multicanonical simulations. *Phys. Rev. B*, 75:092202, 2007.

[324] J. L. F. Abascal and C. Vega. The water force field: Importance of quadrupolar interactions. *J. Phys. Chem. C*, 111:15811, 2007.

[325] N. Bjerrum. Structure and properties of ice. *Science*, 115:385–390, 1952.

[326] K.S. Pitzer. *J. Am. Chem. Soc.*, 60:1140, 1959.

[327] R. Howe. *J. Chem.*, C1:599, 1987.

[328] E. Lindahl, B. Hess, and D. van der Spoel. Gromacs 3.0: A package for molecular simulation and trajectory analysis. *J. Molecular Modeling*, 7:306–317, 2001.

[329] S. W Rick and D.L. Freeman. Proton disorder and the dielectric constant of type ii clathrate hydrates. *J. Chem. Phys.*, 132:054509, 2010.

[330] A. Baranyai, A. Bartok, and A. A. Chialvo. On the re-engineered tip4p water models for the prediction of vapor liquid equilibrium. *J. Mol. Liq.*, 129:120–124, 2006.

[331] J.K.Gregory, D.C. Clary, K. Liu, M.G. Brown, and R.J. Saykally. The water dipole moment in water clusters. *Science*, 275:814–817, 1997.

[332] P. Ren and J.W. Ponder. Amoeba. *J. Phys. Chem. B*, 107:5933, 2003.

[333] H. Docherty, A. Galindo, C. Vega, and E. Sanz. A potential model for methane in water describing correctly the solubility of the gas and the properties of the methane hydrate. *J. Chem. Phys.*, 125:074510, 2006.

[334] G. P. Johari. The electrostatic field and the molecular dipole moment in the polymorphs of ice. *J. Chem. Phys.*, 80:4413, 1984.

[335] K.A. Maerzke and J.I. Siepmann. Effects of an applied electric field on the vapor-liquid equilibria of water, methanol, and dimethyl ether. *J. Phys. Chem. B*, 114:4261, 2010.

[336] S. J. Singer, J. L. Kuo, T. K. Hirsch, C. Knight, L. Ojamae, and M. L. Klein. no se. *Phys. Rev. Lett.*, 94:135701, 2005.

[337] S. J. Singer and C. Knight. Hydrogen bond topology and proton ordering in ice and water clusters. *Advances in Chemical Physics*, in press, 2010.

[338] C. Knight and S. J. Singer. A reexamination of the ice iii/ix hydrogen bond ordering phase transition. *J. Chem. Phys.*, 125:064506, 2006.

[339] V. Buch, H. Groenzin, I. Li, M. J. Shultz, and E. Tosatti. Proton order in the ice crystal surface. *Proc. Natl. Acad. Sci.*, 105:5969, 2008.

[340] D. Pann, Li-Min Liu, G. A. Tribello, B.Slater, A. Michaelides, and E. Wang. Surface energy and surface proton order of the ice ih basal and prism surfaces. *J. Phys. Cond. Mat.*, 22:074209, 2010.

[341] V. Buch, R. Martonak, and M. Parrinello. Exploration of nve classical trajectories as a tool for molecular crystal structure prediction, with tests on ice polymorphs. *J. Chem. Phys.*, 124:204705, 2006.

[342] O. Matsuoka, E. Clementi, and M. Yoshimine. no se. *J. Chem. Phys.*, 64:1351, 1976.

[343] R. Kumar, F. F. Wang, G. R. Jenness, and K. D. Jordan. A second generation distributed point polarizable water model. *J. Chem. Phys.*, 132:014309, 2010.

[344] G.S. Fanourgakis and S.S. Xantheas. The flexible, polarizable, thole-type interaction potential for water (ttm2-f) revisited. *J. Phys. Chem. A*, 110:4100, 2006.

[345] S. W. Rick, S. J. Stuart, and B. J. Berne. Dynamical fluctuating charge force fields: Application to liquid water. *J. Chem. Phys.*, 101:6141, 1994.

[346] I.M. Svishchev and P.G. Kusalik. Electrofreezing of liquid water: A microscopic perspective. *J. Am. Chem. Soc.*, 118:649, 1996.

[347] G.T. Gao, K.T. Oh, and X.C. Zeng. Effect of uniform electric field on homogeneous vapor nucleation and phase equilibria ii. expended simple point charge model water. *J. Chem. Phys.*, 110:2533, 1999.

[348] D. Lu, F. Gygi, and G. Galli. Dielectric properties of ice and liquid water from first-principles calculations. *Phys. Rev. Lett.*, 100:147601, 2008.

[349] T. Matsuoka, S. Fujita, S. Shigerari, and S. Mae. Precise measurement of dielectric anisotropy in ice ih at 39 ghz. *J. Appl. Phys.*, 81:2344, 1997.

[350] J.L. Aragones, L.G. MacDowell, and C. Vega. Dielectric constat of ices and water: A lesson about water interactions. *J. Phys. Chem. A*, 115:5745–5758, 2011.

[351] R. A. Alberty. Use of legendre transforms in chemical thermodynamics. *Pure Appl. Chem.*, 73:1349–1380, 2001.

[352] H.E. Alper and R.M. Levy. Dielectric properties of water. *J. Chem. Phys.*, 91:1242, 1989.

[353] C.R. Song and P.S. Wang. High electric field effects on gigahertz dielectric properties of water measured with microwave microfluidic devices. *Rev. Sci. Inst.*, 81:054702, 2010.

[354] D. Williams. No se. *Chem. Rev.*, 72:203, 1972.

[355] Gerald S. Manning. The molecular theory of polyelectrolyte solutions with applications to the electrostatic properties of polynucleotides. *Quarterly Reviews of Biophysics*, 11: 179–246, 1978.

[356] D.J. Klein, P.B. Moore, and T.A. Steitz. The contribution of metal ions to the structural stability of the large ribosomal subunit. *RNA*, 10:1366–1379, 2004.

[357] Jeffrey Vieregg, Wei Cheng, Carlos Bustamante, and Ignacio Tinoco. Measurement of the effect of monovalent cations on rna hairpin stability. *Journal of the American Chemical Society*, 129:14966–14973, 2007.

[358] Federica Sinibaldi, Barry D. Howes, Giulietta Smulevich, Chiara Ciaccio, Massimo Coletta, and Roberto Santucci. Anion concentration modulates the conformation and stability of the molten globule of cytochrome c. *Journal of Biological Inorganic Chemistry*, 8:663–670, 2003.

[359] M. A. Carignano, E. Baskaran, P. B. Shepson, and I. Szleifer. Molecular dynamics simulation of ice growth from supercooled pure water and from salt solution. *Annals of Glaciology*, 44:44A195, 2006.

[360] D. Zahn. Atomistic mechanism of NaCl nucleation from an aqueous solution. *Phys. Rev. Lett.*, 92:040801, 2004.

[361] I. Okada, Y. Namiki, H. Uchida, M. Aizawa, and K. Itatani. MD simulation of crystal growth of NaCl from its supersaturated aqueous solution. *J. Molec. Liq.*, 118:131, 2005.

[362] Hiroyuki Shinto, Takashi Sakakibara, and Ko Higashitani. Molecular dynamics simulations of water at NaCl(001) and NaCl(011) surfaces. *J. Phys. Chem. B*, 102:1974, 1998.

[363] Y. Yang, S. Meng, L. F. Xu, and E. G. Wang. Dissolution dynamics of NaCl nanocrystal in liquid water. *Phys. Rev. E*, 72:012602, 2005.

[364] Barry Wolf and Sue Hanlon. Structural transitions of deoxyribonucleic acid in aqueous electrolyte solutions. ii. role of hydration. *Biochemistry*, 14:1661–1670, 1975.

[365] Charles C. Hardin, Eric Henderson, Thomas Watson, and Joyce K. Prosser. Monovalent cation induced structural transitions in telomeric dnas: G-dna folding intermediates. *Biochemistry*, 30(18):4460–4472, 1991.

[366] D. Corradini, M. Rovere, and P. Gallo. A route to explain water anomalies from results on an aqueous solution of salt. *J. Chem. Phys.*, 132:134508, 2010.

[367] D. Corradini, P. Gallo, and M. Rovere. Molecular dynamics studies on the thermodynamics of supercooled sodium chloride aqueous solution at different concentrations. *J. Phys. Cond. Mat.*, 22:284104, 2010.

[368] D. Corradini, P. Gallo, and M. Rovere. Effect of concentration on the thermodynamics of sodium chloride aqueous solutions in the supercooled regime. *J. Chem. Phys.*, 130: 154511, 2009. doi: 10.1063/1.3119634.

[369] D. Corradini, M. Rovere, and P. Gallo. Structural properties of high and low density water in a supercooled aqueous solution of salt. *J. Phys. Chem. B*, 115:1461–1468, 2011. doi: 10.1021/jp1101237.

[370] D. Argyris, D. R. Cole, and A. Striolo. Ion-specific effects under confinement: The role of interfacial water. *ACS NANO*, 4:2035, 2010.

[371] Y. S. Lin, B. M. Auer, and J. L. Skinner. Water structure, dynamics, and vibrational spectroscopy in sodium bromide solutions. *J. Chem. Phys.*, 131:144511, 2009.

[372] M. Salanne, C. Simon, P. Turq, and P. A. Madden. Calculation of activities of ions in molten salts with potential application to the pyroprocessing of nuclear waste. *J. Phys. Chem. B*, 112:1177, 2008.

[373] Y. Laudernet, T. Cartailler, P. Turq, and M. Ferrario. A microscopic description of concentrated potassium fluoride aqueous solutions by molecular dynamics simulation. *J.Phys.Chem.B*, 107:2354, 2003.

[374] Marcelo A. Carignano, Paul B. Shepson, and Igal Szleifer. Ions at the ice/vapor interface. *Chem. Phys. Lett.*, 436:99–103, 2007. doi: 10.1016/j.cplett.2007.01.016.

[375] Lubos Vrbka and Pavel Jungwirth. Molecular dynamics simulations of freezing of water and salt solutions. *J. Molec. Liq.*, 134:64–70, 2007. doi: 10.1016/j.molliq.2006.12.011.

[376] Sigurd Bauerecker, Peter Ulbig, Victoria Buch, Lubos Vrbka, and Pavel Jungwirth. Monitoring ice nucleation in pure and salty water via high-speed imaging and computer simulations. *J.Phys.Chem.C*, 112:7631–7636, 2008. doi: 10.1021/jp711507f.

[377] J. Vincze, M. Valisko, and D. Boda. The nonmonotonic concentration dependence of the mean activity coefficient of electrolytes is a result of a balance between solvation and ion-ion correlations. *J. Chem. Phys.*, 133:154507, 2010.

[378] A. P. Hynninen and A. Z. Panagiotopoulos. Simulations of phase transitions and free energies for ionic systems. *Mol.Phys.*, 106:2039, 2008.

[379] T.P. Straatsma and H.J.C. Berendsen. Free-energy of ionic hydration: Analysis of a thermodymamic integration technique to evaluate free-energy differences by molecular-dymamics simulaciont. *J. Chem. Phys.*, 89:5876–5886, 1988.

[380] A.P. Lyubartsev, O.K. Forrisdahl, and A. Laaksonen. Solvation free energies of methane and alkali halide ion pairs: An expanded ensemble molecular dynamics simulation study. *J. Chem. Phys.*, 108:227–233, 1998.

[381] Gerhard Hummer, Lawrence R. Pratt, and Angel E. Garcia. Free energy of ionic hydration. *J. Phys. Chem.*, 100:1206–1215, 1996.

[382] E. G. Noya, M. M. Conde, and C. Vega. Computing the free energy of molecular solids by the einstein molecule approach: Ices xiii and xiv, hard-dumbbells and a patchy model of proteins. *J. Chem. Phys.*, 129:104704, 2008. doi: 10.1063/1.2971188.

[383] I.S. Joung and T.E. Cheatham. Determination of alkali and halide monovalent ion parameters for use in explicit solvated biomolecular simulation. *J. Phys. Chem. B*, 112:9020, 2008.

[384] Josehp E. Mayer. Dispersion and polarizability and the van der waals potential in the alkali halides. *J. Chem. Phys.*, 1:270–279, 1933.

[385] Maurice L. Huggins and Joseph E. Mayer. Interatomic distances in crystals of the alkali halides. *J. Chem. Phys.*, 1:643, 1933.

[386] F.G Fumi and M.P. Tosi. Ionic sizes and born repulsive parameters in the nacl-type alkali halides i. *Journal of Physics and Chemistry of Solids*, 25:31–43, 1964.

[387] D.J. Adams and I.R. McDonald. *J. Phys. C: Solid State Phys.*, 25:00045, 1964.

[388] C. Valeriani, E. Sanz, and D. Frenkel. Rate of homogeneous crystal nucleation in molten nacl. *J. Chem. Phys.*, 122:194501, 2005.

[389] J. L. Aragones, C. Valeriani, E. Sanz, and C. Vega. Melting point of alkali halides by molecular simulation. *J. Chem. Phys.*, Submitted, 2012.

[390] David E. Smith and Liem X. Dang. Computer simulations of nacl association in polarizable water. *J. Chem. Phys.*, 100:3757, 1994.

[391] L.X. Dang and D. E. Smith. Molecular dynamics simulations of aqueous ionic clusters using polarizable water. *J. Chem. Phys.*, 99:6950, 1993.

[392] Lloyd L. Lee. *Hard Spheres and Hard-Core Fluids*, chapter 8. Butterworths, 1988.

[393] Giovanni Bussi, Davide Donadio, and Michele Parrinello. Canonical sampling through velocity rescaling. *J. Chem. Phys.*, 126:014101, 2007.

[394] Berk Hess, Henk Bekker, Herman J. C. Berendsen, and Johannes G. E. M. Fraaije. Lincs: A linear constraint solver for molecular simulations. *J. Comput. Chem.*, 18:1463–1472, 1997.

[395] Jr. Chase. M. nist-janaf thermochemical tables. volume 9. Journal of Physical and Chemical Reference Data Monograph, 1998.

[396] J. Alejandre and J. P. Hansen. Ions in water: From ion clustering to crystal nucleation. *Phys.Rev.E*, 76:061505, 2007.

[397] J. Alejandre, G. A. Chapela, F. Bresme, and J. P. Hansen. The short range anion-h interaction is the driving force for crystal formation of ions in water. *J. Chem. Phys.*, 130:174505, 2009.

[398] M. M. Reif and P. H. Huenenberger. Optimized lennard-jones interaction parameter sets for the alkali and halide ions in water. *J. Chem. Phys.*, 134:144104, 2011.

[399] Ivan Gladich, Paul Shepson, Igal Szleifer, and Marcelo Carignano. Halide and sodium ion parameters for modeling aqueous solutions in tip5p-ew water. *Chem. Phys. Lett.*, 489:113–117, 2010. doi: 10.1016/j.cplett.2010.02.032.

[400] M. Fyta and R. R. Netz. Ionic force field optimization based on single-ion and ion-pair solvation properties: Going beyond standard mixing rules. *J. Chem. Phys.*, 136:124103, 2012.

[401] D.D. Wagman. The nbs tables of chemical thermodynamic properties. selected values for inorganic c1 and c2 organic substances in si units. *J. Phys. Chem. Ref. Data*, 11: supp. 2, 1982.

[402] Jamshed Anwar and Dirk Zahn. Uncovering molecular processes in crystal nucleation and growth by using molecular simulation. *Angewandte Chemie-Int. Edition*, 50:1996–2013, 2011.

[403] M. Lisal, W.R. Smith, and J. Kolafa. Molecular simulation of aqueous electrolyte solubility. 1. the expanded-ensemble osmotic molecular dynamics method for the solution phase. *J. Phys. Chem. B*, 109:12956–12965, 2005.

[404] Manuela Cavallari, Carlo Cavazzoni, and Mauro Ferrario. Structure of nacl and kcl concentrated aqueous solutions by ab initio molecular dynamics. *Molec. Phys.*, 102: 959, 2004.

[405] Erik Wernersson and Pavel Jungwirth. Effect of water polarizability on the properties of solutions of polyvalent ions: Simulations of aqueous sodium sulfate with different force fields. *J. Chem. Theory Comput.*, 6:3233–3240, 2010. doi: 10.1021/ct100465g.

[406] M. Born and D.d. Verh. *Phys. Ges.*, 21:13, 1919.

[407] L. Pauling. The sizes of ions and their influence on the properties of salt-like compounds. *Zeitschrift fur Kristallographie*, 67:377, 1928.

[408] L. Pauling. The influence of relative ionic sizes on the properties of ionic compounds. *J. Am. Chem. Soc.*, 50:1036, 1928.

[409] J.W.E. Lewis, K. Singer, and L.V. Woodcock. Thermodynamic and structural properties of liquid ionic salts obtained by monte carlo simulations. *J. Chem. Soc. Faraday Trans.*, 71:301, 1975.

[410] D.J. Adams and I.R. McDonald. *J. Phys. C: Solid State Phys.*, 7:2761, 1974.

[411] K. Chen, X. Zhu, and J.J. Wang. Molecular dynamics studies of phase transitions of kbr cluster. *Chinese journal of Inorganic Chemistry*, 20:1050, 2004.

[412] X. Zhu. Molecular dynamics studies of homegeneus nucleation in supercooled cluster of sodium bromide. *J. Molec. Structure-Theochem.*, 680:137, 2004.

[413] T. Zykova-Timan, U. Tartaglino, D. Ceresoli, W. Sekkal-Zaoui, and E. Tosatti. Nacl nanodroplet on nacl(100) at the melting point. *Surf. Sci.*, Volumes 566-568, Part 2:794–798, 2004.

[414] T.Zykova-Timan, C.Valeriani, E.Sanz, D.Frenkel, and E.Tosatti. Irreducible finite-size effects in the surface free energy of nacl crystals from crystal-nucleation data. *Phys. Rev. Lett.*, 100:036103, 2008.

[415] D. M. Eike, J. F. Brennecke, and E. J. Maginn. *J. Chem. Phys.*, 122:014115, 2005.

[416] E.A. Mastny and J.J. de Pablo. Direct calculation of solid-liquid equilibria from density-of-states monte carlo simulations. *J. Chem. Phys.*, 122:124109, 2005.

[417] R. Boehler, M. Ross, and D.B. Boercker. Melting of lif and nacl to 1 mbar: Systematics of ionic solids at extreme conditions. *Phys. Rev. Lett.*, 78:4589, 1997.

[418] R. Boehler, M. Ross, and D.B. Boercker. High-pressure melting curves of alkali halides. *Phys. Rev. B*, 53:556, 1996.

[419] A.B. Belonoshko, R. Ahuja, and B. Johansson. Molecular dynamics of lif melting. *Phys. Rev. B*, 61:11928, 2000.

[420] A.B. Belonoshko and L.S. Dubrovinsky. Molecular dynamics of nacl (b1 and b2) and mgo (b1) melting: Two-phase simulation. *Am. Mineral.*, 81:303, 1996.

[421] J. L. Aragones, E. Sanz, and C. Vega. Solubility of nacl in water by molecular simulation revisited. *J. Chem. Phys.*, Accepted, 2012.

[422] H. A. Lorentz. Ueber die anwendung des satzes vom virial in der kinetischen theorie der gase. *Annalen der Physik*, 12 pp:127–136, 1881.

[423] D. Berthelot. Sur le melange des gaz. *Comptes rendus hebdomadaires des seances de l Academie des Sciences*, 126:1703–1855, 1898.

[424] A. J. C. Ladd and L. V. Woodcock. Triple-point coexistence properties of the lennard-jones system. *Chem. Phys. Lett.*, 51:155, 1977.

[425] A. J. C. Ladd and L. V. Woodcock. Interfacial and coexistence properties of lennard-jones system at triple point. *Molec. Phys.*, 36:611–619, 1978.

[426] S. Yoo, X. C. Zeng, and J. R. Morris. The melting lines of model silicon calculated from solid-liquid coexisting phases. *J. Chem. Phys.*, 120:1654, 2004.

[427] D. A. Kofke. Solid-fluid coexistence for inverse-power potentials. *Phys. Rev. Lett.*, 74: 122–125, 1995.

[428] R. Agrawal and D. A. Kofke. Thermodynamic and structural properties of model systems at solid-fluid coexistence. i. fcc and bcc soft spheres. *Molec. Phys.*, 85:23–42, 1995.

[429] Shuichi Nose. A molecular dynamics method for simulations in the canonical ensemble. *Molec. Phys.*, 52:255, 1984.

[430] W. G. Hoover. Canonical dynamics: Equilibrium phase-space distributions. *Phys. Rev. A*, 31:1695, 1985.

[431] J. Akella, S.N. Vaidya, and G.C. Kennedy. Melting of sodium chloride at pressures to 65 kbar. *Phys. Rev.*, 185:1135, 1969.

[432] J. Kolafa and I. Nezbeda. Fortran code for the kolafa and nezbeda equation of state. *Sklogwiki*, www.sklogwiki.org, 2010.

[433] J. K. Johnson, E. A. Muller, and K. E. Gubbins. Equation of state for lennard-jones chains. *J. Phys. Chem.*, 98:6413, 1994.

[434] A.R. Ubbelohde. In *The molten state of matter melting and crystal structure*. John Wiley and Sons, 1978.

[435] N.H. March and M.P. Tosi. In *Coulomb liquids*. Academic Press, 1984.

[436] B. Wunderlich. In *Thermal analysis of polymeric materials*. Springer, 2005.

[437] Q. An, L. Zheng, R. Fu, S. Ni, and S.Luo. Solid-liquid transitions of sodium chloride at high pressures. *J. Chem. Phys.*, 125:154510, 2006.

[438] G.J. Janz. In *Molten Salts Handbook*. Academic Press, 1967.

[439] C. McBride, E.G. Noya, J.L. Aragones, M.M. Conde, and C. Vega. The phase diagram of water from quantum simulations. *Phys. Chem. Chem. Phys.*, Accepted, 2012.